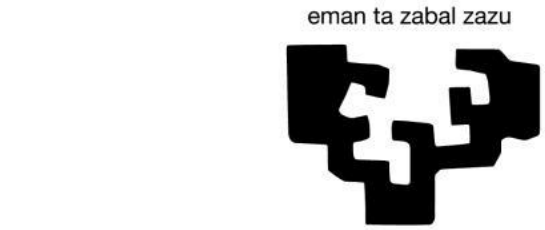

CRYSTALLIZATION AND MORPHOLOGY OF MULTIPHASIC POLYMERIC SYSTEMS: RANDOM COPOLYMERS, NANOCOMPOSITES AND POLYMERS WITH COMPLEX CHAIN TOPOLOGIES.

RICARDO ARPAD PÉREZ CAMARGO

PhD. THESIS

Polymer Science and Technology Department,
Faculty of Chemistry.

Donostia/San Sebastián, 2018

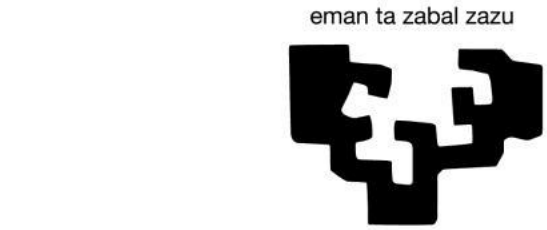

CRYSTALLIZATION AND MORPHOLOGY OF MULTIPHASIC POLYMERIC SYSTEMS: RANDOM COPOLYMERS, NANOCOMPOSITES AND POLYMERS WITH COMPLEX CHAIN TOPOLOGIES.

by

RICARDO ARPAD PÉREZ CAMARGO

Advisor

PROF. ALEJANDRO JESÚS MÜLLER SÁNCHEZ.

Polymer Science and Technology Department,

Faculty of Chemistry.

Donostia/San Sebastián, 2018

ABSTRACT

Thermal, structural, and morphological characterization were performed in several multiphasic polymeric systems. The characterization techniques were differential scanning calorimetry (DSC), X-rays of wide and small angle (WAXS and SAXS, respectively), atomic force and polarized light optical microscopy (AFM and PLOM, respectively) and nuclear magnetic resonance (^{13}C or ^{1}H NMR). The aim of such characterization is to understand the influence of changing certain parameters, such as topology, molecular architecture, comonomer content in copolymers, components of a blend, among others, in the crystallization of polymers and copolymers.

Random copolyesters, branch copolymers (*i.e.*, linear, stars and combs) with gradient distributions, lignin-based systems, blends of polyesters with carbon nanotubes and blends of cyclic and linear chains were the materials selected for the present work. The main findings and conclusions of each system are shown below.

Random copolyesters

Different random copolyesters (*i.e.*, poly (butylene succinate-*ran*-butylene adipate) (PBSA), poly (butylene succinate-*ran*-propylene succinate) (PPBS), poly (butylene adipate-*ran*-propylene adipate) (PPBA)) were employed in a wide composition range (*i.e*., 80:20, 60:40, 50:50, 40:60 and 20:80 molar compositions) and thermally, structurally and morphologically characterized. They showed an isodimorphic behaviour characterized by: the crystallization of all copolymer compositions, a pseudo-eutectic behaviour of the thermal properties as a function of comonomer composition, the presence of two different crystalline structures depending on the comonomer composition and changes in the unit cell parameters of the majority components with comonomer inclusion (*i.e.*, the minority component). Such characteristics were used as criteria to determine the isodimorphic character in random copolymers.

In addition, in those systems with an "even-odd" CH_2 number (*i.e.*, PPBS and PPBA) in their comonomers, a competition in the crystallization ability of the parent components was found. The crystallization ability of the PBA was higher than the PPA, therefore the pseudo-eutectic point was shifted to PPA-rich compositions, instead of

intermediate compositions (*e.g.*, as in the PBSA system). A similar behaviour was found for PPBS but only in the first heating scans, due to the slow crystallization (*i.e.*, days) of PPS. It is worth noting that the poly (propylene succinate-*ran*-propylene adipate) ("odd-odd" CH_2 number) were also studied, but no crystallization occurred under the conditions tested.

Besides studies under non-isothermal conditions at constant cooling and heating rates, rate-dependent studies were performed in the PBSA copolymers. It is worth noting that the PPBS and PPBA were also studied with different cooling rates, but only one cooling condition allows the crystallization of all compositions.

In the rate-dependent studies of PBSA, it was found that changes in cooling rates influence significantly the intermediate compositions (*i.e.*, 50:50 and 40:60). At low cooling rates, despite the coincident crystallization of both phases, the subsequent heating scan reflects a larger peak for the PBS-rich phase and a small shoulder for the PBA-rich phase, which indicates that the PBS-rich phase crystallization is favoured in the 50:50 compositions. In contrast, at high cooling rates, 50:50 PBSA is not able to crystallize during cooling, but it can crystallize during subsequent heating (*i.e.*, by cold crystallization) in a sequential manner, in which the first component that crystallizes is the PBA-rich phase and then an overlap occurs between the cold-crystallization of the PBS-rich phase and the melting process of the PBA rich phase crystals, therefore the melting process also occurs sequentially. In the case of 40:60 PBSA, fast cooling rates avoid the crystallization of the PBS-rich phase; therefore the only component which crystallizes is the PBA rich phase.

Branch copolymers

Poly (ethylene sulfide) (ES) and poly (propylene sulfide) (PS) were copolymerized as gradient and semi-random copolymers (*i.e.*, two comonomer addition protocols were used) with different molecular architectures, *i.e.*, linear, star and combs, and different degrees of polymerization (DP) of their arms (*i.e.*, different arm lengths). The samples used were linear, 4- and 8-armed stars, and combs, in a comparison where each arm had a gradient primary structure and DP of 10, 20 and 30. The influence of the monomeric distribution, topology, number of arms and DP on the thermal properties was studied.

In this work, it was confirmed that the crystallinity degree of these copolymers containing both a crystallizable (ES) and non-crystallizable monomer (PS) strongly depends on: (1) the primary structure (length of ES:PS gradients) and on (2) the presence of topological restrictions introduced by branching. On the other hand, it was confirmed the much higher order obtained in gradient polymers, in comparison to the semi-random ones.

Successive Self-nucleation and Annealing (SSA) technique allows deconvoluting a broad melting endotherm into individual thermal fractions, thanks to the ability of these copolymers to undergo thermal fractionation based on the interruption of the linear crystallizable sequences (ES) by non-crystallizable ones (PS). SSA results confirmed that polymers with longer ES sequences/gradients (addition protocol ***a***) had higher melting temperature thermal fractions (reflecting their much broader melting range) and were confirmed to have a higher crystalline mass fraction by WAXS.

Chain topology (*i.e.*, branching) on the other hand impairs the capacity of ES sequences to crystallize; in general, increasing branching content resulted in a reduced capacity to crystallize, and a strong reduction of crystallization and melting temperatures, relevant enthalpies, annealing capacity and lamellar thickness.

Stars and combs showed clear differences, *e.g.*, in combs the key melting/crystallization temperatures/enthalpies did not further decrease with increasing number of arms. This may be the result of combs showing a chain crowding that allows for easier – although possibly intramolecular - packing (‘parallel’ vs. convergent) or of the topological constrains for crystallization being released as the number of arms (or chain length) surpasses a saturation value.

Lignin-based systems

Two lignin based systems were studied. On one hand, poly (ε-caprolactone)-*grafted*-lignin (PCL-*g*-lignin) copolymers with 2 to 37 wt% lignin were employed to study the effect of lignin on the morphology, nucleation and crystallization kinetics of PCL. On the other hand, poly (lactic acid) (PLA) with *D*-lactide content of 1.2 wt% was melt mixing with 3 wt% of industrial (*i.e.*, untreated) lignin (Kraft or Organosolv) and for comparison purposes with ultrafine talc. The morphology, structure and behaviour of the blends under non-isothermal and isothermal conditions were studied.

The PCL-*g*-lignin reveals a strong dependency of the crystallization rate on lignin content, since there is a competition: lignin nucleation and PCL-*g*-lignin intermolecular interactions, which determines the crystallization behaviour of PCL-*g*-lignin. At low lignin contents (2-5 wt%) the nucleation effect of lignin dominates the behaviour since only a limited number of hydrogen bonds between lignin and PCL can be established. In fact, the nucleation efficiency (*NE*) values obtained demonstrate that lignin is a super-nucleating agent or is very close to being one, at low lignin contents.

Upon increasing lignin content beyond 5 wt%, the nucleation effect progressively declines as the intermolecular interactions limit the diffusion of PCL chains. Lignin contents of 29 and 37 wt% induce very large antinucleation effects in the samples. The hydrogen bonding interactions are equivalent to physical crosslinks that limit crystallization and lamellar sizes, as gathered from the large decreases in both crystallization and melting points. Additionally, the overall crystallization kinetics is slow down to values much lower than in PCL. SSA experiments indicate that the interactions are so strong that they act as crosslinks that limit the annealing capabilities of PCL.

In the case of PCL/kraft (KL) or organosov (OL) lignin and PLA/ultrafine talc (UT), it was found that both lignins (*i.e.*, KL and OL) promote the nucleation of PLA effectively (with a nucleating efficiency, *NE* of approximately 30%); however UT is a much better nucleating agent (*NE* of about 80%). The lignin and talc addition do not affect the spherulitic growth rate, whereas they increase the overall crystallization rate in the following order: PLA/UT>PLA/KL>PLA/OL>PLA in correspondence with the *NE* obtained. The industrial lignins can accelerate PLA crystallization by their nucleating action while preserving biobased and biodegradable character of the PLA/nucleating agent mixture.

Blends with carbon nanotubes

Three approaches for the incorporation of multiwalled carbon nanotubes (MWCNTs) in polymeric matrices were used: (a) blends of PCL with pristine MWCNTs (*i.e.*, nanocomposites), (b) blends of PCL with MWCNT-*g*-PCL (*i.e.*, nanohybrids) and (c) blends of PCL or PBS with MWCNT in a masterbatch based on polycarbonate (PC)/MWCNTs were employed. In (a) PCL was blended with pristine MWCNTs and with (b) a nanohybrid obtained from the same MWCNT but grafted with

low molecular weight PCL. In both (a) and (b), concentrations of 0.25 to 5 wt % of MWCNT and MWCNT-*g*-PCL were used. In (c) the nanocomposites were prepared by melt blending PCL or PBS with PC/MWCNT masterbatch. The nanocomposites contained 0.5, 1.0, 2.0 and 4.0 wt% MWCNTs.

Super-nucleation effects were found in (a) and (b). However, in (b) a competition between the plasticization effect of the low molecular weight grafted PCL chains and the nucleation effect of the MWCNT were found. This competition illustrates the greater complexity of nanohybrid systems with respect to nanocomposites. Nanohybrids with 1 wt% or less MWCNTs exhibit lower crystallization rates than nanocomposites, as a consequence of the plasticization action of low molecular weight grafted PCL chains.

Nucleating effects were found in (c). This effect is low due to the limited phase mixing between the PC-rich and PCL-rich phases. Only a limited quantity of MWCNTs can penetrate the PCL-rich phase and therefore contribute in nucleating PCL, while most of MWCNTs agglomerated in the PC-rich phase at high MWCNT loadings (*i.e.*, 4 wt%). It is worth noting that despite the nucleating effect, a reduction in the percentage of crystallinity of PCL is observed especially at high PC concentrations, as the PC-rich phase is able to crystallize in view of the plasticization effect of the PCL component.

A similar behaviour is found in the PBS/(PC/MWCNTs) systems. In this case the partial miscibility of the PBS and PC causes the crystallization of the PC-rich phase. The MWCNTs were able to nucleate the PBS-rich phase at low loading contents (below 4 wt%), indicating that some of the MWCNTs were able to transfer from the PC-rich to the PBS-rich phase. However, when the content of MWCNTs reached 4 wt%, the PBS-rich phase was antinucleated. This was explained by the agglomeration of MWCNTs which remained encapsulated inside the PC-rich phase and the decreased ability of the PBS chains to nucleate. Such lower nucleation density may have arisen by a combination of reasons: impurities transfer from PBS-rich to PC-rich phase and increased T_g value of the PBS-rich phase in comparison to neat PBS.

Cyclic and linear polymers and their blends

Cyclic poly (ε-caprolactone) (C-PCL) model chains were synthesized by a ring closure click chemistry technique. Identical linear PCL precursor chains of equivalent molecular weight were also prepared. Cyclic/linear (C/L) PCL blends were prepared in

solution with the following compositions: 95/5, 90/10 and 80/20. Two sets of blends with PCL samples of different number average molecular weights (3 and 12 kg/mol) were studied. The blends were analyzed by PLOM and advanced DSC techniques that included non-isothermal and isothermal crystallization studies and thermal fractionation by SSA. Adding small amounts of L-PCL chains (*i.e.*, 5 and 10 wt%) to C-PCL molecules produce dramatic synergistic reductions in the crystallization rate of cyclic molecules that are much larger that those expected on the basics of a simple mixing rule. All properties that are related to crystal formation and melting are affected leading to significant reductions in nucleation rate, crystallization and melting temperatures, spherulitic growth and overall crystallization rates, as well as annealing capacity for both molecular weights.

The results above can be explained by the generation of threading effects between linear and ring molecules that increase entanglement density and reduce molecular diffusion and relaxation.

In contrast, when the amount of L-PCL chains reaches 20 wt% a significant recovery of a simple mixing law behaviour is obtained.

In general terms, each modification of the polymers studied in this work (chemical modification, topology, or addition of nanofillers or other polymers), brings different responses in the structure and thermal properties as well as on the crystallization kinetics of the materials under study, whose understanding is of great importance for the basic comprehension and the development of potential applications of such materials. It is worth noting that almost all the materials used in this work are biodegradable and in some cases can be used for medical applications, therefore this work might help to tailor the properties of these different multiphasic polymeric systems.

RESUMEN

La caracterización térmica, estructural y morfológica de distintos sistemas multifásicos fue realizada, por medio de distintas técnicas, tales como: calorimetría diferencial de barrido (DSC), rayos X de ángulo grande y ángulo pequeño (WAXS y SAXS, respectivamente), microscopía de fuerza atómica (AFM) y óptica de luz polarizada (PLOM) y resonancia magnética nuclear (NMR). El objetivo de la caracterización de estos materiales fue comprender la influencia de cambiar parámetros como la topología, arquitectura molecular, tipo de comonómero en copolímeros, componentes de mezcla, entre otros, en la cristalización de polímeros y copolímeros.

Copolímeros al azar, copolímeros ramificados (lineales, estrellas y tipo peine) con distribución tipo gradiente, sistemas basados en lignina, mezclas de poliésteres con nanotubos de carbono y mezclas de polímeros cíclicos y lineales fueron los materiales multifásicos seleccionados para el presente trabajo. Los principales hallazgos y conclusiones de cada uno de los sistemas arriba mencionados son presentados a continuación:

Copolímeros al azar

Diferentes copoliésteres al azar (poli (butilen sucinato-*ran*-butilen adipato) (PBSA), poli (butilen sucinato-*ran*-propilen sucinato) (PPBS) y poli (butilen adipato-*ran*-propilen adipato) (PPBA)) fueron empleados en un amplio rango de composiciones molares (80:20, 60:40, 50:50, 40:60 y 20:80) y caracterizados térmica, estructural y morfológicamente. Los copolímeros mostraron un comportamiento isodimórfico caracterizado por: cristalización en todas las composiciones, comportamiento pseudo-eutéctico de las propiedades térmicas en función del contenido de comonómero, presencia de dos estructuras cristalinas diferentes dependiendo de la composición de comonómero y cambios en los parámetros de red producto de la inclusión del comonómero minoritario. Las características mencionadas fueron empleadas como criterio para determinar el carácter isodimórfico de copolímeros al azar.

Adicionalmente, en aquellos copolímeros con una relación de átomos de carbono "impar-par" (PPBS y PPBA) en sus comonómeros, fue encontrado un efecto competitivo en la cristalización producto de las diferentes capacidades de cristalización de los componentes puros (PBS vs PPS y PBA vs PPA). La capacidad de cristalización del PBA es mayor que la del PPA, por ello el punto pseudo-eutéctico se desplazó hacía

las composiciones ricas en PPA, en lugar de mantenerse en composiciones intermedias (*ej*., como en el PBSA). Un comportamiento similar fue encontrado en el PPBS pero solo en los primeros barridos de calentamiento, debido a la lenta cristalización (de días) del PPS. Es importante destacar que a pesar de que el poli (propilen sucinato-*ran*-propilen adipato) cuya relación de átomos de carbono es "impar-impar" fue estudiado, no fue posible encontrar las condiciones para su cristalización.

Además de los estudios no-isotérmicos, estudios dependientes de la velocidad de enfriamiento fueron realizados en el PBSA. Cabe destacar que los sistemas PPBS y PPBA también fueron estudiados a diferentes velocidades de enfriamientos, pero sólo fue posible cristalizarlos en todas las composiciones a bajas velocidades (*e.j.,* 1 ºC/min).

En los estudios dependientes de la velocidad se encontró en el PBSA que los cambios en la velocidad de enfriamiento afectan de manera significativa a las composiciones intermedias (50:50 y 40:60). A bajas velocidades de enfriamiento, a pesar de la cristalización coincidente de ambas fases, los subsiguientes barridos de calentamiento reflejan un pico de fusión significativo de la fase rica en PBS y un pequeño hombro para la fase rica en PBA, lo cual indica que la cristalización de la fase rica en PBS se encuentra favorecida en la composición 50:50. Por el contrario, a altas velocidades de enfriamiento, la composición 50:50 no logra cristalizar durante el enfriamiento, pero es capaz de hacerlo durante el subsecuente calentamiento (debido a la cristalización en frío) de una manera secuencial, en la cual la fase rica en PBA es la primera en cristalizar, y luego ocurre un solapamiento entre la fusión de dicha fase (el PBA funde de manera secuencial) y la cristalización en frío de la fase rica en PBS, posteriormente la fusión de la fase rica en PBS ocurre de manera secuencial. En el caso de la composición 40:60, altas velocidades de enfriamiento evitan la cristalización de la fase rica en PBS, por tanto sólo cristaliza la fase rica en PBA.

Copolímeros ramificados

Copolímeros de poli (etilen sulfóxido) (ES) y poli (propilen sulfóxido) (PPS) fueron copolimerizados con distribuciones tipo gradiente y semi-azar (debido a los protocolos de adición de comonómeros empleados), diferentes arquitecturas moleculares, lineal, estrella y tipo peine; y distintos grados de polimerización en cada brazo, es decir diferentes longitudes de brazos.

Las muestras empleadas fueron lineales, estrellas de 4 y 8 brazos y peines de 10, 15 y 20 brazos, cada una de estas muestras tenía una estructura primaria tipo gradiente y con grados de polimerización de 10, 20 y 30. Se estudió la influencia de la distribución de monómero, topología, número de brazos y grado de polimerización en las propiedades térmicas.

En este trabajo, se confirmó que el grado de cristalinidad de estos copolímeros que contienen tanto una unidad cristalizable (ES) como una no-cristalizable (PS), depende fuertemente de: (1) la estructura primaria (la relación de los gradientes de longitud ES:PS) y (2) las restricciones topológicas producto de la introducción de ramificaciones. Por otra parte, se confirmó que un mayor orden se obtiene en los copolímeros tipo gradiente, en comparación con los copolímeros con distribución tipo semi-azar.

Estudios por medio de la técnica de fraccionamiento de pasos sucesivos de autonucleación y recocido (SSA) permitieron deconvolucionar picos de fusión anchos en fracciones individuales, gracias a la habilidad de fraccionamiento de estos copolímeros, producto de la interrupción de secuencias cristalizables lineales (ES) por las no cristalizables (PS). Los resultados de SSA mostraron que los copolímeros con mayores secuencias/gradientes de unidades ES (protocol de adición ***a***) presentaron mayores temperaturas de fusión en su fraccionamiento (reflejado en un rango de fusión más amplio) y una mayor fracción másica cristalina que fue confirmada por ensayos de WAXS.

La topología de la cadena (ramificaciones) limita la capacidad de las secuencias cristalizables de ES; en general los incrementos en el contenido de ramas resultan en una reducción en la capacidad de cristalización, y una fuerte reducción de las temperaturas de cristalización y fundido, las entalpías, capacidad de recocido, y espesores lamelares.

Las topologías tipo estrellas y peines mostraron claras diferencias, *e.j.*, en los peines la temperaturas de fusión/cristalización así como sus respectivas entalpías no decrecieron con el incremento del número de brazos. Esto podría ser debido a que la aglomeración de cadena permite un empaquetamiento más sencillo, aunque posiblemente intramolecular (paralelo *vs* convergente) o las restricciones topológicas para cristalizar son liberadas o aligeradas cuando el número de brazos (o longitud de la cadena) sobrepasa el valor de saturación.

Sistemas basados en lignina

Se estudiaron dos sistemas basados en lignina. Por una parte, se emplearoncopolímeros de poli (ε-caprolactona)-*injertada*-lignina (PCL-*g*-lignina) con 2 a 37 % en peso de lignina para estudiar el efecto de la lignina en la morfología, nucleación y cinética de cristalización de la PCL. Por otra parte, se mezcló el poli (ácido láctico) (PLA) con contenido de *D*-lactida de 1.2% en peso con 3% de lignina industrial (sin tratamiento químico) (lignina del tipo kraft o organosolv) y con fines comparativos también con talco ultrafino. La morfología, estructura y compartimiento bajo condiciones no isotérmicas e isotérmicas fueron estudiados.

La velocidad de cristalización de la PCL-*g*-lignina revela una fuerte dependencia con el contenido de lignina, ya que existe una competición: el efecto nucleante de la lignina y las interacciones intermoleculares de la PCL-*g*-lignina, las cuales determinan el comportamiento de cristalización de estos materiales. A bajos contenidos de lignina (2-5%) el efecto nucleante domina, ya que solo un número limitado de puentes de hidrógeno se pueden establecer entre la lignina y la PCL. De hecho, los valores de eficiencia de nucleación (NE) obtenidos demuestran a bajos contenidos de lignina, que ésta es un agente super-nucleante de la PCL o está muy cerca de serlo.

A medida que se incrementa el contenido de lignina más allá del 5 % el efecto nucleante de la misma decrece, producto de las interacciones intermoleculares que limitan la difusión de las cadenas de PCL. Altos contenidos de lignina, de 29 a 37% inducen un significativo efecto anti-nucleante en las muestras. Los puentes de hidrógeno se comportan como entrecruzamientos físicos, los cuales limitan la cristalización y longitudes cristalinas. Esto es evidenciado en los altos decrecimientos en los puntos de cristalización y fusión. Adicionalmente, la cinética de cristalización global decrece a valores mucho más bajos en comparación a la PCL. Asimismo, los experimentos de SSA indican que las interacciones son tan fuertes que al actuar como entrecruzamientos limitan las capacidades de recocido de la PCL.

En el caso de las mezclas de PLA/lignina kraft (KL) o organosolv (OL) y PLA/talco ultrafino (UL), se encontró que ambas ligninas (KL y OL) promueven efectivamente la nucleación (con *NE* de alrededor de 30%); sin embargo el UT es un mejor agente nucleante (*NE* de 80%). La adición de lignina y talco no afectan la velocidad de crecimiento esferulítico, pero incrementan la velocidad de cristalización global en el siguiente orden: PLA/UT>PLA/KL>PLA/OL>PLA, lo cual se corresponde

con las *NE* obtenidas. Las ligninas industriales aceleran la cristalización del PLA por su acción nucleante mientras preservan el carácter biodegradable de las mezclas PLA/agente nucleante.

Mezclas basadas en nanotubos de carbono

Se emplearon tres maneras de incorporación de nanotubos de carbono multicapas (MWCNTs) en matrices poliméricas: (a) mezclas de PCL con nanotubos de carbono puros (nanocompuestos), (b) mezclas de PCL con MWCNT-*g*-PCL (nanohibrídos) y (c) mezclas de PCL o PBS con MWCNT en masterbatch basados en policarbonato (PC)/MWCNT. En (a) y en (b) las mezclas fueron realizadas con concentraciones de 0.25 a 5% de MWCNT y MWCNT-*g*-PCL, respectivamente. En (c) los nanocompuestos fueron preparados por mezclado en fundido de PCL o PBS con masterbatch de PC/MWCNT. Los nanocompuestos contienen 0.5, 1.0, 2.0 y 4.0 % de MWCNTs.

Se encontraron efectos super-nucleantes en (a) y (b). Sin embargo, en (b) se encontró un efecto competitivo entre el efecto nucleante de los MWCNT y el efecto plastificante de las cadenas de bajo peso molecular de PCL injertadas a los MWCNT. Esta competencia ilustra la complejidad de los sistemas nanohíbridos respecto a los nanocompuestos. Los nanohíbridos con 1% o menos de MWCNT exhiben menores velocidades de cristalización que los nanocompuestos, como consecuencia de la acción plastificante de las cadenas injertadas de PCL de bajo peso molecular

En (c) también se encontró un efecto nucleante. Este efecto es bajo debido a las limitaciones en el mezclado de las fases ricas en PC y PCL. Debido a ello solo una cantidad limitada de MWCNTs puede penetrar a la fase rica en PCL y por tanto contribuir a su nucleación, mientras que la mayoría de los MWCNTs se aglomeran en la fase rica en PC a altos contenidos de MWCNT (*e.j.*, 4%). Es importante destacar que a pesar del efecto nucleante, una reducción de porcentaje de cristalinidad de la PCL es observada, especialmente a altas concentraciones de PC, producto de que la fase rica en PC puede cristalizar debido al efecto plastificante de la PCL.

Un comportamiento similar es encontrado en los sistemas de PBS/(PC/MWCNT). En este caso la miscibilidad parcial del PBS y la PC causa la cristalización de la fase rica en PC. A pesar de ello los MWCNTs pueden nuclear a la fase rica en PBS a bajos contenidos de carga (menores a 4%), lo cual indica que algunos

de los MWCNTs son transferidos de la fase rica en PC a la fase rica en PBS. Sin embargo, cuando los contenidos de MWCNTs alcanzan el 4 %, la fase rica en PBS es anti-nucleada. Este comportamiento es explicado por la aglomeración de MWCNTs que se mantiene encapsulado dentro de la fase rica en PC y decrece la habilidad de las cadenas de PBS de ser nucleadas. La baja densidad de nucleación puede haber surgido por la combinación de las siguientes razones: impurezas transferidas desde la fase rica en PBS a la fase rica en PC y al incremento de la temperatura de transición vítrea de la fase rica en PBS en comparación al PBS puro.

Polímeros cíclicos y lineales y sus mezclas

Se utilizaron cadenas modelo de PCL cíclicas (C-PCL) que fueron sintetizadas en la Universidad de Tulane por medio de la técnica química de cierre de anillo tipo "click". Precursores lineales de PCL idénticos con pesos moleculares equivalentes también fueron preparados. Se prepararon mezclas de PCL cíclica/lineal (C/L) en solución en las siguientes composiciones: 95/5, 90/10 y 80/20. Dos sets de mezclas de PCL con diferente peso molecular promedio en número (3 y 12 kg/mol) fueron estudiados. Las mezclas fueron analizadas por microscopía óptica de luz polarizada y técnicas avanzadas de DSC que incluyen estudios no-isotérmicos, cristalizaciones isotérmicas y fraccionamiento térmico vía SSA. La adición de pequeñas cantidades de cadenas de L-PCL (5 y 10 %) a moléculas de C-PCL produce una fuerte reducción sinergistica en la velocidad de cristalización de las moléculas cíclicas mayor de lo esperado de acuerdo a una ley de mezclas. Todas las propiedades relacionadas con la formación cristalina y el fundido se ven afectadas, conduciendo a significativas reducciones en la velocidad de nucleación, temperaturas de cristalización y fundido, crecimiento esferulítico y velocidades de cristalización global, así como capacidad de recocido para ambos pesos moleculares.

Los resultados arriba descritos pueden ser explicados por la generación de efectos de enhebramiento entre cadenas lineales y moléculas cíclicas que incrementan la densidad de enredos y reducen la difusión y relajación molecular.

En contraste, cuando las cantidades de cadenas de L-PCL alcanzan un 20% se obtiene una significativa recuperación del comportamiento esperado en una ley de mezcla.

En términos generales, cada modificación en los sistemas estudiados en este trabajo (modificación química, topológica, o adición de nanopartículas u otros polímeros) produjo diferentes respuestas en la estructura y las propiedades térmicas, así como en la cinética de cristalización de estos materiales, de los cuales su entendimiento es de gran importancia desde el punto de vista de comprensión de estudios básicos y del desarrollo de potenciales aplicaciones. Es importante destacar que casi todos los materiales empleados en este trabajo son biodegradables y en algunos casos tienen un potencial uso en aplicaciones biomédicas, por lo cual este trabajo podría ayudar a adaptar las diferentes propiedades de los materiales multifásicos estudiados a determinadas aplicaciones.

Dedicatoria

A mi familia, gracias por apoyarme de una manera u otra a pesar del gran sacrificio de no poder verlos y abrazarlos en estos años (sobre todo a ti Be, Papi y Dami (deseo conocerte pronto sobrinito lindo), y todos los miembros de la familia en Venezuela, Chile, y Estados Unidos). Espero poder seguir haciendo carrera fuera de nuestra Venezuela, y así tener la oportunidad de brindarles más apoyo y probablemente verlos.

En especial, se lo dedico a usted Mami, ha sido mi motorcito, mi apoyo y una mujer maravillosa. Y para ti Eve, a pesar de que eres la menor, eres un gran ejemplo, te admiro mucho y estoy orgulloso de ti, y de todo lo que estás haciendo.

Agradecimientos

Cuándo aplique para el obtener la beca, una de las razones era la oportunidad de crecer, conocer muchas culturas, maneras de pensar y hacer las cosas, y todo ello lo he logrado, por tanto agradezco la oportunidad que he tenido de vivir esta experiencia. En especial gracias Profesor Alejandro, quién es la persona que lo ha hecho posible, es un gran ejemplo, al cual admiro por su dedicación, disciplina, cultura, y la gran persona que es. Ha sido una bonita experiencia ver cómo ha hecho crecer al grupo, empezando por usted, que tiene unas estadísticas impresionantes cada año, en congresos, artículos, capítulos de libros, estudiantes, tesis dirigidas y proyectos aprobados; y siguiendo con los laboratorios, que por medio de proyectos ha logrado dotarlos de nuevo espacio físico así como la adquisición de más equipos de laboratorio (los DSC, nuestros caballos de batalla, varios estuvieron bajo mi responsabilidad en estos años) y miembros del grupo con excelente calidad humana (de muchísimas culturas). Gracias también por ver muchas veces (cuándo quizás yo no lo veía) el potencial que tengo, y exigirme más, de esa manera he logrado crecer, y creo que he respondido de una buena manera con muy buenos resultados. Igualmente gracias por la oportunidad de poder conocer por medio de estancias lugares cómo Tainan en Taiwán, y Halle en Alemania, y por medio de congresos, Arabia Saudita, Génova y Burgos (no es internacional, pero es muy bonito). Espero que siga formando a excelentes estudiantes y el grupo siga creciendo. Y que la finalización de este paso, solo sea un hasta pronto.

Gracias a todos los miembros del grupo, han sido años compartiendo con Nerea e Idoia (mis primeras compañeras de ofi), gracias por el tiempo de desconexión en los almuerzos, y algunos almuerzos de grupo e idas a sidrería, aquí también incluyo a Eider. Luego Jordana, gracias por tu amistad en mis primeros años y por ser un gran ejemplo, ya seré tu futuro colega venezolano. A los italianos, Matteo, Giacomo, Alice, Loris, y Greta, han sido todos excelentes conmigo, muchas gracias ragazzi, y último pero no menos importante, Samuele, a pesar de compartir sólo dos meses contigo, has sido un gran amigo dentro y fuera del laboratorio. También han estado Filippo, eres un crack, y

Seif (de Argelia), eres una excelente persona y un trabajador incansable. Gracias a ambos por mostrarme Génova.

No todas las personas que han venido de otro país han sido de Italia, cómo tenemos un grupo muy plural, también tenemos a Maryam (de Irán), Irma y Jorge (de México), gracias por su ayuda, en especial a Irma por las estructuras químicas, y Maryam y Jorge, por la amistad, y a todos por sus preguntas que siempre me hacen preguntarme cosas y buscar soluciones. También tuvimos a Thandi y Elaine (de Sudáfrica), Andrew (de Estados Unidos) que es una persona realmente brillante.

Luego, también hemos tenido a una pasante muy especial de Venezuela, Ana Gabriela, mi pequeña gigante, no te imaginas lo mucho que me ayudaste al empezar, y lo mucho que te agradezco estar en esos momentos. Además de pasantes, hemos tenidos post-docs (no muchos, la verdad, pero estoy seguro que en el futuro habrán más), cómo Borja, de verdad has sido una persona muy inspiradora, por tu mente brillante, y tu gran amistad y calidad humana. Jon, también eres excelente, aportándonos tus ideas de estancias afuera, con una gran capacidad escribiendo proyectos y por supuesto capacidad analítica. Finalmente, para cerrar con nuestro grupo, gracias a Agurtzane y Manoli, por ayudarme en todo lo concerniente a la universidad. También gracias por los momentos compartidos con Juan, Evis y el Prof. Puig de la USB, ha sido un verdadero placer verlos de nuevo.

Quiero también agradecer a todas las personas de las que he tenido la oportunidad de aprender, cómo los grupos del Profesor Woo y del Profesor Thurn-Albretch, de verdad que son grupos excelentes. Las personas del sincrotrón, del cual ya perdí la cuenta de cuántas veces he ido, compartiendo junto a Borja, Jordana, Nerea, Jon, Eider, Leire Meabe, Laurent, Laura y Luca. A todas esas personas con las que he intercambiado ideas para lograr excelentes publicaciones. Y por supuesto, a los técnicos del DSC, en especial a Manuel que nos ha ayudado a mantener nuestros equipos operativos, sé que he sido un pesado con tantos e-mails, pero siempre los han contestado de una manera agradable.

Gracias a la Profesora Rose Mary Michell, por leer mi tesis, y darme un feedback tan positivo, es bueno saber cuándo las cosas se hacen bien. Prof. Dong, thank you for read my thesis as well, and for the excellent report.

Ahora, el doctorado no es algo que sólo se desarrolla en la universidad, también fuera necesitamos un gran apoyo para mantener nuestra vida en equilibrio. Por ello, hay alguien muy especial a quién agradezco, que ha sido cómo mi familia vasca acá en Donosti, Jes, gracias por siempre estar pendiente de mí, no sabes lo que vale un "¿cómo estás?", "¿cómo está tú familia?", "leí esto sobre Venezuela", "te apoyó hermano", o lo que vale alguna invitación a cenar, al monte, un café o una caña, conversar de la vida o simplemente a trabajar codo con codo montando pantallas, jeje, si no lo sabes, te lo digo, vale muchísimo, y siempre lo tendré presente, y no te olvidaré hermano. Y por supuesto, gracias por ayudarme a encontrar una especie de doctorado paralelo bailando, que me ha ayudado a ganar confianza y conocer personas increíbles. También gracias a toda la familia Kandela, Clo, Karina, Maitane y Jenny, muchas gracias por las clases y el cariño, Jenny gracias por haberme invitado al café de tu boda, cenas, y por siempre estar pendiente de mí. Luego gracias a todas esas personas con las que empecé, de las cuáles aún se mantienen María, Mar, Gorka, Mikel y Vanesa y mis compis de congresos Gorka y Julen. También gracias a las personas nuevas, que hacen que el grupo tan bonito vaya creciendo, en especial a Ander, que será mi futuro colega.

En Alemania, he tenido la oportunidad de encontrar a Vanesa (quién se graduó de Ingeniero de Materiales, mención Polímeros conmigo), Vane, muchas gracias por todo el apoyo que me has brindado en Alemania, mostrándome como desplazarme, la uni, mi casa, y por supuesto los momentos compartidos, con juegos de mesa, con Ohjin (tu esposo), y las clases de Tango. De verdad ha sido muy bonito volver a verte, y saber que estas muy bien. Espero que volvamos a repetir. Y hablando de personas que me han ayudado a mostrarme ciudades, gracias Antonio por ayudarme en mis primeros días en Donosti. También deseo darle las gracias a aquellas personas que a la distancia han estado pendientes de mi progreso, Guery mi gran amigo de carrera, la Profesora María Luisa y Freddy, espero que a todos les esté yendo muy bien en Estados Unidos, Canadá y Brasil.

A pesar de que incluí a mi familia en la dedicatoria, quiero agradecerles aquí también. Por estar ahí siempre, y regalarme bonitas experiencias. Eve y Be, han tenido a Evita y Dami, mis bellos sobrinos, de verdad que han sido una bendición. Sólo he tenido la oportunidad de conocer a Eva, pero Be a Dami también lo llevo en mi corazón. Me encanta poder ir a Barcelona a visitarte Eve, Diego, y a la linda Eva, que a pesar de estar pequeñita, me ha enamorado, con lo rápido que creces y por siempre recordarme, y

espero que ya cuándo aprendas a leer más, puedas leer estas breves palabras y sepas que también me has ayudado a crecer. Eve, también gracias por la oportunidad que me has dado cuándo has podido traer a Mami, y así verla aunque sea unos días. Bien sea allá en Barcelona o acá en San Sebastián.

Finalmente gracias a una persona muy especial que ha compartido los nervios y a veces estrés de los meses finales de escritura de nuestras tesis, así como todo el papeleo. Probablemente compartiremos el depósito, y practicaremos nuestras defensas. Gracias por el apoyo que me has brindado, por nuestras conversaciones y bellas experiencias, y gracias porque de una manera u otra me has ayudado a crecer y a creer, Erika, no sabes todo lo que significas para mí.

TABLE OF CONTENTS

LIST OF TABLES xiv

LIST OF FIGURES……..... xvii

CHAPTER I. GENERAL INTRODUCTION AND OBJETIVES

1.1 GENERAL INTRODUCTION ..... - 1 -

1.2 OBJECTIVES ..... - 3 -

GENERAL OBJETIVE..... - 3 -

SPECIFIC OBJECTIVES ..... - 3 -

CHAPTER II .GENERAL CONCEPTS

2.1 Semicrystalline Polymers and their models ..... - 5 -

2.1.1 Fringed micelle-model ..... - 5 -

2.1.2 Chain folded model ..... - 6 -

2.2 Polymer Crystallization..... - 8 -

2.3 Morphological and Structural Analysis of Materials: Small and Wide-Angle X-rays Scattering (SAXS and WAXS), synchrotron radiation and microscopy techniques ..... - 9 -

2.4 Crystallization theories..... - 19 -

2.5 Self-Nucleation (SN) and Successive Self-Nucleation and Annealing (SSA)..... - 25 -

2.6 References ..... - 32 -

CHAPTER III. EXPERIMENTAL PART

3.1 Materials..... - 36 -

3.1.1 Copolyesters..... - 36 -

3.1.2 Copolymers of poly (propylene sulfide-*co*-ethylene sulfide)..... - 40 -

3.1.3 Lignin-based materials: Lignin-*g*-PCL and PLA/lignin blends. ..... - 44 -

3.1.4 PCL/carbon nanotubes, PCL or PBS/(PC/MWCNT) nanocomposites with different contents of carbon nanotubes. ..... - 46 -

3.1.5 Cyclic, linear and blends of cyclic/linear PCL..... - 51 -

3.2 Methods..... - 54 -

3.3 References ..... - 65 -

CHAPTER IV. CRYSTALLIZATION OF RANDOM COPOLYESTERS: ISODIMORPHIC BEHAVIOUR.

4.1. General Introduction ..... - 68 -

4.2. Results and Discussions ..... - 78 -

4.1.1. PBSA random copolymers analysis. ..... - 79 -

4.1.2. PPBA random copolymers. ..... - 116 -

4.1.3. PPBS and PPSA random copolymers. ..... - 121 -

4.3. Conclusions ..... - 122 -

4.4. References ..... - 123 -

CHAPTER V. The influence of chain primary structure and topology (branching) on crystallization and thermal properties

5.1. General Introduction ..... - 127 -

5.2. Results and Discussion ..... - 130 -

5.2.1. Successive Self-Nucleation and Annealing (SSA) ..... - 139 -

5.2.2. Wide Angle X-ray Scattering (WAXS) ..... - 143 -

5.2.3. Small Angle X-ray Scattering (SAXS) ..... - 146 -

5.2.4. General comparison ..... - 147 -

5.3. Conclusions ..... - 149 -

5.4. References ..... - 150 -

CHAPTER VI. NUCLEATION EFFICIENCY AND CRYSTALLIZATION OF LIGNIN-BASED MATERIALS

6.1. General Introduction ..... - 152 -

6.2. Results and Discussion ..... - 154 -

6.2.1. PCL-*g*-lignin ..... - 154 -

6.2.2. PLA/lignins and PLA/talc blends ..... - 174 -

6.3. Conclusions ..... - 192 -

6.4. References ..... - 193 -

CHAPTER VII. BIODEGRADABLE POLYMERS/CARBON NANOTUBES BLENDS

7.1. Results and Discussion ..... - 199 -

7.1.1. Nanocomposites and Nanohybrids ..... - 199 -

7.2.1. Blends of PCL and PBS with a PCL/MWCNT masterbatch ..... - 211 -

7.2. Conclusions ..... - 232 -

7.3. References ..... - 234 -

CHAPTER VIII. CYCLIC AND LINEAR POLYMERS AND THEIR BLENDS

8.1. General Introduction ..... - 241 -

8.2. Results and Discussion ..... - 242 -

8.2.1. Blends of C-PCL with small amounts of L-PCLs ..... - 242 -

8.3. Conclusions ..... - 261 -

8.4. References ..... - 261 -

CHAPTER IX. APPENDIX

9.1 Synthesis of PPBA, PPBS and PPSA ..... - 266 -

9.2 Appendix of Chapter IV. ..... - 269 -

9.3 Appendix Chapter V ..... - 280 -

9.4 Appendix Chapter VI. ..... - 284 -

9.5 Appendix Chapter VII. ..... - 290 -

9.6 Appendix Chapter VIII. ..... - 317 -

9.7 References ..... - 319 -

List of Related Publications ..... - 321 -

Other Publications from academic collaborations ..... - 322 -

LIST OF TABLES

Table 3.1. Samples molar composition, molar masses (M_n and M_w), dispersity index ($Đ$), and Sequence distribution determined by ^{13}C NMR (L_{MA}, L_{MB} and R) .....- 36 -

Table 3.2. Characterization data for the polysulfides prepared in this work[a]. .....- 43 -

Table 3.3. Samples description. .....- 46 -

Table 3.4. Characteristics and nomenclature of the materials employed. .....- 50 -

Table 3.5. Weight percentages of the components in the nanocomposites. .....- 51 -

Table 3.6. Weight percentages of the components in the nanocomposites. .....- 52 -

Table 3.7. Number–Average Molecular Weight (M_n) and Dispersity ($Đ= M_w/M_n$) Data for the Synthesized PCL Samples[a] .....- 53 -

Table 4.1. List of isodimorphic random aliphatic copolymers reported in the literature after 2009. .....- 73 -

Table 4.2. Thermal transitions and relevant enthalpy values obtained from the DSC scans presented in Figure 4.2 (T_g) and 4.3 (standard scans)[*] .....- 86 -

Table 4.3. Signal fractions obtained through NMR experiments for neat PBS and PBA and their copolymers. .....- 106 -

Table 5.1. Relevant calorimetric quantities obtained from DSC scans in Figure 5.1, 5.2 and 5.3[*] .....- 135 -

Table 5.2. Calculated diffraction spacings (d) according to Bragg´s law, 2θ angles and calculated mass fraction of crystals ($X_{c,WAXS}$) from WAXS patterns. .....- 146 -

Table 5.3. Long period (d^*) values obtained at RT for PPS-*co*-PES copolymers with different topologies and a fixed DP (30) and calculated from the q_{max}. The percentages of crystallinity calculated by WAXS ($X_{c,WAXS}$), as well as the lamellar thickness estimated from it (l), are also reported. .....- 147 -

Table 6.1. Thermal properties (crystallization (T_c) and melting temperature (T_m)) obtained from Figure 6.1. The enthalpies of crystallization and melting (ΔH_c and ΔH_m), as well as the values of crystallinity (X_c) have been normalized by the weight fraction of PCL in the sample. .....- 156 -

Table 6.2. Parameters obtained from fitting the Lauritzen and Hoffman theory to the data of Figure 6.3. R^2 is the correlation coefficient for the Lauritzen and Hoffman linear plots. Equation 2.15 (see Chapter II. General Concepts) yields a value of σ=7.01 erg/cm^2. .....- 165 -

Table 6.3. Spherulitic growth rate (G) values as function of isothermal crystallization temperature (T_c) for neat PLA and PLA compounds. .....- 176 -

Table 6.4. Differential scanning calorimetry data of neat and nucleated PLA. .....- 177 -

Table 6.5. Nucleation Efficiency of UT, KL and OL for the prepared PLA/talc and PLA/lignin compounds .....- 184 -
Table 6.6. Parameters obtained from fitting the Lauritzen and Hoffman Theory to the data of Figure 6.16. .....- 187 -
Table 6.7. Isothermal crystallization data and acceleration factors (AF). .....- 189 -
Table 6.8. Molecular weight properties of PLA and nucleated PLA compounds. .....- 190 -
Table 6.9. TGA and DTGA characteristics of PLA and nucleated PLA compounds. .....- 192 -

Table 7.1. Crystallization temperature (T_c) shift (difference between the T_c value of neat PCL and the T_c value of the PCL with CNTs) for different PCL/CNT systems reported in the literature. .....- 201 -
Table 7.2. Crystallization and melting temperatures, normalized heat of crystallization and fusion, and degree of crystallinity (X_c) for the nanocomposites.....- 204 -
Table 7.3. Calculated values of *d*-spacing (from WAXS experiments) and long period (*d**, obtained from SAXS experiments) for the neat PCL and its nanocomposites.....- 217 -
Table 7.4. Summary of tensile testing results for neat PCL and the nanocomposites. .....- 231 -
Table 8.1. Thermal Transitions and Relevant Enthalpy Values Obtained from DSC Scans Presented in Figure 8.1* .....- 245 -
Table 8.2. Parameters obtained from fitting the Lauritzen and Hoffman theory to the data of Figure 8.4* .....- 251 -
Table 9.1. Bragg´s angle and *d*-spacings obtained at -40 ºC, after cooling at the indicated cooling rates. .....- 270 -
Table 9.2. Lamellar long periods calculated from q_{max} obtained by SAXS for PBS, PBA and PBSA samples at 5 and 50 ºC/min. .....- 273 -
Table 9.3. Calculated diffraction spacings (*d*) according to the Bragg´s law for linear (a), star 4-arms and comb samples of 10, 15 and 20 arms at different temperatures.....- 282 -
Table 9.4. Parameters obtained by fitting the Avrami theory for neat PCLs .....- 285 -
Table 9.5. Parameters obtained by fitting the Avrami theory for low lignin contents. .....- 285 -
Table 9.6. Parameters obtained by fitting the Avrami theory for intermediate lignin contents. ...- 285 -
Table 9.7. Parameters obtained by fitting the Avrami theory for high lignin contents. .....- 286 -
Table 9.8. Parameters obtained by fitting the Avrami theory..... 289
Table 9.9. Parameters obtained by fitting the Avrami theory to the data obtained by isothermal crystallization experiments of non-functionalized samples. .....- 290 -
Table 9.10. Parameters obtained by fitting the Avrami theory to the data obtained by isothermal crystallization experiments of functionalized samples.....- 292 -

Table 9.11. Solid-like yield complex modulus for the materials under study at T = 70 °C. - 299 -
Table 9.12. Calculated values of d-spacing (from WAXS experiments) and long period (d^*, obtained from SAXS experiments) for the neat PBS and its nanocomposites. ..... - 304 -
Table 9.13. Kinetic parameters for all the investigated samples during isothermal crystallization. 310
Table 9.14. Kinetic parameters for all the investigated samples during isothermal crystallization. 314
Table 9.15. Parameters for neat PCL. and the PCL/(PC/MWCNTs) nanocomposites..... - 316 -
Table 9.16. Parameters from the isothermal crystallization kinetics analyses for neat PBS and the PBS/(PC/MWCNTs) nanocomposites. ..... - 316 -
Table 9.17. Summary of tensile testing results for neat PBS and the nanocomposites. ..... - 316 -
Table 9.18. Parameters Obtained by Fitting the Avrami Theory to the 3kg/mol samples. .. - 317 -
Table 9.19. Parameters Obtained by Fitting the Avrami Theory to 12 kg/mol samples. ..... - 317 -
Table 9.20. Parameters Obtained from Fitting the Lauritzen and Hoffman Theory. - 318 -

LIST OF FIGURES

Figure 2.1. WAXS from (a) polystyrene, showing a diffuse halo from amorphous sample and (b) highly crystalline polyethylene, showing sharp "powder" rings. [11] .....- 14 -

Figure 2.2. (a) Scattered intensity (black dotted line) of PCL with Porod fit (light gray line). The continuous line gives the sum of the Porod scattering and a background (dashed line) due to density fluctuations. (b) Function $16\pi^3[P\text{-}Is^4]w$ as calculated from $I(s)$ (dotted lines). The continuous line is the result of the simulation giving the result d_a=8.80 nm, σ_a=4.20 nm, d_c=7.65 nm and σ_c=0.85 nm. (c) Correlation function and (d) Resulting interface distribution function $K''(z)$ after a discrete cosine transformation (dotted lines) and simulation (thick continuous line). For the simulation the first three contributions h_a, h_c and $-2h_{ac}$ are indicated additionally.[6] .....- 18 -

Figure 2.3. Avrami plots obtained through the Origin ® plug in developed by Lorenzo et al. [13] .....- 22 -

Figure 2.4. Lauiritzen and Hoffman plots obtained through the Origin ® plug in developed by Lorenzo et al.[13] .....- 25 -

Figure 2.5. (a) DSC cooling scans (at 10°C/min) for PP after 5 min at the indicated T_s. (b) Subsequent heating scans (at 10°C/min) after the cooling runs shown in (a). (c) Representation of the self-nucleation domains for PP homopolymer on top of the standard DSC melting trace. Data points represent peak crystallization temperatures (plotted on the right hand side y axis) as a function of T_s values (plotted on the x axis as temperature).[28] .....- 28 -

Figure 2.6. DSC heating scans (10 °C/min) for (a) PE[25] and (b) 11U4, before and after SSA fractionation.[28] ..... - 30 -

Figure 3.1. (*A*) The persistence length of chains with identical composition (1:1 ES/PS) is inversely proportional to the slope of the plot of $(Mw2[\eta])1/3$ vs. $Mw1/2$. Our analysis stops at the quantification of the slopes without explicitly calculating the persistence lengths, because of the likely large uncertainties in a) the intrinsic viscosity values obtained from GPC measurements (non-zero shear) and b) the values of mass per unit length of the polymers (used to calculate the persistence length from the slopes), which in gradient polymers inherently vary along the chain. (*B*) Left: Plots of R_g and $R_{\square}$ vs. molecular weight for all polymers with 1:1 ES/PS composition. $R_{\square}$ is obtained as viscometric radius ($R\eta = (3\eta Mw)1/3$ [31]); the approximation $RH \approx R\eta$ is assumed valid in the melt, and to at least a qualitative extent in solution too ($R\eta RH \approx 1 \div 1.2$[33]). *(C)* Right: plots of the shape parameter $RGRH$ vs. molecular weight and of the Mark-Houwink parameter a vs. degree of branching; in both cases it is apparent that already 8-armed stars are rather compact structures and combs are increasingly similar to hard spheres ($RGRH \leq 1, a \leq 0.4$).....- 44 -

Figure 3.2. Schematic representation of a self-nucleation (SN) experiment.[20] .....- 57 -
Figure 3.3. *SSA* thermal protocol schematic representation. Cooling and Heating scans are performed at a constant scanning rate.[20] .....- 58 -
Figure 4.1. Melting point (m.p) as a function of number of C atoms for diacids (α, ω-alkenedicarboxylic acids) (HOOC-$(CH_2)_{n-2}$-COOH, *n*=2-10).[31].....- 77 -
Figure 4.2. (a) DSC heating scans performed after quenching PBS, PBA and their copolymers samples. (b) Glass transition temperatures (T_g), taken from (a), as a function of PBA content, the fits to the Fox and Gordon-Taylor equations are also shown.....- 80 -
Figure 4.3. Cooling DSC scans (a, c) from the melt and subsequent heating scans (at 20 ºC/min) (b,d) for the indicated homopolymers and random copolymers samples at 5 (a,b) and 50 (c,d) ºC/min. .....- 82 -
Figure 4.4. Variation of (a) T_c, (b) ΔH^n_c, (c) T_m and (d) ΔH^n_m as a function of PBA content taken during cooling at 5 ºC/min and in the subsequent heating. The shadowed region indicates the pseudo-eutectic point. .....- 84 -
Figure 4.5. WAXS diffractograms of PBS, PBA and their copolymers taken at -40 ºC after being cooled at (a) 5 and (b) 50 ºC/min. .....- 88 -
Figure 4.6. *d*-spacing, obtained after cooling from the melt at (a) 5 and (b) 50 ºC/min, of characteristic planes as a function of the PBA content in the PBSA copolymers.....- 90 -
Figure 4.7. (a) WAXS patterns and *d*-spacing of characteristic planes as a function of the PBA content in the PBSA copolymers, obtained after cooling from the melt at 5 ºC/min.....- 92 -
Figure 4.8. SAXS patterns of PBS, PBA and their copolymers taken at -40 ºC after being cooled at (a) 5 and (b) 50 ºC/min; (c) calculated lamellar thickness for the d^* values presented in (a). .....- 94 -
Figure 4.9. SAXS patterns obtained in a microfocus X-rays equipment in a wide range of *q* at (a) 21ºC (b) -40 ºC and (c) 10 ºC below the melting peak of each material.....- 96 -
Figure 4.10. Interface distribution function for all the samples. .....- 97 -
Figure 4.11. Amorphous and crystalline thickness (da and dc, respectively) as a function of PBA content for all the samples. The distribution of each phase is represented as an error bar...- 98 -
Figure 4.12. Phase Images of all the samples taken at 23 ºC, for PBS-rich compositions: (a) PBS, (b) 80:20, (c) 60:40 and (d) 50:50 PBSA; and for PBA-rich compositions: (e) PBA, (f) 20:80 and (g) 40:60 PBSA. .....- 99 -
Figure 4.13. Height, Phase and Amplitude AFM Images of 50:50 PBSA during step-heating. The temperature (*T*) of each step is indicated at the left. .....- 101 -
Figure 4.14. Height, Phase and Amplitude AFM Images of 40:60 PBSA during step-heating. The temperature (*T*) of each step is indicated at the left. .....- 103 -

Figure 4.15. ^{13}C CP MAS NMR spectra of PBA (top) and PBA (bottom). Note that the signals at 30 and 35 ppm in the PBS and PBA spectra are not overlaped.....- 104 -
Figure 4.16. ^{13}C CP MAS NMR spectra of 80:20, 60:40, 50:50, 40:60 and 20:80 PBSA random copolymers. The arrows indicate the PBS and PBA signals in each copolymer.....- 106 -
Figure 4.17. Crystalline, interphase (crystalline+amorphous) and amorphous fraction (X_c, X_{ra} and X_a, respectively) for PBS (left-axis) and PBA (right-axis) as a function of PBA Content.....- 106 -
Figure 4.18. 50:50 PBSA (a) cooling scans to -40 ºC at different cooling rates and (b) subsequent heating scans performed at 20 ºC/min. The values indicated to the right of each figure indicate the cooling rates applied in ºC/min. .....- 108 -
Figure 4.19. 40:60 PBSA (a) cooling DSC scans at different cooling rates and (b) subsequent heating scans performed at 20 ºC/min. The values indicated to the right of each figure indicate the cooling rates applied in ºC/min. .....- 110 -
Figure 4.20. (a) WAXS diffractograms (at different temperatures) obtained during heating after cooling the 50:50 PBSA sample at 50 ºC/min and (b) DSC heating scans, for a sample with identical thermal history. The cold-crystallization (C.C.) and melting processes are indicated. The red shadows as well as red color on the numbers are employed to highlight the PBA-rich phase thermal events while the blue shadows as well as blue color on the numbers are used for the corresponding PBS-rich phase. The heating scans (for both WAXS and DSC) were performed at 10 ºC/min. The values indicated to the right of figure (a) indicate the temperature at which the patterns were taken. The arrows indicate the main reflections for PBA (see pattern taken at 10 ºC) and PBS (see pattern taken at 20 ºC).....- 111 -
Figure 4.21. WAXS diffractograms taken during (a) cooling at 1 ºC/min and (b) subsequent heating at 10 ºC/min for 40:60 PBSA copolymer. The values indicated to the right of each figure correspond to the temperature at which the patterns were taken. .....- 113 -
Figure 4.22. Polarized light optical micrographs for (a) PBS (b) 80:20 PBSA (c) 60:40 PBSA, (d) 50:50 PBSA, (e) PBA, (f) 20:80 PBSA and (g) 40:60 PBSA taken at -40 ºC after cooling from the melt at 5 ºC/min. The temperature at which the first spherulites appear, or onset crystallization temperature, is indicated under each micrograph. .....- 115 -
Figure 4.23. (a) Cooling at 1 ºC/min and subsequent (b) heating scan at 20 ºC/min for PPBA copolymers. (c) T_m (*i.e.*, obtained from Figure 4.23b) as a function of PBA content. .....- 119 -
Figure 4.24. (a) WAXS patterns and (b) *d*-spacings as a function of the PBA content, for all the PPBA samples. - 120 -

Figure 5.1. DSC cooling (***A***) and subsequent heating (***B***) scans obtained for linear (a) and (b) copolymers with different DPs (*i.e.*, 10, 20 and 30). .....- 132 -

Figure 5.2.DSC (A) cooling and (B) heating scans for linear and star copolymers with different number of arms (*i.e.*, 2, 4 and 8) and variable DP (*i.e.*, DP of 10, 20 and 30).....- 133 -
Figure 5.3. DSC (A) cooling and (B) heating scans for linear and comb copolymers with different number of arms (*i.e.*, 10, 15 and 20) and a fixed DP of 30. A variable DP (i.e., 10, 20 and 30) is presented for the comb with 15 arms.....- 134 -
Figure 5.4.(***A***) Crystallization onset temperatures ($T_{c,onset}$) and end melting temperatures ($T_{m,end}$), (***B***) crystallization (ΔH^n_c) and melt (ΔH^n_m) normalized enthalpies as a function of number of arms, for linear, star and comb samples with different DPs. The solid lines represent guides to the eye. The dashed lines separate the behaviour of linear, star and combs samples.....- 137 -
Figure 5.5. Final heating runs after SSA thermal fractionation for P(PS-*co*-ES) linear copolymers obtained by protocols ***a*** and ***b***, with DP=10, 20 and 30.....- 141 -
Figure 5.6. Final heating runs after SSA thermal fractionation for P(PS-*co*-ES) copolymers with linear and stars topologies and variable DP (*i.e.*, DP=10, 20 and 30).....- 142 -
Figure 5.7. Final heating runs after SSA thermal fractionation for P(PS-*co*-ES) linear and combs copolymers with different number of arms (i.e., 10, 15 and 20) at a fixed DP of 30 and variable DP (*i.e.*, DP=10, 20 and 30) for the 15 arms sample.....- 143 -
Figure 5.8. WAXS patterns for (A) 8 arms star P(PS-*co*-ES) copolymers with variable DP (10, 20 and 30: $S\_(PS_5\text{-}ES_5)_8$, $S\_(PS_{10}\text{-}ES_{10})_8$, $S\_(PS_{15}\text{-}ES_{15})_8$) and SAXS patterns (B) for P(PS-*co*-ES) copolymers with different chain topologies (linear, star and combs) and fixed DP (30) at 25 ºC.....- 145 -
Figure 5.9.A summary of key parameters measured/calculated in this study on polymers with DP 30 per arm and a 1:1 PS:ES ratio. All parameters are normalized against the values presented by the linear (formally 2-armed) polymer obtained with method ***a***. The data for the linear polymer obtained via repeated monomer addition (method ***b***) are presented in red. The Mark-Houwink parameter *a* and the shape parameter $RGRH$ are reported in blue to distinguish these dilute solution (hence single molecule) parameters from those referring to bulk materials, which are represented by black empty symbols.....- 148 -
Figure 6.1 DSC cooling and subsequent heating scans at 20 °C/min for (a), (b) neat PCLs and (c), (d) PCL-*g*-lignin copolymers. The plots are normalized by the weight of the PCL fraction in the sample. The red color was used for the neat materials and the blue one for the copolymers...- 155 -
Figure 6.2. Variation of (a) T_c (b) T_m (c) ΔH_c and (d) ΔH_m as a function of lignin Content. ΔH_c and ΔH_m were normalized by the mass of PCL in the PCL-*g*-lignin copolymer. The solid lines represent guides to the eye. .....- 157 -

Figure 6.3. Overall crystallization rate ($1/\tau_{50\%}$) as a function of isothermal crystallization temperature for (a) neat PCLs (b) PCL[15] and PCLs with different lignin contents. The solid lines represent fits to the Lauritzen and Hoffman theory. .....- 160 -

Figure 6.4. (a) Values of $1/\tau_{50\%}$ as a function of Lignin content at different constant values of T_c. (b) Values of T_c as a function of Lignin content at $1/\tau_{50\%}$=1.0 min^{-1}. The plots contains experimental data points (Exp.) and values extrapolated (Ext.) from the LH fittings to the data shown in Figure 6.3. The solid lines represent guides to the eye. .....- 162 -

Figure 6.5. Avrami index values for: (a) neat PCLs and (b) PCL-*g*-lignin samples. .....- 164 -

Figure 6.6. Values of K_g as a function of Lignin Content. The solid line is a guide to the eye.....- 166 -

Figure 6.7. Standard DSC heating scans for (a) PCL[15] and (b) PCL[127]. The vertical lines indicate the temperatures at which the materials experience their self–nucleation Domain transitions. The data points represent T_c (right hand side *y* axis) as a function of T_s (using the *x* temperature axis). *DI*, *DII* and *DIII* stand for the different self-nucleation domains of the samples. .....- 169 -

Figure 6.8. Nucleation efficiency (*NE*) of lignin in PCL-*g*-lignin samples. The efficiency was calculated using reference crystallization parameters from both PCL[15] (low AAL) and PCL[127] (high AAL), see equation 6 and text. .....- 170 -

Figure 6.9. Final heating run after SSA thermal fractionation for (a) Neat PCLs (b) PCL-*g*-lignin, the endotherms were normalized by the real PCL mass. .....- 171 -

Figure 6.10. Peak melting point of the highest melting point SSA fractions as a function of lignin content. For comparison purposes the T_m (see Figure 6.1) values after non-isothermal crystallization also are plotted. The solid lines represent guides to the eye. .....- 172 -

Figure 6.11. A schematic cartoon illustrating one possible way for PCL chains in PCL-g-lignin to undergo thickening during annealing. The *not–to–scale* square represents hydrogen bonding between PCL and lignin (see text). Acting like a physical crosslink, they prevent that chain fragments around them can enter PCL crystals: (a) Intermediate lignin contents with a low density of hydrogen bonds and (b) High lignin contents with higher density of hydrogen bonds. - 173 -

Figure 6.12. Polarized Light Optical Micrographs of spherulitic morphology of PLA and nucleated PLA compounds at 130 °C taken at the indicated times (scale: 100 μm). .....- 175 -

Figure 6.13. DSC (a) cooling and (b) subsequent heating scans for neat PLA and its blends with the indicated lignin and UT. .....- 178 -

Figure 6.14. (a,b)WAXS diffractograms for all samples taken at 25 ºC (after cooling from the melt at 2 ºC/min) and (b) SAXS patterns for PLA taken during heating at 5 ºC/min at different temperatures, respectively, after previously cooling the samples at 2 ºC/min. .....- 181 -

Figure 6.15. Self-nucleation of neat PLA. (a) DSC cooling scans from T_s (after the 5 min isothermal step at T_s was completed) and (b) DSC subsequent heating scans after the cooling scans shown in (a). .....- 183 -

Figure 6.16. Overall crystallization rate ($1/\tau_{50\%}$) as a function of isothermal crystallization temperature for neat PLA and its blends with UT, KL and OL. The solid lines represents fits to the Lauritzen and Hoffman (LH) theory. .....- 186 -

Figure 6.17. (a) TGA and (b) DTGA curves of PLA and nucleated PLA.....- 191 -

Figure 7.1. DSC cooling and heating scans at 20 °C/min for the indicated nanocomposites and nanohybrids. .....- 203 -

Figure 7.2. Influence of MWCNT content on (a) crystallization and (b) peak melting temperatures. .....- 203 -

Figure 7.3. Self-nucleation behavior of neat PCL for selected self-nucleation temperatures (T_s). (a) DSC cooling scans from T_s and (b) DSC subsequent heating scans (see text). .....- 206 -

Figure 7.4. MWCNTs efficiencies as nucleating agents for PCL_xM_y and PCL_xNH_y nanocomposites. .....- 207 -

Figure 7.5. (a) Variation of $1/\tau_{50\%}$ (inverse of half-crystallization time) values as a function of the crystallization temperature for PCL_xM_y and PCL_xNHy samples. Solid lines indicate fittings to the Lauritzen and Hoffman theory. Selected pairs of samples (nanocomposites versus nanohybrids) are compared for MWCNT contents of (b) 0.25, (c) 0.5 and (d) 3 wt%. .....- 209 -

Figure 7.6. Influence of MWCNTs on (a) the crystallization temperature at $1/\tau_{50\%}$= 0.2 min^{-1} and on (b) the overall crystallization rate at T_c = 52 °C for the indicated blends. Different symbols are used for experimental (Exp.) and extrapolated (Ext.) data points. .....- 210 -

Figure 7.7. DSC cooling and second heating curves for the selected 73/(23/4) w/w PCL/(PC/MWCNTs) nanocomposite. The arrows indicate the crystallization and melting of the PC rich phase in the blends. .....- 212 -

Figure 7.8. (a, c) WAXS diffractograms taken at selected isothermal temperatures; (b, d) SAXS patterns taken at the selected isothermal temperatures for PCL-based (a,b) and PBS-based (c,d) nanocomposites, respectively. .....- 214 -

Figure 7.9. WAXS patterns taken during the heating at 5 ºC min^{-1} after the isothermal step at 46 ºC and 90.5 ºC for (a, c) (93/6/1) and (b, d) (73/23/4) PCL/(PC/MWCNTs) and PBS/(PC/MWCNTs), respectively. .....- 216 -

Figure 7.10. DSC heating curves for neat PCL and the PCL/(PC/MWCNTs) nanocomposites, showing the glass transitions around -60 °C. .....- 218 -

Figure 7.11. DSC (a, c) cooling and (b, d) second heating curves at 20 °C min^{-1} of neat PCL, PBS and the PCL/(PC/MWCNTs), PBS/ (PC/MWCNTs) nanocomposites. .....- 220 -

Figure 7.12. DSC crystallization and second heating melting temperatures as a function of MWCNTs content for neat PCL, PBS and the PCL/(PC/MWCNTs), PBS/(PC/MWCNTs) nanocomposites. A linear fit and a polynomial fit for the experimental data of T_m and T_c, respectively, are used to guide the eye. ..... - 221 -

Figure 7.13. (a) DSC cooling scans for neat PCL after 5 min at the indicated T_s, and (b) subsequent heating scans after the cooling runs shown in (a). ..... - 221 -

Figure 7.14. Dependence of (a) crystallization and (b) melting peak temperatures of neat PCL on T_s ..... - 222 -

Figure 7.15. Nucleation efficiency as a function of MWCNTs content for (a) PCL-based and (b) PBS-based nanocomposites. The experimental points are fitted with a polynomial fit in order to guide the eye. ..... - 222 -

Figure 7.16. Overall crystallization rate ($1/\tau_{50\%}$) as a function of isothermal crystallization temperature (T_c) for PCL and PBS-based nanocomposites. The red solid lines represent fits to the LH theory. ..... - 226 -

Figure 7.17 (a) Crystallization temperature as a function of MWCNTs content at constant $1/\tau_{50\%}$ = 0.5 min^{-1}; (b) overall crystallization rate as a function of MWCNTs content at constant T_c = 47 °C. ..... - 226 -

Figure 7.18. Relative crystallinity (X_c) as a function of isothermal crystallization temperature (T_c) for neat PCL and the PCL/(PC/MWCNTs) nanocomposites. ..... - 227 -

Figure 7.19. (a) Inverse of half crystallization times ($1/\tau_{50\%}$) (b) Normalized crystallization constant of the Avrami model ($K^{1/n}$) and (c) Avrami index (n) as a function of the isothermal crystallization temperature (T_c) for all the samples. ..... - 228 -

Figure 7.20. Stress-strain curves for neat PCL and the nanocomposites. ..... - 231 -

Figure 8.1. DSC cooling (a and c) and subsequent heating (b and d) scans at 20 °C/min for 3 (a and b) and 12 kg/mol (c and d) samples of neat L–PCL and C–PCL and their blends at the indicated compositions. The red (top) and blue (bottom) curves represent neat C-PCL and L-PCL, respectively, whereas the green curves (middle) represent the C/L blends at the indicated compositions. ..... - 243 -

Figure 8.2. DSC heating scans (performed at 20 °C/min) after previous cooling scans at the indicated cooling scans for a 3 kg/mol C–PCL sample ..... - 244 -

Figure 8.3. Values of crystallization (T_c) and melting temperature (T_m) (represented in the right and left handed axis, respectively) as a function of C–PCL content for (a) 3 kg/mol samples and (b) 12 kg/mol samples. The straight solid line indicated the behavior predicted by a simple mixing law. ..... - 247 -

Figure 8.4. Spherulitic growth rate (G) as a function of isothermal crystallization temperature (T_c) for neat L–PCL and C–PCL of 3 kg/mol and their blends. Solid lines represent fits to the

Lauritzen and Hoffman equation. Typical spherulites of C-PCL, L-PCL and their 95/5 blend are also shown. ..... - 248 -

Figure 8.5. Spherulitic growth rate (G) as a function of C–PCL content at selected crystallization temperatures (T_c) for 3 kg/mol samples. The solid lines represent a simple mixing rule. The unfilled symbols represent the values extrapolated from LH fittings to the data shown in Figure 8.4. ..... - 249 -

Figure 8.6. The K_g^G secondary nucleation rate constant derived by the fitting of the data of Figure 8.4 with the LH theory, as a function of the C–PCL content for 3 kg/mol C/L blends. ..... - 253 -

Figure 8.7. Overall crystallization rate ($1/\tau_{50\%}$) as a function of isothermal crystallization temperature for neat C–PCL and L–PCL and their blends: (a) 3 kg/mol and (b) 12 kg/mol.- 254 -

Figure 8.8. Values of $1/\tau_{50\%}$ as a function of C–PCL content at different constant values of T_c for C/L blends of (a) 3 kg/mol and (b) 12 kg/mol. The plots contains experimental data points indicated by filled symbols and values extrapolated from LH fittings to the data shown in Figure 8.7, indicated by unfilled symbols. ..... - 255 -

Figure 8.9. Examples of experimental DSC crystallization isotherms and their fittings with the Avrami equation for (a) C–PCL of 3 kg/mol at T_c=45 °C, L–PCL and C/L 95/5 of 3 kg/mol at 40 °C of 3 kg/mol and (b) C–PCL, L–PCL, C/L 90/10 of 12 kg/mol at 39 °C. ..... - 256 -

Figure 8.10. K_g^τ as a function of the C–PCL content for C/L blends of (a) 3 kg/mol and (b) 12 kg/mol. ..... - 257 -

Figure 8.11. Comparison between the final heating run after SSA thermal fractionation and the standard second heating scan for neat C–PCL and L–PCL of 3 kg/mol. The fractionation windows was of 3 °C. Red (top 2) and blue (bottom 2) curves represent neat C-PCL and L-PCL, respectively. ..... - 259 -

Figure 8.12. Final heating run after SSA thermal fractionation for neat C–PCL and L–PCL and their 90/10 C/L blends of 3 kg/mol. The fractionation window was of 3 °C. Red (top) and blue (bottom) curves represent neat C-PCL and L-PCL, respectively, whereas the green (middle) curve represents the 90/10 C/L blend. ..... - 260 -

Figure 9.1. Cooling and subsequent DSC heating scan for 50:50 and 40:60 PBSA copolymers. The arrows indicate the assignment of the peaks for PBS and PBA rich phases.[3] ..... - 269 -

Figure 9. 2. WAXS patterns obtained during heating the 60:40 PBSA from -40 to 95ºC at 10 ºC/min after cooling the sample until -40ºC at 50 ºC/min. ..... - 270 -

Figure 9.3. WAXS patterns of (a and b) 20:80 and (c) 40:60 PBSA copolymers taken during the heating after cooling at (a) 5 and (b and c) 50 ºC/min. ..... - 272 -

Figure 9.4. WAXS patterns of PBA taken during the heating after cooling at (a) 5 and (b) 50 ºC/min. The PBA at -40 ºC in (a) corresponds to the α phase, whereas in (b) to the β phase.- 273 -

Figure 9.5. Height and amplitude images taken at RT for all the samples.....- 275 -

Figure 9.6. Lorentz fitting for NMR curves for 80:20 and 20:80 PBSA.....- 276 -

Figure 9.7. (a) SAXS patterns (at different temperatures) and (b) DSC heating scan, of the 50:50 PBSA obtained during the heating after cooling the sample at 50 ºC/min. The d^* values are plotted in the left *y*-axis on (b). The heating scans (on SAXS and DSC) were performed at 10 ºC/min.....- 276 -

Figure 9.8. (a) SAXS patterns (at different temperatures) and (b) DSC heating scan, of the 40:60 PBSA obtained during the heating after cooled the sample at 1 ºC/min. The d^* values are plotted in the left *y*-axis on (b). The heating scans (on SAXS and DSC) were performed at 10 ºC/min. .....- 277 -

Figure 9.9. Micrographs of 50:50 PBSA at (a) -40 ºC and (b) 40 ºC, after previous cooling at 5 ºC/min. .....- 278 -

Figure 9.10. (a) First heating DSC scans for PPBS random copolymers, performed at 20 ºC/min. (b) T_m (*i.e.*, obtained from the first heating) as a function of PBS Content. .....- 278 -

Figure 9.11. (a) Cooling at 1 ºC/min and subsequent (b) heating scans at 20 ºC/min performed for the PPBS copolymers. .....- 279 -

Figure 9.12. (a) Cooling and subsequent (b) heating scans performed for the PPSA copolymers. The rate taken was 20 ºC/min.....- 279 -

Figure 9.13. WAXS patterns of (A) linear and star and (B) combs PPS-*co*-PES copolymers with fixed DP of 30. .....- 280 -

Figure 9.14. WAXS patterns of the samples taken at the indicated temperatures for (A) linear (a); (B) star-4 arms and (C) comb 15-arms copolymers with DP of 30. .....- 281 -

Figure 9.15. SAXS patterns of (A) linear (a); (B) star 4-arms; (C) comb 10-arms and (D) comb 15-arms copolymers with DP of 30 taken at the indicated temperatures. The *d**-value obtained from the maximum is labelled. .....- 283 -

Figure 9.16. TEM micrograph of isothermally crystallized PCL and PCL-g-lignin samples at 40, 35, 30 and 25°C for 6 h at each step for (a) PCL^{127} (b) $PCL_{29}^{13.7}$ (c) and (d) $PCL_6^{24.4}$....- 284 -

Figure 9.17. Spherulitic growth rate (G) as a function of crystallization temperature (T_c) for PLA and its nucleated compounds. .....- 286 -

Figure 9.18. Micrographs taken for PLA and its blends at the indicated temperatures (i.e., 130, 125 and 122 ºC). .....- 287 -

Figure 9.19. (a) WAXS patterns during the heating at 122 ºC after previously cooled the sample at 2 ºC min^{-1} (b) SAXS *d*-spacing obtained during heating at 5 ºC/min. .....- 288 -

Figure 9.20. Reduced shear storage (G'_{bT}) modulus versus reduced angular frequency (ω_{aT}) of the materials studied at T_R=70 °C. (a) PCL_xM_y and (b) PCL_xNH_y. 294
Figure 9.21. Reduced magnitude of the complex viscosity ($|\eta^*|\ b_T/a_T$) versus reduced angular frequency of the materials studied at T_R= 70 °C. (a) PCL_xM_y and (b) PCL_xNH_y..... 295
Figure 9. 22. Power law exponents of G' and $|\eta^*|$ obtained by fitting of the lowest frequencies. 296
Figure 9.23. (a) Magnitude of the complex viscosity *versus* magnitude of the complex modulus of selected samples: (○) $PCL_{99.75}M_{0.25}$, (▽) $PCL_{99.5}M_{0.5,}$ (◇) $PCL_{99}M_1$, (●) $PCL_{99.75}NH_{0.25}$, (▼) $PCL_{99.5}NH_{0.5,}$ (◆) $PCL_{99}NH_1$. Lines represent the converted creep results to oscillatory data. (b) Extrapolation procedure using the creep results applied to obtain $|G^*|_0$ when $1/|\eta^*|\rightarrow 0$. 297
Figure 9.24. (a) Shear creep compliance, J_c, as a function of creep time for selected materials at T=70 °C. Applied shear stress, τ_0: (○) 6.25 Pa, (□) 12.5 Pa and (△) 25 Pa for PCL and (■) 50 Pa, (●) 75 Pa and (▲) 100 Pa for $PCL_{99}M_1$. Dotted lines indicate the extrapolated slope of the flow region for PCL. (b) Shear creep compliance, J_c, as a function of creep time at T=70 °C for pure PCL (dashed line); MWCNT samples: (○) $PCL_{99.75}M_{0.25}$, (▽) $PCL_{99.5}M_{0.5,}$ (◇) $PCL_{99}M_1$; and the NH samples (●) $PCL_{99.75}NH_{0.25}$, (▼) $PCL_{99.5}NH_{0.5,}$ (◆) $PCL_{99}NH_1$. The curves of the samples with 0.5 and 1 wt% MWCNT content in (b) have been vertically shifted for a better visualization, as indicated in the graph. .....- 298 -
Figure 9.25. Linearization of the compositional dependence of the yield 'plateau' modulus for the systems under study. The line is the best fit to eq. 9.1. .....- 300 -
Figure 9.26. Reduced magnitude of the complex viscosity, obtained from oscillatory and transformed creep experiments, *versus* reduced angular frequency of selected samples: (□) PCL, (○) $PCL_{99.75}M_{0.25}$, (▽) $PCL_{99.5}M_{0.5,}$ (◇) $PCL_{99}M_1$, (◁) $PCL_{97}M_3$, (solid line) $PCL_{99.75}NH_{0.25}$, (dashed line) $PCL_{99.5}NH_{0.5}$, (dotted line) $PCL_{99}NH_{1,}$ (dash-dotted line) $PCL_{97}NH_3$. .....- 301 -
Figure 9.27. DSC (a) cooling and (b) second heating curves for neat polycarbonate (PC) and the 73/(23/4) w/w PBS/(PC/MWCNTs) nanocomposite. The zoomed regions correspond to the crystallization (see a) and melting (see b) of PC in the nanocomposites and its absence in the neat PC. .....- 303 -
Figure 9.28. Heating of PCL and PBS after isothermal crystallization at 41 and 90.5 ºC, respectively. .....- 304 -
Figure 9.29 DMA (a) loss modulus (E'') and (b) tan δ curves for the PCL based blends. ...- 305 -
Figure 9.30. Glass transition temperatures of neat PCL and the PCL/(PC/MWCNT) nanocomposites as a function of MWCNT content. .....- 305 -
Figure 9.31. DMA (a) loss modulus (E'') and (b) tan δ curves for the PBS-based blends. .- 305 -

Figure 9.32. Glass transition temperatures of neat PBS and the PBS/(PC/MWCNTs) nanocomposites as a function of MWCNTs content (The corresponding PC content is indicated in the top x-axis). The Fox extrapolation T_g data was obtained using the *tan* δ values. .....- 306 -
Figure 9.33. SEM micrographs for the PCL/(PC/MWCNT) nanocomposites, respectively, containing (a) 1.0, (b) 2.0, and (c) 4.0 wt % MWCNTs.....- 307 -
Figure 9.34. Figure 8. High and low magnification TEM micrographs for (a,d) 1.0 wt %, (b,e) 2.0 wt %, and (c,f) 4.0 wt % MWCNTs in the PCL/(PC/MWCNT) nanocomposites.....- 308 -
Figure 9.35. (a) Low and (b,c) high magnification AFM phase images for the 73/(23/4) *w*/*w* PCL/(PC/MWCNT) nanocomposite. .....- 309 -
Figure 9.36.(a) DSC cooling scans for neat PBS after 5 min at the indicated T_s, and (b) subsequent heating scans after the cooling runs shown in (a).....- 309 -
Figure 9.37. (a) Overall half-crystallization rate (the solid lines indicated the Lauritzen and Hoffman fitting); (b) Normalized crystallization constant of the Avrami model ($k^{1/n}$) and (c) Avrami index (n) as a function of the isothermal crystallization temperature (T_c) for all the samples..... 313
Figure 9.38. Stress-strain curves for neat PBS and the nanocomposites.....- 316 -
Figure 9.39. Final heating scan run after SSA thermal fractionation for C and L-PCLs and their C/L blends of 3kg/mol. The fractionation window was 3 ºC. Red and blue curves represent C-PCL and L-PCL, respectively, whereas green curves represent the C/L blends. - 319 -

CHAPTER I
GENERAL INTRODUCTION AND OBJETIVES

1.1 GENERAL INTRODUCTION

Polymers have been developed in order to substitute natural and synthetic products, as well as provide new products which respond to specific applications. In the family of thermoplastics, polyolefins are the simplest in terms of composition; additionally they are extremely versatile, and can be used to obtain a wide range of products. However, due to their nature (*i.e.*, they are petroleum derivatives whose chains are non-biodegradable) and their easy production, pollution problems have been created. The extensive use of polyolefins have created disposal problems that are not easily solve because their low degradation rates. Therefore, nowadays some researchers are focused on the substitution of polyolefins through the creation of versatile products which can be also biodegradable and extensively used in a wide range of applications.

A wide range of new materials has been developed or improved in order to find suitable substitutes to the oil derivatives. Besides this motivation, new materials have been created for technologically and biomedical applications, as well.

Taking into account the necessity to provide materials which respond to specific targets, several advances have been done in different fields. For instance, from the point of view of synthesis, new complex initiators, catalizers, additives, among others, as well as new techniques of synthesis have been developed. Such advances have resulted in the production of new homopolymers and copolymers with different comonomer distribution, as well as different chain topologies. On the other hand, additives such as new plasticizers and nucleating agents or polymers that have these functions, and nanomaterials have been developed, allowing the introduction of new blends of polymers and additives with the aim to tailor properties for specific applications.

In general, as the complexity of the material is increased, the complexity in their behaviour increases as well. As expected, the potential use of these materials requires a deep comprehension of their behaviour.

As was mentioned above, there are many forms in which new materials can be obtained, either by the creation of them or by the improvement of materials that already exist. For instance, the distribution of comonomer sequences in a copolymer (*i.e.*, random, gradient, block, grafted, among others), the molecular architecture, (*i.e*., star, comb, eight-shape, among others) as well as the topology (*i.e*., cyclic and linear topologies), and the blend of polymeric matrix with nanofillers (*e.g*., in order to create nanocomposites) are only some of the most common ways to modified polymeric materials reported in the literature. These modification strategies can produce materials with different final properties. At the same time, such modifications also change the behaviour of the materials, bringing questions related to their influence in the final behaviour.

It is well know, that the crystallization behaviour is directly related to the final properties of the materials and can be evaluated without large quantities of material, therefore a way to understand any modification in new materials is through their structural, morphological and thermal characterization, and depending on the obtained properties, these materials could be further developed, or discarded.

The main aim of this PhD. thesis is to determine how the changes in the length of crystallizable sequences in random copolymers, the inclusion of small groups or even grafted chains on the main chain, the molecular architecture as well as the molecular topology and the type of nanofillers (*e.g.*, carbon nanotubes in blends) influences the properties of these multiphasic systems, with at least one crystallizable component. In order to determine this influence, the structure, morphology and thermal properties with special emphasis on the crystallization behaviour will be assessed.

The base materials selected for the present work are mainly biodegradable materials, like poly (ε-caprolactone), poly (butylene succinate) and polylactide. In addition, poly (propylene sulfide) and poly (ethylene sulfide) are investigated due to their medical applications.

The relevance of the current research in these subjects will be presented in the following chapters: *IV*. Crystallization of random copolyesters: Isodimorphic behaviour; *V*. The influence of chain primary structure and topology (branching) on crystallization and thermal properties. *VI*. Nucleation efficiency and crystallization of Lignin-based materials; *VII*. Biodegradable polymers/carbon nanotubes blends and *VIII*. Cyclic and linear polymers and their blends.

1.2 OBJECTIVES

GENERAL OBJETIVE

The aim of this work is to study the structure, morphology and thermal properties, as well as crystallization kinetics of multiphasic polymeric systems. In order to fulfill this objective, the following systems were selected: random biodegrable copolyesters with crystallizable parent components, statistical and semi-random copolymers with a crystallizable and non-crystallizable components based on sulfides and with different molecular architecture (linear, star and comb); lignin based materials (PCL-*g*-lignin and PLA/lignin and PLA/talc blends), blends of commercial biodegradable polymers with commercial MWCNT masterbatch and blends of biodegradable polymers with cyclic and linear topologies.

SPECIFIC OBJECTIVES

Random Copolyesters

- To determine the crystallization mode (isomorphism, isodimorphism and comonomer exclusion) of the random copolyesters.
- To analyze the rate-dependent behavior of PBS-*ran*-PBA at intermediate compositions.
- To analyze the influence of the odd-even effect in the crystallization mode of random copolymers in PBA-*ran*-PPA and PBS-*ran*-PPS

Poly (propylene sulfide-co-ethylene sulfide) statistical and semi-random copolymers with different molecular architectures (linear, stars and combs)

- To determine the influence of the molecular architecture on the thermal properties of the copolymers.
- To determine the influence of the comonomer addition protocol on the thermal properties of the copolymers.

Lignin-based materials

- To determine how the incorporation of lignin can affect the thermal properties, nucleation efficiency and crystallization kinetics of PCL-*g*-lignin materials and PLA/lignin blends.

Blends of biodegradable polymers with MWCNT masterbatch

- To determine how the thermal properties, nucleation efficiency and crystallization kinetics of PCL are affected by the incorporation of MWCNTs in: PCL/MWCNT nanocomposites and PCL/f-MWNCNT nanohybrids.
- To determine how MWCNTs can affect the thermal properties, nucleation efficiency and crystallization kinetics in PBS/(PC/MWCNT) and PCL/(PC/MWCNT)

Blends of biodegradable polymers with cyclic and linear topologies

- To determine the influence of the topology in the thermal properties, morphology and crystallization kinetics of cyclic/linear PCL blends.

CHAPTER II .

GENERAL CONCEPTS

The main focus of this thesis is to study the structure, morphology and crystallization behavior of different multiphasic materials, therefore basics concepts on the structural analysis of the materials, crystallization as well as the main crystallization theories, are going to be explained in this Chapter. Additionally, the main features of advanced differential scanning calorimetry (DSC) techniques, such as Self-Nucleation (SN) and Successive Self-nucleation and Annealing (SSA) are going to be described. A specific introduction related to the specific multiphasic system under study will be presented in each Chapter (IV to VIII) of the Results and Discussion.

2.1 Semicrystalline Polymers and their models

The crystallization of polymers occurs far from the equilibrium. This behaviour has been attributed to the long chain nature of polymers, which make them difficult to disentangle and to achieve a regular conformation, aligning chains parallel to each other forming ordered crystallites. These factors are the origin of the semicrystalline nature of polymers: only a fraction of the units composing the long chains is able to attain the ordered arrangement required by the crystalline phases.[1] X-ray diffraction experiments have demonstrated that polymers never crystallize 100%, hence they are always semi-crystalline. [2]

In order to describe the semicrystalline character of the polymers, some models have been proposed. Among them, the most important are: fringe-micelle and chain folded models, which are described as follow:

2.1.1 Fringed micelle-model

It is essentially based on a two-phase system, characterized by crystalline and amorphous regions. The crystalline regions are composed by stacks of short lengths of different macromolecular chains, aligned parallel to each other. In contrast, the amorphous region is constituted by disordered sequences, which can be interconnected

by two different ordered portions of the chain. The key feature in this model is that one molecule participates in more than one crystallite (see Scheme 2.1) since the molecular contour length (typically around 100 nm) is at least ten times longer than the experimentally measured size of crystallites. The model easily accounts for the dissipation of molecular order from the crystalline to the amorphous regions; it also explains the mechanical properties of semicrystalline polymers based on the physical linkages (fringes) between ordered regions.[1] The model also explains the existence of fibrillar crystallites and predicts their growth direction normal to the chain axis.[3] However, this model is clearly inadequate to justify the development and optical properties of more complex morphologies entities, such as the spherulites, usually found in melt crystallized polymers.[1]

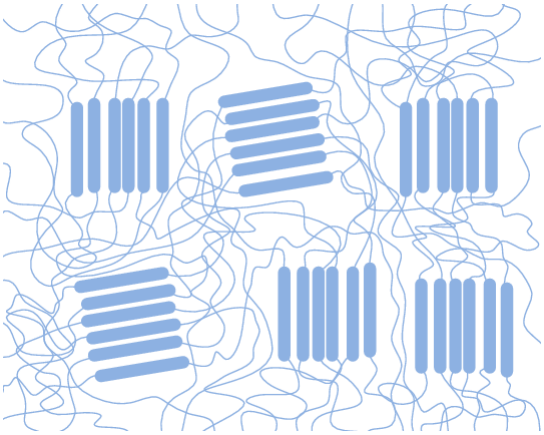

Scheme 2.1. Illustration of the fringed micelle model.[3]

2.1.2 Chain folded model

Chain folding was first introduced by Storks in 1938. However, his proposal was unnoticed by the scientific community.[2]

In 1957, three independent articles published by Keller, Till and Fisher reported that single crystals were 10 nm thick platelets with regular facets and with the chain direction perpendicular to the lamellar surface. Therefore, Andrew Keller postulated chain folding to the fact that crystal lamellae were much thinner than the length of the polymer chain (see Scheme 2.2).[2] The origin of chain folding has been assigned to intramolecular secondary crystal nucleation at the crystal growth front, characterized by a lower free-energy barrier than for intermolecular secondary nucleation. [4]

The folded chain model were based on the adjacent re-entry concept, where chain are assumed to come back and forth into one lamella and form loops with identical lengths (see Scheme 2.2a).[3]

Shortly afterwards, the "switchboard model" (see Scheme 2.2b) was proposed. In this model an irregular re-entry model based on variable lengths of chain loops (see Scheme 2.2b) in the lamella was proposed. These chains are proposed to enter in neighbouring crystals.[3]

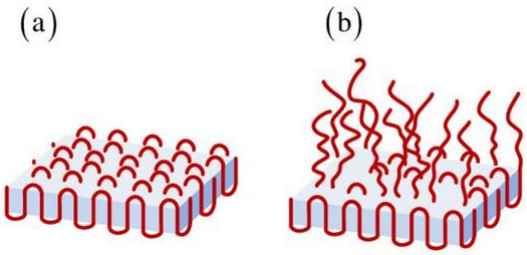

Scheme 2.2.A schematical view of a lamella in (a) adjacent re-entry and (b) switchboard models. [3]

The switchboard model with a total random reentry is physically impossible, as chain packing in the interfacial region would lead to unfeasible density values. In the crystallization from the melt, chain folding still prevails, but not necessarily with tight adjacent chain folding and with chains that can meander from one lamella to a neighboring lamella (tight chains).

The crystallization process can occurs from solution or from the melt state. In the former, the molecules which add to a growing single crystal from a dilute solution are not in strong competition with other polymer molecules. In contrast, crystal growth from concentrated molten state is very different, since the molecules are entangled and any polymer molecule could add to several specific crystal surfaces simultaneously. Melt-grown crystals have the same shape as solution-grown single crystals in most respects. They are lamella-shaped with a thickness-to-width ratio of 0.01-0.001. A typical feature of melt crystallized samples, is the crystal stack. The lamellae of the stacks are almost parallel and the amorphous component is located in the space between the crystal lamellae.[2] Melt crystallization however is characterized by the radial growth of lamellae in spherical units termed spherulites.

The crystallization process in this work is studied by X-ray diffraction, DSC techniques and the application of analytical crystallization theories, which are explained below.

2.2 Polymer Crystallization

The crystallization of polymers can be divided in (a) Primary and (b) Secondary crystallization.

(a) Primary Crystallization: The process leading to the formation of ordered phases in an undercooled isotropic polymer melt is usually classified as primary crystallization. This process results in a partially crystalline solid. The primary crystallization consists of two different steps: nucleation (*i.e.*, primary nucleation) and growth (*i.e.*, secondary nucleation). Primary nucleation can occur by spontaneous aggregation of polymeric chain segments (homogeneous nucleation) or by the attachment of chains into existing heterogeneities (heterogeneous nucleation), a process characterized by a much smaller free energy barrier than that of homogeneous nucleation. After primary nuclei are formed, these grow by secondary nucleation processes of chains that progressively attach to the existing nuclei. The process of secondary nucleation is also referred to as polymer crystal growth. When a polymer crystallizes from the melt, primary crystallization ends when spherulites impinged on one another. This typically occurs around the half-crystallization time of the entire overall crystallization process.

(b) Secondary Crystallization: After spherulites impinged on one another, the crystallization process slows down and several complementary processes can happen: the crystallization of intraspherulitic material, in-filling of spherulites through the secondary nucleation of daughter lamellae (intra-spehulitic crystallization), and thickening of previously formed lamellae. Additionally, the refinement of existing crystals, through the removal of lattice distortions, and a combination of thickening and re-crystallization are also possible.

2.3 Morphological and Structural Analysis of Materials: Small and Wide-Angle X-rays Scattering (SAXS and WAXS), synchrotron radiation and microscopy techniques

In polymer science, the term *morphology* generally refers to form and organization on a size scale above the atomic arrangement but smaller than the size and shape of the whole sample. The term *structure* refers to the local atomic and molecular details. The characterization techniques used to determine structure differ somewhat from those used to determine morphology, although there is some overlap, as a result the terms *morphology* and *structure* are commonly used interchangeably. On one hand, X-ray, electron and optical scattering techniques and a range of other analytical tools are commonly applied to determine the *structure* of polymers. X-rays scatterings for example, permits the determination of interatomic ordering and chain packing.[5] On the other hand, the *morphology* of polymers is determined by a wide range of optical, electron and scanning probe microscopy techniques.[5]

Polymers crystallize only partially (in fact crystalline polymers are more correctly termed *semycristalline* as their measured densities differ from those obtained for perfect crystals [5]) and exhibit a nanoscopic semicrystalline morphology, which determines their macroscopic properties. The simplest crystallization case is when during crystallization from the melt, thin crystalline lamellae with thickness d_c grow separated by amorphous regions with thickness d_a. The sum of both is the long period L, with a typical size on the order of a few nm (*e.g.*, 10 nm) (see Scheme 2.3)

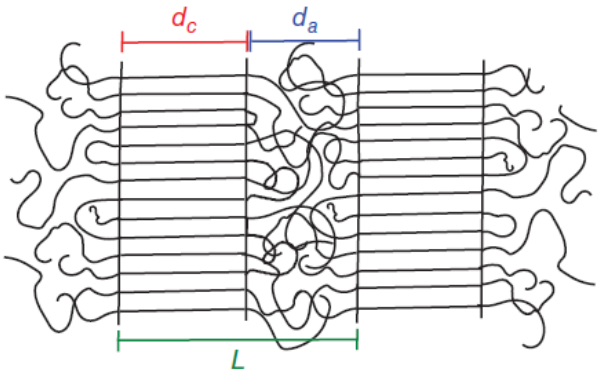

d_a=amorphous thickness

d_c=crystalline thickness

L=long period=d_a+d_c

Scheme 2.3. Schematic of the lamellar structure of a semycristalline polymer, consisting of crystalline lamellae with thickeness d_c and amorphous regions with thickness d_a. The long period is $L=d_a+d_c$

Typically after crystallization from quiescent melt, the lamellar stacks are part of larger spherulitic superstructures (they consist of a great number of lamellar crystals and lamellar stacks, and its size ranges from 0.5 μm to several milimiters[2]) and are isotropically distributed within the sample. Such morphology can be evaluated by several techniques like polarized light optical microscopy (PLOM), Atomic Force microscopy (AFM), scanning (SEM) and electron microscopy (TEM), which give detailed qualitative insights about semicrystalline morphology typically from a small part of the sample. [6]

The spherulites are microscopic units or structures with spherical optical symmetry [2] which compose the bulk crystallized material. Their name derives from the Greek word for ball or globe. [2] These structures exhibit radial symmetric growth of the lamellae from a central nucleus with the molecular chain direction perpendicular to the growth direction. The polymer chains therefore run tangential to the spherulite radius. A schematic representation is shown in Scheme 2.4.

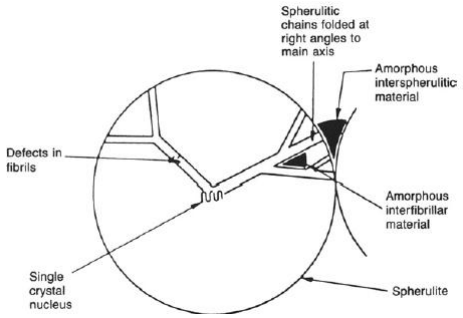

Scheme 2.4. Schematic of spherulite structure.[5]

The structure consists of radiating lamellae with amorphous material between the lamellae and between individual spherulites. Although the shape of the growing spherulites is round, spherulites generally impinge upon one another during cooling, resulting in polyhedral shapes in the final product.[5]

There are certain features of the spherulites which can be studied by polarized optical light microscope. These features are: the maltese cross pattern, the sign of the spherulite and the banding pattern.

If we consider the radial growth of lamellae, then a spherulite has two refractive indices: the tangential (n_t) and radial (n_r) refractive indices. Therefore the sign of a spherulite can be defined. [2] The origin of these refractive indices is that polymer crystals are highly anisotropic in electron density because they have strong covalent bonds along the chain axes, whereas laterally the cohesion of the crystals is achieved by much weaker bonds, like Van der Waals or hydrogen bonds. This anisotropy explains the change in refractive index, *n*. The anisotropy of molecular chains can be explained by the refractive index ellipsoid (see Scheme 2.5)

The indicatrix of a crystal can be defined as an ellipsoid whose radii indicate the magnitude of the refractive index for light vibrating parallel to the radial direction. For isotropic media, the indicatrix is a sphere; for uniaxial crystals (like birefringent crystals typically formed by polymers) it is an ellipsoid of revolution with the optic axis as the rotational axis. The light that passes through a polarizer A can be considered as separated into two components vibrating parallel to the optic axis (extraordinary ray) and normal to the optic axis (ordinary ray). After traversing a uniaxial crystal with thickness "*a*", the two rays have a phase difference Δ (given in degrees), determined by the thickness of the crystal and the refractive index difference; $\Delta = 360\ a\ (n_o - n_e)/\lambda$, where λ is the wavelength of the light. The conditions for light extinction in between crossed polars are:[7]

Isotropic effect: the matter/crystal is optically isotropic, like in amorphous materials (unoriented), cubic crystals or an accidental coincidence of refractive indices.

Thickness compensation: The phase difference Δ is a multiple of 180°

Amplitude Zero effect: The indicatrix is aligned in such a way, that one of its axis is parallel to the polarizer or analizer. In this case, the ray of the second component has an amplitude equal to zero. This is the origin of the Maltese Cross.

Zero Birefringence effect: The indicatrix is aligned in such a way that the light ray travels parallel to the optic axis and the refractive indices are equal in all vibration directions. This is the effect that originates the banding extinction pattern in spherulites.

Accidental effect: several birefringent structures overlap and cause an orientation or compensation effect.

Negative spherulites with $n_t > n_r$ have a higher proportion of the chains in the circumferential planes than along the radius of the spherulites, in this case the second

and fourth quadrants of a spherulite are blue. Conversely, when the first and third quadrants of a spherulites are blue, the spherulite is considered positive ($n_t<n_r$).[2, 8]

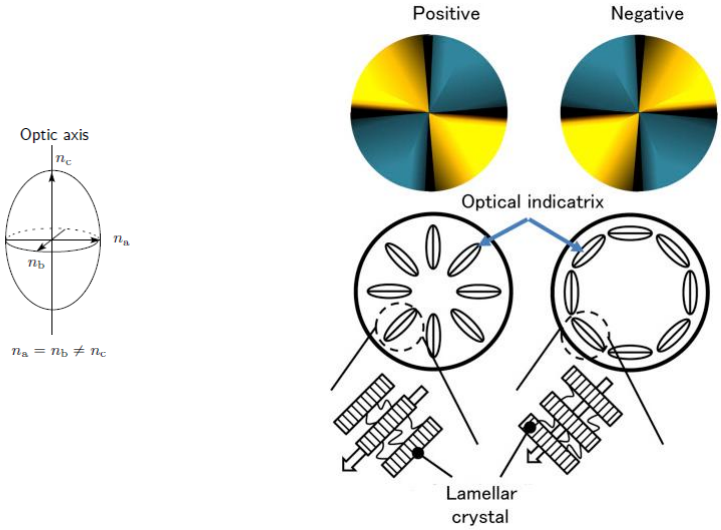

Scheme 2.5. Models of positive and negative spherulites. The optical ellipsoid is represented on the left.[8]

In addition to the sign of the spherulites, another feature that can be detected is the presence of unbanded and banded (ring-banded) spherulites. This feature is basically an extinction pattern. The extinction occurs when the direction of the optical axis (molecular chains) is parallel to the trayectory of the polarized light (see Scheme 2.6). It is commonly believed that the periodic extinction of ringed spherulites is produced by lamellar twisting along the radial direction during crystal growth (see Scheme 2.6), although other hyphothesis can be found in the work of Woo and Lugito. [9]

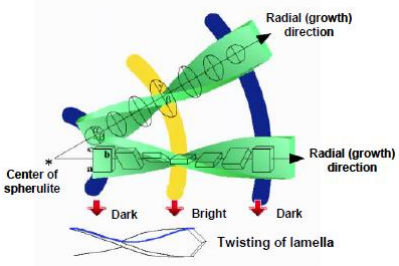

Scheme 2.6. Schematic representation of the lamella twisting and the periodic extinction pattern in polyethylene.

Banding often appears in polyethylene samples as well other materials, which have been crystallized at a relatively high degree of supercooling, *i.e.*, at low temperatures.[2]

SAXS

Small-Angle X-ray Scattering (SAXS) is able to give representative quantitative information about the structure, obtained from an average over macroscopic samples. Generally, features on a length scale of 1 to 100 nm are accessible by SAXS, which corresponds to the typical size for the structure parameters of semicrystalline polymers. It is worth noting that the X-rays used in diffraction have wavelengths lying approximately in the range of 0.5-2.5 Å, whereas the wavelength of visible light is of the order of 6000 Å. X-rays therefore occupy the region between gamma and ultraviolet rays in the complete electromagnetic spectrum (see Scheme 2.7).[10]

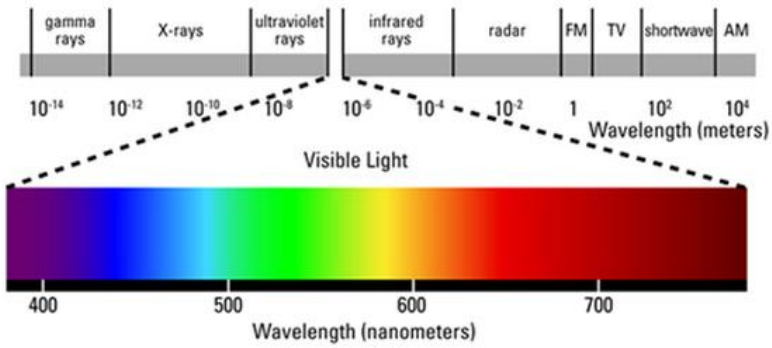

Scheme 2.7. Electromagnetic spectrum.

WAXS

The X-ray region in Scheme 2.7, not only allows studying SAXS but also WAXS. The Wide-Angle X-ray scattering (WAXS) or Wide-Angle X-ray diffraction (WAXD) is an x-ray technique that is often used to determine the crystalline structure of different materials including polymeric materials. This technique specifically refers to the analysis of Bragg peaks scattered to wide angles ($2\theta > 1^{\circ}$) which by Bragg´s law implies that they are caused by subnanometer–sized structures.[11]

The expression of Bragg´s law was derived by the English physicist Sir W.H. Bragg and his son Sir W.L. Bragg in 1913 to explain why the cleavage faces of crystals appears to reflect X-rays beams at certain angles of incidence. Their observation is an example of X-ray wave interference.

The law states that when the x-ray is incident onto a crystal surface, its angle of incidence, θ, will reflect back with a same angle of scattering, θ. And, when the path difference, d is equal to an integer number, n, of wavelength λ, a constructive interference will occur. In other words, Bragg´s law provides the condition for a plane wave to be diffracted by a family of lattice planes, as is show in Equation 2.1

$$2d \sin\theta = n\lambda \qquad \text{Eq. 2.1}$$

where d is the interplanar spacing (path difference), θ the angle between the wave vector of the incident plane wave and the lattice planes (the angle between incident ray and the scatter plane), λ is the wavelength and n is an integer, the order of the reflection.

Since in the WAXS studies, amorphous structures yield scattering halos (broad peaks) whereas crystalline structures are characterized by Bragg peaks (see Figure 2.1), WAXS is therefore a good monitor of crystallinity in the sample.

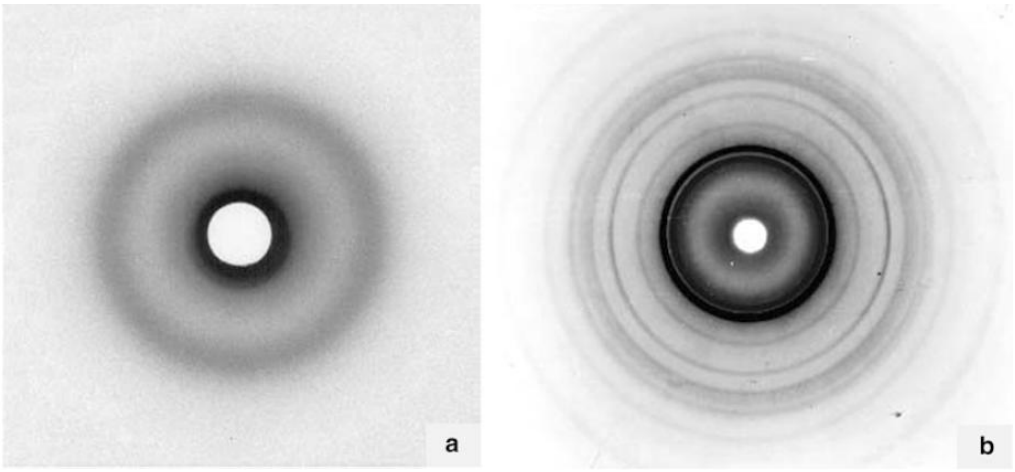

Figure 2.1. WAXS from (a) polystyrene, showing a diffuse halo from amorphous sample and (b) highly crystalline polyethylene, showing sharp “powder” rings. [11]

WAXS patterns can be resolved intro contributions from crystalline and amorphous reflections. The degree of crystallinity is then calculated as:

$$X_c = \frac{I_c}{I_c + I_a} \qquad \text{Eq. 2.2}$$

In Equation 2.2, I_c is the diffracted intensity from all resolved crystalline reflections, I_a the diffraction intensity under the amorphous halo and (I_c+I_a) the total intensity. It is worth noting that the crystallinity degree can be calculated by DSC experiments, as well, as is shown in Equation 2.3.

$$X_{c,DSC} = \frac{\Delta H_f}{\Delta H_f^0} \qquad \text{Eq. 2.3}$$

where ΔH_f is the measured heat of fusion and ΔH_f^0 is the heat of fusion of 100% crystalline polymer.

By knowing X_c and the long period (L) determined by SAXS, a rough approximation of the average lamellar thickness (l) of the material can be obtained as follow (see Equation 2.4):

$$l = X_c . L \qquad \text{Eq. 2.4}$$

Other forms to obtain the lamellar thickness are going to be shown below. In fact, from the analysis of SAXS patterns, there are specific functions that can be applied in order to deconvolute the SAXS pattern.

Correlation Function and Interface Distribution Function

The morphology of a semicrystalline polymer can be described as a lamellar two-phase system consisting of crystalline and amorphous phases with different electron densities and with sharp boundaries between them. This structure gives rise to a peak in the scattering intensity at scattering vector, *s*, from which the average long period, *L*, can be determined.[6]

The correlation function considers that typically the lateral dimensions of the lamellar stacks in the sample are large compared to the interlamellar distance *L*; therefore, only the electron density distribution along the normal of the lamellar stacks, here denoted as *z*-direction, changes within the relevant length scale of SAXS experiments (1-100 nm). Scheme 2.8 shows the structure of an ideal lamellar stack and the corresponding electron density along the *z*-direction. The crystalline regions have a

higher electron density ρ_c than the average value ρ, whereas the amorphous parts have a lower electron density ρ_a. [6]

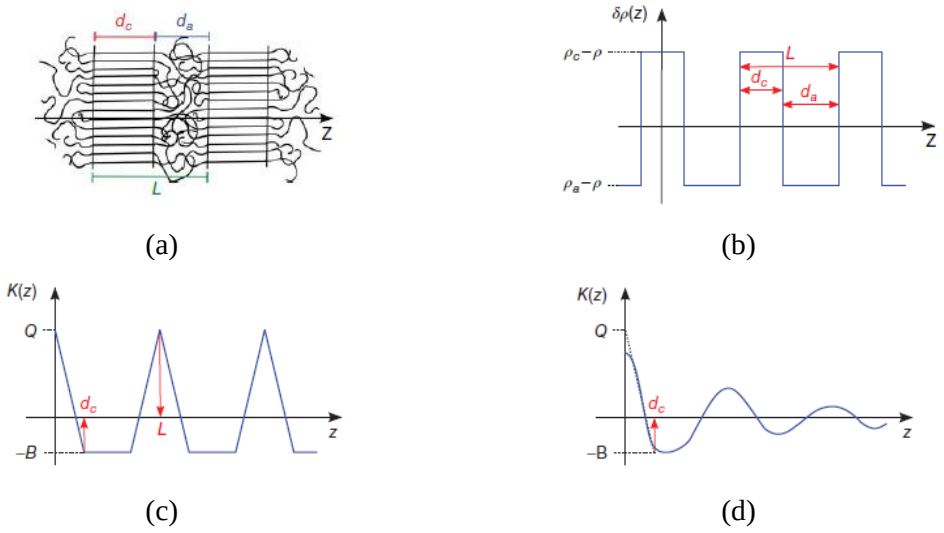

Scheme 2.8. (a) Ideal lamellar stack with *z*-direction along the lamellar normal; (b) Electron density difference along *z*-direction; (c) Correlation function for an ideal lamellar stack and (d) Effect of deviations from ideality. [6]

In Scheme 2.8c, the so-called "self-correlation triangle" is shown centered at the origin reflecting the electron density correlation within a lamella. *Q* (maximum value of *K(z)* on Scheme 2.8c) does not depend on the detailed structure; therefore, *Q* is often called the invariant. Scheme 2.8c also shows that *K*(z) decreases linearly to a minimum value, namely the baseline, *B*. If the crystallinity is smaller than 50% (θ_c<0.5) this minimum position correspond to the crystalline thickness d_c. Otherwise, it correspond to the amorphous thickness d_a and θ_c have to be replace by θ_a=1-θ_c. [6]

The second maximum in *K*(z) is located at the long period *L*. It is worth noting that in a real system, deviations from the ideal structure exist, for example variations of the lamellar and crystalline thickness or diffuse interphases.[6] This is illustrated in Scheme 2.8d. In this case, around the origin *K*(z) is flattened and the first minimum does not necessary reach the value of the baseline anymore. In addition, higher order maxima of *K*(z) are damped due to thickness variations of the crystalline and amorphous phase, leading to an overestimated long period. [6]

The one-dimensional correlation function *K*(z) can be calculated directly from *I*(*s*), and is expressed as in Equation 2.5. For more details of its devivation, see reference [6]

$$K(z) = 2\int_0^{\infty} 2\pi s^2 I_{abs}(s)\cos(2\pi sz)ds \qquad \text{Eq.2.5}$$

In order to overcome the drawbacks of applying *K*(z), another way of analyzing SAXS data of a lamellar two-phase system is the interface distribution function. For an ideal lamellar two-phase system, the second derivative of the one-dimensional correlation function *K´´*(z) has only contributions at positions that correspond to the distance of any two-interphases, with the first three giving the structure parameters d_a, d_c and *L*.[6] Scheme 2.9 shows the correlation function and the first and second derivative *K´*(z) and *K´´*(z).

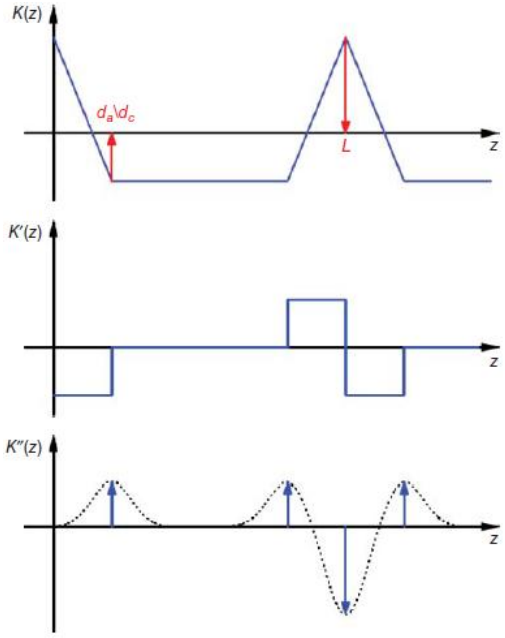

Scheme 2.9. Correlation function *K*(z) for an ideal lamellar stack (see Scheme 2.8a) and the first and second derivatives *K´*(z) and *K´´*(z). Deviations from the ideal lamellar structure lead to a broadening (dotted line) of the δ-peaks (arrows).[6]

K´´(z) can be described as a sum of distribution functions, where h_c(z) denotes the distribution of crystalline thicknesses and h_a(z) the distribution of amorphous thicknesses. h_{ac}(z) is the distribution of the long period, that is, one amorphous plus one crystalline thickness. [6] The *K´´*(z) is expressed as follow:

$$K''(z) = 16\pi^3 \int_0^{\infty} \left[\lim_{s\to\infty} I_{abs}(s)s^4 - s^4 I_{abs}(s)\right]\cos(2\pi sz)ds \qquad \text{Eq. 2.6}$$

The functions shown above (Equations 2.5 and 2.6) allow obtaining the mentioned parameters which can be important for polymer characterization. Figure 2.2 shows experimental results for PCL, in which information about the crystallinity was necessary in order to assign the crystalline and amorphous peaks.

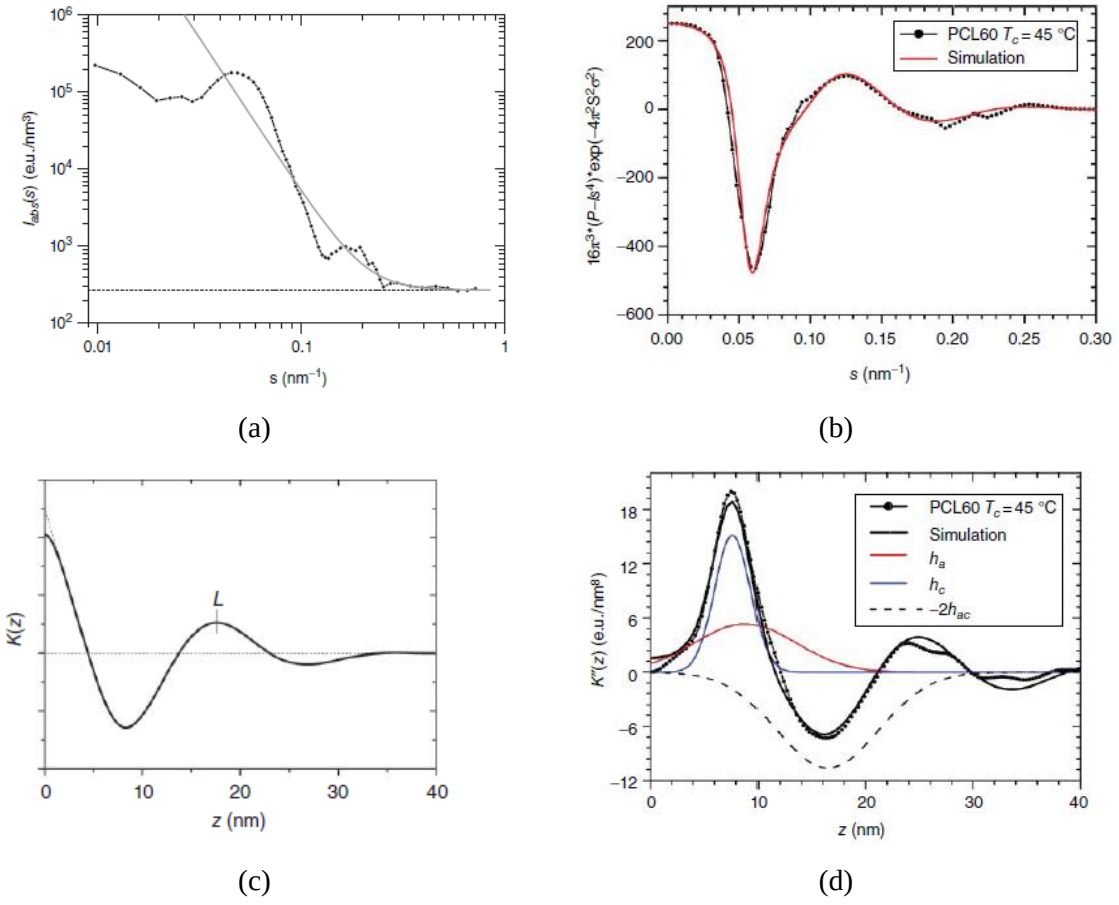

Figure 2.2. (a) Scattered intensity (black dotted line) of PCL with Porod fit (light gray line). The continuous line gives the sum of the Porod scattering and a background (dashed line) due to density fluctuations. (b) Function $16\pi^3[P\text{-}Is^4]w$ as calculated from $I(s)$ (dotted lines). The continuous line is the result of the simulation giving the result d_a=8.80 nm, σ_a=4.20 nm, d_c=7.65 nm and σ_c=0.85 nm. (c) Correlation function and (d) Resulting interface distribution function $K''(z)$ after a discrete cosine transformation (dotted lines) and simulation (thick continuous line). For the simulation the first three contributions h_a, h_c and $-2h_{ac}$ are indicated additionally.[6]

It is important to remark that from the raw data the scattering intensity as a function of the scattering vector is needed (see Figure 2.2a), which is fitted with the Porod fit, and then a discrete cosine transformation is applied. In this way the interface distribution function can be calculated. Moreover, the crystalline and amorphous

thickness (d_c and d_a, respectively) as well as their distributions (σ_c and σ_a, respectively) are obtained.

2.4 Crystallization theories

There are two general categories for studying crystallization kinetics of polymers: bulk or volumetric analysis, and crystal growth analysis. [12] In this work, the Avrami theory which works to analyze the bulk growth and the Lauritzen and Hoffman theory with the crystal growth are going to be used in Chapters VI-VIII, and are described below:

Avrami Theory

The Avrami theory works to analyze partially the bulk growth, since it assumes that the volume does not change (note that a polymer tends to shrink during crystallization), and it do not take into account the secondary crystallization and crystal perfecting. [12] The Avrami theory cannot perfectly describe the entire overall crystallization kinetics of a polymer material, nevertheless it provides an easy to use analytical expression that is able to fit the data, at least in the primary crystallization range.

The Avrami equation was developed to quantify the transition between liquid-solid states. Therefore, such equation is useful in the crystallization of polymers, since they go through melt to crystalline state. The Avrami equation can be expressed as follow:[13]

$$1 - V_c(t - t_0) = \exp(-K\,(t - t_0)^n) \qquad \text{Eq. 2.7}$$

where t is the experimental time, t_0 is the induction time, V_c is the relative volumetric transformed fraction, n is the Avrami index, and K is the overall crystallization rate constant. Note that the term 1-V_c corresponds with the amorphous fraction, and it adopts the value of 1 when the crystallization has not started, but it starts when 1-V_c<1.

From Equation 2.7, the relative volumetric transformed fraction can be calculated (see Equation 2.8) as:

$$V_c = \frac{W_c}{W_c + \left(\frac{\rho_c}{\rho_a}\right)(1 - W_c)} \quad \text{Eq.2.8}$$

where ρ_c and ρ_a are the fully crystalline and fully amorphous polymer densities, respectively, and W_c is the crystalline mass fraction that can be calculated (see Equation 2.9) as:

$$W_c = \frac{\Delta H(t)}{\Delta H_{total}} \quad \text{Eq.2.9}$$

where ΔH_{total} is the maximum enthalpy value reached at the end of isothermal crystallization process and $\Delta H(t)$ is the enthalpy variation as a function of the time spent at a given crystallization temperature. Both above mentioned enthalpy values are obtained by integration of the experimental isothermal data.

In order to obtain the Avrami parameters, Equation 2.7 is linearized (see Equation 2.10) as follows:

$$ln[-\ln(1 - V_c(t - t_0)] = \ln(k) + nln(t - t_0) \quad \text{Eq.2.10}$$

From this expression an Avrami plot can be obtained if $log\ (-ln(1-V_c))$ is plotted versus $log\ (t-t_0)$. If the crystallization kinetics follows the Avrami equation, then a straight line should be obtained with slope equals to n and the intercept equals to K (see Figure 2.3, Avrami Fitted range)

The Avrami index can be considered as a sum of two terms (see refs. [13-15]), as shown in Equation 2.11:

$$n = n_d + n_n \quad \text{Eq. 2.11}$$

where n_d represents the dimensionality of the growing crystals, and it only can take integer number, this mean 1, 2 and 3, corresponding with structures of 1, 2 and 3 dimensions. The term n_n represents the nucleation, which depends on the nucleation time. The n_n can take the extreme values of 0 (instantaneous nucleation) and 1 (sporadic

nucleation) or values in between this two, when the nucleation rate is in between sporadic and instantaneous. In general, the combination of n_d and n_n, gives the different structures indicated on Table 2.1., when only the extreme values of instantaneous or sporadic nucleation are considered.

Table 2.1. Description of the different combination of n_d and n_n. Note that *I* is refer to instantaneous and *S* to Sporadic growth.

Avrami Inxex (*n*)	n_d	n_n	**Description**
1	1	0	Rod (I)
2	1	1	Rod (S)
2	2	0	Axialite (I)
3	2	1	Axialite (S)
3	3	0	Spherulite (I)
4	3	1	Spherulite (S)

The crystallization half-time, $t_{50\%}$ (time needed to achieve 50% of the relative crystallinity of polymer, which means 1-V_c=0.5) can be calculated (see Equation 2.12) as follows:

$$t_{50\%} = \left(\frac{\ln\left(1 - V_c\right)}{k}\right)^{1/n} = \left(\frac{-ln0.5}{k}\right)^{1/n} \qquad \text{Eq.2.12}$$

The plots which can be obtained from the Avrami equation and its linealization are shown in Figure 2.3. These plots were obtained from the Origin ® plug-in developed by Lorenzo et al. [13]

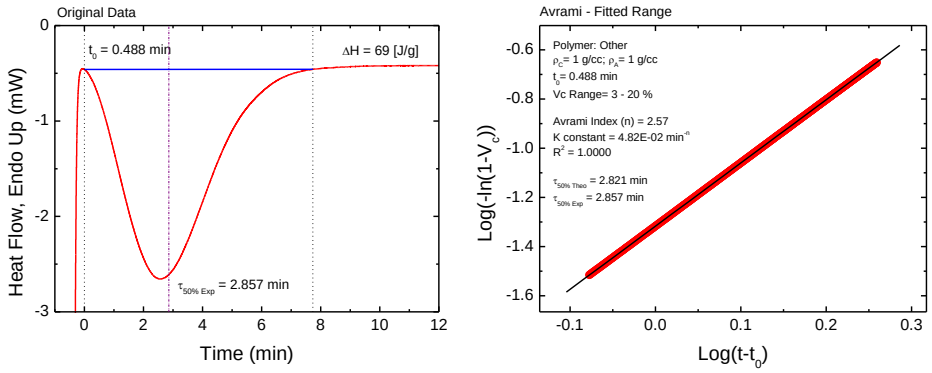

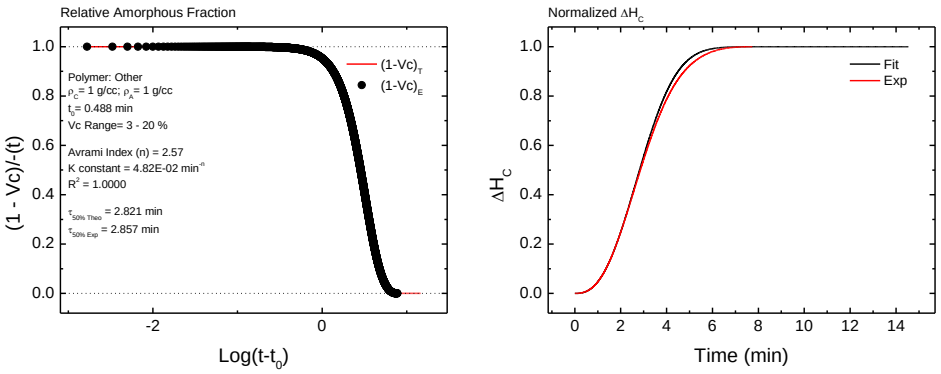

Figure 2.3. Avrami plots obtained through the Origin ® plug in developed by Lorenzo et al. [13]

Lauritzen and Hoffman theory

The Lauritzen and Hoffman theory is one of the earliest theory derived to specifically model polymer chain crystallization based on a kinetic basis. [12] Although the theory has received much criticism lately, [12, 16-20] it is still useful since its relatively simple analytical expression (Equation 2.13) can be used to fit experimental data over a wide supercooling range. [19, 21-25] The theory can be applied for both spherulitic growth rate (*i.e.*, experimental data obtained by PLOM) and overall crystallization rate (*i.e.*, data obtained by DSC). In the case of the spherulitic growth rate ($G\ (T)$), the LH equation can be expressed as a function of the supercooling (ΔT) according to:[12, 16, 20, 26, 27]

$$G(T) = G_0 \exp\left(\frac{-U^*}{R\ (T_c - T_\alpha}\right) exp\left(\frac{-K_g^G}{T_c \Delta T_f}\right) \qquad \text{Eq.2.13}$$

where G_0 is a pre-exponential growth rate constant. The first term is controlled by diffusion, and U^* is the activation energy for the transport of the macromolecules to the growth front (a value of 1500 cal/mol is usually employed), R is the gas constant, and T_c is the isothermal crystallization temperature. T_α is the temperature at which chain mobility ceases, and it is usually taken as T_g- 30 (K). The second term is the secondary nucleation term where ΔT is the supercooling defined as $T_m^{\ 0}$-T_c, with $T_m^{\ 0}$ as the equilibrium melting point, which can be calculated according to the Hoffman-Weeks extrapolation (H-W) as is show below. The factor f is a temperature correction term

equal to $2T_c/(T_c+T_m^0)$, and K_g^G is a secondary nucleation constant that is proportional to the energy barrier for spherulitic growth.
The value of K_g^G can be expressed as: [12, 16, 20, 26, 27]

$$K_g^G = \frac{jb_0\sigma\sigma_e T_m^0}{k\Delta h_f} \quad \text{Eq.2.14}$$

where j is determined by the operating regime (see below) and is equal to 4 for regime I and III and is taken as 2 for regime II; b_0 is the width of the chain, σ is the lateral surface free energy, σ_e is the fold surface free energy, k is the Boltzmann constant, and Δh_f is the heat of fusion of a perfect crystal. The following equations allow the calculation of σ (and therefore σ_e) and q, the work done by the chain to form a fold:

$$\sigma = 0.1\Delta h_f\sqrt{a_0 b_0} \quad \text{Eq.2.15}$$

$$q = 2a_0 b_0 \sigma_e \quad \text{Eq.2.16}$$

Where a_0b_0 is the cross-sectional area of the chain.

The Lauritzen and Hoffman theory analyzes the growth data according to the competition between the rate of deposition of secondary nuclei (i) and the rate of lateral surface spreading (g), resulting in three different regimes:

- Regime I: occurs when $i<<g$ and may be found at very low ΔT.
- Regime II: i is the order of g and occurs at moderate ΔT.
- Regime III: $i>g$ and is found at very high ΔT.

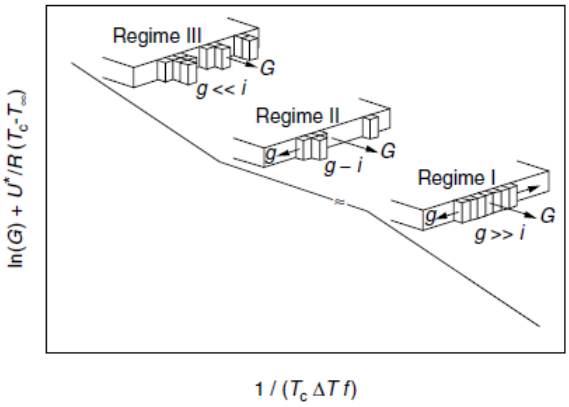

Regime I	$g>>i$
Regime II	$g\approx i$
Regime III	$g<<i$

Scheme 2.10. Schematic representation of LH regimes.[12]

The overall crystallization kinetics (not only the spherulite growth rate) is determined by the contributions of both nucleation and growth. The L-H theory can be applied not only to the spherulites growth rate but also to the isothermal crystallization kinetics data collected by DSC. In the latter case, the Equation 2.17 is as follow:

$$\frac{1}{\tau_{50\%}}(T) = G_0^{\tau} exp\left(\frac{-U^*}{R(T_c - T_\alpha)}\right) exp\left(\frac{-K_g^{\tau}}{T\Delta Tf}\right) \qquad \text{Eq.2.17}$$

Notice that the superscript τ is use to indicate that the parameters depend on the experimental data obtained by DSC, whereas the superscript G indicate that the parameters were obtained from the PLOM experimental data. The Equations 2.14 to 2.16 can be used with the DSC data.

The experimental data to apply the Lauritzen and Hoffman Theory can also be analyzed with the Origin ® plug in developed by Lorenzo et al.[13] The plots generated are show in Figure 2.4

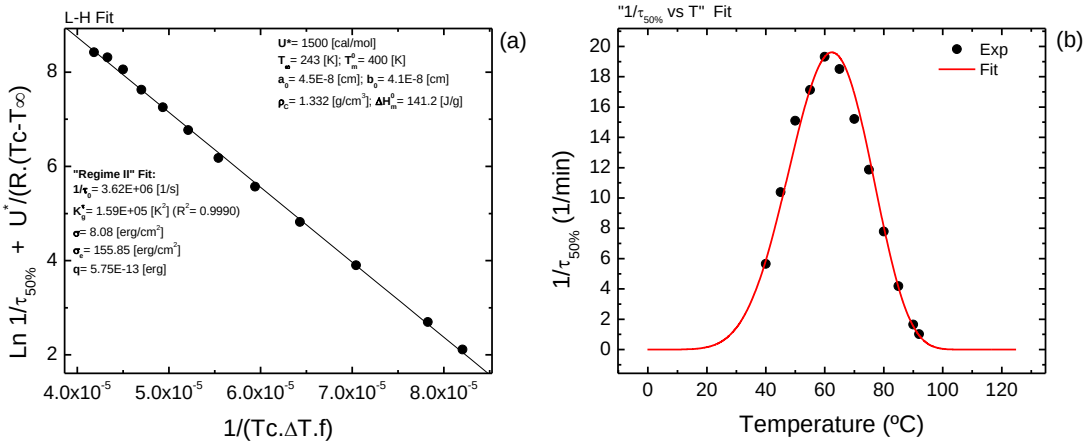

Figure 2.4. Lauiritzen and Hoffman plots obtained through the Origin ® plug in developed by Lorenzo et al.[13]

It is worth noting that similar plots are obtained when the data from PLOM experiments is used. However, it is important to remark that the K_g^G values should be lower than the K_g^τ ones, since the latter includes nucleation and growth, whereas the first includes only the spherulite growth.

2.5 Self-Nucleation (SN) and Successive Self-Nucleation and Annealing (SSA)

2.4.1 Self Nucleation

Self Nucleation is a thermal procedure for the production of self-seeds or self-nuclei within a polymer melt, so that nucleation density can greatly increase. In principle, the best nucleation agents for any polymer are their own crystal fragments or chain segments with residual crystal memory. [28-32] It is worth noting that the nature and origin of such residual crystal memory have been recently investigated through rheological and dielectric measurements. These works have found that the self-nucleated melt do not obey the time-temperature superposition principle, contrary to fully isotropic melts. Such rheological thermocomplexity constitutes the first physical evidence of the presence of melt heterogeneities, which act as self-nuclei when the melt is cooled and recrystallizes.[33]

The SN technique was originally devised by Keller et al.[32] to aid the preparation of single crystals from solution. Fillon et al.[30] extended the study of SN by employing DSC.[29] Fillon et al.[30] defined Domains of SN for isotactic PP. These SN domains can be defined as follow:

Domain I or melting Domain: The polymer is under *Domain I* when complete melting occurs and the crystalline history of the material is erased.
Domain II or exclusive SN Domain: In this domain, the sample is heated to high enough temperatures to melt most crystals but low enough to produce self-nuclei. In *Domain II* T_c is shifted to higher temperatures (as it is proportional to nucleation density), and in the subsequent melting scans no traces of annealing can be seen.
Domain III or SN and annealing Domain: When T_s is too low, partial melting is produced and unmolten crystals are annealed during the 5 minutes at T_s. The subsequent melting scans in *Domain III* reveal the endotherm(s) which were originally present in the standard sample and a new endotherm as a result of the anneled crystals.

Scheme 2.11 provides an schematic diagram to illustrate at a molecular level the different self-nucleation Domains. In Domain I the materials melts completely and the chains adopt an isotropic random coil conformation. In Domain II two possibilities have been considered: At the higher temperature end (where the DSC trace has already attain the baseline after melting or in some cases well above the peak melting temperature of Domain II the melt just retains some residual segmental orientation that constitutes the crystalline memory that allows the polymer to exhibit self-nucleation. At the lower temperature end of Domain II, small crystals fragments survive melting and constitute self-nuclei. Finally in Domain III, partial melting and annealing of unmolten crystals co-exist.

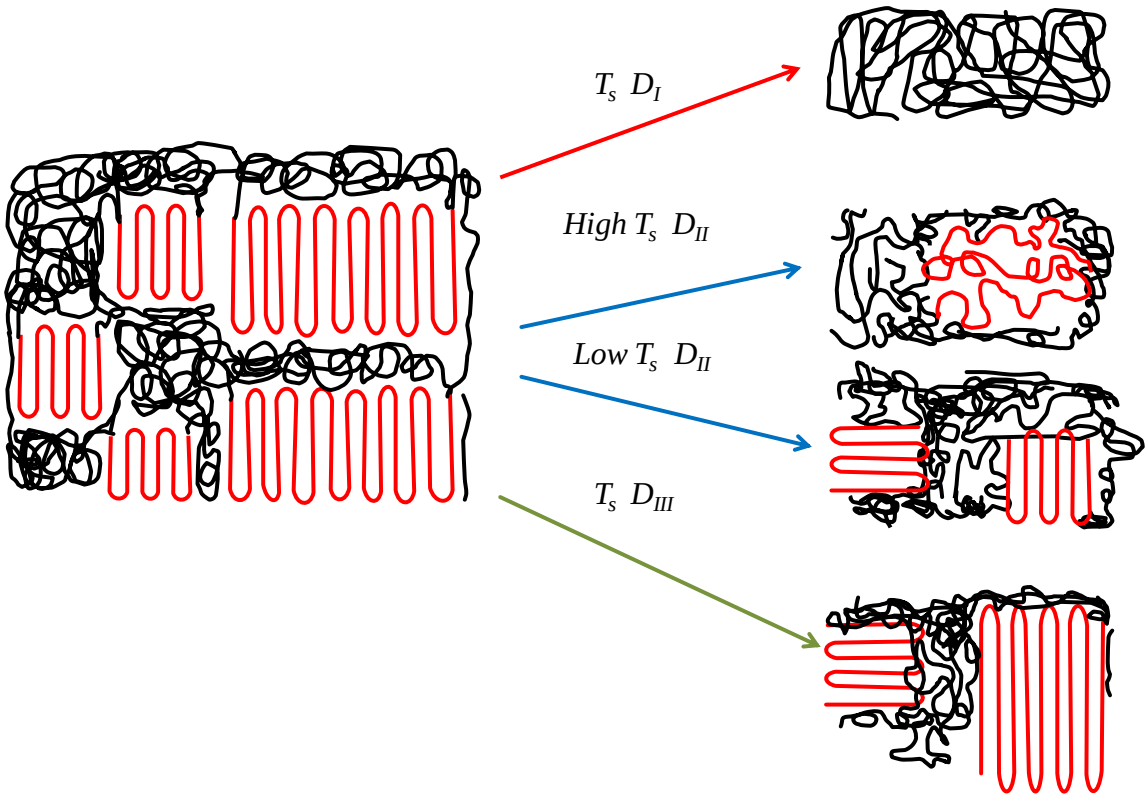

Scheme 2.11. Schematic molecular representation of the different self-nucleation *Domains.*[28]

From the experimental point of view, an example of the obtained information during a SN test, is shown in Figure 2.5, which presents DSC runs obtained during self-nucleation of an isotactic polypropylene sample (PP). The cooling scans after thermal conditioning at the indicated T_s temperatures are shown in Figure 2.5a while the subsequent heating scans are presented in Figure 2.5b.

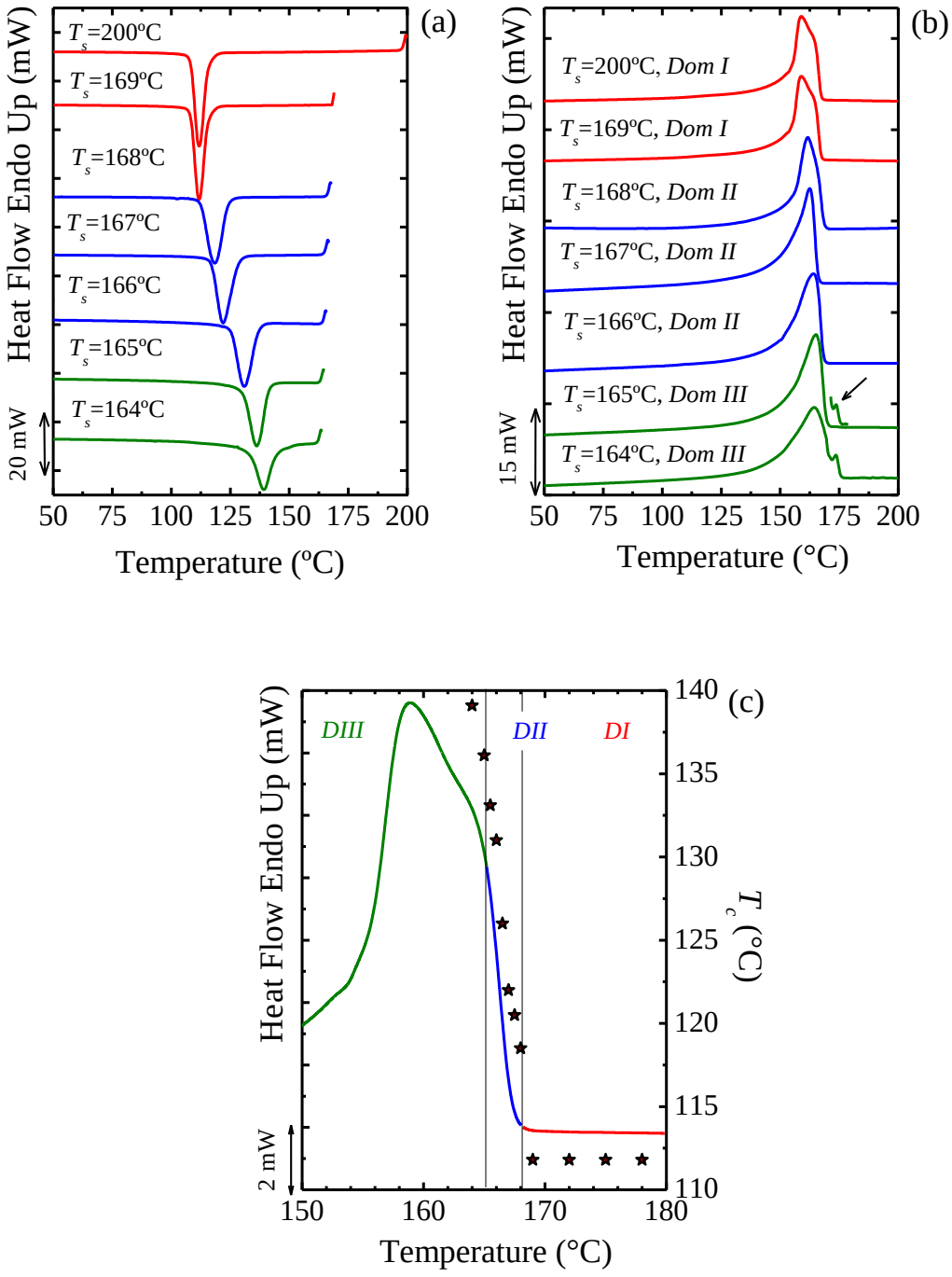

Figure 2.5. (a) DSC cooling scans (at 10°C/min) for PP after 5 min at the indicated T_s. (b) Subsequent heating scans (at 10°C/min) after the cooling runs shown in (a). (c) Representation of the self-nucleation domains for PP homopolymer on top of the standard DSC melting trace. Data points represent peak crystallization temperatures (plotted on the right hand side y axis) as a function of T_s values (plotted on the x axis as temperature).[28]

Figure 2.5a shows the changes in T_c according to the SN *Domain*, whereas Figure 2.5b show the changes in the melting peaks with the indicated SN *Domains* of the PP used as an example.

Nucleation Efficiency Scale

One of the best ways to quantitatively assess the nucleation efficiency of an additive is by comparing its effect on a given polymeric matrix with that of self-nuclei. We have employed the self-nucleation scale derived by Fillon et al. [30, 34] The scale has been used for nanocomposites previously. [35-43]

The nucleation efficiency (*NE*) can be calculated according to the expression:

$$NE) = \frac{T_{c,NA} - T_{c,pol}}{T_{c,max} - T_{c,pol}} \qquad \text{Ec.2.18}$$

where $T_{c,NA}$ is the T_c peak value determined in a DSC cooling scan for the polymer (pol) with the nucleating agent (*NA*), $T_{c,\,pol}$ is the T_c peak for the neat polymer (*pol*) and $T_{c,\,max}$ is the maximum peak crystallization temperature determined after the polymer has been self-nucleated at the ideal self-nucleation temperature, $T_{s,\,ideal}$ (*i.e.*, the self-nucleation temperature that produces maximum self-nucleation without annealing). [29, 30, 34]

2.4.2 Successive Self-Nucleation and Annealing

The thermal fractionation applied in the SSA technique exploits the molecular segregation capacity exhibited by semicrystalline polymeric systems when they are isothermally crystallized or annealed. [28]

SSA was designed and implemented by Müller et al.[44] in 1997 and it was recently review.[28] It is conceptually based on the sequential application of self-nucleation and annealing steps to a polymer specimen.[44] The SSA protocol is shown in Chapter III. Experimental Part.

Figure 2.6 shows an example of the DSC final heating, at 20 ºC/min from the lower temperature limit up to the melt state (higher temperature limit), of two samples

which where fractionated by using the SSA technique. In this final step, the result of the SSA fractionation or fractionation profile is revealed.

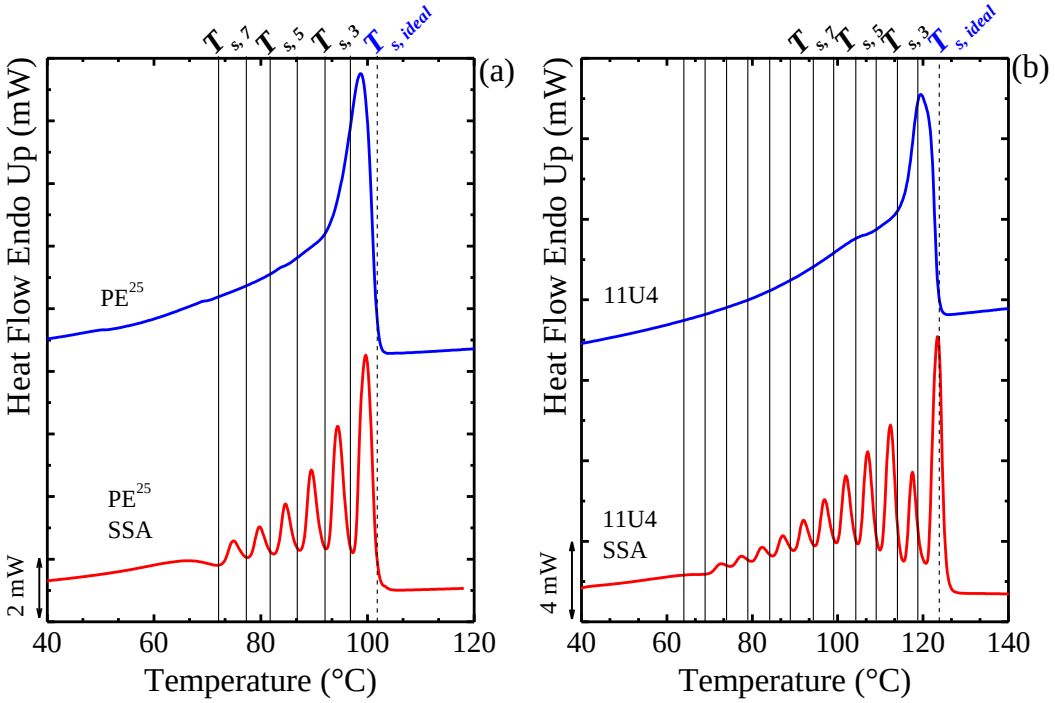

Figure 2.6. DSC heating scans (10 °C/min) for (a) PE^{25} and (b) 11U4, before and after SSA fractionation.[28]

Figure 2.6 shows examples of two different polyethylene samples. The standard non-isothermal heating runs are presented after controlled coolings from the melt at 10 ºC/min. Final heating runs after SSA treatments are also included. The SSA thermal protocols were applied to each sample starting from their corresponding $T_{s,\,ideal}$.

The commercial ethylene/α-olefin copolymer denoted 11U4 is a linear low density polyethylene (LLDPE) synthesized by Ziegler-Natta type catalysis.[29, 44, 45] The hydrogenated polybutadiene (PE^{25}) sample contains 90 wt. % 1,4-units, a number average molecular weight of 25 kg/mol and a polydispersity index (*PDI*) of 1.02. It is denoted in this work as PE^{25}, where the superscript indicates the M_n value in kg/mol.

The SSA fractionation profile in Figure 2.6a shows a series of melting peaks for PE^{25}corresponding to the melting of crystallites with different mean lamellar thickness formed and annealed at each T_s. The SSA final DSC heating scan shows the effects of the accumulation of 7 self-nucleation and annealing steps using T_s values ranging from 102 to 72 °C, every 5 °C. Since 102 °C is the ideal self-nucleation temperature for this PE^{25}, [29, 46] the thermal treatment at $T_{s,\,ideal}$ does not cause any annealing. Therefore,

only 6 steps of the SSA procedure were able to produce annealing. Figure 2.6a shows 6 sharp melting peaks of PE[25] obtained after SSA plus an additional broad melting peak (at around 65 °C) corresponding to the melting of crystals formed during cooling from the lowest T_s employed. The observed distribution of melting peaks is unimodal and reflects the random distribution of 1,2 units in the PB precursor, *i.e.*, the distribution of the resulting ethyl branches along the polyethylene backbone.

For the 11U4 sample, 12 thermal cycles were applied starting from the ideal self-nucleation temperature, *i.e.*, 124 °C. Therefore, 11 sharp meeting peaks are appreciated in Figure 2.6b corresponding to those T_s temperatures that produced annealing and thermal fractions. The bimodal distribution of melting points is very clear after SSA when it is correctly performed starting from $T_{s,\,ideal}$. The effect of selecting the appropriate T_s can be very important, especially when a SCBD need to be inferred or calculated from the fractionated sample DSC heating scan.[45] In fact, if the wrong first T_s is employed, SSA may yield a unimodal distribution of melting points for this sample which would be against its well known bimodal distribution of SCB.

In order to apply a correct SSA protocol, there are certain variables that have to be controlled.

The most important variables to design a successful SSA thermal protocol are:

(a) The first T_s temperature to be used in SSA. As extensively discussed in the previous section, the ideal self-nucleation temperature ($T_{s,ideal}$) should be employed as the first T_s.

(b) The time spent at T_s. This variable has been previously studied by Müller and Arnal. [29] Increasing fractionation time beyond 5 min at each T_s does not significantly improve fractionation by SSA in general terms. A time of 5 min is suitable for most applications.

(c) The fractionation window. Fractionation windows lower than 2.5 ºC lead to very poor fractionation (see reference [29]). Normally 5 ºC is suitable for most applications except in cases where fractionation capacity is low, like in linear (defect free) polymeric chains. In those cases, increasing the width of the fractionation window to 10 ºC is convenient.

(d) Scanning rates. SSA has been typically performed employing a constant sample mass (approximately 10 mg) and various heating rates (5, 10 and 20 °C/min). [44, 45] However, Pijpers et al.[47] introduced high speed

calorimetry concepts that were advantageously applied to thermal fractionation experiments. Müller et al.[29, 46, 48] performed SSA at faster heating rates while reducing sample mass. They performed SSA experiments employing rates as high as 50 °C/min in a conventional Perkin Elmer PyrisTM 1 DSC equipped with an intracooler device. They have also employed the SSA technique with a differential fast scanning chip-calorimeter (FSC) Flash DSC-1 from Mettler Toledo, coupled with a intracooler device. Müller et al. found that FSC is an ideal technique to study the kinetics of the very early stages of the molecular segregation processes that produce thermal fractionation by SSA. In fact, they found that the quality of the thermal fractionation obtained in 10 seconds by FSC is equivalent to that of conventional DSC (t_s=300 s). The resolution at high and low scanning rates is almost identical, when the mass has been conveniently reduced to avoid any superheating effects. A slight shift of the melting point of each fraction to higher temperatures is noticeable, although it is less than 1.1 °C when the scan rate is increased ten times (from 5 to 50 °C/min).[46]

2.6 References

[1] F. Azurri, in: Dipartimento di Chimica e Chimica Industriale, Università degli Studi di Genova, Genoa, Italy, 2004.
[2] U.W. Gedde, Polymer Physics, Springer Netherlands, 2013.
[3] R. Dargazany, V.N. Khiêm, E.A. Poshtan, M. Itskov, Constitutive modeling of strain-induced crystallization in filled rubbers, Physical Review E 89 (2014) 022604.
[4] X. Jiang, G. Reiter, W. Hu, How Chain-Folding Crystal Growth Determines the Thermodynamic Stability of Polymer Crystals, The Journal of Physical Chemistry B 120 (2016) 566-571.
[5] L.C. Sawyer, Polymer Microscopy, Springer Netherlands, 2012.
[6] A. Seidlitz, T. Thurn-Albrecht, Small-Angle X-ray Scattering for Morphological Analysis of Semicrystalline Polymers, in: Polymer Morphology, 2016.
[7] B. Wunderlich, CHAPTER III - The Crystal Morphology, in: B. Wunderlich (Ed.) Macromolecular Physics, Academic Press, 1973, pp. 178-379.
[8] T. Kabe, T. Sato, K.-i. Kasuya, T. Hikima, M. Takata, T. Iwata, Transition of spherulite morphology in a crystalline/crystalline binary blend of biodegradable microbial polyesters, Polymer 55 (2014) 271-277.
[9] E.M. Woo, G. Lugito, Origins of periodic bands in polymer spherulites, Eur. Polym. J. 71 (2015) 27-60.
[10] B.D. Cullity, S.R. Stock, Elements of X-ray Diffraction, Pearson education limited, 2013.

[11] D. Lamba, Wide-Angle X-Ray Scattering (WAXS), in: E. Drioli, L. Giorno (Eds.) Encyclopedia of Membranes, Springer Berlin Heidelberg, Berlin, Heidelberg, 2016, pp. 2040-2042.
[12] J.E. Mark, Physical Properties of Polymers Handbook, Springer New York, 2007.
[13] A.T. Lorenzo, M.L. Arnal, J. Albuerne, A.J. Müller, DSC isothermal polymer crystallization kinetics measurements and the use of the Avrami equation to fit the data: Guidelines to avoid common problems, Polym. Test. 26 (2007) 222-231.
[14] V. Balsamo, N. Urdaneta, L. Pérez, P. Carrizales, V. Abetz, A.J. Müller, Effect of the polyethylene confinement and topology on its crystallisation within semicrystalline ABC triblock copolymers, Eur. Polym. J. 40 (2004) 1033-1049.
[15] A.J. Müller, V. Balsamo, M.L. Arnal, Nucleation and Crystallization in Diblock and Triblock Copolymers, in: V. Abetz (Ed.) Block Copolymers II, Springer Berlin Heidelberg, Berlin, Heidelberg, 2005, pp. 1-63.
[16] G. Strobl, A Multiphase Model Describing Polymer Crystallization and Melting, in: G. Reiter, G. Strobl (Eds.) Progress in Understanding of Polymer Crystallization, Springer Berlin Heidelberg, 2007, pp. 481-502.
[17] M. Muthukumar, P. Welch, Modeling polymer crystallization from solutions, Polymer 41 (2000) 8833-8837.
[18] M. Muthukumar, Commentary on theories of polymer crystallization, European Physical Journal E 3 (2000) 199-202.
[19] A.T. Lorenzo, A.J. Müller, Estimation of the nucleation and crystal growth contributions to the overall crystallization energy barrier, Journal of Polymer Science, Part B: Polymer Physics 46 (2008) 1478-1487.
[20] J.M. Schultz, Polymer Crystallization: The Development of Crystalline Order in Thermoplastic Polymers, American Chemical Society, 2001.
[21] A.J. Müller, J. Albuerne, L. Marquez, J.M. Raquez, P. Degée, P. Dubois, J. Hobbs, I.W. Hamley, Self-nucleation and crystallization kinetics of double crystalline poly(p-dioxanone)-b-poly(ε-caprolactone) diblock copolymers, Faraday Discuss. 128 (2005) 231-252.
[22] M.A. Sabino, J. Albuerne, A. Müller, J. Brisson, R.E. Prud'homme, Influence of in vitro hydrolytic degradation on the morphology and crystallization behavior of poly(p-dioxanone), Biomacromolecules 5 (2004) 358-370.
[23] S. Andjelić, D. Jamiolkowski, J. McDivitt, J. Fischer, J. Zhou, R. Vetrecin, Crystallization study on absorbable poly(p-dioxanone) polymers by differential scanning calorimetry, J. Appl. Polym. Sci. 79 (2001) 742-759.
[24] W. Scott Lambert, P.J. Phillips, Crystallization kinetics of low molecular weight fractions of branched polyethylenes, Macromolecules 27 (1994) 3537-3542.
[25] A.T. Lorenzo, M.L. Arnal, A.J. Müller, A. Boschetti-De-Fierro, V. Abetz, Nucleation and isothermal crystallization of the polyethylene block within diblock copolymers containing polystyrene and poly(ethylene-alt-propylene), Macromolecules 40 (2007) 5023-5037.
[26] J.I. Lauritzen, J.D. Hoffman, Theory of Formation of Polymer Crystals with Folded Chains in Dilute Solution, Journal of Research of the National Bureau of Standards-A. Physics and Chemistry 64 (1960) 73-102.
[27] J.D. Hoffman, J.I. Lauritzen, Crystallization of Bulk Polymers With Chain Folding: Theory of Growth of Lamellar Spherulites, Journal of Research of the National Bureau of Standards-A. Physics and Chemistry 65 (1961) 297-336.

[28] A.J. Müller, R.M. Michell, R.A. Pérez, A.T. Lorenzo, Successive Self-nucleation and Annealing (SSA): Correct design of thermal protocol and applications, Eur. Polym. J. 65 (2015) 132-154.
[29] A.J. Müller, M.L. Arnal, Thermal fractionation of polymers, Prog. Polym. Sci. 30 (2005) 559-603.
[30] B. Fillon, J.C. Wittmann, B. Lotz, A. Thierry, Self-nucleation and recrystallization of isotactic polypropylene (α phase) investigated by differential scanning calorimetry, J. Polym. Sci., Part B: Polym. Phys. 31 (1993) 1383-1393.
[31] A.T. Lorenzo, M.L. Arnal, J.J. Sánchez, A.J. Müller, Effect of annealing time on the self-nucleation behavior of semicrystalline polymers, Journal of Polymer Science, Part B: Polymer Physics 44 (2006) 1738-1750.
[32] D.J. Blundell, A. Keller, A.J. Kovacs, A new self-nucleation phenomenon and its application to the growing of polymer crystals from solution, Journal of Polymer Science Part B: Polymer Letters 4 (1966) 481-486.
[33] L. Sangroniz, D. Cavallo, A. Santamaria, A.J. Müller, R.G. Alamo, Thermorheologically Complex Self-Seeded Melts of Propylene–Ethylene Copolymers, Macromolecules 50 (2017) 642-651.
[34] B. Fillon, B. Lotz, A. Thierry, J.C. Wittmann, Self-nucleation and enhanced nucleation of polymers. Definition of a convenient calorimetric "efficiency scale" and evaluation of nucleating additives in isotactic polypropylene (α phase), J. Polym. Sci., Part B: Polym. Phys. 31 (1993) 1395-1405.
[35] M. Trujillo, M.L. Arnal, A.J. Müller, E. Laredo, S. Bredeau, D. Bonduel, P. Dubois, Thermal and Morphological Characterization of Nanocomposites Prepared by in-Situ Polymerization of High-Density Polyethylene on Carbon Nanotubes, Macromolecules 40 (2007) 6268-6276.
[36] A.J. Müller, M.L. Arnal, M. Trujillo, A.T. Lorenzo, Super-nucleation in nanocomposites and confinement effects on the crystallizable components within block copolymers, miktoarm star copolymers and nanocomposites, Eur. Polym. J. 47 (2011) 614-629.
[37] D. Priftis, G. Sakellariou, N. Hadjichristidis, E.K. Penott, A.T. Lorenzo, A.J. Müller, Surface modification of multiwalled carbon nanotubes with biocompatible polymers via ring opening and living anionic surface initiated polymerization. Kinetics and crystallization behavior, J. Polym. Sci., Part A: Polym. Chem. 47 (2009) 4379-4390.
[38] M. Trujillo, M.L. Arnal, A.J. Müller, M.A. Mujica, C. Urbina De Navarro, B. Ruelle, P. Dubois, Supernucleation and crystallization regime change provoked by MWNT addition to poly(ε-caprolactone), Polymer 53 (2012) 832-841.
[39] A. Kovalcik, R.A. Pérez-Camargo, C. Fürst, P. Kucharczyk, A.J. Müller, Nucleating efficiency and thermal stability of industrial non-purified lignins and ultrafine talc in poly(lactic acid) (PLA), Polym. Degrad. Stab. 142 (2017) 244-254.
[40] T. Gumede, A. Luyt, M. Hassan, R. Pérez-Camargo, A. Tercjak, A. Müller, Morphology, Nucleation, and Isothermal Crystallization Kinetics of Poly(ε-caprolactone) Mixed with a Polycarbonate/MWCNTs Masterbatch, Polymers 9 (2017) 709.
[41] R.A. Pérez, J.V. López, J.N. Hoskins, B. Zhang, S.M. Grayson, M.T. Casas, J. Puiggalí, A.J. Müller, Nucleation and antinucleation effects of functionalized carbon nanotubes on cyclic and linear Poly(ε-caprolactones), Macromolecules 47 (2014) 3553-3566.

[42] R.A. Pérez–Camargo, G. Saenz, S. Laurichesse, M.T. Casas, J. Puiggalí, L. Avérous, A.J. Müller, Nucleation, Crystallization, and Thermal Fractionation of Poly (ε-Caprolactone)-Grafted-Lignin: Effects of Grafted Chains Length and Lignin Content, J. Polym. Sci., Part B: Polym. Phys. 53 (2015) 1736-1750.
[43] J.F. Vega, J. Fernández-Alcázar, J.V. López, R.M. Michell, R.A. Pérez-Camargo, B. Ruelle, J. Martínez-Salazar, M.L. Arnal, P. Dubois, A.J. Müller, Competition between supernucleation and plasticization in the crystallization and rheological behavior of PCL/CNT-based nanocomposites and nanohybrids, J. Polym. Sci., Part B: Polym. Phys. 55 (2017) 1310-1325.
[44] A.J. Müller, Z.H. Hernández, M.L. Arnal, J.J. Sánchez, Successive self-nucleation/annealing (SSA): A novel technique to study molecular segregation during crystallization, Polym. Bull. 39 (1997) 465-472.
[45] M.L. Arnal, V. Balsamo, G. Ronca, A. Sánchez, A.J. Müller, E. Cañizales, C. Urbina de Navarro, Applications of Successive Self-Nucleation and Annealing (SSA) to Polymer Characterization, J. Therm. Anal. Calorim. 59 (2000) 451-470.
[46] A.T. Lorenzo, M.L. Arnal, A.J. Müller, A.B. De Fierro, V. Abetz, High speed SSA thermal fractionation and limitations to the determination of lamellar sizes and their distributions, Macromol. Chem. Phys. 207 (2006) 39-49.
[47] V. Mathot, M. Pyda, T. Pijpers, G. Vanden Poel, E. van de Kerkhof, S. van Herwaarden, F. van Herwaarden, A. Leenaers, The Flash DSC 1, a power compensation twin-type, chip-based fast scanning calorimeter (FSC): First findings on polymers, Thermochim. Acta 522 (2011) 36-45.
[48] A.J. Müller, A.T. Lorenzo, M.L. Arnal, Recent Advances and Applications of "Successive Self-Nucleation and Annealing" (SSA) High Speed Thermal Fractionation, Macromolecular Symposia 277 (2009) 207-214.

CHAPTER III.
EXPERIMENTAL PART

In this Chapter the materials as well as methods used in each topic are explained in detail.

3.1 Materials

3.1.1 Copolyesters

The materials employed in Chapter IV are indicated in Table 3.1. These are copolyesters synthesized and provided by the BioTeam of Prof. Lúc Áverous from Strasbourg University (France). The main difference between these copolyesters are their chain lengths and their main characteristics are summarized in Table 3.1.

Table 3.1. Samples molar composition, molar masses (M_n and M_w), dispersity index ($Đ$), and Sequence distribution determined by ^{13}C NMR (L_{MA}, L_{MB} and R)

System	Composition	Molecular Weight (kg/mol)		$Đ$	Sequence distribution study*		
		M_n	M_w		L_{MA}	L_{MB}	R
PBS	100:0	29.1	56.2	1.9	-	-	-
PBA	100:0	26.8	47.0	1.8	-	-	-
PPA	100:0	28.6	46.5	1.6	-	-	-
PPS	100:0	35.2	57.9	1.6	-	-	-
PBS-*ran*-PBA	80:20	29.8	56.9	1.9	4.2	1.3	0.99
(PBSA)	60:40	18.7	30.3	1.6	2.6	1.6	1.01
	50:50	24.7	50.0	2.0	1.9	1.9	1.02
	40:60	30.3	53.8	1.8	1.8	2.4	0.99
	20:80	32.0	55.2	1.7	1.3	3.8	1.03
PPA-*ran*-PBA	80:20	29.4	50.0	1.7	4.3	1.3	1.01
(PPBA)	60:40	20.0	32.0	1.6	2.5	1.6	1.04
	50:50	29.7	47.5	1.6	2.0	2.1	0.98
	40:60	35.2	56.3	1.6	1.6	2.6	1.00
	20:80	34.9	62.8	1.8	1.3	4.5	1.02

PPS-*ran*-PBS	80:20	31.7	53.9	1.7	4.1	1.4	0.96
(PPBS)	60:40	32.9	61.9	1.9	2.6	1.7	0.98
	50:50	29.8	53.6	1.8	2.0	2.1	0.98
	40:60	23.7	37.9	1.6	1.7	2.4	1.00
	20:80	38.6	65.6	1.7	1.3	4.9	0.98
PPS-*ran*-PPA	80:20	38.2	64.4	1.7	4.6	1.3	1.00
(PPSA)	50:50	36.4	68.1	1.9	2.0	2.0	1.01
	20:80	24.0	40.6	1.7	1.3	4.5	1.02

*L_{MA} is the sequence length of comonomer A (PBS, PPA or PPS) and L_{MB} the sequence length of comonomer B (PBA, PBS). R is the degree of randomness defined as $1/L_{MA}+1/L_{MB}$.

The details of the preparation of PBSA copolymers are presented below:

Biobased succinic acid (SA) (99.5%) was kindly supplied by BIOAMBER (France). SA was bioproduced by fermentation of glucose (from wheat or corn) and obtained after a multistep process based on several purifications, evaporation and crystallization stages. 1,4-butanediol (BDO) (99%), methanol (≥99.6%) and chloroform (99.0-99.4%) were purchased from SIGMA-ALDRICH. Adipic acid (99%), titanium (IV) isopropoxide (TTIP) (98+%) and extra dry toluene (99.85%) were supplied by ACROS. All reactants were used without further purification. All solvents used for the analytical methods were of analytical grade.

Organometallic synthesis of copolyesters

Aliphatic copolyesters were synthesized by a two-stage melt polycondensation method (polycondensation and post-polycondensation). Syntheses were performed in a 50 mL round bottom flask with a distillation device in order to remove by-products of the reaction (mostly water). All reactions were performed with a diol (BDO)/acid (SA and/or AA) molar ratio of 1.1:1. During the first step (esterification), the reaction mixture was maintained under a constant argon flux and stirred at 300 rpm. The temperature of the reactor was set to 200 ºC for 3 h. After 3 h of oligomerization, the remaining by-product of the reaction was removed by distillation under reduced pressure (200 mbar for 5 min), and then the proper amount (0.1 mol % *vs.* the respective amount of diacid) of a 5 wt.% solution

of TTIP in extra dry toluene was introduced inside the reactor. The reaction mixture was heated to 210 ºC under a constant argon flux for 45 min.

In the second step (post-polycondensation), the temperature of the reactor was slowly increased to 230 ºC and the pressure was decreased stepwise over periods of 5 min at 100, 50 and 25 mbar, respectively, in order to avoid uncontrolled foaming and to minimize oligomer evaporation, which is a potential issue during the melt polycondensation. Finally, the pressure was decreased to 1-3 mbar and the post-polycondensation continued for about 3-4 h. At the end, the synthesized polyester was cooled, dissolved in chloroform and precipitated into a large volume of vigorously stirred cold methanol. Thereafter, the precipitate was filtered, washed with methanol and dried under reduced pressure in an oven at 40 ºC for 24 h. A schematic representation of the synthesis is shown in Scheme 3.1.

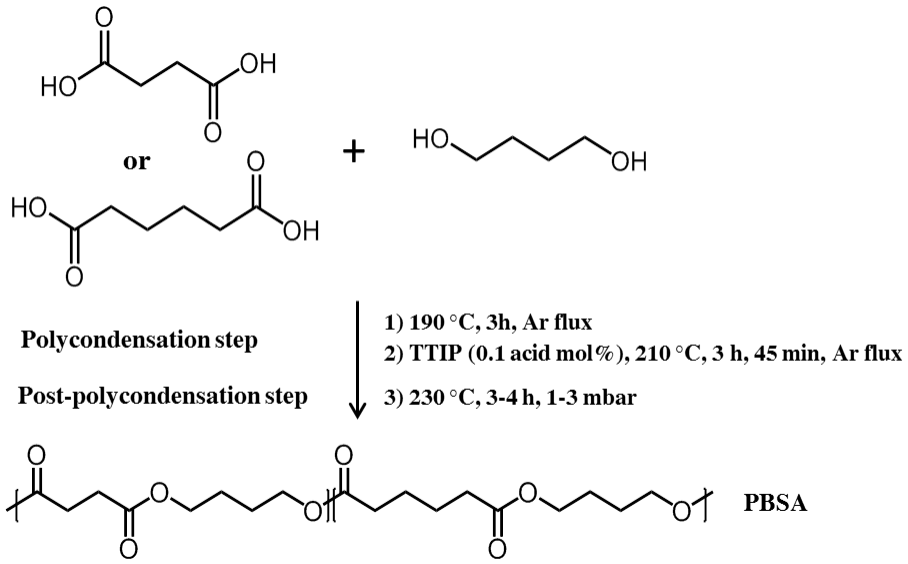

Scheme 3.1. Reaction procedure for PBSA synthesis.

Chemical structures characterizations (SEC & NMR)

^{1}H-and ^{13}C-NMR spectra of polyesters were obtained with a BRUKER 400 MHz. $CDCl_3$ was used as solvent to prepare solutions with concentrations of 8-10 and 30-50 mg/mL for ^{1}H-NMR and ^{13}C-NMR, respectively. The number of scans was set to 128 for ^{1}H-NMR and at least 5,000 for ^{13}C-NMR. Calibration of the spectra was performed using

the $CDCl_3$ peak (δ_H = 7.26 ppm, δ_C = 77.16 ppm). The composition between succinate and adipate segments in all the PBSA copolyesters employed in the present work were determined using ^{1}H-NMR by comparing the integration of signals at δ = 2.62 ppm and δ = 2.32 ppm assigned to methylene protons in α of ester functions in succinate and adipate segments, respectively (see Equation 3.1).

$$\chi_{succinate} = \frac{I_{2.62}}{I_{2.62} + I_{2.32}} \quad (3.1)$$

Number- (M_n) and weight-average (M_w) molecular weights and the dispersity ($Đ$) of the PBSA copolymers were determined in chloroform by size exclusion chromatography (SEC), using a SHIMADZU liquid chromatograph. The columns used were PLGel Mixed-C and PLGeL 100 Å. A refractive index detector was employed and chloroform as eluent at a flow rate of 0.8 mL/min. The apparatus was calibrated with linear polystyrene standards from 162 to 1,650,000 g/mol. The molar composition as well as M_n, M_w and $Đ$ are shown in Table 3.1.

Sequence distribution study of copolyesters

The sensitivity of the ^{13}C-NMR to small differences in the chemical environment enabled us to determine the different triad structures presented on Scheme 3.2. Three different triads: SBS (succinate-butylene-succinate), SBA (succinate-butylene-adipate) and ABA (adipate-butylene-adipate) are present in PBSA chains. BDO moieties are present in all three triads and exhibit four distinct ^{13}C chemical shifts according to their surrounding environment. The splitting of signals assigned to PBS and PBA (carbon atoms a_1, a_2, a_3 and a_4 in Scheme 3.2) enable the calculation of the average sequence length of BS and BA units (L_{BS} and L_{BA}, respectively) and the degree of randomness (R) according to Equation 3.2 to 3.4.

$$L_{BS} = 1 + \frac{2 \times I_{SBS}}{I_{SBA-S} + I_{SBA-A}} \quad (3.2)$$

$$L_{BA} = 1 + \frac{2 \times I_{ABA}}{I_{SBA-S} + I_{SBA-A}} \quad (3.3)$$

$$R = \frac{1}{L_{BS}} + \frac{1}{L_{BA}} \quad (3.4)$$

where I_{SBS}, I_{SBA-S}, I_{SBS-A} and I_{ABA} are integration of peaks assigned to methylene carbons in α of the ester functions (δ ~ 64 ppm) in butyl segments of SBS,

BA and ABA triads for PBSA copolyesters.

If R is equal to 1, the terpolyester is randomly distributed. If R=2, the terpolyester is strictly alternated. If R tends to 0, the terpolyester shows a block tendency. L_{BS}, L_{BA} and R calculated values are summarized in Table 3.1.

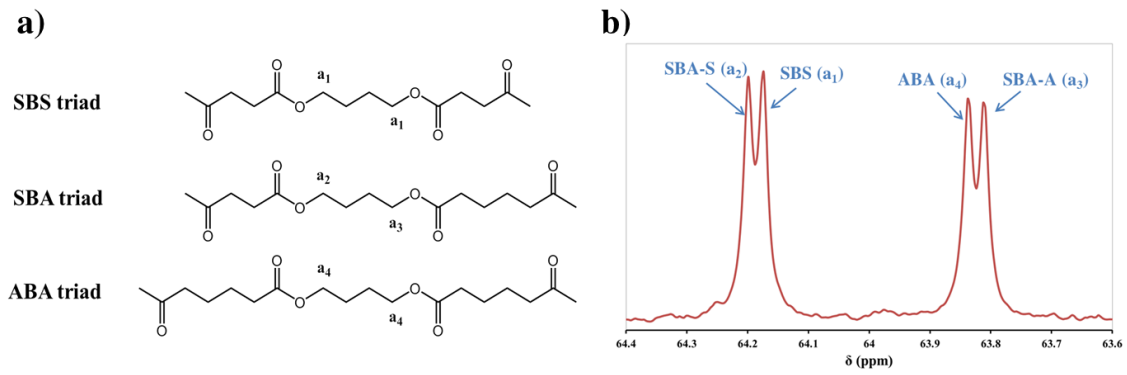

Scheme 3.2. (a) Possible triads of PBSA copolymers, (b) ^{13}C-NMR spectra of 50:50 PSBA centered at δ ~ 64 ppm.

Similarly to the description shown above, the other copolyesters were synthesized. More details are shown in the Section 9.1 of the Appendix and references. [1, 2]

3.1.2 Copolymers of poly (propylene sulfide-*co*-ethylene sulfide)

In Chapter V, a series of copolymers formed by polypropylene and polyethylene sulfide (PPS and PES, respectively) were used. These materials were prepared and molecularly characterized by the team of Prof. Nicola Tirelli. The details are presented below:

All chemicals were used as received from suppliers unless otherwise stated. Ethylene sulphide (ES), propylene sulfide (PS), ethyl 2-bromoacetate, sodium methoxide, tributylphosphine, acetyl chloride, potassium chloride, tetrabutylammonium bromide, allyl bromide, thioacetic acid and 2,2′-(ethylenedioxy)diethanethiol were purchased from Sigma-Aldrich (Gillingham, UK). Dichloromethane, dimethylformamide (DMF), methanol and tetrahydrofuran (THF) were purchased from Fisher Scientific UK Ltd (Loughborough, UK). Azobisisobutyronitrile (AIBN) was purchased from Fluka (Gillingham, UK) and recrystallized from warm methanol before use.

Polymer synthesis

Copolymers of propylene sulfide and ethylene sulfide, with different architectures were synthesized according to a literature protocol,[3] which was recently applied to the preparation of branched chains.[4]

Synthesis of initiators. The initiators were prepared as thioacetates and then deprotected *in situ*; the referenced literature provides the details of the synthetic procedures for the bifunctional (S,S'-((ethane-1,2-diylbis(oxy))bis(ethane-2,1-diyl)) diethanethioate) (DOD),[3] the tetra- and octafunctional (respectively tetrakis(3-thioacetyl propanoxy) pentaerithrytol and octakis(3-thioacetyl propanoxy)bis) and the 10-, 15- and 20-armed combs, as per previous works[4] which briefly, were synthesised firstly from the polymerization of thioglycidyl propargyl ether from the bifunctional DOD initiator to produce an oligoalkyne with an average of 10, 15 and 20 alkyne groups per chain, followed by a the [3+2] Cu-catalysed Huisgen reaction with S-(3-azidopropyl)thioacetate to convert alkyne groups into thioacetates.

Synthesis of polysulfides. The same procedure was adopted for all monomers. 1 mL of degassed DMF containing 1.8, 0.9 or 0.6 mmol of the thioacetate initiators were added to 9 mL of degassed DMF, then adding 2.66, 1.33 or 0.89 mL of tributylphosphine (always corresponding to 6 equiv.s per thioacetate) for the degree of polymerization (DP) 10, 20 or 30 polysulfides, respectively. 1.05 equiv.s (per thioacete) of sodium methoxide were added as a 0.5 M methanol solution and allowed to react for 10 minutes before the addition of PS/ES (18 mmol of episulfide with the PS:ES molar ratio corresponding to 1:0, 3:1 or 1:1); the amount of episulfide were added in one injection (one-shot addition method) or two injections of 9 mmol episulfide with the second injection 45 minutes after the first injection (repeated addition method). 1 hour after the last monomer addition, 3 equiv (per thioacetate) of ethyl 2-bromoacetate were added and allowed to react for a further 3 hours. The mixtures were then concentrated *in vacuo* using a Genevac EZ2 Elite centrifugal evaporator and the residues were dissolved into 40 mL of dichlromethane and extracted against 7 mL of half-saturated brine (x3). The organic phase was separated, dried over Na_2SO_4, filtered and concentrated as above. The resulting oils were then precipitated into 6 mL of methanol three times, decanted and dried under high vacuum for 24 hours in the Genevac EZ2 evaporator followed by a further 24 hours in the vacuum oven at 40 ^{o}C.

Solution characterization

^{1}H NMR spectra were recorded on 1.5 wt%. polymer solutions in deuterated chloroform using a Bruker Avance 300 MHz spectrometer.

Gel permeation chromatography (GPC) was performed using a Polymer Laboratories PL-GPC50 Plus integrated GPC (Polymer Laboratories, UK) assembled with a PLgel 5 μm Guard and two PolyPore 5 μm columns, using triple detection (viscosimetry, refractive index, 2-angle static light scattering). THF was employed as the eluent at a temperature of 30 ^{o}C and a flow rate of 1.0 mL.min^{-1}. The system was calibrated using polystyrene standards of known molecular weight, intrinsic viscosity and dn/dc.

The materials as well as the parameters obtained from their characterization are indicated in Table 3.2

Table 3.2. Characterization data for the polysulfides prepared in this work[a].

	Sample[a]	Arms	Degree of polymerization per arm[b]		$\overline{M_n}$ (g/mol)		Đ	a [c]	End-capping yield (%)[d]
			PS	ES	theor	exp			
LINEAR	*L*_(PS$_{10}$)$_2$	2	9.5	-	1700	1450	1.18	0.97	97
	*L*_(PS$_{20}$)$_2$	2	18.4	-	3200	2870	1.13	1.04	100
	*L*_(PS$_{30}$)$_2$	2	28.9	-	4700	4440	1.15	1.08	99
	*L*_(PS$_{7.5}$-ES$_{2.5}$)$_2$	2	7.1	2.3	1700	1540	1.06	0.96	96
	*L*_(PS$_{15}$-ES$_5$)$_2$	2	15.2	4.9	3100	3100	1.08	1.03	100
	*L*_(PS$_{22.5}$-ES$_{7.5}$)$_2$	2	21.8	7.2	4500	3900	1.08	1.00	100
	***La*_(PS$_5$-ES$_5$)$_2$**	**2**	**5.1**	**5.0**	**1600**	**1650**	**1.32**	**0.93**	**100**
	***La*_(PS$_{10}$-ES$_{10}$)$_2$**	**2**	**9.5**	**9.7**	**2900**	**2240**	**1.19**	**0.97**	**99**
	***La*_(PS$_{15}$-ES$_{15}$)$_2$**	**2**	**14.0**	**14.2**	**4300**	**3730**	**1.09**	**0.99**	**98**
	***Lb*_(PS$_{10}$-ES$_{10}$)$_2$**	**2**	**9.7**	**9.8**	**2900**	**2770**	**1.12**	**0.96**	**100**
	***Lb*_(PS$_{15}$-ES$_{15}$)$_2$**	**2**	**14.5**	**14.3**	**4300**	**3810**	**1.15**	**1.01**	**96**
STAR	*S*_(PS$_{10}$)$_4$	4	9.4	-	3500	3230	1.17	0.75	98
	*S*_(PS$_{20}$)$_4$	4	20.6	-	6500	6610	1.15	0.79	100
	*S*_(PS$_{30}$)$_4$	4	28.5	-	9500	9340	1.08	0.86	99
	*S*_(PS$_{7.5}$-ES$_{2.5}$)$_4$	4	7.5	2.3	3400	3390	1.19	0.73	98
	*S*_(PS$_{15}$-ES$_5$)$_4$	4	15.2	5.1	6200	6090	1.16	0.76	100
	*S*_(PS$_{22.5}$-ES$_{7.5}$)$_4$	4	22.8	7.3	9000	9110	1.09	0.85	100
	***S*_(PS$_5$-ES$_5$)$_4$**	**4**	**5.0**	**4.7**	**3300**	**3160**	**1.08**	**0.82**	**95**
	***S*_(PS$_{10}$-ES$_{10}$)$_4$**	**4**	**10.3**	**10.1**	**6000**	**6320**	**1.05**	**0.85**	**97**
	***S*_(PS$_{15}$-ES$_{15}$)$_4$**	**4**	**14.8**	**14.6**	**8600**	**8210**	**1.07**	**0.91**	**96**
	***S*_(PS$_5$-ES$_5$)$_8$**	**8**	**5.1**	**4.9**	**6800**	**6670**	**1.07**	**0.51**	**99**
	***S*_(PS$_{10}$-ES$_{10}$)$_8$**	**8**	**9.6**	**9.8**	**1100**	**13180**	**1.09**	**0.55**	**100**
	***S*_(PS$_{15}$-ES$_{15}$)$_8$**	**8**	**14.3**	**14**	**17000**	**20630**	**1.26**	**0.59**	**95**
COMB	***C*_(PS$_{15}$-ES$_{15}$)$_{10}$**	**10**	**16**	**14.5**	**24000**	**26050**	**1.24**	**0.48**	**100**
	***C*_(PS$_5$-ES$_5$)$_{15}$**	**15**	**5**	**4.4**	**15000**	**13120**	**1.24**	**0.34**	**87**
	***C*_(PS$_{10}$-ES$_{10}$)$_{15}$**	**15**	**10.3**	**9.7**	**25000**	**27880**	**1.19**	**0.37**	**100**
	***C*_(PS$_{15}$-ES$_{15}$)$_{15}$**	**15**	**14**	**14.5**	**35000**	**33900**	**1.21**	**0.42**	**100**
	***C*_(PS$_{15}$-ES$_{15}$)$_{20}$**	**20**	**15.7**	**15.1**	**47000**	**45590**	**1.25**	**0.41**	**100**

[a] The nomenclature reports first the chain topology (L for linear, S for stars, C for combs), then the composition of the arms (PS and ES units) and finally the number of arms. In black we lisy the polymers used for the characterization studies reported below. The PS homo and copolymers listed in grey PS are those that exhibited too low crystallinity and were therefore excluded from further analysis.

[a] Calculated as the integral ratio of main chain protons from PPS methyl peak (1.33-1.46 ppm) or PES repeat unit (-S-CH_2-CH_2-, 2.73-2.81 ppm) and the initiator peak (linear: -S-CH_2-CH_2-O-CH_2-CH_2-O-CH_2-CH_2-S- at 3.60-3.69 ppm, star: C-CH_2-O-CH_2-CH_2-CH_2-S- at 1.70-1.85 ppm or comb: triazole proton at 7.55-7.77 ppm).

[c] *a* (the Mark-Houwink parameter) was calculated from the slope of the log-log MW vs. [η] graph measured from the triple detection method in GPC using the Cirrus MultiOffline GPC/SEC (v3.4) software.

[d] End-capping yield was calculated from ^{1}H NMR by comparing the integral of the CH_3CH_2-O-C(O)- peak of ethyl 2-bromoacetate at 4.12–4.24 ppm to the initiator peaks (as described in [a]).

PS was used as a racemic mixture, leading to polymers with an atactic distribution of the PS units; since the latter are therefore incapable of crystallization, in the copolymers

they will disrupt that of ES sequences, and this will occur in a fashion proportional to degree of ES:PS interdispersion. The synthesis of polymers with ES:PS ratios>0.5 resulted in precipitation during polymerization, whereas an excess PS caused a lack of any significant crystallization (not shown), therefore we limited our crystallization studies to the 50:50 copolymers.

It is worth mentioning that in solution the introduction of branching dramatically changed the macromolecular structure. For example, it is apparent that independently of the nature or the degree of branching, all stars and combs have the same persistence length, (from molecular weight and intrinsic viscosity data through the Bushin–Bohdanecky method,[5-7] Figure 3.1A), which is considerably smaller than that of the linear polymers. This effect is likely to be unrelated to chain flexibility, and stems from a purely geometrical cause, *i.e.*, the 'kink' in the chains in correspondence to branching points.

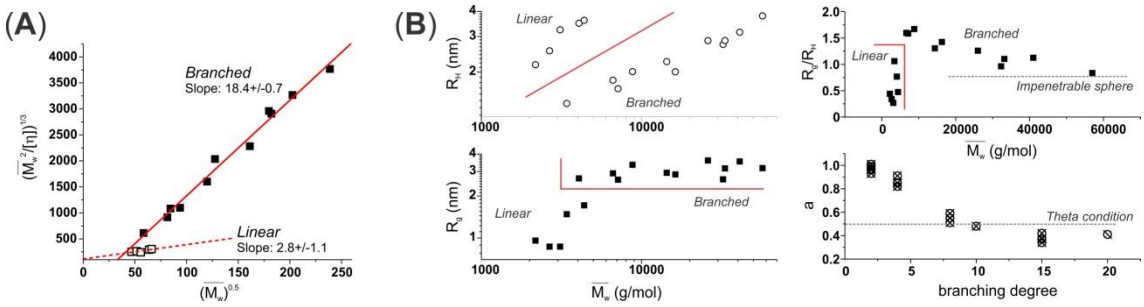

Figure 3.1. (*A*) The persistence length of chains with identical composition (1:1 ES/PS) is inversely proportional to the slope of the plot of $(\frac{\overline{M_w}^2}{[\eta]})^{1/3}$ vs. $\overline{M_w}^{1/2}$. Our analysis stops at the quantification of the slopes without explicitly calculating the persistence lengths, because of the likely large uncertainties in a) the intrinsic viscosity values obtained from GPC measurements (non-zero shear) and b) the values of mass per unit length of the polymers (used to calculate the persistence length from the slopes), which in gradient polymers inherently vary along the chain. (*B*) Left: Plots of R_g and R_H vs. molecular weight for all polymers with 1:1 ES/PS composition. R_H is obtained as viscometric radius ($R_\eta = (3[\eta]\overline{M_w})^{1/3}$ [31]); the approximation $R_H \approx R_\eta$ is assumed valid in the melt, and to at least a qualitative extent in solution too ($\frac{R_\eta}{R_H} \approx 1 \div 1.2$[33]). *(C)* Right: plots of the shape parameter $\frac{R_G}{R_H}$ vs. molecular weight and of the Mark-Houwink parameter *a* vs. degree of branching; in both cases it is apparent that already 8-armed stars are rather compact structures and combs are increasingly similar to hard spheres ($\frac{R_G}{R_H} \leq 1, a \leq 0.4$).

3.1.3 Lignin-based materials: Lignin-*g*-PCL and PLA/lignin blends.

Lignin based materials, Lignin-*g*-PCL and PLA/lignin blends, were prepared by Prof. Lúc Áverous and by Dr. Adriana Kovalcik at Strabourg University (France) and Brno University of Technology (Czech Republic), respectively. The main characteristics of these materials are shown in Table 3.3 and 3.4. Note that in Table 3.4 the characteristics of a PLA/ultrafine talc blend is included for comparisons purposes. The materials were analyzed in Chapter VI.

In the case of PCL-*g*-lignin samples, the lignin employed was an alcaline soda lignin (Protobind 1000) from Green Value SA (Switzerland). Soda lignin is a sulfur-free lignin obtained after extraction and fractionation from wheat straw, with an estimated number average molar mass of around 1120 g mol^{-1}. It is a commercial product that is polydisperse in nature and may contain a mixture of linear and branched chains.

The average number of hydroxyl group/mol of lignin is 5.17, with around 36 wt.% which are aromatic. The glass transition (T_g) of the crude and acetylated lignins are 143 and 117 ºC, respectively.[8]

Soda lignin-based polymers were synthesized by ROP. CL was used as monomer and soda lignin as macroinitiator through its hydroxyl groups. The ROP procedure has been reported previously in [8]. Table 3.3 list the synthesis parameters and the average arm length (AAL) characterization data obtained by ^{1}H NMR. The nomenclature used is PCL_x^y and denotes the approximate lignin composition in wt.% as a subscript, and the approximate AAL of the multiple PCL grafted chains as superscript. AAL number is an estimation of the average degree of polymerization of the grafted PCL chains and is consequence of the synthesis conditions (CL/OH, OH/catalyst molar ratios and reaction times).[8] Table 3.3 shows that to fully assess the grafting of PCL chains onto lignin versus the synthesis of PCL free chains, some blank experiments were carried out synthesizing PCL macromolecules without lignin with the same parameters.

The T_g of PCL-*g*-lignin as well as PCLs was determined by DSC and no differences were found between neat PCL and grafted copolymers indicating that soda lignin and PCL are not miscible.

Table 3.3. Samples description.

Sample	wt % of lignin	CL/OH molar ratio (mol mol^{-1})	AAL
PCL^{127}	0	5	127 (H)
PCL^{15}	0	20	15.0 (L)
PCL^{149}	0	50	149 (H)
$PCL_6^{24.4}$	6	50	24.4 (L)
PCL_{10}^{25}	10	20	25.0 (L)
$PCL_{17}^{16.7}$	17	10	16.7 (L)
PCL_{18}^{20}	18	10	20.0 (L)
$PCL_{29}^{13.7}$	29	5	13.7 (L)
$PCL_{37}^{11.9}$	37	5	11.8 (L)
PCL_2^{44}	2	50	44.0 (I)
$PCL_3^{63.3}$	3	100	63.3 (I)

The letters L, I and H denote low, intermediate and high average arm length (AAL)

In the case of PCL/lignin and PCL/talc blends, the PLA used was Ingeo^{TM} Biopolymer 3251D type (NatureWorks, MN, USA), with a D-lactide content of 1.2% a density of 1.24 g cm^{-3}, a melt flow index (MFI) of 35 g 10 min^{-1} (at 190 ºC and 2.16 kg). The T_g and T_m of PLA resins (moisture in the range of 0.02-0.03 %) were 59.5 and 170.9 ºC, respectively.

Kraft lignin (KL) with M_w 3.8 kDa, $Đ$ of 3.8 and with particle size distribution d90 of 63 μm (Indulin AT, Mead Wescavo corp., USA), and Organosolv lignin (OL) with M_w of 3.2 kDa, $Đ$ of 2.9 and with particle size distribution d90 of 75 μm (Chemicalpoint) were used as a received. Ultrafine talc (UT) (Jetfine 3CA) with particle size distribution d95 of 3.3 μm and specific gravity of 2.78 g cm^{-3} was obtained from Luzenac. It is composed of 62% SiO_2, 31.5% MgO, 0.4% Al_2O_3, 0.3% CaO and 0.2% Fe_2O_3.

PLA and nucleating agents were dried in an oven at 80 ºC for 24 h. Melt blending of neat PLA and PLA with nucleating agents were carried out in a Brabender Plasti-Corder (Brabender 250 EHT, Germany) at a temperature of 190 ºC, a screw speed of 60 rpm for 6

minutes. The samples were code as follows: PLA/UT, PLA/KL, and PLA/OL with a constant amount of 3 wt% nucleating agent.

3.1.4 PCL/carbon nanotubes, PCL or PBS/(PC/MWCNT) nanocomposites with different contents of carbon nanotubes.

Different nanocomposites of PCL/carbon nanotubes, as well as blends of PBS, PCL and a masterbatch of PC/MWNCNT (*i.e.*, PCL/masterbatch and PBS/masterbacth) were employed to investigate the best way to dispersed carbon nanotubes in a polymeric matrix. The discussion of these systems is shown in Chapter VII and the characteristics of these materials are shown in Tables 3.4 to 3.6.

PCL/Carbon Nanotubes nanocomposites and nanohybrids

The Poly (ε-caprolactone) (CAPA 6500) was a commercial sample produced by SOLVAY INTEROX, with a number average molecular weight of 50,000 g/mol. Two types of CNT were employed, functionalized and non-functionalized Multiwall Carbon Nanotubes (MWCNT). The industrial grade NC7000 was produced by NANOCYL (Sambreville, Belgium). The method of synthesis was catalytic carbon vapor deposition (CCVD), the average diameter is 10 nm and their average length is around 2 μm. They contain less than 10 wt% of metal oxide impurities that remain from the catalyst and catalytic support.

In a first step, the MWCNTs were modified by exposing them to a flow of atomic nitrogen (provided from a $Ar+N_2$ microwave plasma)[9] and molecular hydrogen. These functionalized MWCNTs present a grafting of 1 at.% of nitrogen group whose 70% are primary amines groups.[10]

The MWCNT-*g*-PCL nanohybrids were prepared by ROP of ε-CL initiated by primary amine groups grafted onto the MWCNTs and catalyzed by $AlEt_3$. ε -caprolactone (ε-CL, 99%, Fluka) was dried over calcium hydride (93 + %, Acros) for 48 h and, then, distilled under reduced pressure and kept under nitrogen at 4 °C. The triethylaluminum solution ($AlEt_3$, 25 wt.% in toluene, Aldrich) was diluted in dried toluene to obtain a 1 M solution, which was stored under nitrogen atmosphere. The MWCNT-*g*-PCL nanohybrids were prepared by ROP of ε-CL initiated by primary amine groups grafted onto the

MWCNTs (0.5 g) by addition of 1 mL of $AlEt_3$ (1 M) and, then 4 mL of ε-CL (4.12 g). The ROP of ε-CL occurred for 24 h, the reaction system became viscous suggesting that the polymerization took place. The reaction medium was poured in a large excess of heptane to selectively precipitate the PCL-grafted MWCNTs and any 'free' (non-grafted) PCL that could be formed directly in solution via homogeneous initiation from hydroxyl impurities present in the medium. After drying, the obtained gray powder contained a mixture of MWCNT-*g*-PCL nanohybrids and 'free' PCL chains which could be removed by washing the product with toluene via Soxhlet extraction for 1 day. After Soxhlet extraction of 'free' PCL chains with toluene, we determined by TGA analyses that the composition of MWCNT-*g*-PCL + 'free' PCL chains sample is: 20 wt% of MWCNTs, 7 wt% of grafted PCL and 73 wt% of 'free' PCL.

To determine the number-average molecular weight (M_n) of grafted polymer chains, the common strategy consists in breaking the bonds between MWCNTs and the grafted polymer and to analyze the so-formed homopolymer by Gel Permeation Chromatography (GPC). [11] However, this strategy cannot be used to characterize our samples because the polymer chains are linked via a covalent amide bond at the MWCNT surface and amide bonds are known to be more stable than ester bonds of PCL. Nevertheless, by GPC, we determined the number average molecular weight (M_n) of 'free' PCL chains to be equal to 12,000 g/mol with dispersity ($Đ$) of 2.1. Therefore, knowing the quantity of PCL chains covalently grafted per gram of MWCNTs and the primary amine content per gram of MWCNTs, assuming that each NH_2 groups effectively participates in the initiation of ε-CL polymerization, the number average molecular weight of grafted PCL chains can be estimated to be 500-1,000 g/mol (see ref.[10]). This value is lower than the entanglement molecular weight, M_e=3,000 g/mol, reported for PCL.[12] Thus, the final weight composition of the PCL sample filled with MWCNT-*g*-PCL + PCL (3 wt% of MWCNTs) was 3 wt% of MWCNTs, 1 wt% of grafted PCL, 11 wt% of 'free' low molecular weight PCL chains and 85 wt% of the high molecular weight PCL matrix (CAPA6500).

The PCL (*i.e.*, CAPA 6500) was blended with 0.25, 0.3, 0.5, 0.75, 1, 2 and 3 % w/w of the previously prepared MWCNT-*g*-PCL (*i.e.*, nanohybrids) and up to 5 % w/w of non-functionalized MWCNT (*i.e.*, nanocomposites), respectively. Table 3.4 reports the sample

nomenclature (*i.e.*, M refers to unmodified MWCNT and NH refers to nanohybrid and corresponds to the modified MWCNT (MWCNT-*g*-PCL) employed in this work.

Table 3.4. Characteristics and nomenclature of the materials employed.

Name	**MWCNT (%wt)**	***g*-PCL (wt%)**	**Free PCL (wt%)**	**Matrix (wt%)**	**Total PCL (wt%)**
PCL	0	-	-	-	100
$PCL_{99.75}M_{0.25}$	0.25	-	-	-	99.75
$PCL_{99.3}M_{0.3}$	0.3	-	-	-	99.7
$PCL_{99.5}M_{0.5}$	0.5	-	-	-	99.5
$PCL_{99.25}M_{0.75}$	0.75	-	-	-	99.25
$PCL_{99}M_{1}$	1	-	-	-	99
$PCL_{98}M_{2}$	2	-	-	-	98
$PCL_{97}M_{3}$	3	-	-	-	97
$PCL_{95}M_{5}$	5	-	-	-	95
$PCL_{99.75}NH_{0.25}$	0.25	0.1	0.9	98.75	99.75*
$PCL_{99.5}NH_{0.5}$	0.5	0.2	1.8	97.5	99.5*
$PCL_{99.25}NH_{0.75}$	0.75	0.3	2.7	96.25	99.25*
$PCL_{99}NH_{1}$	1	0.4	3.7	95	99*
$PCL_{98}NH_{2}$	2	0.7	7.3	90	98*
$PCL_{97}NH_{3}$	3	1.0	11	85	97*

**In the nanohybrid, the total PCL is equal to the sum of g-PCL, 'free' PCL and PCL of the matrix. In contrast, in the nanocomposites, the total PCL is equal to the PCL added in the blend.*

PCL/masterbatch

A commercial PCL (CAPA 6500, Perstorp, United Kingdom) was purchased from Southern Chemicals (Johannesburg, South Africa). It has a density of 1.1 g cm^{-3}, a melting temperature of 58-60 °C, and a degree of crystallinity of ~ 35%. Its weight-average molecular weight (M_w) and number-average molecular weight (M_n) were measured by GPC, resulting in 113,400 g mol^{-1} and 73,620 g mol^{-1}, respectively, with a polydispersity index (M_w/M_n) of 1,54.

A conductive masterbatch based on 85% low viscosity polycarbonate (Makrolon® 2205 grade, M_w of 20,100 g mol^{-1} [13]) loaded with 15 wt% of MWCNTs (industrial grade NC7000) was obtained from Nanocyl (Sambreville, Belgium). It has a density of 1.175 g cm^{-3}. The average diameter and length of the MWCNTs were respectively 10 nm and 3-4 µm. The carbon nanotubes contained more than 90% carbon and less than 10% metal oxide impurities.

The nanocomposites were prepared by melt mixing in a twin-screw extruder (Thermo Scientific HAAKE Mini Lab II) operated under compressed air (100 rpm, 160 °C, 10 min). After extrusion, the samples were compression moulded at 160 °C for 5 min under 50 kPa using a hydraulic melt press. The calculated weight percentages of the different components in each of the investigated nanocomposites are given in Table 1.

Table 3.5. Weight percentages of the components in the nanocomposites.

PCL (%)	PC (%)	MWCNTs (%)
100	0	0
97	2.55	0.45
93	5.95	1.05
87	11.05	1.95
73	22.95	4.05

PBS/masterbatch

A commercial poly (1,4-butylene succinate) (PBS), extended with 1,6-diisocyanatohexane, was purchased from Sigma-Aldrich (Johannesburg, South Africa).

It has a density of 1.3 g cm^{-3} at 25 °C and a melting temperature of 120 °C. The weight-average molecular weight (M_w) of PBS was 63,000 g mol^{-1} [17].

A conductive masterbatch based on 85% low viscosity polycarbonate (Makrolon® 2205 grade, M_w of 20,100 g mol^{-1} [13]) loaded with 15 wt% of MWCNTs (industrial grade NC7000), was obtained from Nanocyl (Sambreville, Belgium). It has a density of 1.175 g cm^{-3}. The average diameter and length of the MWCNTs were respectively 10 nm and 3-4 μm. The MWCNTs contained more than 90% carbon and less than 10% metal oxide impurities.

The nanocomposites were prepared by melt mixing in a twin-screw extruder (Thermo Scientific HAAKE Mini Lab II at the University of Pretoria, South Africa) operated under compressed air (100 rpm, 160 °C, 10 min). After extrusion, the samples were compression moulded at 160 °C for 5 min under 50 kPa using a hydraulic melt press. The calculated weight percentages of the different components in each of the investigated nanocomposites are given in Table 3.6.

Table 3. 6. Weight percentages of the components in the nanocomposites.

PBS (%)	PC (%)	MWCNTs (%)
100	0	0
97	2.55	0.45
93	5.95	1.05
87	11.05	1.95
73	22.95	4.05

3.1.5 Cyclic, linear and blends of cyclic/linear PCL

Different topologies (i.e., cyclic versus linear) and their blends were studied (see Chapter VII). These materials were prepared by Prof. Grayson and are shown in Table 3.7.

Scheme 3.3 illustrates the synthetic pathway employed to obtain the linear PCL precursors and the corresponding cyclic molecules of almost identical molecular weights. Scheme 3.3 summarizes the three fundamental steps needed to prepare the

materials (for further details see references [14, 15]). *Step 1* (see scheme 3.3a): the L–PCL–OH linear precursor was synthesized by using the tin octanoate–catalyzed, ring opening polymerization of ε–caprolactone from a 3–azido propanol initiator. *Step 2* (see scheme 3.3b): A *bis*–functional linear precursor with complementary azide and alkyne end groups was prepared by esterification of the terminal hydroxyl with 1–pentynoic anhydride.[14] *Step 3* (see scheme 3.3c): cyclization reactions of the linear precursors were performed by Cu (I) catalyzed azide–alkyne cycloaddition (CuAAC) under high dilution. [15]

The polymers were characterized by GPC, NMR,[14] MALDI–TOF MS and ion mobility spectrometry[16] (see Table 3.7). These techniques were employed in order to verify the absence of any substantial amount of linear impurities [17, 18] and to confirm the nearly quantitative cyclization of the linear precursors.

Table 3.7. Number–Average Molecular Weight (M_n) and Dispersity ($Đ = M_w/M_n$) Data for the Synthesized PCL Samples[a]

	M_n			$Đ$	
Polymer	***GPC[b]***	***GPC[c]***	***MALDI***	***GPC***	***MALDI***
L–PCL 3k	6970	3440	3140	1.15	1.03
C–PCL 3k	4560	2180	3200	1.15	1.03
L–PCL 12k	22310	12000	12000	1.12	1.03
C–PCL 12k	19830	10580	12000	1.15	1.04

[a]Data calculated by gel permeation chromatography (GPC) and matrix-assisted laser desorption ionization (MALDI) mass spectrometry. [b]Calibration based upon linear polystyrene standards. [C]Corrected value for PCL [18] using M_n (PCL)=0.259 $M_n(\mathrm{PS})^{1.073}$.

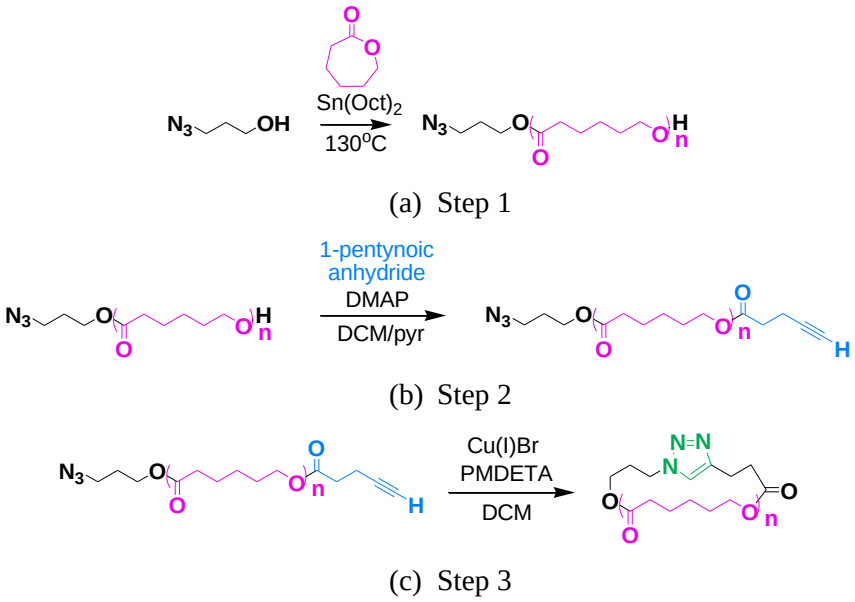

(a) Step 1

(b) Step 2

(c) Step 3

Scheme 3.3. Synthetic pathway employed to obtain: (a) *Step 1*: L–PCL–OH (b) *Step 2*: *bis*–functional precursors and (c) *Step 3*: C–PCL.

The C–PCL/L–PCL (C/L) blends were prepared by solution mixing in chloroform (99.4 purity) using different compositions of cyclic and linear PCL of an average number molecular weight (M_n) of 3 and 12 kg/mol. In this manner, the following C/L blends were obtained: C/L 95/5, 90/10 and 80/20, and these blend compositions were examined at two different molecular weights, namely 3 and 12 kg/mol.

Neat cyclic and linear PCLs were dissolved in chloroform and blended in the desired ratios employing magnetic stirrers in closed reservoirs. The solvent was evaporated in a fume hood at ambient temperature. Then the films were dried under vacuum at 40 °C until the samples achieved a constant weight. These preparation conditions were employed for neat components and their blends.

3.2 Methods

3.2.1 Differential Scanning Calorimetry (DSC)

DSC measurements were performed to the materials indicated above in **a** and **b**, in a DSC 8500 equipped with an intracooler 3, whereas the materials indicated in **c**, **d** and **e** were analyzed with a DSC Pyris 1, both from PERKIN ELMER. The DSCs operated under ultrahigh purity nitrogen, and were calibrated with dodecane, indium and zinc standards. Approximately 5 mg of each sample were used in DSC pans, for the entire test. The different tests applied to the different samples are listed below:

- **Non-Isothermal DSC Scans**

In general, the cooling and heating rate selected was 20 ºC/min. However, some materials like those presented in Chapter IV, required cooling rates in a range from 1 to 50 ºC/min, and a subsequent heating rate of 20 ºC/min. Additionally, in those systems in which it was possible to determine the glass transition temperature, a faster cooling rate (*i.e.*, ballistic cooling) was employed.

- **Isothermal DSC Scans**

The isothermal tests were performed following the protocol of Lorenzo et al.[19], *i.e.*, using a previous test in order to determine the minimum isothermal crystallization temperature in which the material could be cooled down without crystallizing during such cooling. The protocol consists in erasing the thermal history of the material and then cooling down the sample until a selected temperature (*e.g.*,

generally the onset crystallization temperature obtained during a non-isothermal cooling scan is employed as a starting reference temperature). The cooling rate to be use is the faster cooling rate that allows the selected crystallization temperature. Note that this rate would be the same in the isothermal test. Once the material reaches the selected temperature, it is immediately heated up. If a melting peak appears during the heating scan, it means that the material was able to crystallize during the previous cooling, therefore a higher T_c is needed. The same protocol has to be repeated until no melting peak during the subsequent heating is found. In consequence, the selected T_c values which do not generate any peak during the subsequent heating scan would be the minimum T_c, and then the initial T_c to be used in the isothermal test.

Once $T_{c,min}$ is determined, the isothermal test can be performed. The isothermal test consists on cooling down the sample from the melt at a controlled cooling rate, until a selected T_c, starting by the $T_{c,\,min}$. Then the sample is kept at the set temperature for a crystallization time (t_c) until saturation is reached. Finally the sample is subsequently heated in order to record the melting behaviour of the isothermally crystallized sample, specifically the resulting T_m at that specific T_c. With the data of T_c and T_m, the equilibrium melting temperature can be determined using the Hoffman-Weeks extrapolation, by plotting the observed T_m as a function of T_c to observe the intersection of this line with another line with a slope equal to 1 ($T_m=T_c=T_m^0$).

- **Self-Nucleation (SN)**

Self-nucleation is a thermal procedure for the production of self-seeds or self-nuclei within a polymer melt, so that nucleation density can be greatly increased. In principle, the best nucleating agent for any polymer are its own crystal fragments or chain segments with residual crystal memory.[1,17-19]

The SN procedure is schematically shown in Figure 3.2 and can be described as follows: [1,17]

(a) Erasure of thermal history and crystalline memory. The sample is kept in the melt for 3 minutes at a temperature of 25-30 °C above its peak melting temperature. All thermally sensitive nuclei will be destroyed leaving only temperature resistant heterogeneous nuclei of unknown nature (catalyst residues, impurities or any other type of heterogeneities).

(b) Creation of a "standard" semi-crystalline state. The sample is cooled down from the melt at a constant rate (typically 10 or 20ºC/min) to a minimum temperature, low enough to allow the sample to crystallize until saturation. The peak crystallization temperature recorded during this cooling scan is the "standard" crystallization temperature (or standard T_c), since it is only a function of the density of thermally stable nuclei in the sample. The sample is held at the minimum temperature for 3 minutes.

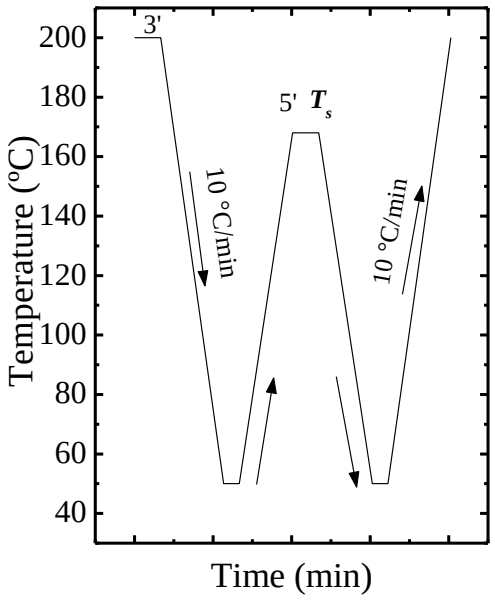

Figure 3.2. Schematic representation of a self-nucleation (SN) experiment.[20]

(c) Thermal conditioning at a temperature denoted T_s (where the sample could melt, self-nucleate or self-nucleate and anneal). The sample is heated at a constant rate (the same rate employed in step (b)) from the chosen minimum temperature up to a selected self-seeding or self-nucleation temperature (commonly denoted T_s), and then the sample is held at this T_s temperature for 5 minutes.

(d) Subsequent cooling at a constant rate from T_s down to the minimum temperature chosen in step (b).

(e) Final melting. Subsequent heating at a constant rate (the same rate as in steps (b) through (d)) from the minimum temperature chosen in (b) up to the maximum melting temperature established in step (a).

The most important parameters during SN are: 1) the heating and cooling rates employed, 2) the T_s temperature, and 3) the time spent at T_s.[20]

From the SN test could be defined three Domains which were described in Chapter II. General Concepts.

- **Successive Self-nucleation and Annealing (SSA)**

In order to design a correct SSA protocol, SN must be performed previously. Once SN is performed (as described above), $T_{s,\ ideal}$ is determined. SSA can now be designed by employing $T_{s,\ ideal}$ as the first T_s of the thermal protocol schematically shown in Figure 3.3.

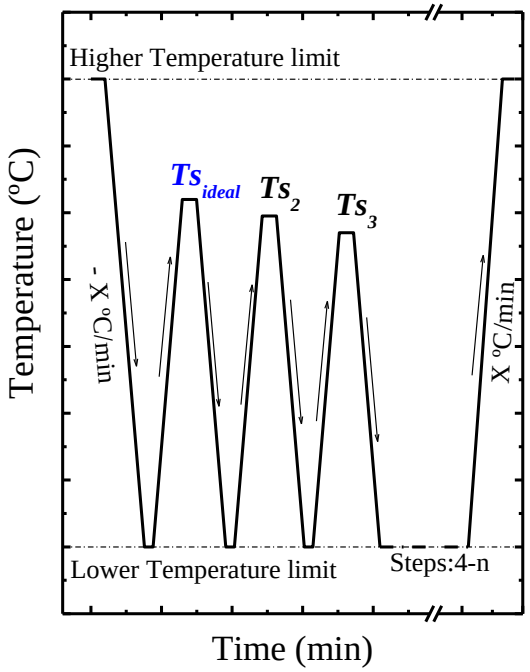

Figure 3.3. *SSA* thermal protocol schematic representation. Cooling and Heating scans are performed at a constant scanning rate.[20]

Figure 3.3 shows that the first two steps of SSA are identical to the SN protocol described above (Figure 3.2). The correct SSA thermal protocol can be described as:

(A) Preparation steps to achieve a reference ideal self-nucleated state.

(a) Erasure of previous thermal history by heating to a higher temperature limit (Figure 3.2) where crystalline memory disappears (usually at 30 ºC above the melting peak of the sample).

(b) Creation of the initial "standard" semi-crystalline state by cooling the sample from the melt at 20 ºC/min. For the sake of clarity, a constant heating and cooling rate of 20 ºC/min is assumed in this sample protocol (other rates could be used too). The effect of scanning rates will be examined below.

(c) The sample is heated at 20 ºC/min from the lower temperature limit to the ideal self-nucleation temperature ($T_{s,\,ideal}$) determined in a previous SN experiment.

(d) The sample is held at $T_{s,\,ideal}$ for 5 min. During this first step the sample is only self-nucleated and no annealing or fractionation occurs during this first step. After this first step the sample is saturated with the maximum number of self-nuclei since $T_{s,\,ideal}$ was employed (see SN section above). Hence, in this step the sample achieves a reference morphology given by the maximum nucleation density generated. This is a crucial first step in the SSA protocol and one that is often ignored in the literature. Selecting the first T_s for SSA randomly or at the end of the melting trace does not guarantee a reference state for the following fractionation steps.

(e) Cooling from $T_{s,\,ideal}$. The sample is cooled at 20 ºC/min from $T_{s,\,ideal}$ to the lower temperature limit, the polymer will crystallize after having been ideally self-nucleated achieving a reference semi-crystalline state.

(B) Thermal fractionation by SSA.

(f) The sample is heated at 20 ºC/min from the lower temperature limit to T_{s2}. The difference in temperature between $T_{s,\,ideal}$ and T_{s2} is usually set at 5°C. This is the fractionation window (ΔT_f) since it determines the width of the thermal fraction and it should be kept constant throughout the SSA experiment. The sample is held at T_{s2} for 5 min. This is the isothermal fractionation time (t_s) and it should be kept constant for all SSA steps. T_{s2} is within *Domain III*, hence it produces annealing of unmolten crystals and self-nucleation of the molten polymer when the sample is cool down. Some isothermal crystallization at T_{s2} also occurs. During the 5 min at T_{s2} the first thermal fraction is generated in the sample (due to the isothermal crystallization and annealing

process that takes place). This first thermal fraction will be "refined" by the subsequent thermal cycles applied by SSA (although it will be mostly affected by the cooling from T_{s2} and subsequent heating to T_{s3}).

(g) The sample is cooled at 20 ºC/min from T_{s2} down to the lower temperature limit. During cooling, the molten part of the sample will be self-nucleated by all surviving self-nuclei plus all the crystals that were created and annealed during the 5 min at T_{s2}.

(h) The sample is heated from the lower temperature limit at 20 ºC/min up to T_{s3}. All the crystal population that melts below T_{s3} will disappear, while the second fraction is created during the 5 min at T_{s3}. At the same time the first fraction will be "refined" by further annealing.

(i) Steps similar to (g) and (h) are repeated at progressively lower T_s temperatures as indicated in Figure 3.2 until the full width of the melting range has been encompassed.

(C) Melting of the SSA fractionated sample.

The sample is heated at 20 ºC/min from the lower temperature limit up to the melt state (higher temperature limit). In this final step, the result of the SSA fractionation or fractionation profile is revealed.[20]

3.2.2 Polarized Light Optical Microscopy (PLOM)

A PLOM Olympus BX51 was employed incorporating a λ plate in between the polarizers at 45º to facilitate observation and determine the sign of the birefringence. The microscope was equipped with an Olympus SC50 digital camera. A Linkam LNP95 hot stage, which was connected to liquid nitrogen, was coupled to the equipment.

Film samples of the selected materials were prepared by solution casting using chloroform as a solvent (i.e., 4 wt%). The polymer solution was deposited on a glass slide at ambient temperature to form thin films that were uncovered (no cover glass was employed). The cast samples were dried by evaporating the solvent under a hood at controlled temperature for at least 24 hours. These uncovered samples were first heated to an adequate temperature in order to erase the thermal history and then crystallize from the melt by cooling until -40 ºC at a selected cooling rate (*i.e*, 5, 10 and 50 ºC/min). These procedure was employed those samples used in Chapter IV. For the

other samples, the preparation of the film was from the melt, due to difficulties in the dissolution process or because they were blends, whose morphology can be altered by using a solution casting preparation.

3.2.3 Atomic Force Microscopy (AFM)

AFM measurements were performed by our group in the PBSA (Chapter IV), whereas the other AFM measurements reported in this work corresponds to collaborations with other groups. However, the process of preparation of the AFM samples is similar.

For the PBSA samples, solution at 2 and 4 wt% in chloroform were prepared for measurements at room temperature and with a temperature ramp (temperature-dependent measurements), respectively.

The "holder" of these solutions was a piece of silicon wafer, which was previously washed. The washing procedure is as follow:

- Cleaning with pressure air.
- Cleaning in distilled water and then the silicon wafer was maintain in distilled water for 30 minutes.
- Cleaning with pressure air.
- Cleaning in sulfuric acid for 30 minutes. Then the sample was removed from the acid and put in distilled water placed on a petri dish.
- Cleaning in distilled water.
- Cleaning with pressure air.

Immediately after the cleaning process described above, one drop of solution was placed in the cleaned silicon wafer. Then, the silicon wafer was placed in a spin coating equipment, in which a program of 2000 rpm per 60 seconds was selected. After the spin coating process finalized, the sample was placed in a vacuum oven and the sample was heated until 150 ºC per 30 minutes, in order to achieve a homogeneous film, and then the sample was cooled down until room temperature overnight at approximately 0.1 ºC/min.

The AFM NanoWizard I from JPK Instruments equipped with a heatable sample holder was used. Cantilevers were purchased from NT-MDT. Measurements in the net repulsive regimen were performed with NSG30 cantilevers (k=40 N/m and w_0=320 kHz) with an excitation frequency $w<w_0$ and a free amplitude in the range of 60 nm. For neat attractive measurements, softer NSG03 cantilevers (k=1.74 N/m and w_0=90 kHz) were used, and a free amplitude of about 45 nm and an excitation frequency $w>w_0$ were chosen. To ensure measuring in the net attractive regime, amplitude and phase distance curves were checked before imaging. AFM height images were corrected by plane and line leveling, whereas amplitude and phase images were corrected only by line leveling with the software Gwyddion. [21]

3.2.4 Nuclear Magnetic Resonance (NMR)

All samples were investigated using a time efficient but non-quantitative cross polarization (CP) ^{13}C magic angle spinning MAS NMR technique.

NMR measurements were performed at ^{1}H and ^{13}C Larmor frequencies of 400.16 and 100.06 MHz, respectively, on BRUKER spectrometers equipped with a 4 mm double-resonance magic-angle spinning (MAS) probe at a spinning frequency of 5 kHz. For high-field measurements the sample was packed into a 4 mm ZrO_2 MAS rotor in the form of a small cylinder. A BVT3000 heater was used for temperature regulation with the bearing air as heat transfer medium. The temperature accuracy amounted to ± 1 K and the temperature gradient over the sample was in the range of 0.5 K. The repetition delay was chosen to be 2 s. [22]

^{13}C CP MAS NMR spectra: The effect of the cross polarization sequence is to transfer the high polarization of protons to the less polarized ^{13}C atoms. But this effect is non quantitative since both phases of the sample (crystalline and amorphous) are not polarized according to their mass ratio. For short contact times (time of polarization transfer) the transfer of polarization to ^{13}C-atoms occurs only from the closest ^{1}H atoms (for the more rigid regions of the sample). With increasing contact times, protons, which have a higher distance to the ^{13}C-atoms, also contribute to the transfer. Accordingly, a ^{13}C CP MAS NMR spectra with short contact time (< 50 s) yields

mostly the information of the crystalline (more rigid) part of the sample, whereas with higher contact times also the amorphous (more mobile) parts will be detected. Another advantage of this technique is its time efficiency, since the shorter T_1 relaxation time of the protons (shorter compared to the T_1 of ^{13}C) determines the repeating time (recycle delay) of the experiment.

^{1}H time domain measurements: The acquired signal in the domain is a superposition of three components: the rigid part, the mobile-amorphous region and an intermediate state, the so-called “rigid-amorphous" phase which has an intermediate mobility. The decay of the signal depends on the homonuclear dipolar coupling: In the crystalline region with a low mobility, the resulting strong dipolar coupling will lead to a fast decay of the signal. In the amorphous phase with a higher mobility the signal will decay slower, since the dipolar couplings are averaged by the fast motion (far above T_g). The decay of the rigid-amorphous signal exhibits a value between the corresponding values of the crystalline and the mobile phase.

3.2.5 X-rays: Small and Wide-Angle X-rays Scattering (SAXS/WAXS)

X-rays experiments were performed in the ALBA synchrotron (Barcelona, Spain), and the European Synchrotron Radiation Facility (Grenoble, France). Measurements in Laboratory equipments were performed in the Martin Luther University (Halle-Salle, Germany) and in Centro de Física de Materiales (CFM) (CSIC-UPV/EHU) - Materials Physics Center (MPC) (Donostia-San Sebastián, Spain) for the copolyesters systems and copolysulfides ones, respectively. The characteristics of each equipment are as following:

X-rays at lab-scale

A BRUKER D8 Advance diffractometer working in parallel beam geometry with CuK_α transition photons of wavelength λ=1.54 Å was employed for WAXS measurements. A linear detector by LYNXEYE was used with an active area of 14.4 mm *x* 16 mm. The experiments were performed in reflection mode (θ-2θ configuration), varying the scattering angle 2θ from 10 to 30 º with step of 0.05 º. The measuring time was 10 s/point.

SAXS experiments were performed with a RIGAKU 3-PINHOLE PSAXS-L equipment operating at 45 kV and 0.88 mA. A MICROMAX-002+ X-ray generator

system was employed. This system is composed of a microfocus sealed tube source module and an integrated X-ray generator unit which also produces CuK_α transition photons. Both flight path and sample chamber are under vacuum. A two-dimensional multiwire X-ray detector (Gabriel design, 2D-2000X) was used. The azimuthally averaged scattered intensities were measured as a function of wave vector q, and $q=4\pi\lambda^{-1}sin\theta$. Reciprocal space calibration was performed using silver behenate as standard. The samples were films that were placed in a LINKAM Scientific Instruments THMS 600 temperature controller (range -196 to +600 ºC, stability <0.1 ºC) in transmission geometry, with sample-detector distances of 2 m and 50 cm. Measuring times of 20 min were employed. In some cases, when the material was in the rubbery state, the films could not be measured, as they flow out of the measuring spot. Measurements were only performed on samples that had enough dimensional stability during measurements.

In temperature-dependent experiments, patterns were taken at room temperature and during heating. This equipment was employed in Chapter V for PPS, PES and their copolymers.

In the case of PBSA, complementary measurements were performed using an X-ray generator of rotating anode type with Cu target from Rigaku operated at 2.4 kW. A confocal optics from Osmic provided monochromatic CuK_α radiation. The x-ray beam was collimated by a system of three pinholes. At the position of the sample, the size of the beam was ~350 μm. The flight path was fully evacuated and the scattered radiation was detected by a Bruker Hi-Star multiwire proportional chamber. The data were collected as frames of 1024*x*1024 pixels and later on calibrated using silver behenate. The accessible q range was 0.01 $Å^{-1}<q<0.14$ $Å^{-1}$. To control the temperature of the samples, a hot stage from Linkam was used. Heat conduction paste was used for good thermal contact between the holder and the hot stage in vacuum.[23] The thermal protocol employed for the samples is show schematically in Scheme 3.4.

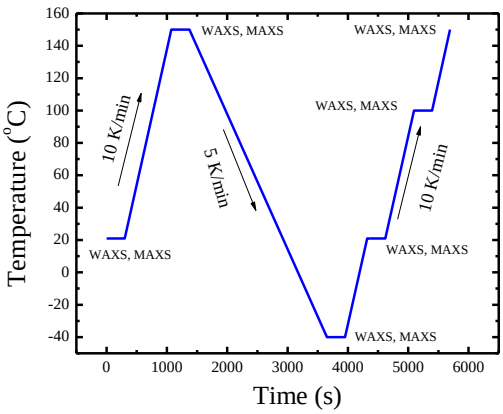

Scheme 3.4. Schematic representation of the thermal protocol employed to take the WAXS and SAXS patterns. The WAXS and SAXS patterns were taken during 300 s and 600 s, respectively, at 21 º C (sample as a received), then at 30 ºC above the melting temperature of the material. Then the samples were cooled down until -40 ºC and heating up with holding steps at 21 ºC, at 10 degrees below the melting temperature of the material and 30 ºC above the melting temperature of the material.

X-rays with synchrotron radiation

In the ALBA synchrotron simultaneous WAXS and SAXS were performed at the beamline BL11-NCD (samples in Chapter IV and VII) and BL11-NCD-SWEET (in this case the SAXS detector was a Pilatus 1M3S from dielectrics, with an active area of 168.7 (width)*x*179.4 (height) mm, pixel size 172 μm^2) (samples in Chapter VI). The samples were placed in DSC pans, and the DSC pans were put on a Linkam THM600 hot stage couple to a liquid nitrogen system. The hot stage was programmed to perform the cooling and subsequent heating (*i.e.*, therefore recording the crystallization and melting process) and at the same time register the SAXS/WAXS patterns. The energy of the x-rays source was 12.4 keV (λ=1.0 Å). In the SAXS configuration, the sample-detector (ADSC Q315r detector, Poway, CA, USA) with a resolution of 3070*x*3070 pixels, pixel size 102 μm^2 distance was 6495.0 mm with a tilt angle of 0º, whereas in the WAXS configuration, the sample-detector (Rayonix LX255-HS detector, Evanston, IL, USA) with resolution of 1920*x*5760 pixel, pixel size of 44 μm^2 distance was 132.6 mm with a tilt angle of 21.2º. The intensity profile was output as the plot of the scattering intensity (*I*) vs scattering vector, $q=4\pi sin\theta\lambda^{-1}$, where λ is the x-ray wavelength and 2θ is the scattering angle. The scattering vector was calibrated using silver behenate (SAXS) and chromium (III) oxide (WAXS).

In the ESRF the X-rays were also performed simultaneously at the beamline BM26-B at the European Synchrotron Radiation Facility (ESRF) in Grenoble, France. The energy of x-ray source was 12 keV (λ=0.1033 nm), and sample-to-detector distances of 274 and 2946 mm for WAXS and SAXS, respectively. Two Pilatus detectors (300 k and 1 M) with 172*x*172 μm pixel size were used to record the scattering pattern at wide and small angle. The scattering vector was calibrated using silver behenate (SAXS) and alumina powder (WAXS). Scattering data were also corrected for background scattering. The samples were placed in DSC pans, and the DSC pans were put on a Linkam DSC600 hot stage couple to a liquid nitrogen system. The hot stage was programmed to perform the cooling and subsequent heating (*i.e.*, therefore recording the crystallization and melting process) and at the same time register the SAXS/WAXS patterns

In the ALBA synchrotron the thermal protocols used were those employed in the DSC, this mean non-isothermal, isothermal, SN and SSA which are explained below, and were performed for the samples in Chapter IV, VI and VII. In the case of the ESRF synchrotron non-isothermal and isothermal test were performed for the PBSA of the Chapter IV.

3.3 References

[1] T. Debuissy, P. Sangwan, E. Pollet, L. Avérous, Study on the structure-properties relationship of biodegradable and biobased aliphatic copolyesters based on 1,3-propanediol, 1,4-butanediol, succinic and adipic acids, Polymer 122 (2017) 105-116.
[2] T. Debuissy, E. Pollet, L. Avérous, Synthesis and characterization of fully biobased poly(propylene succinate-ran-propylene adipate). Analysis of the architecture-dependent physicochemical behavior, J. Polym. Sci., Part A: Polym. Chem. 55 (2017) 2738-2748.
[3] R. d'Arcy, A. Siani, E. Lallana, N. Tirelli, Influence of Primary Structure on Responsiveness. Oxidative, Thermal, and Thermo-Oxidative Responses in Polysulfides, Macromolecules 48 (2015) 8108-8120.
[4] R. d'Arcy, A. Gennari, R. Donno, N. Tirelli, Linear, Star, and Comb Oxidation-Responsive Polymers: Effect of Branching Degree and Topology on Aggregation and Responsiveness, Macromol. Rapid Commun. 37 (2016) 1918-1925.
[5] M. Bohdanecky, New method for estimating the parameters of the wormlike chain model from the intrinsic viscosity of stiff-chain polymers, Macromolecules 16 (1983) 1483-1492.
[6] M.S. Kök, A.S. Abdelhameed, S. Ang, G.A. Morris, S.E. Harding, A novel global hydrodynamic analysis of the molecular flexibility of the dietary fibre polysaccharide konjac glucomannan, Food Hydrocolloids 23 (2009) 1910-1917.
[7] K.S. Seo, G.B. Caflisch, Molecular dimensions and melt rheology of an all-aromatic liquid crystalline polymer, J. Polym. Sci., Part B: Polym. Phys. 39 (2001) 2378-2389.

[8] S. Laurichesse, L. Avérous, Synthesis, thermal properties, rheological and mechanical behaviors of lignins-grafted-poly(ε-caprolactone), Polymer 54 (2013) 3882-3890.
[9] B. Ruelle, S. Peeterbroeck, T. Godfroid, C. Bittencourt, M. Hecq, R. Snyders, P. Dubois, Selective Grafting of Primary Amines onto Carbon Nanotubes via Free-Radical Treatment in Microwave Plasma Post-Discharge, Polymers 4 (2012) 296.
[10] B. Ruelle, S. Peeterbroeck, C. Bittencourt, G. Gorrasi, G. Patimo, M. Hecq, R. Snyders, S.D. Pasquale, P. Dubois, Semi-crystalline polymer/carbon nanotube nanocomposites: Effect of nanotube surface-functionalization and polymer coating on electrical and thermal properties, React. Funct. Polym. 72 (2012) 383-392.
[11] H. Kong, C. Gao, D. Yan, Functionalization of Multiwalled Carbon Nanotubes by Atom Transfer Radical Polymerization and Defunctionalization of the Products, Macromolecules 37 (2004) 4022-4030.
[12] J. Gimenez, P. Cassagnau, A. Michel, Bulk polymerization of ε-caprolactone: Rheological predictive laws, J. Rheol. 44 (2000) 527-547.
[13] G.R. Kasaliwal, A. Göldel, P. Pötschke, G. Heinrich, Influences of polymer matrix melt viscosity and molecular weight on MWCNT agglomerate dispersion, Polymer 52 (2011) 1027-1036.
[14] J.N. Hoskins, S.M. Grayson, Synthesis and degradation behavior of cyclic poly(ε-caprolactone), Macromolecules 42 (2009) 6406-6413.
[15] B.A. Laurent, S.M. Grayson, An efficient route to well-defined macrocyclic polymers via "click" cyclization, J. Am. Chem. Soc. 128 (2006) 4238-4239.
[16] J.N. Hoskins, S. Trimpin, S.M. Grayson, Architectural differentiation of linear and cyclic polymeric isomers by ion mobility spectrometry-mass spectrometry, Macromolecules 44 (2011) 6915-6918.
[17] J.N. Hoskins, S.M. Grayson, Cyclic polyesters: Synthetic approaches and potential applications, Polymer Chemistry 2 (2011) 289-299.
[18] P. Dubois, I. Barakat, R. Jerome, P. Teyssie, Macromolecular engineering of polylactones and polylactides. 12. study of the depolymerization reactions of poly(ε-caprolactone) with functional aluminum alkoxide end groups, Macromolecules 26 (1993) 4407-4412.
[19] A.T. Lorenzo, M.L. Arnal, J. Albuerne, A.J. Müller, DSC isothermal polymer crystallization kinetics measurements and the use of the Avrami equation to fit the data: Guidelines to avoid common problems, Polym. Test. 26 (2007) 222-231.
[20] A.J. Müller, R.M. Michell, R.A. Pérez, A.T. Lorenzo, Successive Self-nucleation and Annealing (SSA): Correct design of thermal protocol and applications, Eur. Polym. J. 65 (2015) 132-154.
[21] A.-K. Löhmann, T. Henze, T. Thurn-Albrecht, Direct observation of prefreezing at the interface melt–solid in polymer crystallization, Proceedings of the National Academy of Sciences 111 (2014) 17368-17372.
[22] K. Schäler, A. Achilles, R. Bärenwald, C. Hackel, K. Saalwächter, Dynamics in Crystallites of Poly(ε-caprolactone) As Investigated by Solid-State NMR, Macromolecules 46 (2013) 7818-7825.
[23] I. Gunkel, T. Thurn-Albrecht, Thermodynamic and Structural Changes in Ion-Containing Symmetric Diblock Copolymers: A Small-Angle X-ray Scattering Study, Macromolecules 45 (2012) 283-291.

CHAPTER IV.

CRYSTALLIZATION OF RANDOM COPOLYESTERS: ISODIMORPHIC BEHAVIOUR

4.1.General Introduction

Copolymers synthesis offers the ability to alter the properties of homopolymers in a desired direction by the introduction of the appropriately chosen second repeating unit. In this way, the desired properties of two different homopolymers are combined in a single copolymer. The magnitudes of properties, such as crystallinity, flexibility, crystallization and melting temperature, as well as glass transition temperature are generally altered, and even the directions of these changes can be selected depending on whether statistical, alternating or block copolymers are involved.[1]

The most commonly produced copolymers, due to their versatility and simplicity are the random copolymers, in which the final properties are generally in between the properties of the parent components or co-monomers.

Random copolymers are those in which the probability of finding a given constitutional repeating unit at any given site is independent of the nature of the adjacent position. The term "*random copolymer*" is occasionally used for copolymers with the additional restriction that the constitutional repeating units are present in equal amounts. Therefore, random copolymers are a special case of statistical copolymers, in which statistical laws, *e.g.*, Markovian statistics (*i.e.*, first- or second-order) are obeyed. Although, it is worth noting that random copolymers obeys Bernoullian statistics (*i.e.*, zero-order Markovian statistics).[1]

Random copolymerization is a simple synthetic strategy of combining the properties of two distinct homopolymers. It provides random covalent links between different comonomers, therefore ensuring total melt miscibility, at variance with the typical immiscible polymer blends. Their thermal and mechanical properties can be tailored by changing the composition of the copolymer.

This work deals with the crystallization of random copolyesters, which are very important polymeric materials due to the fact that many of them can be biobased and

biodegradable. Their hydrolytic degradation rates strongly depend on their chemical structure, degree of crystallinity and morphology. Their morphology and crystallinity can also influence their mechanical properties, permeability to gases and thermal stability.[2]

The crystallization of random copolymers is a complex function of the chemical structure of the repeating units involved, molar ratio of comonomers and molecular weight. In general, the crystallization of random copolymers depends on whether the crystalline phase is pure or if the co-units enter into the crystallite, either in equilibrium or as a defect. This is reflected on both the crystallization and in the subsequent melting, generating three different behaviours, in copolymers with crystallizable parent components.

Scheme 4.1 represents the three general ways in which random copolymers can crystallize, as deduced from the trends of how the thermal transitions vary as a function of copolymer composition. The thermal transitions represented as examples in Scheme 4.1 are those typically determined by non-isothermal Differential Scanning Calorimetry (DSC) experiments. In addition, for the sake of clarity, cartoons of how the comonomeric units are located into the crystal lattice in these three crystallization models are also shown.

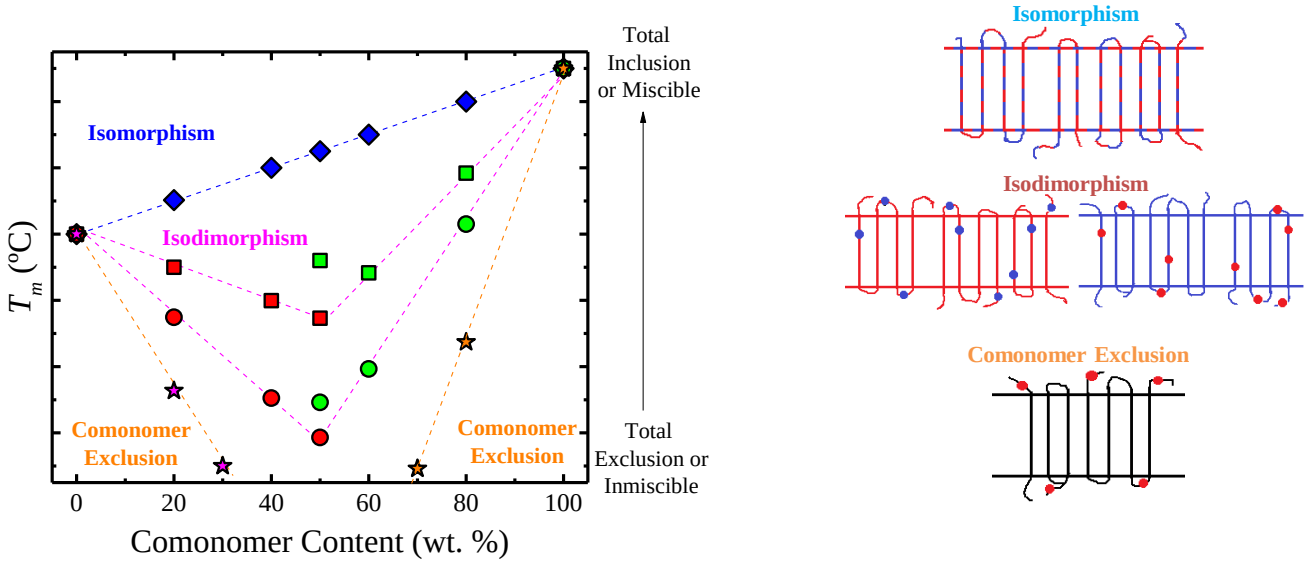

Scheme 4.1. Schematic representation of the different melting temperature, T_m, trends as a function of comonomer content (left).[2] Cartoons of the models of the different crystallizations modes (right) described on the left.

Provided that the two crystallizable repeating units meet strict molecular requirements, the copolymers can crystallize in the same crystal lattice, in the entire composition range. In other words, the two comonomeric units along the chain can co-crystallize regardless of composition. Therefore, the two comonomers can be considered miscible in the crystalline state. This case is referred to in Scheme 4.1 as total inclusion of comonomers in a single crystal lattice or isomorphic behaviour (see the corresponding cartoon (Isomorphism) at the right of the Scheme 4.1). Thermal and structural properties, such as melting temperatures and lattice parameters, typically show linear dependence on composition (see Scheme 4.1).

The concept of isomorphism in the polymer field was first considered by Natta et al.[3] According to Allegra and Bassi [4], the requirements to observe macromolecular isomorphism in random copolymers are: *(i)* approximately same shape, volume and compatible conformations of the different monomer units, *(ii)* analogous chain conformation, lattice symmetry and dimensions of the crystalline phase of the "parent" homopolymers, *(iii)* total miscibility in the melt of the comonomers and *(iv*) similar rate of crystallization of the two parent homopolymers. As a result, a total inclusion of both comonomers in the crystalline lattice occurs, and the composition of the crystal perfectly reflects the one of the polymer chain. Because of the specific conditions to be met, only four random copolyesters have been reported to exhibit isomorphic crystallization: poly (hexamethylene gluarate-*ran*-hexamethylene azelate) (P(HG-*ran*-HA)),[5] poly (ε-caprolactone-*ran*-2-oxepane-1,5-dione) (P(CL-*ran*-OPD)),[6] poly (ε-caprolactone-*ran*-ω-pentadecalactone) (P(CL-*ran*-PDL)),[7] and poly (butylene succinate-*ran*-butylene fumarate) (P(BS-*ran*-BF)).[8]

When the two homopolymers (A and B) do not share a common crystalline structure, but they still have similar repeating units, an isodimorphic behavior of the random copolymers (A-*ran*-B) constituted by the respective repeating units can result. A partial inclusion of comonomer A in the unit cell of homopolymer B crystals is typically observed for copolymers with composition rich in B units, and *vice versa*. However, the inclusion is only partial, *i.e.*, the concentration of comonomer A in the B crystals is lower than its concentration in the polymer chain. Since both comonomers can be hosted in the crystals of the majority component (comonomer A in the B crystals, and comonomer B in the A crystals), a "pseudo-eutectic" trend of the thermal

properties (melting and crystallization temperatures, as well as their enthalpies) is obtained ((see the T_m as function of comonomer composition (left) and the corresponding cartoon (isodimorphic case) at the right of the Scheme 4.1).

As represented in Scheme 4.1, isodimorphic copolymers are characterized by a homopolymer-A-rich crystalline phase in one side of the pseudo-eutectic region and a homopolymer-B-rich crystalline phase on the other side of the eutectic region. While isodimorphic copolymers can still crystallize in the entire composition range, the melting temperature of the two crystalline phases is depressed by the presence of the included second comonomer, until a minimum value is reached for an intermediate composition. As will be show below, recently, three phases have been found at the eutectic region, *i.e.*, mixed amorphous phase, homopolymer-A-rich crystalline phase and homopolymer-B-rich crystalline phase. This is the reason behind the double data points represented at the eutectic composition in Scheme 4.1. More precisely, the term pseudo-eutectic point or pseudo-eutectic region should be preferred, since the three phases are not in thermodynamic equilibrium. Hence, at the pseudo-eutectic region the copolymers can display double crystalline superstructural morphologies (see below).

According to the literature, there are no general rules that can unambiguously predict if a copolymer will display isodimorphism or not. In fact, even in those cases where the comonomers have similar chemical structures and are miscible in the amorphous phase, the possibility of forming a mixed crystalline unit cell, or in other words the efficiency of comonomer inclusion, is not easily determined. In spite of this, some features affecting isodimorphic behavior have been highlighted in the literature. For instance, a homopolymer with a large unit cell is expected to include more easily a comonomer whose respective homopolymer presents a smaller unit cell.[9] Also, a comonomer with an even number of methylene groups in the repeating unit will most likely include similar even CH_2 comonomers in its unit cell, and exclude those with odd number of carbon atoms in their chemical structure. [5, 10] These empirical rules, related to the miscibility of the comonomers in the crystalline state are not always strictly obeyed. However, below the important rules for this chapter are going to be described.

Scheme 4.1 show two curves for the isodimorphic case from top to bottom, representing different degrees of inclusion of the comonomers in the homopolymer crystal lattice. With a higher degree of inclusion, the crystallization/melting behavior deviates less from the isomorphic case. In contrast, when the comonomer units are largely excluded from the crystals, even though the copolymer may still able to crystallize in all compositions, the thermal response will be closer to that of a copolymer characterized by a complete rejection of the co-units to the amorphous phase, discussed in the following.

When comonomer B is completely rejected from the crystalline structure of the major component (comonomer A) (see the corresponding cartoon (comonomer exclusion) at the right of the Scheme 4.1), the transition temperatures and enthalpies are strongly depressed as the content of comonomer B increases in the random copolymer, and there exists a range of copolymer compositions where the copolymer remains completely amorphous. Random copolymers with complete exclusion, where symmetrical compositions do not crystallize are very common and constitute the most commonly reported case in the literature.[2]

Several examples of isodimorphic copolyesters, mainly poly (hydroxyalkanoates), were reported in the review of Pan et al., in 2009.[11] In Table 4.1 more recent works on random aliphatic copolyesters and one work in unsaturated copolyester ((poly (butylene succinate-*ran*-*cis*-butene succinate))[12], are summarized indicating for each system the type of comonomers and the melting points of each homopolymer. It was note that in most of the cited studies, the co-crystallization of the co-units in the whole composition range was observed, but the isodimorphic behavior of the systems is seldom discussed in detail.

Table 4.1. List of isodimorphic random aliphatic copolymers reported in the literature after 2009.

System	Acid Group		Alcohol group	T_m (ºC)	Reference
PHS	Succinic acid	+	1,6- Hexanediol	52.6	[13]
P(HS-*ran*-HA)	Adipic Acid	+	1,6- Hexanediol	54	
P(HS-*ran*-HSu)	Suberic acid	+	1,6- Hexanediol	63.3	
P(HS-*ran*-HSe)	Sebacic acid	+	1,6- Hexanediol	64.3	
P(HS-*ran*-HD)	Dodecanedioic acid	+	1,6- Hexanediol	70	
P(HS-*ran*-HA)	Succinic acid	+	1,6- Hexanediol	57	[14]
	Adipic Acid	+	1,6- Hexanediol	62	
P(HSe-*ran*-HA)	Sebacic acid	+	1,6- Hexanediol	68.9	[15, 16]
	Adipic Acid	+	1,6- Hexanediol	60	
P(PS-*ran*-ES)	Succinid acid	+	1,3-propanediol	45.4	[10]
	Succinic acid	+	ethylene glycol	105.5	
P(BS-*ran*-HS)	Succinic acid	+	1,4-butanediol	113.8	[17]
	Succinic acid	+	1,6- Hexanediol	51	
P(HG-*ran*-HP)	Glutaric acid	+	1,6- Hexanediol	30.3	[5]
	Pimelic acid	+	1,6- Hexanediol	49.9	
P(HP-*ran*-HA)	Pimelic acid	+	1,6- Hexanediol	49.9	
	Azelaic acid	+	1,6- Hexanediol	53	
P(HG-*ran*-HA)	Glutaric acid	+	1,6- Hexanediol	30.3	
Isomorphic	Azelaic acid	+	1,6- Hexanediol	53	
P(BS-*ran*-BAz)	Succinic acid	+	1,4-butanediol	115	[18-20]
	Azelaic acid	+	1,4-butanediol	41	
P(BS-*ran*-BA)	Succinic acid	+	1,4-butanediol	114	[21]
	Adipic Acid	+	1,4-butanediol	51-59	
PHSu	Suberic acid	+	1,6- Hexanediol	63.8	[22]
P(HSu-*ran*-HSe)	Sebacic acid	+	1,6- Hexanediol	65	
P(HSu-*ran*-HA)	Adipic Acid	+	1,6- Hexanediol	59.4	
P(HA-*ran*-BA)	Adipic Acid	+	1,6- Hexanediol	59.8	[23]

	Adipic Acid	+	1,4-butanediol	51.2		
P(PS-*ran*-BS)	Succinic acid	+	1,3-propanediol	50		[24]
	Succinic acid	+	1,4-butanediol	116		
P(PA-*ran*-BA)	Adipic Acid	+	1,3-propanediol	48		
	Adipic Acid	+	1,4-butanediol	58		
	Monomer A		**Monomer B**	**T_m (ºC)**		**Reference**
P(LLA-*ran*-L-2HB)	L-lactic acid	+	L-2hydroxybutanoic acid	165	101	[25]
PB-*ran*-Manx	diol 2,4:3,5-di-O-methylene-D-mannitol(Manx)	+	Poly(dimethyle succinate)	111.5	125	[26]
P(BS-*ran*-CL)	Poly(butylene succinate)	+	Poly(ε-caprolactone)	110	55	[27]
P(BL-*ran*-CL)	Poly(ϒ-butyrolactone)	+	Poly(ε-caprolactone)	63.5	57.6	[28]
P(BL-*ran*-VL)	Poly(ϒ-butyrolactone)	+	Poly(σ-valerolactone)		58.6	
P(CL-*ran*-DL)	Poly(ε-caprolactone)	+	Poly(ω-pentadecalactone)	52	92	[29]
P (BS-*ran*-*c*BS)	Poly (butylene succinate)	+	Poly (*cis*-butene succinate)	68.8	21.4	[12]

In this work, we consider that in order to determine whether random copolyesters are isodimorphic, the points indicated on Scheme 4.2 should be met.

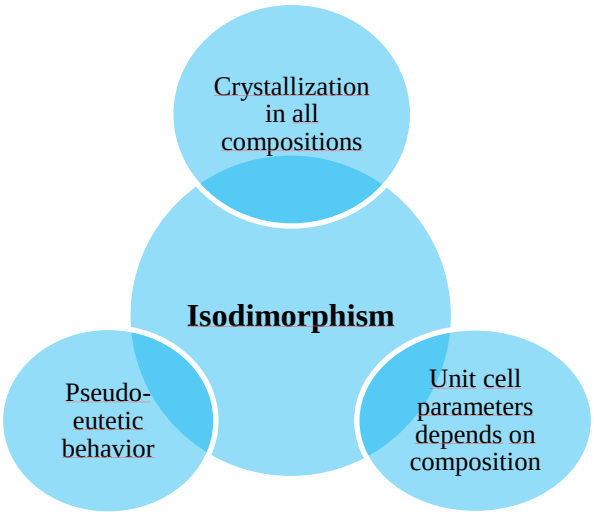

Scheme 4.2. Schematic representation of the criteria followed in this work to determine the isodimorphic character of random copolyesters.

Scheme 4.2 shows that when a random copolyester is able to crystallize in all the composition range, with a pseudo-eutectic behaviour in the T_m *versus* comonomer content curve, and with changes in the unit cell parameters with composition, then it can be considered isodimorphic. The different evidences of isodimorphism could be obtained by Differential scanning calorimetry (DSC) characterization which can efficiently highlight the pseudo-eutectic feature of the thermal transitions, as well as the crystallization in all the compositions. Deeper information is obtained by Wide and Small Angle X-Ray Scattering (WAXS/SAXS), since the partial inclusion of the minority co-unit in the crystalline unit cell (*i.e.*, note that such inclusion leads to changes in the unit cell parameters) of the major component impacts the structure and morphology at different levels. Others techniques that can provide useful information are: infrared spectroscopy (FT-IR), Polarized Light Optical Microscopy (PLOM) and nuclear magnetic resonance (NMR).[2]

The above described criteria, with the suitable techniques, were used in four different copolyesters in the present work. It is important to remark that such criteria have been applied in previous works, by Arandia et al.[18], Safari et al.[27] and Pérez-Camargo et al.[21]

As we mentioned above, there are some factors that can influence in some of the features of the isodimorphic behaviour. For instance, the chemical structure of the comonomers strongly influence in the position of the eutectic point.

In general, since both comonomers are semicrystalline, the position of the eutectic point is determined by the competition on the crystallization of both comonomers, whereas the miscibility reflects the compatible extent of comonomer in each crystal lattice. [12]

The competition ability is influenced by the stiffness or length of comonomer unit. The comonomer unit which owns stronger stiffness or longer chain length always has stronger competition in isodimorphism. The latter point means that the homopolyester with more methylene number (*i.e.*, lower density of ester groups) has stronger crystallization ability and more stabilized crystalline structure [30]. However, as we already mentioned, some of the empirical rules are not strictly obeyed.

In the case of P (BS-*co*-*c*BS), despite the *c*BS and BS have the same length and the *c*BS is stiffer, it is the BS the one that dominates the crystallization, due to its ability to adopt *trans*-configuration in comparison with the *c*BS which adopt *cis*-configuration because of the double bonds. [12]

The difference between all-*trans* and *cis*-configuration is due to the *trans*-configuration being more symmetrical and stretched, and favouring the formation of stable and perfect crystals. In contrast, the *cis* isomer introduces “kinks” into the main chain due to the geometrical effect associated with the *cis* unit having both ester linkages on the same side of the *cis*-carbon double bonds, which results in the formation of randomly coiled chains in the copolyesters. Consequently, it is hard to form a perfect crystal for the *cis*-butene unit; therefore its crystallization is weaker in comparison with the *trans*-butylene units.[12]

Another interesting effect which can alter the isodimorphic behaviour despite the similar number of carbon atoms is the “odd-even effect”. This perturbation could affect significantly the melting point. The melting temperatures of aliphatic polyesters with an odd number of CH_2 units are lower than those containing an even number. The alternation of melting temperatures in this particular series is found throughout the organic chemistry of low molecular weight substances, including the *n*-alkanes. Graphically the “odd-even effect” is reflected when the melting temperatures are plotted as a function of the number of carbon atoms (see Figure 4.1), and the well-known zigzag line is observed. As the number of carbon atoms is increased the difference in

melting temperatures in between successive odd-even polymers decreases. There is an indication that for a sufficiently high number of carbon atoms this effect will vanish.

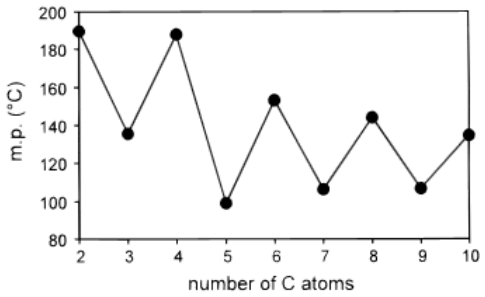

Figure 4.1. Melting point (m.p) as a function of number of C atoms for diacids (α, ω-alkenedicarboxylic acids) (HOOC-$(CH_2)_{n-2}$-COOH, *n*=2-10).[31]

The reason for the "odd-even effect" on the melting temperatures has usually been attributed to different positions of the ordered planar zigzag conformation resulting in different alignments of the carbonyl group. It has been pointed out that ΔH_u alternates with carbon number in an opposite manner to the melting temperature. Consequently enthalpy differences cannot be the cause of alternation. The alternation must result from differences in entropies of fusion.[32]

The even-odd effect described above leads to even-even poly (alkylene dicarboxylate)s synthesized from even diacids with even diols having good mechanical strength. In contrast, odd-odd poly (alkylene dicarboxylate)s are characterized by slow biodegradation rate and poor toughness. As a result, in order to obtain materials with tailorable and tunable properties, even-odd random copolymers have been designed. [12, 30] It is worth noting that compared with even diacids, odd diacids used as monomers could enhance degradation rate of polyesters, since odd carbon atoms make packing of polymer chains difficult and thereby lead to reduced crystallinity and increased degradability.[30]

In the work presented in this chapter, random copolymers based on PBS, PBA, PPS and PPA are used.

The PBS used is a commercial sample. This homopolymer represented 11.4% of the biodegradable homopolyesters used in the world in 2017.[33] It is one of the newest biopolymers, currently produced by combining succinic acid and 1,4-butanediol. PBS is a biodegradable synthetic aliphatic polyester whose properties are often favorably compared to LDPE or PP.[34] It is a highly crystalline polyester in comparison to other aliphatic polyesters, such as poly (ethylene succinate), poly (ethylene adipate), poly

(butylene adipate), among others. Moreover, PBS features a higher melting temperature (above 110 ºC) which is crucial for applications at a high temperature range. The physical properties of PBS are directly comparable to those of traditional and non-biodegradable polymers such as PE and PP. In particular, PBS shows good tensile strength, impact strength, moderate rigidity and hardness, typical of tough polymer properties. However, PBS has a glass transition temperature of -31 ºC, not high enough for its use in rigid packaging where stiffness and thermal resistance are priority requisites. In the molten state, PBS shows low melt strength and low melt viscosity because of the high linear chain structure, which limits its applications in thermoplastic processing, foaming and filming.[34]

The high crystallinity of PBS provides good mechanical properties but involves a low biodegradation rate. The properties of PBS have been tailored through different strategies, depending on the target: random and block copolymers, chain branching, PBS composites and nanocomposites, among others, are some of the strategies used in order to improve the PBS properties.[34]

4.2.Results and Discussions

The crystallization behaviour under non-isothermal and isothermal conditions, as well as the structure and morphology of random copolyesters was studied through different techniques, such as differential scanning calorimetry (DSC), polarized light optical and force atomic microscopy (PLOM and AFM), simultaneous Wide and Small Angle X-rays scattering (WAXS and SAXS) with and without synchrotron radiation and Cross-Polarization Magic Angle Spinning nuclear magnetic resonance (CP-MAS ^{13}C NMR). The random copolymers that were studied and their main characteristics are indicated in Table 3.1 of the Experimental part (see Chapter III). These random copolymers are: poly (butylene-*ran*-butylene adipate) (PBSA), poly (propylene adipate-*ran*-butylene adipate) (PPBA), poly (propylene succinate-*ran*-butylene succinate) (PPBS), and poly (propylene succcinate-*ran*-propylene adipate) (PPSA). Since these systems have different repeating units, the influence of its length (*e.g.*, odd or even number of CH_2 in the repeating unit of the comonomer) is study. The results and discussions are divided by systems. In each system the employed techniques are indicated.

4.1.1. PBSA random copolymers analysis.

PBSA copolymers were the materials (amongst all employed here) that allow a deeper comprehension of the isodimorphic behaviour due to their characteristics, therefore, they were studied in greater detail.

a. Non-Isothermal DSC scans

Non-isothermal DSC scans were used to evaluate the glass transition temperature (T_g) as a function of the comonomer composition (see Figure 4.2) in order to obtain an evidence of the miscibility of PBSA copolymers. Additionally, the non-isothermal DSC scans were used to determine the thermal transitions of the materials, such as crystallization (T_c) and melting (T_m) temperatures, as well as their respectively enthalpies (ΔH_c and ΔH_m) under rate-dependent experiments.

Figure 4.2 shows DSC heating traces for the random copolymers and their corresponding homopolymers after they were quenched from the melt (using ballistic cooling as indicated in the experimental section). All copolymers exhibit a single glass transition temperature (T_g) in between the T_g values of the homopolymers, as expected for random copolymers (their random sequence structure was determined by ^{1}H-NMR, shown above) that form a miscible amorphous phase. The presence of a single phase in the melt was also corroborated by standard and rate-dependent (see section below) SAXS experiments.

Figure 4.2b shows a plot of T_g values versus composition. The T_g values decrease with increasing PBA content, as expected, since there are four methylene groups in the butylene adipate repeating unit, which makes PBA more flexible in comparison with PBS. Such differences in chain flexibility account for the 25 ºC difference in between the T_g values of PBA and PBS.[35]

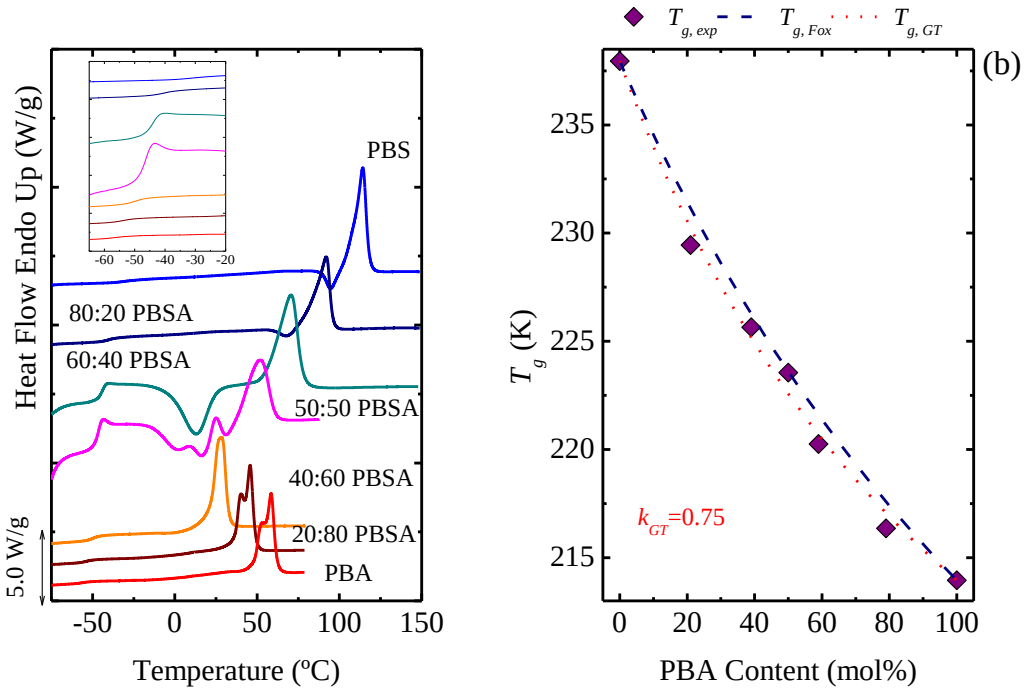

Figure 4.2. (a) DSC heating scans performed after quenching PBS, PBA and their copolymers samples. (b) Glass transition temperatures (T_g), taken from (a), as a function of PBA content, the fits to the Fox and Gordon-Taylor equations are also shown.

Figure 4.2a shows that samples that are able to crystallize during the previous ballistic quenching display weak glass transitions that can only be clearly seen if a close up is made in the curve.[36] In contrast, the intermediate compositions of 60:40 and 50:50 PBSA show a large endothermic jump associated with the change in heat capacity experienced by the material during T_g, followed by cold-crystallization. For these samples, the crystallization during fast cooling was hindered and this evidences the composition dependent behavior of the samples.

Figure 4.2b shows a non-linear dependence of the T_g as a function of the PBA content that can be approximately described by the semi-empirical Fox equation,[37] although it is even better fitted by the Gordon-Taylor equation:[38]

$$T_{g,PBSA} = \frac{w_{PBA}T_{g,PBA} + k_{GT}(1 - w_{PBA})T_{g,PBS}}{w_{PBA} + k_{GT}(1 - w_{PBA})} \qquad \text{Eq.4.1}$$

where $T_{g,PBA}$ and $T_{g,PBS}$ are the glass transition temperature of PBA and PBS, respectively; w_{PBA} the mass fraction of PBA, and k_{GT} the Gordon-Taylor parameter.

The Gordon-Taylor equation fitted well the experimental data with k_{GT} = 0.75. As a result, $T_{g,\,PBSA}$ can be predicted for all composition range using Equation 4.1.

Rate dependent DSC analyses were performed. Cooling rates of 5 and 50 ºC/min were selected, whereas the subsequent heating scans were always performed at 20 ºC/min. The DSC cooling and heating curves are shown in Figure 4.3.

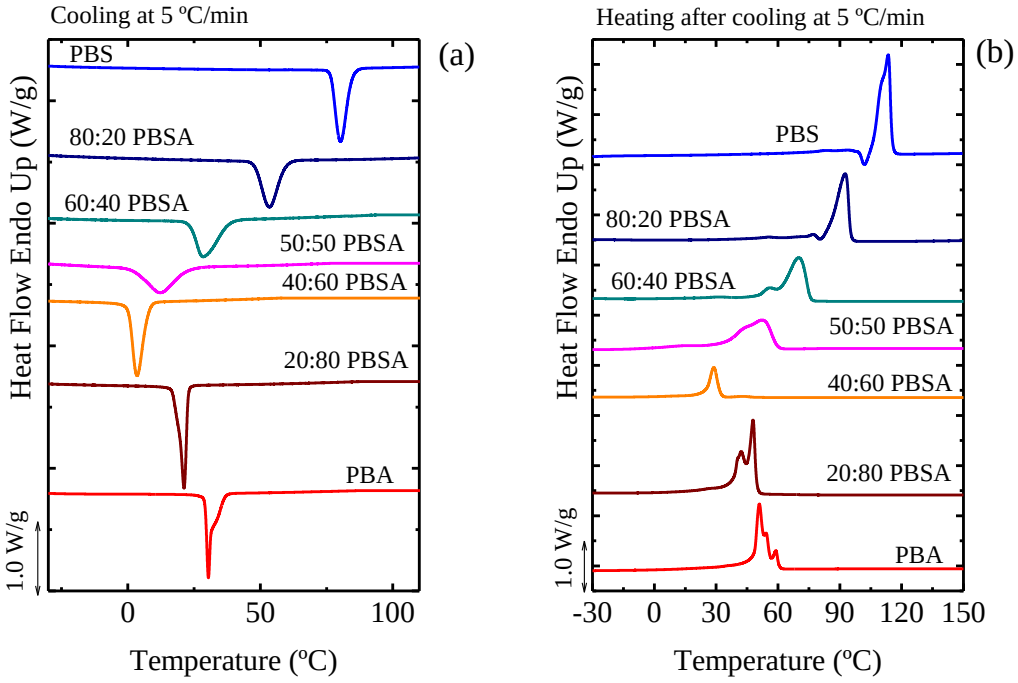

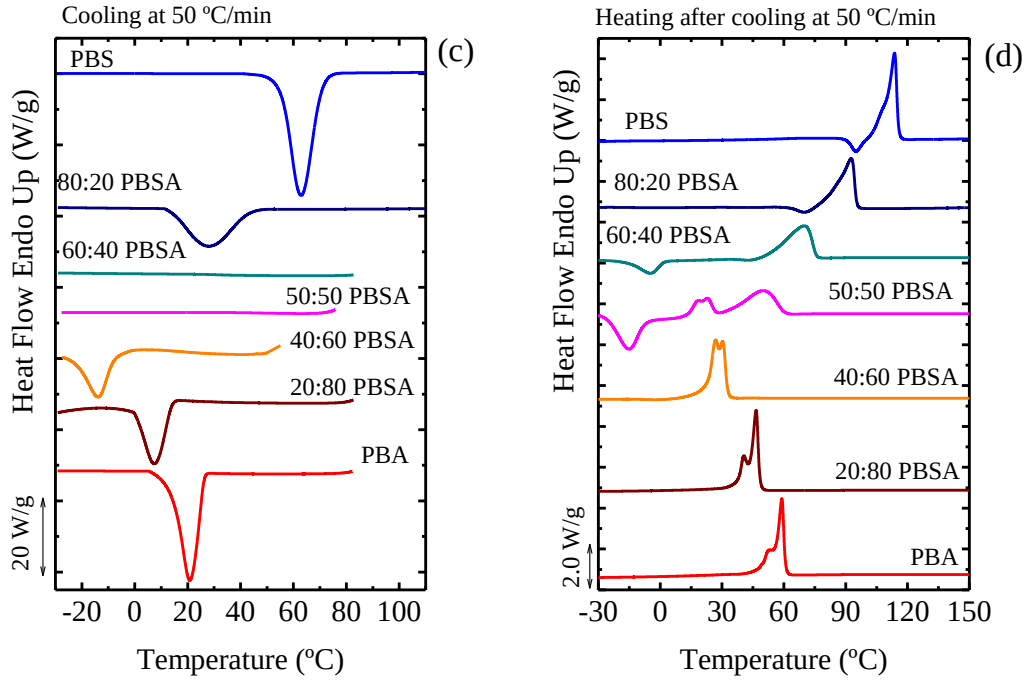

Figure 4.3. Cooling DSC scans (a, c) from the melt and subsequent heating scans (at 20 ºC/min) (b,d) for the indicated homopolymers and random copolymers samples at 5 (a,b) and 50 (c,d) ºC/min.

Figure 4.3 shows cooling and heating DSC scans for both 5 and 50 ºC/min cooling rates, in which all compositions of PBSA copolymers are able to crystallize. A related remarkable point to consider is that all copolymer samples are able to crystallize, despite their randomness. This is a characteristic behavior of isodimorphic copolymers.[18] Such copolymers can crystallize in unit cells that resemble those of the homopolymers, but with inclusions of the second component repeating units, as demonstrated in the previous section.

Figure 4.3a shows that all samples exhibit a single crystallization peak during cooling from the melt, which is sharper or broader depending on composition.

The subsequent heating scans are shown in Figure 4.3b. PBS and PBS-rich compositions exhibit cold-crystallization during heating followed by melting. In contrast, PBA-rich copolymers do not exhibit cold-crystallization. PBA and PBA-rich copolymers display bimodal melting. WAXS analysis (see Figure 4.5) indicates that these samples are polymorphic. Neat PBA exhibits the α or β phase depending on the previous cooling rate (see Figure 4.5a and b, respectively), whereas in the PBA-rich compositions, the β phase is the dominant polymorphic form regardless of the cooling

rate (see Figure 4.5b). Such predominance of the β phase is apparently induced by the inclusion of PBS within the crystal lattice of PBA. Therefore, the bimodal melting of the PBA-rich compositions (see Figure 4.3) is attributed to the polymorphic nature of PBA,[39-43] since a switch from the less stable β phase to the more stable α phase typically occurs during heating, especially when the samples were previously cooling at 50 ºC/min (see Figure 4.3b).

For the PBS-rich phase, the α phase is the dominant one. Therefore, the bimodal melting peaks in these cases are probably due to partial melting and reorganization during the heating scan.[18]

At intermediate compositions (*i.e.*, 50:50 and 40:60 PBSA), both PBS and PBA-like phases have similar chances to crystallize. Figure 4.3a and b show broader crystallization and melting peaks and even multiple peaks. A single exothermic peak is always observed during cooling indicating that coincident crystallization of both phases is occurring. This can be demonstrated by the detection of two sequential melting peaks upon heating. In fact, the coincident crystallization and sequential melting can be better observed in Figure 9.1 (see Chapter IX. Appendix), where a close up of the DSC traces of Figure 4.3a and b is presented. This sequential melting was also evidenced by X-rays and AFM experiments.

It is worth noting that in PBS/PBA blends, fractionated[39] and sequential crystallization[44] have been reported instead of the coincident crystallization process that has been found in this work for PBSA random copolymers.

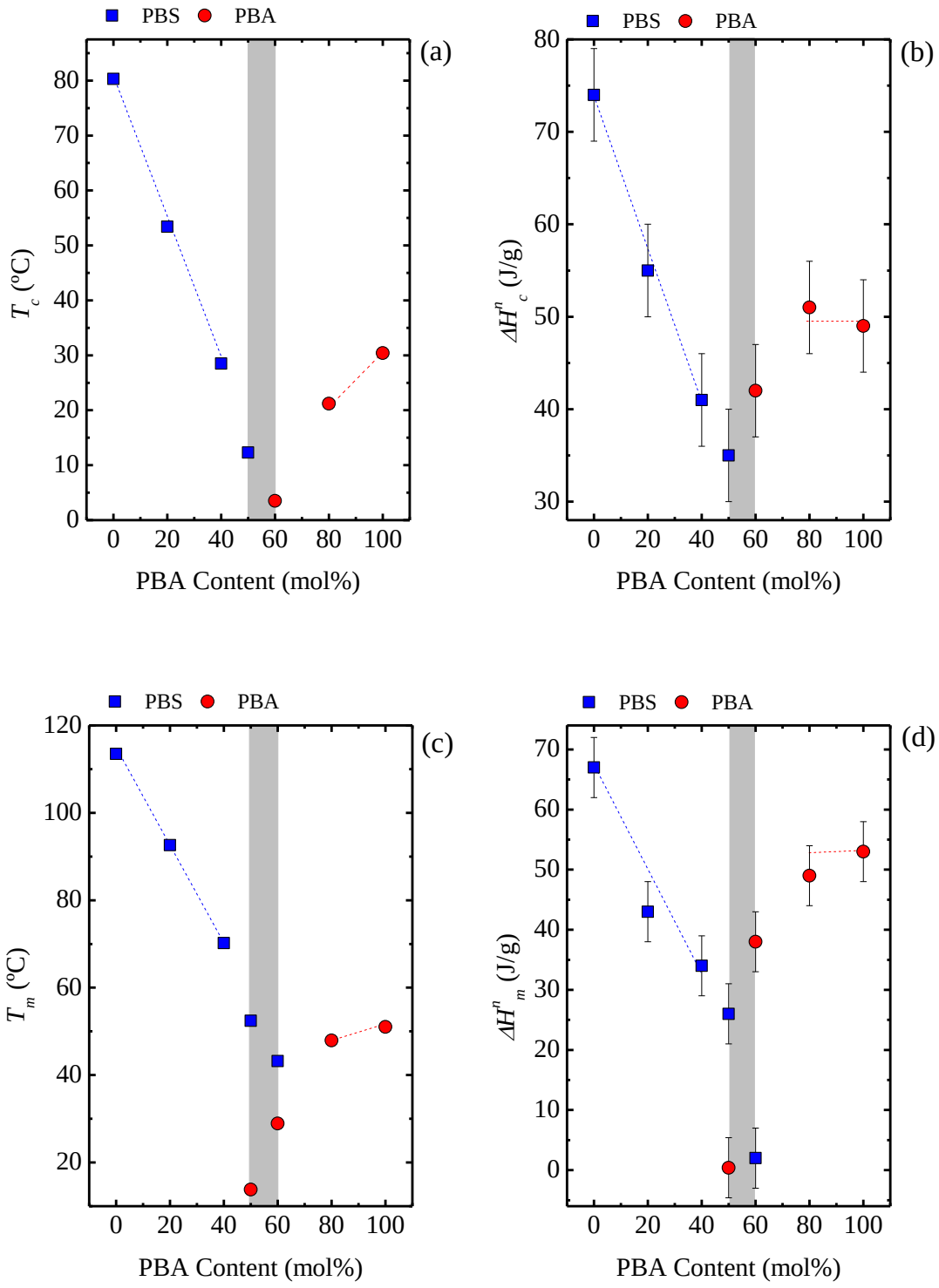

Figure 4.4. Variation of (a) T_c, (b) ΔH^n_c, (c) T_m and (d) ΔH^n_m as a function of PBA content taken during cooling at 5 ºC/min and in the subsequent heating. The shadowed region indicates the pseudo-eutectic point.

Figure 4.4 shows how the crystallization and melting temperatures and enthalpies (after cooling at 5 ºC/min) depend on the composition of the copolymers (see

also Table 4.2). Figure 4.4 also shows the characteristic pseudo-eutectic like behavior of isodimorphic random copolymers. Three zones can be distinguished. Left of the pseudo-eutectic point, the incorporation of PBA within the copolymer induces the plasticization of PBS, as the random copolymers are miscible. This behavior causes a decrease of the calorimetric properties of PBS with increasing adipate unit content, until they go through a minimum at a copolymer composition close to equimolarity (shadowed region), and then they increase towards the value of PBA. The reductions of melting point and heat of fusion as a function of composition indicate that even though some co-monomer incorporation is possible (as indicated by the WAXS results presented above), most of the minority co-monomer units act as defects that are excluded from the crystalline regions limiting crystallinity and reducing lamellar size (see also the corresponding Figure 4.4c).[35, 45] The miscibility between the two types of co-monomer units also induces changes in supercooling as the equilibrium melting point will be a function of composition. These changes in supercooling also contribute to the large dependence of the calorimetric properties on composition.

The pseudo-eutectic like behavior is in agreement with others copolyesters systems and in fact was also obtained in PBSA copolymers, but without the sequential melting at intermediate compositions by Tserki et al.[35]

According to the thermal behavior presented in Figure 4.4, the pseudo-eutectic point corresponds to a PBA content of 60 and 50 mol% (see shadowed region). On each side of the pseudo-eutectic point, the copolymers crystallize solely in the PBS-like (PBA content <50 mol%) or PBA-like (PBA content >60 mol%) crystal lattice.

Figure 4.3c shows that crystallization at intermediate compositions (*i.e.*, PBA content of 40 and 50 mol%) is inhibited, but in the subsequent heating scans (Figure 4.3d) cold-crystallization and melting peaks are displayed.

Figure 4.3d shows the subsequent heating scans after cooling at 50 ºC/min. Almost all materials show similar curves to those obtained at lower cooling rates. However, for the 60:40 and 50:50 PBSA copolymers, a cold-crystallization is clearly observed followed by one and two melting peaks, respectively.

In the 60:40 case, no evidences of the crystallization of the PBA-rich phase was found (*i.e.*, by WAXS, see Figure 9.2 in the Appendix). In the 50:50 PBSA copolymer case, a cold-crystallization process followed by the sequential melting of the two phases can be observed in Figure 4.3d. The endothermic peak at low temperature corresponds to the melting of PBA-rich phase crystals, whereas the peak at higher temperatures

corresponds to the melting of PBS-rich phase crystals (see Figure 4.3d). Therefore, the 50:50 PBSA is the only copolymer that is able to develop a double crystalline structure during cold-crystallization from the glassy state. In fact, during the cold-crystallization process, the PBA-rich phase will crystallizes first, followed by the PBS-rich phase crystallization. However, the cold-crystallization of the PBS-rich phase and the melting of the PBA-rich phase occur in the same temperature range and are overlapped, as it will be demonstrated below employing temperature-resolved WAXS.

Even though the 40:60 PBSA copolymer crystallizes in a coincident fashion (*i.e.*, the crystallization of both phases occurs in the same temperature range and the exotherms are overlapped into a single process) when it is cooled at 5 ºC/min, the PBA-rich phase crystallization is favored over the PBS-rich phase when a cooling rate of 50 ºC/min was used. As a result, no PBS-rich phase crystals are formed and no melting point corresponding to PBS-rich phase is observed in Figure 4.3d.

Table 4.2. Thermal transitions and relevant enthalpy values obtained from the DSC scans presented in Figure 4.2 (T_g) and 4.3 (standard scans)*

Sample	$T_{g,onset}$ (ºC)	$T_{c,end}$ (ºC)	$T_{c,peak}$ (ºC)	$T_{c,onset}$ (ºC)	$\Delta H^n c$ (J/g)	$T_{m,onset}$ (ºC)	$T_{m,peak}$ (ºC)	$T_{m,end}$ (ºC)	$\Delta H^n{}_m$ (J/g)
PBS	-35.2	76.7	80.3	84.6	74	106.4	113.5/109.9	115.3	67
80:20 PBSA	-43.7	48.1	53.4	59.2	55	84.6	92.6	95.2	43
60:40 PBSA	-46.9	24.2	28.5	37.3	41	60.5	70.2/55.3	75.6	34
50:50 PBSA	-49.0	4.9	12.3	20.6	35	4.1 34.6	13.8 52.4/43.7	26.7 59.5	0.4 26
40:60 PBSA	-52.9	0.4	3.5	7.7	42	25 37.2	28.5 43.2	32.1 48.1	38 2
20:80 PBSA	-56.8	18.8	21.2	22.8	51	44.4	47.9/42.0	49.6	49
PBA	-59.2	29.3	30.4/34.1	31.4	49	48.3	51.0/54.5/59.1	54.1	53

*Onset glass transition temperature ($T_{g,onset}$), onset crystallization temperature ($T_{c,onset}$), peak crystallization temperature ($T_{c,peak}$), normalized crystallization enthalpy (ΔH^n_c), onset melting temperature ($T_{m,onset}$), peak melting temperature ($T_{m,peak}$), normalized melting enthalpy (ΔH^n_m).

b. Simultaneous WAXS/SAXS experiments.

WAXS results

As we mentioned in the general introduction, one of the most important techniques to determine whether a random copolymer is isodimorphic or not, is to prove that they have two crystalline phases corresponding to each parent component. Moreover, when one of these rich-phases crystallizes, it should allow the partial

inclusion of the comonomer into its crystal lattice and *viceversa*. Such inclusion might generate an increase of the *d*-spacings, as a result of the unit cell distortion. In addition, at the pseudo-eutectic point two crystalline phases coexist at the same time and are observed directly (*i.e.*, at room temperature after applying a specific thermal protocol, or in the samples as a received) or indirectly (*i.e.*, during the heating of the samples after applying an specific thermal protocol). In the latter, when one of the phases melts, allows to clearly observing the presence of the other one, as a result of a sequential melting.

It is worth noting that the coexistence of the two crystalline phases (with the inclusion of the other comonomer) constitutes a strong evidence of isodimorphic behaviour. Despite that the NMR technique employed in the present work does not allow to determine where the comonomer is included, it can determine if the two comonomers have crystalline phases, as will be show below.

The WAXS patterns shown in Figure 4.5 were measured after cooling the samples from the melt to -40 ºC at 5 and 50 ºC/min (Figure 4.5a and b, respectively). Table 9.1 in the Appendix lists all the reflections and *d*-spacings calculated by employing Bragg´s law (see Equation 2.1 on Chapter II. General Concepts), which are also labeled in Figure 4.5.

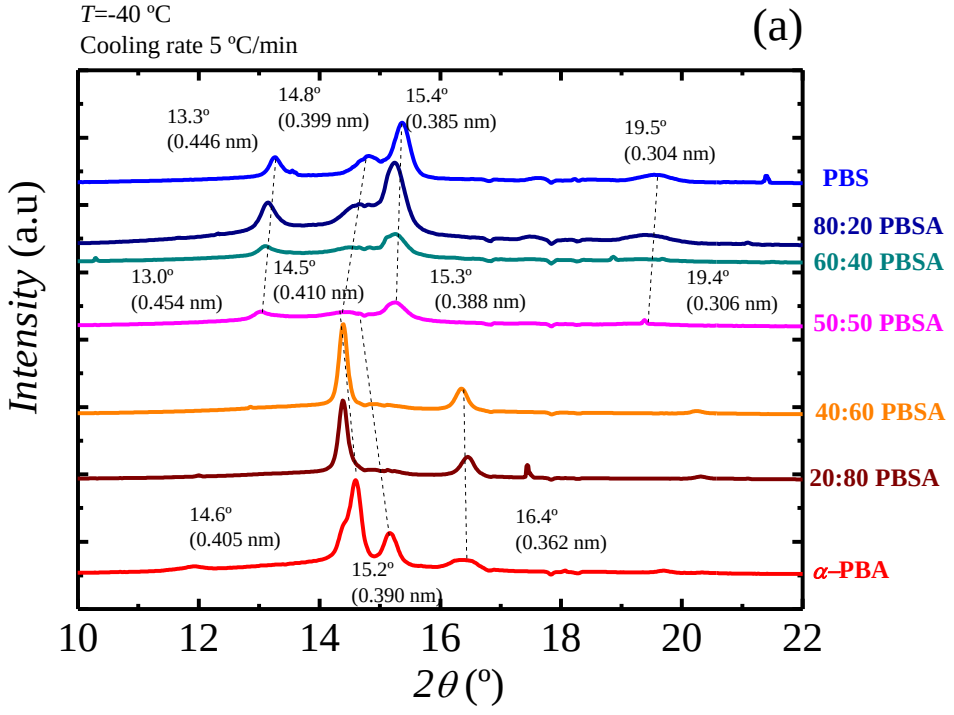

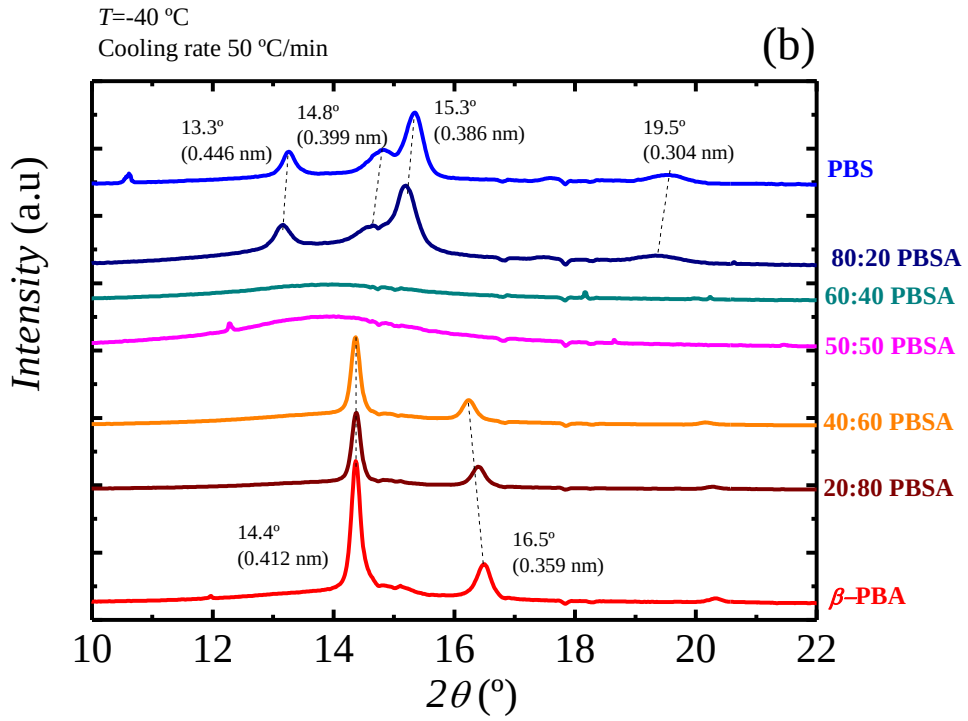

Figure 4.5. WAXS diffractograms of PBS, PBA and their copolymers taken at -40 ºC after being cooled at (a) 5 and (b) 50 ºC/min.

The most intense reflections observed in the WAXS spectrum of PBS appear at 0.446 and 0.385 nm and correspond to the *(020)* and *(110)* planes. Moreover, medium intense reflections were observed at 0.399 and 0.304 nm and can be assigned to the *(021)* and *(111)* planes [35, 39, 45-47] of the monoclinic unit cell[13] of *α*-PBS[46, 48] (with the following cell parameters: *a*=5.232 Å, *b*=9.057Å, *c*=10.900 Å and *γ*=123.87º).[46, 47]

In contrast, the most intense reflections observed for neat PBA appear at 0.405 and 0.362 nm, with a medium intense reflection at 0.390 nm, corresponding to the *(110)*, *(021)* and *(020)* planes[35, 39-41, 45, 46] of the monoclinic unit cell of the *α*-PBA (with cell parameters *a*=6.70 Å, *b*=8.00 Å, *c*=14.20 Å and *γ*=45.50º).[45]

Figure 4.5a (for samples cooled at 5 ºC/min) reveals that a transformation from *α*-PBA crystals in neat PBA to *β*-PBA-rich phase occurs for PBA-rich copolymers (*i.e.*, 20:80 and 40:60 PBSA copolymers). Additionally, a change from *β* to *α*-PBA phase also occurs during heating for the 20:80 PBSA copolymer (see Figure 9.3 on the Appendix).

The more thermodynamically stable *α* form in neat PBA is formed preferentially upon slow cooling at 5 ºC/min. A switch to the less stable *β* phase occurs in PBA-rich copolymers, as a consequence of the incorporation of PBS units in chains.

A similar control of PBA polymorphic crystallization in isodimorphic copolymers is reported in the case of in poly (hexamethylene adipate-*ran*-butylene adipate) (P(HA-*ran*-BA), where the increase of HA units in the copolyester favors the formation of the *β*-PBA form crystals as well.[23] The authors explain this effect by considering that HA units are better "tolerated" in the lattice of *β*-PBA rather than in the one of *α*-phase crystals. This is a consequence of lattice matching between *β*-phase PBA and the crystal structure of PHA.[23]

While in the present case of PBSA copolymers a clear lattice matching between PBS and *β*-PBA structures is not apparent, from the polymorphic crystallization we can deduce that the free energy penalty for including BS units in the cell of the PBA *β*-phase crystals is less severe in comparison to the one needed to host them into the *α*-phase.

It is worth mentioning that the differential partitioning of co-units between the different polymorphs has been often invoked to explain the effect of comonomer on polymorph selection in other semicrystalline polymers. An important example is the case of isotactic copolymers of propene with other alkenes (ethylene, 1-butene, 1-hexene), where the orthorhombic *γ*-form replaces the monoclinic *α*-phase with increasing co-unit content.[49, 50]

When PBA is cooled rapidly, at 50 ºC/min, the most intense reflection appears at 0.412 nm with a medium intense reflection at 0.359 nm, which correspond to *(110)* and *(020)* planes of the orthorhombic unit cell of the kinetically favored *β*-PBA phase (*a*=5.06 Å, *b*=7.35 Å and *c*=14.67 Å).[51-55] The presence of *β*-PBA-rich phase can be observed for PBA-rich copolymers (*i.e.*, 20:80 and 40:60 PBSA copolymers) at -40 ºC in Figure 2b. If the PBA-rich copolymer samples are subsequently heated, they undergo a series of transformations, from the *β* phase, passing through a mixture of *β*+*α* phases and finally reaching the more stable *α*-PBA form at higher temperatures (see Figure 9.3 and 9.4 on the Appendix). These results can be attributed to the mobility gain during the heating that might expand the cell and allow the inclusion of the PBS co-monomer even in the *α*-PBA phase. Other hypothesis is a partial exclusion of the PBS co-monomer in order to allow the transformation from *β* to *α*-PBA.

Summarizing the previous results, WAXS experiments show that *β*-PBA phases are favored either by fast cooling (in both PBA and PBA-rich copolymers) or by the

presence of PBS in slowly cooled PBA-rich copolymer samples (*i.e.*, PBSA copolymers cooled at 5 ºC/min).

In Figure 4.5b (*i.e.*, fast cooling rates) the 60:40 and 50:50 PBSA copolymers are not able to crystallize, this result is in line with SAXS and DSC evidences that will be shown below. Nevertheless, according to Figure 4.5, for both cases (slow and fast cooling), the crystal structure changes from PBS-like unit cells to PBA-like unit cells (either α or β) with increasing PBA composition.

Isodimorphic copolymers are characterized by the inclusion of one of the co-monomers in at least one of the present phases. In order to ascertain the possible isodimorphism, the *d*-spacings of the samples were calculated from the main reflections (see Table 9.1 on the Appendix) and plotted in Figure 4.6. According to Figure 4.6, *d*-spacing values are not constant with composition, but shift in comparison with the main components. These shifts can be interpreted as increases in unit cell dimensions that are needed to accommodate co-units of the minority co-monomer inside the crystals.

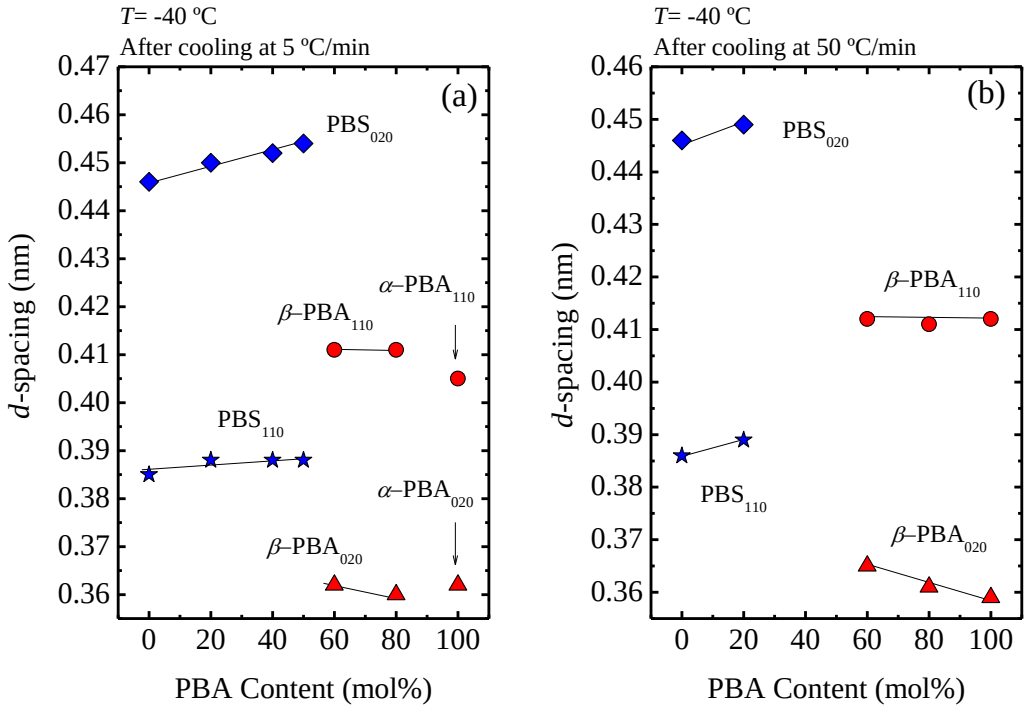

Figure 4.6. *d*-spacing, obtained after cooling from the melt at (a) 5 and (b) 50 ºC/min, of characteristic planes as a function of the PBA content in the PBSA copolymers.

For the PBS-rich phase, Figure 4.6 shows evidences of clear changes in *d*-spacings with PBA content. These changes can be explained by the inclusion of a small amount of PBA repeating units within PBS-like unit cells. Therefore, co-crystals of PBS

and PBA are formed. However, according to the small changes in *d* values and the fact that in PBS-rich compositions, WAXS shows the characteristic reflections of PBS unit cells, it can be inferred that co-monomer incorporation is limited.

In the case of PBA-rich compositions, the situation is complicated by the change from α to β PBA phases as explained above (see Figure 4.6a). Nevertheless, the results are consistent with a small inclusion of PBS units within the β-PBA unit cells for the 20:80 and 40:60 PBSA copolymers, as judged by the changes in the *d*-spacings of the *(020)* planes of the β-PBA phase unit cells with PBS addition in the copolymer (at least when the samples are cooled at 50 ºC/min).

The changes observed in *d*-spacings in Figure 4.6, together with the DSC results shown below, where a pseudo-eutectic point is clearly observed, are consistent with isodimorphic behavior. Furthermore, SAXS results also indicate that two different crystalline phases are formed with distinct lamellar thicknesses that are composition dependent.

The results obtained above both by WAXS and DSC demonstrate that isodimorphic behavior is present in the PBSA copolymer samples in view of their similar chemical structure.

WAXS experiments were also performed with X-ray laboratory equipment, under the same thermal protocol (*i.e.*, cooling at 5 ºC/min until -40 ºC) applied in the synchrotron measurements. The WAXS results for these experiments and the calculated *d*-spacings are presented in Figure 4.7.

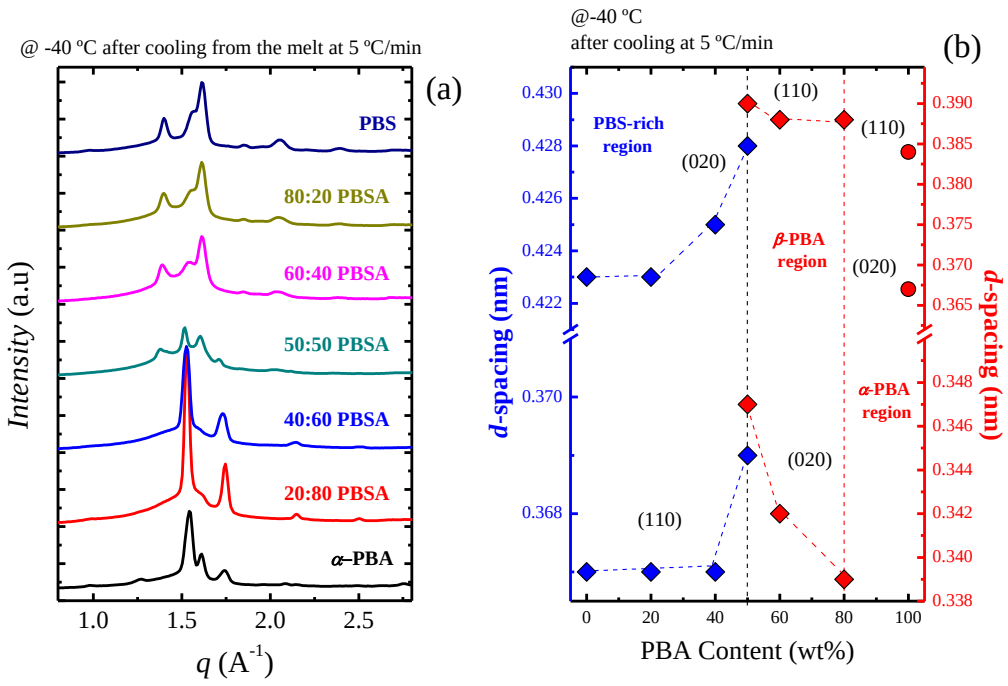

Figure 4.7. (a) WAXS patterns and *d*-spacing of characteristic planes as a function of the PBA content in the PBSA copolymers, obtained after cooling from the melt at 5 ºC/min.

The WAXS patterns show in Figure 4.7 corroborate the results obtained by synchrotron measurements. However, there is one feature that can be differentiated: At the 50:50 composition, the presence of the main peaks of the PBS as well as the ones of PBA is clear, whereas in the synchrotron WAXS patterns the results seems to be dominated by the PBS-rich phase. This could be attributed to the way in which the sample was held, since in the synchrotron DSC pans were used and this might partially mask the signal. In contrast in the microfocus WAXS measurements, the beam makes direct contact with the sample, because it is located in the central hole of the circular holder. Moreover, a thermal wax is used in the circular holder in order to increase the thermal conductivity between the hot stage and the holder, and therefore the sample.

Even though the calculated *d*-spacings have the difficulties of the *α*-*β* transitions in the PBA, an additional experimental data is obtained due to the PBA signal in the 50:50 PBSA random copolymer (see Figure 4.7a).

In the case of the PBS it is clear that the *d*-spacing slightly change in the 80:20 compositions, but as PBA is added the changes are larger and reach a maximum value at the intermediate composition (note that the *d*-spacing at the 50:50 PBSA can be

measured for PBS and PBA). A similar behaviour is shown for the PBA, but as mentioned in Figure 4.5 and 4.6, in between the neat PBA and the 20:80 PBSA a change from α to β-PBA occurs due to the presence of PBS.

SAXS results

SAXS patterns were obtained under the same conditions as WAXS patterns. The Lorentz representation was chosen to analyze the results, by plotting the product of intensity and the square of the scattering vector q as a function of q. Figure 4.8 shows clear maxima that represent the scattering from lamellar stacks.

The long periods d^* were estimated by Equation 4.2 and they are listed in Table 9.2 (see the Appendix). The experimentally obtained long period values were used for labeling the peaks in Figure 4.8.

$$d^* = \frac{2\pi}{qmax} \qquad \text{Eq.4.2}$$

Figures 4.8a and b show that neat PBA samples (*i.e.*, in its α and β polymorphic forms) have long periods at lower q-values in comparison with those of PBS, while the PBSA copolymers are characterized by long periods located at intermediate q-values.

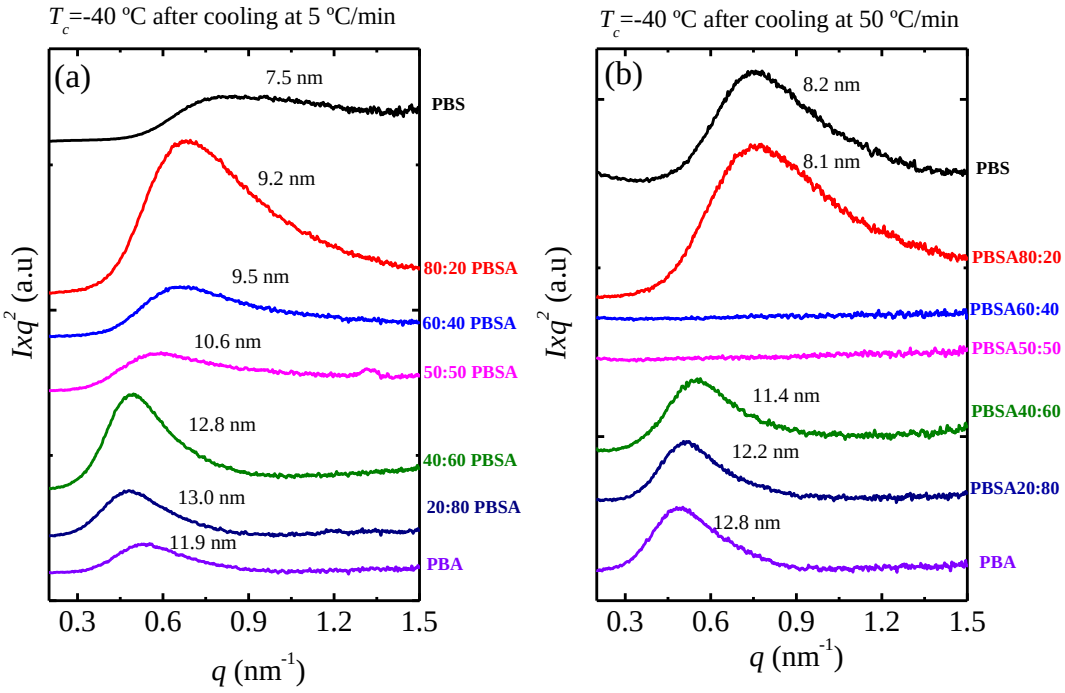

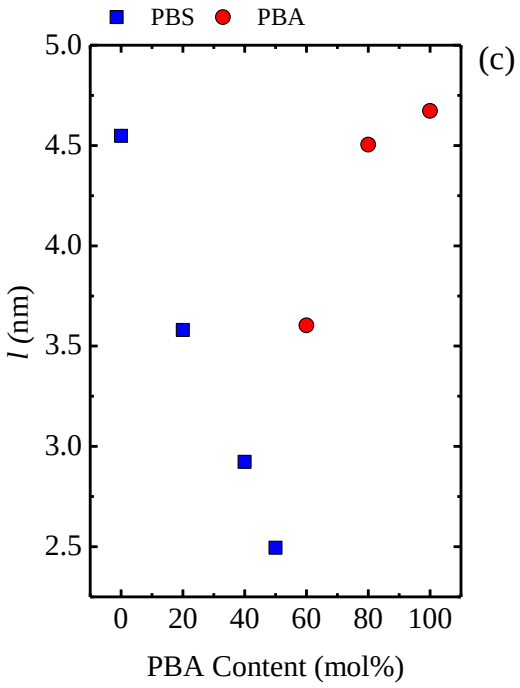

Figure 4.8. SAXS patterns of PBS, PBA and their copolymers taken at -40 ºC after being cooled at (a) 5 and (b) 50 ºC/min; (c) calculated lamellar thickness for the d^* values presented in (a).

Figures 4.8a and b show a single long period (d^*) for all the samples (represented by a single maximum in the curve), even at intermediate compositions. These single d^* values are obtained regardless of the previous cooling conditions (*i.e.*, cooling rates of 5 or 50 ºC/min) and of composition. Even for those intermediate compositions, where the two phases could potentially crystallize, it would be difficult to observe two long periods since Figure 4.8 shows that both PBS and PBA homopolymers exhibit similar long periods.

Lamellar thickness values were calculated according to Equation 4.3. They are plotted as a function of PBA content in Figure 4.8c for samples cooled at 5 ºC/min.

$$l = d^*.x_v \qquad \text{Eq.4.3}$$

In Equation 4.3, x_v is the crystalline volume fraction, which can be approximated to the mass fraction of crystals (x_m), determined from Equation 4.4, since the density of the different materials has not been measured:

$$x_v \approx x_m = \left(\frac{\Delta H_m^n}{\Delta H_{m,100\%}}\right) \qquad \text{Eq.4.4}$$

where ΔH^n_m is the normalized melting enthalpy of the component under consideration (see Table 4.2) and $\Delta H_{m,100\%}$ is the enthalpy of fusion of a 100% crystalline sample. Values of 110.5 and 135 J/g determined from the groups contribution method as proposed by Van Krevelen[56] were used for PBS and PBA, respectively.[35, 40, 45]

Figure 4.8c shows how the *l* values of the PBS-rich composition copolymers decreases with the increase of the PBA content. A similar effect is observed for the PBA-rich copolymers. The reduction in *l* values is a consequence of co-monomer incorporation into the chains that limit the length of crystallizable sequences. In fact, for these PBSA copolymers, the *l* values exhibit a pseudo-eutectic like behavior as a function of composition.

When the samples are cooled rapidly (see Figure 4.8b), d^* values experience changes for both homopolymers and random copolymers. At 50 ºC/min, the 60:40 and 50:50 PBSA copolymers are not able to crystallize. This is consistent with the WAXS results (discussed above) and DSC data (shown below).

In order to further understand the SAXS results, SAXS patterns in a wider range of *q* values were obtained in laboratory SAXS equipment, as shown in Figure 4.9, and then analyzed with the "so called" interface distribution function. It is worth noting that this function is accurate for a two face system, this mean a crystalline and an amorphous face. The accuracy of the function with a four face system (two crystalline and two amorphous phases) was tested in this work.

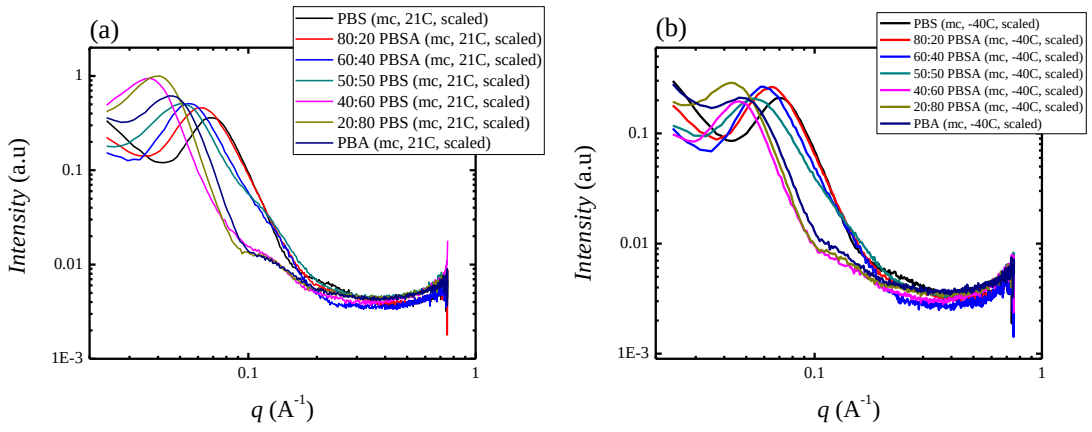

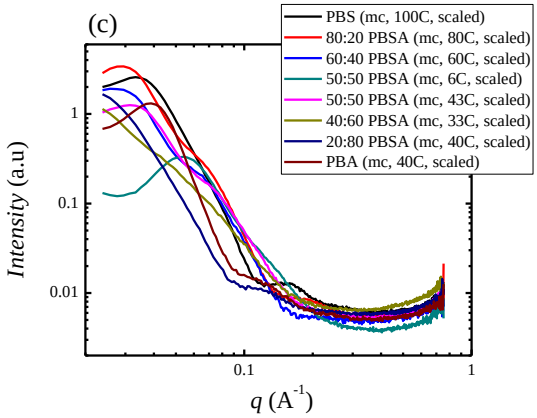

Figure 4.9. SAXS patterns obtained in a microfocus X-rays equipment in a wide range of *q* at (a) 21ºC (b) -40 ºC and (c) 10 ºC below the melting peak of each material.

Figure 4.9 shows that the signal in the copolymers is shifted to lower *q* in comparison with the main parent components, as a result of an increase of the long period. The maximum long period corresponds to the intermediate composition. This behaviour is the same independently of the temperature, although at 10 degrees below the melting point of each sample, the shift to lower *q* is even higher.

According to the previous evidence obtained by DSC, the increase obtained in the long period could be related with the decrease of the crystallinity of the samples (*i.e.*, due to an increase of the amorphous thickness). The results of the interface distribution function (see Figure 4.10) corroborates the results of the previous hypothesis

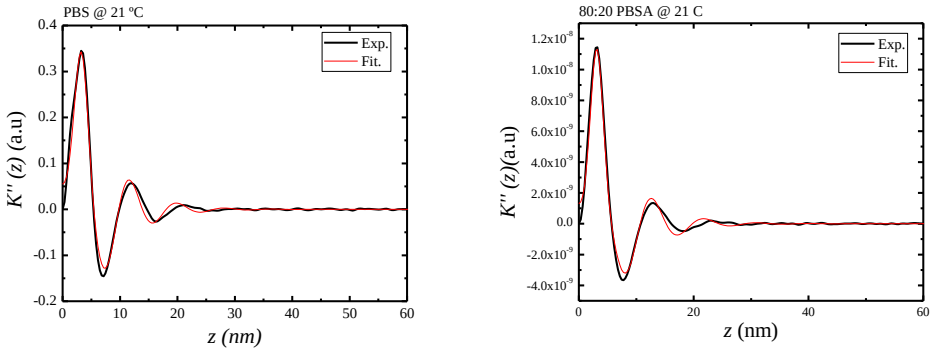

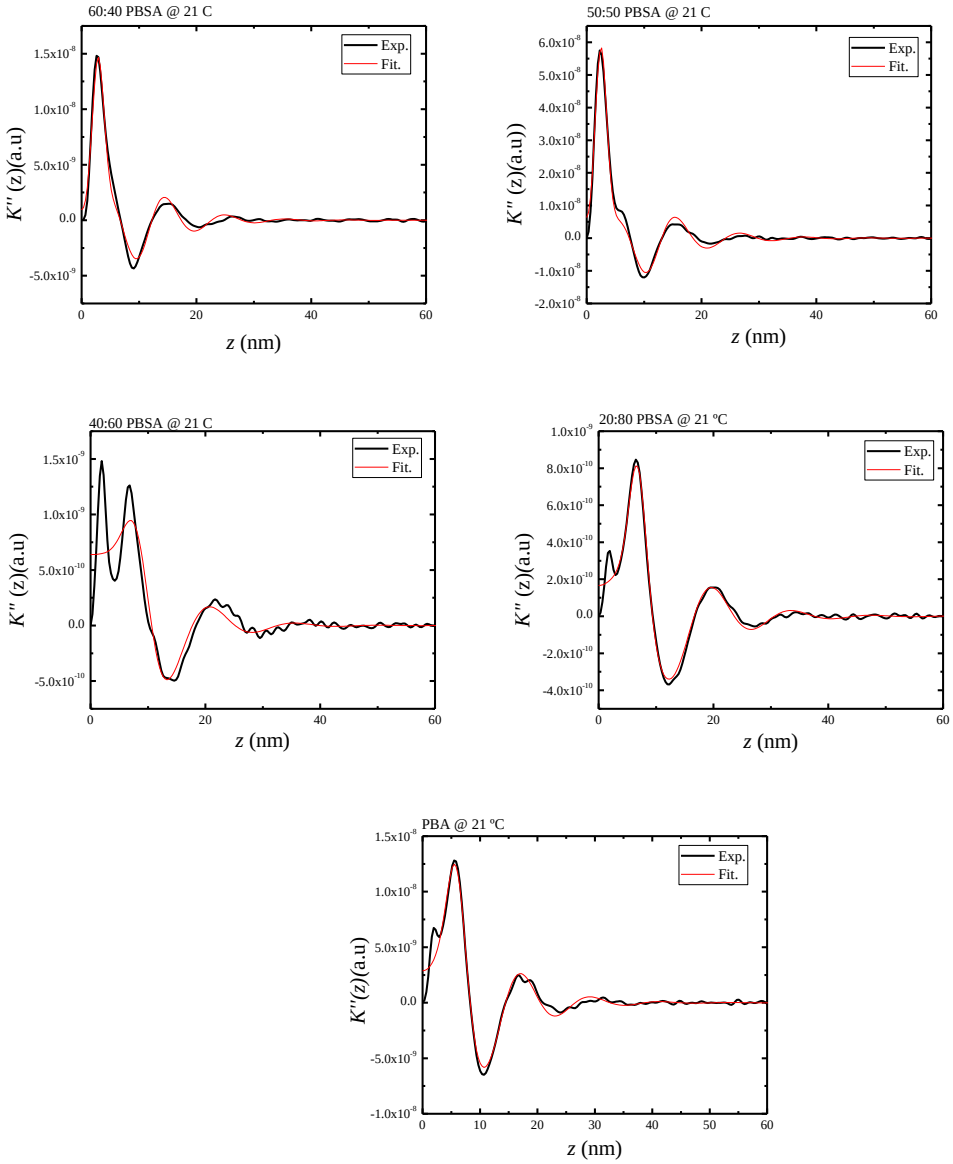

Figure 4.10. Interface distribution function for all the samples.

Figure 4.10 shows that the model could fit the experimental data for the parent components and the extreme compositions (80:20 and 20:80), whereas in the intermediate compositions the function seems to be not accurate. Despite of this, the results of the model are show in Figure 4.10.

The interface distribution function is able to predict the thickness of the crystalline (d_c) and amorphous layer (d_a), as well as their distribution (σ_c and σ_b). Taking into account the crystallinity obtained by DSC and WAXS experiments, the values corresponding to d_a and d_c were assigned, and plotted as a function of the PBA content in Figure 4.11.

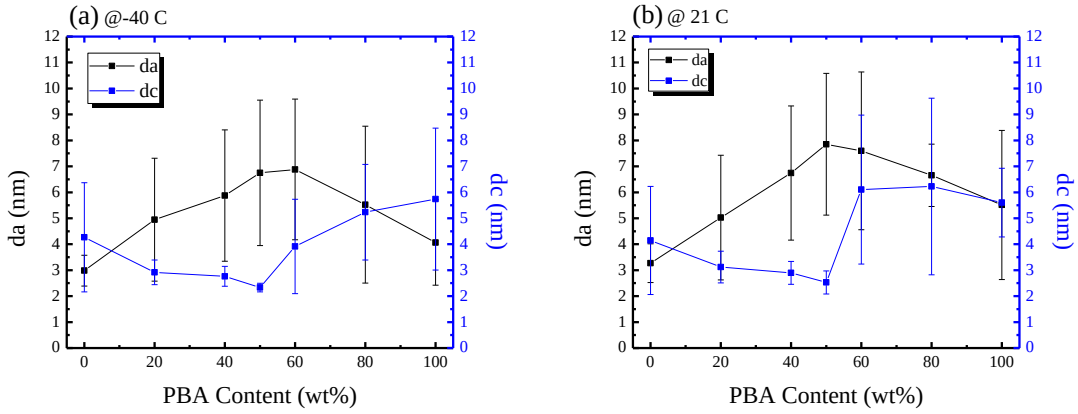

Figure 4.11. Amorphous and crystalline thickness (da and dc, respectively) as a function of PBA content for all the samples. The distribution of each phase is represented as an error bar.

Despite that the interface distribution function has its drawbacks for these copolymers, the trend obtained is similar to the one observed in Figure 4.8c. For instance, the d_c values decrease with the increase of PBA until the eutectic point and then start to increase until they reach values similar to the values of the PBA parent component. Moreover, the lamellar thickness of the crystal is in the same range of those calculated by the product of the d^* and the crystallinity degree.

AFM Results

AFM measurements were taken at room temperature for all the samples (*i.e.*, after previous preparation of the films (with ~1.5 μm of thickness, see section 3.2.3 in Chapter III. Experimental Part) and temperature-dependent experiment were used for the intermediate compositions (*i.e.*, 50:50 and 40:60 PBSA).

Figure 4.12 show the phase AFM images for all the samples (the height and amplitude images are show in Figure 9.5 of the Appendix). On these images, differences between the lamellas of the parent components, PBS and PBA cannot be distinguished. This is an expected behaviour and is in line with the SAXS results, since similar lamellar thickness were obtained for the parent components.

The different orientation of the lamellae shown in Figure 4.12 correspond to flat on and edge on lamellae. These orientations are attributed to the preparation of the film by spin-coating, in which factors like the wetting properties of the material, the

interaction substrate-material and the spin coating rate can induce such lamellar distribution and orientation.

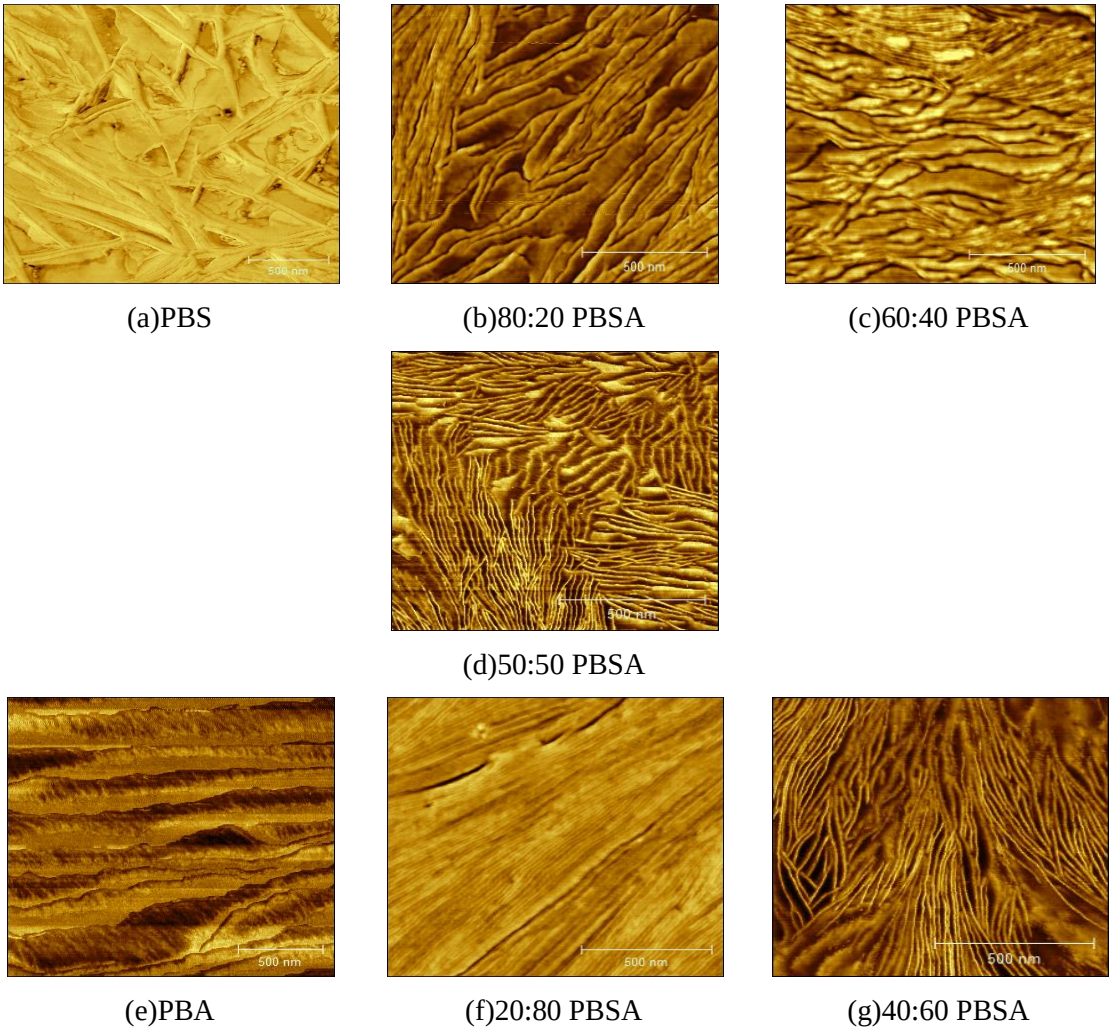

(a)PBS (b)80:20 PBSA (c)60:40 PBSA

(d)50:50 PBSA

(e)PBA (f)20:80 PBSA (g)40:60 PBSA

Figure 4.12. Phase Images of all the samples taken at 23 ºC, for PBS-rich compositions: (a) PBS, (b) 80:20, (c) 60:40 and (d) 50:50 PBSA; and for PBA-rich compositions: (e) PBA, (f) 20:80 and (g) 40:60 PBSA.

Despite the AFM images (see Figure 4.12) do not show clear differences between PBS-rich and PBA-rich lamellae, the lamellae of the PBS-rich compositions seem to be disordered, this means with different orientations, whereas in the PBA-rich compositions the lamellae are oriented and very flat. However, there is no torsion of the lamellae in the PBS-rich compositions, as is expected due to the ring-band patterns shown below (See Figure 4.22).

Besides the different orientation of the lamellae according to the material, Figure 4.12 shows differences between the parent components and the copolymers, as well. For instance, the lamellae of the PBS-rich copolymers seems to become thinner as

the PBA content is increased, due to the change in supercooling induced by the presence of the PBA and *viceversa*.

Figure 4.13 and 4.14 shows the temperature-dependent study performed in the 50:50 and 40:60 PBSA, respectively. The thermal protocol applied before heating (*i.e.*, in the hot stage incorporated on the AFM) ensures that at RT both PBA-rich and PBS-rich phases are semi-crystalline.

Figure 4.13 shows the sequential melting of the material. At the beginning the lamellae of the PBA-rich phase are the predominant ones, and they start to disappear (see T=35 ºC) as the temperature increases (see temperatures at the left of Figure 4.13). At high temperatures the PBA-rich lamellae are molten (see T=39 ºC) and the PBS-rich lamellae are not visible, since the molten PBA-rich phase covers the PBS-rich crystals. However, underneath the molten PBA-rich phase, there should be some oriented material which corresponds to the PBS-rich lamellae, as such material only disappears completely near the PBS-rich crystals melting temperature (see T=56 ºC), as expected for the 50:50 PBSA (see non-isothermal DSC scans in Figure 4.3). It is interesting that when the PBS-rich lamellae are the dominant ones, the colors in the phase images are inverted; this could be attributed to the parameters employed in the measurements, and to the soft material (*i.e.*, molten PBA-rich phase) which covers the more rigid one (*i.e.*, PBS-rich phase). It is possible that experiments in the net attractive mode might provide better images of the PBS-rich lamellae.

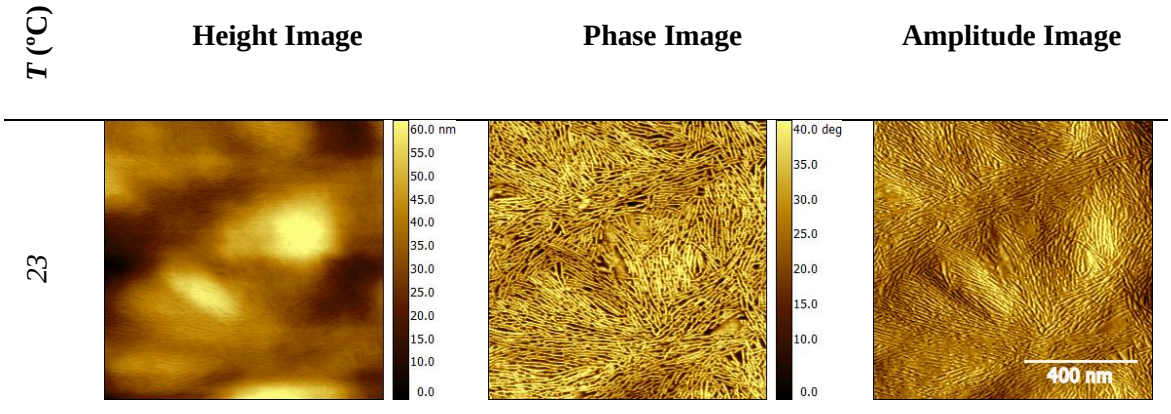

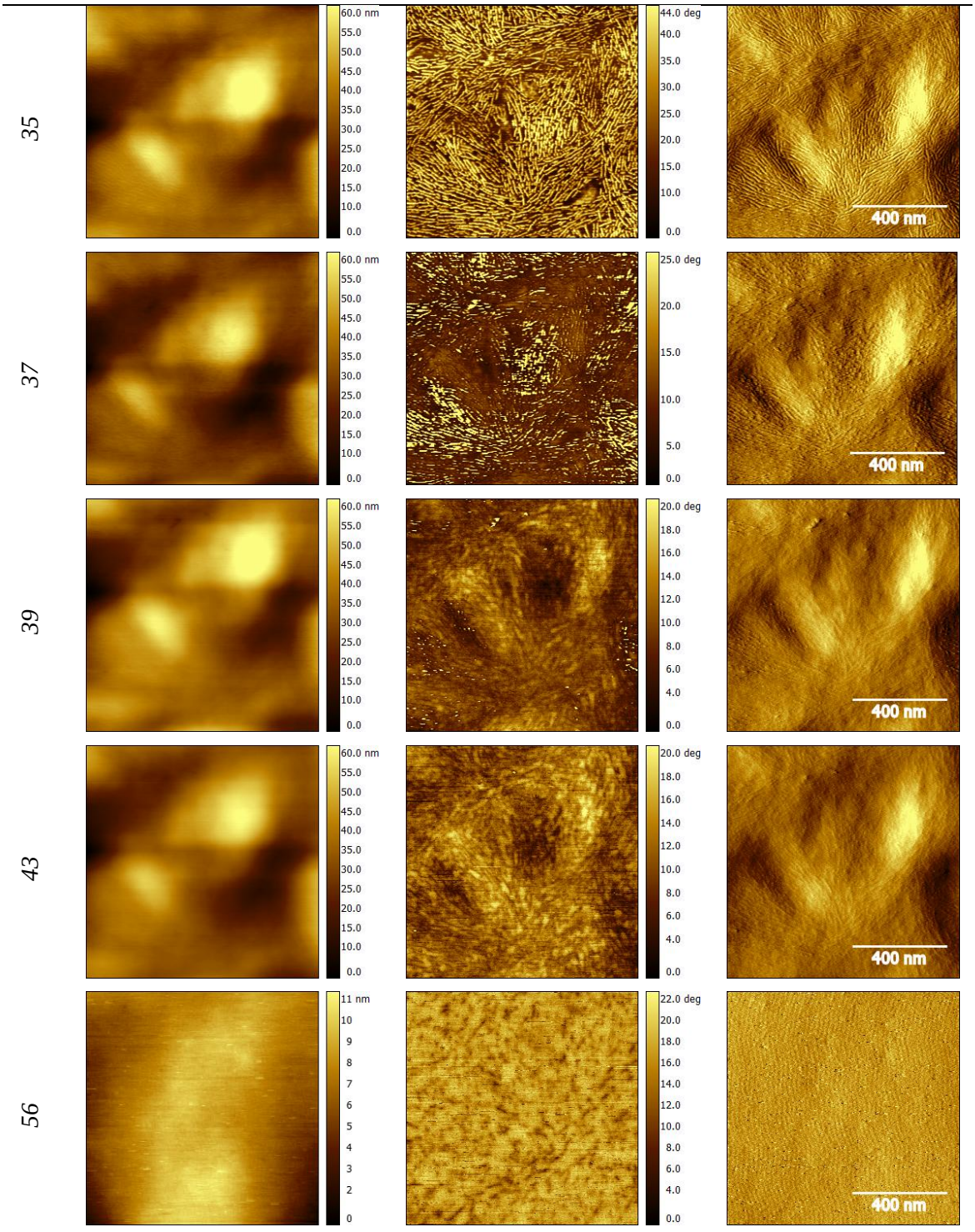

Figure 4.13. Height, Phase and Amplitude AFM Images of 50:50 PBSA during step-heating. The temperature (*T*) of each step is indicated at the left.

T (ºC)	**Height Image**	**Phase Image**	**Amplitude Image**

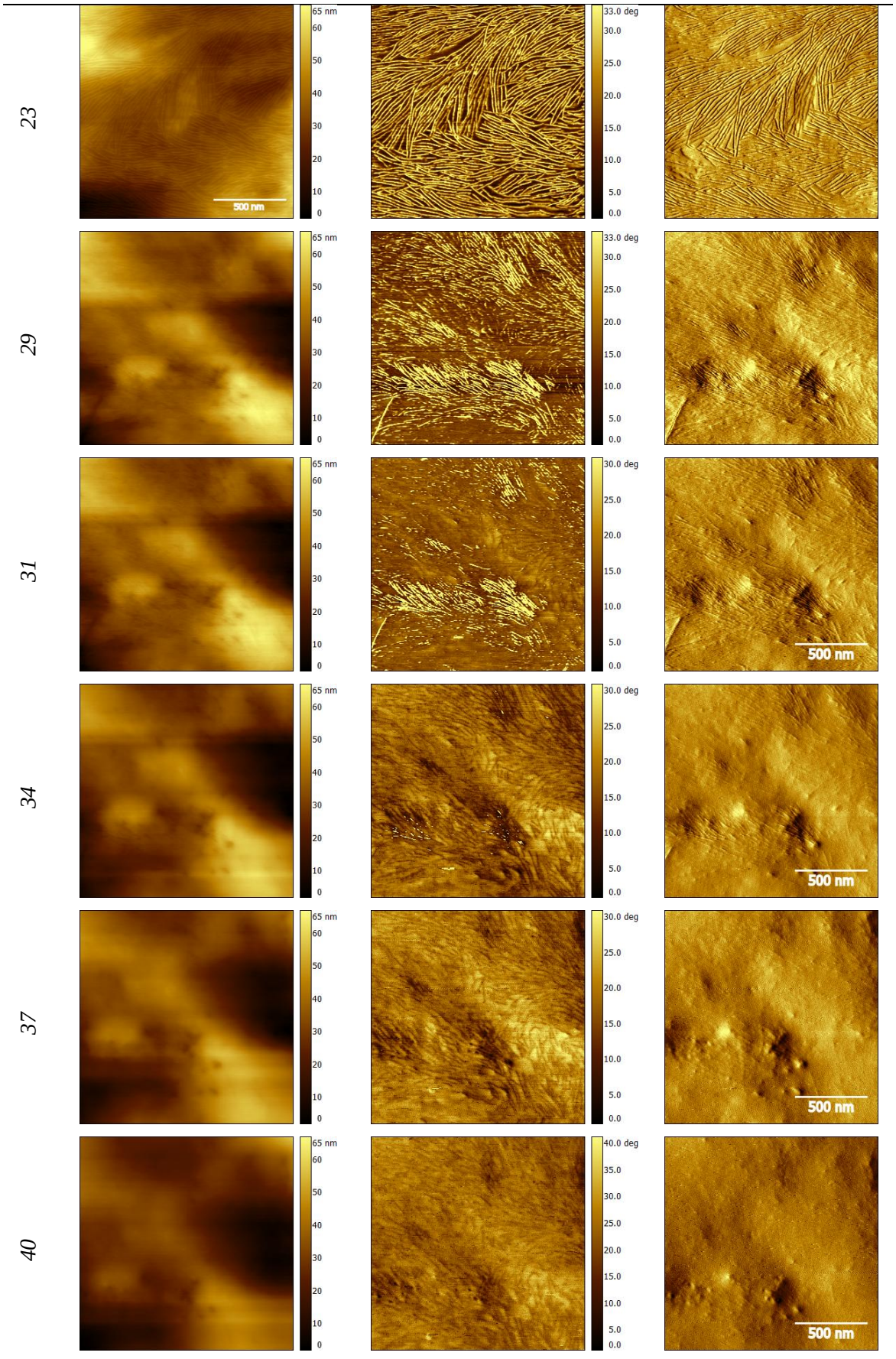
23
29
31
34
37
40
65 nm
60
50
40
30
20
10
0
33.0 deg
30.0
25.0
20.0
15.0
10.0
5.0
0.0
40.0 deg
35.0
500 nm

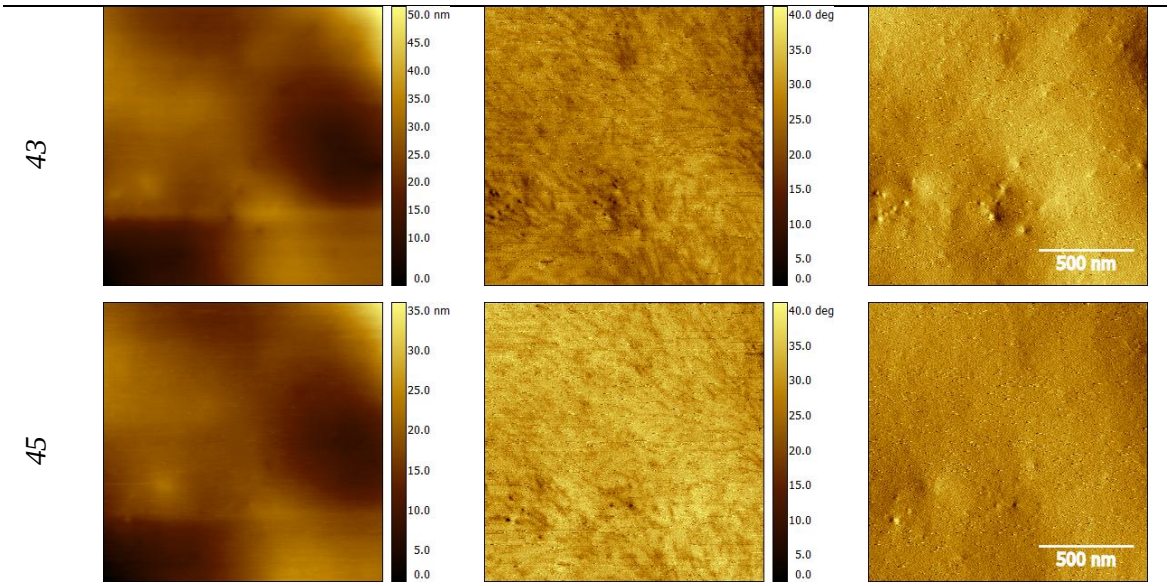

Figure 4.14. Height, Phase and Amplitude AFM Images of 40:60 PBSA during step-heating. The temperature (*T*) of each step is indicated at the left.

Figure 4.14 shows a sequential melting of the 40:60 PBSA, similar to the previous case of the 50:50 PBSA. Again, when the sample is heated, the PBA-rich lamellae start to disappear, and the molten material is spread over the sample and covers the remaining lamellae, therefore the PBS-rich lamellae are not clearly observed. Despite this, after the PBA-rich crystals completely melt, there are some oriented structures underneath the molten material that seems to correspond to PBS-rich lamellae. In fact, such structures start to disappear at 40 ºC, and disappear entirely when the melting temperature of PBS-rich crystals is reached. Therefore, such changes evidence the sequential melting of the PBA-rich and PBS-rich lamellae.

c. Nuclear Magnetic Resonance

NMR experiments were performed to all the samples at RT. The technique employed is cross-polarization magic angle spinning NMR, and is based on the transfer of protons to the carbon atoms. This technique allows differentiating rigid and mobile phases. At short contact times, the transfer of protons occurs from the closest ones, which correspond to the rigid phase. In contrast, higher contact times imply the transfer is at higher distances (*i.e.*, mobile phase). As a result, the rigid phase, the intermediate or interlayer phase and the mobile phase can be detected by this technique. However, this technique does not allow to determine whether one comonomer is inside the crystal lattice of the other, but allows to detect that the comonomer is in a phase which might

be rigid. Moreover, the X_c obtained by this method are qualitative and other methods are needed in order to obtain quantitative X_c (*e.g.*, direct ^{13}C NMR)

Figure 4.15 show the ^{13}C CP MAS NMR spectra of the neat components. It is observed that some signals of the PBS and PBA are overlapping, around 175 and 25 ppm, however there is a signal of the PBS at 30 ppm which is not present on the PBA, and a signal of the PBA at 35 ppm which is not present in the PBA. Therefore, following these signals the behaviour of the PBS and PBA components within the copolymers could be analyzed, as shown in Figure 4.16.

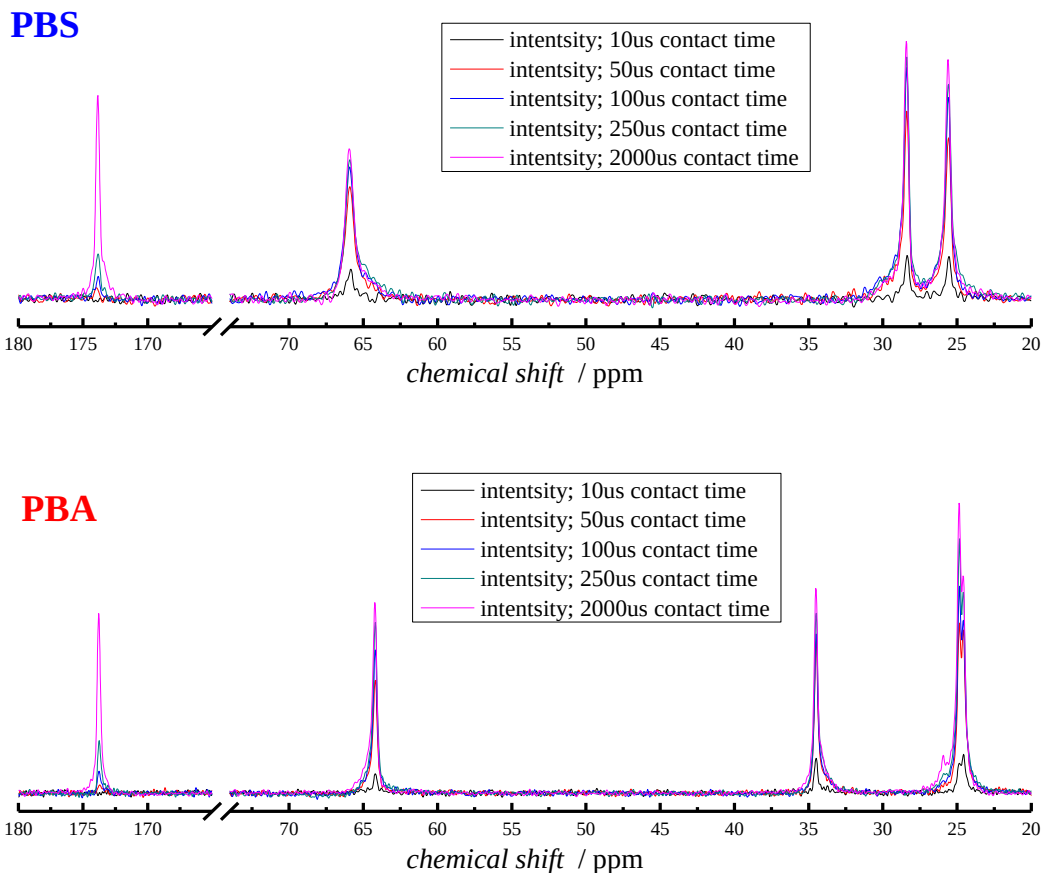

Figure 4.15. ^{13}C CP MAS NMR spectra of PBA (top) and PBA (bottom). Note that the signals at 30 and 35 ppm in the PBS and PBA spectra are not overlaped.

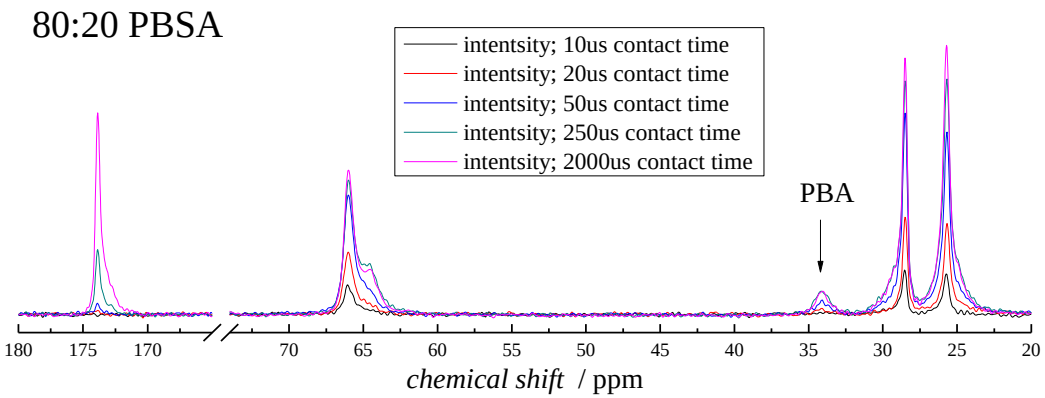
80:20 PBSA
intentsity; 10us contact time
intentsity; 20us contact time
intentsity; 50us contact time
intentsity; 250us contact time
intentsity; 2000us contact time
PBA
180 175 170 70 65 60 55 50 45 40 35 30 25 20
chemical shift / ppm

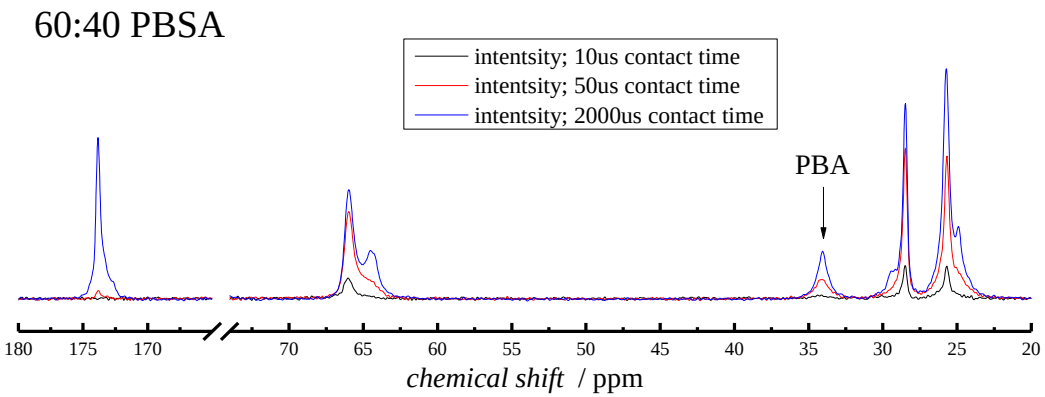
60:40 PBSA
intentsity; 10us contact time
intentsity; 50us contact time
intentsity; 2000us contact time
PBA
180 175 170 70 65 60 55 50 45 40 35 30 25 20
chemical shift / ppm

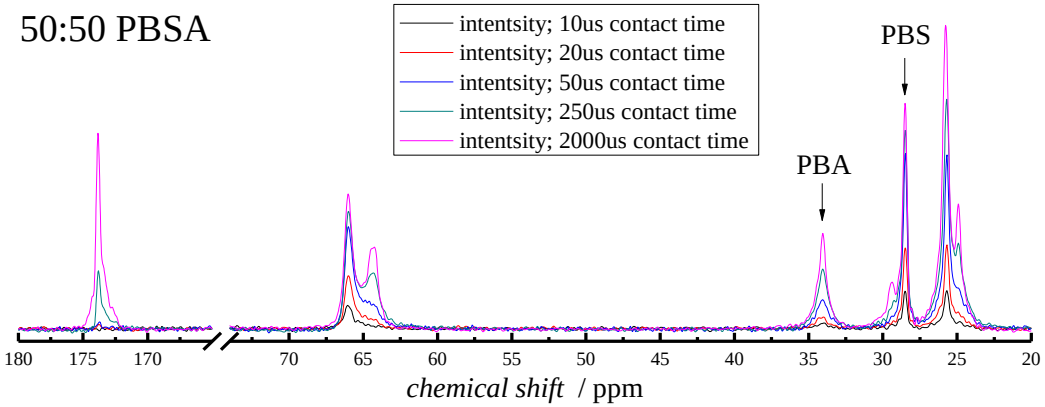
50:50 PBSA
intentsity; 10us contact time
intentsity; 20us contact time
intentsity; 50us contact time
intentsity; 250us contact time
intentsity; 2000us contact time
PBS
PBA
180 175 170 70 65 60 55 50 45 40 35 30 25 20
chemical shift / ppm

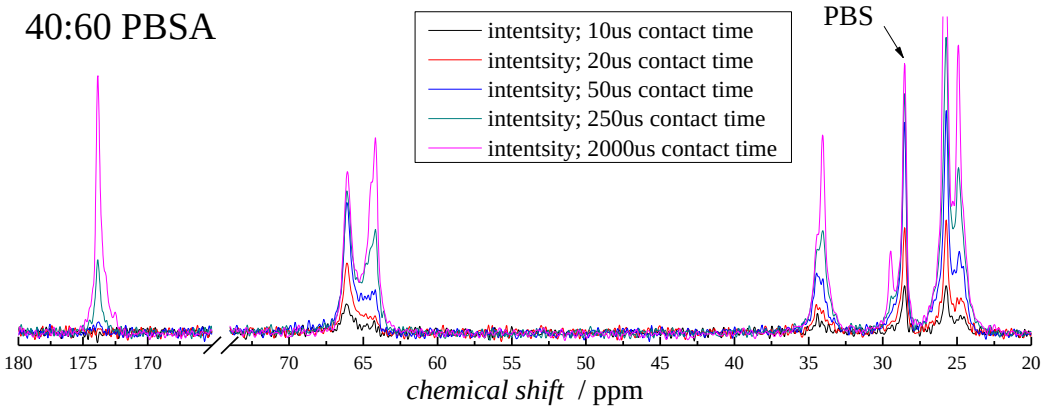
40:60 PBSA
intentsity; 10us contact time
intentsity; 20us contact time
intentsity; 50us contact time
intentsity; 250us contact time
intentsity; 2000us contact time
PBS
180 175 170 70 65 60 55 50 45 40 35 30 25 20
chemical shift / ppm

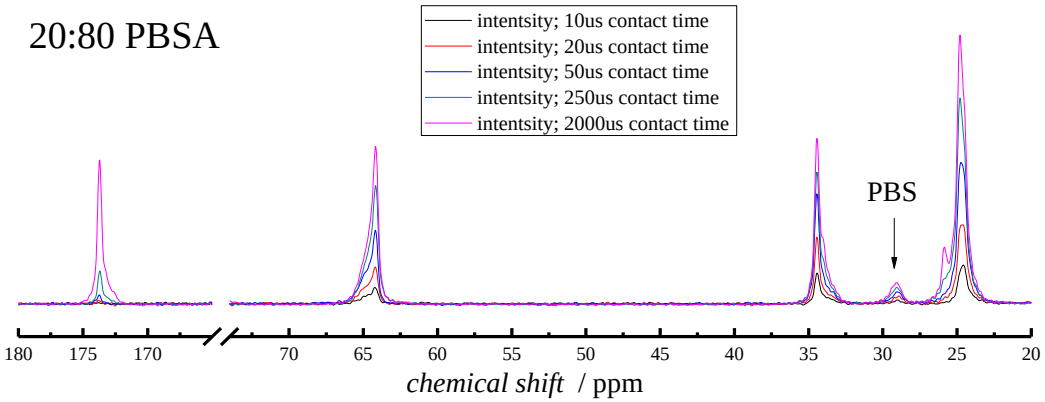

Figure 4.16. ^{13}C CP MAS NMR spectra of 80:20, 60:40, 50:50, 40:60 and 20:80 PBSA random copolymers. The arrows indicate the PBS and PBA signals in each copolymer.

Figure 4.16 shows an increase in the PBS and PBA signal with the increase of PBS or PBA in the copolymer. Therefore, the signal of the one component into the other can be deconvoluted using a Lorentz function in order to obtain the crystalline, interlayer and amorphous fraction (see an Example on Figure 9.6 in the Appendix). The obtained values from the signal at 30 and 35 ppm are shown in Table 4.3 and Figure 4.17.

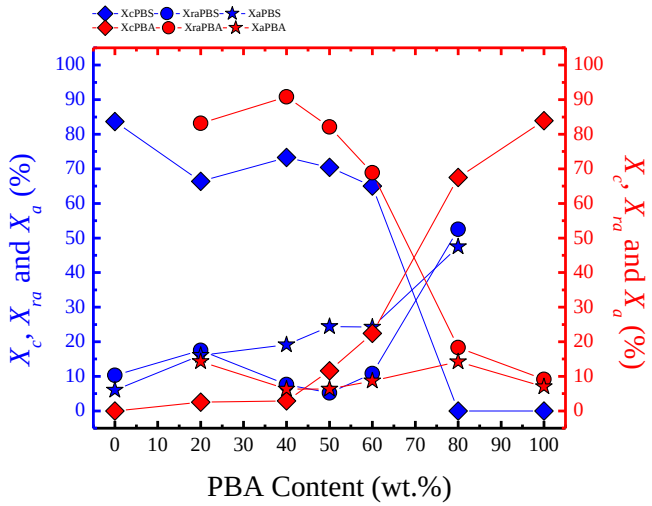

Figure 4.17. Crystalline, interphase (crystalline+amorphous) and amorphous fraction (X_c, X_{ra} and X_a, respectively) for PBS (left-axis) and PBA (right-axis) as a function of PBA Content.

Table 4.3. Signal fractions obtained through NMR experiments for neat PBS and PBA and their copolymers.

Sample	Signal fraction of the PBS component (^{13}C)	Signal fractions of the PBA component (^{13}C)

	X_c	X_{ra}	X_a	X_c	X_{ra}	X_a
PBS	83.7	10.3	6.0	-	-	-
80:20 PBSA	66.4	17.5	16.1	2.5	83.2	14.3
60:40 PBSA	73.3	7.6	19.1	2.9	90.8	6.3
50:50 PBSA	70.4	5.2	24.4	11.6	82.1	6.3
40:60 PBSA	65.0	10.8	24.2	22.4	68.9	8.7
20:80 PBSA	0	52.5	47.5	67.5	18.3	14.2
PBA	-	-	-	83.9	9.1	7.0

Table 4.3 shows that PBS is able to crystallize in a larger quantity in the PBA-rich compositions than the PBA in the PBS-rich compositions. For instance, in the 40:60 PBSA the value of X_c is higher for the PBS than for the PBA, despite the fact that the PBA is the majority component. However, in the 60:40 PBSA the value of X_c is lower for the PBA than the PBS, since PBS is the rich component. This behaviour evidences the higher crystallization ability of the PBS.

d. Temperature and rate dependent experiments

DSC rate dependent experiments

In order to better understand the sequential and coincident crystallization processes of the 50:50 and 40:60 PBSA copolymers, rate dependent experiments were performed.

Figure 4.18a shows cooling scans from the melt at different cooling rates corresponding to the 50:50 PBSA copolymer. Figure 4.18b, on the other hand, shows the subsequent heating scans performed at the constant rate of 20 ºC/min.

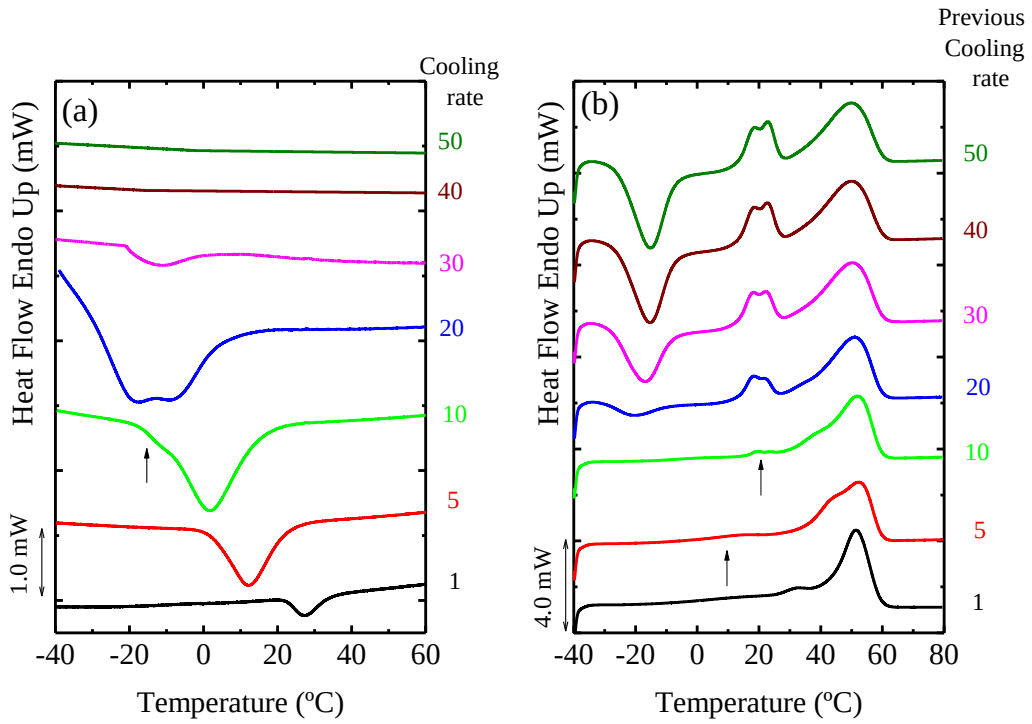

Figure 4.18. 50:50 PBSA (a) cooling scans to -40 ºC at different cooling rates and (b) subsequent heating scans performed at 20 ºC/min. The values indicated to the right of each figure indicate the cooling rates applied in ºC/min.

Figure 4.18 shows that, when the 50:50 PBSA copolymer is cooled at a very slow rate (*i.e.*, at 1 ºC/min), only the PBS-rich phase is able to crystallize, as indicated by the single crystallization exotherm and subsequent melting peak at temperatures that are higher than the melting point of the PBA-rich phase. As the cooling rate is increased, the PBA -rich phase is able to undergo crystallization as well. For the sample cooled at 5 ºC/min, even though a single crystallization peak is registered (*i.e.*, coincident crystallization), the subsequent heating shows a very small melting endotherm or shoulder at temperatures that are characteristic of the PBA-rich phase (which is indicated with an arrow in Figure 4.18b) and a large melting peak at higher temperatures that corresponds to the melting of PBS-rich crystals.

A similar behavior to that observed at 5 ºC/min is observed at 10 ºC/min, except for the fact that during crystallization, a low temperature shoulder can be seen, which attributed to the crystallization of the PBA-rich phase (signaled with an arrow in Figure 4.18a). A small melting endotherm at low temperatures can also be seen on the heating curve corresponding to the melting of the small population of PBA-rich phase crystals (also indicated with an arrow in Figure 4.18b). The bimodality of the crystallization

exotherm is easily seen in the sample cooled at 20 ºC/min in Figure 4.18a, as well as the evident melting of PBA-rich phase crystals at around 20 ºC following a cold-crystallization exotherm.

Increasing the cooling rate to values higher or equal to 40 ºC/min prevents the crystallization of the 50:50 copolymer (also corroborated by WAXS studies). Upon subsequent heating, a very large cold-crystallization exotherm is observed followed by sequential melting. In the next section, WAXS studies during heating shows that in such rapidly cooled samples, the large cold-crystallization exotherm corresponds to the crystallization of the PBA-rich crystal phase. As temperature is increased, the melting of the PBA-rich crystals overlaps with the cold-crystallization of the PBS-rich phase until temperatures above 30 ºC are reached, at which the PBS-rich crystals start melting.

According to results presented above for the 50:50 PBSA copolymer sample, as the PBS-rich phase crystallization becomes more kinetically limited (upon increasing cooling rates), the PBA-rich phase is able to crystallize. Therefore, the coincident crystallization during cooling from the melt switches to a sequential process when cooled from the melt at 10 or 20 ºC/min and finally to a sequential cold-crystallization during heating (for completely amorphous 50:50 PBSA samples).

Similar rate dependent experiments were performed to the 40:60 PBSA copolymer and the results are shown in Figure 4.19.

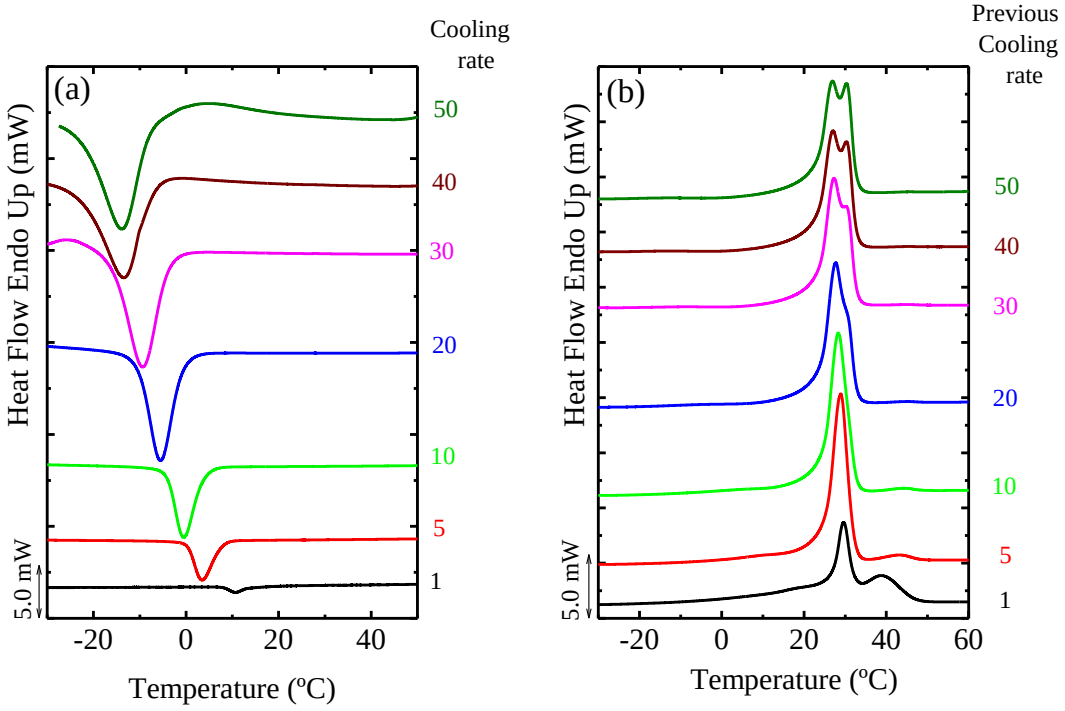

Figure 4.19. 40:60 PBSA (a) cooling DSC scans at different cooling rates and (b) subsequent heating scans performed at 20 ºC/min. The values indicated to the right of each figure indicate the cooling rates applied in ºC/min.

Figure 4.19a shows a single crystallization peak at all the selected cooling rates for the 40:60 PBSA. At high cooling rates (*i.e.*, >20 ºC/min) this peak corresponds to the PBA-rich phase only. This behavior was corroborated by WAXS experiments, (see Figure 9.3 on Supporting information), in which β to α-PBA phase transformation was observed during the heating of the 40:60 PBSA copolymer, whereas such transformation is inhibited when the PBS is able to crystallize.

At low cooling rates (*i.e.*, <20 ºC/min) the single crystallization peak (see Figure 4.19a) correspond to the coincident crystallization of the PBS- and PBA-rich phases, which melt sequentially in the subsequent heating scans (*e.g.*, 1 ºC/min in Figure 4.19b). As the cooling rate is decreased, the melting peak at higher temperatures, which corresponds to the PBS-rich phase, is increased. Therefore, when PBS is the minority phase (40 mol%), it will only be able to crystallize under favorable thermodynamic conditions, such as slow cooling rates, since it only crystallizes before the PBA-rich phase has started its crystallization.

WAXS rate dependent experiments

By employing DSC experiments, the conditions to promote double crystallization in the 50:50 and 40:60 PBSA copolymers were determined. These conditions were employed to perform parallel X-ray experiments.

Figure 4.20a shows WAXS patterns of the 50:50 PBSA copolymer taken during heating immediately after the sample was rapidly cooled from the melt at 50 ºC/min. The corresponding DSC heating scan is presented in Figure 4.20b indicating the changes experienced by the sample, as determined by the WAXS results of Figure 4.20a.

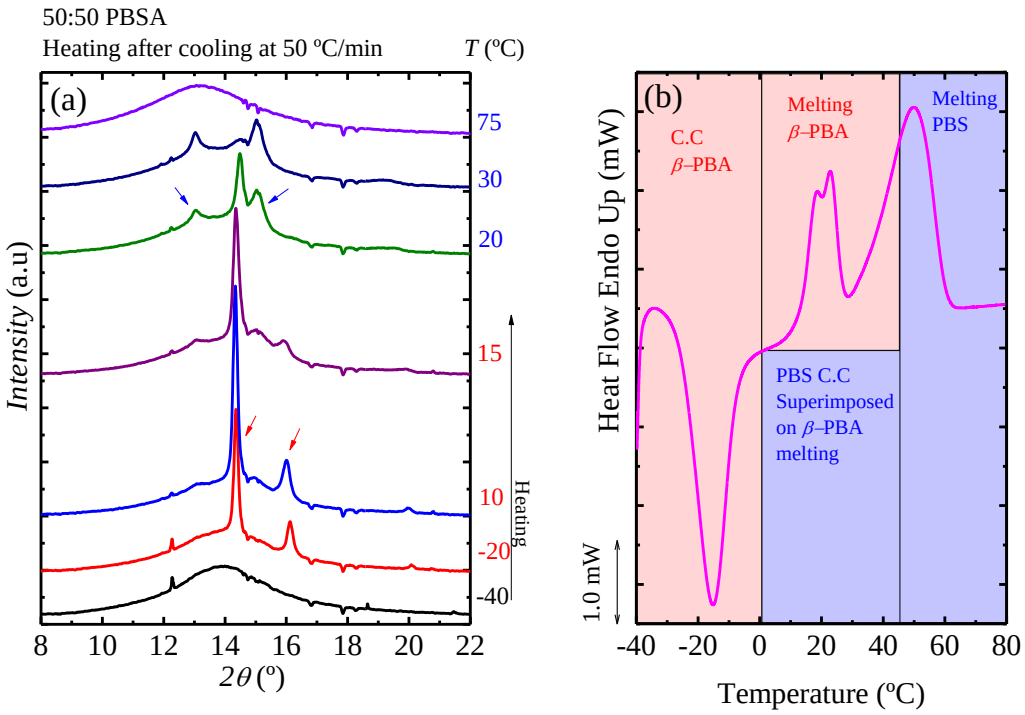

Figure 4.20. (a) WAXS diffractograms (at different temperatures) obtained during heating after cooling the 50:50 PBSA sample at 50 ºC/min and (b) DSC heating scans, for a sample with identical thermal history. The cold-crystallization (C.C.) and melting processes are indicated. The red shadows as well as red color on the numbers are employed to highlight the PBA-rich phase thermal events while the blue shadows as well as blue color on the numbers are used for the corresponding PBS-rich phase. The heating scans (for both WAXS and DSC) were performed at 10 ºC/min. The values indicated to the right of figure (a) indicate the temperature at which the patterns were taken. The arrows indicate the main reflections for PBA (see pattern taken at 10 ºC) and PBS (see pattern taken at 20 ºC).

Figure 4.20a shows WAXS spectra obtained during heating for the 50:50 PBSA copolymer from the amorphous state (*i.e.*, T_c of -40 ºC), after cooling the sample at 50 ºC/min. As the temperature is increased, the PBA-rich phase starts to crystallize at -20 ºC, which corresponds to the cold-crystallization shown in Figure 4.20b. A shoulder at ~15º, in between the two main reflections of the PBA-rich crystalline phase (~14 and 16º), and a weak signal at 13º, which correspond to the PBS-rich phase crystals, appear just at the end of the cold-crystallization of the PBA-rich phase at approximately 5 ºC (data not shown). Then, an increase in intensity of the PBS-rich crystal reflections and a simultaneous decrease of the PBA-rich crystal reflections are recorded in between 15 and 20 ºC, indicating that PBA-rich crystals melt and the PBS-rich phase undergoes

cold-crystallization. Finally, at 30 ºC, only the signals of the PBS-rich crystals remain, until they disappear at higher temperatures (*i.e.*, > 60 ºC) upon melting.
It is worth noting that the transition from β phase to α PBA-rich phase is inhibited by the crystallization of the PBS.

A different behavior is obtained for the 40:60 PBSA copolymer. When the material is cooled from the melt at 1 ºC/min, coincident crystallization of both phases is detected by DSC, as the exotherms corresponding to the crystallization of the two phases overlap (see Figure 4.20a). However, *in situ* WAXS experiments show that the PBS-rich phase starts its crystallization at slightly higher temperatures (*i.e.*, 2 ºC) than the PBA-rich phase. Figure 4.21a shows representative WAXS diffractograms during cooling from the melt at 1 ºC/min. Segmented blue and red lines are used to indicate the PBS and PBA reflections. It can be appreciated that PBS crystal reflections can be first seen at 10 ºC as temperature is decreased, while β-PBA reflections only appear at 8 ºC. Nevertheless, most of the crystallization process occurs at temperatures below 8 ºC in a coincident fashion in agreement with the DSC results.

Figure 4.21b shows WAXS diffractograms for the 40:60 PBSA copolymer taken during heating. The characteristic reflections of β-PBA start to decrease in intensity at 25 ºC, and disappear completely at 29 ºC because the β-PBA rich phase melts. Then, PBS characteristic signals disappear at higher temperatures, as the PBS-rich phase crystals melt, in agreement with the sequential melting detected by DSC experiments (see Figure 4.20b). It is worth noting that also in this sample β to α-PBA phase transformation is inhibited by the presence of PBS in the copolymer. The same conditions for the WAXS rate dependent experiments were used in SAXS and the results are shown in Figures 9.7 and 9.8 (Appendix).

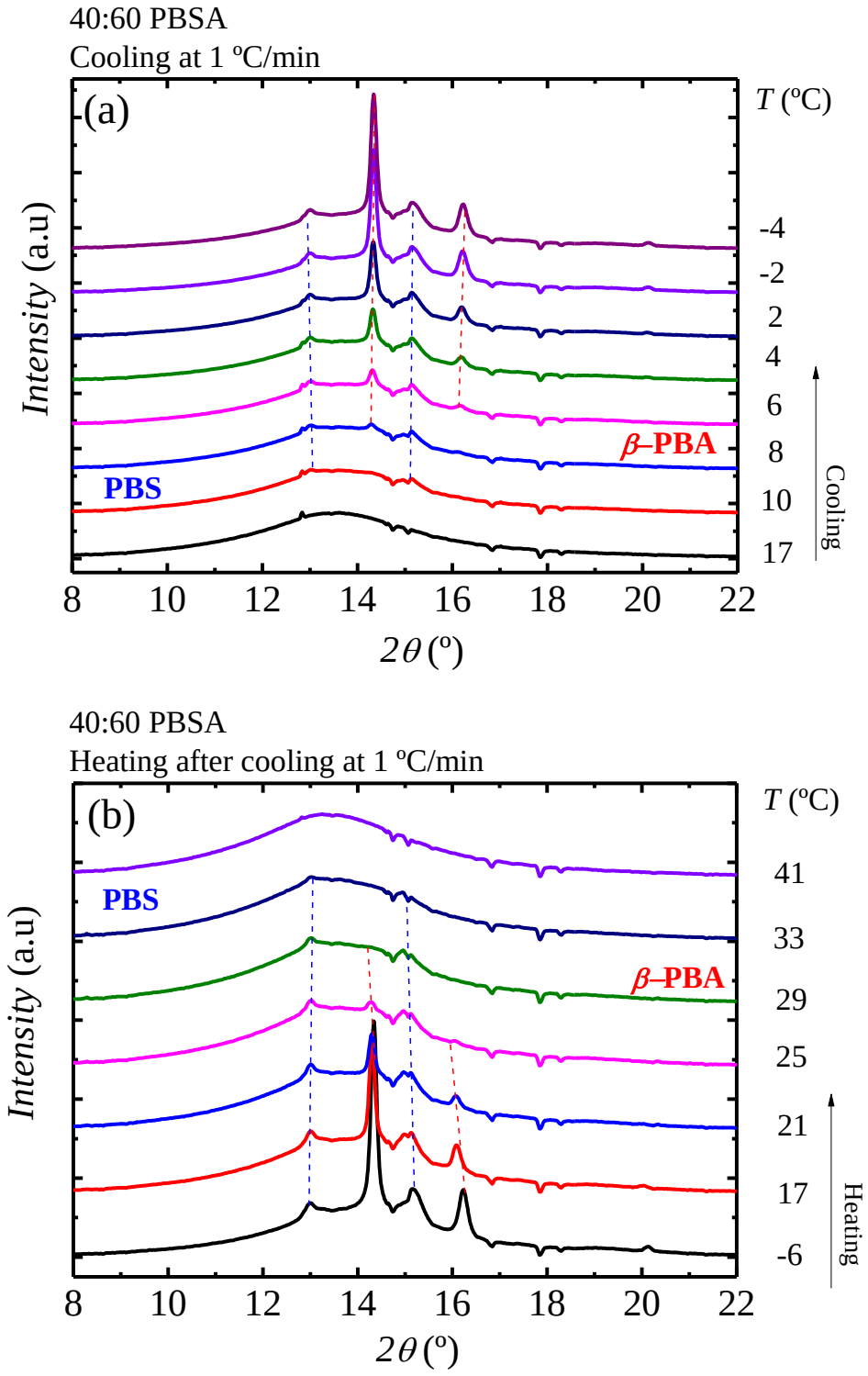

Figure 4.21. WAXS diffractograms taken during (a) cooling at 1 ºC/min and (b) subsequent heating at 10 ºC/min for 40:60 PBSA copolymer. The values indicated to the right of each figure correspond to the temperature at which the patterns were taken.

The results of the previous experiments have shown that these isodimorphic random copolymers have a strong temperature and rate-dependence under non-isothermal test. In order to further understand these copolymers, isothermal test were

performed with different techniques. The following section is related to the behaviour of the PBSA random copolymers under isothermal conditions.

e. Spherulitic morphology.

The PLOM was used to observe the morphology of the different copolymers, as well as to follow their spherulitic growth rate.

The morphological study was performed by cooling the samples from the melt to -40 ºC at 5 ºC/min. Micrographs were taken when spherulites were already impinged and the onset crystallization temperature is indicated in Figure 4.22.

Figure 4.22 shows two kinds of morphologies depending on which is the dominant phase. Therefore, for the PBS or PBA-rich compositions, the morphology approximately resembles that exhibited by the parent homopolymer.

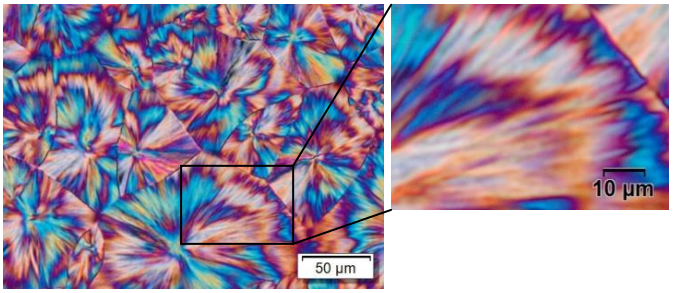

(a) PBS, 80 ºC

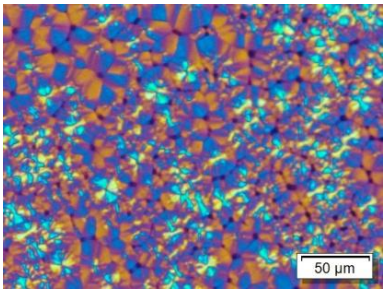

(e) PBA, 34 ºC

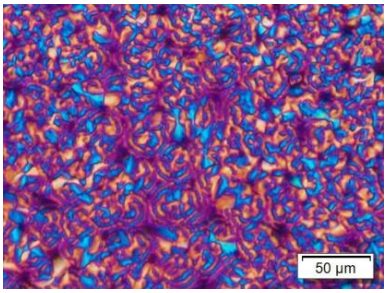

(b) 80:20 PBSA, 52 ºC

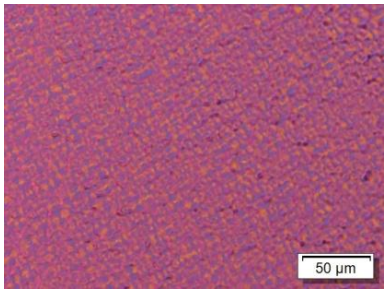

(d) 50:50 PBSA, 11 ºC

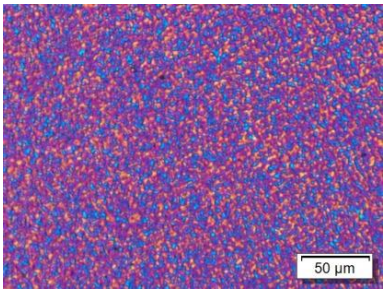

(f) 20:80 PBSA, 21 ºC

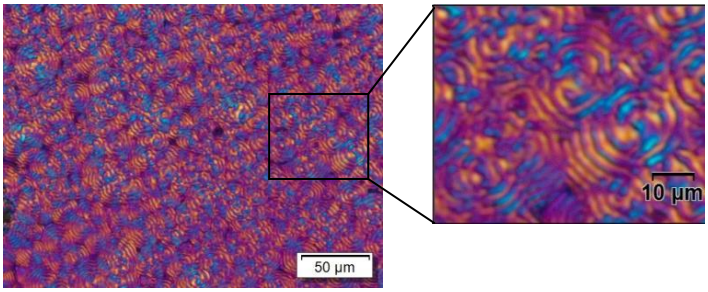

(c) 60:40 PBSA, 27 ºC

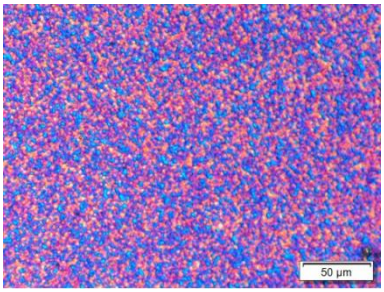

(g) 40:60 PBSA, 3 ºC

Figure 4.22. Polarized light optical micrographs for (a) PBS (b) 80:20 PBSA (c) 60:40 PBSA, (d) 50:50 PBSA, (e) PBA, (f) 20:80 PBSA and (g) 40:60 PBSA taken at -40 ºC after cooling from the melt at 5 ºC/min. The temperature at which the first spherulites appear, or onset crystallization temperature, is indicated under each micrograph.

The micrographs shown in Figure 4.22 (a, b and c) correspond to PBS-rich compositions (they are generally crystallized at higher temperatures than PBA-rich compositions). All these samples display negative spherulites with more or less defined ring band patterns, as shown in the inserts of Figure 4.22a and d. Ring banded spherulites have been reported in the literature at temperatures below[46] and up to 80 ºC[57] under isothermal conditions for neat PBS. In addition, banding has been also reported for 80:20 PBSA copolymer spherulites by Ren et al.[46]

The ring band patterns in Figure 4.22 (a, b and c) go from diffuse (in neat PBS, see Figure 4.22a and its close-up) to well defined (in the copolymers, see Figures 4.22b and c, in which a close-up is inserted) as the BA content increases. Furthermore, a decrease in band spacing, which is related to a decrease in the crystallization temperature,[46] has been observed as PBA content increases (80:20 and 60:40 PBSA). In fact, the onset crystallization temperature also decreases with PBA content (see the onset T_c values below each micrograph in Figure 4.22). Such morphological changes, added to the increase in the nucleation density as the PBA content is increased, are attributed to changes in supercooling imposed by changing composition.

Figure 4.22 (e and f) shows the morphologies obtained for PBA-rich compositions, which correspond to negative spherulites without ring band patterns. PBA morphology is a complex subject, since it is reported that PBA in its two polymorphic forms (*i.e.*, α and β-form) shows negative spherulites without ring band patterns and when these forms coexist (*i.e.*, mixture α+β) the ring band pattern appears.[39] However, it is also reported that both α and β-PBA form can show banding and mixed morphologies.[51] For instance, according to Liu et al.[51] isothermally crystallized PBA (*i.e.*, with M_n of 5.2 kg/mol) at 30 ºC exhibits both ringless α form and ring-banded β form spherulites, and this behavior depends on the rate of nucleation and radial growth of α and β crystals.

In the present case, in the PBA and PBA-rich compositions, banding is absent and WAXS results after cooling at 5 ºC/min indicate spherulites with predominant α or β phases form, respectively. The increase in nucleation density and the decrease in the onset crystallization temperatures, observed as PBS is added to the PBA-rich

copolymers, are attributed to the change in supercooling resulting from the composition changes.

At intermediate compositions (see Figure 4.22d and g), the high number of nuclei complicates the morphological observations at the micron scale. In spite of this, the birrefringent texture observed for the 50:50 PBSA copolymer is similar to those found in PBS-rich compositions, whereas for the 40:60 PBSA copolymer the texture is similar to those present in PBA-rich compositions. In fact, after prepared the samples for AFM observations, the spin-coated samples were observed and the results corroborate the previous observation (*i.e.*, ring-band spherulities for 50:50 PBSA and ringless spherulites for 40:60 PBSA).

In summary, the superstructural morphology is dominated by the majority component in the copolymer at compositions away from the pseudo-eutectic point (lower than 40% of the component in consideration).

As will be demonstrated below, in copolymers with compositions close to 50:50 both PBS-rich and PBA-rich phases can crystallize. It is worth noting that since the PBA-rich phase is molten when the PBS-rich phase starts to crystallize, the latter templates the morphology. Therefore, the PBA-rich phase crystallizes inside the previously formed PBS-rich phase spherulites. This template-like behavior has been reported in PBS/PBA blends,[58] in which PBS forms open structures (*i.e.*, in comparison with the regular spherulites) due to the addition of PBA.

When samples of intermediate composition are heated, changes in birefringence are observed (see Figure 9.9 on the Appendix) and these changes are related to the sequential melting of PBA-rich and PBS-rich phases, which were observed through DSC, X-rays and AFM measurements. Therefore, both PBA- and PBS-rich phases can crystallize when the composition is close to 50:50 (*i.e.*, double crystallization).

4.1.2. PPBA random copolymers.

PPBA random copolymers have a combination of odd-even number of CH_2 in their comonomers, instead of even-even number of CH_2 as in the PBSA random copolymers. Moreover, in the PPBA the functional group is the same in each comonomer, adipic acid instead of a combination of functional groups as in the PBSA

copolymers (see Schematic representation in Scheme 4.3). These characteristics are going to determine the behaviour of PPBA copolymers.

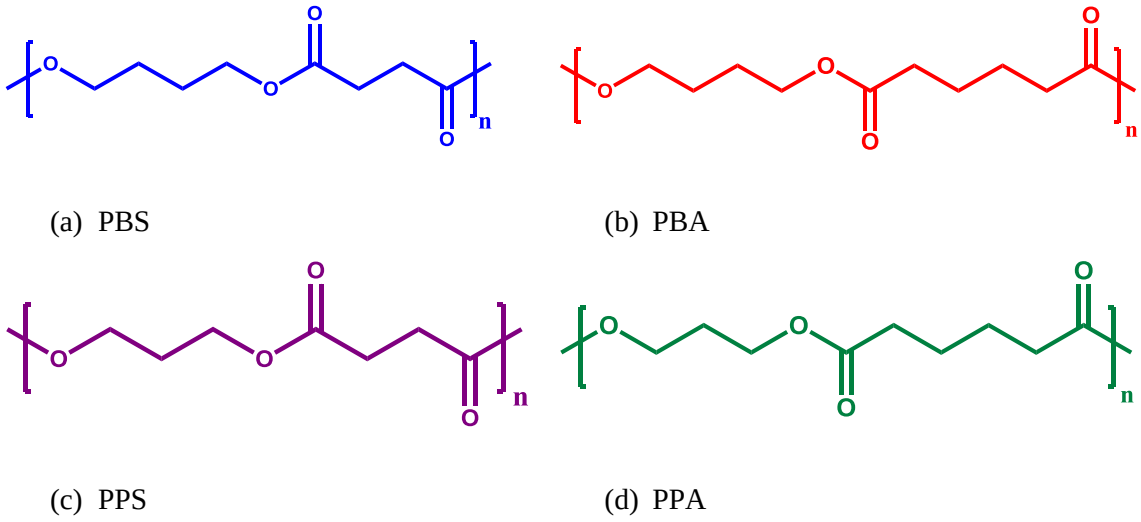

(a) PBS (b) PBA

(c) PPS (d) PPA

Scheme 4.3. Chemical structures of (a) PBS, (b) PBA, (c) PPS and (d) PPA. Note that 4 -C- are in between two oxygens in the repeat unit of (a) PBS and (b) PBA, whereas 3 -C- are present in equivalent positions for (c) PPS and (d) PPA.

Even though the difference between the repeating units of PPA and PBA is only one CH_2, it has been reported in the literature that polyesters with an even and odd number of CH_2s in their repeating unit exhibit different behaviors. Polyesters with an odd number of CH_2 crystallize significantly slower, according to the literature, than those with an even number of CH_2. This effect is commonly reflected on the melting temperatures and it has been usually attributed to different positions of the ordered planar zigzag chain conformation resulting in different alignments of the carbonyl group. These different positions must generate differences in entropies of fusion affecting the crystallization and melting of the material. [59]

Since, the crystallization of a random copolymer is determined by the crystallization ability of each comonomer, it is expected that those comonomers that have similar crystallization ability would compete and the composition at which the crystal transition occurs between one crystal type to the other (*i.e.*, the composition of the pseudo-eutectic point) would be located at intermediate compositions (as in the PBSA copolymer). This crystallization ability is influenced by the length of the comonomer unit, therefore the comonomer unit which has longer chain length has stronger competition. [12]

When two comonomers have different crystallization ability, the composition at which the crystal transition between one crystal type to the other occurs would be located at compositions richer in the comonomer with lower crystallization ability. The reason of such behaviour is the dominant role played by the comonomer with greater crystallization ability. As we will show below, such behaviour correspond to that found in PPBA copolymer, in which the PBA has a stronger crystallization ability in comparison with PPA.

a. Non-isothermal DSC scans

Figure 4.23 shows the DSC cooling scans performed at 1 ºC/min and the subsequent heating at 20 ºC/min for PPBA random copolymers. Such slow cooling rate was selected since it is the only one that allows crystallization of all compositions, especially for the 80:20 PPBA. In fact, PPBA copolymers were studied by Debuissy et al.[24] and they did not find any signal of crystallization for the 80:20 PPBA when it was cooled down at 5 ºC/min.

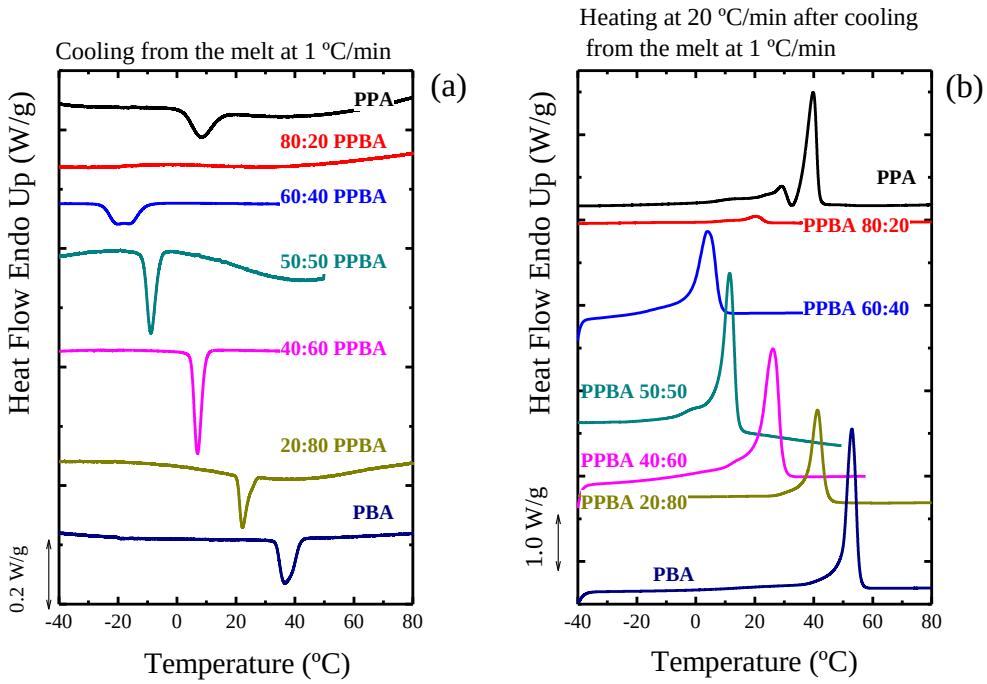

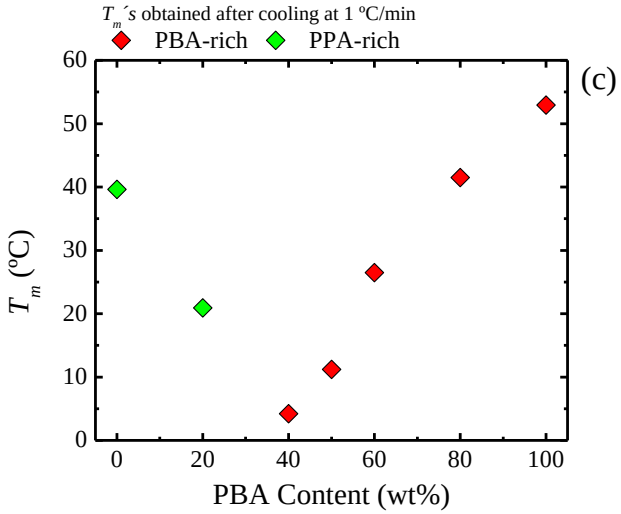

Figure 4.23. (a) Cooling at 1 ºC/min and subsequent (b) heating scan at 20 ºC/min for PPBA copolymers. (c) T_m (*i.e.*, obtained from Figure 4.23b) as a function of PBA content.

Figure 4.23 shows sharp and defined cooling peaks for all compositions, except for the 80:20 PPBA. In this case, a wide crystallization range is displayed, and the weak melting peak recorded in the subsequent scan appears at higher temperatures than that for 60:40 PPBA. Taking into account the melting behaviour of the PPBA copolymers, they show a pseudo-eutectic behaviour (see Figure 4.23c) which differs from the PBSA copolymers in: (a) Unlike the PBSA, double melting peaks are not present, or at least there are not easily observable. This behaviour may be attributed to the closer melting temperatures of PPA and PBA. (b) The eutectic point in the PPBA copolymers seems to be located at compositions in between 60:40 and 80:20 PPBA (see Figure 4.23c), which are significantly lower than 50:50 and 40:60 PBSA pseudo-eutectic compositions of the PBSA copolymers. This shift in the eutectic composition is attributed to the slow crystallization rate of the PPA component, which made that even at high contents of PPA, the crystallization of the PBA dominates over that of PPA. This is related to the stronger competition of the PBA comonomer, due to its longer repeating unit length.

b. X-rays experiments.

Figure 4.24 shows the WAXS patterns for the PPBA systems. These patterns were obtained at different temperatures, as some of the materials are molten at room temperature, therefore *in situ* experiments were necessary to obtain their WAXS patterns.

Despite the different thermal histories, two crystalline structures are observed. The 20:80, 40:60, 50:50 and 60:40 PPBA correspond to the *β*-PBA. Although, it is worth noting that the latter composition shows a shoulder at lower *q* that could indicate the presence of some PPA crystals. In contrast, the 80:20 PPBA shows a pattern which resembles neat PPA (note that this pattern is used for comparison purposes since it was obtained under isothermal conditions). The behaviour shown in Figure 4.24 indicates that the pseudo-eutectic point is located at a composition in between 60:40 and 80:20. This result is in line with the DSC data.

It is worth noting that as expected, the eutectic point is not located at intermediate composition. Such location of the eutectic point is attributed to the slow crystallization rate of the PPA or what is the same, the higher crystallization ability of the PBA. As we mentioned before, this crystallization ability differences are caused by the "odd-even effect".

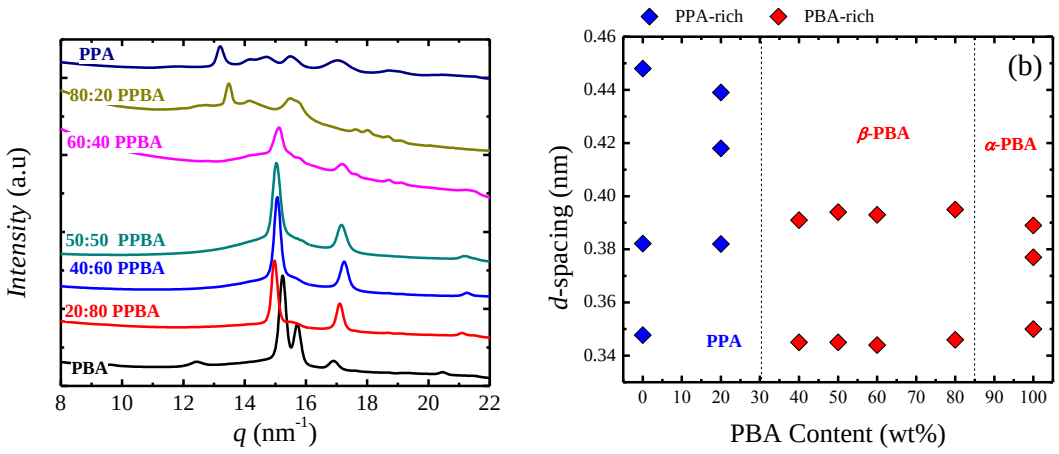

Figure 4.24. (a) WAXS patterns and (b) *d*-spacings as a function of the PBA content, for all the PPBA samples.

Figure 4.24b shows that the *d*-spacing does not change progressively and shows jumps between the different crystalline phases instead. For instance, there is a jump from *α* to *β*-PBA. Then the *β*-PBA phase dominates the crystallization and it is maintained from the 20:80 PPBA until the 60:40 PPBA. A final change occurs from the *β*-PBA to the PPA-rich phase. In this latter phase, an increase of the *d*-spacing is recorded for some of the main planes of the PPA, which could indicate PBA comonomer inclusion.

From the quantitatively point of view it is difficult to conclude that PPBA copolymer is isodimorphic according to Figure 4.24b. However, the qualitative changes, seems to indicate the inclusion of the PPA into the PBA, due to the change from α to β, and *viceversa* due to the changes on the *d*-spacing.

4.1.3. PPBS and PPSA random copolymers.

The PPBS copolymers only showed crystallinity when they were recovered and purified after their synthesis. During the first DSC heating run, they displayed melting peaks (see Figure 9.10 in Appendix). After their thermal history was erased, they were not able to crystallize anymore, even when cooling rates as slow as 1 ºC/min were employed (see Figure 9.11 in Appendix). Therefore, it is hypothesized that PPBS copolymers will crystallize only under extremely low cooling rates (or from solution), or by employing holding times of days above T_g, due to the slow crystallization of the PPS.

In the case of PPSA random copolymers, none of the compositions studied was able to crystallize (see Figure 9.12 in Appendix), even though the only difference between the comonomers (with respect to PPBS) is the functional groups (adipate *vs* succinate). Despite the similarities between PPS and PPA comonomers, the latter is able to crystallize due to the absence of butylene adipate (BA) unit defects and the presence of adipic acid (AA) segments (instead of succinic acid (SA) segments) which increases the crystallization rate.[24] However, both comonomers have slow crystallization rates in comparison with PBS and PBA comonomers.

It is worth noting that the PBSA copolymers are able to crystallize for all compositions. However, only one CH_2 less (therefore with an odd number of CH_2s in the repeating unit, instead of an even one) in each comonomer produces copolymers that do not show crystallization or melting, therefore the PPSA system was discarded for further studies. This generates two questions that could be studied in future works: Can a copolyester formed by two comonomers with odd numbers of CH_2 crystallize? Is the crystallization of copolyesters formed by two comonomers with odd numbers of CH_2 dependent on the length of the chain (*e.g.*, propylene vs pentylene)?

4.3.Conclusions

Different combinations of monomers were prepared via polycondensation in order to obtain random copolymers. Three of these copolymers are able to crystallize in all the composition ranges (taking into account the first heating scan for PPBS). According to the results, the crystallization is favoured in the PBSA copolymers, whereas in the PPBA and PPBS, the combination of odd and even monomers difficult the crystallization, as a result of the presence of PPA and PPS, respectively. In fact, the presence of PPS in PPBS copolymers hinders the crystallization in all compositions under the studied conditions. However, it can be hyphotesized that the melting peak in the first heating of all compositions, is the result of a previous crystallization from solution. After melting, the material may need days in order to crystallize at temperatures between T_g and T_m. Therefore, under such conditions (*i.e.*, crystallization of days) PPBS copolymer might be isodimorphic. In contrast, in PPSA copolymers, the combination of PPA and PPS results in the lack of crystallization for any composition under the testing conditions employed in this work.

PBSA and PPBA are isodimorphic according to the results obtained in this work. In the PBSA copolymers, the pseudo-eutectic points is located at intermediate compositions (50:50 and 40:60), whereas in the PPBA systems it is located at PPA rich compositions (*i.e.*, 80:20 PPBA) due to the higher crystallization ability of the PBA in comparison with the PPA. Since, PPBA shows difficulties to crystallize; the studies through different techniques were focused on the PBSA, which is an easier system to study.

PBSA random copolymers are isodimorphic, since each phase allows the inclusion of the minority comonomer. Moreover, the calorimetric properties exhibit a pseudo-eutectic behaviour. Around the eutectic point, which correspond to two compositions (*i.e.*, 50:50 and 40:60 PBSA), a double crystallization process, which strongly depends on cooling rates, was observed.

For all copolymers, the inclusion of PBS repeating units in the co-crystals forces the PBA-rich phase to crystallize in its kinetically favoured crystalline phase (*i.e.*, β-PBA). This behaviour could be ascribed to less severe energy penalty for the BS units into the PBA-rich β-phase lattice, in comparison to inclusion into the α-phase.[21]

4.4.References

[1] G. Odian, Principles of Polymerization, Wiley, 2004.
[2] R.A. Pérez-Camargo, I. Arandia, M. Safari, D. Cavallo, N. Lotti, M. Soccio, A.J. Müller, Crystallization of isodimorphic aliphatic random copolyesters: Pseudo-eutectic behavior and double-crystalline materials, Eur. Polym. J. 101 (2018) 233-247.
[3] G. Natta, P. Corradini, D. Sianesi, D. Morero, Isomorphism phenomena in macromolecules, Journal of Polymer Science 51 (1961) 527-539.
[4] G. Allegra, I.W. Bassi, Isomorphism in synthetic macromolecular systems, in: Fortschritte der Hochpolymeren-Forschung, Springer Berlin Heidelberg, Berlin, Heidelberg, 1969, pp. 549-574.
[5] Y. Yu, L. Sang, Z. Wei, X. Leng, Y. Li, Unique isodimorphism and isomorphism behaviors of even-odd poly(hexamethylene dicarboxylate) aliphatic copolyesters, Polymer 115 (2017) 106-117.
[6] J.-P. Latere Dwan'Isa, P. Lecomte, P. Dubois, R. Jérôme, Synthesis and Characterization of Random Copolyesters of ε-Caprolactone and 2-Oxepane-1,5-dione, Macromolecules 36 (2003) 2609-2615.
[7] G. Ceccorulli, M. Scandola, A. Kumar, B. Kalra, R.A. Gross, Cocrystallization of Random Copolymers of ω-Pentadecalactone and ε-Caprolactone Synthesized by Lipase Catalysis, Biomacromolecules 6 (2005) 902-907.
[8] H.-M. Ye, R.-D. Wang, J. Liu, J. Xu, B.-H. Guo, Isomorphism in Poly(butylene succinate-co-butylene fumarate) and Its Application as Polymeric Nucleating Agent for Poly(butylene succinate), Macromolecules 45 (2012) 5667-5675.
[9] V. Siracusa, M. Gazzano, L. Finelli, N. Lotti, A. Munari, Cocrystallization phenomena in novel poly(diethylene terephthalate-co-thiodiethylene terephthalate) copolyesters, J. Polym. Sci., Part B: Polym. Phys. 44 (2006) 1562-1571.
[10] G.Z. Papageorgiou, D.N. Bikiaris, Synthesis and Properties of Novel Biodegradable/Biocompatible Poly[propylene-co-(ethylene succinate)] Random Copolyesters, Macromol. Chem. Phys. 210 (2009) 1408-1421.
[11] P. Pan, Y. Inoue, Polymorphism and isomorphism in biodegradable polyesters, Prog. Polym. Sci. 34 (2009) 605-640.
[12] Y. Yu, Z. Wei, L. Zheng, C. Jin, X. Leng, Y. Li, Competition and miscibility of isodimorphism and their effects on band spherulites and mechanical properties of poly(butylene succinate-co-cis-butene succinate) unsaturated aliphatic copolyesters, Polymer 150 (2018) 52-63.
[13] Y. Yu, Z. Wei, C. Zhou, L. Zheng, X. Leng, Y. Li, Miscibility and competition of cocrystallization behavior of poly(hexamethylene dicarboxylate)s aliphatic copolyesters: Effect of chain length of aliphatic diacids, Eur. Polym. J. 92 (2017) 71-85.
[14] X. Li, Z. Hong, J. Sun, Y. Geng, Y. Huang, H. An, Z. Ma, B. Zhao, C. Shao, Y. Fang, C. Yang, L. Li, Identifying the Phase Behavior of Biodegradable Poly(hexamethylene succinate-co-hexamethylene adipate) Copolymers with FTIR, The Journal of Physical Chemistry B 113 (2009) 2695-2704.
[15] Z. Liang, P. Pan, B. Zhu, T. Dong, L. Hua, Y. Inoue, Crystalline Phase of Isomorphic Poly(hexamethylene sebacate-co-hexamethylene adipate) Copolyester: Effects of Comonomer Composition and Crystallization Temperature, Macromolecules 43 (2010) 2925-2932.
[16] X. Li, J. Sun, Y. Huang, Y. Geng, X. Wang, Z. Ma, C. Shao, X. Zhang, C. Yang, L. Li, Inducing New Crystal Structures through Random Copolymerization of Biodegradable Aliphatic Polyester, Macromolecules 41 (2008) 3162-3168.

[17] B. Tan, S. Bi, K. Emery, M.J. Sobkowicz, Bio-based poly(butylene succinate-co-hexamethylene succinate) copolyesters with tunable thermal and mechanical properties, Eur. Polym. J. 86 (2017) 162-172.
[18] I. Arandia, A. Mugica, M. Zubitur, A. Arbe, G. Liu, D. Wang, R. Mincheva, P. Dubois, A.J. Müller, How Composition Determines the Properties of Isodimorphic Poly(butylene succinate-ran-butylene azelate) Random Biobased Copolymers: From Single to Double Crystalline Random Copolymers, Macromolecules 48 (2015) 43-57.
[19] A. Díaz, L. Franco, J. Puiggalí, Study on the crystallization of poly(butylene azelate-co-butylene succinate) copolymers, Thermochim. Acta 575 (2014) 45-54.
[20] R. Mincheva, A. Delangre, J.-M. Raquez, R. Narayan, P. Dubois, Biobased Polyesters with Composition-Dependent Thermomechanical Properties: Synthesis and Characterization of Poly(butylene succinate-co-butylene azelate), Biomacromolecules 14 (2013) 890-899.
[21] R.A. Pérez-Camargo, B. Fernández-d'Arlas, D. Cavallo, T. Debuissy, E. Pollet, L. Avérous, A.J. Müller, Tailoring the Structure, Morphology, and Crystallization of Isodimorphic Poly(butylene succinate-ran-butylene adipate) Random Copolymers by Changing Composition and Thermal History, Macromolecules 50 (2017) 597-608.
[22] Z. Liang, P. Pan, B. Zhu, Y. Inoue, Isomorphic crystallization of aliphatic copolyesters derived from 1,6-hexanediol: Effect of the chemical structure of comonomer units on the extent of cocrystallization, Polymer 52 (2011) 2667-2676.
[23] Z. Liang, P. Pan, B. Zhu, Y. Inoue, Isomorphic Crystallization of Poly(hexamethylene adipate-co-butylene adipate): Regulating Crystal Modification of Polymorphic Polyester from Internal Crystalline Lattice, Macromolecules 43 (2010) 6429-6437.
[24] T. Debuissy, P. Sangwan, E. Pollet, L. Avérous, Study on the structure-properties relationship of biodegradable and biobased aliphatic copolyesters based on 1,3-propanediol, 1,4-butanediol, succinic and adipic acids, Polymer 122 (2017) 105-116.
[25] H. Tsuji, T. Sobue, Cocrystallization of monomer units in lactic acid-based biodegradable copolymers, poly(l-lactic acid-co-l-2-hydroxybutanoic acid)s, Polymer 72 (2015) 202-211.
[26] C. Lavilla, A. Alla, A. Martínez de Ilarduya, S. Muñoz-Guerra, High Tg Bio-Based Aliphatic Polyesters from Bicyclic d-Mannitol, Biomacromolecules 14 (2013) 781-793.
[27] C. Ciulik, M. Safari, A. Martínez de Ilarduya, J.C. Morales-Huerta, A. Iturrospe, A. Arbe, A.J. Müller, S. Muñoz-Guerra, Poly(butylene succinate-ran-ε-caprolactone) copolyesters: Enzymatic synthesis and crystalline isodimorphic character, Eur. Polym. J. (2017).
[28] M. Hong, X. Tang, B.S. Newell, E.Y.X. Chen, "Nonstrained" γ-Butyrolactone-Based Copolyesters: Copolymerization Characteristics and Composition-Dependent (Thermal, Eutectic, Cocrystallization, and Degradation) Properties, Macromolecules 50 (2017) 8469-8479.
[29] K. Wang, Y.-G. Jia, X.X. Zhu, Two-Way Reversible Shape Memory Polymers Made of Cross-Linked Cocrystallizable Random Copolymers with Tunable Actuation Temperatures, Macromolecules 50 (2017) 8570-8579.
[30] Y. Yu, Z. Wei, Y. Liu, Z. Hua, X. Leng, Y. Li, Effect of chain length of comonomeric diols on competition and miscibility of isodimorphism: A comparative study of poly(butylene glutarate-co-butylene azelate) and poly(octylene glutarate-co-octylene azelate), Eur. Polym. J. 105 (2018) 274-285.
[31] V.R. Thalladi, M. Nüsse, R. Boese, The Melting Point Alternation in α,ω-Alkanedicarboxylic Acids, J. Am. Chem. Soc. 122 (2000) 9227-9236.

[32] L. Mandelkern, Crystallization of Polymers: Volume 1, Equilibrium Concepts, Cambridge University Press, 2002.
[33] T. Haider, C. Volker, J. Kramm, K. Landfester, F.R. Wurm, Plastics of the future? The impact of biodegradable polymers on the environment and on society, Angewandte Chemie (International ed. in English) (2018).
[34] S. Kalia, L. Avérous, Biodegradable and Biobased Polymers for Environmental and Biomedical Applications, Wiley, 2016.
[35] V. Tserki, P. Matzinos, E. Pavlidou, D. Vachliotis, C. Panayiotou, Biodegradable aliphatic polyesters. Part I. Properties and biodegradation of poly(butylene succinate-co-butylene adipate), Polym. Degrad. Stab. 91 (2006) 367-376.
[36] J. Zhang, W. Zhu, C. Li, D. Zhang, Y. Xiao, G. Guan, L. Zheng, Effect of the biobased linear long-chain monomer on crystallization and biodegradation behaviors of poly(butylene carbonate)-based copolycarbonates, RSC Advances 5 (2015) 2213-2222.
[37] R.J. Young, P.A. Lovell, Introduction to Polymers, Third Edition, Taylor & Francis, 2011.
[38] M. Gordon, J.S. Taylor, Ideal copolymers and the second-order transitions of synthetic rubbers. i. non-crystalline copolymers, Journal of Applied Chemistry 2 (1952) 493-500.
[39] J. Yang, P. Pan, L. Hua, Y. Xie, T. Dong, B. Zhu, Y. Inoue, X. Feng, Fractionated crystallization, polymorphic crystalline structure, and spherulite morphology of poly(butylene adipate) in its miscible blend with poly(butylene succinate), Polymer 52 (2011) 3460-3468.
[40] E.M. Woo, M.C. Wu, Thermal and X-ray analysis of polymorphic crystals, melting, and crystalline transformation in poly(butylene adipate), J. Polym. Sci., Part B: Polym. Phys. 43 (2005) 1662-1672.
[41] Z. Gan, K. Kuwabara, H. Abe, T. Iwata, Y. Doi, Metastability and Transformation of Polymorphic Crystals in Biodegradable Poly(butylene adipate), Biomacromolecules 5 (2004) 371-378.
[42] Z. Gan, H. Abe, Y. Doi, Temperature-Induced Polymorphic Crystals of Poly(butylene adipate), Macromol. Chem. Phys. 203 (2002) 2369-2374.
[43] T. Dong, W. Kai, Y. Inoue, Regulation of Polymorphic Behavior of Poly(butylene adipate) upon Complexation with α-Cyclodextrin, Macromolecules 40 (2007) 8285-8290.
[44] H.-j. Wang, H.-p. Feng, X.-c. Wang, P.-y. Guo, T.-s. Zhao, L.-f. Ren, X.-h. Qiang, Y.-h. Xiang, C. Yan, Effects of crystallization temperature and blend ratio on the crystal structure of poly(butylene adipate) in the poly(butylene adipate)/poly(butylene succinate) blends, Chin. J. Polym. Sci. 32 (2014) 488-496.
[45] M.S. Nikolic, J. Djonlagic, Synthesis and characterization of biodegradable poly(butylene succinate-co-butylene adipate)s, Polym. Degrad. Stab. 74 (2001) 263-270.
[46] M. Ren, J. Song, C. Song, H. Zhang, X. Sun, Q. Chen, H. Zhang, Z. Mo, Crystallization kinetics and morphology of poly(butylene succinate-co-adipate), J. Polym. Sci., Part B: Polym. Phys. 43 (2005) 3231-3241.
[47] H.-M. Ye, Y.-R. Tang, J. Xu, B.-H. Guo, Role of Poly(butylene fumarate) on Crystallization Behavior of Poly(butylene succinate), Industrial & Engineering Chemistry Research 52 (2013) 10682-10689.
[48] Y. Ichikawa, H. Kondo, Y. Igarashi, K. Noguchi, K. Okuyama, J. Washiyama, Crystal structures of α and β forms of poly(tetramethylene succinate), Polymer 41 (2000) 4719-4727.

[49] I.L. Hosier, R.G. Alamo, P. Esteso, J.R. Isasi, L. Mandelkern, Formation of the α and γ Polymorphs in Random Metallocene−Propylene Copolymers. Effect of Concentration and Type of Comonomer, Macromolecules 36 (2003) 5623-5636.
[50] C. De Rosa, F. Auriemma, O.R. de Ballesteros, L. Resconi, I. Camurati, Crystallization Behavior of Isotactic Propylene−Ethylene and Propylene−Butene Copolymers: Effect of Comonomers versus Stereodefects on Crystallization Properties of Isotactic Polypropylene, Macromolecules 40 (2007) 6600-6616.
[51] J. Liu, H.-M. Ye, J. Xu, B.-H. Guo, Formation of ring-banded spherulites of α and β modifications in Poly(butylene adipate), Polymer 52 (2011) 4619-4630.
[52] E. Pouget, A. Almontassir, M.T. Casas, J. Puiggalí, On the Crystalline Structures of Poly(tetramethylene adipate), Macromolecules 36 (2003) 698-705.
[53] R. Minke, J. Blackwell, Single crystals of poly(tetramethylene adipate), Journal of Macromolecular Science, Part B 18 (1980) 233-255.
[54] G. Lugito, E.M. Woo, Intertwining lamellar assembly in porous spherulites composed of two ring-banded poly(ethylene adipate) and poly(butylene adipate), Soft Matter 11 (2015) 908-917.
[55] G.Z. Papageorgiou, V. Tsanaktsis, D.N. Bikiaris, Crystallization of poly(butylene-2,6-naphthalate-co-butylene adipate) copolymers: regulating crystal modification of the polymorphic parent homopolymers and biodegradation, CrystEngComm 16 (2014) 7963-7978.
[56] D.W. Van Krevelen, K. Te Nijenhuis, Chapter 5 - Calorimetric Properties, in: Properties of Polymers (Fourth Edition), Elsevier, Amsterdam, 2009, pp. 109-128.
[57] Z. Gan, H. Abe, Y. Doi, Crystallization, Melting, and Enzymatic Degradation of Biodegradable Poly(butylene succinate-co-14 mol ethylene succinate) Copolyester, Biomacromolecules 2 (2001) 313-321.
[58] H. Wang, Z. Gan, J.M. Schultz, S. Yan, A morphological study of poly(butylene succinate)/poly(butylene adipate) blends with different blend ratios and crystallization processes, Polymer 49 (2008) 2342-2353.
[59] L. Mandelkern, The Crystalline State, in: J. Mark, K. Ngai, W. Graessley, L. Mandelkern, E. Samulski, J. Koening, G. Wignall (Eds.) Physical Properties of Polymers, Cambridge University Press, 2004, pp. 209-315.

CHAPTER V.

The influence of chain primary structure and topology (branching) on crystallization and thermal properties

5.1. General Introduction

Variations in primary structure and topology (*e.g.*, branching) can strongly affect the crystallization and thermal properties of copolymers. For instance, different chain structures, such as linear, star and comb-like structure, have different conformational sequences, therefore they typically exhibit differences in their crystallization behavior.

The differences on the crystallization and thermal properties of copolymers, allows tailoring the properties of some materials by changing their structure and topology. When the materials are biocompatible, the main goal of such changes is to obtain materials that can be used in biomedical applications. Among these materials, specifically for inflammation processes, polysulfides can be found. Polysulfides have been extensively studied as oxidation-responsive materials, owing to the biological relevance of oxidation phenomena. Indeed, oxidants (reactive oxygen species, ROS) play a key role in a variety of cellular phenomena, including mitosis, angiogenesis, tumorigenesis and above all inflammatory pathologies and a number of materials have been developed to perform ROS-responsive actions with a therapeutic value.[1-4] Some of these materials are based on organic sulfides, where the oxidation of hydrophobic sulfur(II) atoms to more hydrophilic sulfoxide or sulfone determines a phase transition (*e.g.*, a solubilisation) of the material,[5] which can be used for example as a circulating nanocarrier[6] for *e.g.*, site-specific drug release in a ROS-responsive fashion[7] or to transduce a chemical signal such as glucose (*via* glucose oxidase) into a measurable output signal.[8] Importantly, the responsive behaviour depends not only on the nature of the oxidant,[9-11] but also on details of the polysulfide architecture, in particular the primary structure[12] and the degree of branching.[13]

However, in addition to evaluating the final influence of the macromolecular architecture on the oxidative response, it is important to separate the direct effects (*e.g.*, short-range hindrance by groups neighbouring sulphur atoms) from those that are

mediated by the capacity of producing ordered structures and by the presence of topological restrictions.

In order to clarify the links between macromolecular architecture and long-range order capacity in polysulfides; specifically, we focused on how the latter are affected by primary structure (order of repeating units) and by branching (single or multiple branching points) in copolymers comprising a crystallisable with a non-crystallizable repeating unit (Scheme 5.1). The former is propylene sulfide (PS); atactic poly (propylene sulfide) (PPS, obtained from racemic PS) is an amorphous polymer with a low T_g,[14] soluble in most organic solvents.[12] The crystallizable unit is closely related to PS, but devoid of the methyl group: ethylene sulfide (ES). The regularity of the ES repeating units makes its homopolymer, poly (ethylene sulfide) (PES), highly crystalline, with a high melting point (*i.e.*, 205-210 ºC)[15, 16] and very poor solubility (only in drastic conditions such as nitrobenzene at temperatures higher than 170 ºC).

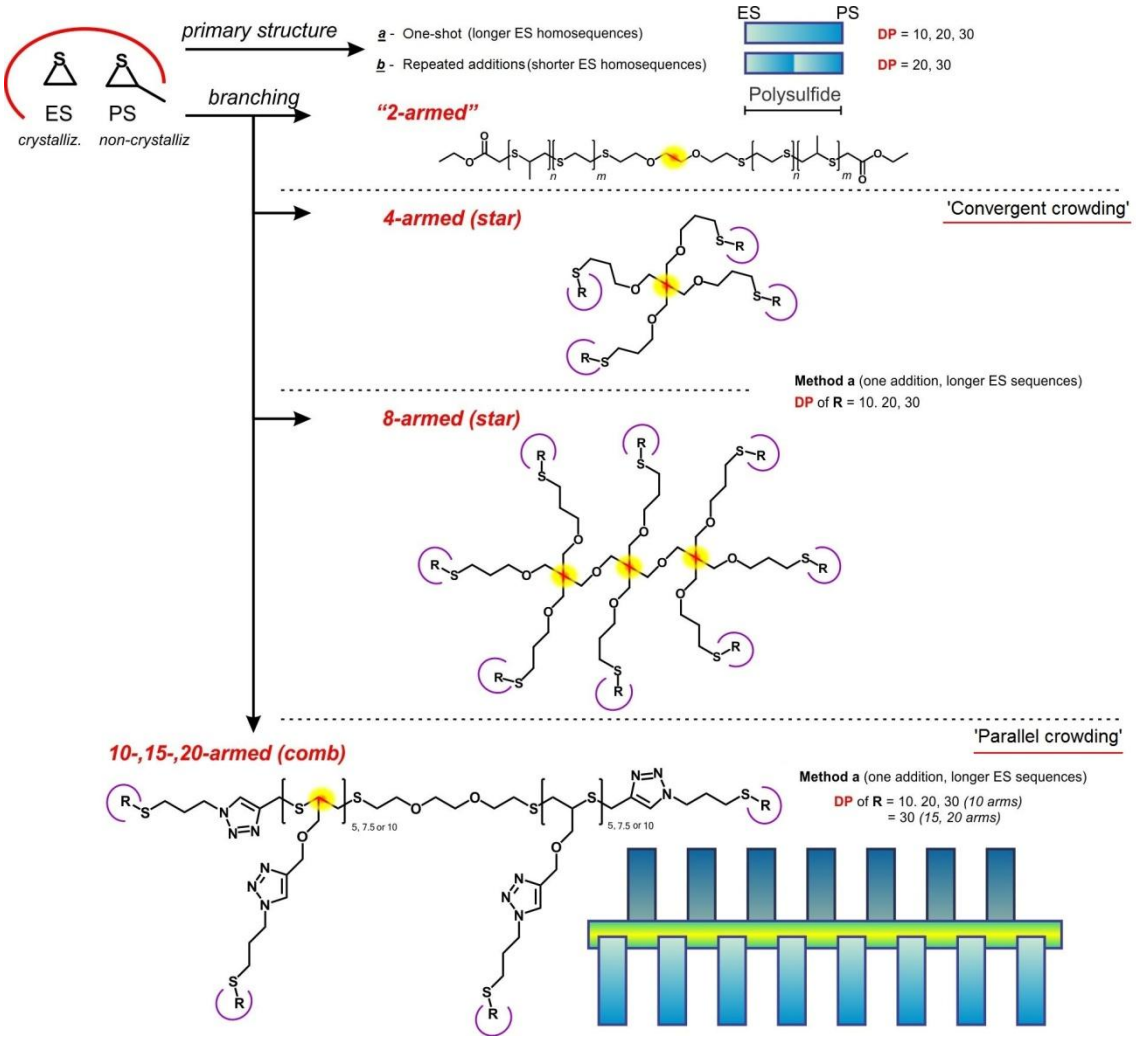

Scheme 5.1. Polymer architectures investigated in this study. In linear polymers, the polysulfide chains were produced through a single addition of the monomer mixture (protocol ***a***; single, longer gradient chains), or through repeated additions (protocol ***b*** shorter, double gradient; closer to a random distribution); in the scheme we colour-code ES in white and PS in blue to show the different gradient structures. The side chains of the branched polymers were prepared only with single gradient structure. Please note that for simplicity of presentation, the polysulfide chains (ES/PS copolymers) are replaced by the symbol 'R' in the branched structures.

If present in sufficiently long sequences, ES units can crystallize in copolymeric structures. PES, for example, confers crystallinity to block copolymers with isoprene, butadiene or styrene.[17] Due to the high tendency to crystallize, an ordered assembly can be obtained also with very short blocks; for example, ES sequences as short as three (oligo (ethylene sulfide), OES) allow association and gelation of PEG-OES copolymers,[18] and it has been shown that when ES is copolymerized with other

episulfides, including PS, the homosequences (ES-rich blocks) formed due to the higher reactivity of ES (r_{ES} = 0.58, r_{PS} = 3.11) allow for the formation of crystalline phases.[12]

P (PS-*co*-ES) were successfully prepared by employing two different protocols of anionic ring-opening copolymerization that provide different primary structures: 1) protocol ***a***, a one-shot addition of all monomers to the initiators, which leads to gradient (blocky) structures (due to the higher reactivity ratio of ES to PS[12]); and 2) protocol ***b***, repeated additions of the monomer mixture, which produce shorter gradients along the chain; this determines a local ES/PS ratio that deviates less from that of the feed, and due to the presence of shorter homosequences of the crystallisable unit, the copolymers should exhibit a lower tendency to crystallize. Further, the copolymers obtained through the one-shot addition protocols were also produced in different chain topologies following procedures described in a recent paper[13]: linear macromolecules obtained from a bifunctional initiator (theoretically a 2-armed star topology) were compared to 'real' branched polymers with a 4- and 8-armed star structure produced from multifunctional initiators, and to comb polymers (10, 15 and 20 arms); the latter were obtained through the polymerization of propargyl episulfide, followed by click reaction with an azide-containing thioacetate, which was finally used to initiate the side-chain copolymerization of ES/PS. In all cases, the degree of polymerization (DP) was also varied, using DP=10, 20 or 30 per arm, which for linear polymers correspond to a total DP of 20, 40 or 60 monomeric units.

The influence of these variables (*i.e.*, addition protocol, number of arms and degree of polymerization) on the morphology, nucleation and crystallization were studied by polarized optical microscopy, differential scanning calorimetry and X-ray scattering.

5.2. Results and Discussion

Thermal analysis of the copolymers described thus far (*i.e.*, linear obtained by both protocols of addition, stars and combs with different DP) was carried out by DSC (in Table 3.2 of Chapter III (section 3.1.2) the characterization data for the polysulfides prepared in this work is reported as well as their nomenclature). The nomenclature of the samples is as follows: *Xh*_$(PS_y\text{-}ES_z)_a$, where "X" is L for linear, S for star and C for comb, "h" can be a or b depending on the addition protocol used, "Y" and "Z" are the degree of polimerization of each comonomer, therefore Y+Z is the degree of

polimerization per copolymer (DP). Finally "a" is the number of arms. For instance, *La*_$(PS_5\text{-}ES_5)_2$ is a linear copolymer with a DP of 10, which was synthesized with protocol a.

The DSC results for linear and star copolymers can be seen respectively in Figures 5.1 and 5.2, whereas the DSC scans results for comb copolymers, which display a similar trend, are shown in Figure 5.3. The data obtained from the DSC traces of all the samples are summarized in Table 5.1.

Longer vs. shorter gradients (protocol ***a*** vs. protocol ***b***). Cooling scans after erasing thermal history and subsequent heating scans were measured with DSC (Figure 5.1) with most samples exhibiting a bimodal crystallization and melting. The longer gradient copolymers (*La* in Figure 5.1) are characterized by a much broader crystallization and melting range than those obtained by the sequential addition method (*Lb* in Figure 5.1). The longer gradient copolymers contain on average longer crystallizable sequences which can form thicker lamellae that melt at higher temperatures. However, they also contain shorter crystallisable units which will crystallize and melt at lower temperatures. Therefore, the distribution of crystal sizes produced in the longer gradient copolymer is much broader than in those copolymers prepared with shorter gradients. In the case of shorter gradients, the average crystallizable sequence lengths are shorter. Therefore, the calorimetric differences observed between copolymers prepared by the two addition methods reflect the difference in monomer distribution throughout the copolymer chains.

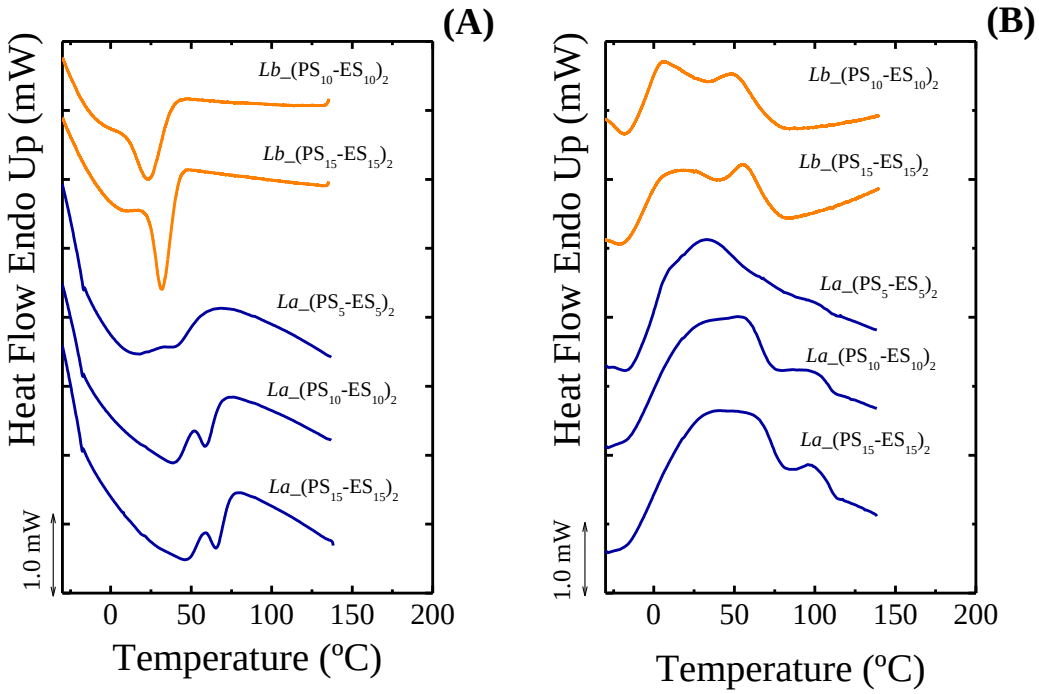

Figure 5.1. DSC cooling (***A***) and subsequent heating (***B***) scans obtained for linear (a) and (b) copolymers with different DPs (*i.e.*, 10, 20 and 30).

Increasing the DP of P(PS-*co*-ES) resulted in an increase of both the crystallization (T_c) and melting (T_m) temperatures, as expected for samples of increasing molecular weight (Figure 5.1, and quantitatively summarized in Table 5.1). The effect of the molecular weight on first order transition temperatures usually saturates as chain length reaches a critical value, which may be between DP values of 20 and 30, as the differences between their T_c and T_m values is negligible (Figure 5.2B).

Chain topology and molecular weight influence. Due to their higher crystallinity and higher T_c and T_m of the longer gradient copolymers, all branched macromolecules were prepared through protocol ***a***, investigating the effect of DP and number of arms on DSC cooling scans (after erasing thermal history) and subsequent heating scans (performed at 20 ºC/min), as shown in Figures 5.2 (*i.e.*, star copolymers) and 5.3 (*i.e.*, comb copolymers). The data calculated from the DSC scans (Figures 5.1, 5.2 and 5.3) are also summarized in Table 5.1.

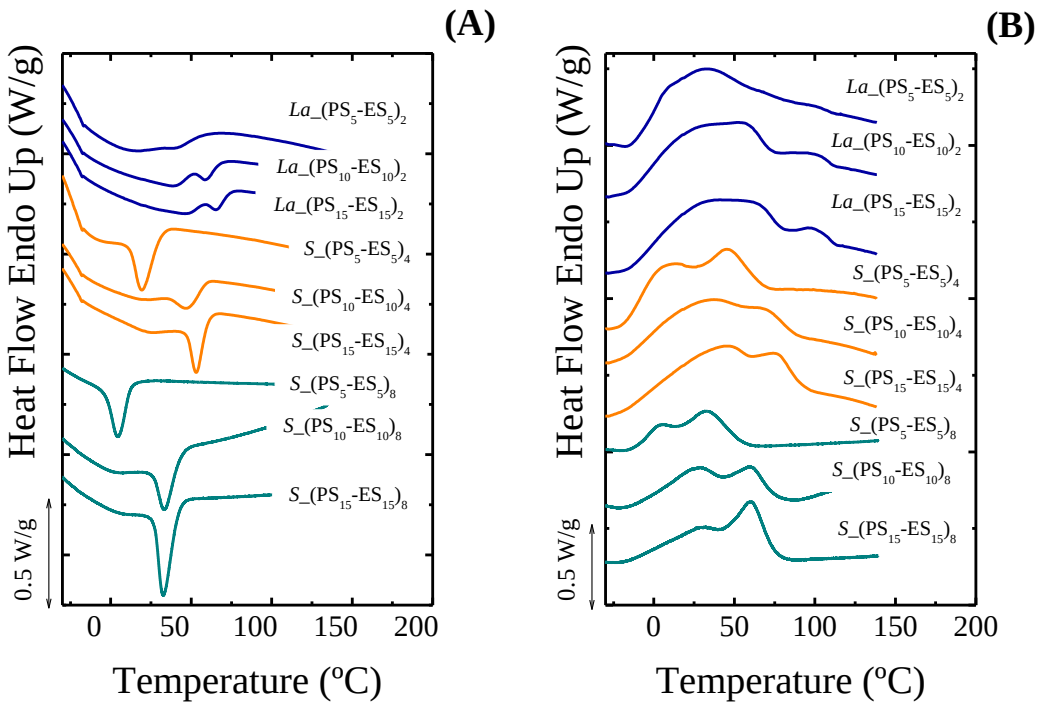

Figure 5.2.DSC (A) cooling and (B) heating scans for linear and star copolymers with different number of arms (*i.e.*, 2, 4 and 8) and variable DP (*i.e.*, DP of 10, 20 and 30).

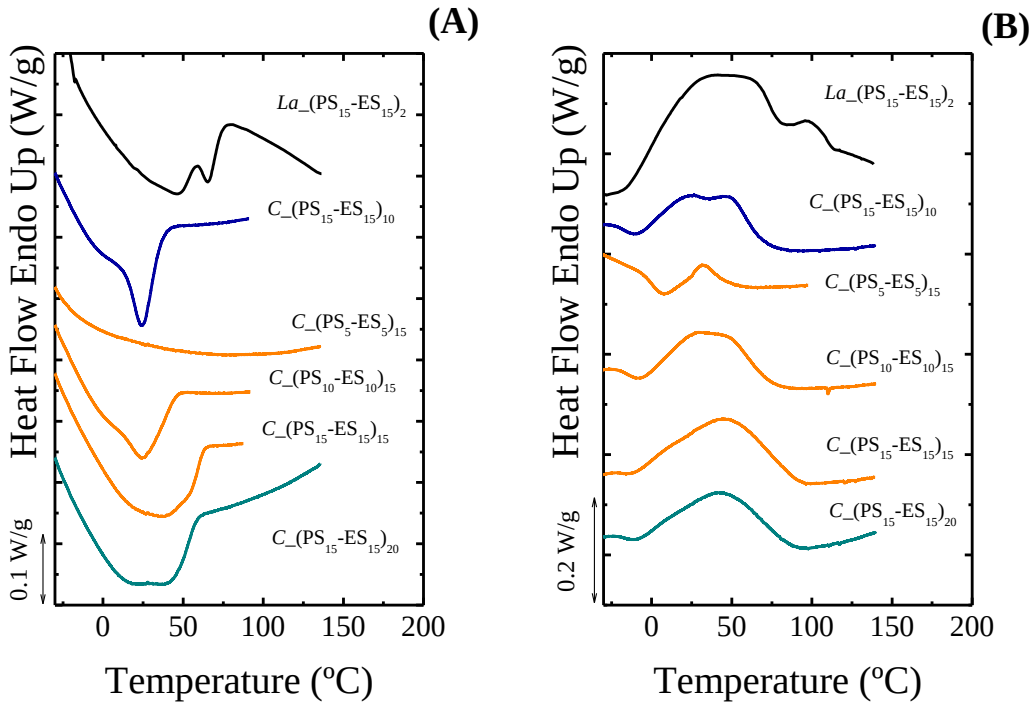

Figure 5.3. DSC (A) cooling and (B) heating scans for linear and comb copolymers with different number of arms (*i.e.*, 10, 15 and 20) and a fixed DP of 30. A variable DP (i.e., 10, 20 and 30) is presented for the comb with 15 arms.

In general, both crystallization and melting occurred in a wide range of temperatures with bimodal exothermal and endothermal transitions, respectively, while the heat flow values were also very small (see *y*-axis scale bars), indicating low levels of crystallinity (see later WAXS measurements). It was found that the onset crystallization temperature ($T_{c,\ onset}$), as well as the end melting temperature ($T_{m,\ end}$), could better characterize the changes experienced by the material in comparison to peak values, as a result of the presence of two or more peaks and the extreme temperature width of the exothermal and endothermal first order transitions. Similar behaviour was found for comb copolymers in Figure 5.3. Note that the linear sample has a higher onset crystallization temperature and a higher final melting temperature than any of the combs. It should be remembered that DP values are reported per arm.

Table 5.1. Relevant calorimetric quantities obtained from DSC scans in Figure 5.1, 5.2 and 5.3*

Sample	$T_{c,onset}$ (ºC)	$T_{c,peak}$ (ºC)	ΔH^n_c (J/g)	$T_{m,peak}$ (ºC)	$T_{m,end}$ (ºC)	ΔH^n_m (J/g)	$X_{c,WAXS}$ (%)
*La*_$(PS_5\text{-}ES_5)_2$	67.4	(12.3)42.2	88	30.0 (98.0)	112.9	104	-
*La*_$(PS_{10}\text{-}ES_{10})_2$	78.5	(38.8)59.3	96	35.7(100.4)	115.9	98	-
*Lb*_$(PS_{10}\text{-}ES_{10})_2$	49.5	23.6	28	4.7(50.7)	83.8	34	-
*La*_$(PS_{15}\text{-}ES_{15})_2$	82.2	(45.5)66.0	88	37.4(98.4)	117.2	106	34
*Lb*_$(PS_{15}\text{-}ES_{15})_2$	53.0	31.8	38	8.6(57.2)	85.0	44	13
*S*_$(PS_5\text{-}ES_5)_4$	42.5	(-3.3)19.5	54	10.2(44.4)	76.1	68	-
*S*_$(PS_{10}\text{-}ES_{10})_4$	65.3	(18.5)48.2	82	36.7(70.1)	94.7	92	-
*S*_$(PS_{15}\text{-}ES_{15})_4$	69.1	(25.1)53.3	82	44.1(76.8)	102.4	96	30
*S*_$(PS_5\text{-}ES_5)_8$	22.4	4.3	24	3.85(47.8)	61.8	30	15
*S*_$(PS_{10}\text{-}ES_{10})_8$	48.1	33.2	38	27.1(60.7)	79.8	38	24
*S*_$(PS_{15}\text{-}ES_{15})_8$	50.4	32.7	44	26.2(60.4)	82.9	44	28
*C*_$(PS_{15}\text{-}ES_{15})_{10}$	-	-	-	31.7[c]	60.6	4	-
*C*_$(PS_5\text{-}ES_5)_{15}$	55.2	25.7	24	31.9	87.0	28	-
*C*_$(PS_{10}\text{-}ES_{10})_{15}$	46.9	24.2	24	23.7(47.9)	85.5	28	16
*C*_$(PS_{15}\text{-}ES_{15})_{15}$	65.3	18.4	42	47.8	99.2	42	20
*C*_$(PS_{15}\text{-}ES_{15})_{20}$	64.5	18.1	32	42.5	95.1	34	19

*onset ($T_{c,onset}$) and peak ($T_{c,peak}$) crystallization temperatures, peak ($T_{m,peak}$) and end ($T_{m,\ end}$) melting temperatures, crystallization (ΔH^n_c) and melting (ΔH^n_m) normalized enthalpies, calculated mass of crystals ($X_{c,\ WAXS}$) from WAXS patterns. [a] One-shot monomer addition or protocol (a) and [b] sequential monomer addition or protocol (b) [c] before the melting a cold crystallization occurs at: $T_{cc,\ onset}$=-2.9 ºC, $T_{cc,\ peak}$=6.3 ºC, $T_{cc,\ end}$=18.4 ºC and a normalized cold crystallization enthalpy of 3 J/g.

As shown in Figure 5.4, peak crystallization and melting temperatures appeared to show three regions in their dependency on the number of arms. At any given DP, the linear polymers have higher values for thermal transitions and enthalpies, stars decreased their values with increasing number of arms, and combs in most cases reached a plateau or even increased. Such behaviour is attributed to the topological restrictions induced by the increasing crowding, which hinders crystallization.

Another general trend that can be appreciated in Figure 5.4 is that as DP increases there are small increases in melting temperature and even in crystallinity, especially for samples with a higher number of arms.

A more detailed analysis of each specific case is given below.

1) ***Linear copolymer***s. Since linear copolymers are free of topological restrictions, their size is the main factor affecting crystallization; however, an increase in DP only modestly changed their thermal properties, since their values tend to saturate at DP =20, (almost identical values at DP 20 and 30). It is also worth noting that the ES gradient of the polymer with DP 10 and that with DP 20 (protocol ***b***) are identical, yet all indicators show that the latter has a markedly lower crystallinity; this effect may be a result of slower diffusion of the larger polymer, or maybe more likely due to the fact that the ES sequences in the centre of the polymer are less easily accommodated into a crystalline arrangement.

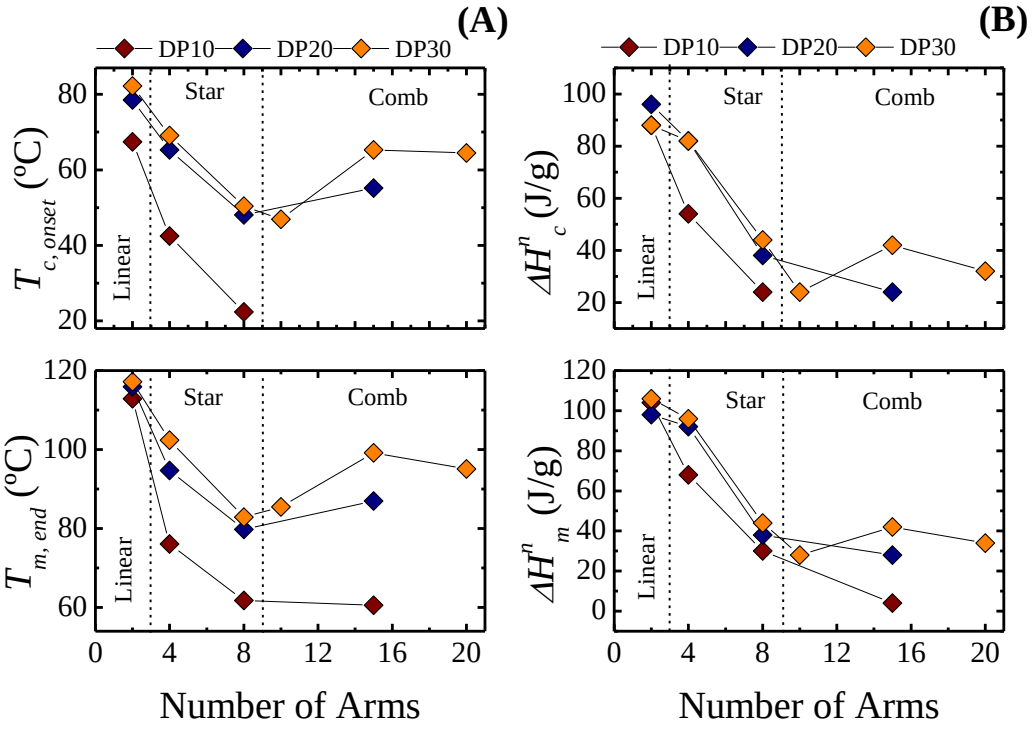

Figure 5.4.(***A***) Crystallization onset temperatures ($T_{c,onset}$) and end melting temperatures ($T_{m,end}$), (***B***) crystallization (ΔH^n_c) and melt (ΔH^n_m) normalized enthalpies as a function of number of arms, for linear, star and comb samples with different DPs. The solid lines represent guides to the eye. The dashed lines separate the behaviour of linear, star and combs samples.

2) Star copolymers. Crowding around branching points typically limits the conformational freedom of polymer chains, reducing their flexibility and diffusion,[19] and hence decrease their ability to crystallize in comparison to linear analogues. This effect should decrease with increasing length of the arms, therefore higher DP would correspond to higher crystallinity.

$T_{c,onset}$ and $T_{m,end}$, as well as crystallization and melting enthalpies increased as DP increased in the 4 and 8 arm stars. This is consistent with the nucleation observations presented above (see Figure 5.1) and shows that the topological restrictions of the central branching point may have been at least partially compensated when the ES homosequences extend further from it. In the case of the lowest DP (*i.e.*, 10), the topological restrictions for the stars to crystallize are the strongest and increase as the number of arms increases, as judged by the dramatic decrease in crystallization and

melting temperatures (as well as associated enthalpies) that can be observed in Figure 5.4.

3) Comb copolymers. The combs with 15 and 20 arms behaved differently from star copolymers (see comb region on Figure 5.4): the values of $T_{c,\ onset}$, $T_{m,end}$ increased (instead of decreasing) as the number of arms increased, and the crystallization and melting enthalpies stopped decreasing; this would appear to indicate a higher crystallizability of combs *vs*. stars. As for the star polymers, also for the combs; crystallization can only take place in the side chains: their main chain is atactic. Therefore, any comb/star difference should be ascribed to the different packing density of the side chains. In the melt, flexible polymer chains are typically assumed to adopt a conformation analogous to a theta state; however, chains that are already contracted/globular in solution, are likely to maintain this state as also demonstrated by the almost globular structure of the combs (Mark-Houwink parameter a<0.5, see Table 3.2 in Chapter III. Experimental Part). It could be argued that the side chains in the combs experience a sort of 'parallel crowding' (= high packing density; please refer also to Scheme 5.1), not dissimilarly to chains of hyperbranched polystyrene that are supposed to undergo radial stretching in the melt (and show 'excess' anisotropy).[20] This situation may facilitate intramolecular crystallization, whereas the 'convergent crowding' of the stars, whose arms are likely to be less tightly packed (higher values of $\frac{R_G}{R_H}$ and a; Figure 3.1 of the Experimental Part) of may only rely on the increasingly difficult intermolecular crystallization; this would rationalize why combs with 15 and 20 arms (high coil compaction already in solution: parameter a=0.42 or 0.41, respectively) are significantly more crystalline than the corresponding stars. It is worth mentioning that the values of the Mark-Houwink a parameter ranged from around 1 for linear polymers to less than 0.5 for combs, indicating that the polymer coils clearly became more compact with increasing degree of branching.

The behaviour of combs with DP=10 is different, and dominated by the problems of crystallization of these short sequences. DSC cooling scans provide clear evidence of their retarded crystallization (see Figure 5.3A): the ES sequences within the comb copolymer with 15 arms of DP=10 are not able to crystallize during cooling and

they undergo cold-crystallization during the subsequent heating scan followed by melting (see Figure 5.3B).

In summary, using short chains with identical composition and primary structure, their crystallinity very strongly decreases with increasing branching, and this does not appear to be due to the more compact morphology of combs. This can be an important indication of: sensitivity to the actual length of the ES sequences and may indicate that comb crystallization possibly proceeds in a predominantly intramolecular fashion.

5.2.1. Successive Self-Nucleation and Annealing (SSA)

The thermal fractionation by SSA yields multiple endothermic peaks that correspond to the melting of the different fractions produced by the applied thermal protocol. Each peak represents the melting of a population of lamellae with specific mean lamellar thickness, *i.e.*, a thermal fraction. Typically, the average lamellar thickness values increase as T_m increases and the largest lamellar thickness corresponds to the longest uninterrupted ES sequence. Melting peaks are identified with numbers: the highest melting temperature (melting peak 1) corresponds to thermal fraction 1, *i.e.*, the annealed population produced mainly during a 5' holding time at $T_{s,1}$, although the successive steps might have also some limited influence on the size of the fraction. Thermal fraction 2 is produced at $T_{s,2}$ and so on.

The frequent interruption of ES sequences facilitates their segregation, and this caused excellent fractionation in all samples, as shown by a peak separation where the DSC baseline is typically reached. This clear separation is essentially the deconvolution of a standard DSC curve into thermal fractions, which can therefore provide much more detailed information than standard DSC measurements.

1) Linear copolymers. In Figure 5.5 solid lines indicate the T_s values employed for the fractionation, while the dashed line corresponds to the $T_{s,\,ideal}$ for the linear ***a*** copolymer, which is also the first T_s temperature employed for all samples (*i.e.*, linear, stars and combs). SSA fractionation profiles are a necessary reflection of the chain primary structure,[21-26] due to the impossibility for PS to crystallize, and indeed a clear difference between protocols ***a*** and ***b*** can be seen. The copolymers with longer ES sequences possess the highest melting point fractions, (fractions 1 to 3) whereas the

melting range of those with shorter ES sequences shifted to lower temperatures, and $T_{s,1}$ to $T_{s,3}$ did not produce any detectable thermal fractions. The influence of DP is small for both linear copolymers *La* and *Lb*. Even though as DP increases, chain length also increases, there are only small changes in the fractionation capacity. The *La* and *Lb* copolymers with the highest and the lowest DP show the same number of thermal fractions, however, as DP increases, the areas under the highest temperature fractions increase. This result indicates that as DP increases, the longest uninterrupted linear ES sequences that constitute the lamellar crystals melt at the highest temperature peaks (*i.e.*, fractions 1, 2 and 3) are more abundant. It is worth noting that the maximum melting peak (corresponding to the melting of fraction 1) after SSA treatment is around 114 ºC, which is almost half of the reported value for the equilibrium melting point of ES homopolymer (*i.e.*, 215.6 ºC).[16] This is due to the short length of the crystallizable sequences of ES, which on the other hand is also responsible for the remarkable fractionation of the samples.

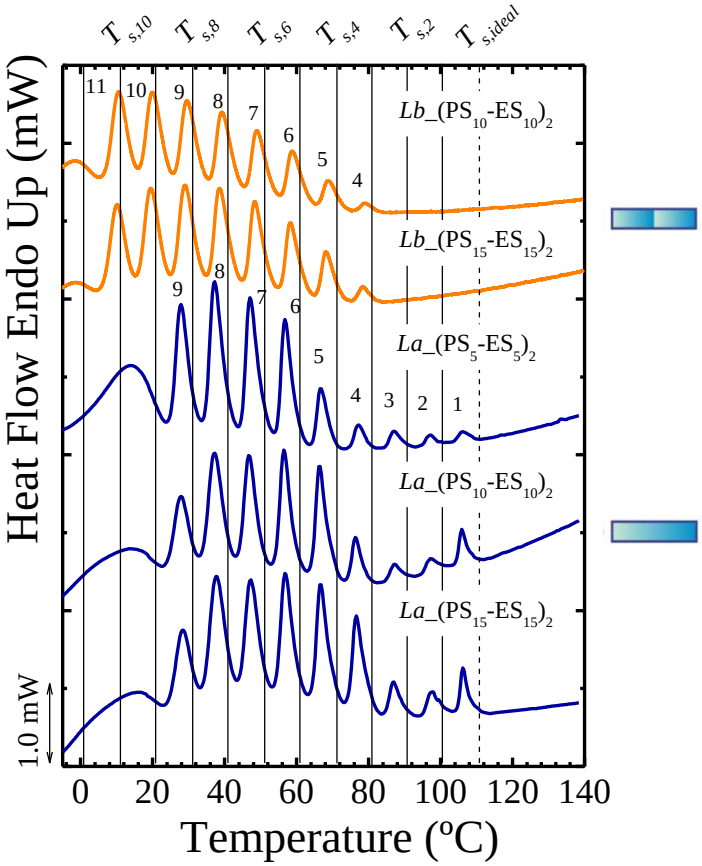

Figure 5.5. Final heating runs after SSA thermal fractionation for P(PS-*co*-ES) linear copolymers obtained by protocols ***a*** and ***b***, with DP=10, 20 and 30.

2) Star copolymers. Both the stars and linear polymers presented in Figure 5.6 in principle have the same primary structure (longer gradients, protocol ***a***), but fraction 1 was only present in the latter. If a comparison is made of the SSA fractionation profile at constant DP, it can be clearly seen that the topological restrictions, which increase with arm number, provoke the gradual disappearance of several of the highest melting point thermal fractions. These topological restrictions should be maximum near the junction points (at the centre of the stars), where in fact the longest uninterrupted PES linear sequences are located; hence as the number of arms increases, confinement increases and these segments cannot crystallize. On the other hand, upon increasing arm length (*i.e.*, DP), the topological constraints are gradually released and Figure 5.6 shows how some higher melting point fractions are indeed recovered in the stars. As fractionation profiles suffer important changes due to variations in chain topology (linear chains versus star chains), the interpretation of these profiles in terms of only comonomer distribution is no longer possible.

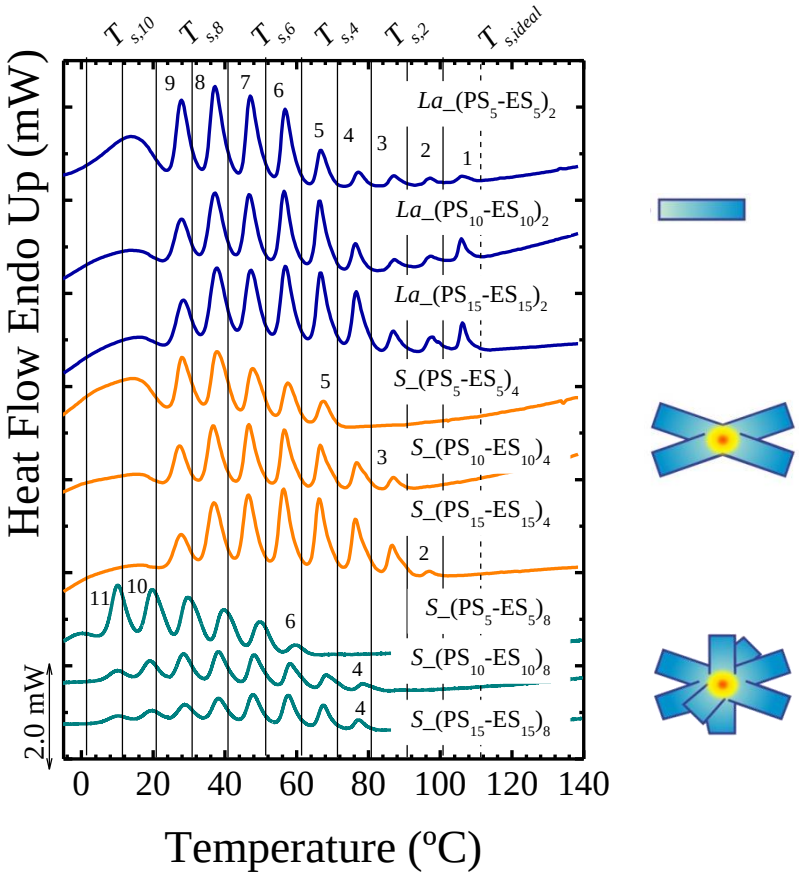

Figure 5.6. Final heating runs after SSA thermal fractionation for P(PS-*co*-ES) copolymers with linear and stars topologies and variable DP (*i.e.*, DP=10, 20 and 30).

3) Comb copolymers. In this analysis, we have varied both the number of arms (10, 15 and 20) and the DP (10, 20 and 30), again keeping fixed the primary structure and using a linear polymer as a reference (see Figure 5.7). First, the trend towards increasing crystallinity with increasing DP is similar to what is observed for stars: in this respect the behaviour of the 15-armed comb is analogous to that of *e.g.* 8-armed star. With low DP (DP 10) arms, combs also continued the trend of decreasing crystallinity with increasing branching: the first detectable fraction is that of peak 1 for the linear reference, peak 5 and 6 respectively for the 4- and 8-armed stars, and only peak 7 for the 15-armed comb. A significant difference, on the other hand, is seen at high DP (DP 30): the first detectable fraction is peak 1 for the linear polymer, peak 2 and 4 respectively for the 4- and 8-armed stars, peak 4, and 3 (slight recovery of crystallinity) for the 10-, 15- and 20-armed combs.

Therefore, SSA broadly confirms the hypotheses discussed on the basis of the DSC scans: for side chains with very short ES gradients (low DP), branching always appears to have a monotonous and detrimental effect on the presence of thicker lamellar crystals; for longer ES gradients, on the contrary, the parallel crowding of combs appears to allow the chains to regain some of the order. And again, these observations may support an intramolecular nature of the crystallization of the branched materials.

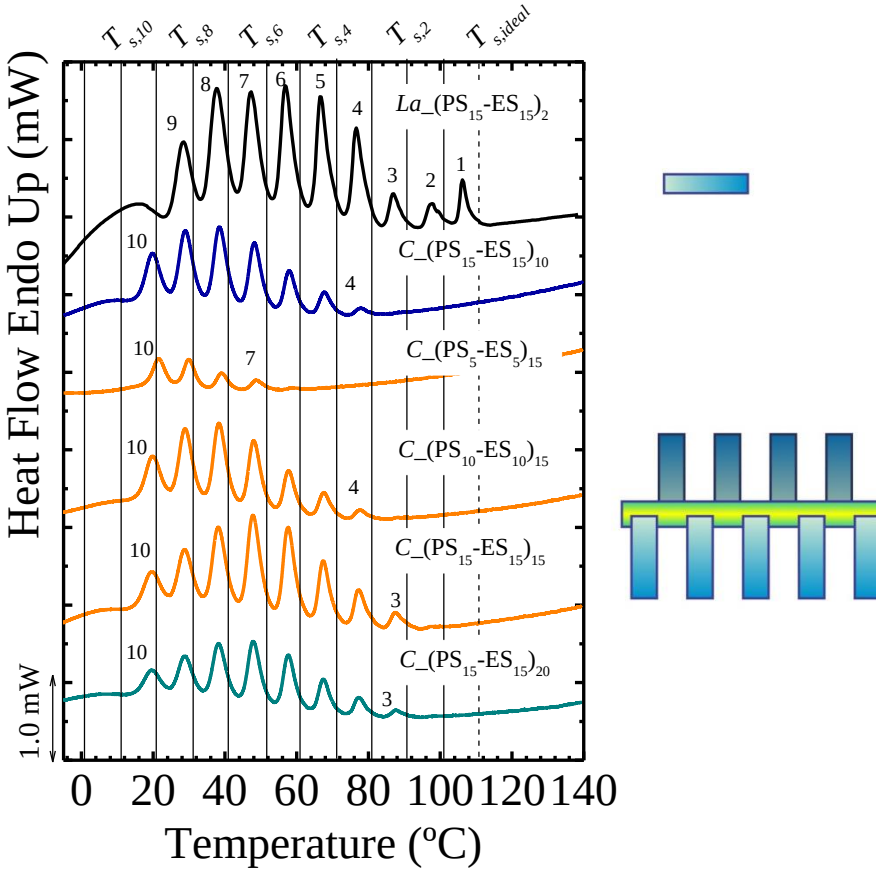

Figure 5.7. Final heating runs after SSA thermal fractionation for P(PS-*co*-ES) linear and combs copolymers with different number of arms (i.e., 10, 15 and 20) at a fixed DP of 30 and variable DP (*i.e.*, DP=10, 20 and 30) for the 15 arms sample.

5.2.2. Wide Angle X-ray Scattering (WAXS)

WAXS patterns were measured at RT (25 ºC) for all the samples (previously cooled from the melt at 20 ºC/min to reproduce the same thermal history applied by DSC) with a fixed DP of 30 (see Figure 9.13 and 9.14 in the Appendix).

In WAXS patterns (Figure 5.8A, Table 5.2), it is easy to see the presence of a main peak and a shoulder/secondary peak for all samples, which indicates that crystals have the same unit cell regardless of the chain topology and the DP of the arms. It is noteworthy that the shape of these diffraction maxima does not change significantly with temperature until melting occurs (temperature-dependent WAXS and SAXS patterns are included in the Appendix, see Figure 9.14, 9.15 and Table 9.3). The reflections appear at 2θ angles of 20 and 24º (diffraction spacings $d = \lambda/2\sin\theta$, of 0.439 and 0.370 nm, respectively); they would therefore correspond to the *(100)* and *(101)* planes of the orthorhombic PES unit cell (*a*=8.50 Å, *b*=4.95 Å and *c* (fibre axis) =6.70 Å),[27] which is reasonable since ES is the only crystallizable component. It must be said, however, that only few works have applied X-ray diffraction to PES homopolymer,[27] and even its structure was determined by electron diffraction.[27, 28] To our knowledge, in the only report about P(ES-*co*-PS) copolymers (but prepared at low conversion, and therefore differing from ours in the gradient structure), Roggero et al.[29] reported an increase of the crystalline PES unit cell volume to accommodate the PS methyl groups in the crystal lattice, albeit with no X-ray evidence supporting this conclusion. In our case, the diffraction spacings were not significantly different among all different copolymers examined to draw the same conclusion (Table 5.2).

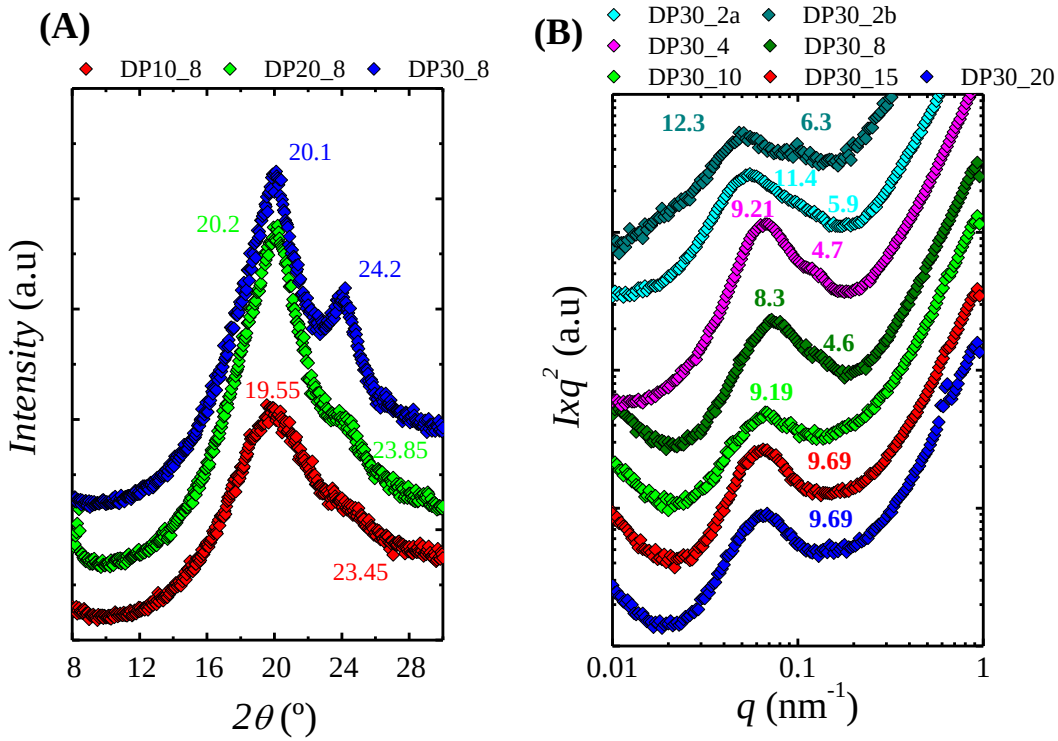

Figure 5.8. WAXS patterns for (A) 8 arms star P(PS-*co*-ES) copolymers with variable DP (10, 20 and 30: *S_(*PS_5-$ES_5)_8$, *S_(*PS_{10}-$ES_{10})_8$, *S_(*PS_{15}-$ES_{15})_8$) and SAXS patterns (B) for P(PS-*co*-ES) copolymers with different chain topologies (linear, star and combs) and fixed DP (30) at 25 ºC.

Differently from their location, the reflection intensity depended both on topology and DP. For instance, the intensity of both reflections increased with DP (Figure 5.8A), indicating that the crystal fraction is increasing. The *(101)* reflection in the sample with DP=30 is the most intense of the three samples in Figure 5.8A, while in the sample with DP=10 the shoulder is barely visible; similar changes were found for all samples (see Figure 5.3 and 9.13 in the Appendix). The software PEAKFIT was employed to deconvolve WAXS patterns into amorphous and crystalline contributions, obtaining the degree of crystallinity by dividing the area under a crystalline peak by the total area under the diffractogram (column 3 ($X_{c,WAXS}$), Table 5.2). This analysis broadly confirmed the calorimetric results: a) longer gradients yield larger crystalline fractions than shorter gradients, both when they were obtained varying primary structure or DP; b) decreasing crystallinity with increasing branching, with a slight gain with longer combs.

Table 5.2. Calculated diffraction spacings (*d*) according to Bragg´s law, *2θ* angles and calculated mass fraction of crystals ($X_{c,WAXS}$) from WAXS patterns.

Sample	*2θ* (º)	*d* (nm)	$X_{c,\,WAXS}$ *(%)*
*La*_$(PS_{15}\text{-}ES_{15})_2$	20.2/24.0	0.439/0.370	34
*Lb*_$(PS_{15}\text{-}ES_{15})_2$	20.3/23.8	0.437/0.373	13
*S*_$(PS_{15}\text{-}ES_{15})_4$	20.0/23.6	0.443/0.377	30
*S*_$(PS_5\text{-}ES_5)_8$	19.5/23.5	0.454/0.379	15
*S*_$(PS_{10}\text{-}ES_{10})_8$	20.2/23.9	0.439/0.372	24
*S*_$(PS_{15}\text{-}ES_{15})_8$	20.1/24.2	0.441/0.367	28
*C*_$(PS_{15}\text{-}ES_{15})_{10}$	20.0/23.4	0.443/0.380	16
*C*_$(PS_{15}\text{-}ES_{15})_{15}$	20.3/24.2	0.437/0.367	20
*C*_$(PS_{15}\text{-}ES_{15})_{20}$	20.3/24.1	0.437/0.369	19

5.2.3. **Small Angle X-ray Scattering (SAXS)**

SAXS patterns were measured at 25 ºC for all the samples (previously cooled from the melt at 20 ºC/min to reproduce the same thermal history as that applied by DSC). The Lorentz representation was chosen to analyse the SAXS results, by plotting the product of the intensity of diffracted X-rays and the square of the scattering vector q as a function of q. A clear maximum that represent the scattering from lamellar stacks was observed in the SAXS patterns of all samples (see Figure 5.8B for DP 30). This is associated with the average distance between adjacent lamellae, or long period d^* (column 3 in Table 5.3), which can be estimated as $d^* = \frac{2\pi}{qmax}$ (peaks in Figure 5.8B are labelled according to their d^* values). Since the peak was generally well pronounced, a fair amount of lamellar stacking must have always been present, also for low-crystallinity samples.

We have also calculated a probably more informative parameter: the lamellar thickness *l*, $l = X_v . d^*$, where X_v is the crystalline volume fraction. Here, since accurate density measurements would be needed to obtain the crystalline volume fraction, we have replaced it with the crystalline mass fraction determined from WAXS (third and fourth column in Table 5.3).

Table 5.3. Long period (d^*) values obtained at RT for PPS-*co*-PES copolymers with different topologies and a fixed DP (30) and calculated from the q_{max}. The percentages of crystallinity calculated by WAXS ($X_{c,WAXS}$), as well as the lamellar thickness estimated from it (*l*), are also reported.

Sample	q_{max} (A^{-1})	d^* (nm)	$X_{c,WAXS}$ *(%)*	*l* *(*nm*)*
*La*_PS_{15}-ES_{15}	0.05512	11.41	34	3.84
*Lb*_PS_{15}-ES_{15}	0.04821	12.31	13	1.56
S_4_PS_{15}-ES_{15}	0.06821	9.21	30	2.75
S_8_PS_{15}-ES_{15}	0.07609	8.26	13	1.11
C_{10}_P_{15}-ES_{15}	0.06840	9.19	16	1.51
C_{15}_P_{15}-ES_{15}	0.06485	9.69	20	1.89
C_{20}_P_{15}-ES_{15}	0.06485	9.69	19	1.81

In short, d^* and *l* followed qualitatively the same pattern previously seen for DSC results, especially SSA, and for the crystal fractions calculated from WAXS. All decreased with increasing branching in stars and then slightly increased for longer combs, and they also further confirmed the loss of order in the linear polymers prepared via repeated monomer addition (method ***b***).

5.2.4. General comparison

We have graphically summarized (Figure 5.9) the influence of branching on the various parameters investigated in this study, namely ΔH_c, ΔH_m, X_c, *d*, *l* and the temperature of

the highest peak in SSA. These parameters offer different perspectives over the capacity of these polymers to assemble in an ordered fashion; this is confirmed by the very low values of most parameters (except *d*) for the linear polymers with irregular primary structure (obtained through method ***b***). All parameters coherently show a loss of order with increasing branching for stars, and a stabilization/slight regain for combs.

Interestingly, a similar branching-dependent trend is also seen in shape/compactness parameters measured in solution, *i.e.*, the Mark-Houwink *a* parameter and the shape parameter $\frac{R_G}{R_H}$; this trend indicates that the macromolecules grow increasingly compact and are unlikely to form entanglements in solution, to the limit of behaving as impenetrable spheres. Clearly, these parameters reflect dimension and conformation of the polymers in dilute solution, which, differently from the bulk, are typically dominated by excluded volume effects. Yet, it seems logical to see a parallel in that the same cause (branching) in solution overcomes the excluded volume-dependent swelling, determining the coil collapse into increasingly compact globular structures, and in the bulk leads to the progressive loss of intermolecular order and possibly to the build-up (in combs) of some forms of intramolecular order.

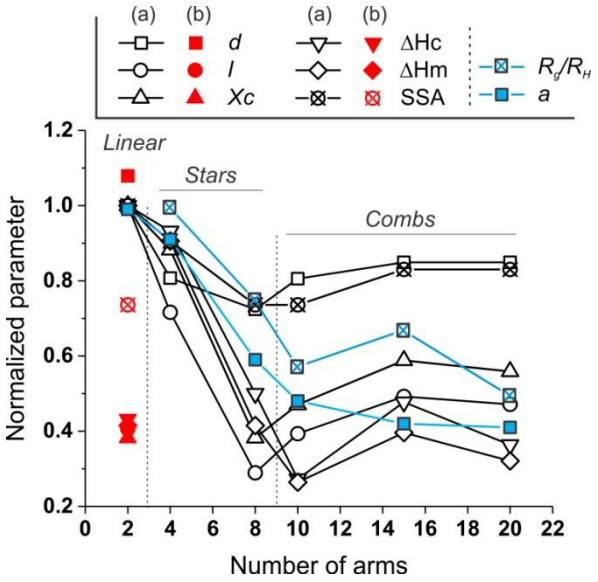

Figure 5.9.A summary of key parameters measured/calculated in this study on polymers with DP 30 per arm and a 1:1 PS:ES ratio. All parameters are normalized against the values presented by the linear (formally 2-armed) polymer obtained with method ***a***. The data for the linear polymer obtained via repeated monomer addition (method ***b***) are presented in red. The Mark-Houwink parameter *a* and the shape

parameter $\frac{R_G}{R_H}$ are reported in blue to distinguish these dilute solution (hence single molecule) parameters from those referring to bulk materials, which are represented by black empty symbols.

5.3.Conclusions

We have confirmed that the degree of crystallinity of a copolymer containing both a crystallizable (ES) and non-crystallizable monomer (PS) strongly depends on 1) the primary structure (length of ES:PS gradients) and on 2) the presence of topological restrictions introduced by branching.

SSA generated thermal fractions based on molecular segregation of the crystallisable sequences (due to the interruptions of the non-crystallizable monomer units), allow us to probe polymers with a broad melting temperature in significantly greater depth than standard DSC alone. This confirmed that polymers with longer ES sequences/gradients (addition protocol ***a***) had higher temperature thermal fractions (reflecting their much broader melting range) and were confirmed to have a higher crystalline mass fraction by WAXS.

Chain topology (*i.e.*, branching) on the other hand conferred a strong steric barrier on the capacity of ES sequences to crystallize; in general, increasing branching resulted in a reduced capacity to crystallize, with crystallization and melting temperatures, relevant enthalpies, annealing capacity and lamellar thickness all strongly decreasing. It is intriguing that this trend mirrors that of the polymer coil compactness (Mark-Houwink parameter *a* and $\frac{R_G}{R_H}$ ratio), which indicates the decreasing availability of the chain for topological interactions (such as entanglements).

Stars and combs showed clear differences, *e.g.*, in combs the key melting/crystallization temperatures/enthalpies did not further decrease with increasing number of arms. This may be the result of combs showing a chain crowding that allows for easier – although possibly intramolecular - packing (‘parallel’ vs. convergent) or of the topological constrains for crystallization being released as the number of arms (or chain length) surpasses a saturation value.

Here we have therefore demonstrated that branching allows for a very fine tuning of the local order in polysulfides, which also likely includes a balance between intra- and intermolecular assembly. This can pave the way to a detailed control over *e.g.*, solubility and diffusion of low MW compounds (drugs) in these matrices, with clear applications in drug delivery (loading and release kinetics).

5.4.References

[1] S.H. Lee, M.K. Gupta, J.B. Bang, H. Bae, H.-J. Sung, Current Progress in Reactive Oxygen Species (ROS)-Responsive Materials for Biomedical Applications, Advanced Healthcare Materials 2 (2013) 908-915.
[2] C.D. Vo, G. Kilcher, N. Tirelli, Polymers and Sulfur: what are Organic Polysulfides Good For? Preparative Strategies and Biological Applications, Macromol. Rapid Commun. 30 (2009) 299-315.
[3] E. Lallana, N. Tirelli, Oxidation-Responsive Polymers: Which Groups to Use, How to Make Them, What to Expect From Them (Biomedical Applications), Macromol. Chem. Phys. 214 (2013) 143-158.
[4] R. d'Arcy, N. Tirelli, Fishing for fire: strategies for biological targeting and criteria for material design in anti-inflammatory therapies, Polym. Adv. Technol. 25 (2014) 478-498.
[5] A. Napoli, M. Valentini, N. Tirelli, M. Muller, J.A. Hubbell, Oxidation-responsive polymeric vesicles, Nat Mater 3 (2004) 183-189.
[6] A. Rehor, H. Schmoekel, N. Tirelli, J.A. Hubbell, Functionalization of polysulfide nanoparticles and their performance as circulating carriers, Biomaterials 29 (2008) 1958-1966.
[7] D. Missirlis, R. Kawamura, N. Tirelli, J.A. Hubbell, Doxorubicin encapsulation and diffusional release from stable, polymeric, hydrogel nanoparticles, Eur. J. Pharm. Sci. 29 (2006) 120-129.
[8] A. Rehor, N.E. Botterhuis, J.A. Hubbell, N.A.J.M. Sommerdijk, N. Tirelli, Glucose sensitivity through oxidation responsiveness. An example of cascade-responsive nano-sensors, J. Mater. Chem. 15 (2005) 4006-4009.
[9] P. Hu, N. Tirelli, Scavenging ROS: Superoxide Dismutase/Catalase Mimetics by the Use of an Oxidation-Sensitive Nanocarrier/Enzyme Conjugate, Bioconjugate Chem. 23 (2012) 438-449.
[10] D. Jeanmaire, J. Laliturai, A. Almalik, P. Carampin, d.A. Richard, E. Lallana, R. Evans, R.E.P. Winpenny, N. Tirelli, Chemical specificity in REDOX-responsive materials: the diverse effects of different Reactive Oxygen Species (ROS) on polysulfide nanoparticles, Polymer Chemistry 5 (2014) 1393-1404.
[11] P. Carampin, E. Lallana, J. Laliturai, S.C. Carroccio, C. Puglisi, N. Tirelli, Oxidant-Dependent REDOX Responsiveness of Polysulfides, Macromol. Chem. Phys. 213 (2012) 2052-2061.
[12] R. d'Arcy, A. Siani, E. Lallana, N. Tirelli, Influence of Primary Structure on Responsiveness. Oxidative, Thermal, and Thermo-Oxidative Responses in Polysulfides, Macromolecules 48 (2015) 8108-8120.

[13] R. d'Arcy, A. Gennari, R. Donno, N. Tirelli, Linear, Star, and Comb Oxidation-Responsive Polymers: Effect of Branching Degree and Topology on Aggregation and Responsiveness, Macromol. Rapid Commun. 37 (2016) 1918-1925.
[14] E. Nicol, T. Nicolai, D. Durand, Dynamics of Poly(propylene sulfide) Studied by Dynamic Mechanical Measurements and Dielectric Spectroscopy, Macromolecules 32 (1999) 7530-7536.
[15] E.H. Catsiff, M.N. Gillis, R.H. Gobran, Poly(ethylene sulfide). II. Thermal degradation and stabilization, Journal of Polymer Science Part A-1: Polymer Chemistry 9 (1971) 1271-1292.
[16] A. de Chirico, L. Zotteri, Crystallization and glass transitions of polyethylene sulphide and polyisobutylene sulphide, Eur. Polym. J. 11 (1975) 487-490.
[17] W. Cooper, P.T. Hale, J.S. Walker, Elastomeric block polymers from ethylene sulphide, Polymer 15 (1974) 175-186.
[18] C.E. Brubaker, D. Velluto, D. Demurtas, E.A. Phelps, J.A. Hubbell, Crystalline Oligo(ethylene sulfide) Domains Define Highly Stable Supramolecular Block Copolymer Assemblies, ACS Nano 9 (2015) 6872-6881.
[19] Y. Tezuka, Topological Polymer Chemistry: Progress of Cyclic Polymers in Syntheses, Properties, and Functions, World Scientific, 2013.
[20] S.B. Kharchenko, R.M. Kannan, Role of Architecture on the Conformation, Rheology, and Orientation Behavior of Linear, Star, and Hyperbranched Polymer Melts. 2. Linear Viscoelasticity and Flow Birefringence, Macromolecules 36 (2003) 407-415.
[21] A.J. Müller, R.M. Michell, R.A. Pérez, A.T. Lorenzo, Successive Self-nucleation and Annealing (SSA): Correct design of thermal protocol and applications, Eur. Polym. J. 65 (2015) 132-154.
[22] A.J. Müller, M.L. Arnal, Thermal fractionation of polymers, Progress in Polymer Science (Oxford) 30 (2005) 559-603.
[23] A.J. Müller, Z.H. Hernández, M.L. Arnal, J.J. Sánchez, Successive self-nucleation/annealing (SSA): A novel technique to study molecular segregation during crystallization, Polym. Bull. 39 (1997) 465-472.
[24] A.T. Lorenzo, M.L. Arnal, A.J. Müller, A.B. De Fierro, V. Abetz, High speed SSA thermal fractionation and limitations to the determination of lamellar sizes and their distributions, Macromol. Chem. Phys. 207 (2006) 39-49.
[25] A.J. Müller, A.T. Lorenzo, M.L. Arnal, Recent advances and applications of "successive self-nucleation and annealing" (SSA) high speed thermal fractionation, Macromolecular Symposia 277 (2009) 207-214.
[26] A.T. Lorenzo, M.L. Arnal, A.J. Müller, M.C. Lin, H.L. Chen, SAXS/DSC analysis of the lamellar thickness distribution on a SSA thermally fractionated model polyethylene, Macromol. Chem. Phys. 212 (2011) 2009-2016.
[27] Y. Takahashi, H. Tadokoro, Y. Chatani, Structure of polyethylene sulfide, Journal of Macromolecular Science, Part B 2 (1968) 361-367.
[28] B. Moss, D.L. Dorset, Poly(ethylene sulfide): Reevaluation of the electron diffraction structure analysis, Journal of Macromolecular Science, Part B 22 (1983) 69-77.
[29] A. Roggero, L. Zotteri, A. Proni, A. Gandini, A. Mazzei, Syntheses and properties of ethylene sulphide-isobutylene sulphide copolymers and their unsaturated terpolymers, Eur. Polym. J. 12 (1976) 837-842.

CHAPTER VI.

NUCLEATION EFFICIENCY AND CRYSTALLIZATION OF LIGNIN-BASED MATERIALS

6.1.General Introduction

Lignin is the second most abundant biopolymer after cellulose.[1] It constitutes a natural aromatic polymer that accounts for up to 18-35 wt% of wood. Lignin can be extracted from ligno-cellulosic biomass (wood and annual plants) which are often byproducts of different industries (*e.g.*, paper, biofuel, etc). Lignin chemical structure is a function of the extraction process employed. The glass transition temperature (T_g) of lignin is around 130-160 ºC.[2] The main reactive sites in lignin are aliphatic and aromatic hydroxyl groups. Such hydroxyl groups make a potential reactive building block for synthesis of new macromolecular architectures.[1, 3] Lignin molecules have strong intermolecular interactions that cause a high T_g. Although at temperatures well above T_g the molecular motions of lignin are enhanced, its processability is still insufficient.[2] One approach to improve the potential of lignin is grafting it to mobile chains, such as PCL. This graft polymerization might help to avoid the poor dispersion of lignin, due to its propensity to self-aggregate. Moreover, it is an attractive approach to covalently modify the surface of lignin, resulting in lignin–based copolymers.[4] Another approach in order to take advantage of the lignin properties is to use it without any purification or any other treatment as a nucleating agent.[5]

Despite some promising properties, the applicability of PLA is restricted by its slow crystallization, high brittleness, low softening temperature and a high tendency to shrinkage (during polymer processing and storage). Given these limitations, the best way to improve its properties and enhance its application range is to prepare blends, copolymers or to reinforce it with various inorganic and organic fillers.[5]

The production of new compounds and mixtures based on PLA, as well as the modification of polymer processing methods, are under constant development to meet industrial customer´s needs.[5]

A number of nucleating agents based on (1) inorganic materials, *e.g.*, talc and kaolin [6, 7] (2) organic materials, *e.g.*, sorbitol derivatives,[8] oxalamide derivatives,[9] aromatic phosphonates,[5] aromatic sulphonates,[10, 11] benzoyl hydrazide compounds[12-14] (3) inorganic-organic hybrid materials, *e.g.*, epoxy functionalized poly (hedral oligomeric silsesquioxane),[15] and (4) oligomers or polymers, *e.g.*, lignin[16, 17] or (5) hybrids based on inorganic material and polymer[18] have been studied.

The essential requirements for nucleating agents are their good dispersion in PLA, high nucleation efficiency at low concentrations and to induce the crystallization into preferred crystalline forms. The following nucleating agents are commercially available for PLA: talc, kaolin, calcium carbonate, ethylenebis (12-hydroxystearylamide) (EBHSA), ethylene bis-steramide (EBS), N, N´, N´´-tricyclohexyl-1,3,5-benzenetricarboxylamide (TMC-328), 1,3:2,4-Dibenzylidene-D-sorbitol (DBS), Ecopromote, phthalhydrazide, tetramethylenedicarboxylic dibenzoylhydrazide (TM-306), potassium salt of 5-dimethyl sulfoisothalate (Lak-301).[5] Other non-commercial crystal nucleating agents for PLA have been synthesized and investigated, such as various inorganic and organic materials like hydrazide compounds,[5, 13, 14, 19] *myo*-Inositol,[20] benzenetricarboxylamide (BTA) derivatives,[9] amino acids and poly (amino acids),[21] phenylphosphonic acid zinc salt,[22] bibenzoylhydrazinepropane (BBP).[23] The effective concentration of inorganic materials was found to be in the range of 1-5 wt% depending on their efficiency. Nano- and micro-talc are amongst the most effective nucleating agents for PLA.

A number of PLA blends with physically and chemically modified lignins have been studied. [16, 18, 24-38] Only a few works have employed commercial lignins without additional chemical modifications as additives for PLA in concentrations up to 5 wt%.[16, 26, 29] Some authors have shown that the addition of lignin can improve the thermal stability of PLA.[26, 30, 31] Other studies confirmed the existence of PLA-lignin interactions (carbonyl groups of PLA with hydroxyl groups of lignin) and formation of hydrogen bonds.[24, 31, 32, 39-41] The ability of lignins (derived from cornstalk[16]) and lignin nanoparticles (LNP) prepared by stem explosion and

enzymatic modified pristine lignin[17, 38] to serve as nucleating agents for the heterogeneous crystallization of PLA has been demonstrated by non-isothermal DSC and polarized light optical microscopy analyses.

Some works have reported anti-nucleation effects of several types of lignin (*i.e.*, almond shell lignin,[26] Kraft-lignin derived from lignoBoost process[29, 31] organosov lignin from birch wood [31] and methanol fractionated softwood Kraft lignin (Indulin AT) [40] on PLA.

The use of lignin without chemical modifications (*i.e.*, industrial lignin) represents an interesting approach from the industrial point of view, since its cost would be much lower.

In this chapter the nucleating capacity of lignin is evaluated in both (a) PCL-*g*-lignin copolymers and (b) PLA/industrial lignin and PLA/talc blends. In (a) and (b) the techniques employed were: DSC, in which the nucleating efficiency was determined by self-nucleation experiments employing the Fillon et al. [42] nucleating efficiency scale. Additionally, the overall crystallization kinetics, as well as the morphology was evaluated.

6.2. Results and Discussion

The results and discussion of this Chapter, are divided in the following sections: 6.2.1 PCL-*g*-lignin and 6.2.2.PLA/lignins and PLA/talc blends.

6.2.1. PCL-*g*-lignin

Non-Isothermal DSC Scans

Non-isothermal DSC scans were conducted in all the samples (see their characteristics in Table 3.3 in Chapter III. Experimental Part) at 20 ºC/min. The DSC cooling and heating curves are shown in Figure 6.1. The relevant thermal parameters obtained from these DSC data are listed in Table 6.1.

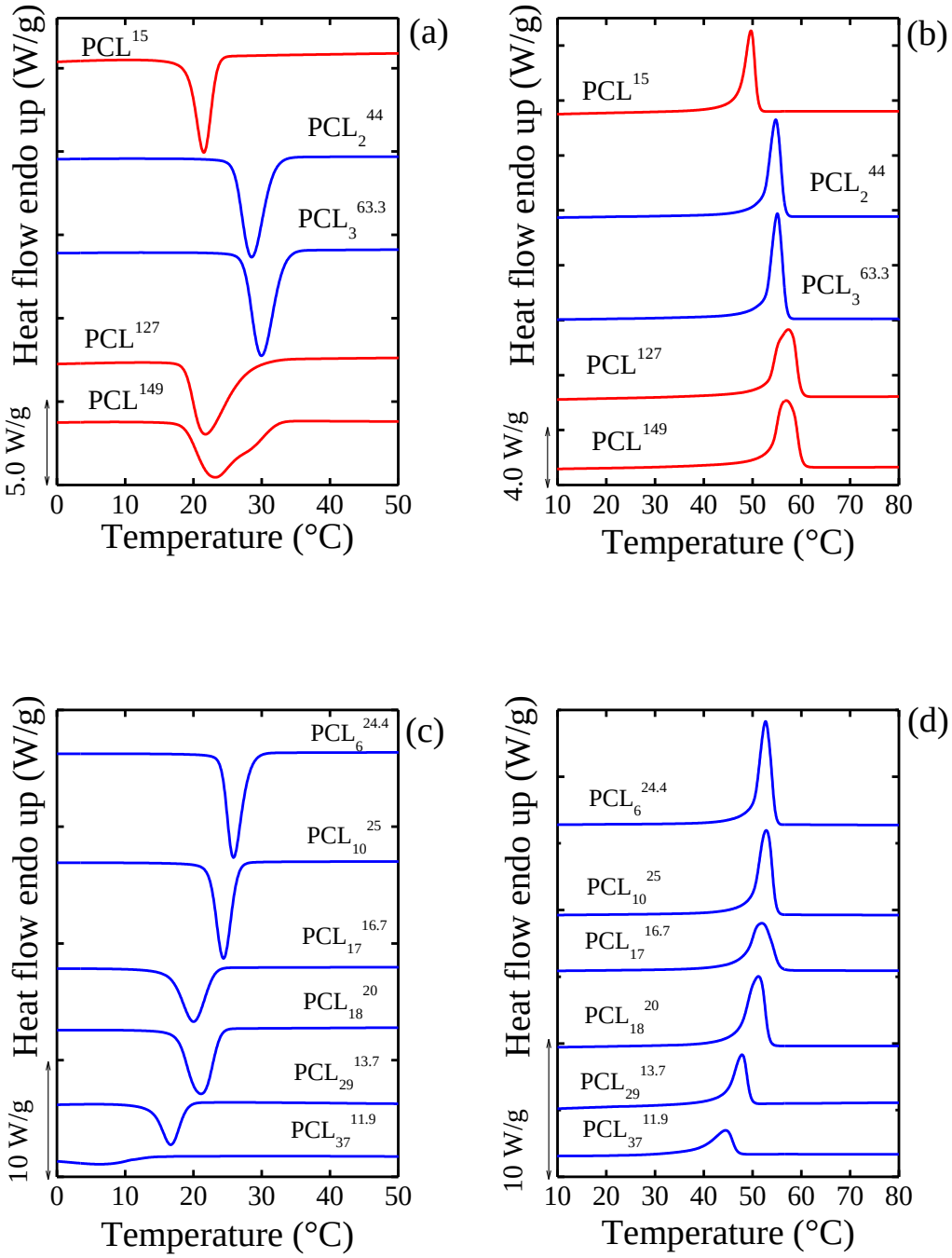

Figure 6.1 DSC cooling and subsequent heating scans at 20 °C/min for (a), (b) neat PCLs and (c), (d) PCL-*g*-lignin copolymers. The plots are normalized by the weight of the PCL fraction in the sample. The red color was used for the neat materials and the blue one for the copolymers.

Table 6.1. Thermal properties (crystallization (T_c) and melting temperature (T_m)) obtained from Figure 6.1. The enthalpies of crystallization and melting (ΔH_c and ΔH_m), as well as the values of crystallinity (X_c) have been normalized by the weight fraction of PCL in the sample.

Samples	Cooling			Second Heating		
	T_c (°C)	ΔH_c (J/g)	X_c (%)	T_m (°C)	ΔH_m (J/g)	X_c (%)
PCL[15]	21.5	53	39	49.7	58	43
PCL[127]	21.7	77	57	55.2/57.3	85	63
PCL[149]	23.2	79	58	56.9	86	63
PCL_2[44]	28.5	69	51	54.7	73	54
PCL_3[63.3]	30.0	74	55	55.1	77	57
PCL_6[24.4]	25.9	76	56	52.7	81	59
PCL_{10}[25]	24.4	69	51	52.8	74	55
PCL_{17}[16.7]	20.0	59	43	51.9	64	47
PCL_{18}[20]	21.1	70	51	51.2	77	56
PCL_{29}[13.7]	16.7	39	29	47.9	46	34
PCL_{37}[11.9]	7.1	10	7	44.5/58.1	30	22

Table 6.1 shows that as the average arm length (AAL) value increases for neat PCLs (from 15 to 149), both the peak crystallization temperature (T_c) and the peak melting temperature (T_m) increase. This result represents the expected behavior for any crystallizable polymer as the molar mass increases, and similar trends have been previously reported for PCLs.[43, 44]

In the case of the PCL–*g*–lignin copolymers the behavior is more complex, as it depends on the lignin content besides the AAL value (see Table 6.1). Figure 6.2 shows plots for selected calorimetric properties as a function of lignin content. In Figure 6.2, lines to guide the eye are drawn through data points corresponding to samples with low AAL values, for which a wide range of lignin contents is available. All the calorimetric properties in Figure 6.2 go through a maximum at lignin contents below 10 wt%.

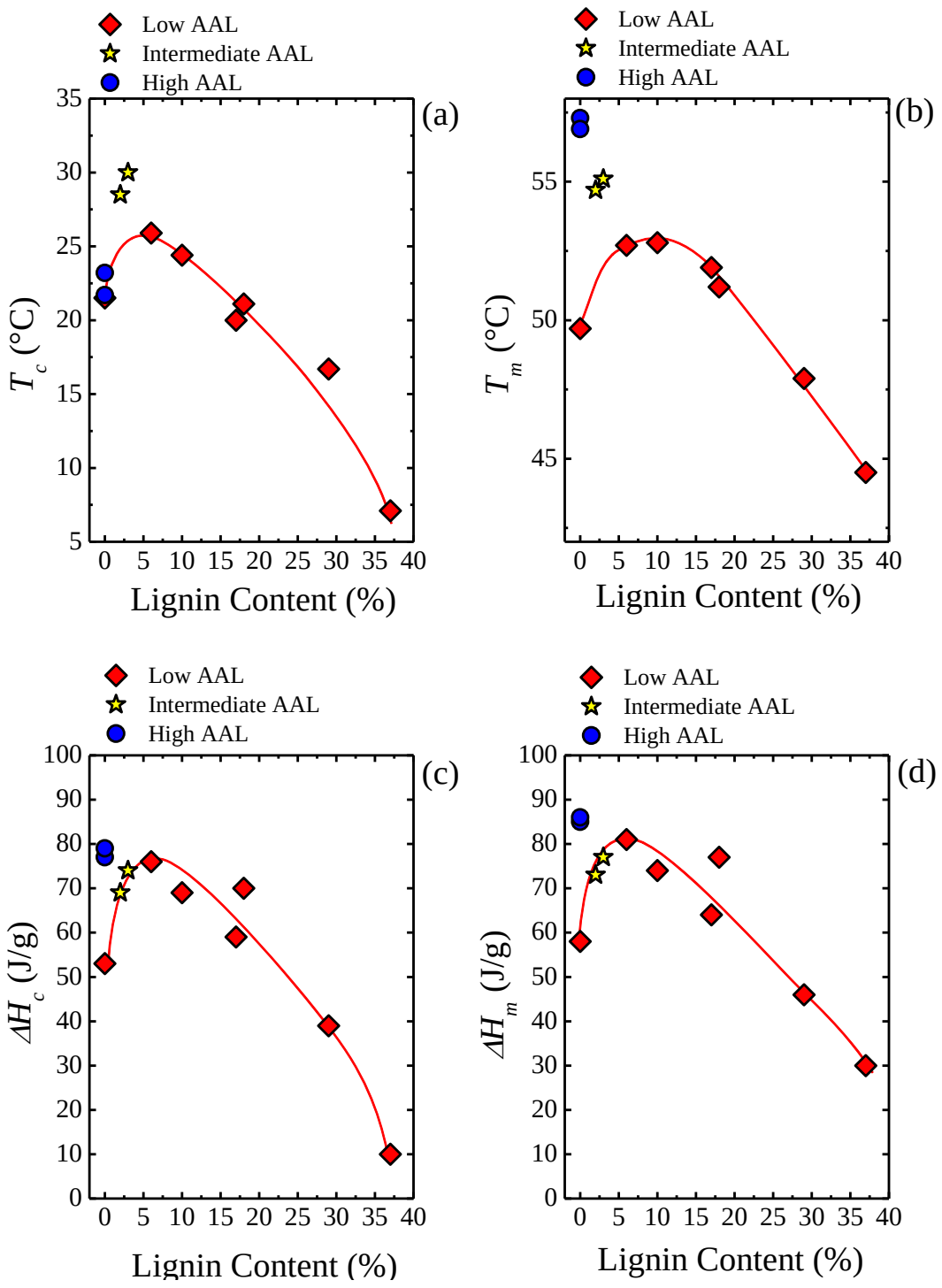

Figure 6.2. Variation of (a) T_c (b) T_m (c) ΔH_c and (d) ΔH_m as a function of lignin Content. ΔH_c and ΔH_m were normalized by the mass of PCL in the PCL-*g*-lignin copolymer. The solid lines represent guides to the eye.

Figure 6.2 shows that as the AAL value increases for neat PCLs, both T_c and the T_m increase. This result represents the expected behavior for any crystallizable polymer as the molar mass increases, and similar trends have been previously reported for PCLs [43, 44]

The T_c (Figure 6.2a) is proportional to the nucleation density. Hence, at low lignin contents (lower than 10%), lignin is nucleating PCL, since T_c values increase by about 5 ºC with respect to neat PCL. This result is consistent with the cross-hatched lamellar morphology present in the grafted copolymers with low lignin contents (Figure 9.16a and 9.16b of the Appendix) The nucleating effect that causes the increase in T_c is also reflected in the subsequent heating scans in an increase in T_m values (Figure 6.2b). The T_m has a lower sensibility to nucleation and anti–nucleation than T_c, as a consequence of the metastable nature of the polymeric crystals, especially under non–isothermal conditions. Hence, the T_m shifts are lower in comparison with those displayed by T_c. Additionally, the latent heats of crystallization, during cooling from the melt, and melting, during subsequent heating, also increase in the lignin range where nucleation is detected.

The nucleating effect of lignin on the PCL-*g*-lignin copolymers reaches a maximum value at or below 10% lignin (Figure 6.2). Higher quantities of lignin progressively cause less nucleation until at about 18% lignin content, the copolymers behave (within the error of the measurements) similar to neat PCL. For lignin contents higher than 20% an anti-nucleation effect is clearly seen, since T_c values drop well below that corresponding to neat PCL. A quantification of the efficiency of nucleation and anti-nucleation as well as the possible origin of the phenomenon will be presented in the next sections.

Since PCL was grown from the OH groups of lignin by ROP, the grafting between PCL and lignin occurs at one of the chain ends of PCL. Therefore, there is no interruption of the linear crystallizable sequences of PCL by the grafting reaction. However, steric effects (near the grafted chain end with lignin), intermolecular interactions and topological confinement can affect the nucleation and crystallization of PCL chains.

In a previous work, Laurichesse et al.[1, 3] reported that samples with lignin contents of 46 and 48 wt% and CL/OH ratios of 5 mol.mol^{-1} were amorphous materials. Only when CL/OH ratios were higher than 5 mol.mol^{-1} PCL chains were able to crystallize. However, in the present work, the two samples with lignin contents of 29 and 37 wt % also have CL/OH ratios of 5 mol.mol^{-1} and they are able to crystallize, albeit at temperatures lower than 20 ºC. In fact, the sample with 37% crystallizes at much lower temperatures and with a very broad crystallization exotherm (below 10 ºC and its crystallization continues down to 0 ºC and below), see Figure 6.1c. Hence, it is not surprising that at lignin contents higher than 37% the samples were not able to crystallize at all.

Isothermal DSC Scans

Isothermal crystallization experiments were performed by DSC in order to measure the half-crystallization time ($\tau_{50\%}$) and determine the overall crystallization kinetics of the samples. The inverse of the half-crystallization time ($1/\tau_{50\%}$) provides an experimental measure of the overall crystallization rate (which includes both nucleation and growth).

Figure 6.3 shows the overall crystallization rate as a function of the temperature for neat PCLs (Figure 6.3a) and PCL-*g*-lignin copolymers (Figure 6.3b). PCLs with higher AAL values (PCL^{127} and PCL^{149}) need lower supercoolings to crystallize in comparison with PCL^{15}. Figure 6.3a shows solid lines that corresponds to mathematical fits to the Lauritzen and Hoffman theory (see Chapter II. General Concepts), which can be used in this case to have an idea of the extrapolated behavior of the low AAL sample to higher T_c values. Extrapolating the overall crystallization rate trends with T_c, the crystallization rate increases with AAL values at constant T_c (in the range of high T_c values, above 30 ºC).

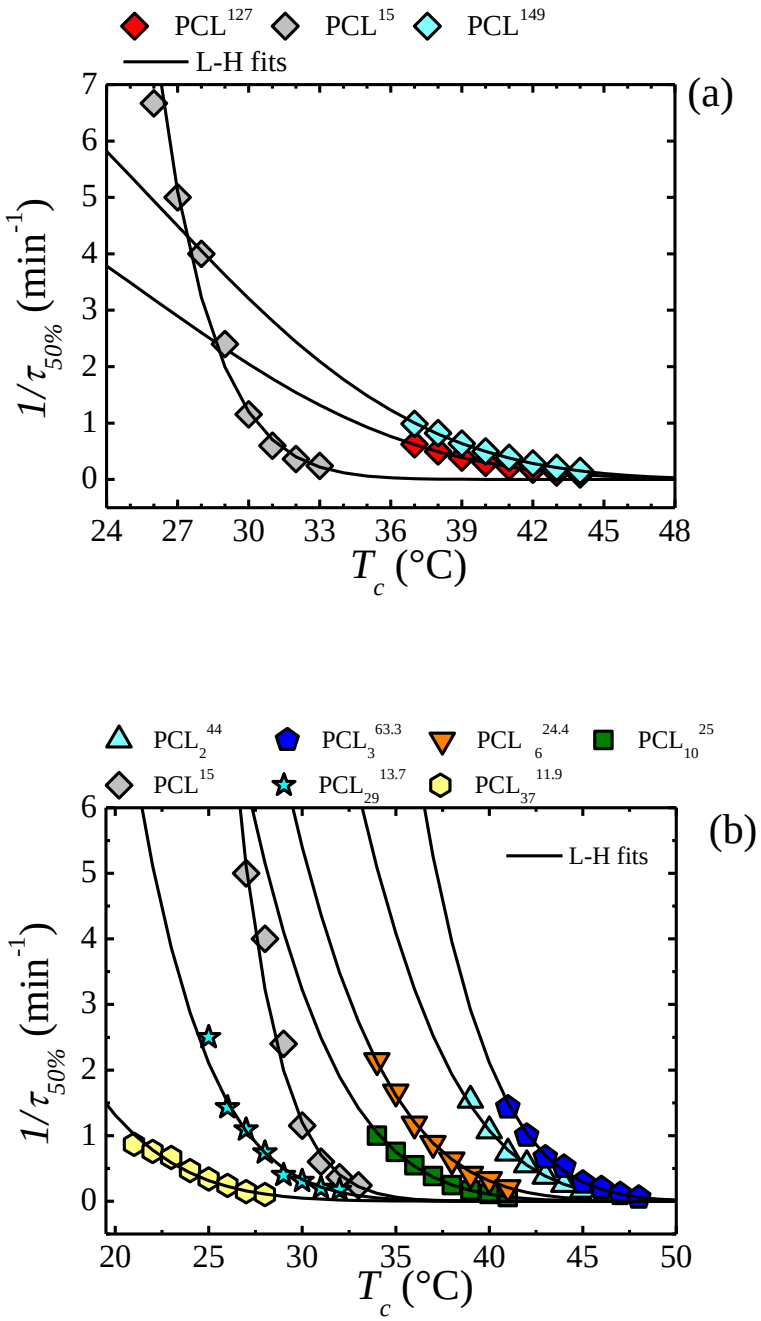

Figure 6.3. Overall crystallization rate ($1/\tau_{50\%}$) as a function of isothermal crystallization temperature for (a) neat PCLs (b) PCL^{15} and PCLs with different lignin contents. The solid lines represent fits to the Lauritzen and Hoffman theory.

The differences observed in Figure 6.3a are related to the average molar mass values of the samples. Both polyethylene and PCL have complex dependences of their crystallization rate with molar mass. Previous works[45-49] have demonstrated that their crystallization rate first increases as the molar mass increases, until a maximum is

reached. After the maximum, the crystallization rate usually decreases with molar mass. In the present case, the results obtained suggest that these three PCL samples are in the molar mass range where the crystallization rate (at constant crystallization temperature) increases with increases in chain length. At low molar masses, the overall crystallization rate increases with AAL, since shorter chains experience a higher nucleation barrier [45-49].

The crystallization rate behavior of the PCL-*g*-lignin copolymers is shown in Figure 6.3b. The data points corresponding to PCL^{15} are included for comparison purposes. This neat PCL sample was selected since it has AAL values closer to most of the copolymer samples.

Figure 6.3b shows that lignin content has a significant effect on the crystallization rate of PCL. Taking PCL^{15} as a reference material that does not contain lignin, two clear general trends can be observed in Figure 6.3b. Firstly, PCL-*g*-lignin samples with lignin contents lower than 10 wt% exhibit shifts of their overall crystallization rate versus temperature curves to lower supercoolings. These results imply an acceleration of the overall crystallization kinetics which is consistent with a nucleation effect under isothermal conditions. These results agree with the non-isothermal results presented above. Secondly, the samples with lignin contents higher than 10 wt% display shifts of their overall crystallization rate versus temperature curves to higher supercoolings. These results correspond to a retardation of the overall crystallization kinetics which is consistent with the anti-nucleation effect detected under non-isothermal conditions.

The samples with 17 and 18% lignin (i.e., $PCL_{17}^{16.7}$ and PCL_{18}^{20}) have very similar crystallization kinetics to PCL^{15} and were not included in Figure 6.3b for the sake of clarity.

The results presented in Figure 6.3b can be better analyzed by representing the overall crystallization rate (given by $1/\tau_{50\%}$) at constant temperature as a function of lignin content as shown in Figure 6.4a. Additionally, a plot of the crystallization temperature needed to achieve a constant crystallization rate is shown in Figure 6.4b.

For both representations, experimental and extrapolated data (employing the Lauritzen and Hoffman theory) were employed.

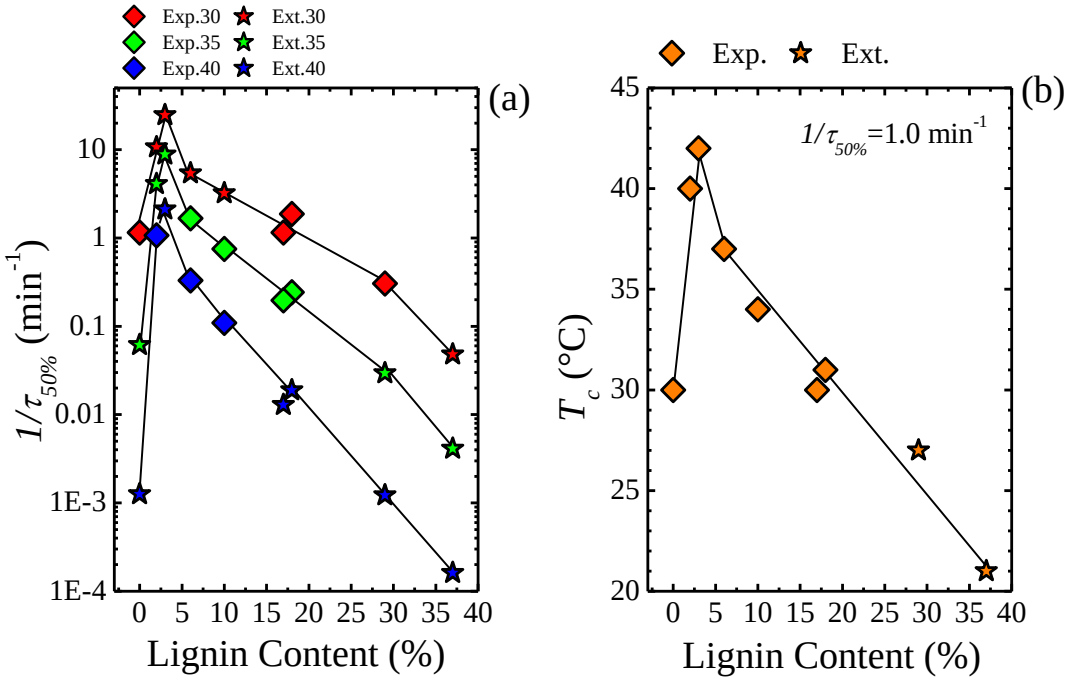

Figure 6.4. (a) Values of $1/\tau_{50\%}$ as a function of Lignin content at different constant values of T_c. (b) Values of T_c as a function of Lignin content at $1/\tau_{50\%}$=1.0 min^{-1}. The plots contains experimental data points (Exp.) and values extrapolated (Ext.) from the LH fittings to the data shown in Figure 6.3. The solid lines represent guides to the eye.

Figure 6.4a shows a complex trend with lignin content where the data falls into three categories:

(1) A sharp increase in overall crystallization rate at constant T_c values is observed (notice the logarithmic scale in the y axis) with lignin content until a maximum value that always corresponds to 3% lignin. This acceleration of overall crystallization rate is mainly due to the nucleation effect that small quantities of lignin have on PCL. However, part of the effect is also due to differences in AAL content, since the reference sample is one with low PCL content (i.e., PCL[15]) while samples with 2 and 3% lignin are copolymers where PCLs have intermediate AAL contents (*i.e.*,

PCL_2^{44} and $PCL_3^{63.3}$). As explained above, the crystallization rate increases with AAL content (Figure 6.4a) at constant T_c temperatures.

(2) After the maximum in Figure 6.4a, the crystallization rate decreases with further increases in lignin contents. PCL-*g*-lignin samples with lignin contents of 6 and 10% still show higher values of crystallization rates at the constant temperatures selected in Figure 6.4a as compared to PCL^{15}, indicating that nucleation effects are still present even though of lower efficiencies. When lignin content in the copolymers reaches 17-18%, the crystallization rate becomes the same as that of PCL^{15} signaling that all nucleation effects have disappeared.

(3) Finally, when lignin contents higher than 20% are present in the PCL-*g*-lignin samples, a stronger decrease (as judged by the higher negative slope) in crystallization rate sets in. Additionally, the crystallization rates of samples $PCL_{29}^{13.7}$ and $PCL_{37}^{11.9}$ are much lower than that of PCL^{15} for all the crystallization temperatures selected in Figure 6.4a. The behavior is consistent with anti-nucleation effects.

The behavior observed in Figure 6.4 is similar for all the three isothermal crystallizations selected. The relative differences observed in the values of $1/\tau_{50\%}$ are expected on the basis of the dependence of the crystallization kinetics with the temperature (Figure 6.4a). A similar trend that corresponds well with the three categories explained above can also be seen in the representation employed in Figure 6.4b.

The isothermal crystallization data obtained by DSC was analyzed using the Avrami equation [50, 51]. The fits to the Avrami equation were performed using the Origin® plug in developed by Lorenzo et al.[50]. The procedure employed and examples of the results are presented in Chapter II. General Concepts.

The values of the overall crystallization rate constant *K* and its variation with lignin content are consistent with the results presented in Figures 6.3 and 6.4, as expected from the excellent fits obtained in the primary crystallization range (see Table 9.4 to 9.7 in the Appendix). The Avrami index values obtained for neat PCLs and PCL-*g*-lignin samples are presented in Figure 6.5.

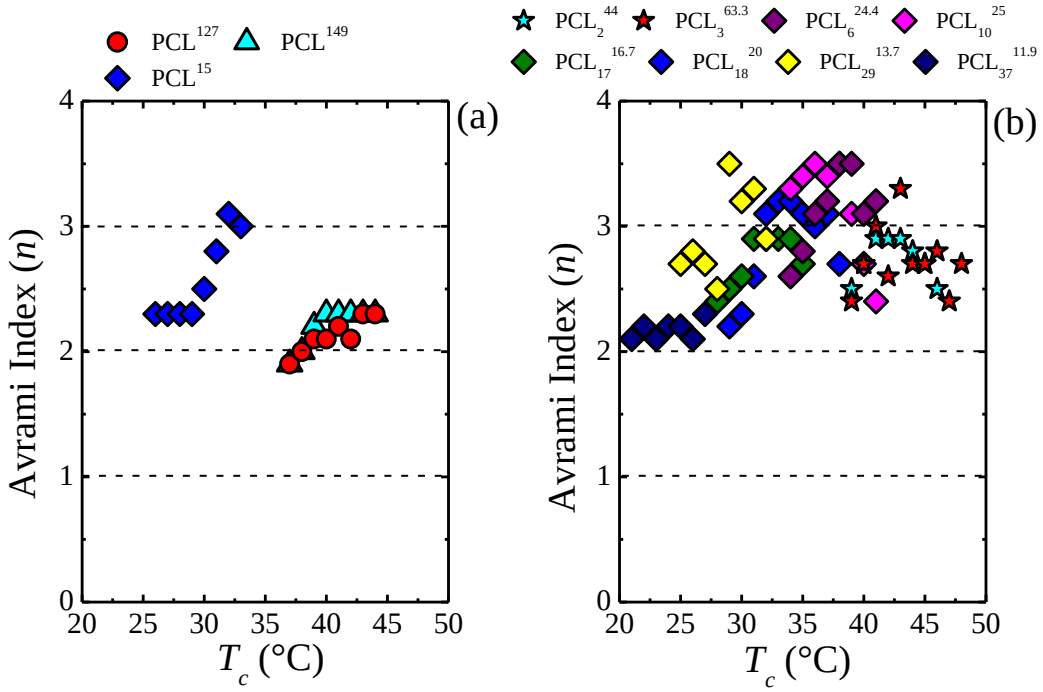

Figure 6.5. Avrami index values for: (a) neat PCLs and (b) PCL-*g*-lignin samples.

The Avrami index values (*n*) are within 2–3 for neat PCLs depending on the temperature (Figure 6.5a). A value of 2 is associated with instantaneous axialites (*i.e.*, superstructural aggregates composed of a two dimensional aggregates of lamellae) while 3 can be due to instantaneous spherulites or sporadic axialites. As T_c increases the Avrami index tends to increase. This is a typical trend, since nucleation becomes more sporadic as temperature increases.

In the case of PCL-*g*-lignin, Figure 6.5b shows that most Avrami index values are between 2-3 (with very few data points at 3.5). No significant trends can be seen as a function of lignin content. In previous works, nanocomposites of *in situ* polymerized polyethylene onto carbon nanotubes (PE/CNT) were prepared and their crystallization kinetics studied in detail. The results showed a decrease in the Avrami index with CNT content that was correlated with confinement effects provoked by the interactions of CNT surfaces with PE molecules, together with space filling restrictions caused by inert residual alumina (coming from the catalysis system employed). The Avrami index

progressively reduced from a value of 2 for neat PE to values close to 1 (and even lower for large CNT contents). An Avrami index of 1 is also commonly seen in confined block copolymer phases (see ref.[43]). Confinement causes a nucleation control on the overall crystallization kinetics, as a result the kinetics becomes first order (for details, see reference [43]).

Taking into account the results obtained in Figure 6.5, in the case of PCL-*g*-lignin, no reduction of Avrami index with lignin content is observed, hence significant confinement effects are not present. The overall crystallization kinetics is still determined by contributions of both nucleation and growth. Hence, it was decided to apply the Lauritzen and Hoffman (LH) nucleation and growth theory to the isothermal crystallization kinetics data collected by DSC (see details on Chapter II. General Concepts). The parameters obtained from the LH theory are presented on Table 6.2.

Table 6.2. Parameters obtained from fitting the Lauritzen and Hoffman theory to the data of Figure 6.3. R^2 is the correlation coefficient for the Lauritzen and Hoffman linear plots. Equation 2.15 (see Chapter II. General Concepts) yields a value of σ=7.01 erg/cm^2.

Sample	K_g [K^2]	σ_e[erg/cm^2]	qx10^{13}[erg]	R^2
PCL^{15}	556517	617.4	22.8	0.98943
PCL^{127}	190611	211.5	7.80	0.9996
PCL^{149}	186919	207.4	7.65	0.99975
PCL$_2$^{44}	218293	242.2	8.94	0.99890
PCL$_3$$^{63.3}$	230857	256.1	9.45	0.99582
PCL$_6$$^{24.4}$	260565	289.1	10.7	0.99777
PCL$_{10}$^{25}	302146	335.2	12.4	0.99909
PCL$_{17}$$^{16.7}$	382751	424.6	15.7	0.98657
PCL$_{18}$^{20}	375574	416.7	15.4	0.97795
PCL$_{29}$$^{13.7}$	463640	514.4	19.0	0.98337

$PCL_{37}^{11.9}$	470335	521.8	19.2	0.98990

The data presented in Figure 6.3 was fitted to the Lauritzen and Hoffman theory and represented as solid lines. The parameters derived from the fittings are listed in Table 6.2. The T_m^o value obtained in a recent work for linear PCL[52] as well as the procedure suggested by Lorenzo and Müller.[50] have been used.

Table 6.2 shows, in the case of neat PCLs, values that are reasonably expected in view of the crystallization behavior of these materials (Figure 6.3a). The samples that crystallize at lower supercoolings are those with higher molar mass and they have values of K_g or σ_e that reflect a lower free energy barrier for overall crystallization in comparison with PCL^{15}. Since σ_e, q and K_g are all linearly dependent on one another, their trends are similar.

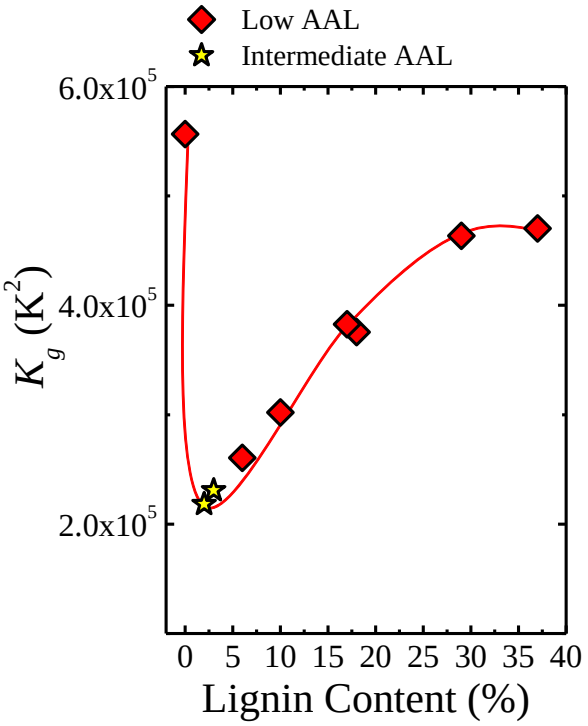

Figure 6.6. Values of K_g as a function of Lignin Content. The solid line is a guide to the eye.

Figure 6.6 shows how the parameter K_g depends on lignin content. At very low lignin contents, K_g sharply decreases as the nucleation effect of lignin reduces the free energy barrier for crystallization. At larger lignin contents K_g increases, and in the range where anti-nucleation sets in, its value saturates. However, the values of K_g at very large lignin contents are not higher than that of PCL[15], a result that is not expected based on the experimental results presented in Figure 6.3. The LH theory nevertheless qualitatively describes the large changes in overall crystallization free energy as lignin content increases in the copolymers.

Laurichesse et al.[1] performed previously Fourier Transformed Infrared Spectroscopy (FTIR) studies on their PCL-*g*-lignin samples. They found that the peak position corresponding to O–H stretching band shifts from 3357 to 3342 cm^{-1} in PCL-*g*-lignin samples with CL/OH ratios of 5 $mol.mol^{-1}$ (in the present work, the samples with 29 and 37 wt% of lignin have a CL/OH ratio of 5 $mol.mol^{-1}$). These significant shifts were attributed to the formation of intermolecular hydrogen bonding between carbonyl groups of PCL and phenolic and aliphatic hydroxyl groups of lignin. Additionally, evidences of strong interactions were obtained by rheological tests, in which these samples exhibited a specific behavior of cross–linked-like polymers, with a plateau at low frequencies.[1]

In order to detect hydrogen bonding formation by FTIR, the amount of such interactions needs to be significant, a condition fulfilled in the samples with high lignin content and the highest free OH groups content. (ref. [1])

The results presented so far can be explained considering a competition between nucleation and intermolecular hydrogen bonding formation. At low lignin contents, the nucleation effect of lignin on PCL predominates and the overall crystallization kinetics is accelerated. As with the majority of nucleating agents, the effect of lignin saturates at around 5%. At higher lignin contents, the effects of intermolecular interactions start increasing and anti-nucleation effects eventually appear. When lignin contents are higher than 20% (*i.e.*, in samples with 29 and 37 wt% lignin with a CL/OH ratio of 5 $mol.mol^{-1}$), hydrogen bonding predominates limiting chain diffusion up to a point where the overall rate of crystallization drops below that of neat PCL. An additional minor

factor that may be limiting nucleation and diffusion is the steric effect present near the PCL chain ends grafted to lignin. These steric effects will also tend to increase as lignin content increases in the samples.

Self-Nucleation Experiments and Nucleation efficiency

One of the best ways to quantitatively assess the nucleation efficiency of an additive is by comparing its effect on a given polymeric matrix with that of self-nuclei. An efficiency scale has been derived by Fillon et al.[42, 53]. The scale has been used to calculate the efficiency of nucleation of several nanocomposites [43, 44, 54, 55]. The nucleation efficiency (*NE*) can be calculated according to the Equation 2.18 presented in Section 2.4.2 of Chapter II. General Concepts.

Self-nucleation was applied to PCL^{15} and PCL^{127} in order to determine the ideal self-nucleation temperature of two PCL neat samples with different molar mass, which are need it in order to determine the *NE*. The self-nucleation process of PCLs has been studied before ref. [43, 44, 54, 55]. Hence, only the final results are presented in Figure 6.7. The peak crystallization temperature is constant in *Domain I* or complete melting domain. When T_s is lower than a specific temperature the samples crosses over from *Domain I* to *Domain II*. T_c values increase exponentially in *Domain II* or self-nucleation domain because self-nucleation significantly increases the nucleation density of the sample. *Domain II* is wider and extends to temperatures well above the melting point for PCL^{127} in comparison to PCL^{15}. This is a consequence of the higher crystalline memory of the sample with a larger molar mass, a result in agreement with recent data on model PCLs.

The ideal self-nucleation temperatures for PCL^{15} and PCL^{127} are 26.9 and 35.9 ºC respectively. These temperatures were used as $T_{c,max}$ in equation 2.18 to determine the nucleation efficiency taking into account two different reference PCLs. Figure 6.8 shows the results. The value of *NE* depends on which reference PCL is employed for its calculation.

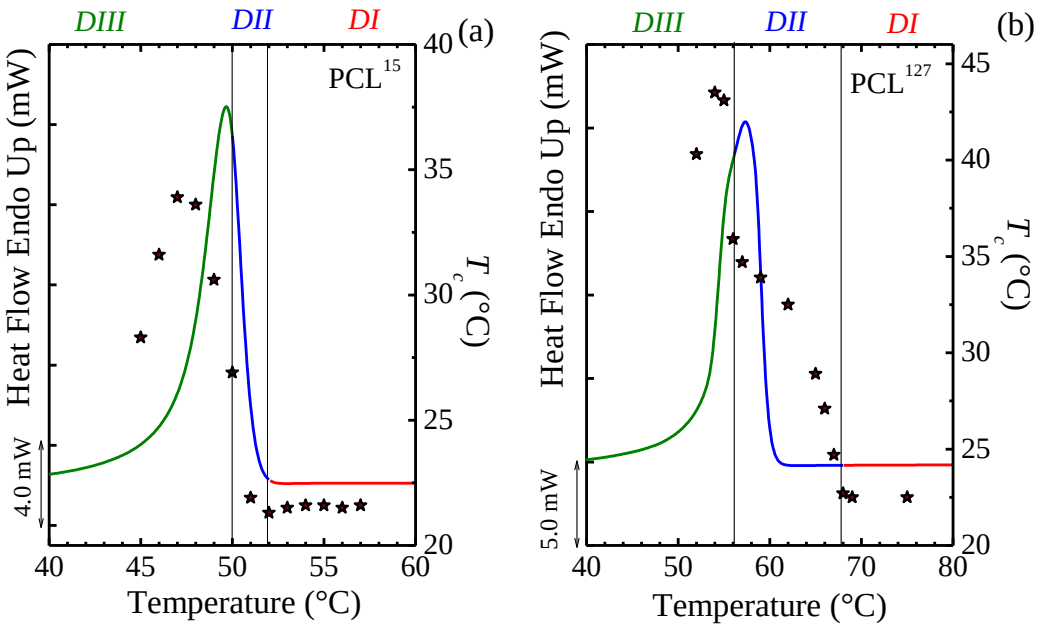

Figure 6.7. Standard DSC heating scans for (a) PCL[15] and (b) PCL[127]. The vertical lines indicate the temperatures at which the materials experience their self–nucleation Domain transitions. The data points represent T_c (right hand side *y* axis) as a function of T_s (using the *x* temperature axis). *DI*, *DII* and *DIII* stand for the different self-nucleation domains of the samples.

PCL[15] has a low AAL value, as well as most of the PCL-*g*-lignin samples (see Table 6.1). Hence, using PCL[15] as a reference value to calculate *NE*s makes sense for most of the copolymer samples containing lignin. However, for samples with intermediate AAL values, *NE*s may be overestimated as such samples exhibit higher peak crystallization temperatures as a result of both nucleating effects and higher molar mass values. On the other hand, if PCL[127] is used as a reference, *NE* values at low lignin contents will be underestimated since all PCL-*g*-lignin samples have lower molar mass.

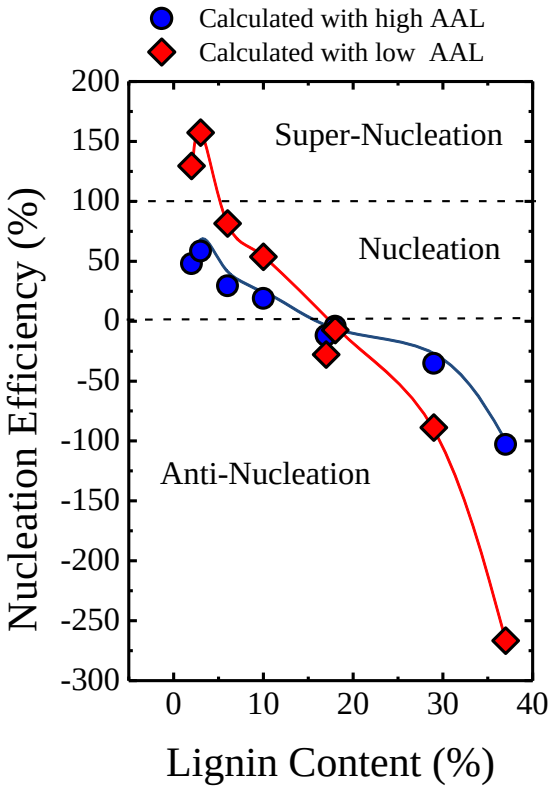

Figure 6.8. Nucleation efficiency (*NE*) of lignin in PCL-*g*-lignin samples. The efficiency was calculated using reference crystallization parameters from both PCL[15] (low AAL) and PCL[127] (high AAL), see equation 6 and text.

Regardless of AAL differences in the samples, the trends observed in Figure 6.8 (which can be considered as the minimum and maximum possible values for *NE*) clearly indicate that lignin is a good (or excellent depending on the reference value) nucleating agent for PCL samples with 5% grafted lignin or less. Super-nucleation would indicate that lignin is a better nucleating agent than PCL self-nuclei. Multi-wall carbon nanotubes are known to produce super-nucleation effects in HDPE and PCL[43, 44, 55]. In the present case, super-nucleation is only obtained for two samples where *NE* may be overestimated since they correspond to samples with intermediate AAL values, as explained above.

Samples with more than 20% lignin exhibit the strongest anti-nucleation effect regardless of the reference values employed to calculate *NE*. Once more, such large

effects are probably due to the hydrogen bonding between PCL and lignin molecules previously detected by FTIR in similar samples (ref. [1]).

Successive Self-Nucleation and Annealing (SSA)

As indicated in Figure 6.7, self-nucleation of PCL^{127} yielded a $T_{s,ideal}$ value of 56 ºC. An SSA protocol was therefore designed employing as the first T_s temperature, a value of 56 ºC for all samples, as indicated in the experimental part (see Chapter II. Experimental Part). Figure 6.9 shows the final heating runs after SSA was applied to all samples. In these heating scans, the effects of SSA protocol are revealed as multiple melting points. Each melting peak corresponds to a thermal fraction. As $T_{s,ideal}$ only produces self-nucleation without annealing (ref. [56]), the 6 steps SSA protocol applied only produces 5 thermal fractions.

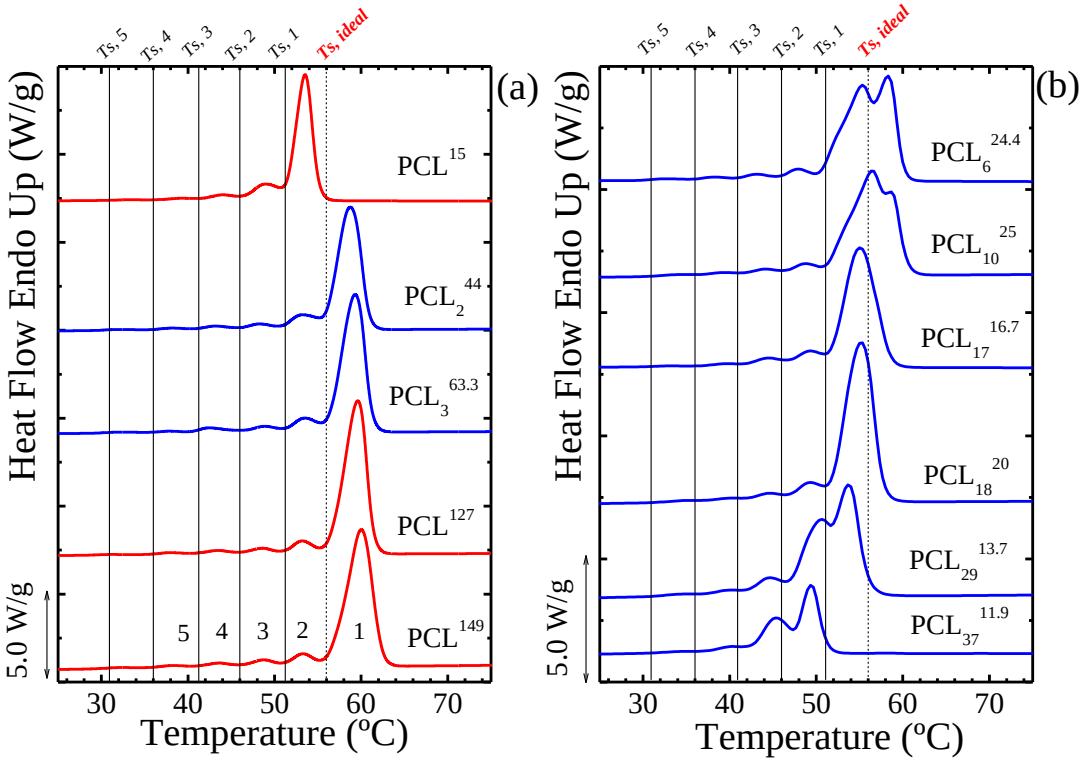

Figure 6.9. Final heating run after SSA thermal fractionation for (a) Neat PCLs (b) PCL-*g*-lignin, the endotherms were normalized by the real PCL mass.

Figure 6.9a shows the melting process of SSA fractionated neat PCL samples. For PCL[149], the numbers inserted on the DSC scan represent the different thermal fractions. Hence, thermal fraction 1 melts at temperatures above $T_{s,ideal}$ (at approx. 60 ºC) and was produced during the annealing experienced by the sample when $T_{s,1}$ was applied. Fraction 2 melts at around 53 ºC and was produced by the annealing at $T_{s,2}$, and a similar situation holds for the other fractions. Notice that vertical lines have been plotted to indicate the T_s values used during SSA. More details on SSA can be found in a recent review (see ref.[56]).

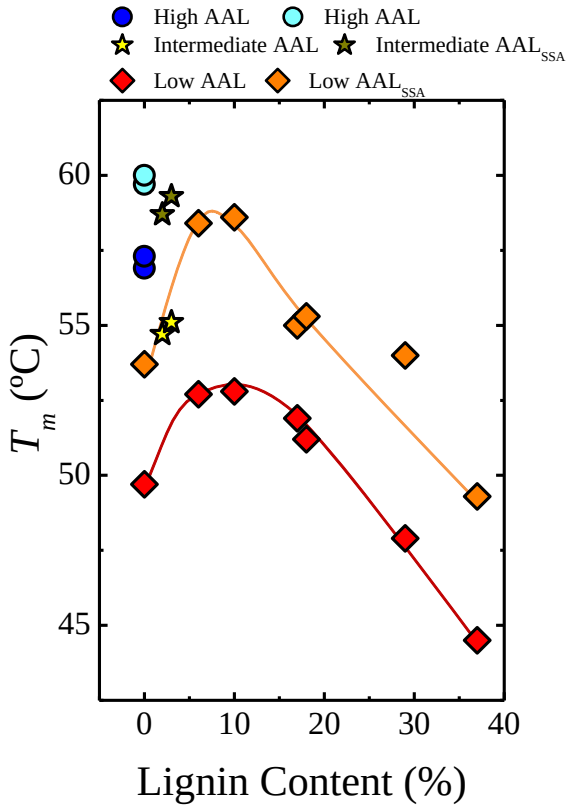

Figure 6.10. Peak melting point of the highest melting point SSA fractions as a function of lignin content. For comparison purposes the T_m (see Figure 6.1) values after non-isothermal crystallization also are plotted. The solid lines represent guides to the eye.

SSA promotes crystal thickening by successive annealing and therefore melting points tend to increase as compared to non-isothermally or isothermally crystallized samples. In Figure 6.9a, it should be noticed how fraction 1 is missing from PCL[15], because it originally melts at lower temperatures than PCL[127] or PCL[149] as a result of its

much lower average molar mass. The PCL-*g*-lignin samples with intermediate AAL values and 2 or 3% lignin exhibit similar behavior as neat PCL samples with high AAL values, but with slightly lower T_m values for fraction 1, as expected.

Figure 6.9b shows SSA final DSC scans for PCL-*g*-lignin samples with different lignin contents in the range 6-37%. A progressive depletion of the highest melting point fraction (*i.e.*, fraction 1) is seen as the content of lignin increases, until at 17-18% it disappears almost completely. When the lignin content is 29%, fraction 1 is not present and fraction 2 is the most important in terms of melting point and area. Finally, when the lignin content is 37%, fraction 2 also disappears and fraction 3 becomes the dominant fraction of the distribution.

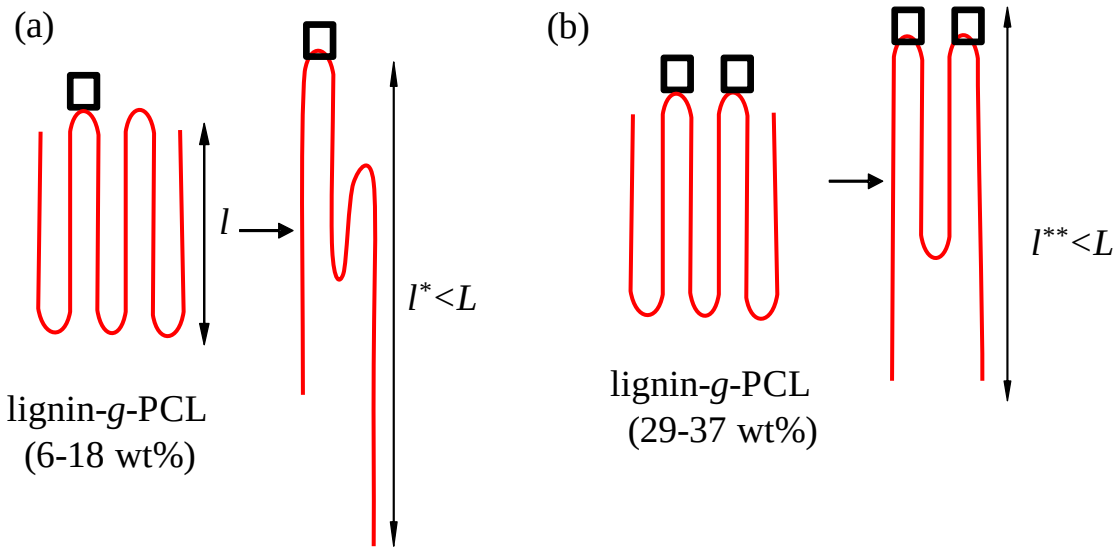

Figure 6.11. A schematic cartoon illustrating one possible way for PCL chains in PCL-g-lignin to undergo thickening during annealing. The *not–to–scale* square represents hydrogen bonding between PCL and lignin (see text). Acting like a physical crosslink, they prevent that chain fragments around them can enter PCL crystals: (a) Intermediate lignin contents with a low density of hydrogen bonds and (b) High lignin contents with higher density of hydrogen bonds.

Figure 6.10 plots the peak melting point of the highest melting point SSA fractions, as a function of lignin content. For comparison purposes, the T_m values obtained after

non-isothermal crystallization (Figure 6.1b) are also plotted in Figure 6.10. Very similar trends are obtained after SSA except for the fact that melting points are approximately 4 ºC higher than those obtained by non-isothermal crystallization. These higher T_m values are expected as SSA induces annealing of the samples. It is remarkable that the hydrogen bonds cause melting point depression for lignin samples with more than 20% lignin survive after successive annealings, indicating that they can act as physical crosslinks in a way schematically depicted in Figure 6.11.

6.2.2. PLA/lignins and PLA/talc blends

As we mention on the introduction of this Chapter, the feasibility of using industrial lignin without any purification or other treatment step might be useful in order to nucleate the PLA and at the same time avoid the increase of the overall cost of PLA products. In this section PLA and Organosolv (PLA/OL) and Kraft (PLA/KL) lignin blends were study and for comparison purposes these blends are compared with PLA/ultrafine talc (PLA/UT) blend. The characteristics of these materials are show in Chapter III. Experimental Part, in Section 3.1c.

Morphology, nucleation and spherulitic growth rate determined by PLOM

Figure 6.12 displays polarized light optical micrographs, which were taken at different times. Spherulites in neat PLA and nucleated PLA isothermally crystallized from the melt at a T_c of 130 ºC can be observed.

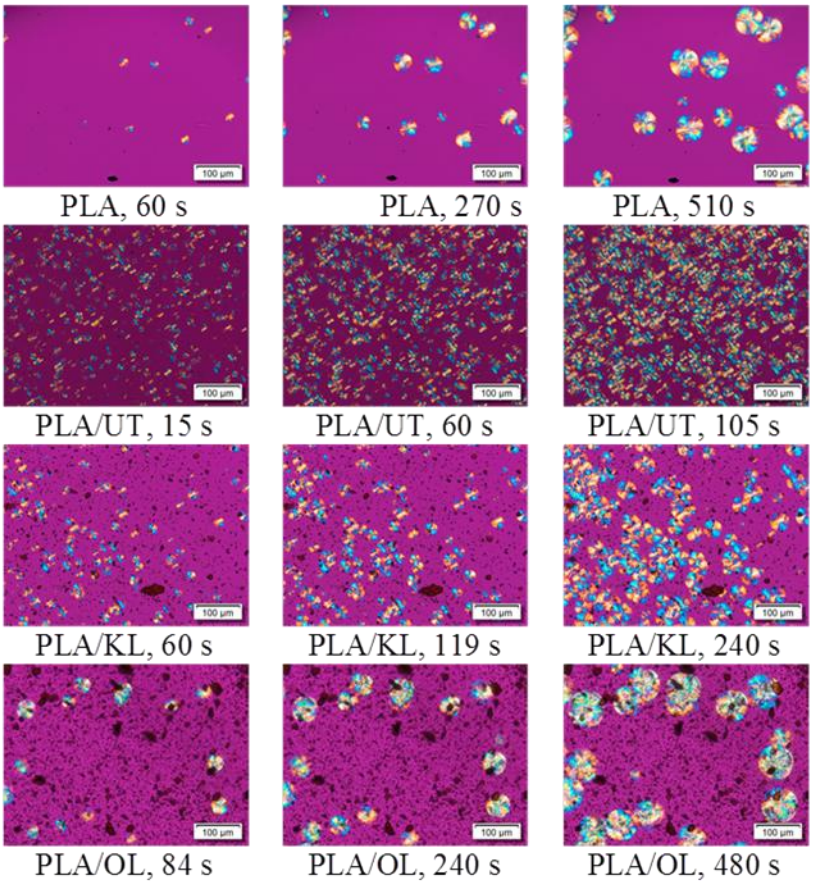

Figure 6.12. Polarized Light Optical Micrographs of spherulitic morphology of PLA and nucleated PLA compounds at 130 °C taken at the indicated times (scale: 100 μm).

Neat PLA and nucleated PLAs exhibit clear negative spherulites (indicated by the characteristic yellow color of the 1st and 3rd quadrants and the blue color of the 2nd and 4th quadrants when a red-sensitive tint plate is used), since neither the lignins nor UT alters the morphology of neat PLA. However, nucleated PLA shows a larger number of spherulites, formed at shorter times, in comparison with neat PLA. This indicates the nucleation activity of all tested nucleating agents such as UT, Kraft lignin and Organosolv lignins in PLA. When the micrographs of nucleated PLAs are compared, the UT shows a good dispersion in the PLA matrix and a remarkable nucleating capacity and nucleation rate (*i.e.*, in only 105 seconds the micrograph of PLA/UT shows a higher number of nuclei in comparison with any of the other systems). The dark spots clearly visible in the micrographs of PLA/lignin samples are due to lignin aggregates. It is clear that the distribution of lignins (KL and OL) in PLA matrix

is not optimal. It must be noted that although lignins can act as nucleating agents (see next section), the presence of agglomerates may negatively influence the mechanical properties of PLA/lignin composites.

Since lignin structure is complex and some reports of plasticization effects caused by lignin have been published [57-59], the spherulitic growth rate (G) as a function of the isothermal crystallization temperature (T_c) was determined. It is expected that due to plasticization effects (if they are present) the value of G should increase as chain mobility also increases in a plasticized polymer. Table 6.3 reports the spherulitic growth rates of neat PLA and PLA containing the different nucleating agents (a plot of G versus T_c can be found in the Appendix, see Figure 9.17). Within the error of the measurements, there is no significant difference between the values of growth rates of the different samples when compared at identical crystallization temperatures. These results show that neither lignins nor UT cause any plasticization on PLA. The additives, therefore, can only affect the nucleation capacity of PLA but not its crystal growth. Micrographs at different supercoolings (*i.e.* different T_c) were taken and are shown in Figure 9.18 (See the Appendix). They are consistent regarding differences between UT and lignins with the observations in Figure 6.12, already discussed above.

Table 6.3. Spherulitic growth rate (G) values as function of isothermal crystallization temperature (T_c) for neat PLA and PLA compounds.

T_c (ºC)	G (µm min^{-1})			
	PLA	PLA/UT	PLA/KL	PLA/OL
125	3.1 ± 0.1	-	3.4 ± 0.1	3.3 ± 0.2
127	3.3 ± 0.1	-	3.4 ± 0.1	3.7 ± 0.1
129	3.3 ± 0.1	3.1 ± 0.7	3.5 ± 0.2	3.6 ± 0.2
130	3.2 ± 0.1	3.5 ± 0.2	3.6 ± 0.2	-
131	3.2 ± 0.1	-	-	3.5 ± 0.1
132	-	3.2 ± 0.2	-	-

134	3.3 ± 0.1	-	3.5 ± 0.1	3.2 ± 0.2
135	3.2 ± 0.1	-	3.5 ± 0.1	-
137	-	2.8 ± 0.2	-	-
140	-	2.5 ± 0.1	-	-

Non-isothermal crystallization behavior

DSC cooling and heating scans are presented in Figure 6.13 while Table 6.4 lists obtained calorimetric data.

Table 6.4. Differential scanning calorimetry data of neat and nucleated PLA.

Sample	**Cooling cycle**		**2nd heating cycle**										
	T_c (°C)	ΔH_c (J g^{-1})	Tg (°C)	$\Delta C_{p,DSC}$ (J g^{-1}°C^{-1})	MAF (%)	RAF (%)	$T_{c,c1}$ (°C)	$\Delta H_{c,c1}$ (J.g^{-1})	$T_{c,c2}$ (°C)	$\Delta H_{c,c2}$ (J.g^{-1})	T_m (°C)	ΔH_m (J g^{-1})	CF (%)
PLA	93.5	8	58	0.476	56.5	18.0	95.5	25.4	154.2	3	167.7	52.1	25.5
PLA/UT	115.9	47	59	0.243	15.1	22.8	-	-	-	-	163.6/169.9	56.0	62.1
PLA/KL	102.2	38	58	0.242	16.8	25.5	-	-	-	-	160.5/168.5	52.1	57.8
PLA/OL	101.1	38	58	0.248	18.3	26.7	-	-	-	-	160.5/168.1	49.6	55.0

MAF – mobile amorphous fraction

RAF – rigid amorphous fraction

CF – crystalline phase

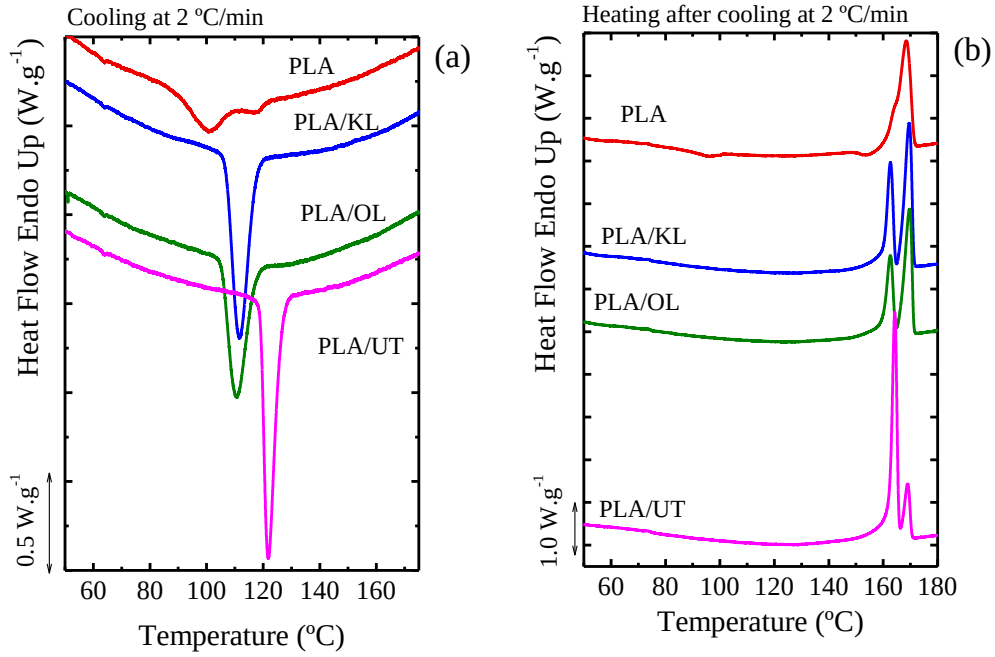

Figure 6.13. DSC (a) cooling and (b) subsequent heating scans for neat PLA and its blends with the indicated lignin and UT.

Figure 6.13a shows a broad bimodal crystallization process with a main exothermic peak at 93 °C (T_c) for neat PLA. After addition of both lignins and talc, this exothermic signal becomes monomodal, larger and sharper. The crystallization peaks are shifted to higher T_c, as a result of the nucleating effect, induced by both lignins and UT. UT is a more efficient nucleating agent, as the crystallization temperature of PLA/UT is the highest in Figure 6.13a. The changes in T_c are proportional to the nucleation density within the samples. The second heating curves show (Figure 6.13b) that neat PLA exhibits a glass transition temperature at approximately 58 ºC (not shown here) followed by a cold crystallization peak at 95.5 ºC and finally a melting peak at 167.7 ºC preceded by a second cold crystallization. The melting peak for neat PLA is asymmetric and if a close-up is made of the DSC trace, a lower temperature shoulder can be observed, which indicates the presence of a superimposed lower melting peak. In the case of the samples with nucleating agent, the double melting peaks are very clear.

All nucleated PLA compounds display double melting peaks without the presence of the cold crystallization peak (see Figure 6.13b). On one side, the disappearance of the cold crystallization peak proves that all tested additives are effective as nucleating agents since all samples with additives can crystallize until saturation during the cooling scan.

The possible reasons for double melting in PLA can be summarized as follows: (I) the presence of two types of average lamellar crystals with different lamellar thickness [60]; (II) A polymorphic behavior of PLLA, as the PLA crystal structure could change from the less stable α' phase to the more stable α phase during heating [61]; (III) the melting/recrystallization of unstable crystals during the heating scan [62, 63].

For the determination of Rigid Amorphous Fraction (RAF) in the samples, a three-phase model was implemented by considering that the semi-crystalline structure of PLA can be described by a crystalline fraction (CF), a mobile amorphous fraction (MAF) and a rigid amorphous fraction (RAF). [64-66]

It is interesting to note that in a recent reference, Klonos et al. [66] studied polymer nanocomposites of PLLA and fillers of different geometry (nanoparticles (3D), carbon nanotubes (1D) and graphene nanosheets (2D). They found that at the same filler content (1%), CF and RAF increased with filler addition in an order that correlated with the increased aspect ratio of the nanofillers. Hence they suggested that RAF could be correlated with PLA crystals rather than with NPs. They considered that their nanofillers acted as nucleating agents promoting crystallization but at the same time the interaction of the filler with PLA could cause topological restrictions limiting diffusion thereby reducing crystallinity degree and crystallization rate. In the present work, as Table 6.4 indicates, the RAF values only change significantly from neat PLA to nucleated PLA, as expected in view of the large crystallinity degree differences. However, comparing the values of CF, RAF and MAF for the samples with the different fillers employed in our work, no significant differences can be observed beyond the experimental uncertainty (around 10%). Therefore, we do not think differences in RAF may affect the results presented for the PLA loaded with the different fillers.

Nevertheless, a more detailed investigation into the influence of RAF is outside the scope of the present work.

In order to investigate the origin of these double melting peak, *in-situ* synchrotron X-rays experiments were performed and the results are provided in Figure 6.14.

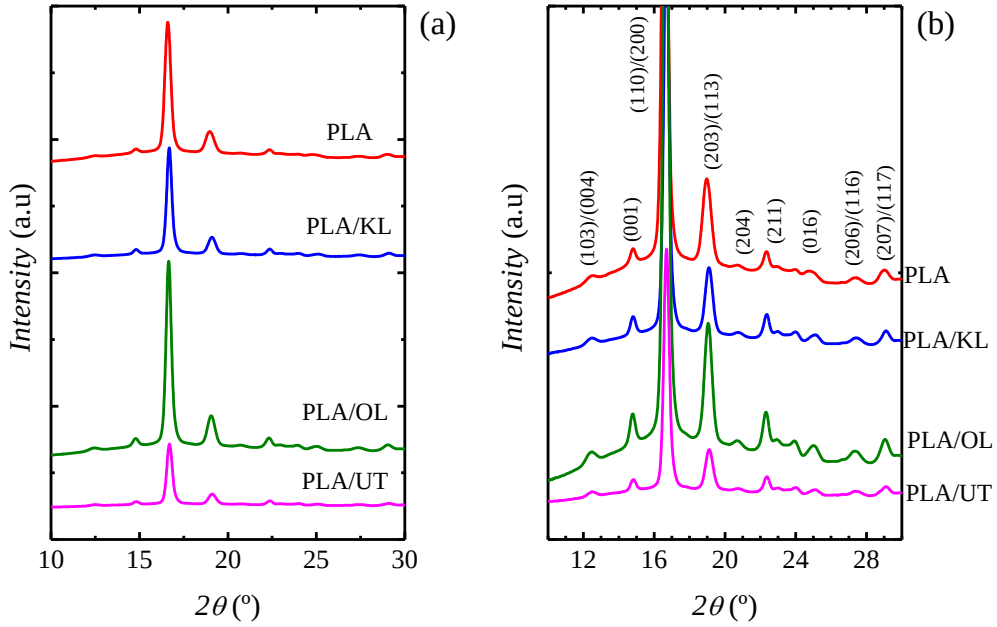

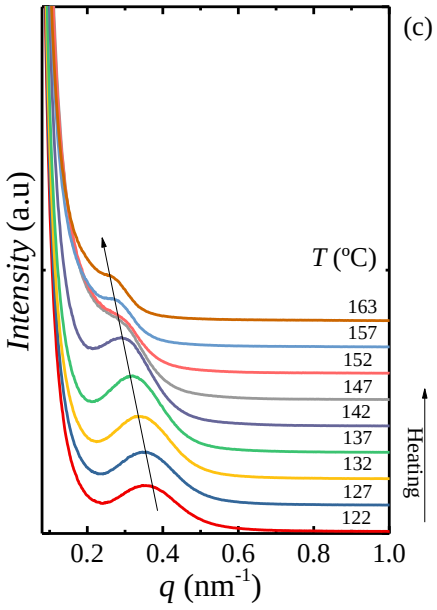

Figure 6.14. (a,b)WAXS diffractograms for all samples taken at 25 ºC (after cooling from the melt at 2 ºC/min) and (b) SAXS patterns for PLA taken during heating at 5 ºC/min at different temperatures, respectively, after previously cooling the samples at 2 ºC/min.

All samples were first cooled down from the melt at 2 ºC min^{-1} and then subsequently heated at 5 ºC min^{-1} in order to reproduce the same thermal history as in Figure 6.13. During heating, WAXS and SAXS patterns were measured. Figure 6.14a displays the WAXS patterns taken at 25 ºC. All samples exhibit reflections at 2θ of 12.5; 14.9; 16.6; 19.0; 20.7; 22.4; 24.8; 27.4 and 28.9 º and correspond to the crystalline planes (103)/(004); (011); (110)/(200), (304)/(113), (204), (211), (016), (206)/(116) and (207)/(117) of the more stable α-PLLA phase, with orthorhombic unit cells with the following parameters: a = 10.73, b = 6.14 and c = 29.04 Å [67]. A related point to consider is that the peaks at 12.5, 20.7 and 28.9 º are characteristics for the α-phase and do not appear in the α'phase. In summary, all detected reflections correspond to the α-PLLA phase, independently of the nucleating agent used. In fact, close examination of the WAXS patterns indicated the total absence of the α' phase at all temperatures examined until crystals melt. These results indicate that the presence of lignin as well as the fast cooling process (50 ºC min^{-1}) does not promote the formation of the α'phase (see Figure 9.19a on the Appendix). Therefore, polymorphism of PLLA can be

excluded in the present work and should not be considered as a possible reason for double melting.

SAXS experiments were also performed and the results clearly showed that only one well defined scattering peak was present in all samples, with and without fillers. This maximum is due to the scattering of the crystalline lamellae stacks in PLA and can be assigned to the long period. Figure 6.14b provides an example of the SAXS measurements performed during heating at 5 ºC/min as a function of temperature. The long period or *d-spacing* of the scattering peaks can be calculated by Bragg´s law, and plotted as a function of temperature (see Figure 9.19 on the Appendix). The *d*-spacing increases as temperature increases in the range 120-140 ºC even before any significant melting has been detected by DSC indicating crystal annealing processes. After 140 ºC the increases in *d*-spacing are more pronounced as expected. The results obtained by SAXS clearly indicate that the samples are characterized by a single population of lamellar crystals and we can rule out the existence of two discrete populations of PLA crystals with distinct melting points. Therefore, the most likely explanation for the observed bimodal distribution of melting points in the sample is a complex reorganization (or partial melting/recrystallization/melting) of the crystals during the heating scans. A similar conclusion has been reached recently by Santoja-Blasco et al. by performing DSC experiments at various heating rates in double melting PLA samples of different molecular weights.[68]

Nucleation efficiency

The SN protocol described in the experimental part (see Chapter II. General Concepts) was used for the evaluation of the effectiveness of industrial lignins and talc as nucleating agents for PLA. In order to obtain the $T_{c,\,max}$ at the lowest T_s of *Domain II*, SN experiments were performed for neat PLA and the results are shown in Figure 6.15.

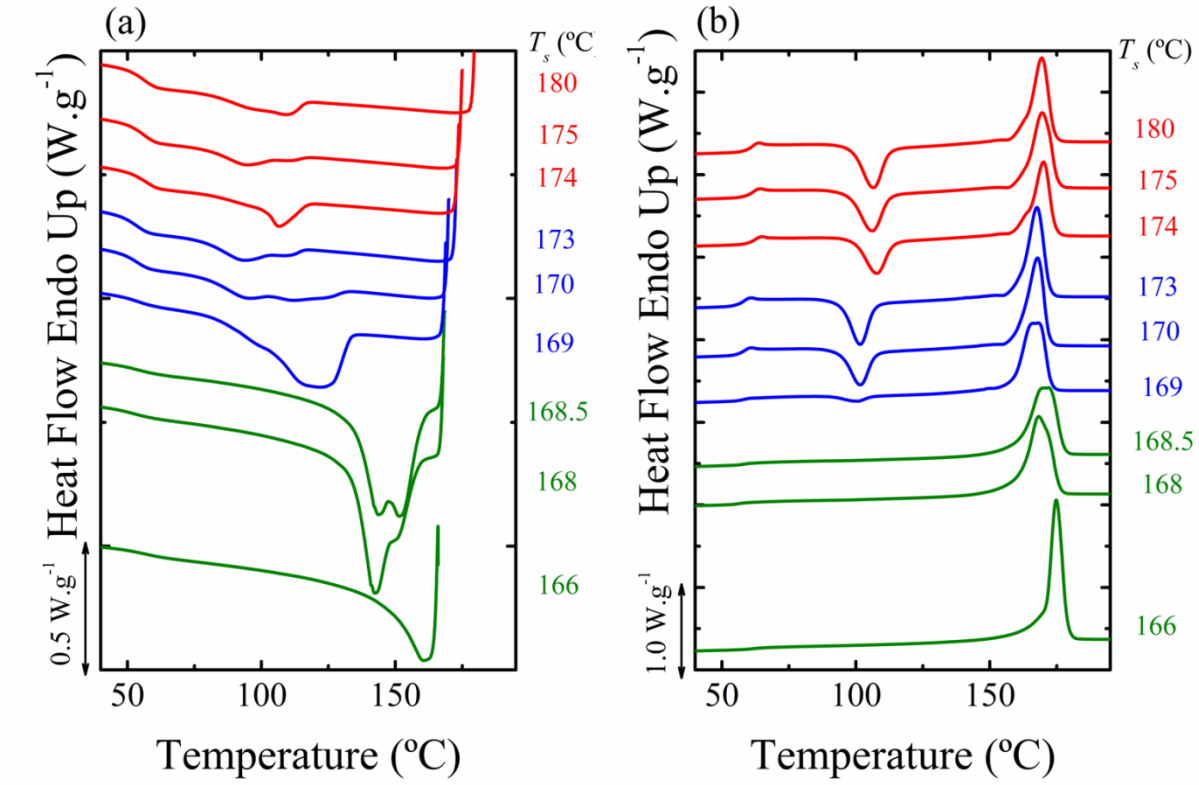

Figure 6.15. Self-nucleation of neat PLA. (a) DSC cooling scans from T_s (after the 5 min isothermal step at T_s was completed) and (b) DSC subsequent heating scans after the cooling scans shown in (a).

Figure 6.15a shows that the cooling scans present broad exotherms at high T_s (*i.e.*, *Domain I*) that become sharper at the lowest T_s of *Domain II* and in *Domain III*. This is attributed to the nucleating effect of self-nuclei (in *Domain II*) and self-nuclei and unmolten crystals (in *Domain III*) that enhanced the crystallization of the PLA. Heating scans displayed in Figure 6.15b show that the characteristic cold crystallization peak of neat PLA becomes smaller or disappears at the lowest T_s of *Domain II* and in *Domain III*, respectively. Based on the SN test, we have determined that the T_s of 169 ºC is the ideal self-nucleation temperature (*i.e.*, the T_s value that causes the maximum nucleation without annealing or the lowest T_s value within *Domain II*).

The *NE* of lignins and UT was calculated based on the crystallization behavior of neat PLA, self-nucleated PLA and nucleated PLA using the Equation 2.18 (See Chapter II. General Concepts)

The values determined by SN and non-isothermal DSC tests, as well as the calculated *NE* are summarized in Table 6.5.

Table 6.5. Nucleation Efficiency of UT, KL and OL for the prepared PLA/talc and PLA/lignin compounds

Sample	$T_{c,\,NA}$ (ºC)	$T_{c,\,PLA}$ (ºC)	$T_{c,\,max}$ (ºC)	***NE* (%)**
PLA	-	93.5	121.4	-
PLA/UT	115.9	-	-	80
PLA/KL	102.2	-	-	31
PLA/OL	101.1	-	-	27

Table 6.5 shows the calculated values of *NE* of industrial lignins and ultrafine talc. The results indicate that ultrafine talc is the best nucleating agent with a very high *NE* of 80%. Similar *NE* value of 81% for 1.5 wt% talc (Luzenac A3, d95 < 3 μm) in PLA (M_w = 120 kg.mol^{-1}, PLA from Futerro, Belgium with the content of 4% *D*-lactide) was reported by Carbone et al. [21].

Zhang et al. [69] determined a *NE* of only 14% for 0.5 wt% talc with a particle size of about 12 μm in PLLA (M_w = 155 kg.mol^{-1}, Corbion Purac). Additionally to the content of *D*-lactide in PLA, particle size of talc and molecular weight of PLA may also play a role on the *NE* values of talc.

NE values of about 27 - 31% of Organosolv lignin and Kraft lignin were determined in this work, for the first time, as far as we are aware for PLA/lignin compounds. UT is the best nucleating agent, but lignins also display a significant effect.

Since, *NE* of nucleating agents highly depends on their physical (particle size, shape, and morphology) and chemical (structural composition) properties as well; different *NE* values could be attributed to distinct values of nucleation energy barriers [7, 21, 70]. Based on the results, the particle size seems to be a major factor influencing the nucleation efficiency of additives.

Isothermal crystallization behavior determined by DSC

The inverse of the half-crystallization times obtained from isothermal crystallization experiments, which were performed by DSC using freshly dried samples in hermetically sealed aluminum pans, provide an experimental measure of the overall crystallization rate that includes both nucleation and growth contributions. Figure 6.16 shows the overall crystallization rate as a function of isothermal crystallization temperature for neat PLA, PLA/talc and PLA/lignin compounds.

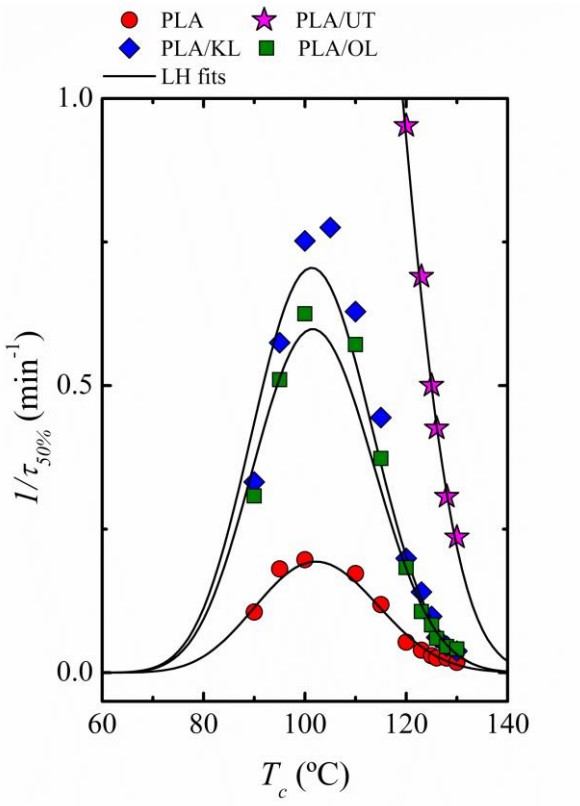

Figure 6.16. Overall crystallization rate ($1/\tau_{50\%}$) as a function of isothermal crystallization temperature for neat PLA and its blends with UT, KL and OL. The solid lines represents fits to the Lauritzen and Hoffman (LH) theory.

In Figure 6.16 it is observed that neat PLA, as well as nucleated PLA samples, exhibit the typical bell shape dependence on $1/\tau_{50\%}$ as a function T_c. In the case of the PLA/UT, the high nucleating effect of the UT controls the overall crystallization rate. Therefore only the nucleation dependence or nucleation control could be observed. On the other hand, all PLA samples with nucleating agents show an acceleration of $1/\tau_{50\%}$ in comparison with neat PLA in all the range of T_c values employed here. This behavior is due to the nucleating action of lignin and UT.

The $1/\tau_{50\%}$ values of PLA samples increase as follow: $1/\tau_{50\%}$ (PLA) < $1/\tau_{50\%}$ (PLA/OL) < $1/\tau_{50\%}$ (PLA/KL) < $1/\tau_{50\%}$ (PLA/UT). This behavior is consistent with the DSC results and the differences in nucleation efficiencies obtained above.

The data obtained during DSC isothermal crystallization experiments were analyzed using the Avrami fit, Equation 2.10 and Figure 2.3 (see Chapter II. General Concepts).

The overall crystallization rate constant *k* (see values on Table 9.8, Appendix) must be expressed as $k^{1/n}$ in order to obtain rate values expressed in s^{-1}. Once transformed in quantities with identical units, these complex overall crystallization rate constants follow the same trend observed in Figure 6.16, as expected.

The Avrami index values obtained by fitting the theory to the experimental data did not show significant differences between neat PLA and PLA with nucleating agents. The *n* values for all samples are in the range from 2.5 to 3.5, which indicates three-dimensional superstructures (*i.e.*, spherulites) that were nucleated instantaneously or sporadically, depending on T_c values.[71] These results correspond with the observations made by PLOM, in which spherulitic structures were found in all cases.

Figure 6.16 shows solid lines that correspond to mathematical fits to the Lauritzen and Hoffman (LH) theory, which can be applied to the DSC overall crystallization data. The LH theory could not be applied to the growth rate data presented in Table 6.6, in view of the limited temperature range in which satisfactory measurements were obtained and the large data scatter.

Table 6.6. Parameters obtained from fitting the Lauritzen and Hoffman Theory to the data of Figure 6.16.

Sample	$K_g^{\tau}\times10^{-5}$ **(K^2)**	σ **(erg cm^{-2})**	σ_e **(erg cm^{-2})**	$q\times10^{12}$ **(erg)**	R^2
PLA	11.9	6.14	668	3.11	0.9957
PLA/UT	9.91	6.14	562	2.61	0.9981
PLA/KL	11.2	6.14	634	2.95	0.9958
PLA/OL	11.0	6.14	623	2.90	0.9966

The inverse of the experimental half-crystallization time ($1/\tau_{50\%}$ (T)) based on Lauritzen and Hoffman model can be expressed as a function of ΔT as was shown in Chapter II. General Concepts.

The equilibrium melting point was calculated by the Hoffman-Weeks extrapolation and an approximate value of 215 ºC was obtained for all the samples. This value is in the range of T_m^0 values previously reported in the literature [72-74].

The LH parameters, which are shown in Table 6.6 were calculated from the data in Figure 6.16 by employing the Origin ® plug in developed by Lorenzo et al.[75] The employed values were U = 1500 cal mol^{-1}; a_0 = 4.1x10^{-8} cm, b_0 = 5.17 × 10^{-8} cm, ΔH_m=93.7 J g^{-1}; ρ_c = 1.359 g cm^{-3} and $T_{g\text{-}30}$ = 27.2 ºC. Table 5 shows the parameters obtained by the fits which represent both nucleation and growth since they have been derived from the isothermal crystallization kinetics data.

Table 6.6 shows that the nucleation effect of UT, KL and OL induces a reduction in the energy barrier for nucleation and growth (as K_g^{τ} is reduced). The high nucleation capacity of the UT is also reflected in the LH parameters, since the PLA/UT shows the lowest K_g^{τ} value, whereas the PLA/lignin compounds show intermediate values (*i.e.*, lower than PLA but higher than PLA/UT).

In a previous work [76], an acceleration factor (*AF*) defined as the ratio, $\frac{1/\tau_{50\%,NA}}{1/\tau_{50\%,neat}}$, of the overall crystallization rate of the polymer with a nucleating agent ($1/\tau_{50\%NA}$) and the overall crystallization rate of the neat polymer ($1/\tau_{50\%,neat}$) was employed for comparison purposes, since *NE* has not been determine for all polymer/nucleating pairs reported in the literature. In this way, $AF > 1$ indicates a nucleation effect, whereas $AF < 1$ indicates an anti-nucleation effect. It is worth noting that $1/\tau_{50\%}$ values can strongly depend on the selected T_c, thus the *AF* cannot directly quantify nucleation efficiency.

Table 6.7 shows that PLA/UT exhibits the higher values of *AF* followed by the PLA/KL and PLA/OL, which are qualitatively consistent with calculated *NE* values reported in this work. *AF* values of PLA/lignins systems have not been reported in the literature so far, since as far as the authors are aware, this is the first time that isothermal

crystallization tests have been performed on PLA/lignin compounds. *AF* factors of PHB, PET, PP and PCL with lignin calculated and compared in the work of Pérez-Camargo et al. [76] show that the nucleation ability of lignins depends on the polymer matrix in which they were incorporated. The origin of lignin and their physical and chemical properties could also affect their nucleation ability. It is accepted that talc is a very effective commercial inorganic nucleating agent and it is commonly used as a reference for comparing with other nucleating agents [21, 62, 77, 78]. Table 6.7 shows *AF* values of talc (with particles size about 10 μm) calculated based on the results of Battegazzore et al. [79] It can be seen that *AF* values depend on the concentration of talc as well as on *Tc*.

Table 6.7. Isothermal crystallization data and acceleration factors (AF).

Polymer/nucleating agent system	**Nucleating agent (%)**	$1/\tau_{50\%}$ **(T_c) (min^{-1}) (ºC)**	***AF* (T_c)**	**Reference**
PLA/UT	3	0.95 - 0.24 (120 - 130)	17.9 - 13.1 (120 - 130)	(this work)
PLA/KL	3	0.63 - 0.04 (110 - 130)	3.6 - 2.1 (110 - 130)	(this work)
PLA/OL	3	0.57 - 0.04 (110 - 130)	3.3 - 2.3 (110 - 130)	(this work)
PLA/talc	1	0.23 - 0.15 (100 - 110)	19 - 17.4 (100 - 110)	[77]
PLA/talc	2.5	0.33 - 0.16 (100 - 110)	27.2 - 19 (100 - 110)	[77]
PLA/talc	5	0.36 - 0.21	29.1 - 23.3	[77]

		(100 - 110)	(100 - 110)	
PLA/talc	10	0.46 - 0.24	37 - 28.1	[77]
		(100 - 110)	(100 - 110)	
PLA/talc	15	0.5 - 0.25	41 - 29.5	[77]
		(100 - 110)	(100 - 110)	

Thermal stability of PLA and nucleated PLA compounds

PLA is polyester with limited thermal stability and narrow thermal processing window. Some additives may contribute to the loss of molecular weight of PLA during melt processing. Therefore it is necessary for the practical use of nucleating agents to determine their influence on the thermal stability of PLA. Table 6.8 shows molecular weight properties of PLA and nucleated PLA compounds after melt mixing at 190 °C for 6 min. The results indicate a very slight decrease in M_n in samples with nucleating agents as compared to PLA, but given the experimental errors involved in GPC molecular weight determinations (of the order of 5-10%), the differences are not considered being significant.

Table 6.8. Molecular weight properties of PLA and nucleated PLA compounds.

Sample	$\boldsymbol{M_n}$ **(kDa)**	$\boldsymbol{M_w}$ **(kDa)**	$\boldsymbol{Đ}$
PLA	76	123	1.6
PLA/UT	73	117	1.6
PLA/KL	68	107	1.6
PLA/OL	69	110	1.6

The thermogravimetric curves and thermal data obtained under nitrogen atmosphere for PLA and nucleated PLA compounds are presented in Figure 6.17 and

Table 6.9. TGA results show that PLA has an onset degradation temperature of 351 °C. In the samples with nucleating agents, the temperature decreases between 2 and 6 ºC. Similarly, the values at 50% weight loss were very slightly shifted to the lower temperatures due to the presence of nucleating agents. It can be concluded that the addition of 3 wt% of lignins, as well as ultrafine talc, do not influence the thermal processing window of PLA.

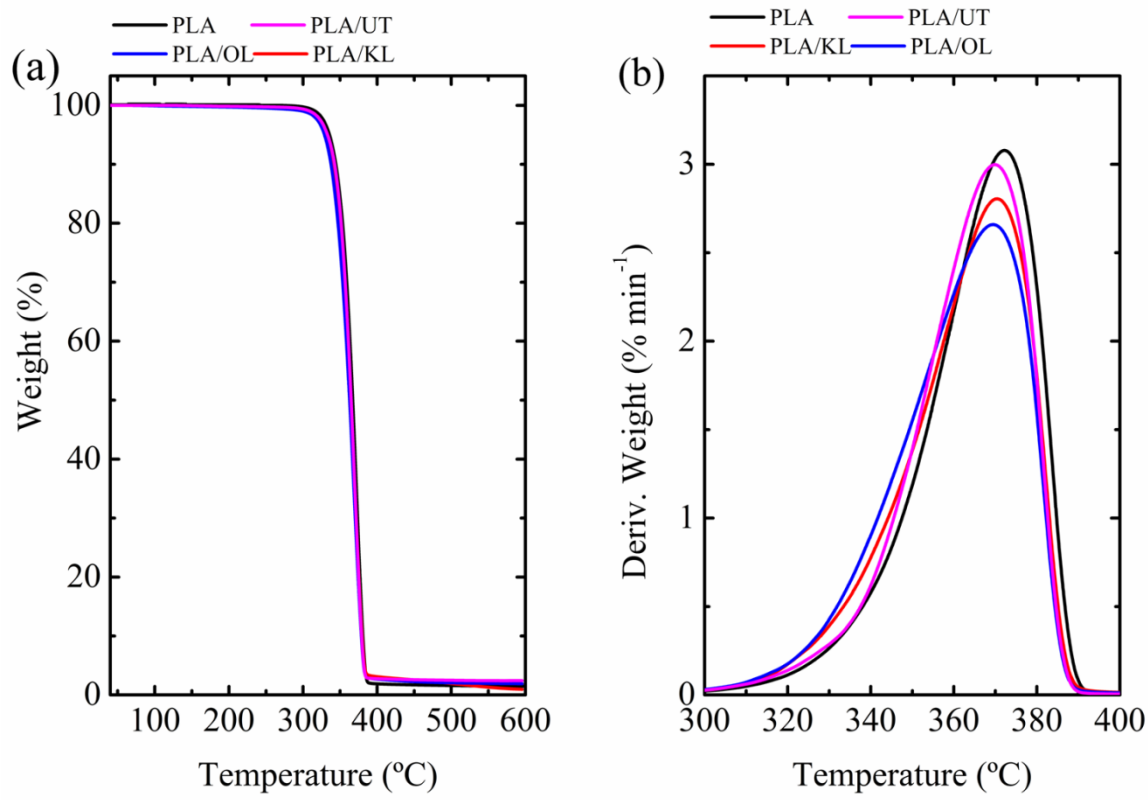

Figure 6.17. (a) TGA and (b) DTGA curves of PLA and nucleated PLA.

Table 6.9. TGA and DTGA characteristics of PLA and nucleated PLA compounds.

Sample	T_{onset} **(°C)**	$T_{10\%}$ **(°C)**	$T_{50\%}$ ***(°C)***	***DTGA peak value (°C)***
PLA	351	344	367	372
PLA/UT	349	343	365	370
PLA/KL	347	339	365	371
PLA/OL	345	338	363	370

* T_{onset} – onset of the thermal decomposition, $T_{10\%}$, $T_{50\%}$ - temperatures with 10 and 50% mass loss of sample, DTGA peak value – maximum degradation temperature

6.3.Conclusions

In the case of the PCL-*g*-lignin, it was found that the competition between lignin nucleation and intermolecular interactions determines the crystallization behavior. At low lignin contents (2–5 wt %), the nucleation effect of lignin dominates the behavior since only a limited number of hydrogen bonds between lignin and PCL can be established.

Evidences of the nucleating effect of lignin were gathered in terms of morphological changes (TEM) and calorimetric properties (DSC). The *NE* values obtained demonstrate that lignin is a super-nucleating agent or it is very close to being one, at low lignin contents. Upon increasing lignin content beyond 5 wt %, the nucleation effect progressively declines as the intermolecular interactions limit the diffusion of PCL chains. Lignin contents of 29 and 37 wt % induce very large antinucleation effects in the sample. The hydrogen bonding interactions, previously documented by FTIR and rheology analysis, are equivalent to physical crosslinks that limit crystallization and lamellar sizes, as gathered from the large decreases in both crystallization and melting points. Additionally, the overall crystallization kinetics is slow down to values much lower than in neat PCL. SSA experiments indicate that the interactions are so strong that they act as crosslinks that limit the annealing capabilities of PCL.

The results shown in this work illustrate how the thermal properties of PCL can be tailored by grafting onto soda lignin, which presents a high potential as renewable aromatic building block. Other specific properties such as antioxidant, antifungal, and

fire-resistance properties would be also a strong function of the architecture and composition of such copolymers and should be investigated.

PLA was melt mixed with 3 wt% of different nucleating agents: Kraft lignin, Organosolv lignin and ultrafine talc. The nucleating efficiency was determined after self-nucleation studies of the PLA employed. Both lignins promote the nucleation of PLA effectively (*NE* of approximately 30%); however ultrafine talc is a much better nucleating agent (*NE* of about 80%). It was demonstrated that the spherulitic growth rate is not affected by the addition of any of the three nucleating agents employed here.

The overall crystallization rate, on the other hand, increases in the order: PLA/UT > PLA/KL > PLA/OL > PLA, in correspondence to the *NE* of the additives. The Lauritzen and Hoffman theory revealed that Kraft and Organosolv lignins, as well as ultrafine talc, reduce the energy barrier for nucleation and growth. Our results showed that industrial lignins can accelerate PLA crystallization by their nucleating action while preserving the biobased and biodegradable character of the PLA/nucleating agent mixture.

6.4.References

[1] S. Laurichesse, L. Avérous, Synthesis, thermal properties, rheological and mechanical behaviors of lignins-grafted-poly(ε-caprolactone), Polymer 54 (2013) 3882-3890.
[2] T. Hatakeyama, Y. Izuta, S. Hirose, H. Hatakeyama, Phase transitions of lignin-based polycaprolactones and their polyurethane derivatives, Polymer 43 (2002) 1177-1182.
[3] S. Laurichesse, L. Avérous, Chemical modification of lignins: Towards biobased polymers, Prog. Polym. Sci. 39 (2014) 1266-1290.
[4] Y.-L. Chung, J.V. Olsson, R.J. Li, C.W. Frank, R.M. Waymouth, S.L. Billington, E.S. Sattely, A Renewable Lignin–Lactide Copolymer and Application in Biobased Composites, ACS Sustainable Chemistry & Engineering 1 (2013) 1231-1238.
[5] A. Kovalcik, R.A. Pérez-Camargo, C. Fürst, P. Kucharczyk, A.J. Müller, Nucleating efficiency and thermal stability of industrial non-purified lignins and ultrafine talc in poly(lactic acid) (PLA), Polym. Degrad. Stab. 142 (2017) 244-254.
[6] X. Shi, G. Zhang, V.T. Phuong, A. Lazzeri, Synergistic Effects of Nucleating Agents and Plasticizers on the Crystallization Behavior of Poly(lactic acid), Molecules 20 (2015).
[7] S. Ouchiar, G. Stoclet, C. Cabaret, V. Gloaguen, Influence of the Filler Nature on the Crystalline Structure of Polylactide-Based Nanocomposites: New Insights into the Nucleating Effect, Macromolecules (Washington, DC, U. S.) 49 (2016) 2782-2790.

[8] W.-C. Lai, Thermal Behavior and Crystal Structure of Poly(l-lactic acid) with 1,3:2,4-Dibenzylidene-d-sorbitol, The Journal of Physical Chemistry B 115 (2011) 11029-11037.
[9] P. Ma, Y. Xu, D. Wang, W. Dong, M. Chen, Rapid Crystallization of Poly(lactic acid) by Using Tailor-Made Oxalamide Derivatives as Novel Soluble-Type Nucleating Agents, Industrial & Engineering Chemistry Research 53 (2014) 12888-12892.
[10] V. Nagarajan, K. Zhang, M. Misra, A.K. Mohanty, Overcoming the Fundamental Challenges in Improving the Impact Strength and Crystallinity of PLA Biocomposites: Influence of Nucleating Agent and Mold Temperature, ACS Applied Materials & Interfaces 7 (2015) 11203-11214.
[11] V. Nagarajan, A.K. Mohanty, M. Misra, Crystallization behavior and morphology of polylactic acid (PLA) with aromatic sulfonate derivative, J. Appl. Polym. Sci. 133 (2016).
[12] T. Xu, A. Zhang, Y. Zhao, Z. Han, L. Xue, Crystallization kinetics and morphology of biodegradable poly(lactic acid) with a hydrazide nucleating agent, Polym. Test. 45 (2015) 101-106.
[13] Y.-H. Cai, Y.-H. Zhang, L.-S. Zhao, Role of N,N'-bis(1H-benzotriazole) adipic acid acethydrazide in crystallization nucleating effect and melting behavior of poly(L-lactic acid), Journal of Polymer Research 22 (2015) 246.
[14] Y. Fan, J. Zhu, S. Yan, X. Chen, J. Yin, Nucleating effect and crystal morphology controlling based on binary phase behavior between organic nucleating agent and poly(l-lactic acid), Polymer 67 (2015) 63-71.
[15] M. Kodal, H. Sirin, G. Ozkoc, Non-isothermal crystallization kinetics of PEG plasticized PLA/G-POSS nanocomposites, Polym. Compos. 38 (2017) 1378-1389.
[16] C. Mu, L. Xue, J. Zhu, M. Jiang, Z. Zhou, Mechanical and Thermal Properties of Toughened Poly(L-lactic) Acid and Lignin Blends, BioResources; Vol 9, No 3 (2014) (2014).
[17] W. Yang, E. Fortunati, F. Dominici, J.M. Kenny, D. Puglia, Effect of processing conditions and lignin content on thermal, mechanical and degradative behavior of lignin nanoparticles/polylactic (acid) bionanocomposites prepared by melt extrusion and solvent casting, Eur. Polym. J. 71 (2015) 126-139.
[18] A. Grząbka-Zasadzińska, Ł. Klapiszewski, K. Bula, T. Jesionowski, S. Borysiak, Supermolecular structure and nucleation ability of polylactide-based composites with silica/lignin hybrid fillers, J. Therm. Anal. Calorim. 126 (2016) 263-275.
[19] N. Kawamoto, A. Sakai, T. Horikoshi, T. Urushihara, E. Tobita, Nucleating agent for poly(L-lactic acid)—An optimization of chemical structure of hydrazide compound for advanced nucleation ability, J. Appl. Polym. Sci. 103 (2007) 198-203.
[20] Y. Tachibana, T. Maeda, O. Ito, Y. Maeda, M. Kunioka, Biobased myo-inositol as nucleator and stabilizer for poly(lactic acid), Polym. Degrad. Stab. 95 (2010) 1321-1329.
[21] M.J. Carbone, M. Vanhalle, B. Goderis, P. Van Puyvelde, Amino acids and poly(amino acids) as nucleating agents for poly(lactic acid), J. Polym. Eng. 35 (2015) 169-180.
[22] P. Chen, H. Zhou, W. Liu, M. Zhang, Z. Du, X. Wang, The synergistic effect of zinc oxide and phenylphosphonic acid zinc salt on the crystallization behavior of poly (lactic acid), Polym. Degrad. Stab. 122 (2015) 25-35.

[23] G.-X. Zou, Q.-W. Jiao, X. Zhang, C.-X. Zhao, J.-C. Li, Crystallization behavior and morphology of poly(lactic acid) with a novel nucleating agent, J. Appl. Polym. Sci. 132 (2015).
[24] W. Ouyang, Y. Huang, H. Luo, D. Wang, Poly(Lactic Acid) Blended with Cellulolytic Enzyme Lignin: Mechanical and Thermal Properties and Morphology Evaluation, J. Polym. Environ. 20 (2012) 1-9.
[25] M.A. Rahman, D. De Santis, G. Spagnoli, G. Ramorino, M. Penco, V.T. Phuong, A. Lazzeri, Biocomposites based on lignin and plasticized poly(L-lactic acid), J. Appl. Polym. Sci. 129 (2013) 202-214.
[26] O. Gordobil, I. Egüés, R. Llano-Ponte, J. Labidi, Physicochemical properties of PLA lignin blends, Polym. Degrad. Stab. 108 (2014) 330-338.
[27] S. Kim, S. Oh, J. Lee, N. Ahn, H. Roh, J. Cho, B. Chun, J. Park, Effect of alkyl-chain-modified lignin in the PLA matrix, Fibers and Polymers 15 (2014) 2458-2465.
[28] R. Liu, Y. Peng, J. Cao, Y. Chen, Comparison on properties of lignocellulosic flour/polymer composites by using wood, cellulose, and lignin flours as fillers, Compos. Sci. Technol. 103 (2014) 1-7.
[29] M.A.S. Anwer, H.E. Naguib, A. Celzard, V. Fierro, Comparison of the thermal, dynamic mechanical and morphological properties of PLA-Lignin & PLA-Tannin particulate green composites, Composites Part B: Engineering 82 (2015) 92-99.
[30] O. Gordobil, R. Delucis, I. Egüés, J. Labidi, Kraft lignin as filler in PLA to improve ductility and thermal properties, Industrial Crops and Products 72 (2015) 46-53.
[31] I. Spiridon, K. Leluk, A.M. Resmerita, R.N. Darie, Evaluation of PLA–lignin bioplastics properties before and after accelerated weathering, Composites Part B: Engineering 69 (2015) 342-349.
[32] J. Zhu, L. Xue, W. Wei, C. Mu, M. Jiang, Z. Zhou, Modification of Lignin with Silane Coupling Agent to Improve the Interface of Poly(L-lactic) Acid/Lignin Composites, BioResources; Vol 10, No 3 (2015) (2015).
[33] Influence of lignin on morphology, structure and thermal behavior of polylactic acid-based biocomposites, AIP Conference Proceedings 1736 (2016) 020133.
[34] L. Costes, F. Laoutid, M. Aguedo, A. Richel, S. Brohez, C. Delvosalle, P. Dubois, Phosphorus and nitrogen derivatization as efficient route for improvement of lignin flame retardant action in PLA, Eur. Polym. J. 84 (2016) 652-667.
[35] W. Yang, F. Dominici, E. Fortunati, J.M. Kenny, D. Puglia, Effect of lignin nanoparticles and masterbatch procedures on the final properties of glycidyl methacrylate-g-poly (lactic acid) films before and after accelerated UV weathering, Industrial Crops and Products 77 (2015) 833-844.
[36] R. Kumar Singla, S.N. Maiti, A.K. Ghosh, Crystallization, Morphological, and Mechanical Response of Poly(Lactic Acid)/Lignin-Based Biodegradable Composites, Polymer-Plastics Technology and Engineering 55 (2016) 475-485.
[37] C. Vila, V. Santos, B. Saake, J.C. Parajó, Manufacture, Characterization, and Properties of Poly-(lactic acid) and its Blends with Esterified Pine Lignin, 2016.
[38] W. Yang, E. Fortunati, F. Dominici, G. Giovanale, A. Mazzaglia, G.M. Balestra, J.M. Kenny, D. Puglia, Synergic effect of cellulose and lignin nanostructures in PLA based systems for food antibacterial packaging, Eur. Polym. J. 79 (2016) 1-12.
[39] J. Li, Y. He, Y. Inoue, Thermal and mechanical properties of biodegradable blends of poly(L-lactic acid) and lignin, Polym. Int. 52 (2003) 949-955.

[40] R. Chen, M.A. Abdelwahab, M. Misra, A.K. Mohanty, Biobased Ternary Blends of Lignin, Poly(Lactic Acid), and Poly(Butylene Adipate-co-Terephthalate): The Effect of Lignin Heterogeneity on Blend Morphology and Compatibility, J. Polym. Environ. 22 (2014) 439-448.
[41] S. Wang, Y. Li, H. Xiang, Z. Zhou, T. Chang, M. Zhu, Low cost carbon fibers from bio-renewable Lignin/Poly(lactic acid) (PLA) blends, Compos. Sci. Technol. 119 (2015) 20-25.
[42] B. Fillon, B. Lotz, A. Thierry, J.C. Wittmann, Self-nucleation and enhanced nucleation of polymers. Definition of a convenient calorimetric "efficiency scale" and evaluation of nucleating additives in isotactic polypropylene (α phase), J. Polym. Sci., Part B: Polym. Phys. 31 (1993) 1395-1405.
[43] A.J. Müller, M.L. Arnal, M. Trujillo, A.T. Lorenzo, Super-nucleation in nanocomposites and confinement effects on the crystallizable components within block copolymers, miktoarm star copolymers and nanocomposites, Eur. Polym. J. 47 (2011) 614-629.
[44] D. Priftis, G. Sakellariou, N. Hadjichristidis, E.K. Penott, A.T. Lorenzo, A.J. Müller, Surface modification of multiwalled carbon nanotubes with biocompatible polymers via ring opening and living anionic surface initiated polymerization. Kinetics and crystallization behavior, J. Polym. Sci., Part A: Polym. Chem. 47 (2009) 4379-4390.
[45] R.A. Pérez, M.E. Córdova, J.V. López, J.N. Hoskins, B. Zhang, S.M. Grayson, A.J. Müller, Nucleation, crystallization, self-nucleation and thermal fractionation of cyclic and linear poly(ε-caprolactone)s, React. Funct. Polym. 80 (2014) 71-82.
[46] J.G. Fatou, C. Marco, L. Mandelkern, The crystallization kinetics of low-molecular-weight polyethylene fractions, Polymer 31 (1990) 890-898.
[47] J.G. Fatou, C. Marco, L. Mandelkern, The influence of molecular weight on the regime crystallization of linear polyethylene, Polymer 31 (1990) 1685-1693.
[48] L. Mandelkern, J.G. Fatou, K. Ohno, The molecular weight dependence of the crystallization rate for linear polyethylene fractions, Journal of Polymer Science Part B: Polymer Letters 6 (1968) 615-619.
[49] E. Ergoz, J.G. Fatou, L. Mandelkern, Molecular Weight Dependence of the Crystallization Kinetics of Linear Polyethylene. I. Experimental Results, Macromolecules 5 (1972) 147-157.
[50] A.T. Lorenzo, M.L. Arnal, J. Albuerne, A.J. Müller, DSC isothermal polymer crystallization kinetics measurements and the use of the Avrami equation to fit the data: Guidelines to avoid common problems, Polym. Test. 26 (2007) 222-231.
[51] M. Avrami, Granulation, phase change, and microstructure kinetics of phase change. III, The Journal of Chemical Physics 9 (1941) 177-184.
[52] H.H. Su, H.L. Chen, A. Díaz, M.T. Casas, J. Puiggalí, J.N. Hoskins, S.M. Grayson, R.A. Pérez, A.J. Müller, New insights on the crystallization and melting of cyclic PCL chains on the basis of a modified Thomson-Gibbs equation, Polymer (United Kingdom) 54 (2013) 846-859.
[53] B. Fillon, J.C. Wittmann, B. Lotz, A. Thierry, Self-nucleation and recrystallization of isotactic polypropylene (α phase) investigated by differential scanning calorimetry, J. Polym. Sci., Part B: Polym. Phys. 31 (1993) 1383-1393.
[54] R.A. Pérez, J.V. López, J.N. Hoskins, B. Zhang, S.M. Grayson, M.T. Casas, J. Puiggalí, A.J. Müller, Nucleation and antinucleation effects of functionalized carbon

nanotubes on cyclic and linear Poly(ε-caprolactones), Macromolecules 47 (2014) 3553-3566.
[55] M. Trujillo, M.L. Arnal, A.J. Müller, M.A. Mujica, C. Urbina De Navarro, B. Ruelle, P. Dubois, Supernucleation and crystallization regime change provoked by MWNT addition to poly(ε-caprolactone), Polymer 53 (2012) 832-841.
[56] A.J. Müller, R.M. Michell, R.A. Pérez, A.T. Lorenzo, Successive Self-nucleation and Annealing (SSA): Correct design of thermal protocol and applications, Eur. Polym. J. 65 (2015) 132-154.
[57] C. Mu, L. Xue, J. Zhu, M. Jiang, Z. Zhou, Mechanical and thermal properties of toughened poly(L-lactic) acid and lignin blends, BioResources 9 (2014) 5557-5566, 5510 pp.
[58] S. Domenek, A. Louaifi, A. Guinault, S. Baumberger, Potential of Lignins as Antioxidant Additive in Active Biodegradable Packaging Materials, J. Polym. Environ. 21 (2013) 692-701.
[59] A. Cayla, F. Rault, S. Giraud, F. Salaun, V. Fierro, A. Celzard, PLA with intumescent system containing lignin and ammonium polyphosphate for flame retardant textile, Polymers (Basel, Switz.) 8 (2016) 331/331-331/316.
[60] M. Pluta, A. Galeski, Crystalline and supermolecular structure of polylactide in relation to the crystallization method, Journal of Applied Polymer Science 86 (2002) 1386-1395.
[61] M. Yasuniwa, K. Sakamo, Y. Ono, W. Kawahara, Melting behavior of poly(L-lactic acid): X-ray and DSC analyses of the melting process, Polymer 49 (2008) 1943-1951.
[62] M. Yasuniwa, S. Tsubakihara, Y. Sugimoto, C. Nakafuku, Thermal analysis of the double-melting behavior of poly(L-lactic acid), J. Polym. Sci., Part B: Polym. Phys. 42 (2003) 25-32.
[63] Z. Kulinski, E. Piorkowska, Crystallization, structure and properties of plasticized poly(l-lactide), Polymer 46 (2005) 10290-10300.
[64] E. Zuza, J.M. Ugartemendia, A. Lopez, E. Meaurio, A. Lejardi, J.-R. Sarasua, Glass transition behavior and dynamic fragility in polylactides containing mobile and rigid amorphous fractions, Polymer 49 (2008) 4427-4432.
[65] A. Magon, M. Pyda, Study of crystalline and amorphous phases of biodegradable poly(lactic acid) by advanced thermal analysis, Polymer 50 (2009) 3967-3973.
[66] P. Klonos, Z. Terzopoulou, S. Koutsoumpis, S. Zidropoulos, S. Kripotou, G.Z. Papageorgiou, D.N. Bikiaris, A. Kyritsis, P. Pissis, Rigid amorphous fraction and segmental dynamics in nanocomposites based on poly (l–lactic acid) and nano-inclusions of 1–3D geometry studied by thermal and dielectric techniques, European Polymer Journal 82 (2016) 16-34.
[67] M.C. Righetti, M. Gazzano, M.L. Di Lorenzo, R. Androsch, Enthalpy of melting of α′- and α-crystals of poly(l-lactic acid), European Polymer Journal 70 (2015) 215-220.
[68] L. Santonja-Blasco, A. Ribes-Greus, R.G. Alamo, Comparative thermal, biological and photodegradation kinetics of polylactide and effect on crystallization rates, Polym. Degrad. Stab. 98 (2013) 771-784.
[69] X. Zhang, L. Meng, G. Li, N. Liang, J. Zhang, Z. Zhu, R. Wang, Effect of nucleating agents on the crystallization behavior and heat resistance of poly(L-lactide), J. Appl. Polym. Sci. 133 (2016) n/a.

[70] T. Urushihara, K. Okada, K. Watanabe, A. Toda, N. Kawamoto, M. Hikosaka, Acceleration mechanism in critical nucleation of polymers by epitaxy of nucleating agent, Polymer journal 41 (2009) 228-236.
[71] V. Nagarajan, A.K. Mohanty, M. Misra, Crystallization behavior and morphology of polylactic acid (PLA) with aromatic sulfonate derivative, J. Appl. Polym. Sci. 133 (2016) n/a.
[72] R. Vasanthakumari, A.J. Pennings, Crystallization kinetics of poly(l-lactic acid), Polymer 24 (1983) 175-178.
[73] H. Tsuji, Y. Ikada, Properties and morphologies of poly (L-lactide): 1. Annealing condition effects on properties and morphologies of poly (L-lactide), Polymer 36 (1995) 2709-2716.
[74] J. Huang, M.S. Lisowski, J. Runt, E.S. Hall, R.T. Kean, N. Buehler, J. Lin, Crystallization and microstructure of poly (l-lactide-co-meso-lactide) copolymers, Macromolecules 31 (1998) 2593-2599.
[75] A.T. Lorenzo, M.L. Arnal, J. Albuerne, A.J. Mueller, DSC isothermal polymer crystallization kinetics measurements and the use of the Avrami equation to fit the data: Guidelines to avoid common problems, Polym. Test. 26 (2007) 222-231.
[76] R.A. Perez-Camargo, G. Saenz, S. Laurichesse, M.T. Casas, J. Puiggali, L. Averous, A.J. Mueller, Nucleation, Crystallization, and Thermal Fractionation of Poly (ε-Caprolactone)-Grafted-Lignin: Effects of Grafted Chains Length and Lignin Content, J. Polym. Sci., Part B: Polym. Phys. 53 (2015) 1736-1750.
[77] V. Peinado, P. Castell, L. García, Á. Fernández, Effect of Extrusion on the Mechanical and Rheological Properties of a Reinforced Poly (Lactic Acid): Reprocessing and Recycling of Biobased Materials, Materials 8 (2015) 7106-7117.
[78] L. Jiang, T. Shen, P. Xu, X. Zhao, X. Li, W. Dong, P. Ma, M. Chen, Crystallization modification of poly(lactide) by using nucleating agents and stereocomplexation, e-Polym. 16 (2016) 1-13.
[79] D. Battegazzore, S. Bocchini, A. Frache, Crystallization kinetics of poly(lactic acid)/talc composites, eXPRESS Polym. Lett. 5 (2011) 849-858.

CHAPTER VII.

BIODEGRADABLE POLYMERS/CARBON NANOTUBES BLENDS

Carbon nanotubes have been using as nucleating agents for a large number of polymers, due to their excellent conductive properties. However, during the blending process aggregation of CNT frequently occur, causing a loss of their effectiveness. Because of this, an important number of researchers have focused in avoiding such aggregation, therefore chemical ways (*i.e.*, using the approach of grafting to and grafting from) in which the carbon nanotubes are attach to an specific chemical group, or even a polymeric chains have been used. The main problems of these chemical routes are the cost and their escalation process to the industry. For this reason, research has also been focused in achieving good dispersions without using chemical processes. An example of this is the commercial formulation of masterbatches that may be miscible with the polymeric matrix allowing the migration from the masterbatch to the matrix. This strategy is studied and compared with treated carbon nanotubes in the first part of the present chapter.[1]

In the second part of this chapter, biodegradable commercial homopolymers, such as PBS and PCL, were blended with a commercial masterbatch of PC/MWCNT. The blends used were PCL/(PC/MWCNT)[2] and PBS/(PC/MWCNT). These blends were analysed through non-isothermal and isothermal DSC, SAXS/WAXS measurements, and the nucleating efficiency of the masterbatch were evaluated according to the equation proposed by Fillon et al.[3, 4]

7.1.Results and Discussion

7.1.1. Nanocomposites and Nanohybrids

The code of the samples used in this section as well as a detail description of the employed materials and methods are in Table 3.4 and Chapter III. Experimental Part. In general terms the notation PCL_xM_y and PCL_xNH_y are used to specify that the material is a Nanocomposite or a Nanohybrid, respectively.

In Figure 7.1, the clear exothermic peaks during cooling are due to the crystallization of the PCL (Figure 7.1a). In the subsequent heating scans, the sharp endothermic peaks represent the melting of the crystals formed during the previous step (Figure 7.1b).

The crystallization temperature (T_c) is shifted to higher values as the amount of carbon nanotubes increases, for both systems. This behavior has been already reported by several authors in the past and it is associated with the nucleating ability of CNTs. [5-7] MWCNTs possess a large surface/volume ratio that provides an ideal substrate for the nucleation of polymer chains.[8-25]

Figure 7.2a shows the variation of the T_c with MWCNT content. The dramatic increase in T_c (16.2 °C) with only 1 wt% of MWCNT is an example of the nucleating capacity of the unmodified MWCNT. Similarly, the modified MWCNTs are able to increase T_c (15.1 °C) (see $PCL_{99}NH_1$).

In Figure 7.2a it is also observed that T_c is shifted to higher values as the unmodified MWCNT content is increased in the nanocomposites. The increase between 0.25 and 1 wt% of MWCNTs is higher than the one presented in a range of 1 to 3 wt%. This behavior is indicative of a saturation of the nucleating effect after 1 wt% loading with plain MWCNTs.

In contrast, for the modified MWCNTs, *i.e.*, in the nanohybrids, the trend is more complex because of the presence of PCL grafted chains onto the MWCNT surfaces. The grafted MWCNTs have a pearl-necklace like structure for some of the nanotubes. However, all the nanotubes are not covered by the grafted PCL chains. As a consequence, the applied chemical modification disentangles the CNTs but do not cover all the surface of the nanotubes, improving the amount of available MWCNT surface for the PCL nucleation. The drop in T_c values after 0.25 wt% and their recovery at higher loadings are attributed to a competition between the nucleation effect of MWCNT and the plasticization effect of both 'free' PCL and PCL chains attached to the MWCNTs, which have a lower M_n values (*i.e.*, 12,000 and 500-1,000 g/mol, respectively) than the neat PCL matrix (*i.e.*, 50,000 g/mol). As the MWCNT content increases in the hybrid materials, the amount of low M_n PCL chains also increases (see Table 7.1). The low molecular weight PCL needs larger under-cooling than the high molecular weight to crystallize[26]. As a consequence, the shorter chains are molten during the crystallization process

of the matrix, exhibiting a plasticization effect; as a result the undercooling needed by the PCL matrix should be larger as the amount of free PCL increases.

Müller et al. have studied supernucleation[13, 25, 27, 28] effects for PEO-*g*-CNT, PCL-*g*-CNT and PE/CNT *in situ* polymerized nanocomposites. The term supernucleation refers to the nucleation by heterogeneities with efficiencies higher than the own polymer crystal fragments (see Self-nucleation and nucleation efficiency section in Chapter II. General Concepts and Chapter III. Experimental Part). A characteristic of this behavior is a large increase in T_c. Table 7.1 summarizes the results reported in the literature for PCL/CNT systems.

Table 7.1. Crystallization temperature (T_c) shift (difference between the T_c value of neat PCL and the T_c value of the PCL with CNTs) for different PCL/CNT systems reported in the literature.

System	MW or SWCNT (wt%)	Shift in T_c (°C)	Ref.
PCL/CNT	0.5	14	[27]
PCL/MWNT	5	2	[8]
PCL/MWNT	10	9	[9]
	5	10	
PCL-*g*-SWNT	5	14	[11]
PCL-*g*-fMWNT	2	4.5	[29]
PCL/MWCNT	0.25	13.6	This work
	0.3	11.9	
	0.5	14.1	
	0.75	15.3	
	1	16.2	
	2	16.5	
	3	16.7	
PCL/PCL-*g*-MWNT	0.25	16.6	This work
	0.5	13.5	
	0.75	15.3	
	1	15.1	

2	15.6
3	15.7

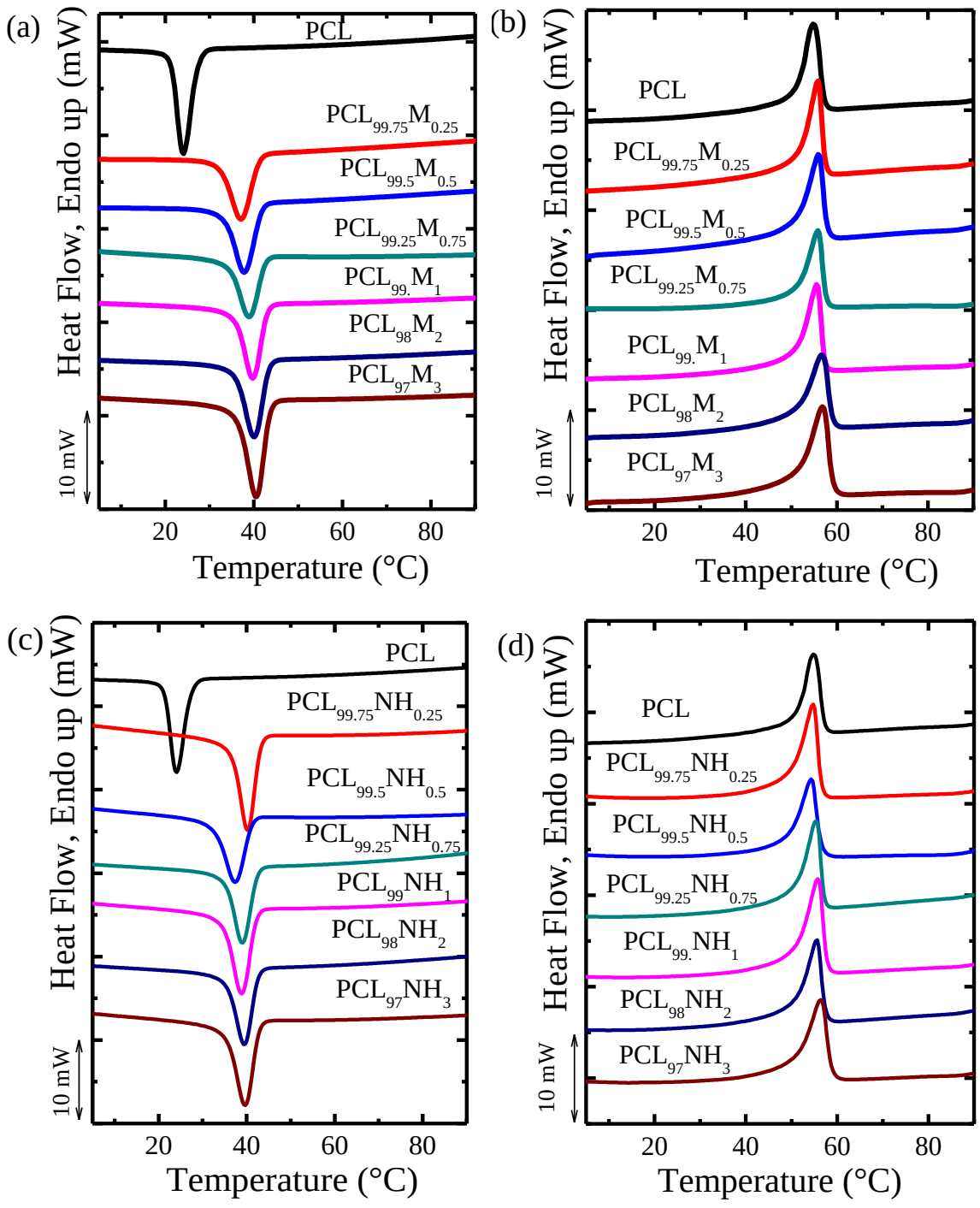
(a)
PCL
PCL99.75M0.25
PCL99.5M0.5
PCL99.25M0.75
PCL99.M1
PCL98M2
PCL97M3
10 mW
Heat Flow, Endo up (mW)
20
40
60
80
Temperature (°C)
(b)
PCL
PCL99.75M0.25
PCL99.5M0.5
PCL99.25M0.75
PCL99.M1
PCL98M2
PCL97M3
10 mW
Heat Flow, Endo up (mW)
20
40
60
80
Temperature (°C)
(c)
PCL
PCL99.75NH0.25
PCL99.5NH0.5
PCL99.25NH0.75
PCL99NH1
PCL98NH2
PCL97NH3
10 mW
Heat Flow, Endo up (mW)
20
40
60
80
Temperature (°C)
(d)
PCL
PCL99.75NH0.25
PCL99.5NH0.5
PCL99.25NH0.75
PCL99.NH1
PCL98NH2
PCL97NH3
10 mW
Heat Flow, Endo up (mW)
20
40
60
80
Temperature (°C)

Figure 7.1. DSC cooling and heating scans at 20 °C/min for the indicated nanocomposites and nanohybrids.

Not all reported works on PCL/CNT result in an increase in T_c. In fact in some cases an anti-nucleation effect has been reported. For instance, Jana et al.[29] reported a small decrease in T_c values for PCL-*g*-CNT nanocomposites prepared by a "grafting to" procedure. This contrasts with their report of a decrease in spherulitic size. The efficiency of a nucleating agent depends on, among other factors, the quality of the dispersion and distribution of the particles. According to the PLOM images showed by Jana et al., the quality of the distribution and dispersion was poor (as many agglomerates were visible), and it is possible that this originated the reduction in crystallization temperature.

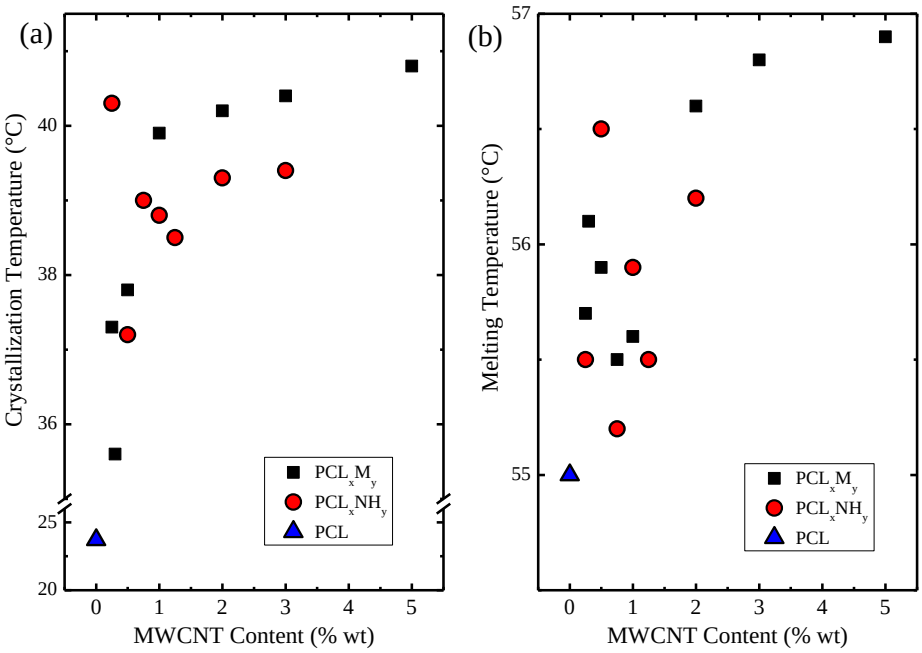

Figure 7.2. Influence of MWCNT content on (a) crystallization and (b) peak melting temperatures.

Figure 7.2b as well as Table 7.2 show that the melting temperature (T_m) remains almost constant (*i.e.*, it changes in between 55 and 57 °C) with the increase of the MWCNT content, as it is expected when a nucleating agent is employed. Although, it is worth mentioning that an increase of T_m has been reported in supernucleated PCL/CNT systems.[13, 27]

Table 7.2 shows the variations of the crystallization degree for both systems. The calculations were performed employing an equilibrium melting enthalpy for a 100% crystalline PCL sample of 136 J/g.[30-32] In both cases, an increase in the degree of crystallinity is observed upon MWCNT addition. In general the increase in MWCNT content results in an increase of X_c, although the trend is not monotonic. For example, the samples $PCL_{99.25}M_{0.75}$ and $PCL_{99.75}M_{0.25}$ exhibit apparent reductions in X_c, but the differences are small and the error in enthalpy determination by DSC can be as large as 10-15%.

Table 7.2. Crystallization and melting temperatures, normalized heat of crystallization and fusion, and degree of crystallinity (X_c) for the nanocomposites.

Sample	T_c (°C)	ΔH_c^n (J/g)	T_m (°C)	ΔH_m^n (J/g)	X_c (%)
PCL	23.7	51	55.0	54	40
$PCL_{99.75}M_{0.25}$	37.3	47	55.7	50	37
$PCL_{99.3}M_{0.3}$	35.6	56	56.1	58	42
$PCL_{99.5}M_{0.5}$	37.8	52	55.9	58	42
$PCL_{99.25}M_{0.75}$	39.0	47	55.5	52	38
$PCL_{99}M_1$	39.9	50	55.6	54	40
$PCL_{98}M_2$	40.2	54	56.6	63	46
$PCL_{97}M_3$	40.4	57	56.8	63	46
$PCL_{95}M_5$	40.8	55	56.9	58	43
$PCL_{99.75}NH_{0.25}$	40.3	65	55.5	69	51
$PCL_{99.5}NH_{0.5}$	37.2	57	56.5	63	46
$PCL_{99.25}NH_{0.75}$	39.0	60	55.2	64	47
$PCL_{99}NH_1$	38.8	68	55.9	76	55
$PCL_{98}NH_2$	39.3	56	55.5	63	45
$PCL_{97}NH_3$	39.4	64	56.2	71	51

The increase of the crystallization degree with the increase of MWCNT content, has also been reported by Trujillo et al.[27] for the PCL/MWCNT system. In contrast, some studies reported a reduction in crystallinity for PCL/CNT and even in functionalized systems.[8-10, 33, 34] The authors explain this unusual behavior due to topological restrictions that constrain the chain diffusion during crystallization.[33] On several reports for nanocomposites of different polymeric matrices, the crystallinity can increase[16, 19, 24, 35-38] or remains unchanged with

CNT addition.[36] Once again, the interactions between the CNT and the polymer chain will determine the crystallization behavior of the system.

Self-nucleation and nucleation efficiency

Self-nucleation experiments (SN) is explained in detail in the Chapter II. General concepts and in the following refererences: [3, 39], whereas the used of the nucleation efficiency from SN data can be seen in reference [4] and in nanocomposites in references [12, 13, 27, 28, 40, 41]

An example of the experiment of self-seeding for the PCL employed in this work is shown in Figure 7.3. Figure 7.3a shows the cooling scans after SN at the indicated T_s and Figure 7.3b shows the subsequent heating scans. After a careful observation of Figure 7.3a (the dashed line indicates the PCL crystallization temperature under standard conditions), it is possible to determine the change in the crystallization temperature without any change in the melting behavior. T_s values higher than 62 ºC are high enough to produce a complete melting process and a homogeneous melt. Lower or equal temperatures to 62 ºC are able to produce self-nucleation in the melt (*Domain II* or self-nucleation Domain), in which T_c will increase with the decrease in T_s, but without changes in the melting scans (i.e., T_m should be the same for all the *Domain II*). Figure 4b shows a change in the melting process at 54 ºC. At this point the melting endotherm shows a second peak at high temperatures indicating the presence of annealed crystals, which means that T_s values lower than 55 ºC belong to *Domain III*. Since 54 ºC belongs to *Domain III*, the ideal T_s should be 55 ºC.

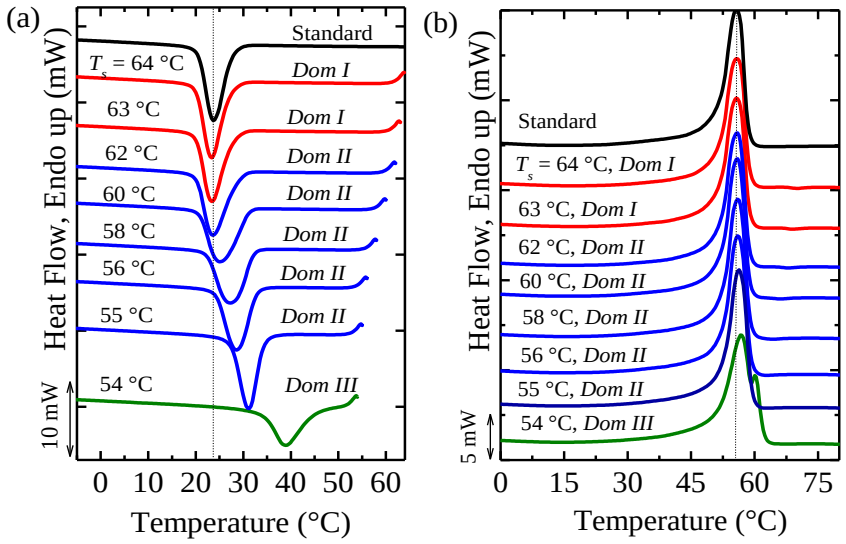

Figure 7.3. Self-nucleation behavior of neat PCL for selected self-nucleation temperatures (T_s). (a) DSC cooling scans from T_s and (b) DSC subsequent heating scans (see text).

Employing the ideal T_s (55 °C), it is possible to find the maximum crystallization temperature ($T_{c,max}$) for the PCL employed here, *i.e.*, 31.3 °C. This $T_{c,\ max}$ was used in the calculation of the nucleation efficiency (*NE*) (see Equation 2.18 on Chapter II. General Concepts) developed by Fillon et al.[4]

The *NE* results are plotted in Figure 7.4. In all the cases the nucleation efficiency is higher than 100%. This remarkable phenomenon is known as supernucleation since the crystallization temperature of the nanocomposites and nanohybrids are always higher than the crystallization temperature of the ideally self-nucleated polymer. The supernucleation has been reported in other systems such as *in situ* polymerized polyethylene on different carbon nanotubes[12, 13] and PEO, and PCL covalently grafted on the surface of CNTs.[13, 28] Trujillo et al.[27] reported for the first time the supernucleation in a simple melt mixed nanocomposite (PCL/CNT). This result indicated that the CNT supernucleation could be dominated by (a) the strong interaction between the polymer and the MWCNT and (b) the dispersion quality of the blend. In the present work the supernucleation effect of the MWCNT is a result of an excellent dispersion of the MWCNT within the polymeric matrix, which can be enhanced when modified MWCNTs are employed. However, the improvement of the dispersion with the modification of MWCNT approach could lead to a decrease of its nucleation capacity, as a result of the agents introduced.

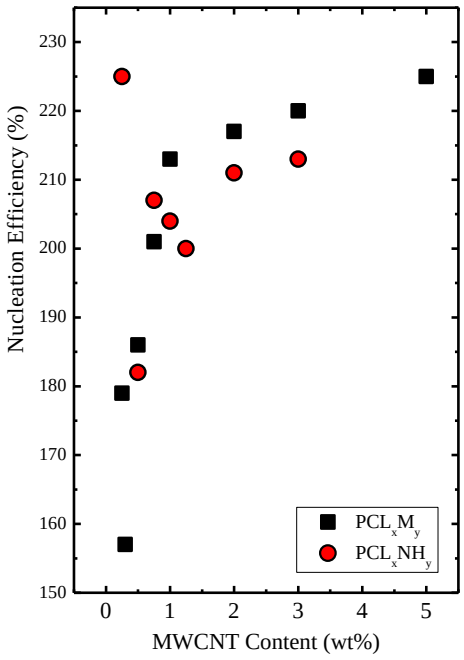

Figure 7.4. MWCNTs efficiencies as nucleating agents for PCL_xM_y and PCL_xNH_y nanocomposites.

Isothermal crystallization experiments

The inverse of the half crystallization time ($1/\tau_{50\%}$) is related to the overall crystallization rate, which is plotted as a function of the crystallization temperature (T_c) in Figure 7.5. From Figure 7.5 it is possible to observe that the T_c range for isothermal crystallization of the PCL is much lower than for the nanocomposites. In the samples with MWCNTs, the supercooling needed for the development of isothermal crystallization is much lower than for neat PCL in view of the supernucleation effect that they cause on the PCL matrix.

A careful comparison of PCL_xM_y versus PCL_xNH_y samples reveals a complex behavior. At lower MWCNT content (0.25 wt%) the nanohybrids exhibit a higher crystallization rate than $PCL_{99.75}M_{0.25}$, but as the MWCNT content is increased (*i.e.*, 0.25 to 1 wt%) the values of $1/\tau_{50\%}$ are closer, and remains almost the same until the MWCNT content reaches the value of 1 wt%, where the sample with pristine MWCNTs (*i.e.*, nanocomposites) has a slightly higher crystallization rate than the nanohybrids.

This behavior in the MWCNT-*g*-PCL could be attributed to two competitive factors: (a) the nucleation ability of the MWCNT and (b) the diluent effect of the low molecular weight PCL chains grafted to the MWCNT. These chains could be acting as plasticizers reducing the

crystallization kinetics. At lower MWCNT content, it is possible to obtain a favorable balance of these two factors and the sample reaches the highest crystallization rate. In contrast, increases of the MWCNTs in the nanohybrids results in an increase of the amount of low molecular weight PCL chains, which, in turns, increases the plasticizer effect.

A third factor may be possible, taking into account the works of Winey and co-workers.[42-46] They proposed that it is possible to modify the diffusion coefficient of a polymer chain when nanoparticles (NP) are present, or even in blends where the NP are grafted to polymer chains. They have reported that if the NPs are grafted to the polymer, the diffusion coefficient goes through a minimum as the NP concentration increases. Away from this minimum, high diffusion values are expected. It could be possible that in the nanohybrids, a concentration of 0.25% MWCNT is within a region where maximum diffusion of polymer chains can occur next to the CNTs, and hence the overall crystallization can be accelerated.

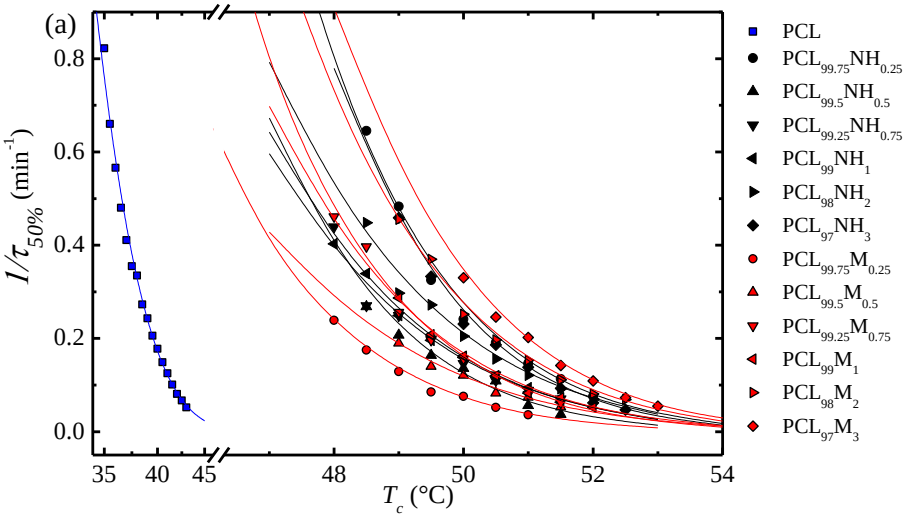

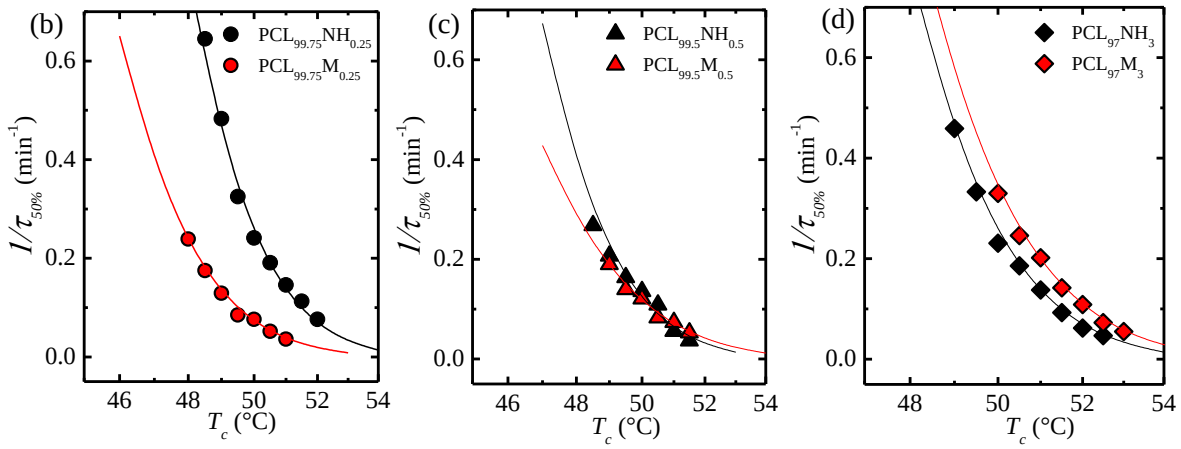

Figure 7.5. (a) Variation of $1/\tau_{50\%}$ (inverse of half-crystallization time) values as a function of the crystallization temperature for PCL_xM_y and PCL_xNHy samples. Solid lines indicate fittings to the Lauritzen and Hoffman theory. Selected pairs of samples (nanocomposites versus nanohybrids) are compared for MWCNT contents of (b) 0.25, (c) 0.5 and (d) 3 wt%.

The supercooling ($\Delta T = T_m^0 - T_c$) is proportional to the enthalpic driving force that a polymer needs to start the crystallization event, the reduction in ΔT is due to a reduction in the energy barrier as a consequence of the nucleating ability of the MWCNTs in both systems. Figure 7.6 shows the values of the crystallization temperature for which the blends reach a constant $1/\tau_{50\%}$ of 0.2 min^{-1} (see Figure 7.6a) and the $1/\tau_{50\%}$ values at a constant T_c of 52 °C (see Figure 7.6b), as a function of the MWCNT content. In Figure 7.6a, it is possible to observe that T_c increases as MWCNT content increases. In other words, that ΔT is smaller when the amount of MWCNTs increases in the blend, suggesting that the presence of MWCNT (either in the PCL_xM_y or PCL_xNH_y) makes the overall crystallization (including both nucleation and growth) more favorable.

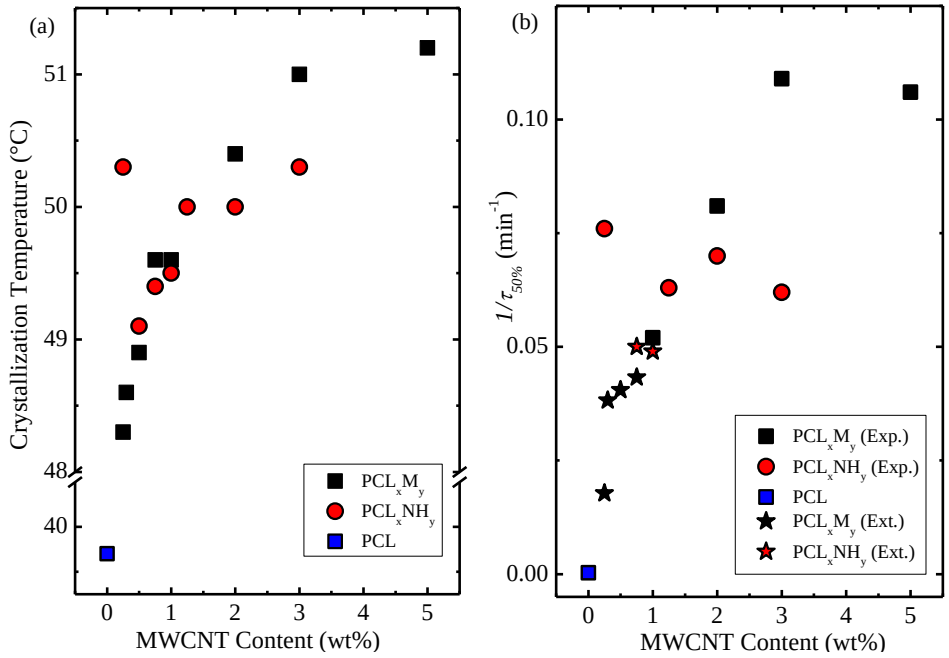

Figure 7.6. Influence of MWCNTs on (a) the crystallization temperature at $1/\tau_{50\%}$= 0.2 min^{-1} and on (b) the overall crystallization rate at T_c = 52 °C for the indicated blends. Different symbols are used for experimental (Exp.) and extrapolated (Ext.) data points.

Figure 7.6b shows that the overall crystallization rate ($1/\tau_{50\%}$) increases with MWCNT content. This change can be attributed to the predominant increase in the nucleation rate. The overall crystallization rate has two components, the nucleation rate and the growth rate. As a consequence of the supernucleation found, a larger amount of nuclei are activated at higher temperature for both systems.

As a result, the rate of nucleation is increased and the overall crystallization is also faster. The difference between the PCL_xM_y and PCL_xNH_y blends is small, suggesting that the modified MWCNTs have a similar activity than neat MWCNTs, except for the lowest content explored (i.e., 0.25 wt%).

The data obtained during the isothermal crystallization experiments were analyzed using the Avrami equation [47, 48]. The details can be seen in Chapter II. General Concepts.

For all the samples studied the fit was very good, even adjusting the data beyond the 50% of conversion. This behavior is not common but has been reported previously in some polyester.[27, 47, 49] The Avrami indexes for PCL are between 2.7 and 3.2 (see Table 9.9 and 9.10 in the Appendix) these values are very close to 3, and correspond to instantaneously nucleated spherulites when they are observed by

polarized light optical microscopy (not shown). On the other hand, the introduction of highly active MWCNTs greatly increases the number of active nuclei and in consequence a fully three-dimensional structure cannot be obtained for all the nanocomposites studied here, and tiny aggregates are obtained instead (not shown) The Avrami index was between 2.6 and 1.7 (see Tables 9.9 and 9.10), however the average was 2.3 and the most common value 2.1. These values correspond to a two dimensional lamellar aggregates that resemble bottle brush morphologies or hybrid shish kebab structures observed in similar nanocomposites.[12, 24, 27, 28] The K values are shown in the Appendix (Tables 9.9 and 9.10). The values of $K^{1/n}$ display a similar tendency than $1/\tau_{50\%}$, since $K^{1/n}$ is also related to the overall crystallization kinetics.

Despite the present chapter is focused on the crystallization of the nanocomposites and nanohybrids, rheological properties were also obtained and are presented in Section 9.5 of the Appendix.

7.2.1. Blends of PCL and PBS with a PCL/MWCNT masterbatch

The main characteristics of the materials used in this section are indicated in Chapter III. Experimental Part, specifically in Tables 3.5 (for PCL-based nanocomposites) and 3.6 (for PBS-based nanocomposites).

Miscibility assessment

The interaction between the components of a polymer blend can be determined from the composition dependence of the glass transition temperature (T_g). If two polymers are completely miscible, only one T_g is observed with its position determined by the composition of the blend. For immiscible polymer blends, two distinct T_gs are observed at the same temperatures as those of the parent homopolymers. However, when the two polymers are partially miscible, there are still two T_gs that will be shifted towards each other, with the degree of shift being dependent on both blend composition and miscibility degree.

In the present case, the T_g of the PC component in the nanocomposites could not be observed through either DSC, DMA or dielectric analysis (DEA), because PCL or

PBS, depending on the case (the major component of the blends, *i.e.*, the matrix) melted at a temperature well below the T_g of PC (DMA analyses could not be performed at temperatures above the T_m of PCL or PBS), and because PC crystallized in the nanocomposites (see crystallization and melting peaks indicated with arrows in Figure 7.7). PC does not normally crystallize, as it has a semi-rigid chemical structure and its crystallization is too slow. However, when plasticizers are added into the PC matrix, its free volume increases, which enhances the mobility of the PC polymer chains and its ability to crystallize can be enhanced [50, 51]. In this case PCL and PBS obviously acted as a plasticizer for PC, a sign of miscibility (either full miscibility or partial miscibility). As PC crystallizes, its T_g is difficult to observe by DSC, as the amount of mobile amorphous fraction per unit mass is very small in the blends. It is worth noting that a similar behaviour occurs for the PBS/(PC/MWCNT) nanocomposites (see Figure 9.27 in the Appendix).

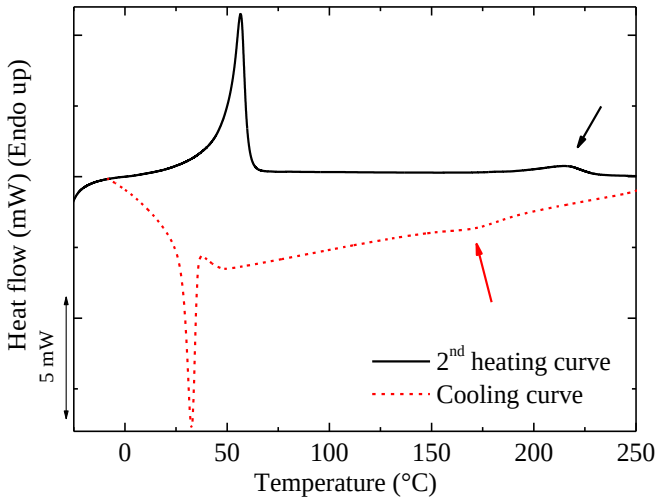

Figure 7.7. DSC cooling and second heating curves for the selected 73/(23/4) w/w PCL/(PC/MWCNTs) nanocomposite. The arrows indicate the crystallization and melting of the PC rich phase in the blends.

The crystallization of the PC component was also confirmed by simultaneous SAXS/WAXS analyses of PCL and the 93/(6/1) w/w PCL/(PC/MWCNTs) and 73/(23/4) w/w PCL/(PC/MWCNTs) nanocomposite samples (see Figure 7.8a and b). The same compositions were studied in PBS/(PC/MWCNTs) nanocomposites (see Figure 7.8c and d). Figure 7.8 depicts the final X-ray patterns taken under the indicated isothermal crystallization temperatures for the above systems. The main WAXS

reflections shown by neat PCL are also present in the nanocomposites, since the MWCNTs in the masterbatch acted only as nucleating agents. The main reflection peaks of PCL are located at q values of 15.2 and 16.8 nm^{-1}, and correspond to the (110) and (200) planes, respectively. It is worth noting that the characteristic shoulder in the PCL at 15.7 nm^{-1} appears in both neat PCL and the nanocomposites and corresponds to the (111) plane. All the reflections are consistent with the reported orthorhombic unit cell of PCL with unit cell parameters a = 7.48, b = 4.98 and c = 17.26 Å.[52] The main WAXS reflections shown by neat PBS are visible in the X-ray patterns of the nanocomposites.

The main reflection peaks of PBS are located at q values of 13.9 and 16.0 nm^{-1}, and correspond to the (002) and (110) planes, respectively. The medium intense reflection at 15.5 nm^{-1}, which corresponds to the (012) plane, as well as the minor reflections at 18.4 and 20.4 nm^{-1}, which correspond to the (12-1) and (111) planes, also appear in all the samples. All the reflections are consistent with the reported monoclinic unit cell of α-PBS with unit cell parameters a = 5.232, b = 9.057 and c = 10.900 Å and γ = 123.87º.

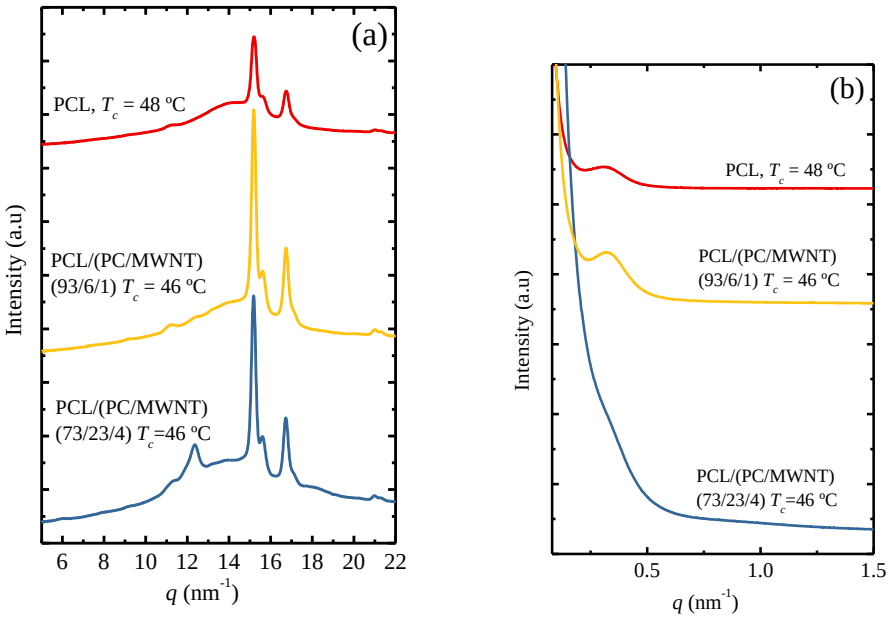

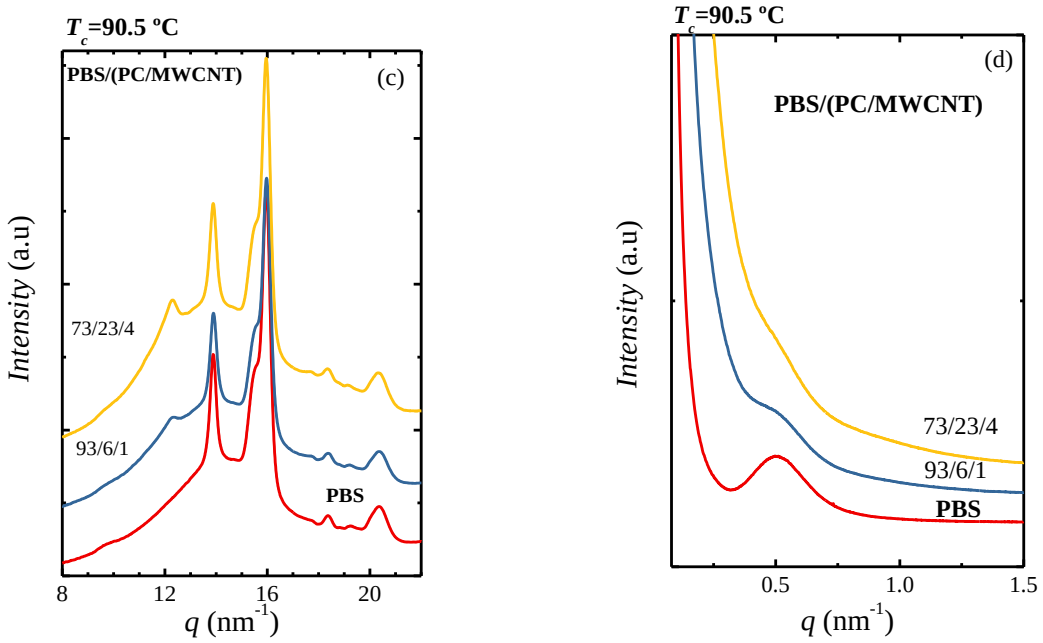

Figure 7.8. (a, c) WAXS diffractograms taken at selected isothermal temperatures; (b, d) SAXS patterns taken at the selected isothermal temperatures for PCL-based (a,b) and PBS-based (c,d) nanocomposites, respectively.

In addition to the PCL unit cell peaks, there is a peak at 12.4 nm^{-1} (equivalent to a 2θ of 17.4º), and this peak becomes pronounced as the PC content in the nanocomposites increases. This peak corresponds to the PC component that is able to crystallize due to the plasticization effect of the PCL, as will be shown in Figure 7.8.It is worth noting that this peak is also present in the PBS-based nanocomposites (see Figure 7.8c)

Figure 7.8b and d shows the SAXS patterns taken at the same condition used in the WAXS experiments for PCL-based and PBS-based nanocomposites, respectively. In these patterns, the PCL signal observed in the neat material and in the nanocomposites with low content of PC is dominant, since the single peak corresponds mainly to the long spacing of PCL lamellae. However, at higher PC content (*i.e.*, 23 wt%), the PC is able to crystallize due to the plasticization effect of the PCL. Therefore, the SAXS signal is not clear due to the overlap of the long spacings generated by the lamellae of PCL and PC. The signal observed is probably an average of these two long spacings. A similar behaviour is observed for the PBS-based system.

For the sake of clarity, WAXS patterns were taken during heating after the isothermal step (see Figure 7.9) for the selected samples of 93/(6/1) and 73/(23/4) w/w PCL/(PC/MWCNTs) (see Figure 7.9a and b) and PBS/(PC/MWCNTs) (see Figure 7.9c

and d) nanocomposites (the heating patterns of the neat samples are shown in Figure 9.28 of the Appendix). Figure 7.9 shows that the PC peak does not disappear when the PCL or the PBS are already molten at T>60 ^{o}C and T>116 ^{o}C, respectively. This behaviour is clearly observed at higher PC content in Figure 7.9b and d. According to this results and the literature,[51] PC is able to crystallize, as mentioned earlier in the discussion, due to the plasticization effect of PCL and PBS, depending on the evaluated nanocomposite, and shows a main reflection at a 2θ angle of 17.1^{o}. The peak at 12.4 nm^{-1} can therefore be attributed to the PC component, which crystallizes as a result of the plasticization effect of the parent homopolymer (either PCL or PBS).

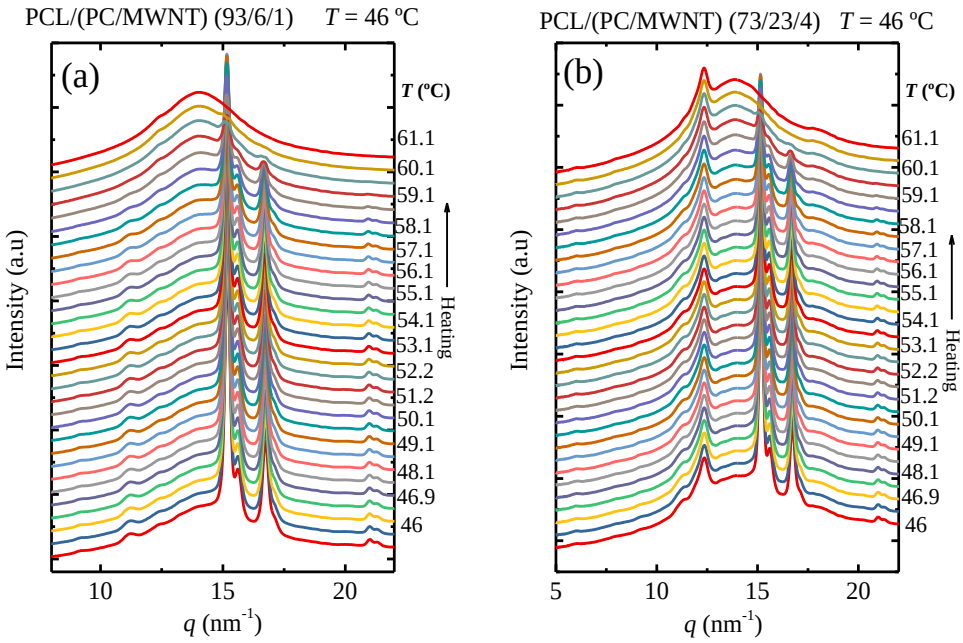

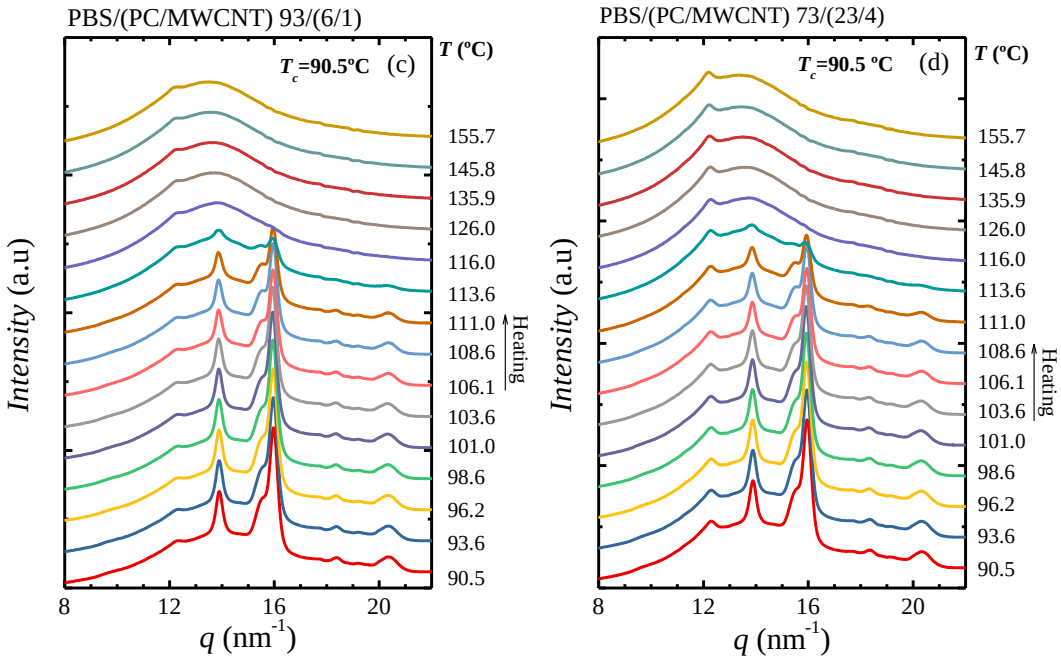

Figure 7.9. WAXS patterns taken during the heating at 5 ºC min^{-1} after the isothermal step at 46 ºC and 90.5 ºC for (a, c) (93/6/1) and (b, d) (73/23/4) PCL/(PC/MWCNTs) and PBS/(PC/MWCNTs), respectively.

The *d*-spacings for all the reflections shown in Figure 7.8a were calculated according to Equation 2.1 (see Chapter II. General Concepts), whereas, the long periods were calculated from the main PCL and PBS peaks in the SAXS patterns in Figure 7.9b and d, respectively. The relevant values are tabulated in Table 7.3 and Table 9.12 for the PBS-based nanocomposites (see Appendix).

The *d*-spacings and the *d** values of neat PCL and the PCL in the nanocomposites are almost the same for neat PCL and low PC contents (*i.e.*, 6 wt%). In the case of 73/(23/4) w/w PCL/(PC/MWCNTs) nanocomposite, the peak related to the PC component is the same as the one reported in the literature (0.464 nm). In the SAXS patterns, an overlap between the long spacings of PC and PCL occurs and that explain the decrease of *d** values in comparison with the other samples. A similar behaviour was found for the PBS-based nanocomposites.

Table 7.3. Calculated values of *d*-spacing (from WAXS experiments) and long period (*d**, obtained from SAXS experiments) for the neat PCL and its nanocomposites.

Sample	*d*-spacing (nm)/(plane)	d^* (nm)
Neat PCL	0.378 (110)	19.8
	0.343 (200)	
	0.400 (111)	
93/(6/1) w/w	0.378 (110)	19.9
PCL/(PC/MWCNTs)	0.344 (200)	
	0.400(111)	
73/(23/4) w/w	0.464*	17.2**
PCL/(PC/MWCNTs)	0.378 (110)	
	0.344 (200)	
	0.400 (111)	

*PC signal

**overlap of PC and PCL signals

The DSC and DMA results in Figures 7.10 and Figure 9.29 (see the Appendix) show little change between the T_g values for neat PCL and PCL within the different nanocomposites. The T_g values from the two techniques are different for the same sample, with $T_{g,DSC} < T_{g,E''} < T_{g,tan\ \delta}$ (See Figure 9.30 on the Appendix). This is well known, as DMA applies not only a heating rate but also a mechanical deformation with a particular frequency, which as a result increases the rate at which T_g is being measured [53-55]. The trends from the different sets of results are, however, the same. The results show that the presence of the masterbatch had little effect on the T_g of PCL, which may be an indication of limited interfacial interaction between the PCL and the PC in the masterbatch. Theoretically, when two polymers are completely miscible, the T_g of the PCL in the blend nanocomposites should have increased to approximate values calculated according to the Fox equation (Equation 7.1).

$$\frac{1}{T_g} = \frac{w_1}{T_{g1}} + \frac{w_2}{T_{g2}} \qquad \text{Eq. 7.1}$$

where T_g is the PCL/PC blend glass transition temperature, and T_{gi} and w_i are the respective glass transitions and weight fractions of PCL and PC. The glass transition

temperatures of PCL obtained from both DSC and DMA did not change much across the composition range, and the values are lower than those predicted by the Fox equation (Figure 9.30, see the Appendix), which could be an indication of immiscibility or partial miscibility between the PCL and PC.

However, a closer inspection of the DSC results (Figure 7.10) shows that the blend containing the highest amount of PC, *i.e.*, 73/(23/4) PCL/(PC/MWCNTs) has a T_g value of approximately 7 ^{o}C higher than neat PCL (see also Figure 9.30, See the Appendix) . DMA results also show an increase in T_g values of this blend with respect to neat PCL (*i.e.*, 3-4 ^{o}C). In fact, Figure 9.30, See the Appendix, shows an increasing trend (much smaller than that predicted by the Fox equation but still significant) of T_g with increases in PC content in the blend.

If complete immiscibility would be present in the blends, no plasticization of PC would have been observed (as indicated by PC crystallization, demonstrated above). Taking into account the results presented so far, we can conclude that the blends are partially miscible. Two phases are formed: (1) A PC rich phase, where a small amount of PCL chains are present and can plasticize the PC component, so that it can crystallize, and (2) A PCL rich phase, where the amount of PC chains present is very small, so that changes in the T_g of the PCL phase are much smaller than those predicted by the Fox equation. Note that a similar behaviour was found for the PBS-based nanocomposites (see Figures 9.31 and 9.32 in the Appendix).

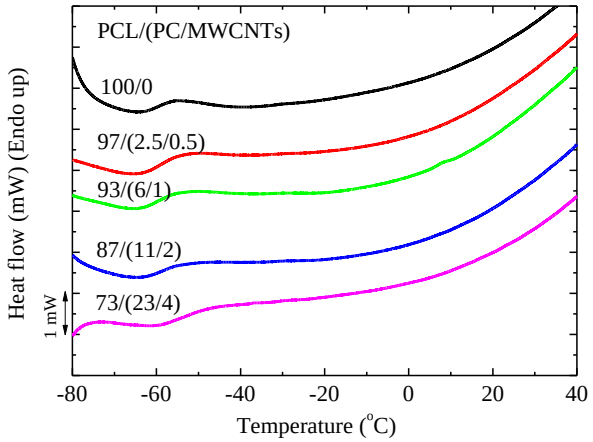

Figure 7.10. DSC heating curves for neat PCL and the PCL/(PC/MWCNTs) nanocomposites, showing the glass transitions around -60 °C.

Non-isothermal DSC

Figure 7.11 shows the DSC (a,c) cooling scans after erasing the, thermal history and (b,d) the subsequent heating scans performed at 20 °C min^{-1} for the different investigated samples. The crystallization peak temperatures (T_c) of PCL in the nanocomposites shifted to higher temperatures as compared to that of neat PCL (Figure 7.11a). The DSC heating curves show little or no change in the melting temperature (T_m) of PCL in the nanocomposites compared to that of neat PCL (Figure 7.11b).

To examine the results presented in Figure 7.11, the T_c and T_m values were plotted in Figure 7.12 as a function of MWCNTs content. The increase in T_c with increasing MWCNTs content is due to the nucleation effect caused by the presence of MWCNTs that penetrated into the PCL rich phase (as was demonstrated morphologically by SEM and AFM images, see Figures 9.33 to 9.35 in the Appendix). However, a saturation of this nucleation effect starts below 2 wt% of MWCNT and it is in line with the percolation threshold of 0.5-1 wt% found it in the previous section. This saturation is related to the aggregation of MWCNTs and the limited diffusion of the MWCNTs with increasing PC content. The T_m remains almost constant with the increase of MWCNTs content, as it is expected when a nucleating agent is used. This is due to the metastable nature of polymer crystals that usually require large increases in T_c values to give rise to T_m values.[27]

In the case of the PBS-based nanocomposites, the T_c of the PBS in the nanocomposites is higher than that of neat PBS up to 2 wt% MWCNTs. The nucleation effect of the MWCNTs is maximum for the 0.5% composition, where probably, the MWCNTs diffusion to the PBS rich phase is maximum considering the partial miscibility with the PC phase. At higher concentrations, there is a decrease in the nucleation effect as indicated by the decrease in T_c values. This effect is probably due to the MWCNTs aggregation in the PC rich phase, which restricted the MWCNTs from diffusing to the PBS rich phase, and could not participate in nucleating PBS. At a concentration of 4% MWCNTs, an antinucleating effect appears, which can only be attributed to the migration of active nucleating heterogeneities from the PBS rich phase to the PC rich phase. At a composition of 4% MWCNTs, the migration of MWCNTs to the PBS rich phase did not occur, probably because of the higher amount of PC content in the blend.

In Figure 7.11d a T_m depression is observed for the PBS component with an increase in the masterbatch content which is related to the melting point depression caused by the partial miscibility with the PC chains in the blend, in addition to the drop in T_c values caused by the nucleation changes. The nucleation action of the MWCNTs is further studied in the next section through self-nucleating experiments.

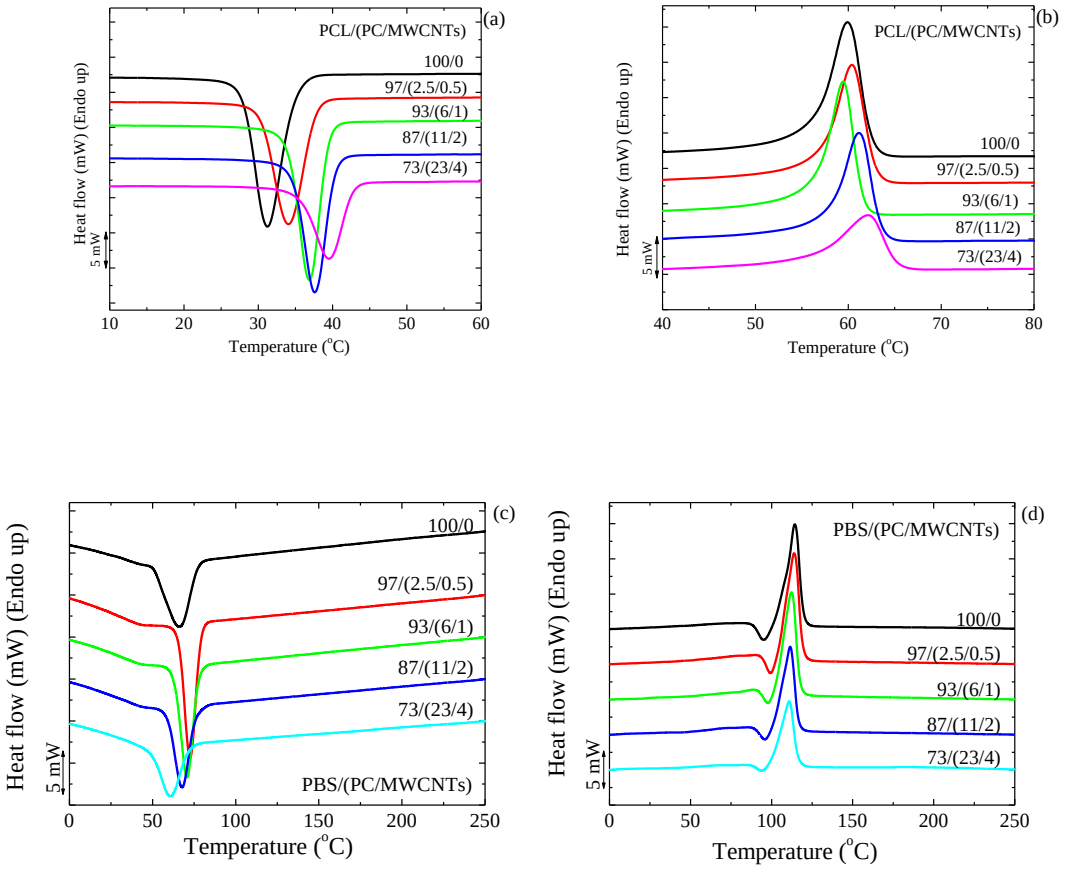

Figure 7.11. DSC (a, c) cooling and (b, d) second heating curves at 20 °C min^{-1} of neat PCL, PBS and the PCL/(PC/MWCNTs), PBS/ (PC/MWCNTs) nanocomposites.

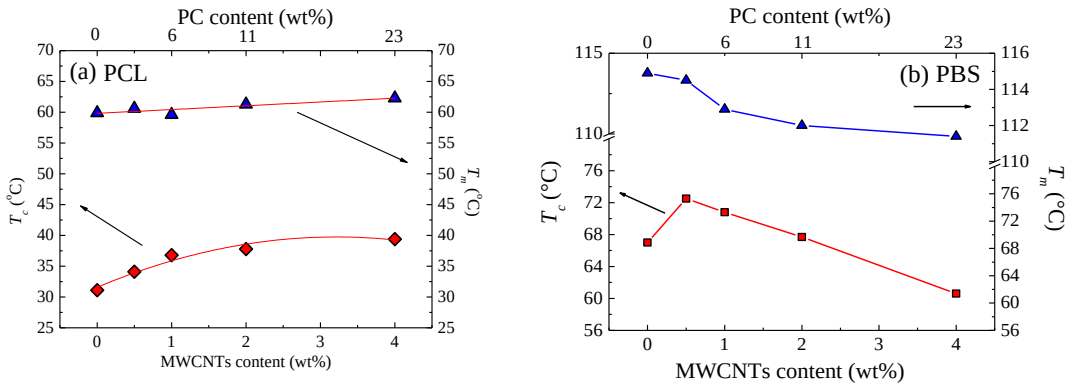

Figure 7.12. DSC crystallization and second heating melting temperatures as a function of MWCNTs content for neat PCL, PBS and the PCL/(PC/MWCNTs), PBS/(PC/MWCNTs) nanocomposites. A linear fit and a polynomial fit for the experimental data of T_m and T_c, respectively, are used to guide the eye.

Self-nucleation (SN)

The efficiency of MWCNTs as nucleating agents was evaluated with the same thermal protocol employed in the previous section [3, 56, 57] and was explained in detail on Chapter II. General Concepts. Figure 7.13 shows the experimental data obtained during an SN experiment for neat PCL (Note that the data corresponding to the PBS can be observed in the Appendix, Figure 9.36). The cooling scans after the isothermal step at T_s are presented in Figure 7.13a and the subsequent heating scans are shown in Figure 7.13b. The dashed line indicates the PCL crystallization and melting temperatures under standard conditions. The three SN domains are described in Chapter II. General Concepts as defined by Fillon et al [3].

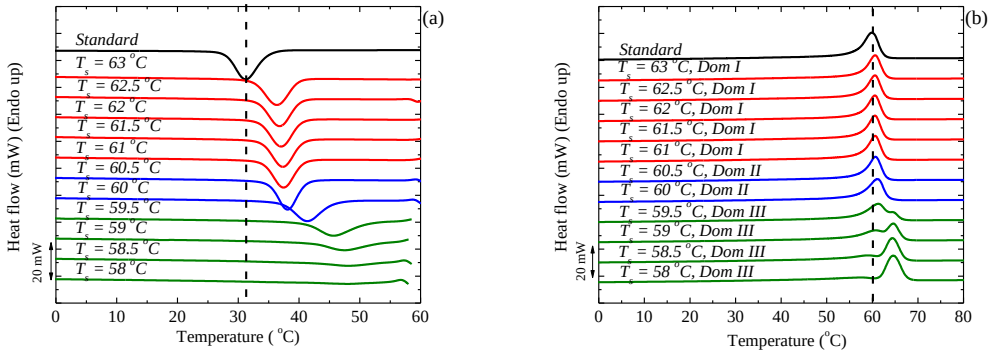

Figure 7.13. (a) DSC cooling scans for neat PCL after 5 min at the indicated T_s, and (b) subsequent heating scans after the cooling runs shown in (a).

For the PCL studied in Figure 7.13, *Domain I* is found at T_s larger or equal to 61 °C, since no change was detected in the T_c when compared to the standard T_c. Both the crystallization and melting DSC scans are identical within *Domain I*. The start of *Domain II* in Figure 7.13a occurred at a T_s = 60 °C, since the sample was self-nucleated without any annealing. Figure 7.13b shows that, at T_s < 60 °C, the melting endotherm exhibits a small high temperature peak that is a result of the melting of annealed crystals. At this T_s, the crystallization exotherm shows a high temperature tail which reveals that the sample is in *Domain III*.

Figure 7.14 shows the location of the three self-nucleation domains for the PCL sample. The vertical dashed lines indicate the temperatures at which the material experiences a self-nucleation domain transition. The T_c values are constant in *Domain I* and increase as the T_s value crosses over to *Domain II*, as expected [3, 56]. Since 60 °C is the lowest T_s value in *Domain II*, it is called the ideal self-nucleation temperature, because it is the temperature at which there is maximum self-nucleation without any annealing. Employing the ideal T_s (60 °C), the T_c corresponding to the ideal T_s should be used as the maximum crystallization temperature ($T_{c,max}$) when determining the nucleation efficiency of the nanofiller. For the PCL used in this study, $T_{c,max}$ is 42.8 °C.

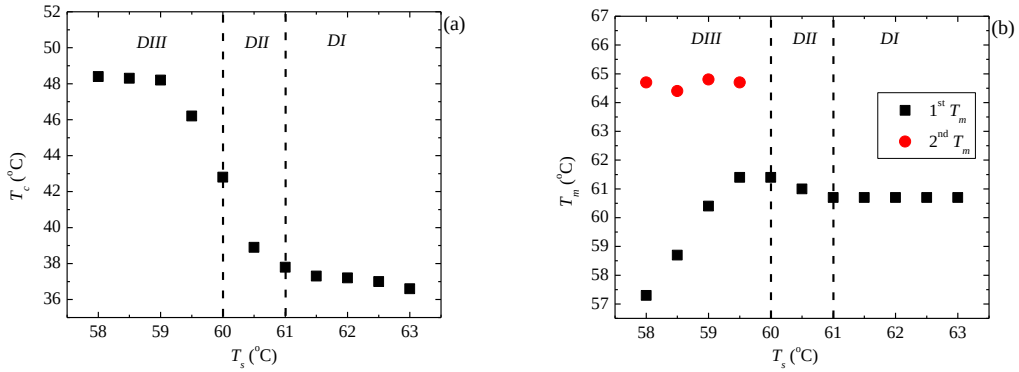

Figure 7.14. Dependence of (a) crystallization and (b) melting peak temperatures of neat PCL on T_s.

The efficiency of the MWCNTs as nucleating agents for the PCL matrix was calculated according to Equation 2.18 (see Chapter II. General Concepts). Figure 7.15a and b, shows the percentage nucleation efficiency of MWCNTs in the PCL/(PC/MWCNTs) and PBS/(PC/MWCNTs) nanocomposites, respectively.

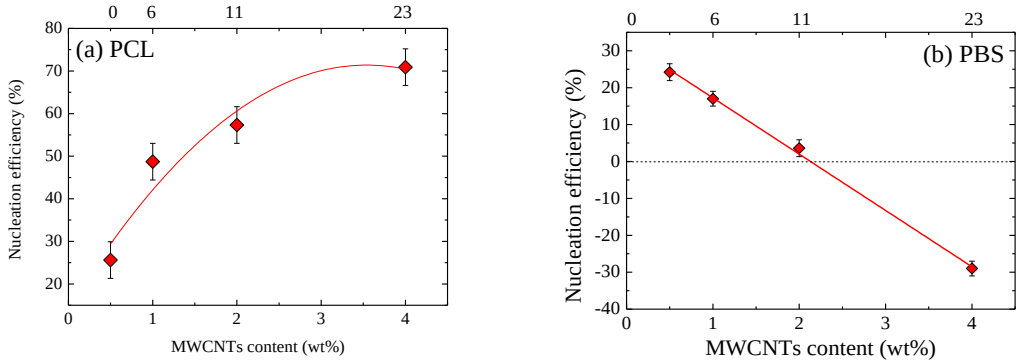

Figure 7.15. Nucleation efficiency as a function of MWCNTs content for (a) PCL-based and (b) PBS-based nanocomposites. The experimental points are fitted with a polynomial fit in order to guide the eye.

The nucleating efficiency of the PCL-based nanocomposites (see Figure 7.15a) increases with increasing MWCNTs content. Notice that if the blends were totally immiscible, the MWCNTs would be trapped inside the PC phase and the increase in MWCNTs would probably cause no increase in nucleation efficiency. In this case, the nucleation efficiency clearly increases with MWCNTs, a result which is also consistent with the partial miscibility of the blends. The fast increase in the nucleation efficiency is observed until 1 wt% MWCNTs, is in line with the DSC results. Above 1 wt% MWCNTs, the increase is slow which correspond to a saturation effect due to agglomeration of MWCNTs and the PC crystallization.

The increase in nucleation efficiency (even if highly significant, up to 70%) is less than expected, as literature results indicate that MWCNTs can super nucleate PCL (*i.e.*, can produce nucleation efficiencies larger than 100% with loading as low as 1% or less).[1, 27] In our case, the nucleating efficiency is lower due to limited phase mixing between the PC rich and the PCL rich phases. Only a limited quantity of MWCNTs can penetrate the PCL rich phase and therefore contribute in nucleating PCL, while most of the MWCNTs agglomerated in the PC rich phase.

In contrast with the PCL, a different behaviour is show in the PBS-based nanocomposites, since it is observed in Figure 7.15b that the nucleation efficiency decreases with increasing MWCNTs content. This is consistent with Figure 7.12b. At the highest MWCNTs content (*i.e.*, 4 wt%), the nucleation efficiency is below 0%. This behaviour is unexpected since negative nucleation efficiencies (*i.e.*, antinucleation effect) have been only reported due to interactions between the polymeric matrix and the nucleating agent, *e.g.*, C-PCL/MWCNT-*g*-L-PCL,[58] polylactide grafted cellulose nanocrystal (CNC-*g*-PLA) was added to poly (β-hydroxybutyrate) (PHB) [55] and PCL-*grafted*-lignin (with high lignin contents).[41] Generally, such interactions make the diffusion of the polymeric matrix difficult. Some of these interactions are hydrogen bonding and threading effects, and it is also reported that the surface modified CNC particles retarded the heterogeneous nucleation of the PHB crystals by restraining the relaxation of neighbouring PHB chain segments.

In the present work, there is no group neither in the PBS matrix nor in the masterbatch that can cause similar interactions. Therefore, two possible reasons for this behaviour are (1) the MWCNT aggregation or (2) its encapsulation in the carrying

polymer (*i.e.*, the PC used in the masterbatch), which might lead to the saturation of the system, or to no contact between MWCNT and the PBS. In both cases, the expected behaviour is a nucleation efficiency equal to zero.

The significant decrease in the nucleation efficiency can only be explained by a complex behaviour in which a migration of heterogeneities from the PBS matrix to the PC in the masterbatch occurs, through the help of the plasticization effect previously reported. Then, the MWCNT could be confined into the PC, due to its crystallization, avoiding the MWCNTs diffusion to the PBS matrix. Therefore, the PBS matrix do not have neither all their heterogeneities nor the MWCNT, and as a result both its crystallization temperature as well as its crystallization kinetics decreases.

Overall isothermal crystallization studied by DSC

The influence of the MWCNTs as well as PC (both components of the masterbatch employed) at different contents, over the isothermal crystallization kinetics of the PCL and PBS is studied. Figure 7.16 shows the inverse of the half crystallization time ($1/\tau_{50\%Exp}$), which is proportional to the overall crystallization rate as a function of isothermal crystallization temperatures (T_c) for neat PCL, PBS and the nanocomposites. The T_c range for neat PCL is lower than for the nanocomposites. This indicates that a larger degree of supercooling is needed for neat PCL to crystallize, while the nanocomposites crystallize more easily than neat PCL, because of the nucleation effect that they cause on the PCL rich phase. In contrast, for the PBS-based nanocomposites the nucleation effect of 0.5% MWCNTs can impact the overall crystallization kinetics (which includes both nucleation and growth) accelerating it. For this composition, the nucleation effect can dominate the behaviour as compared to a possible depression in crystal growth that could be produced by the reduced diffusion of the PBS chains within the PBS rich phase (whose diffusion would be affected by the miscibility with the more rigid PC chains). Increasing the content of MWCNTs to 1% (and also the content of PC in the blend to 6%) produces an equilibration effect between nucleation and growth that matches exactly the crystallization kinetics of neat PBS. Further addition of MWCNTs in the blends produce decreases in the overall crystallization kinetics, as the efficiency of nucleation decreases. The decrease in overall crystallization rate is particularly large

for the blend with 4% MWCNT, a reflection of the antinucleation effect previously discussed.

Another way to examine the results presented in Figure 7.16, is by taking the values of the crystallization temperature for which the blends reach a constant value of $1/\tau_{50\%}$ (*i.e.*, 0.5 and 0.43 min^{-1} for PCL and PBS, respectively) (Figure 7.17a and c) and the $1/\tau_{50\%}$ values at a constant T_c (*i.e.*, 47 and 82 ^oC for PCL and PBS, respectively) (Figure 7.17b and d), as a function of MWCNTs content. Figure 7.17a and c shows the experimental and extrapolated data using the Lauritzen and Hoffman (L-H) theory, which is explained in detail in Chapter II. General Concepts. It is clear in the PCL-based nanocomposites that nucleation produces an interesting practical effect, as a higher T_c value is needed to reach the same overall crystallization rate with increasing MWCNTs content in the PCL-rich phase. This result is in agreement with previous works,[1, 27, 40] where an increase in MWCNTs content resulted in an increase in the T_c of PCL during non-isothermal crystallization. A contrasting behaviour is found on the PBS-based nanocomposites, since in order to obtain a predetermined (arbitrarily chosen) constant crystallization rate, the nanocomposite with only 0.5% MWCNTs needs a lower supercooling than neat PBS, but as the MWCNTs increases (together with PC content in the blends), the supercooling applied to obtain the same rate needs to be substantially increased, even beyond that needed by neat PBS.

In Figure 7.17b, the overall crystallization rate of the PCL rich phase at a constant crystallization temperature increases with MWCNTs loading, due to the nucleating effect of the MWCNTs, as in Figure 7.17a. Similarly, the same trend obtained in Figure 7.17d is found for PBS-based nanocomposite in Figure 7.17c.

Despite the nucleating effect of MWCNTs, a reduction in the percentage crystallinity (X_c) of PCL is observed (see Figure 7.18), especially at high PC contents. It must be remembered (see Table 3.5, Experimental Part) that since the nanocomposites are prepared by mixing PCL and a masterbatch, as the MWCNTs content increases, so does the PC fraction in the blends. This decrease in X_c of the PCL matrix (Figure 7.18), during isothermal crystallization, is due to the presence of the PC rich phase, which is able to crystallize because of the plasticization effect of the PCL component.

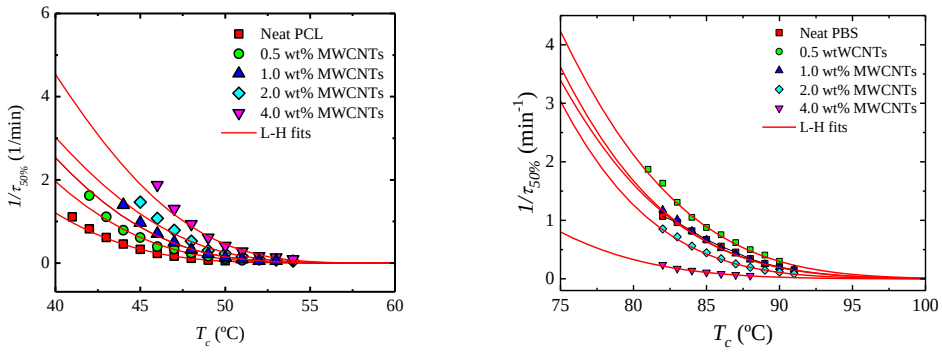

Figure 7.16. Overall crystallization rate ($1/\tau_{50\%}$) as a function of isothermal crystallization temperature (T_c) for PCL and PBS-based nanocomposites. The red solid lines represent fits to the LH theory.

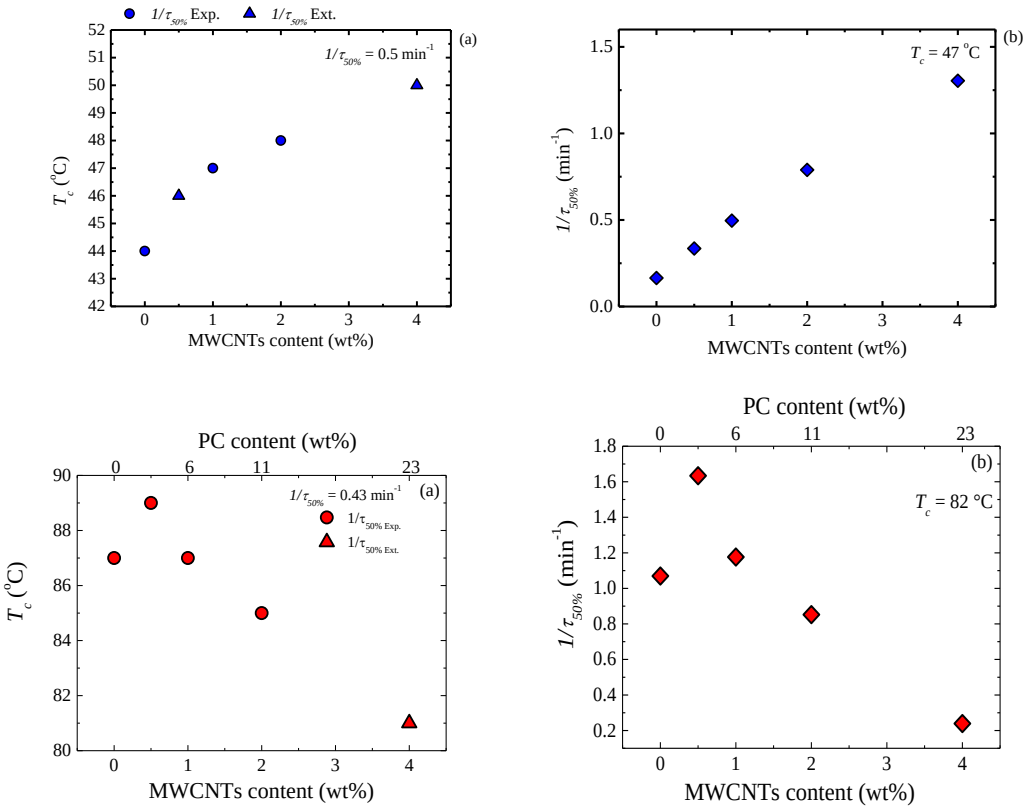

Figure 7.17 (a) Crystallization temperature as a function of MWCNTs content at constant $1/\tau_{50\%}$ = 0.5 min^{-1}; (b) overall crystallization rate as a function of MWCNTs content at constant T_c = 47 °C.

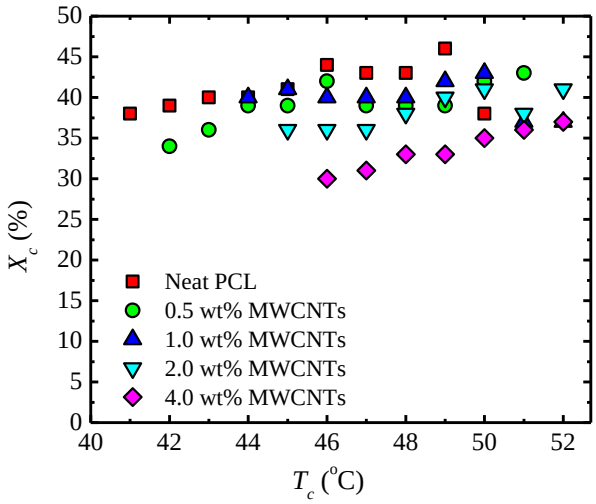

Figure 7.18. Relative crystallinity (X_c) as a function of isothermal crystallization temperature (T_c) for neat PCL and the PCL/(PC/MWCNTs) nanocomposites.

Fitting DSC isothermal data to the Avrami model

The data obtained during the isothermal crystallization experiments were analysed employing the Avrami equation (see Chapter II. General Concepts for more details).

The kinetic parameters for all the investigated samples are plotted in Figure 7.19 and tabulated in Table 9.13 of the Appendix.

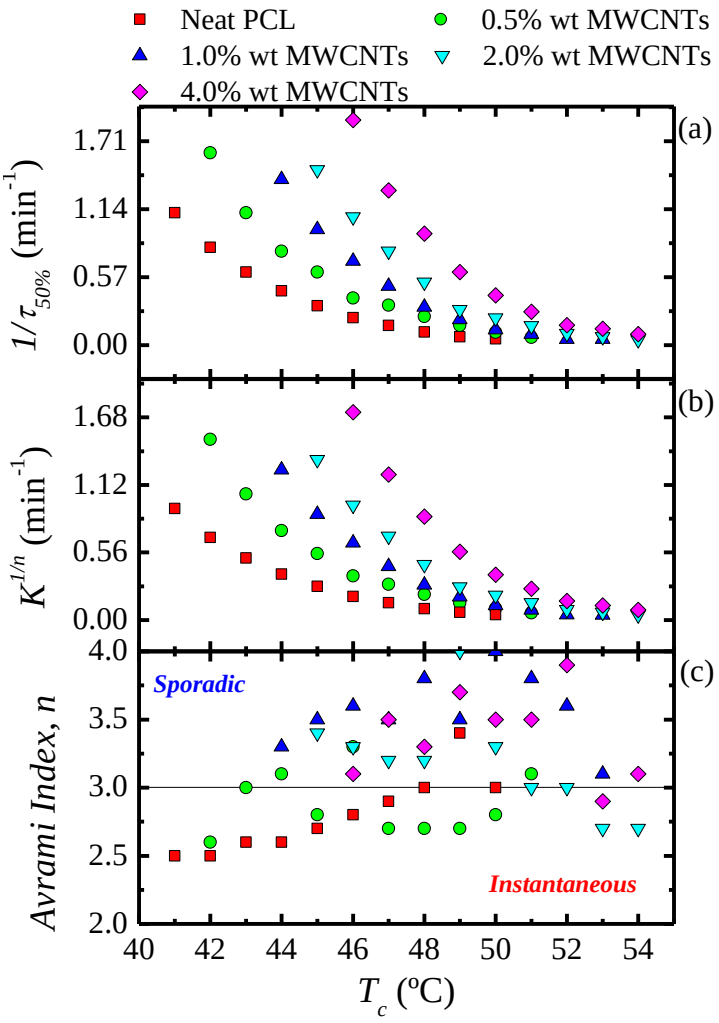

Figure 7.19. (a) Inverse of half crystallization times ($1/\tau_{50\%}$) (b) Normalized crystallization constant of the Avrami model ($K^{1/n}$) and (c) Avrami index (n) as a function of the isothermal crystallization temperature (T_c) for all the samples.

Figure 7.19a shows $1/\tau_{50\%}$ values as a function of T_c, whose trend was explained earlier in the discussion. The same trend is obtained with the $K^{1/n}$ values of the Avrami model (see Figure 7.19b), since this constant is related to the overall crystallization kinetics as well. Figure 7.19c shows the n values for all the samples, which depend on the dimensionality of the crystalline superstructure and on their nucleation kinetics.[47, 59]

The values of n for neat PCL are approximately 3 in the investigated T_c range, which is an expected result for PCL.[1, 27, 40] A value of 3 indicates a spherulitic morphology with instantaneous nucleation, which is commonly observed in PCL homopolymers. Therefore, upon addition of a nucleating agent, one would expect that the Avrami index would remain around 3 or would decrease (as the dimensionality of

growth can switch from 3D to 2D when the nucleation density is greatly enhanced). Higher values than 3 for these PCL nanocomposites are not expected, especially when it has been demonstrated that MWCNTs are effective in nucleating PCL. Further studies are needed in order to understand the explanation of such unexpected results. Elsewhere in the literature,[1, 27, 40] the authors reported decreasing *n* values for the nanocomposites as compared to neat PCL.

The obtained results for the PBS-based nanocomposites are show in Figure 9.37 and Table 9.14, see Appendix.

Overall isothermal crystallization data analysed by the Lauritzen-Hoffman model

The overall crystallization kinetics is determined by contributions of primary nucleation and growth. The Lauritzen-Hoffman (LH) nucleation and growth theory can be applied to the isothermal crystallization kinetics data collected from DSC (See Chapter II. General Concepts for more details)

According to Figure 7.16 the lines can adequately fit the overall crystallization rate as a function of T_c for the explored range. The fittings were useful in order to construct Figure 7.17 by extrapolating unavailable data in specific temperature ranges. Additionally, it was found, as expected and reported before in similar studies,[1, 27, 40] that K_g^{τ} values (proportional to the energy barrier for overall crystallization) decrease when the nanotubes content increases as a result of their nucleating ability (see Table 9.15 of the Appendix).

In contrast, for the PBS-based nanocomposites there is a slight variation of K_g^{τ} values (see Table 9.16 of the Appendix) with increasing masterbatch content, which are in line with the above discussions.

Tensile properties

The mechanical properties of PCL, PBS and the nanocomposites were investigated employing tensile testing. These properties depend upon the interfacial interaction between the nanofiller and the different components in the polymer blend, chain stiffness, and the crystallinities of the individual components in the blend. This implies

that to utilize the reinforcing capability of carbon nanotubes and to maximize the mechanical properties of the nanocomposites, strong interfacial bonding is necessary. The extent of interaction depends on how well the filler is dispersed in the matrix.

Considering that the nanocomposites prepared here involve the increasing addition of both PC and MWCNTs to PCL, it is expected that the ductility of the PCL significantly decreases while the modulus increases. Table 7.4 presents the tensile tests results which partially corroborate the expected trends. The strain at break significantly decreases as the masterbatch content increases (see Figure 7.20), a trend proportional to a reduction in ductility. Additionally, the elastic modulus is not significantly affected, until the maximum amount of masterbatch was used. In this last case, the value increased from 388 MPa for neat PCL to 592 MPa for the nanocomposite.

PC is a more rigid polymer than PCL. In the present blends, PC addition caused a small increase in the T_g of the PCL phase due to the partial miscibility. Additionally, the presence of PC rich inclusions in a PCL matrix can act as stress concentrators that may trigger earlier fracture nucleation and propagation.

On the other hand, MWCNTs are known to increase overall rigidity of the polymer matrix to which they are added, when the dispersion is adequate and when there are strong interactions with the polymer matrix. In this case, the interactions may not be very strong with the PCL matrix and the fact that the density of MWCNTs is higher in the PC rich phase than in the PCL rich phase is probably causing a stronger stress concentration effect and a lower effectiveness in enhancing the elastic modulus of the nanocomposites. This may be the reason why, the positive effect on the elastic modulus can only be obtained at large masterbatch loadings. As both PC and MWCNTs addition are inducing enhanced rigidity and stress concentrations in the PCL matrix, the stress at break is also seen to decrease with masterbatch addition.

Although increases in tensile strength, similar to that of the Young's modulus, have been reported in CNT-filled nanocomposites, the local nature of the shear yielding process, usually leads to constant or even decreasing values as the CNT content increases.[60] In this case, the yield stress of PCL first decreases slightly with masterbatch addition only to recover at the maximum concentration of MWCNTs.

Table 7.4. Summary of tensile testing results for neat PCL and the nanocomposites.

w/w PCL/ (PC/MWCNTs)	σ_b / MPa	ε_b / %	E / MPa	σ_y / MPa
100/0	34.3 ± 12.9	578 ± 151	388 ± 29	16.2 ± 1.9
97/(2.5/0.5)	15.9 ± 7.1	285 ± 152	354 ± 77	13.7 ± 3.3
93/(6/1)	10.3 ± 5.0	154 ± 198	352 ± 28	13.6 ± 1.0
87/(11/2)	6.9 ± 1.9	22.8 ± 2.0	336 ± 33	11.3 ± 4.1
73/(23/4)	15.6 ± 0.9	4.3 ± 0.7	592 ± 62	17.1 ± 1.4

σ_b – stress at break, ε_b – strain at break, E – Young's modulus, σ_y – yield strength

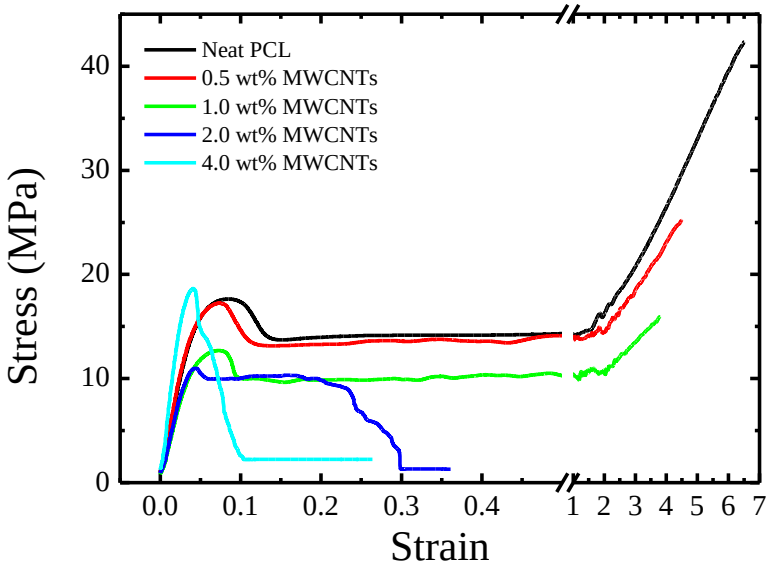

Figure 7.20. Stress-strain curves for neat PCL and the nanocomposites.

In the PBS-based nanocomposites the stress at break shows a decrease with the incorporation of the masterbatch (see Figure 9.38 and Table 9.17 in the Appendix). However, the nanocomposites containing 0.5, 1.0, 2.0 wt% MWCNTs gave almost the same value. The initial drop in tensile stress with the inclusion of the masterbatch in the PBS matrix is the result of the formation of the sea island morphology, with very large dispersed PC rich phase acting as stress concentration regions. PBS loses its localized shear deformation ability to form a neck and instead becomes a fragile material, as cracks nucleate at the dispersed phase and grow to produce earlier fracture. As a consequence the strain at break dramatically drops when the masterbatch is added.

The tensile stress, however, remains fairly high for the samples containing up to 2 wt% MWCNTs, which could be related to the partial miscibility of the blends, where in spite of the large size of the dispersed PC rich phase, there is adhesion between the PC rich and the PBS phase, as manifested in the lack of void formation at the interphase in between the phases, as documented by SEM and AFM. For the 4 wt% MWCNTs nanocomposite, there was a very large drop in the tensile stress. This is probably due to the MWCNTs aggregates within the PC rich phase (in addition to the PC phase crystallization) that result in an increasing chance that the polymer will fracture at a much lower stress.

7.2.Conclusions

The comparative study of the crystallization process of the PCL_xM_y and PCL_xNHy systems shows common behaviors such as the supernucleating action of the carbon nanotubes in the crystallization process and the increase in the rate of crystallization with the content of nanotubes as compared to PCL homopolymer. A novel aspect of this study is the significant influence of the molecular weight of the PCL chains synthesized during the functionalization of the nanotubes, whether they are free or grafted, in the overall crystallization kinetics and therefore in the solidification process of products. The nucleating action of the nanotubes and the plasticizing effect of the low molecular weight PCL chains synthesized during the functionalization have opposite effects on the crystallization kinetics of the nanohybrids. The prevalence of one effect with respect to the other exhibits an interesting dependence with the composition. This competition illustrates the greater complexity of nanohybrid systems with respect to nanocomposites. Nanohybrids with 1 wt% or less MWCNTs exhibit faster crystallization rates than nanocomposites. In contrast, nanohybrid with more than 1 wt% MWCNT exhibit lower crystallization rates than nanocomposites, as a consequence of the plasticization action of low molecular weight PCL chains. The control of the molecular weight of the grafted and ‘free’ chains in nanohybrid systems offers a novel way to tailor the behavior of these systems.

Rheological properties confirm solid-like behavior in the melt for both PCL_xM_y and PCL_xNH_y samples from MWCNT content as low as 0.25 wt%. The results indicate an

effective dispersion of the MWCNT in both families, and a percolation threshold of around 0.23-0.24 wt%, which is one order of magnitude lower than that found in other melt-mixed PCL nanocomposites. The application of the percolation theory to the rheological data confirms a 3D percolated network in the melt, with an exponent t = 2.00. Additionally, from this study an improved performance and processability of the PCL_xNH_y samples can be foreseen, as decreased values of viscosity (up to a 50 %) have been determined in the compositional range 0.25 - 1 wt% of nanohybrids. This result is likely due to the low molecular weight MWCNT-grafted and 'free' PCL present in PCL_xNH_y samples, which compete with the MWCNTs network for these compositions.

In the case of polymer/masterbatch systems, after analysing the DSC, SEM, DMA, TEM and AFM results, it can be concluded that the PC and PCL blends prepared in this work are partially miscible. Two phases were formed: (1) A PC rich phase, where a small amount of PCL chains are present and can plasticize the PC component, so that it can crystallize, and (2) A PCL rich phase, where the amount of PC chains present is very small, so that changes in the T_g of the PCL phase are much smaller than those predicted by the Fox equation. Due to partial miscibility and the establishment of PC rich and PCL rich phases, a fair number of MWCNTs diffused from the PC rich phase to the PCL rich phase as evidenced by the SEM and AFM images, but their diffusion depends on the PC (and MWCNTs content) in the blend.

Standard DSC measurements demonstrated an increase in T_c with increasing MWCNTs content due to the nucleation effect caused by the presence of MWCNTs that penetrated into the PCL rich phase (as was demonstrated morphologically by SEM and AFM images). The nucleating efficiency is however low, due to limited phase mixing between the PC rich and the PCL rich phases. Only a limited quantity of MWCNTs can penetrate the PCL rich phase and therefore contribute in nucleating PCL, while most of the MWCNTs agglomerated in the PC rich phase at high MWCNTs loadings (e.g., 4%). The nucleation effects saturated at 1 wt% MWCNTs content on the PCL rich phase. This was corroborated by the determination of the dielectric percolation threshold which ranged between 0.5-1.0 wt% MWCNTs.

Isothermal crystallization experiments performed by DSC showed an increase in the overall crystallization kinetics of PCL with increases in MWCNTs as a result of their nucleating effect. Despite the nucleating effect of MWCNTs, a reduction in the

percentage crystallinity of PCL was observed especially at high PC contents. This was attributed to the presence of the PC rich phase, which was able to crystallize in view of the plasticization effect of the PCL component.

The thermal conductivities and tensile properties of the nanocomposites were generally enhanced with the addition of MWCNTs.

The PBS/masterbatch blends were partially miscible and formed PC rich and PBS rich phases, while the majority of the MWCNTs were inside the PC rich phase. PBS plasticization caused some PC crystallization. The MWCNTs were able to nucleate the PBS rich phase at low loading contents (below 4%), indicating that some of the MWCNTs were able to transfer from the PC rich to the PBS rich phase, as visualized by AFM. However, when the content of MWCNTs reached 4%, the PBS rich phase was antinucleated. This was explained by the agglomeration of MWCNTs which remained encapsulated inside the PC rich phase and the decreased ability of the PBS chains to nucleate. Such lower nucleation density may have arisen by a combination of reasons: impurities transfer from PBS rich to PC rich phase and increased T_g value of the PBS rich phase in comparison to neat PBS. The isothermal crystallization rate also increased with low contents of MWCNTs, went through a maximum and then decreased in a consistent way with the non-isothermal results.

The thermal conductivities and tensile properties of the nanocomposites varied, but could generally be explained in terms of the observed morphology of the nanocomposites.

7.3.References

[1] J.F. Vega, J. Fernández-Alcázar, J.V. López, R.M. Michell, R.A. Pérez-Camargo, B. Ruelle, J. Martínez-Salazar, M.L. Arnal, P. Dubois, A.J. Müller, Competition between supernucleation and plasticization in the crystallization and rheological behavior of PCL/CNT-based nanocomposites and nanohybrids, J. Polym. Sci., Part B: Polym. Phys. 55 (2017) 1310-1325.

[2] T. Gumede, A. Luyt, M. Hassan, R. Pérez-Camargo, A. Tercjak, A. Müller, Morphology, Nucleation, and Isothermal Crystallization Kinetics of Poly(ε-

caprolactone) Mixed with a Polycarbonate/MWCNTs Masterbatch, Polymers 9 (2017) 709.

[3] B. Fillon, J.C. Wittmann, B. Lotz, A. Thierry, Self-nucleation and recrystallization of isotactic polypropylene (α phase) investigated by differential scanning calorimetry, J. Polym. Sci., Part B: Polym. Phys. 31 (1993) 1383-1393.

[4] B. Fillon, B. Lotz, A. Thierry, J.C. Wittmann, Self-nucleation and enhanced nucleation of polymers. Definition of a convenient calorimetric "efficiency scale" and evaluation of nucleating additives in isotactic polypropylene (α phase), J. Polym. Sci., Part B: Polym. Phys. 31 (1993) 1395-1405.

[5] L. Mandelkern, Crystallization of Polymers: Volume 1, Equilibrium Concepts, Cambridge University Press, 2002.

[6] L. Mandelkern, Crystallization of Polymers: Volume 2, Kinetics and Mechanisms, Cambridge University Press, 2004.

[7] G. Strobl, A Multiphase Model Describing Polymer Crystallization and Melting, in: G. Reiter, G. Strobl (Eds.) Progress in Understanding of Polymer Crystallization, Springer Berlin Heidelberg, 2007, pp. 481-502.

[8] M.D. Sanchez-Garcia, J.M. Lagaron, S.V. Hoa, Effect of addition of carbon nanofibers and carbon nanotubes on properties of thermoplastic biopolymers, Compos. Sci. Technol. 70 (2010) 1095-1105.

[9] T.-M. Wu, E.-C. Chen, Crystallization behavior of poly(ε-caprolactone)/multiwalled carbon nanotube composites, J. Polym. Sci., Part B: Polym. Phys. 44 (2006) 598-606.

[10] T.-M. Wu, E.-C. Chen, Isothermal and nonisothermal crystallization kinetics of poly(ε-caprolactone)/multi-walled carbon nanotube composites, Polymer Engineering & Science 46 (2006) 1309-1317.

[11] C.A. Mitchell, R. Krishnamoorti, Non-isothermal crystallization of in situ polymerized poly(ε-caprolactone) functionalized-SWNT nanocomposites, Polymer 46 (2005) 8796-8804.

[12] M. Trujillo, M.L. Arnal, A.J. Müller, E. Laredo, S. Bredeau, D. Bonduel, P. Dubois, Thermal and Morphological Characterization of Nanocomposites Prepared by in-Situ Polymerization of High-Density Polyethylene on Carbon Nanotubes, Macromolecules 40 (2007) 6268-6276.

[13] A.J. Müller, M.L. Arnal, M. Trujillo, A.T. Lorenzo, Super-nucleation in nanocomposites and confinement effects on the crystallizable components within block

copolymers, miktoarm star copolymers and nanocomposites, Eur. Polym. J. 47 (2011) 614-629.

[14] R. Andrews, M.C. Weisenberger, Carbon nanotube polymer composites, Curr. Opin. Solid State Mater. Sci. 8 (2004) 31-37.

[15] R. Haggenmueller, J.E. Fischer, K.I. Winey, Single Wall Carbon Nanotube/Polyethylene Nanocomposites: Nucleating and Templating Polyethylene Crystallites, Macromolecules 39 (2006) 2964-2971.

[16] B.P. Grady, F. Pompeo, R.L. Shambaugh, D.E. Resasco, Nucleation of Polypropylene Crystallization by Single-Walled Carbon Nanotubes, The Journal of Physical Chemistry B 106 (2002) 5852-5858.

[17] A.R. Bhattacharyya, T.V. Sreekumar, T. Liu, S. Kumar, L.M. Ericson, R.H. Hauge, R.E. Smalley, Crystallization and orientation studies in polypropylene/single wall carbon nanotube composite, Polymer 44 (2003) 2373-2377.

[18] O. Probst, E.M. Moore, D.E. Resasco, B.P. Grady, Nucleation of polyvinyl alcohol crystallization by single-walled carbon nanotubes, Polymer 45 (2004) 4437-4443.

[19] M.L. Minus, H.G. Chae, S. Kumar, Single wall carbon nanotube templated oriented crystallization of poly(vinyl alcohol), Polymer 47 (2006) 3705-3710.

[20] K.P. Ryan, S.M. Lipson, A. Drury, M. Cadek, M. Ruether, S.M. O'Flaherty, V. Barron, B. McCarthy, H.J. Byrne, W.J. Blau, J.N. Coleman, Carbon-nanotube nucleated crystallinity in a conjugated polymer based composite, Chem. Phys. Lett. 391 (2004) 329-333.

[21] S.P. Bao, S.C. Tjong, Mechanical behaviors of polypropylene/carbon nanotube nanocomposites: The effects of loading rate and temperature, Materials Science and Engineering: A 485 (2008) 508-516.

[22] K. Anoop Anand, U.S. Agarwal, R. Joseph, Carbon nanotubes induced crystallization of poly(ethylene terephthalate), Polymer 47 (2006) 3976-3980.

[23] Y. Gao, Y. Wang, J. Shi, H. Bai, B. Song, Functionalized multi-walled carbon nanotubes improve nonisothermal crystallization of poly(ethylene terephthalate), Polym. Test. 27 (2008) 179-188.

[24] G. Xu, L. Du, H. Wang, R. Xia, X. Meng, Q. Zhu, Nonisothermal crystallization kinetics and thermomechanical properties of multiwalled carbon nanotube-reinforced poly(ε-caprolactone) composites, Polym. Int. 57 (2008) 1052-1066.

[25] M. Trujillo, M.L. Arnal, A.J. Müller, S. Bredeau, D. Bonduel, P. Dubois, I.W. Hamley, V. Castelletto, Thermal Fractionation and Isothermal Crystallization of Polyethylene Nanocomposites Prepared by in Situ Polymerization, Macromolecules 41 (2008) 2087-2095.

[26] B. Kalb, A.J. Pennings, General crystallization behaviour of poly(l-lactic acid), Polymer 21 (1980) 607-612.

[27] M. Trujillo, M.L. Arnal, A.J. Müller, M.A. Mujica, C. Urbina De Navarro, B. Ruelle, P. Dubois, Supernucleation and crystallization regime change provoked by MWNT addition to poly(ε-caprolactone), Polymer 53 (2012) 832-841.

[28] D. Priftis, G. Sakellariou, N. Hadjichristidis, E.K. Penott, A.T. Lorenzo, A.J. Müller, Surface modification of multiwalled carbon nanotubes with biocompatible polymers via ring opening and living anionic surface initiated polymerization. Kinetics and crystallization behavior, J. Polym. Sci., Part A: Polym. Chem. 47 (2009) 4379-4390.

[29] R.N. Jana, J.W. Cho, Non-isothermal crystallization of poly(ε-caprolactone)-grafted multi-walled carbon nanotubes, Composites Part A: Applied Science and Manufacturing 41 (2010) 1524-1530.

[30] P.J. Phillips, G.J. Rensch, K.D. Taylor, Crystallization studies of poly(ε-caprolactone).I. Morphology and kinetics, J. Polym. Sci., Part B: Polym. Phys. 25 (1987) 1725-1740.

[31] Q. Guo, G. Groeninckx, Crystallization kinetics of poly(ε-caprolactone) in miscible thermosetting polymer blends of epoxy resin and poly(ε-caprolactone), Polymer 42 (2001) 8647-8655.

[32] S.-W. Kuo, S.-C. Chan, F.-C. Chang, Crystallization kinetics and morphology of binary phenolic/poly(ϵ-caprolactone) blends, J. Polym. Sci., Part B: Polym. Phys. 42 (2004) 117-128.

[33] J.-T. Yeh, M.-C. Yang, C.-J. Wu, C.-S. Wu, Preparation and characterization of biodegradable polycaprolactone/multiwalled carbon nanotubes nanocomposites, J. Appl. Polym. Sci. 112 (2009) 660-668.

[34] F. Buffa, H. Hu, D.E. Resasco, Side-Wall Functionalization of Single-Walled Carbon Nanotubes with 4-Hydroxymethylaniline Followed by Polymerization of ε-Caprolactone, Macromolecules 38 (2005) 8258-8263.

[35] H.-S. Xu, X.J. Dai, P.R. Lamb, Z.-M. Li, Poly(L-lactide) crystallization induced by multiwall carbon nanotubes at very low loading, J. Polym. Sci., Part B: Polym. Phys. 47 (2009) 2341-2352.

[36] Y. Li, Y. Wang, L. Liu, L. Han, F. Xiang, Z. Zhou, Crystallization improvement of poly(L-lactide) induced by functionalized multiwalled carbon nanotubes, J. Polym. Sci., Part B: Polym. Phys. 47 (2009) 326-339.

[37] A.M. Díez-Pascual, M. Naffakh, M.A. Gómez, C. Marco, G. Ellis, M.T. Martínez, A. Ansón, J.M. González-Domínguez, Y. Martínez-Rubi, B. Simard, Development and characterization of PEEK/carbon nanotube composites, Carbon 47 (2009) 3079-3090.

[38] J.Y. Kim, S.I. Han, D.K. Kim, S.H. Kim, Mechanical reinforcement and crystallization behavior of poly(ethylene 2,6-naphthalate) nanocomposites induced by modified carbon nanotube, Composites Part A: Applied Science and Manufacturing 40 (2009) 45-53.

[39] B. Fillon, A. Thierry, J.C. Wittmann, B. Lotz, Self-nucleation and recrystallization of polymers. Isotactic polypropylene, β phase: β-α conversion and β-α growth transitions, J. Polym. Sci., Part B: Polym. Phys. 31 (1993) 1407-1424.

[40] R.A. Pérez, J.V. López, J.N. Hoskins, B. Zhang, S.M. Grayson, M.T. Casas, J. Puiggalí, A.J. Müller, Nucleation and antinucleation effects of functionalized carbon nanotubes on cyclic and linear Poly(ε-caprolactones), Macromolecules 47 (2014) 3553-3566.

[41] R.A. Pérez–Camargo, G. Saenz, S. Laurichesse, M.T. Casas, J. Puiggalí, L. Avérous, A.J. Müller, Nucleation, Crystallization, and Thermal Fractionation of Poly (ε-Caprolactone)-Grafted-Lignin: Effects of Grafted Chains Length and Lignin Content, J. Polym. Sci., Part B: Polym. Phys. 53 (2015) 1736-1750.

[42] C.-C. Lin, K. Ohno, N. Clarke, K.I. Winey, R.J. Composto, Macromolecular Diffusion through a Polymer Matrix with Polymer-Grafted Chained Nanoparticles, Macromolecules 47 (2014) 5357-5364.

[43] A. Karatrantos, R.J. Composto, K.I. Winey, M. Kröger, N. Clarke, Entanglements and Dynamics of Polymer Melts near a SWCNT, Macromolecules 45 (2012) 7274-7281.

[44] M. Mu, N. Clarke, R.J. Composto, K.I. Winey, Polymer Diffusion Exhibits a Minimum with Increasing Single-Walled Carbon Nanotube Concentration, Macromolecules 42 (2009) 7091-7097.

[45] M. Mu, R.J. Composto, N. Clarke, K.I. Winey, Minimum in Diffusion Coefficient with Increasing MWCNT Concentration Requires Tracer Molecules To Be Larger than Nanotubes, Macromolecules 42 (2009) 8365-8369.

[46] J. Choi, N. Clarke, K.I. Winey, R.J. Composto, Fast Polymer Diffusion through Nanocomposites with Anisotropic Particles, ACS Macro Letters 3 (2014) 886-891.

[47] A.T. Lorenzo, M.L. Arnal, J. Albuerne, A.J. Müller, DSC isothermal polymer crystallization kinetics measurements and the use of the Avrami equation to fit the data: Guidelines to avoid common problems, Polym. Test. 26 (2007) 222-231.

[48] M. Avrami, Kinetics of Phase Change. I General Theory, The Journal of Chemical Physics 7 (1939) 1103-1112.

[49] R.M. Michell, A.J. Müller, M. Spasova, P. Dubois, S. Burattini, B.W. Greenland, I.W. Hamley, D. Hermida-Merino, N. Cheval, A. Fahmi, Crystallization and stereocomplexation behavior of poly(D - And L -lactide)-b-poly(N,N-dimethylamino-2-ethyl methacrylate) block copolymers, Journal of Polymer Science, Part B: Polymer Physics 49 (2011) 1397-1409.

[50] Y. Zhang, J.H. Han, Crystallization of high-amylose starch by the addition of plasticizers at low and intermediate concentrations, J Food Sci 75 (2010) N8-16.

[51] V. Balsamo, N. Calzadilla, G. Mora, A.J. Müller, Thermal characterization of polycarbonate/polycaprolactone blends, J. Polym. Sci., Part B: Polym. Phys. 39 (2001) 771-785.

[52] H. Hu, D.L. Dorset, Crystal structure of poly(iε-caprolactone), Macromolecules 23 (1990) 4604-4607.

[53] P. Pötschke, A.R. Bhattacharyya, A. Janke, H. Goering, Melt mixing of polycarbonate/multi-wall carbon nanotube composites, Compos. Interfaces 10 (2003) 389-404.

[54] F.Y. Castillo, R. Socher, B. Krause, R. Headrick, B.P. Grady, R. Prada-Silvy, P. Pötschke, Electrical, mechanical, and glass transition behavior of polycarbonate-based nanocomposites with different multi-walled carbon nanotubes, Polymer 52 (2011) 3835-3845.

[55] J. Guo, Y. Liu, R. Prada-Silvy, Y. Tan, S. Azad, B. Krause, P. Pötschke, B.P. Grady, Aspect ratio effects of multi-walled carbon nanotubes on electrical, mechanical, and thermal properties of polycarbonate/MWCNT composites, J. Polym. Sci., Part B: Polym. Phys. 52 (2014) 73-83.

[56] A.T. Lorenzo, M.L. Arnal, J.J. Sánchez, A.J. Müller, Effect of annealing time on the self-nucleation behavior of semicrystalline polymers, Journal of Polymer Science, Part B: Polymer Physics 44 (2006) 1738-1750.

[57] A.J. Müller, M.L. Arnal, Thermal fractionation of polymers, Prog. Polym. Sci. 30 (2005) 559-603.

[58] R.A. Pérez, M.E. Córdova, J.V. López, J.N. Hoskins, B. Zhang, S.M. Grayson, A.J. Müller, Nucleation, crystallization, self-nucleation and thermal fractionation of cyclic and linear poly(ε-caprolactone)s, React. Funct. Polym. 80 (2014) 71-82.

[59] M. Avrami, Granulation, phase change, and microstructure kinetics of phase change. III, The Journal of Chemical Physics 9 (1941) 177-184.

[60] H. Meng, G.X. Sui, P.F. Fang, R. Yang, Effects of acid- and diamine-modified MWNTs on the mechanical properties and crystallization behavior of polyamide 6, Polymer 49 (2008) 610-620.

CHAPTER VIII.

CYCLIC AND LINEAR POLYMERS AND THEIR BLENDS

8.1. General Introduction

Cyclic polymers differ with their linear analogues in their lack of chain ends. This means that whereas linear chains can take any conformation that is available under the local constraint of excluded volume only, cyclic polymers can never change their state of concatenation and thus provide an additional and global constraint for the conformation statistics.[1] Such topological difference can have a large impact on their molecular behaviour. [2]

Despite that cyclic topology was discovered 60 years ago when Jacob and Wollman[3] concluded that the genetic map of bacterial chromosomes of *Eschericha coli* showed circularity, only recent advances on the preparation of cyclic polymers as well as copolymers with a high degree of purity allows to study the cyclic homopolymers and compared them with their linear analogues.

The synthetic procedures and purification methods employed in the production of ring polymers with high purity have been evolving for decades.[4] In fact, nowadays, new synthetic approaches have allowed the preparation of a wide range of high purity ring polymers, as well as novel and more complex cyclic-based topologies.[5-23] These new synthetic approaches have enabled researchers to study differences between the properties of cyclic and linear polymers, such as the glass transition temperature,[24, 25] melt viscosity and diffusion,[24-29] morphology,[30-32] and crystallization.[29, 33-45]

The studies which compared cyclic and linear homopolymers reported in the literature show contrasting behaviours as well as explanations. In fact, the influence of the cyclic topology posted important questions related to the existing crystallization models. In general terms, there are authors which claim that the crystallization of the cyclic polymers is slower in comparison with the linear ones,[34, 38, 39] whereas others claims the opposite behaviour.[2, 35, 41-44, 46] In a recent work, these differences were attributed to the importance of the purity of the materials as well as their nature.[2] It is important to note that even in simulation studies (*i.e.*, the impurities of the samples is

discarded) contrasting trends are also reported. Sommer et al.[1] corroborated some of the experimental findings of higher crystallization and melting temperatures, as well as faster crystallization kinetics in cyclic polymers, which were related to the direct impact of the entanglement state on the crystallization properties, whereas Muthukumar and Iyer[47] reported the opposite trend, since they found lower melting temperatures for cyclic polymers, due to free energy barriers in the secondary nucleation of cyclic chains.

8.2.Results and Discussion

The main aim of this chapter is to show how small amounts of linear PCL (L-PCL) chains can affect the thermal properties, spherulitic growth rate and overall crystallization kinetics of cyclic PCL (C-PCL). The synthesis and chemical characterization of this material can be seen in Chapter III. Experimental Part, Section 3.1e.

8.2.1. Blends of C-PCL with small amounts of L-PCLs

Figure 8.1 shows DSC cooling scans after erasing thermal history and subsequent heating scans for neat C–PCLs and L–PCLs and their blends. Figure 8.1a and b correspond to the cooling (8.1a) and heating (8.1b) of C/L blends prepared with 3 kg/mol samples, while Figure 8.1c and d present the cooling and heating of 12 kg/mol C/L blends.

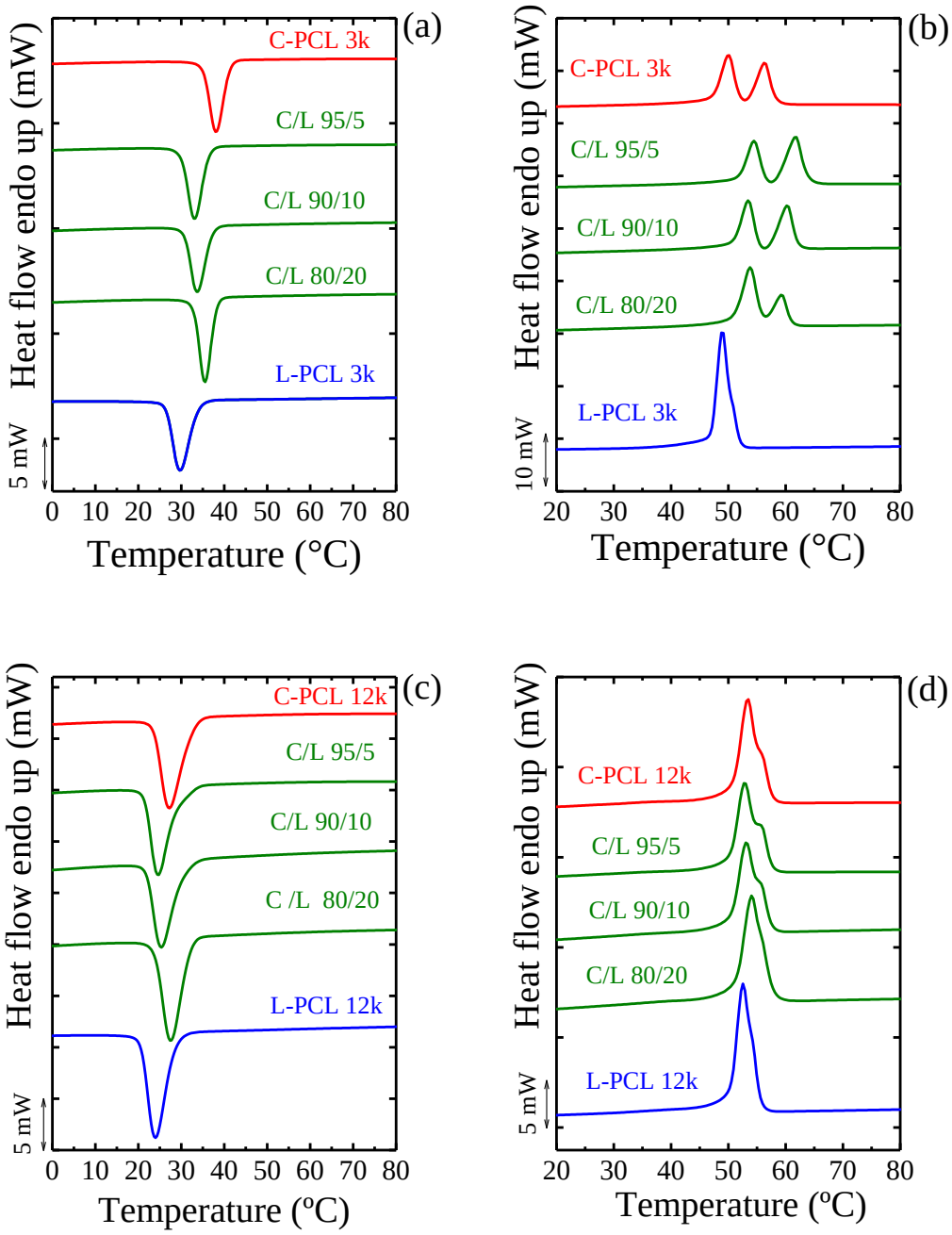

Figure 8.1. DSC cooling (a and c) and subsequent heating (b and d) scans at 20 °C/min for 3 (a and b) and 12 kg/mol (c and d) samples of neat L–PCL and C–PCL and their blends at the indicated compositions. The red (top) and blue (bottom) curves represent neat C-PCL and L-PCL, respectively, whereas the green curves (middle) represent the C/L blends at the indicated compositions.

The differences in both crystallization (T_c) and melting (T_m) temperatures between cyclic and linear PCL can be observed in Figure 8.1. The higher T_c and T_m values of the C–PCL respect to its linear analog for both 3 and 12 kg/mol samples are in agreement with previous works[35-37, 41, 42] in which the differences were attributed to higher supercoolings and faster diffusion of cyclic PCL. It is worth noting that in a recent work of Sommer et al.[1] an alternative explanation is given, since the differences between cyclic and linear polymers are attributed to the direct impact of the entanglement state on the crystalline properties (since kinetics models based on the effective supercooling would lead to the opposite conclusion).

The second DSC heating scans show a double melting peak for neat C–PCLs and their blends (see Figure 8.1b and d). This double melting peak is more pronounced for the samples with 3 kg/mol in comparsion to those with 12 kg/mol. These double melting peaks are due to melting and recrystallization processes during the scan. This is demonstrated for neat 3 kg/mol C-PCL in Figure 8.2.

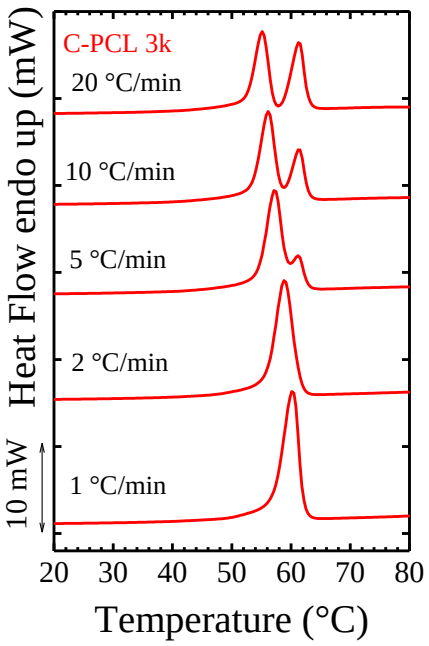

Figure 8.2. DSC heating scans (performed at 20 °C/min) after previous cooling scans at the indicated cooling scans for a 3 kg/mol C–PCL sample.

Figure 8.2 shows DSC heating scans after previous cooling scans at different rates for 3 kg/mol neat C–PCL samples. As the previous cooling rate goes down, the sample has enough time to form more stable crystals that do not undergo recrystallization during subsequent heating scans, hence, the double melting disappears. This result is in agreement with a previous report by Córdova et al.[35] on L–PCL and C–PCL with number average molecular weights of 2 to 7.5 kg/mol.

The relevant thermal parameters obtained from the DSC scans (see Figure 8.1) are listed in Table 8.1.

Table 8.1. Thermal Transitions and Relevant Enthalpy Values Obtained from DSC Scans Presented in Figure 8.1*

Sample	T_c (°C)	ΔH_c (J/g)	T_m (°C)	ΔH_m (J/g)
C–PCL 3k	34.0	68	55.2 (61.3)	70
C/L 3k 95/5	31.2	71	54.5 (61.9)	72
C/L 3k 90/10	32.0	65	53.4 (60.2)	69
C/L 3k 80/20	34.6	69	53.8 (59.2)	73
L–PCL 3k	26.7	74	48.8	78
C–PCL 12k	27.3	60	53.5	67
C/L 12k 95/5	24.7	61	52.7	67
C/L 12k 90/10	25.4	61	53.0	67
C/L 12k 80/20	27.4	61	54.0	66
L–PCL 12k	24.0	69	52.5	73

* Peak crystallization temperature (T_c), Crystallization enthalpy (ΔH_c), Peak melting temperature (T_m), Melting enthalpy (ΔH_m). The enthalpy of crystallization and fusion of 100% crystalline PCL was taken as 136 J/g.[48]

Crystallization and melting enthalpies (see Table 8.1) do not show significant variations by changing blend composition. The effect of M_n on C–PCLs and their linear counterparts has been previously studied by Pérez et al. in a wider molecular weight range.[42]

Figure 8.3 shows plots of T_c and T_m as a function of C–PCL content. Negative deviations from a simple mixing law (indicated as straight lines in Figure 8.3) can be observed in all cases. In the case of T_c, additions of 5 or 10 wt% L-PCL to C-PCL induce a depression of T_c well below the value of neat C-PCL samples for both 3 and 12 kg/mol cases. Such acute decreases in T_c corresponded to anti-nucleation effects that were verified by PLOM, as the nuclei density was significantly reduced.

The negative deviation of the simple mixing rule in Figure 8.3 occurs when small amounts of L–PCL (5 or 10 wt%) are added to C–PCL. Interestingly, adding larger amounts (>20 wt%) leads to a strong recovery in the values of T_c, which become as large as those of neat C-PCL samples. Hence, the anti-nucleation effect completely disappears for 80/20 C/L blends. The observed changes in T_c values are mimicked by similar trends in melting peak with blend composition, also shown in Figure 8.3. The changes in melting points are not as large, as expected in view of the metastable character of polymeric crystals.

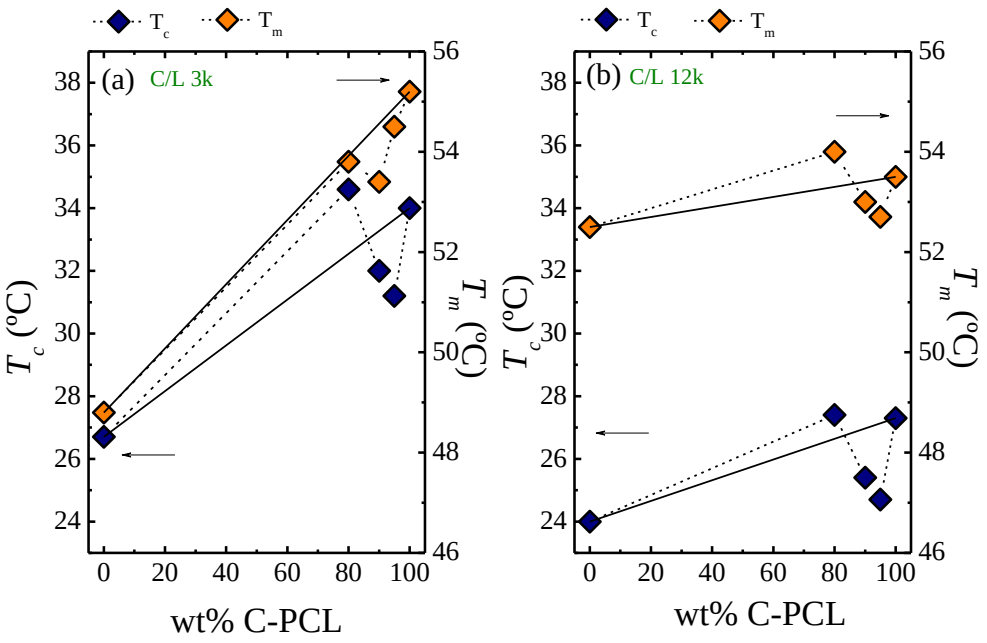

Figure 8.3. Values of crystallization (T_c) and melting temperature (T_m) (represented in the right and left handed axis, respectively) as a function of C–PCL content for (a) 3 kg/mol samples and (b) 12 kg/mol samples. The straight solid line indicated the behavior predicted by a simple mixing law.

The results shown in Figure 8.3 are in agreement with those obtained in a previous work,[43] in which decreases in nucleation density, T_c, T_m and crystallization ability were obtained for a C–PCL/MWNT–*g*–PCL nanocomposite. In this nanocomposite case, nearly 9% of L–PCL chains grafted to MWNT were added to a C-PCL matrix. The results were explained by a threading effect of C–PCL by L–PCL chains. A similar explanation is responsible for the effects displayed in Figure 8.3. A detailed mechanism will be presented below after isothermal crystallization and thermal fractionation results are discussed.

Spherulitic growth rates determined by PLOM

Cyclic and linear PCLs (both 3 and 12 kg/mol samples) crystallize in spherulitic superstructures. Typical spherulites are shown in Figure 8.4. The spherulites of neat L-PCLs, C-PCLs and their blends exhibit the characteristic Maltese Cross extinction patterns with no banding and negative signs (see Figure 8.4). Negative spherulites are characterized by tangential chain axis orientation.[49]

Figure 8.4 also shows the spherulitic growth rates for neat linear and cyclic 3 kg/mol PCL samples and their blends. As expected, neat C–PCL exhibits higher growth rates than L–PCL, as already reported for similar samples with different M_n values.[35, 41, 42] The higher growth rates for cyclic PCLs have been explained by their enhanced supercooling degree, since their equilibrium melting points are higher than their linear analog PCL samples. Additionally, the more compact conformation of cyclic chains in the melt, together with their lower entanglement density lead to lower diffusion coefficients for cyclic PCLs as compared to linear PCLs. These factors produce faster nucleation and faster spherulitic growth rates for cyclic PCL chains.[2, 35, 41-43]

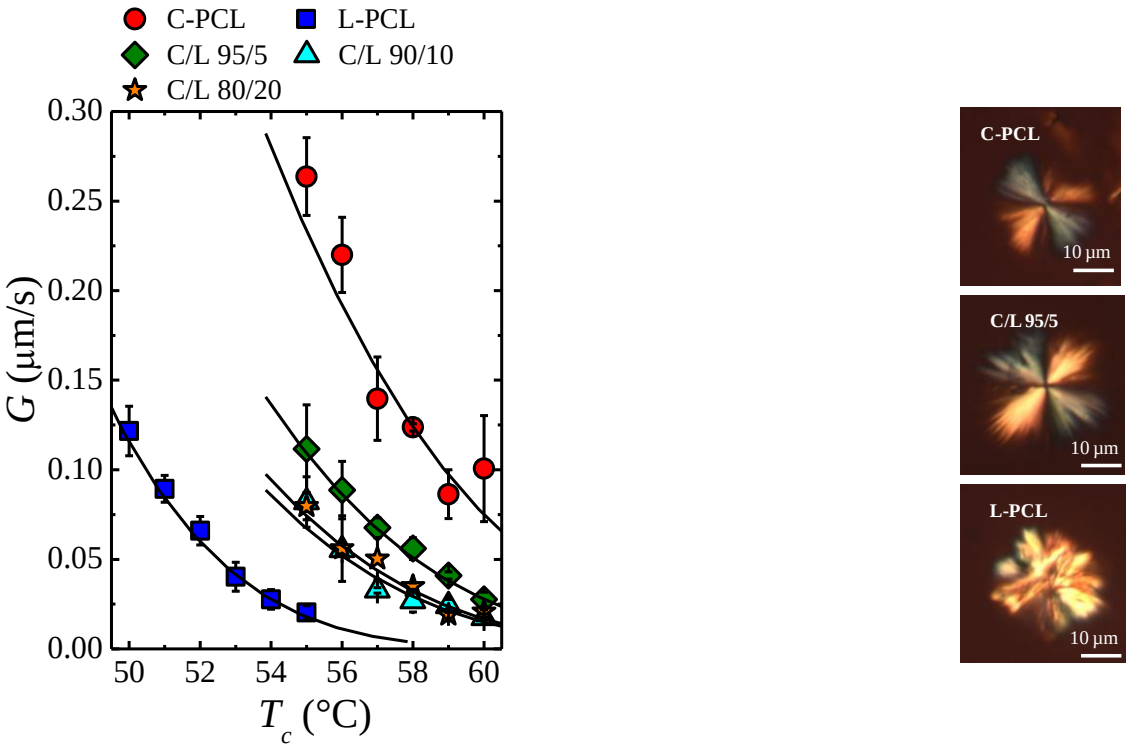

Figure 8.4. Spherulitic growth rate (G) as a function of isothermal crystallization temperature (T_c) for neat L–PCL and C–PCL of 3 kg/mol and their blends. Solid lines represent fits to the Lauritzen and Hoffman equation. Typical spherulites of C-PCL, L-PCL and their 95/5 blend are also shown.

The spherulitic growth rates of the C/L blends are intermediate in comparison to the growth rate values of the C-PCL and the L-PCL (see Figure 8.4). Nevertheless, the trend with composition is highly non-linear. This is illustrated in Figure 8.5 where the growth rate has been plotted as a function of composition for different isothermal crystallization temperatures. A synergistic decrease in growth rate is observed when small amounts of L-PCL chains are added to C-PCL.

The spherulitic growth rate is influenced by both secondary nucleation and by diffusion effects related to the transport of molecules from the melt to the crystalline front. A reduction in spherulitic growth rate can be explained by decreases in diffusion ability of the chains,[49] as a result of melt viscosity increases. McKenna et al.[27] reported an increase of the melt viscosity in blends of polystyrene rings with small amounts of linear polystyrene.

The decrease in growth rate is more significant as crystallization temperatures decrease. As T_c temperatures increase, melt viscosity decreases and diffusion effects are less important.

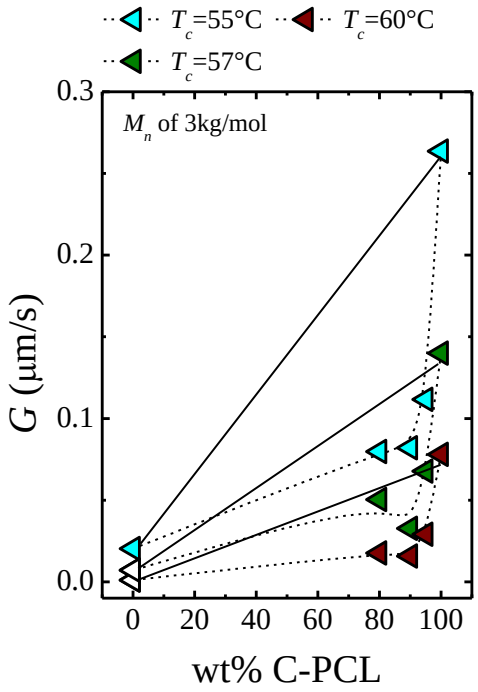

Figure 8.5. Spherulitic growth rate (G) as a function of C–PCL content at selected crystallization temperatures (T_c) for 3 kg/mol samples. The solid lines represent a

simple mixing rule. The unfilled symbols represent the values extrapolated from LH fittings to the data shown in Figure 8.4.

The negative synergistic deviation from a simple rule of mixtures shown in Figure 8.5 can be explained by a threading effect of several ring PCL chains by linear analog chains, which increase entanglement density and reduce the diffusion ability of cyclic PCL chains.

The results shows in Figure 8.5 are in agreement with self–diffusion coefficients (*D*) measurements performed by Nam et al.[50] in PEO cyclic and linear blends. The *D* values of C/L PEO blends reach a minimum at low C–PEO contents (*i.e.*, around 20–40 wt%), followed by an increase towards the value of neat C-PEO. Nam et al.[50] claimed that threaded conformations are present across the entire composition range in their blends.

It is worth noting that in the work of Nam et al.[50, 51] the lowest linear chain content in their C/L PEO blends was 20 wt%. Other results in the literature indicate that very small amounts of linear chains can also have important effects on the properties of cyclic chains.

Kapnistos et al. reported that even 0.07 wt% of linear chains added to cyclic PS could cause significant changes in the rheology, diffusion, chain dynamics and relaxation times of ring molecules.[28] Similar effects have been predicted by computer simulations.[52-60] These studies have shown that cyclic molecules relax and diffuse more slowly than linear chains. Therefore, these threading effects that connect ring and linear chains constitute long lived entanglements which represent strong topological interactions that are capable of slowing down relaxation and chain mobility. [52-60]

In view of the above explained arguments, a threading effect of C–PCL by L–PCL chains reduces the spherulitic growth rates of ring PCL molecules, as shown in Figure 8.6. At low T_c (*i.e.*, 55 °C), the influence of the diffusion in the crystalline growth is higher, whereas as T_c increases (*i.e.*, 57 °C) the crystalline growth is more influenced by nucleation control. Nevertheless, even at such low supercoolings where diffusion is not expected to be predominant, the threading effects survive as indicated

by the reduced values of *G* in the blends as compared to neat C-PCL. The threading effects seem to saturate at 20 wt% L-PCL loadings, in the sense that the rate of decrease in *G* with composition is reduced. This effect is in agreement with the disappearance of the anti-nucleation effect shown in Figure 8.3 when the content of L-PCL is increased to 20 wt% in the blends.

The solid lines in Figure 8.4 are fits to the experimental data performed with the Lauritzen and Hoffman theory (LH) of polymer nucleation and growth.[61-65] The details of LH model were shown in Chapter II. General Concepts, whereas the results obtained are show in Table 8.2.

Table 8.2. Parameters obtained from fitting the Lauritzen and Hoffman theory to the data of Figure 8.4*

Sample	K_g^G (K^2)	σ_e (erg/cm^2)	R^2
C–PCL 3k	107005	115	0.87841
C/L 3k 95/5	122223	132	0.99548
C/L 3k 90/10	127723	138	0.94461
C/L 3k 80/20	117784	128	0.94254
L–PCL 3k	107906	120	0.99417

*R^2 is the correlation coefficient for the Lauritzen and Hoffman linear plots. The superindex *G* in K_g^G is used to indicate that the parameter is derived from spherulitic growth rate data.

The parameters derived from the LH fittings are listed in Table 8.2. These parameters depend strongly on the T_m^0 values used to perform the fit. In this work, the values are taken from a previous paper,[41] where equilibrium melting points were experimentally determined for L–PCL and C–PCL samples with M_n of 7.5 kg/mol. The T_m^0 value is higher for C–PCL than for L–PCL (*i.e.*, 91.2 °C and 80 °C for cyclic and linear PCL respectively).[41] The correlation coefficient is quite low for C-PCL in view of the errors involved in the experimental measurements. Even so, a slightly lower K_g^G value was obtained for C-PCL as compared to L-PCL. Since C-PCL exhibits a faster

spherulitic growth rate at identical T_c values than L-PCL, a lower energy barrier for spherulitic growth is expected (and therefore a lower K_g^G value).

In the case of the C/L blends, the following equation was used to estimate T_m^0 values for the blends at selected compositions:

$$T^0_{m(blend)} = T^0_{m(L)}(\%L) + T^0_{m(C)}(\%C) \qquad \text{Eq.8.1}$$

$T_m^{0}{}_{(L)}$ is the T_m^0 of the neat L–PCL, $T_m^{0}{}_{(C)}$ is the T_m^0 for the neat C–PCL, *(%L)* and *(%C)* are the L–PCL and C–PCL contents in the blend respectively.

After calculating these approximated equilibrium melting points for the blends, the fits to the LH theory were performed as indicated by the solid lines in Figure 8.4 with good agreement with the experimental data. The calculated K_g^G values from the fittings are plotted in Figure 8.6. A synergistic increase in the value of this parameter, which is proportional to the energy barrier for secondary nucleation is clearly observed as small amounts of L-PCL molecules are added to C-PCL. The increases in K_g^G values quantify the topological difficulties that the mixture of linear and cyclic PCL chains encounters to grow spherulites, especially at low L–PCL contents (5 and 10 wt%). The maximum value of K_g^G is observed at 10% L-PCL. At 20 wt% L-PCL the energy barrier for spherulitic growth decreases as the threading effect seems to saturate. These results are fully consistent with the trends observed in Figures 8.3 and 8.5.

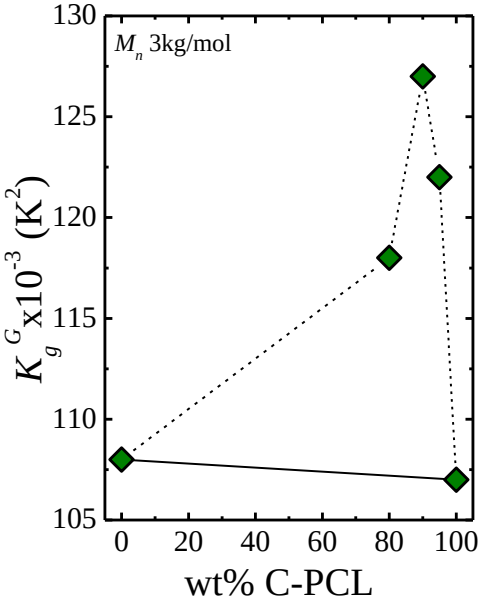

Figure 8.6. The K_g^G secondary nucleation rate constant derived by the fitting of the data of Figure 8.4 with the LH theory, as a function of the C–PCL content for 3 kg/mol C/L blends.

Determination of overall isothermal crystallization rates by DSC

Isothermal crystallization experiments were performed by DSC in order to measure the half–crystallization time and determine the overall crystallization kinetics of the samples. The inverse of the half–crystallization time provides an experimental measure of the overall crystallization rate (which includes both nucleation and growth).

Figure 8.7 shows the overall crystallization rate as a function of the crystallization temperature for linear and cyclic PCL samples and their 3 and 12 kg/mol blends (see Figure 8.7a and b, respectively). As in previous works,[35, 41-43] neat cyclic PCLs exhibit faster overall crystallization rates at identical T_c values than their linear analogs.

Figure 8.4 presents growth rate only. In this case, the *G* value does not depend on primary nucleation effects, only on secondary nucleation or growth. In Figure 8.7, the overall crystallization rate depends on both primary nucleation and growth of the

crystals. Any difference between Figure 8.4 and Figure 8.7 is due to the additional effect of primary nucleation on top of the differences in growth kinetics.

The behavior of the C/L blends in Figure 8.7 is in general terms similar to that in Figure 8.4. The differences in between linear and cyclic PCLs are smaller in the case of 12 kg/mol as compared to 3 kg/mol as expected, since the effect of no end groups is diluted for longer chains relative to shorter chains.[42] Parallel threading effects cause synergistic negative deviations of the rule of mixing for overall crystallization rate as a function of composition as clearly shown in Figure 8.8. The critical molecular weight for the development of entanglements in PCL has been estimated to be between 2.3 and 3 kg/mol.[66, 67] Since the samples employed in this work have M_n values of the same order of magnitude or above the critical molecular weight, the threading effect occurs for both 3 and 12 kg/mol C/L blends.

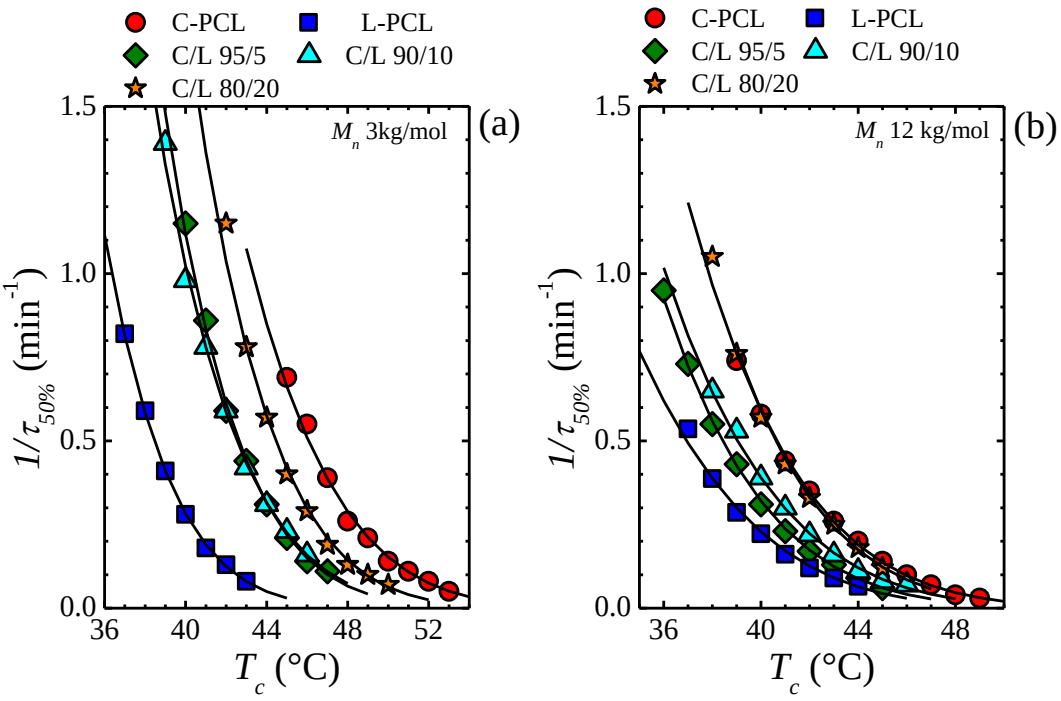

Figure 8.7. Overall crystallization rate ($1/\tau_{50\%}$) as a function of isothermal crystallization temperature for neat C–PCL and L–PCL and their blends: (a) 3 kg/mol and (b) 12 kg/mol.

As in the previous case of Figure 8.4, when T_c increases, the diffusion control decreases and the overall crystallization rate as a function of C–PCL content is closer to the expectations of a simple rule of mixing (see T_c = 45 °C in Figure 8.8b).

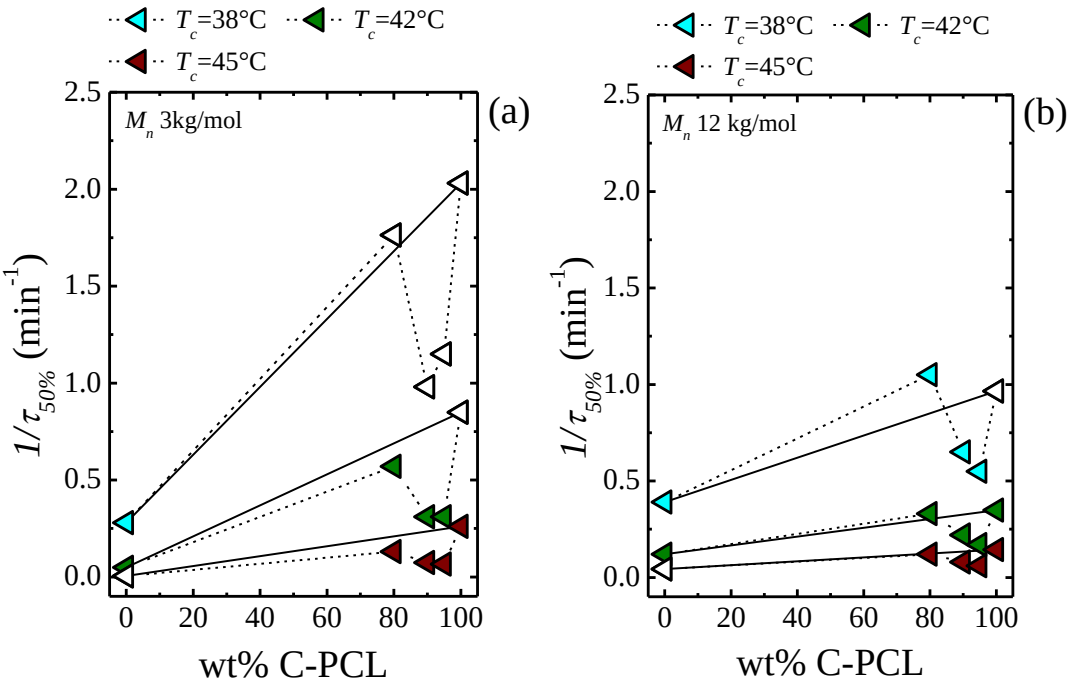

Figure 8.8. Values of $1/\tau_{50\%}$ as a function of C–PCL content at different constant values of T_c for C/L blends of (a) 3 kg/mol and (b) 12 kg/mol. The plots contains experimental data points indicated by filled symbols and values extrapolated from LH fittings to the data shown in Figure 8.7, indicated by unfilled symbols.

The overall crystallization rate can be modelled by the Avrami equation.[68, 69] The details related to the Avrami equation are show in Chapter II. General Concepts.

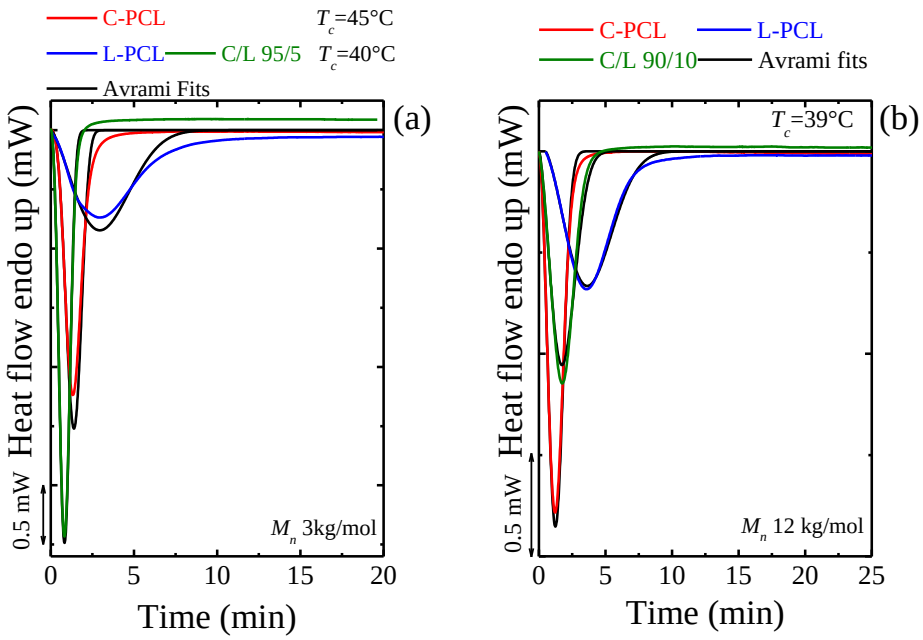

Figure 8.9. Examples of experimental DSC crystallization isotherms and their fittings with the Avrami equation for (a) C–PCL of 3 kg/mol at T_c=45 °C, L–PCL and C/L 95/5 of 3 kg/mol at 40 °C of 3 kg/mol and (b) C–PCL, L–PCL, C/L 90/10 of 12 kg/mol at 39 °C.

Figure 8.9 shows experimental DSC crystallization isotherms and their fittings by the Avrami equation. The selected conversion range in the Origin ® plug-in was 2–35 % (see ref. [68]) although the quality of the fit is outstanding in the primary crystallization range, and up to about 50 % conversion. This can be observed in the Appendix, where Tables 9.18 and 9.19 compare the experimentally half–crystallization times with those predicted by the Avrami equations with excellent agreement.

The Avrami indexes obtained are listed in Tables 9.18 and 9.19 for both types of blends (*i.e.*, C/L blends of 3 and 12 kg/mol respectively). Most *n* values are within 2.5–3 indicating that instantaneous spherulites were formed, a result consistent with PLOM observations.

The Lauritzen and Hoffman theory can also be applied to DSC data if *G(T)* is replaced by the inverse of the experimental half–crystallization time,[61] as is show in Equation 2.17 in Chapter II. General Concepts.

Table 9.20 (see Appendix) shows the parameters obtained by the fits which represent both nucleation and growth since they have been derived from overall crystallization kinetics data. For that reason, the values of K_g^{τ} (see Table 9.20) are larger as compared to K_g^{G} (see Table 8.3) in all cases (see also ref.[61]). On the other hand, the quality of the fits is much better (correlation coefficients larger than 0.99 in all cases, see Table 9.20) in this case, in comparison to those shown in Figure 8.6 and Table 8.3 by growth rate data.

The reduction in the overall crystallization rate of C-PCL as L-PCL is added to the C/L blends produces an increase in the values of K_g^{τ} and σ_e. These increases quantify the topological difficulties that the mixture of linear and cyclic PCL chains encounters to crystallize.

Figure 8.10 shows K_g^{τ} values as a function of C–PCL content for both 3 and 12 kg/mol C/L blends. The behavior "*mutatis mutandis*" is the same as that presented in Figure 8.6 when only growth rate data was employed for the LH fittings. The positive deviation effects are comparatively reduced for the 12 kg/mol blends as expected from the overall crystallization rate data presented in Figure 8.7.

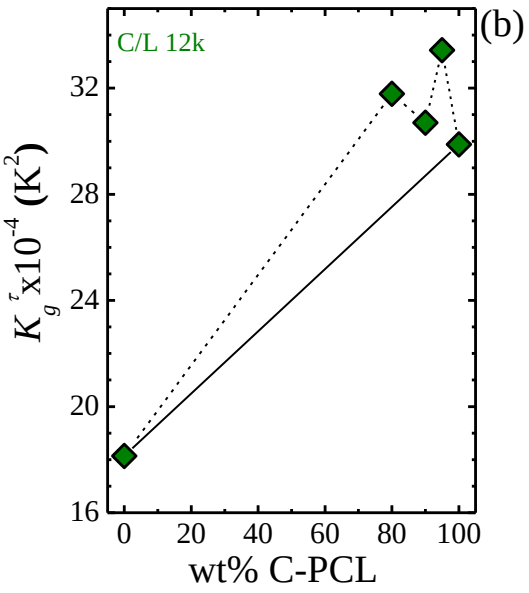

Figure 8.10. K_g^{τ} as a function of the C–PCL content for C/L blends of (a) 3 kg/mol and (b) 12 kg/mol.

According to the results presented in this section, the threading effects obtained by mixing small amounts of linear PCL molecules with cyclic chains can also affect the overall crystallization kinetics in a similar way to spherulitic growth rates.

Successive Self-Nucleation and Annealing (SSA)

Figure 8.11 shows DSC heating scans for linear and cyclic 3 kg/mol PCLs before and after SSA. Vertical lines indicate the values of the T_s temperatures employed for the fractionation. The segmented vertical line corresponds to the T_{sideal} used as the first T_s temperature for all samples. Additionally, for all the samples the numbers inserted on the DSC scan represent the different thermal fractions.

The thermal fractionation by SSA has different effects on the cyclic and linear PCLs. The ideal self-nucleation temperature of C-PCL was employed to fractionate all materials in this series of 3 kg/mol. The SSA protocol employed applied 9 T_s temperatures starting from the ideal T_s value. Therefore, at least in the cyclic material, a total of eight fractions could be potentially produced, since the first T_s is the ideal T_s temperature which does not produce annealing but only self-nucleation.

For the 3 kg/mol C-PCL sample, because of its melting range, only 6 thermal fractions (from *T1* to *T6*, *T7* and *T8* are not detectable) are produced by the SSA protocol applied, as indicated in the close-up shown in Figure 8.11 next to the C-PCL sample after SSA. Fraction 1 corresponds to the material that melts above *T1*. Fraction 2, *T2*, corresponds to the material that melts above *T2* but below *T1*, and so on. Fraction number 1 is the most important fraction in quantity of crystalline material (as indicated by its melting enthalpy) and corresponds to the melting of the thickest lamellae present in the material.

It is interesting to note that the bimodal melting of the 3 kg/mol C-PCL sample before SSA changes after fractionation. After SSA there is no crystal reorganization during heating. SSA promotes self-nucleation and annealing of the crystal population, pushing the crystals closer to equilibrium by thickening. This is the reason why the melting peak of fraction 1 is nearly 5 °C higher than the highest temperature melting peak of the material before SSA.

On the other hand, the 3 kg/mol L-PCL sample melts at much lower temperatures than C-PCL even after SSA. In view of its lower melting point range, in L-PCL, the highest temperature melting peak after SSA corresponds to fraction number 3. For L-PCL, fractions 3, 4, 5 and 6 are clearly visible, while fractions 7 and 8 require a close-up to be noticed.

Previous studies have argued that C-PCL molecules have a much larger capacity to produce crystal thickening during SSA since they have lower entanglement densities as compared to L-PCL molecules.[42, 70] This larger annealing capacity is surprising, since a completely extended linear chain has twice the size of a cyclic molecule of identical length.

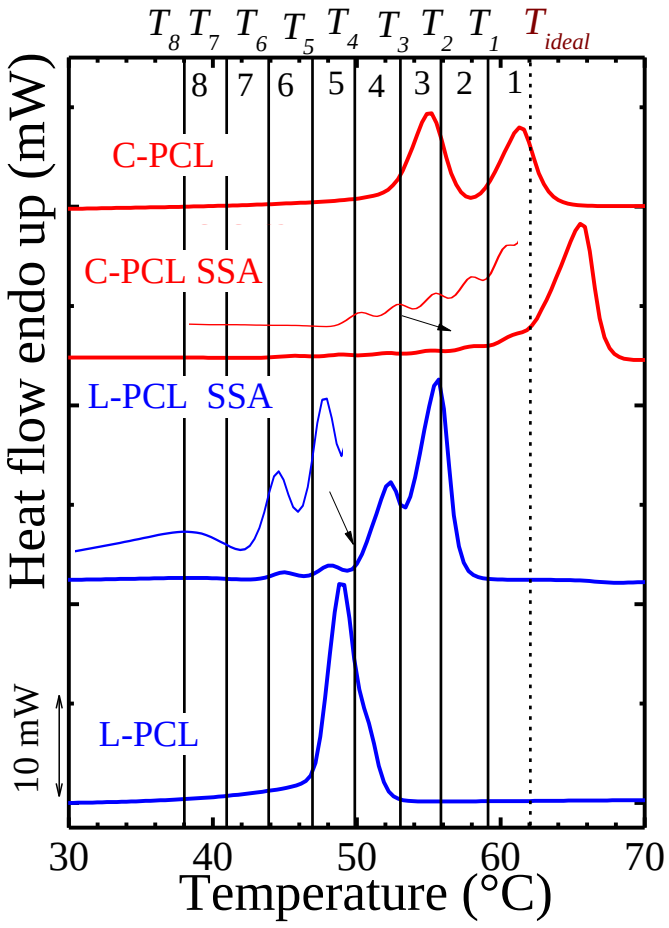

Figure 8.11. Comparison between the final heating run after SSA thermal fractionation and the standard second heating scan for neat C–PCL and L–PCL of 3 kg/mol. The fractionation windows was of 3 °C. Red (top 2) and blue (bottom 2) curves represent neat C-PCL and L-PCL, respectively.

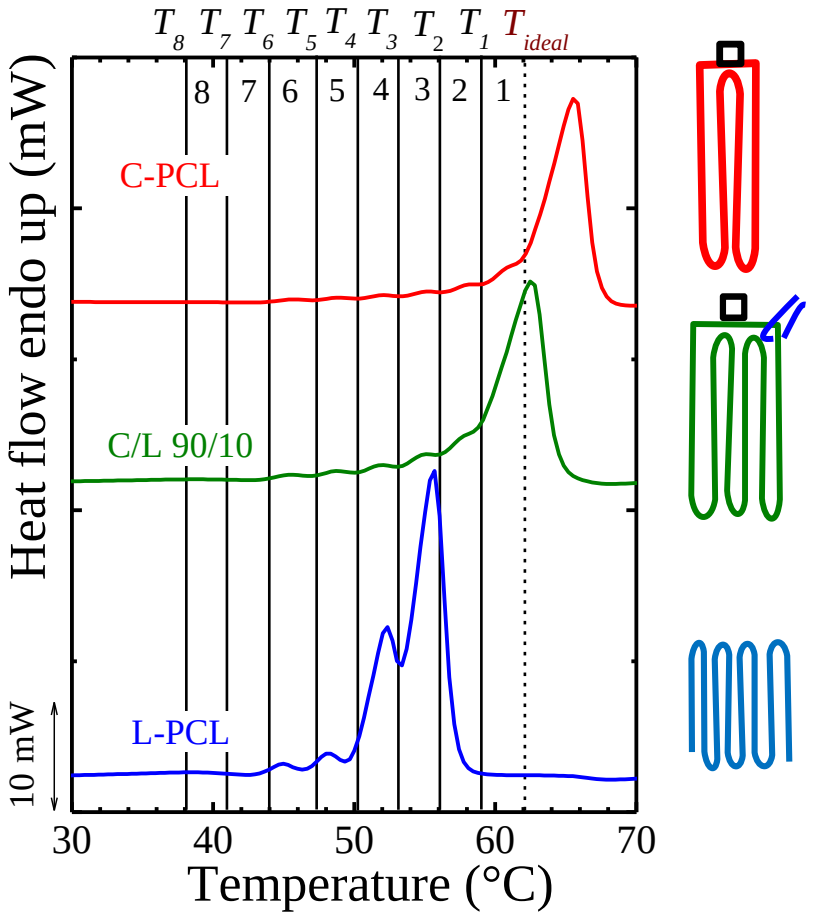

Figure 8.12. Final heating run after SSA thermal fractionation for neat C–PCL and L–PCL and their 90/10 C/L blends of 3 kg/mol. The fractionation window was of 3 °C. Red (top) and blue (bottom) curves represent neat C-PCL and L-PCL, respectively, whereas the green (middle) curve represents the 90/10 C/L blend.

Figure 8.12 shows the final heating scan after thermal fractionation by SSA of the 90/10 C/L blend in comparison to the unblended neat materials. As illustrated in the cartoon next to the DSC traces, in the blend case, the remarkable annealing capacity of C–PCL chains is limited by the threading effect of linear chains. Interestingly, Fraction 1 or melting peak at T_1 is suppressed when the content of L–PCL is 10 wt%. In Figure 9.39 of the Appendix, it is shown that in the case of 5 wt% L-PCL addition, the annealing capacity is closer to that of neat C-PCL and for 20 wt% L-PCL, it is even further reduced as compared to the 10 wt% sample. Similar trends were found for the 12 kg/mol samples (results not shown).

As explained previously, the threading of linear chains through cyclic molecules increase the entanglement density of C-PCL chains. In the case of SSA experiments, these new entanglements limit the annealing capacity of C–PCL.

8.3.Conclusions

Adding small amounts of linear PCL chains to C-PCL molecules produce dramatic synergistic reductions in the crystallization rate of cyclic molecules that are much larger than those expected on the basis of a simple mixing rule. All properties that related to crystal formation and melting are affected leading to significant reductions in nucleation rate, crystallization temperatures, melting temperatures, spherulitic growth rates, overall crystallization rates and annealing capacity. The results can be explained by a threading effect between linear and ring molecules that increase entanglement density and reduce molecular diffusion and relaxation

8.4. References

[1] H. Xiao, C. Luo, D. Yan, J.-U. Sommer, Molecular Dynamics Simulation of Crystallization Cyclic Polymer Melts As Compared to Their Linear Counterparts, Macromolecules 50 (2017) 9796-9806.
[2] R.A. Pérez-Camargo, A. Mugica, M. Zubitur, A.J. Müller, Crystallization of Cyclic Polymers, in: F. Auriemma, G.C. Alfonso, C. de Rosa (Eds.) Polymer Crystallization I: From Chain Microstructure to Processing, Springer International Publishing, Cham, 2017, pp. 93-132.
[3] F. Jacob, E.L. Wollman, Genetic and physical determinations of chromosomal segments in Escherichia coli, Symposia of the Society for Experimental Biology 12 (1958) 75-92.
[4] J.N. Hoskins, S.M. Grayson, Cyclic polyesters: Synthetic approaches and potential applications, Polymer Chemistry 2 (2011) 289-299.
[5] M. Schappacher, A. Deffieux, Controlled Synthesis of Bicyclic "Eight-Shaped" Poly(chloroethyl vinyl ether)s, Macromolecules 28 (1995) 2629-2636.
[6] S. Beinat, M. Schappacher, A. Deffieux, Linear and Semicyclic Amphiphilic Diblock Copolymers. 1. Synthesis and Structural Characterization of Cyclic Diblock Copolymers of Poly(hydroxyethyl vinyl ether) and Linear Polystyrene and Their Linear Homologues, Macromolecules 29 (1996) 6737-6743.
[7] M. Kubo, T. Hayashi, H. Kobayashi, T. Itoh, Syntheses of Tadpole- and Eight-Shaped Polystyrenes Using Cyclic Polystyrene as a Building Block, Macromolecules 31 (1998) 1053-1057.
[8] H. Oike, M. Hamada, S. Eguchi, Y. Danda, Y. Tezuka, Novel Synthesis of Single- and Double-Cyclic Polystyrenes by Electrostatic Self-Assembly and Covalent Fixation with Telechelics Having Cyclic Ammonium Salt Groups†, Macromolecules 34 (2001) 2776-2782.

[9] H. Oike, M. Washizuka, Y. Tezuka, Designing an "A-ring-with-branches" polymer topology by electrostatic self-assembly and covalent fixation with interiorly functionalized telechelicsa having cyclic ammonium groups, Macromol. Rapid Commun. 22 (2001) 1128-1134.
[10] Y. Tezuka, R. Komiya, M. Washizuka, Designing 8-Shaped Polymer Topology by Metathesis Condensation with Cyclic Poly(THF) Precursors Having Allyl Groups, Macromolecules 36 (2003) 12-17.
[11] Z. Jia, Q. Fu, J. Huang, Synthesis of Amphiphilic Macrocyclic Graft Copolymer Consisting of a Poly(ethylene oxide) Ring and Multi-Polystyrene Lateral Chains, Macromolecules 39 (2006) 5190-5193.
[12] H. Li, R. Jérôme, P. Lecomte, Amphiphilic Sun-Shaped Polymers by Grafting Macrocyclic Copolyesters with PEO, Macromolecules 41 (2008) 650-654.
[13] H. Li, R. Riva, R. Jérôme, P. Lecomte, Combination of ring-opening polymerization and "click" chemistry for the synthesis of an amphiphilic tadpole-shaped poly(ε-caprolactone) grafted by PEO, Macromolecules 40 (2007) 824-831.
[14] H. Li, R. Jérôme, P. Lecomte, Synthesis of tadpole-shaped copolyesters based on living macrocyclic poly(ε-caprolactone), Polymer 47 (2006) 8406-8413.
[15] X. Pang, R. Jing, J. Huang, Synthesis of amphiphilic macrocyclic graft copolymer consisting of a poly(ethylene oxide) ring and multi-poly(ε-caprolactone) lateral chains, Polymer 49 (2008) 893-900.
[16] G.-Y. Shi, C.-Y. Pan, Synthesis of Well-Defined Figure-of-Eight-Shaped Polymers by a Combination of ATRP and Click Chemistry, Macromol. Rapid Commun. 29 (2008) 1672-1678.
[17] G.-Y. Shi, L.-P. Yang, C.-Y. Pan, Synthesis and characterization of well-defined polystyrene and poly(ε-caprolactone) hetero eight-shaped copolymers, J. Polym. Sci., Part A: Polym. Chem. 46 (2008) 6496-6508.
[18] Y.Q. Dong, Y.Y. Tong, B.T. Dong, F.S. Du, Z.C. Li, Preparation of tadpole-shaped amphiphilic cyclic PS-b-linear PEO via ATRP and click chemistry, Macromolecules 42 (2009) 2940-2948.
[19] D.E. Lonsdale, M.J. Monteiro, Various polystyrene topologies built from tailored cyclic polystyrene via CuAAC reactions, Chem. Commun. 46 (2010) 7945-7947.
[20] X. Fan, G. Wang, J. Huang, Synthesis of macrocyclic molecular brushes with amphiphilic block copolymers as side chains, J. Polym. Sci., Part A: Polym. Chem. 49 (2011) 1361-1367.
[21] B.A. Laurent, S.M. Grayson, Synthesis of cyclic dendronized polymers via divergent "graft- from" and convergent click "graft-to" routes: Preparation of modular toroidal macromolecules, J. Am. Chem. Soc. 133 (2011) 13421-13429.
[22] G. Wang, X. Fan, B. Hu, Y. Zhang, J. Huang, Synthesis of Eight-shaped Poly(ethylene oxide) by the Combination of Glaser Coupling with Ring-opening Polymerization, Macromol. Rapid Commun. 32 (2011) 1658-1663.
[23] X. Fan, B. Huang, G. Wang, J. Huang, Synthesis of amphiphilic heteroeight-shaped polymer cyclic -[poly(ethylene oxide)- b -polystyrene] 2 via "click" chemistry, Macromolecules 45 (2012) 3779-3786.
[24] E.R. Semlyen, Cyclic Polymers, Springer Netherlands, 2007.
[25] H.R. Kricheldorf, Cyclic polymers: Synthetic strategies and physical properties, J. Polym. Sci., Part A: Polym. Chem. 48 (2010) 251-284.
[26] C.W. Bielawski, D. Benitez, R.H. Grubbs, An "endless" route to cyclic polymers, Science 297 (2002) 2041-2044.

[27] G.B. McKenna, B.J. Hostetter, N. Hadjichristidis, L.J. Fetters, D.J. Plazek, A study of the linear viscoelastic properties of cyclic polystyrenes using creep and recovery measurements, Macromolecules 22 (1989) 1834-1852.
[28] M. Kapnistos, M. Lang, D. Vlassopoulos, W. Pyckhout-Hintzen, D. Richter, D. Cho, T. Chang, M. Rubinstein, Unexpected power-law stress relaxation of entangled ring polymers, Nature Materials 7 (2008) 997-1002.
[29] S. Nam, J. Leisen, V. Breedveld, H.W. Beckham, Dynamics of unentangled cyclic and linear poly(oxyethylene) melts, Polymer 49 (2008) 5467-5473.
[30] K.-S. Lee, G. Wegner, S.L. Hsu, Vibrational spectroscopic studies of linear and cyclic alkanes CnH2n+2, CnH2n with 24⩽n⩽288: Chain folding, chain packing and conformations, Polymer 28 (1987) 889-896.
[31] Z. Yang, G.-E. Yu, J. Cooke, Z. Ali-Adib, K. Viras, H. Matsuura, A.J. Ryan, C. Booth, Preparation and crystallinity of a large unsubstituted crown ether, cyclic heptacosa(oxyethylene)(cyclo-E27, 81-crown-27), studied by Raman spectroscopy, X-ray scattering and differential scanning calorimetry, J. Chem. Soc., Faraday Trans. 92 (1996) 3173-3182.
[32] J. Cooke, K. Viras, G.E. Yu, T. Sun, T. Yonemitsu, A.J. Ryan, C. Price, C. Booth, Large cyclic poly(oxyethylene)s: Chain folding in the crystalline state studied by Raman spectroscopy, x-ray scattering, and differential scanning calorimetry, Macromolecules 31 (1998) 3030-3039.
[33] G.-E. Yu, T. Sun, Z.-G. Yan, C. Price, C. Booth, J. Cook, A.J. Ryan, K. Viras, Low-molar-mass cyclic poly(oxyethylene)s studied by Raman spectroscopy, X-ray scattering and differential scanning calorimetry, Polymer 38 (1997) 35-42.
[34] Y. Tezuka, T. Ohtsuka, K. Adachi, R. Komiya, N. Ohno, N. Okui, A Defect-Free Ring Polymer: Size-Controlled Cyclic Poly(tetrahydrofuran) Consisting Exclusively of the Monomer Unit, Macromol. Rapid Commun. 29 (2008) 1237-1241.
[35] M.E. Córdova, A.T. Lorenzo, A.J. Müller, J.N. Hoskins, S.M. Grayson, A comparative study on the crystallization behavior of analogous linear and cyclic poly(ε-caprolactones), Macromolecules 44 (2011) 1742-1746.
[36] K. Schäler, E. Ostas, K. Schröter, T. Thurn-Albrecht, W.H. Binder, K. Saalwächter, Influence of chain topology on polymer dynamics and crystallization. investigation of linear and cyclic poly(ε-caprolactone)s by 1H solid-state NMR methods, Macromolecules 44 (2011) 2743-2754.
[37] E.J. Shin, W. Jeong, H.A. Brown, B.J. Koo, J.L. Hedrick, R.M. Waymouth, Crystallization of cyclic polymers: Synthesis and crystallization behavior of high molecular weight cyclic poly(ε-caprolactone)s, Macromolecules 44 (2011) 2773-2779.
[38] T. Kitahara, S. Yamazaki, K. Kimura, Effects of topological constraint and knot entanglement on the crystal growth of polymers proved by growth rate of spherulite of cyclic polyethylene, Kobunshi Ronbunshu 68 (2011) 694-701.
[39] H. Takeshita, M. Poovarodom, T. Kiya, F. Arai, K. Takenaka, M. Miya, T. Shiomi, Crystallization behavior and chain folding manner of cyclic, star and linear poly(tetrahydrofuran)s, Polymer (United Kingdom) 53 (2012) 5375-5384.
[40] E.J. Shin, A.E. Jones, R.M. Waymouth, Stereocomplexation in cyclic and linear polylactide blends, Macromolecules 45 (2012) 595-598.
[41] H.H. Su, H.L. Chen, A. Díaz, M.T. Casas, J. Puiggalí, J.N. Hoskins, S.M. Grayson, R.A. Pérez, A.J. Müller, New insights on the crystallization and melting of cyclic PCL chains on the basis of a modified Thomson-Gibbs equation, Polymer (United Kingdom) 54 (2013) 846-859.

[42] R.A. Pérez, M.E. Córdova, J.V. López, J.N. Hoskins, B. Zhang, S.M. Grayson, A.J. Müller, Nucleation, crystallization, self-nucleation and thermal fractionation of cyclic and linear poly(ε-caprolactone)s, React. Funct. Polym. 80 (2014) 71-82.
[43] R.A. Pérez, J.V. López, J.N. Hoskins, B. Zhang, S.M. Grayson, M.T. Casas, J. Puiggalí, A.J. Müller, Nucleation and antinucleation effects of functionalized carbon nanotubes on cyclic and linear Poly(ε-caprolactones), Macromolecules 47 (2014) 3553-3566.
[44] J. Wang, Z. Li, R.A. Pérez, A.J. Müller, B. Zhang, S.M. Grayson, W. Hu, Comparing crystallization rates between linear and cyclic poly(epsilon-caprolactones) via fast-scan chip-calorimeter measurements, Polymer 63 (2015) 34-40.
[45] N. Sugai, S. Asai, Y. Tezuka, T. Yamamoto, Photoinduced topological transformation of cyclized polylactides for switching the properties of homocrystals and stereocomplexes, Polymer Chemistry 6 (2015) 3591-3600.
[46] J.V. Lopez, R.A. Perez-Camargo, B. Zhang, S.M. Grayson, A.J. Muller, The influence of small amounts of linear polycaprolactone chains on the crystallization of cyclic analogue molecules, RSC Advances 6 (2016) 48049-48063.
[47] K. Iyer, M. Muthukumar, Langevin dynamics simulation of crystallization of ring polymers, J Chem Phys 148 (2018) 244904.
[48] R. Patki, K. Mezghani, P.J. Phillips, Crystallization Kinetics of Polymers, in: J.E. Mark (Ed.) Physical Properties of Polymers Handbook, Springer New York, 2007, pp. 625-640.
[49] J.M. Schultz, Polymer Crystallization: The Development of Crystalline Order in Thermoplastic Polymers, American Chemical Society, 2001.
[50] S. Nam, J. Leisen, V. Breedveld, H.W. Beckham, Melt Dynamics of Blended Poly(oxyethylene) Chains and Rings, Macromolecules 42 (2009) 3121-3128.
[51] S. Nam, in: Textile and Fiber Engineering, Georgia Institute of Technology, 2006.
[52] S.F. Henke, S. Shanbhag, Self-diffusion in asymmetric ring-linear blends, React. Funct. Polym. 80 (2014) 57-60.
[53] C.D. Chapman, S. Shanbhag, D.E. Smith, R.M. Robertson-Anderson, Complex effects of molecular topology on diffusion in entangled biopolymer blends, Soft Matter 8 (2012) 9177-9182.
[54] J.D. Halverson, G.S. Grest, A.Y. Grosberg, K. Kremer, Rheology of ring polymer melts: From linear contaminants to ring-linear blends, Phys. Rev. Lett. 108 (2012).
[55] G. Subramanian, S. Shanbhag, Self-diffusion in binary blends of cyclic and linear polymers, Macromolecules 41 (2008) 7239-7242.
[56] R. Vasquez, S. Shanbhag, Percolation of trace amounts of linear polymers in melts of cyclic polymers, Macromol. Theory Simul. 20 (2011) 205-211.
[57] D.G. Tsalikis, V.G. Mavrantzas, Threading of Ring Poly(ethylene oxide) Molecules by Linear Chains in the Melt, ACS Macro Letters 3 (2014) 763-766.
[58] D.G. Tsalikis, T. Koukoulas, V.G. Mavrantzas, Dynamic, conformational and topological properties of ring-linear poly(ethylene oxide) blends from molecular dynamics simulations, React. Funct. Polym. 80 (2014) 61-70.
[59] B.V.S. Iyer, A.K. Lele, S. Shanbhag, What Is the Size of a Ring Polymer in a Ring−Linear Blend?, Macromolecules 40 (2007) 5995-6000.
[60] C.A. Helfer, G. Xu, W.L. Mattice, C. Pugh, Monte Carlo Simulations Investigating the Threading of Cyclic Poly(ethylene oxide) by Linear Chains in the Melt, Macromolecules 36 (2003) 10071-10078.
[61] A.T. Lorenzo, M.L. Arnal, A.J. Müller, A. Boschetti-De-Fierro, V. Abetz, Nucleation and isothermal crystallization of the polyethylene block within diblock

copolymers containing polystyrene and poly(ethylene-alt-propylene), Macromolecules 40 (2007) 5023-5037.
[62] S. Andjelić, D. Jamiolkowski, J. McDivitt, J. Fischer, J. Zhou, R. Vetrecin, Crystallization study on absorbable poly(p-dioxanone) polymers by differential scanning calorimetry, J. Appl. Polym. Sci. 79 (2001) 742-759.
[63] M.A. Sabino, J. Albuerne, A. Müller, J. Brisson, R.E. Prud'homme, Influence of in vitro hydrolytic degradation on the morphology and crystallization behavior of poly(p-dioxanone), Biomacromolecules 5 (2004) 358-370.
[64] A.J. Müller, J. Albuerne, L. Marquez, J.M. Raquez, P. Degée, P. Dubois, J. Hobbs, I.W. Hamley, Self-nucleation and crystallization kinetics of double crystalline poly(p-dioxanone)-b-poly(ε-caprolactone) diblock copolymers, Faraday Discuss. 128 (2005) 231-252.
[65] A.T. Lorenzo, A.J. Müller, Estimation of the nucleation and crystal growth contributions to the overall crystallization energy barrier, Journal of Polymer Science, Part B: Polymer Physics 46 (2008) 1478-1487.
[66] W. Li, R.E. Prud'homme, Orientation and miscibility of poly(ε-caprolactone)/poly(styrene-co-acrylonitrile) mixtures, Polymer 35 (1994) 3260-3267.
[67] D.H.S. Ramkumar, M. Bhattacharya, Steady shear and dynamic properties of biodegradable polyesters, Polymer Engineering & Science 38 (1998) 1426-1435.
[68] A.T. Lorenzo, M.L. Arnal, J. Albuerne, A.J. Müller, DSC isothermal polymer crystallization kinetics measurements and the use of the Avrami equation to fit the data: Guidelines to avoid common problems, Polym. Test. 26 (2007) 222-231.
[69] M. Avrami, Granulation, phase change, and microstructure kinetics of phase change. III, The Journal of Chemical Physics 9 (1941) 177-184.
[70] A.J. Müller, R.M. Michell, R.A. Pérez, A.T. Lorenzo, Successive Self-nucleation and Annealing (SSA): Correct design of thermal protocol and applications, Eur. Polym. J. 65 (2015) 132-154.

CHAPTER IX. APPENDIX

9.1 Synthesis of PPBA, PPBS and PPSA

PPBA and PPBS synthesis

Biobased succinic acid (SA) (99.5%) was kindly supplied by BioAmber (France). SA was bioproduced by fermentation of glucose (from wheat or corn) and obtained after a multistep process based on several purifications, evaporation and crystallization stages. 1,4-BDO (99%), methanol (99.6%), chloroform (99.0-99.4%), chromium(III) acetyl acetonate (97%), 2-chloro-4,4,5,5-tetramethyl-1,3,2-dioxaphospholane (Cl-TMDP, 95%) and cholesterol (>99%) were purchased from Sigma-Aldrich. 1,3-propanediol (1,3-PDO) (98%) and pyridine HPLC grade (99.5þ%) were purchased from Alfa Aesar. Adipic acid (AA) (99%), titanium (IV) isopropoxide (TTIP)(98%) and extra dry toluene (99.85%) were supplied by Acros. All reactants were used without further purification. All solvents used for the analytical methods were of analytical grade.

Aliphatic copolyesters were synthesized by a two-stage melt polycondensation method (esterification and transesterification). Syntheses are performed in a 50 mL round bottom flask with a distillation device to remove by-products of the reaction (mainly water). All reactions were performed with a diol/acid molar ratio of 1.1/1. For each reaction, 10.0 g of diacid (SA or AA) were used and the weight of diols was adjusted according to the composition. During the first step (esterification), the reaction mixture was maintained under a constant argon flux and magnetically stirred at 300 rpm. The reactor temperature was set to 190 ºC for 3 h. After 3 h of oligomerization, the remaining by-products of the reaction was distilled off by reducing the pressure to 200 mbar for 5 min, and then the proper amount (0.1 mol.% of TTIP vs. the amount of diacid used) of a 5 wt% solution of TTIP in extra dry toluene was introduced inside the reactor under a constant argon flux. The reaction mixture was heated to 210 ºC for 45 min. In the second step (transesterification), the reactor temperature was slowly increased to 230 ºC and the pressure was decreased stepwise over period of 5 min at 100, 50 and 25 mbar to avoid excessive foaming and to minimize oligomer sublimation (a potential problem during the melt polycondensation). The transesterification continued for 3-4 h. The global reaction procedure is summarized in Scheme 9.1.

To end, the synthesized polyester was cooled down, dissolved in chloroform, and precipitated into a large volume of vigorously stirred dry ice-cold methanol. Thereafter, the precipitate was filtered with a fine filter (0.45 mm), washed with cold methanol and dried under reduced pressure in an oven at 40 ºC, for 24 h. Lightly colored (ivory white or pale yellow) (co)polyesters were finally obtained. Different poly(1,3-propylene succinate-co-1,4-butylene succinate) (PPBS) and poly(1,3-propylene adipate-co-1,4-butylene

adipate) (PPBA) were synthesized with various 1,3-PDO/1,4-BDO molar ratios (100/0, 80/20, 60/40, 50/50, 40/60, 20/80 and 0/100).[1]

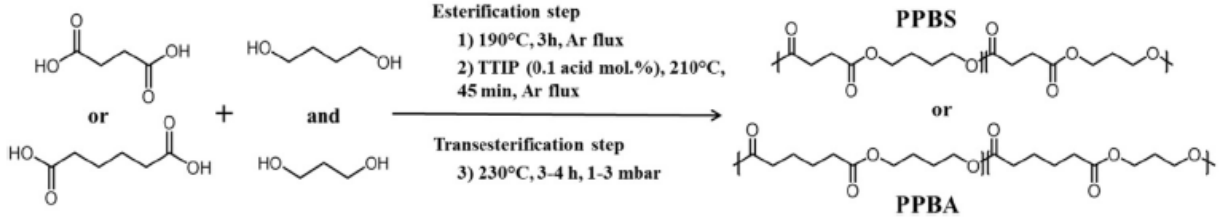

Scheme 9.1. Reaction procedure of PPBS and PPBA.[1]

PPSA synthesis

Biobased SA (99.5%) was kindly supplied by BioAmber (France). SA was bioproduced by fermentation of glucose (from wheat or corn) and obtained after a multistep process based on several purifications, evaporation, and crystallization stages. Methanol (99.6%), chloroform (99.0%–99.4%), chromium(III) acetyl acetonate (97%), 2-chloro-4,4,5,5-tetramethyl-1,3,2-dioxaphospholane (Cl-TMDP, 95%), and cholesterol (> 99%) were purchased from Sigma-Aldrich. 1,3-PDO (98%) and pyridine HPLC grade (99.51%) were purchased from Alfa Aesar. AA (99%), titanium (IV) isopropoxide
(TTIP) (981%), and extra dry toluene (99.85%) were supplied by Acros. All reactants were used without further purification. All solvents used for the analytical methods were of analytical grade.

Aliphatic copolyesters were synthesized by a two-stage melt polycondensation method (esterification and transesterification). Syntheses are performed in a 50-mL round bottom flask with a distillation device to remove all the by-products from the reaction (mostly water). All reactions were performed with a diol (1,3-PDO)/acid (SA and/or AA) molar ratio of 1.1/1.

During the first step (esterification), the reaction mixture was maintained under a constant argon flux and stirred at 300 rpm. The temperature of the reactor was set to 190 8C for 3 h. After 3 h of oligomerization, the remaining byproduct of the reaction was distilled off by reducing the pressure to 200 mbar for 5 min, and then the proper amount (0.1 mol % vs. the respective amount of diacid) of a 5 wt % solution of TTIP in extra dry toluene was introduced inside the reactor. The reaction mixture was heated to 210 ºC under a constant argon flux for 45 min. In the second step (transesterification), the temperature of the reactor was slowly increased to 230 ºC and the pressure was decreased stepwise over periods of 5 min at 100, 50, and 25 mbar, respectively, to avoid excessive foaming and to minimize oligomer sublimation, which is a potential issue during the melt polycondensation. Finally, the pressure was decreased to 1–3 mbar and the transesterification continued for about 3–4 h. The global reaction procedure is summarized in Scheme 9.2.

At the end, the synthesized polyester was cooled down, dissolved in chloroform and precipitated into a large volume of vigorously stirred cold methanol.

Thereafter, the precipitate was filtered, washed with methanol, and dried under reduced pressure in an oven at 40 ºC for 24 h. Ivory white or pale yellow polyesters were finally obtained. Several poly(propylene succinate-co-propylene adipate) (PPSA) were synthesized with different SA/AA molar ratios (100/0, 80/20, 50/50, 20/80, and 0/100). The two homopolyesters are named as PPS and PPA, respectively.[2]

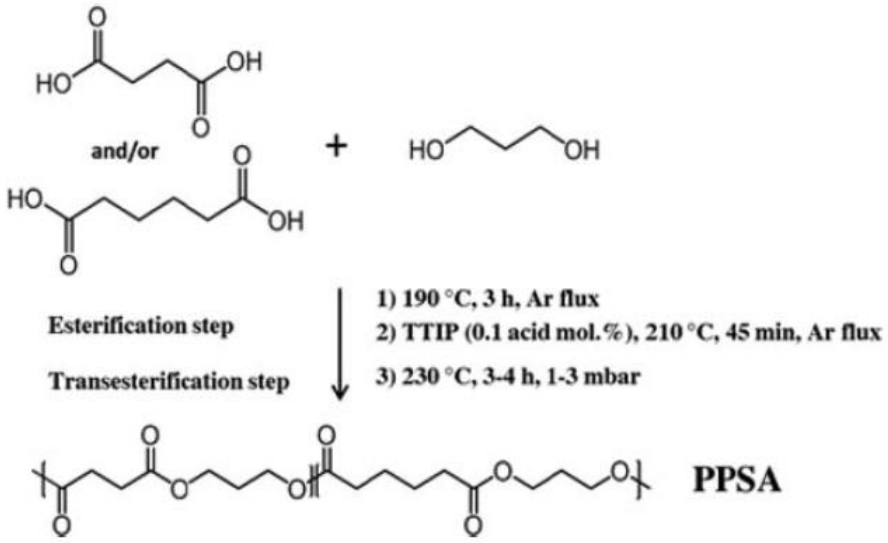

Scheme 9.2. Reaction procedure for PPSA organometallic synthesis.[2]

9.2 Appendix of Chapter IV.

DSC and WAXS experiments

Figure 9.1 shows cooling and heating scans of PBSA intermediate compositions. Note the coincident crystallization during cooling and sequential melting during subsequent heating.

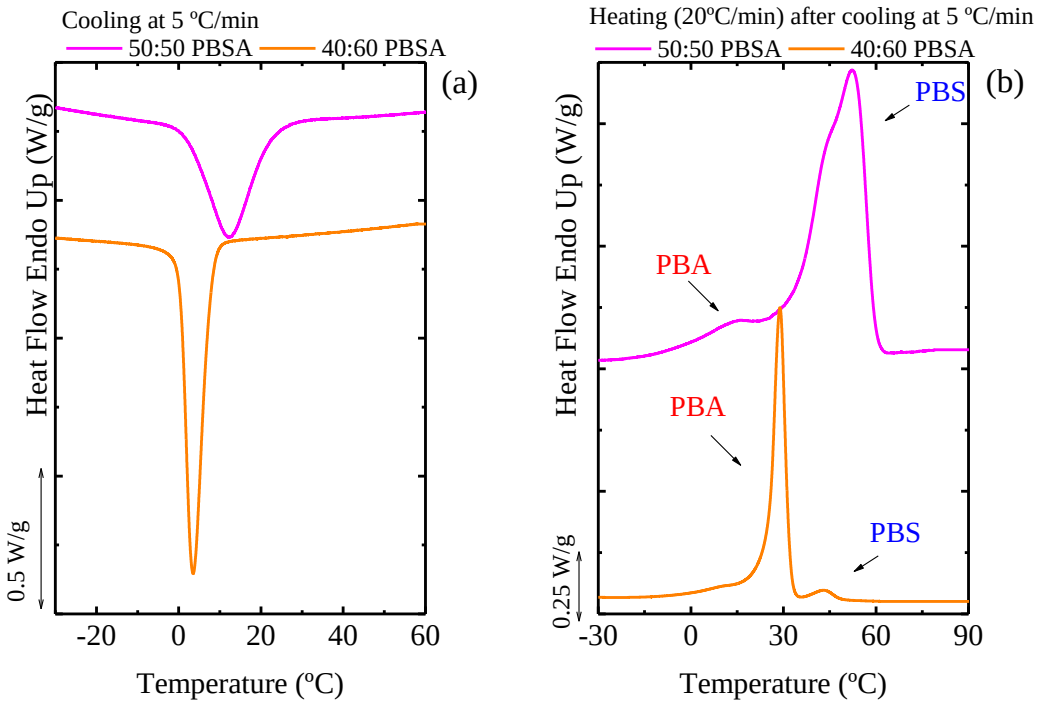

Figure 9.1. Cooling and subsequent DSC heating scan for 50:50 and 40:60 PBSA copolymers. The arrows indicate the assignment of the peaks for PBS and PBA rich phases.[3]

Figure 9.2 shows the WAXS patterns taken during heating from -40 ºC after cooling down the sample at 50 ºC/min. The WAXS patterns demostranted that the crystallization of the 60:40 PBSA was inhibited after such cooling and crystallize during the subsequent heating (cold-crystallization). However, this cold-crystallization during corresponds to the PBS-rich phase. Therefore the PBA is not able to crystallize.

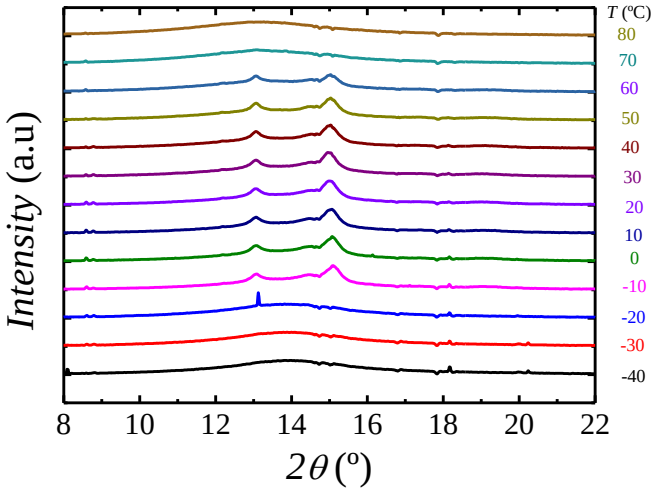

Figure 9. 2. WAXS patterns obtained during heating the 60:40 PBSA from -40 to 95ºC at 10 ºC/min after cooling the sample until -40ºC at 50 ºC/min.

Table 9.1 shows the *d*-spacings for all samples, which were calculated according to Bragg´s law.

Table 9. 1. Bragg´s angle and *d*-spacings obtained at -40 ºC, after cooling at the indicated cooling rates.

Material	**5 ºC/min**		**50 ºC/min**		**1 ºC/min**	
	***2θ* (º)**	***d* (nm)**	***2θ* (º)**	***d* (nm)**	***2θ* (º)**	***d* (nm)**
PBS	13.26	0.446	13.26	0.446	-	-
	14.82	0.399	14.82	0.399	-	-
	15.37	0.385	15.34	0.386	-	-
	19.53	0.304	19.53	0.304	-	-
80:20 PBSA	13.14	0.450	13.16	0.449	-	-
	14.64	0.404	14.64	0.404	-	-
	15.25	0.388	15.20	0.389	-	-
	19.41	0.305	19.32	0.307	-	-
60:40 PBSA	13.10	0.452	-	-	-	-
	14.55	0.407	-	-	-	-
	15.26	0.388	-	-	-	-
	19.29	0.307	-	-	-	-
50:50 PBSA	13.02	0.454	-	-	-	-
	14.45	0.410	-	-	-	-
	15.25	0.388	-	-	-	-
	19.38	0.306	-	-	-	-
40:60 PBSA	14.40	0.411	14.37	0.412	12.99	0.455
	15.13	0.391	14.84	0.399	14.38	0.411
	16.35	0.362	16.23	0.365	15.26	0.388
	20.25	0.293	20.15	0.294	16.32	0.363
	-	-	-	-	20.21	0.293
	-	-	-	-	-	-
20:80 PBSA	14.38	0.411	14.38	0.411	-	-
	15.13	0.391	15.11	0.392	-	-
	16.46	0.360	16.40	0.361	-	-
	20.32	0.292	20.29	0.292	-	-
PBA	14.60	0.405	14.37	0.412	-	-

	15.16	0.390	15.1	0.392	-	-
	16.35	0.362	16.49	0.359	-	-
	19.72	0.301	20.34	0.292	-	-

Figure 9.3 shows the WAXS pattern taken during the heating from -40 ºC after cooling down the 20:80 PBSA samples at 5 and 50 ºC/min and the 40:60 PBSA at 50 ºC/min. Both compositions reflects the change in the PBA from the α to β-phase, due to PBS addition, and the from β to α-PBA upon heating.

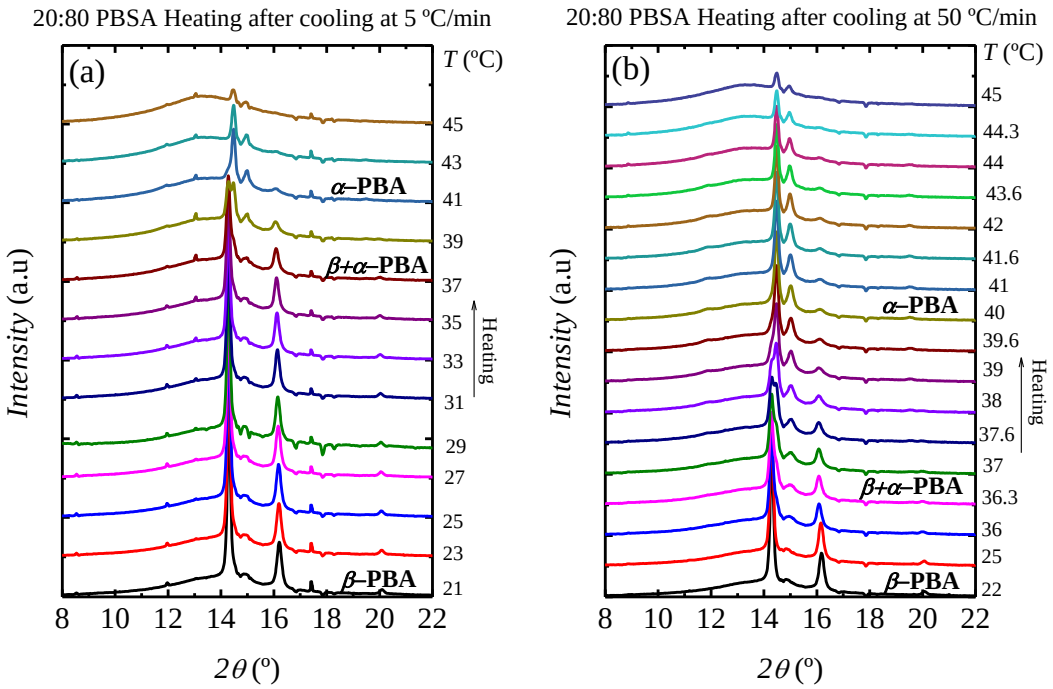

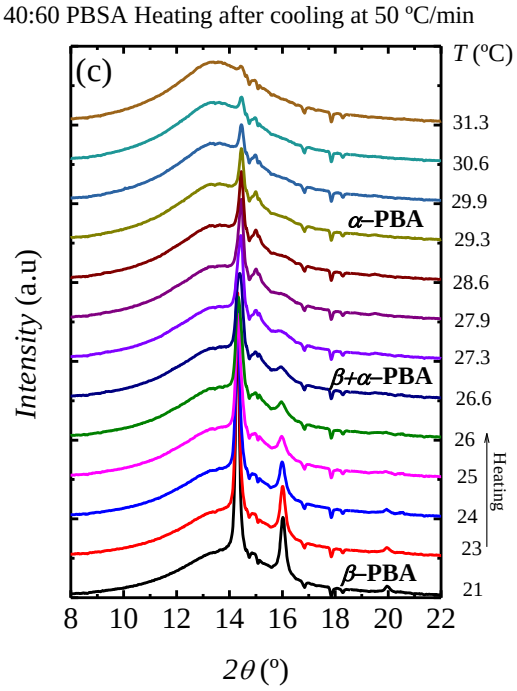

Figure 9.3. WAXS patterns of (a and b) 20:80 and (c) 40:60 PBSA copolymers taken during the heating after cooling at (a) 5 and (b and c) 50 ºC/min.

The polymorphism of neat PBA after cooling at 5 and 50 ºC/min was also evidenced on the subsequent heating scans, in which the α phase does not change during heating (see Figure 9.4a), whereas the β phase changes at 50 ºC to an $\alpha+\beta$ mixed phase and finally to the α phase at approximately 52 ºC (see Figure 9.4b).

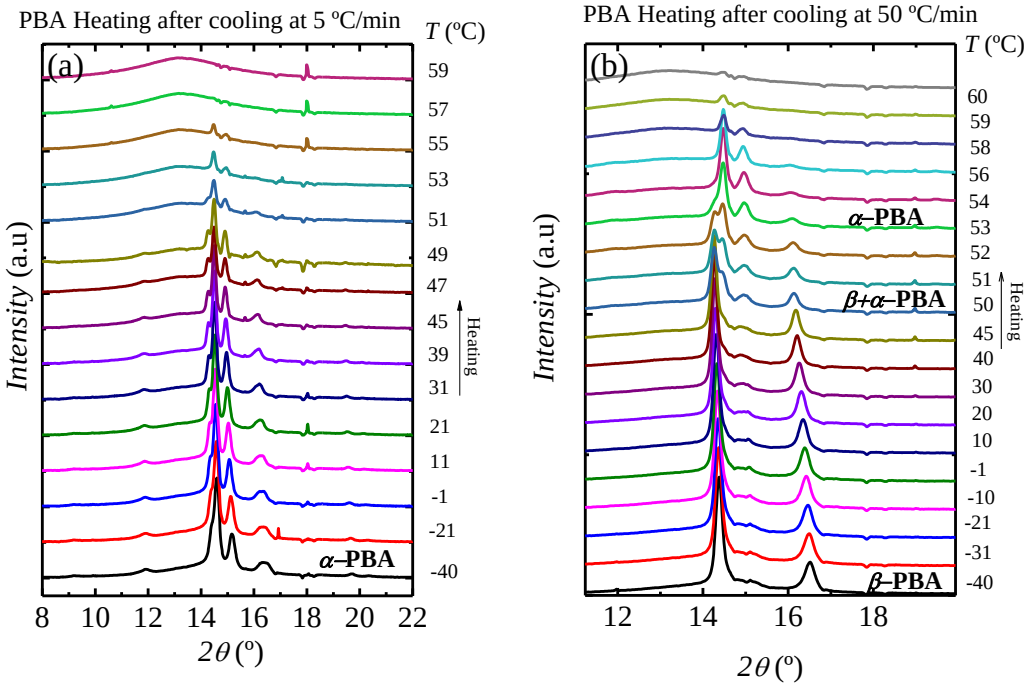

Figure 9.4. WAXS patterns of PBA taken during the heating after cooling at (a) 5 and (b) 50 ºC/min. The PBA at -40 ºC in (a) corresponds to the α phase, whereas in (b) to the β phase.

Table 9.2 shows the lamellar long periods calculated from the SAXS patterns for all the samples.

Table 9.2. Lamellar long periods calculated from q_{max} obtained by SAXS for PBS, PBA and PBSA samples at 5 and 50 ºC/min.

Material	***5 ºC/min***		***50 ºC/min***		***1 ºC/min***	
	q_{max} **(nm^{-1})**	***d**** **(nm)**	q_{max} **(nm^{-1})**	***d**** **(nm)**	q_{max} **(nm^{-1})**	***d**** **(nm)**
PBS	0.834	7.5	0.767	8.2	-	-
80:20 PBSA	0.680	9.2	0.776	8.1	-	-
60:40 PBSA	0.663	9.5	-	-	-	-
50:50 PBSA	0.592	10.6	-	-	-	-
	1.311*	4.8*	-	-	-	-
40:60 PBSA	0.493	12.8	0.551	11.4	0.471	13.3
	1.632*	3.8*	2.091*	3.0*		
20:80 PBSA	0.482	13.0	0.514	12.2	-	-
PBA	0.529	11.9	0.493	12.8	-	-

*These peaks were measurement to demonstrate that correspond to noise signal instead of a second order reflection.

AFM

AFM measurements were performed at room temperature, and the height and amplitude images are show in Figure 9.5.

PBS

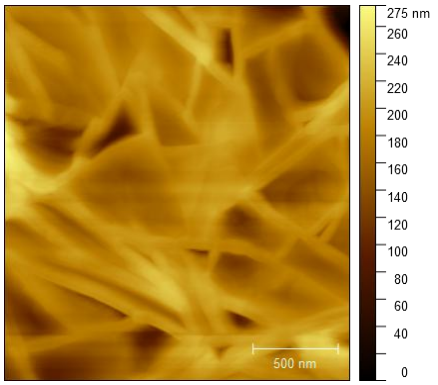

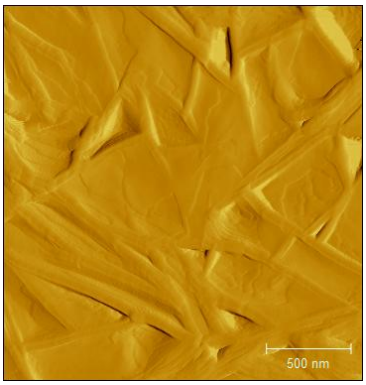

80:20
PBSA

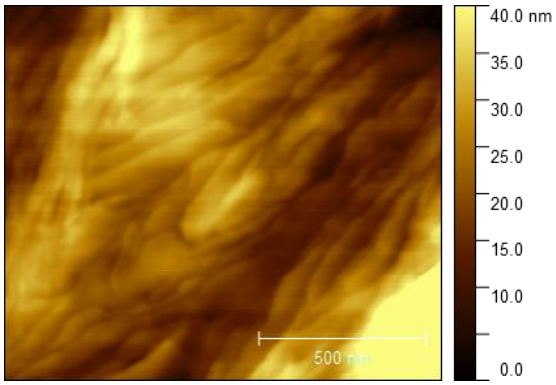

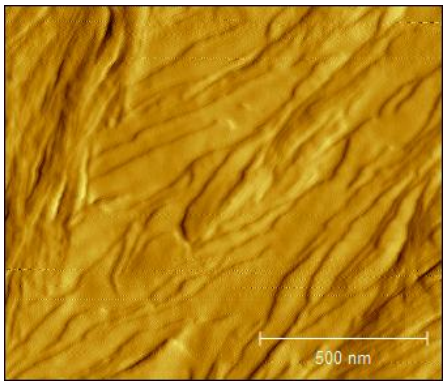

60:40
PBSA

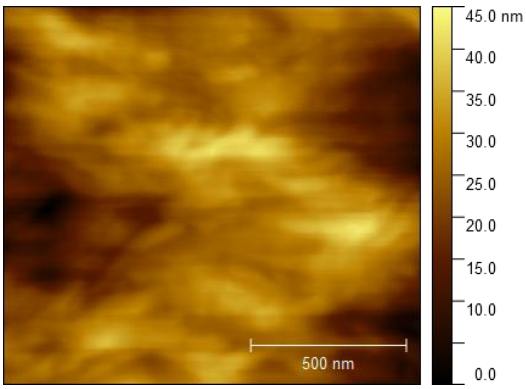

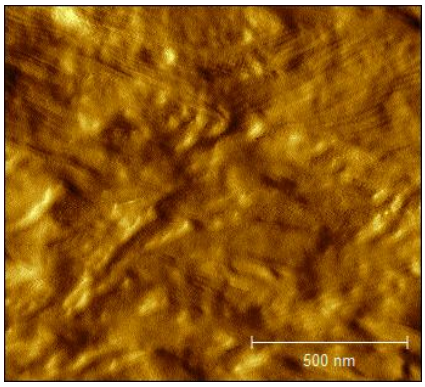

50:50
PBSA

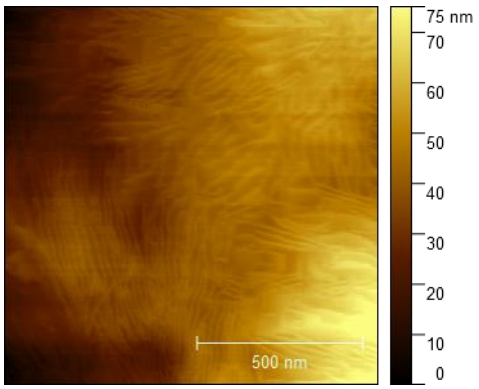

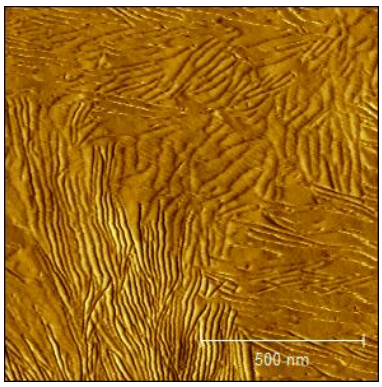

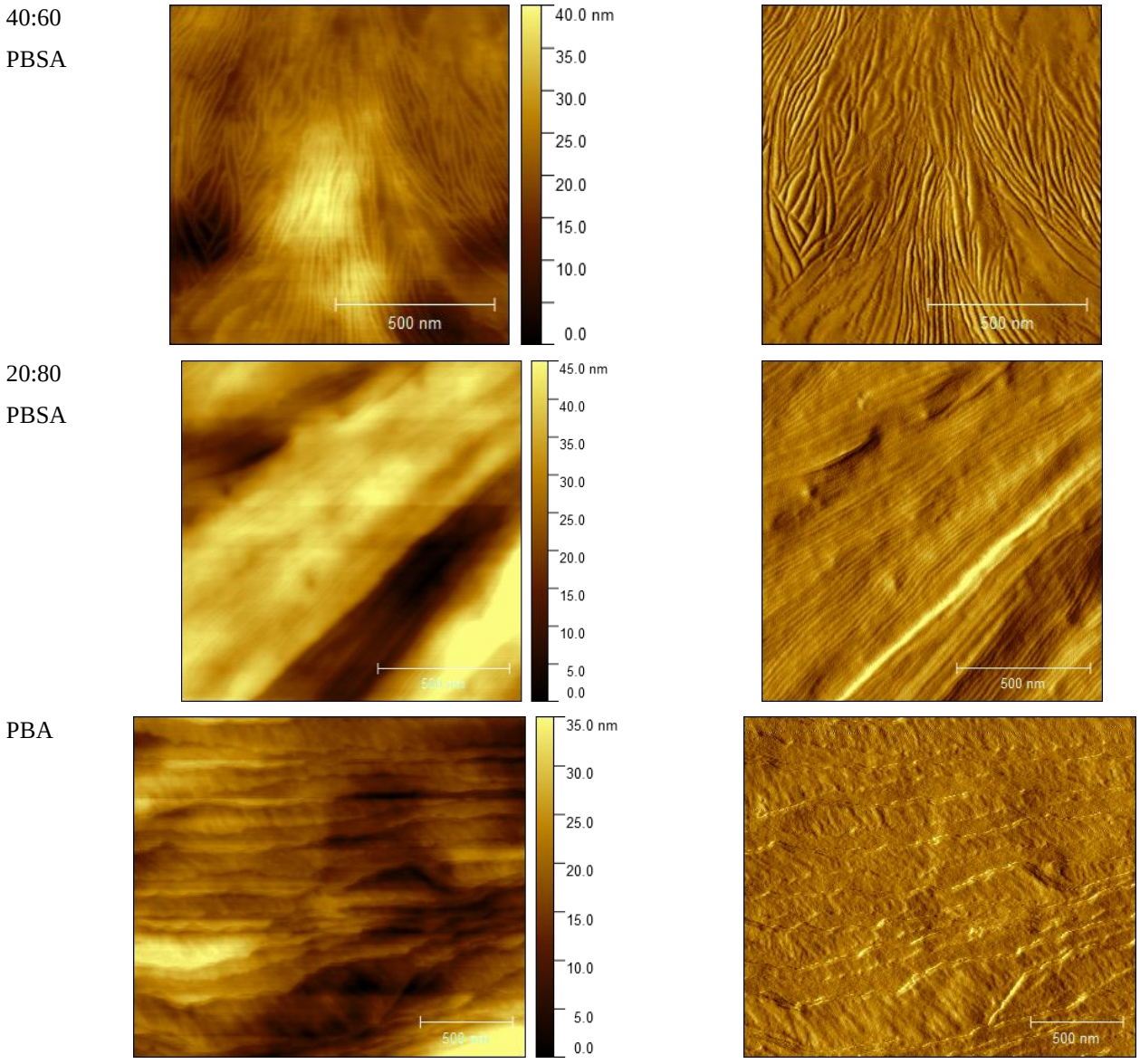

Figure 9.5. Height and amplitude images taken at RT for all the samples.

NMR

In order to determine the % of rigid phase, which correspond to crystal, the interlayer phase (crystals and amorphous phase) and the mobile phase (amorphous) a deconvolution of the selected peaks (i.e., those of the minoritary comonomer, PBA in the 80:20 PBSA and PBS in the 20:80 PBS) is performed. As a result, the contributions of each phase could be estimated, and gives a qualitative idea of the comonomer inclusion. Figure 9.6 shows the Lorentz fits applied to the 80:20 and 20:80 PBSA, as an example.

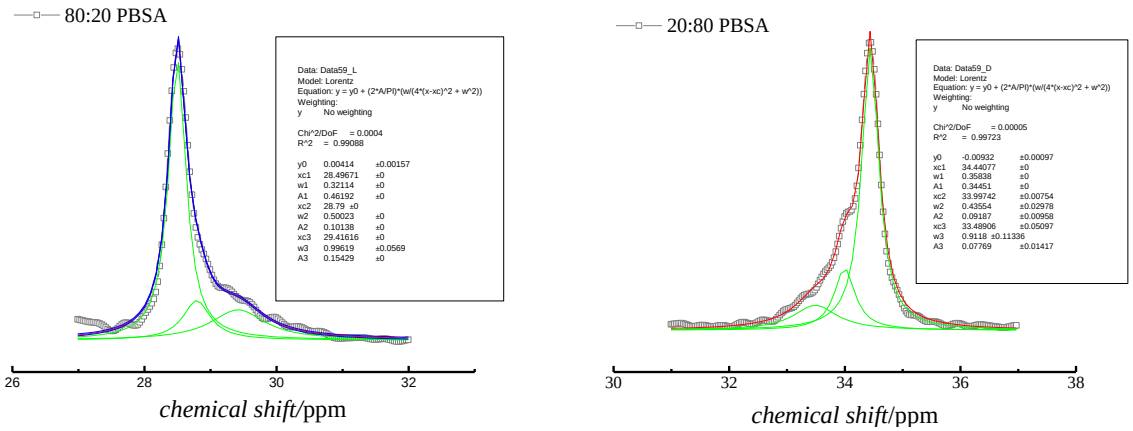

Figure 9.6. Lorentz fitting for NMR curves for 80:20 and 20:80 PBSA.

SAXS

In order to take into account the changes occurring during crystallization and melting of the samples, we performed SAXS during *in-situ* cooling and subsequent heating (as in the WAXS experiments) experiments.

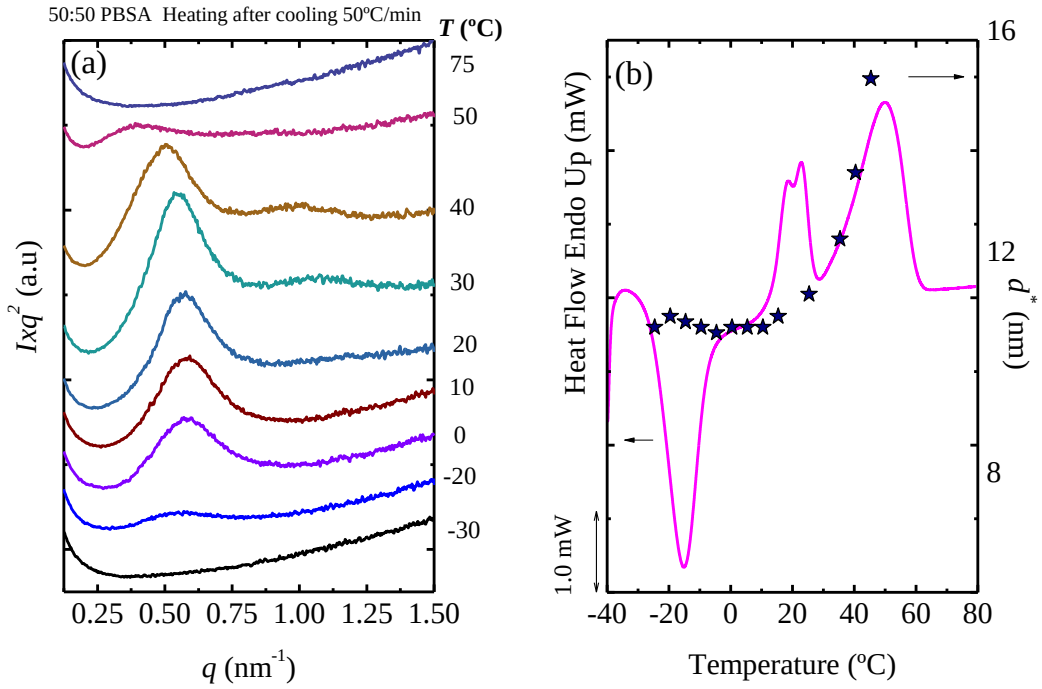

Figure 9.7. (a) SAXS patterns (at different temperatures) and (b) DSC heating scan, of the 50:50 PBSA obtained during the heating after cooling the sample at 50 ºC/min. The d^* values are plotted in the left *y*-axis on (b). The heating scans (on SAXS and DSC) were performed at 10 ºC/min.

In the 40:60 PBSA a coincident crystallization during cooling and sequential melting during heating can be deduced from the SAXS patterns and observed by DSC. Figure 9.8 shows the heating scan after cooling the sample at 1 ºC/min.

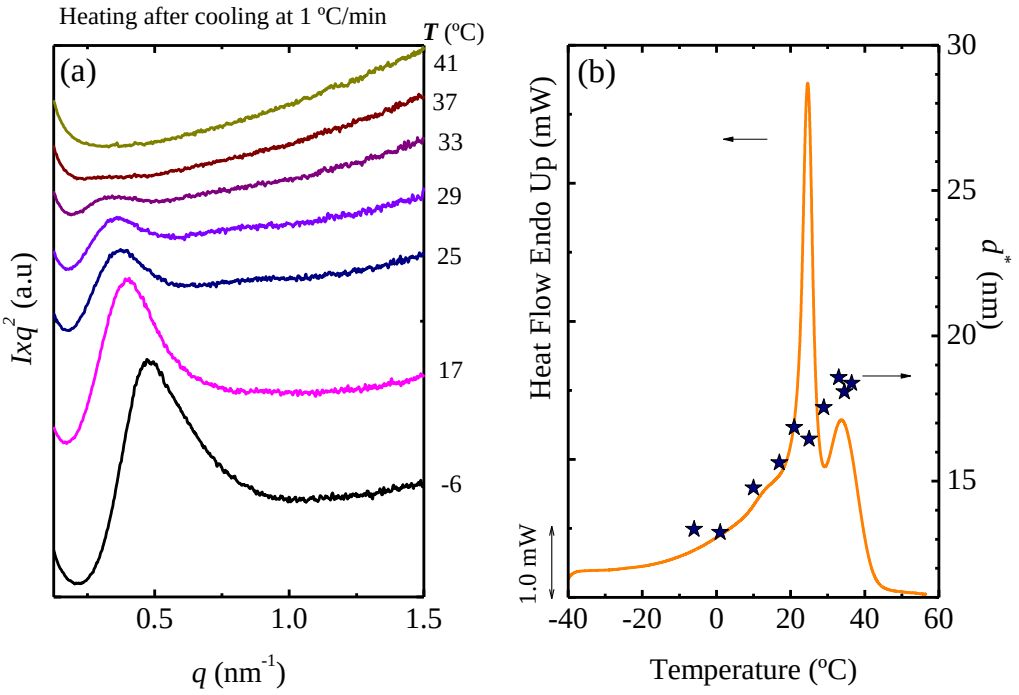

Figure 9.8. (a) SAXS patterns (at different temperatures) and (b) DSC heating scan, of the 40:60 PBSA obtained during the heating after cooled the sample at 1 ºC/min. The d^* values are plotted in the left *y*-axis on (b). The heating scans (on SAXS and DSC) were performed at 10 ºC/min.

PLOM

PLOM micrographs for 50:50 PBSA copolymer were taken after cooling at 5 ºC/min at -40 ºC (Figure 9.9a). Then the sample was heated until 40 ºC (Figure 9.9b), a temperature at which the β-PBA rich phase crystals are molten. The changes in birefringence are shown in Figure 9.9.

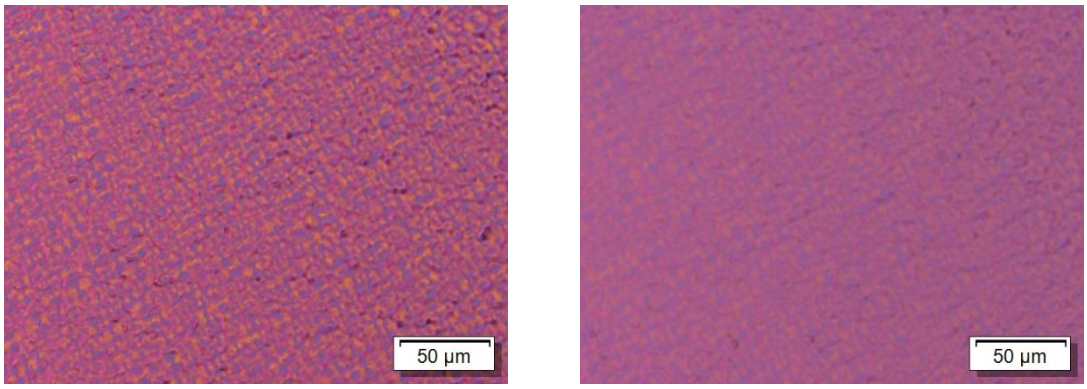

(a) 50:50 PBSA, -40 ºC (b) 50:50 PBSA, 40 ºC

Figure 9.9. Micrographs of 50:50 PBSA at (a) -40 ºC and (b) 40 ºC, after previous cooling at 5 ºC/min.

Figure 9.10a shows the first heating DSC scans for the PPBS samples, whereas Figure 9.9b shows the higher melting points, taken from Figure 9.10a, as a function of the composition. Figure 9.10 and 9.11 shows the cooling and subsequent heating DSC scans for PPBS and PPSA copolymers, respectively.

PPBS and PPSA samples: Non-isothermal DSC experiments.

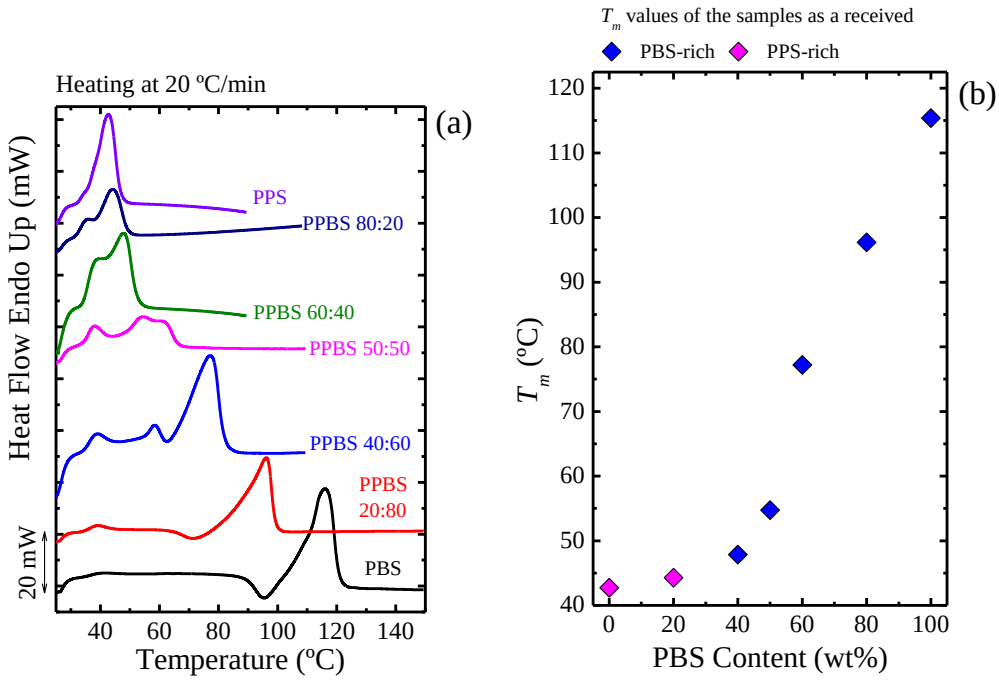

Figure 9.10. (a) First heating DSC scans for PPBS random copolymers, performed at 20 ºC/min. (b) T_m (*i.e.*, obtained from the first heating) as a function of PBS Content.

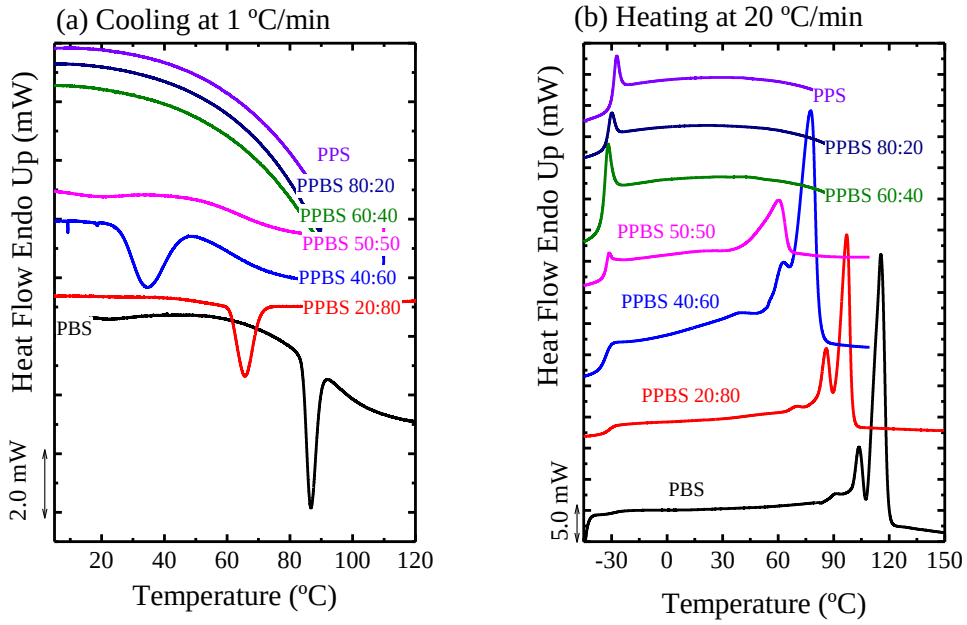

Figure 9.11. (a) Cooling at 1 ºC/min and subsequent (b) heating scans at 20 ºC/min performed for the PPBS copolymers.

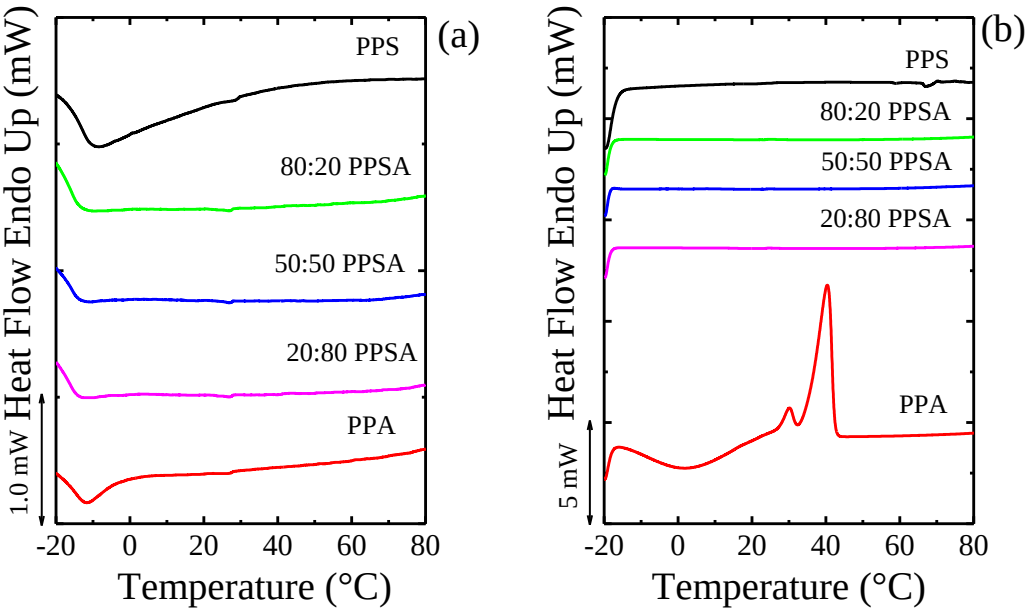

Figure 9.12. (a) Cooling and subsequent (b) heating scans performed for the PPSA copolymers. The rate taken was 20 ºC/min.

9.3 Appendix Chapter V.

WAXS experiments

Figure 9.13 shows WAXS patterns, which were taken at RT for all the samples (linear, star and combs) with a fixed DP of 30.

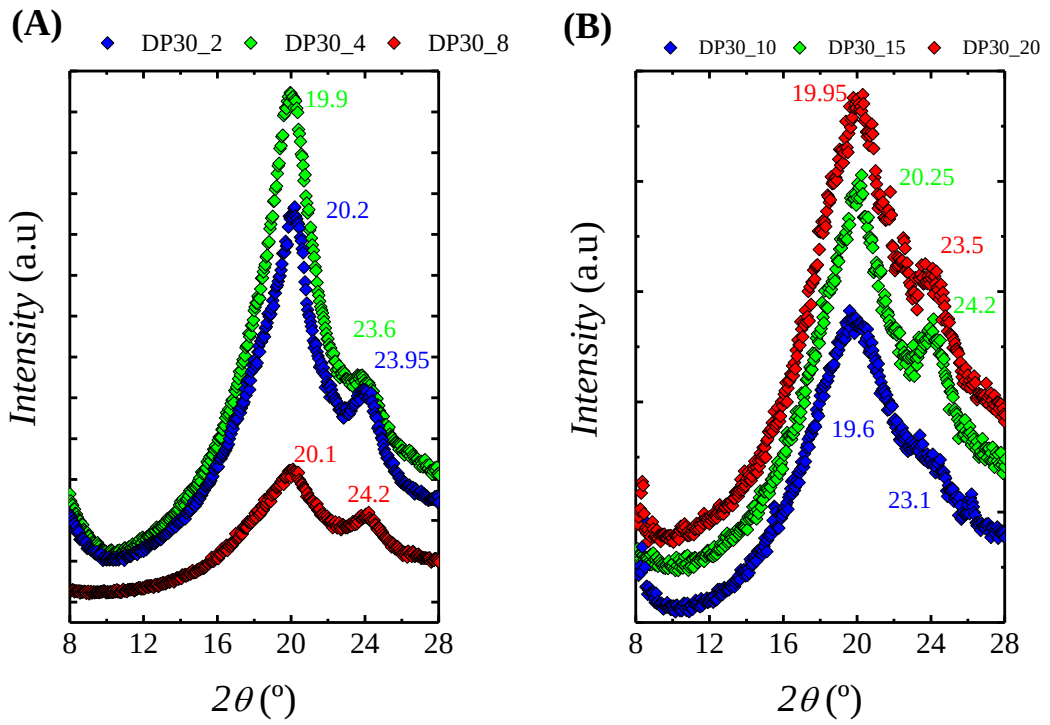

Figure 9.13. WAXS patterns of (A) linear and star and (B) combs PPS-*co*-PES copolymers with fixed DP of 30.

Figure 9.14 shows the WAXS patterns at selected temperatures for the linear (see Figure 9.14A), 8 arm-star (see Figure 9.14B) and 15-arm comb (see Figure 9.14C) copolymers.

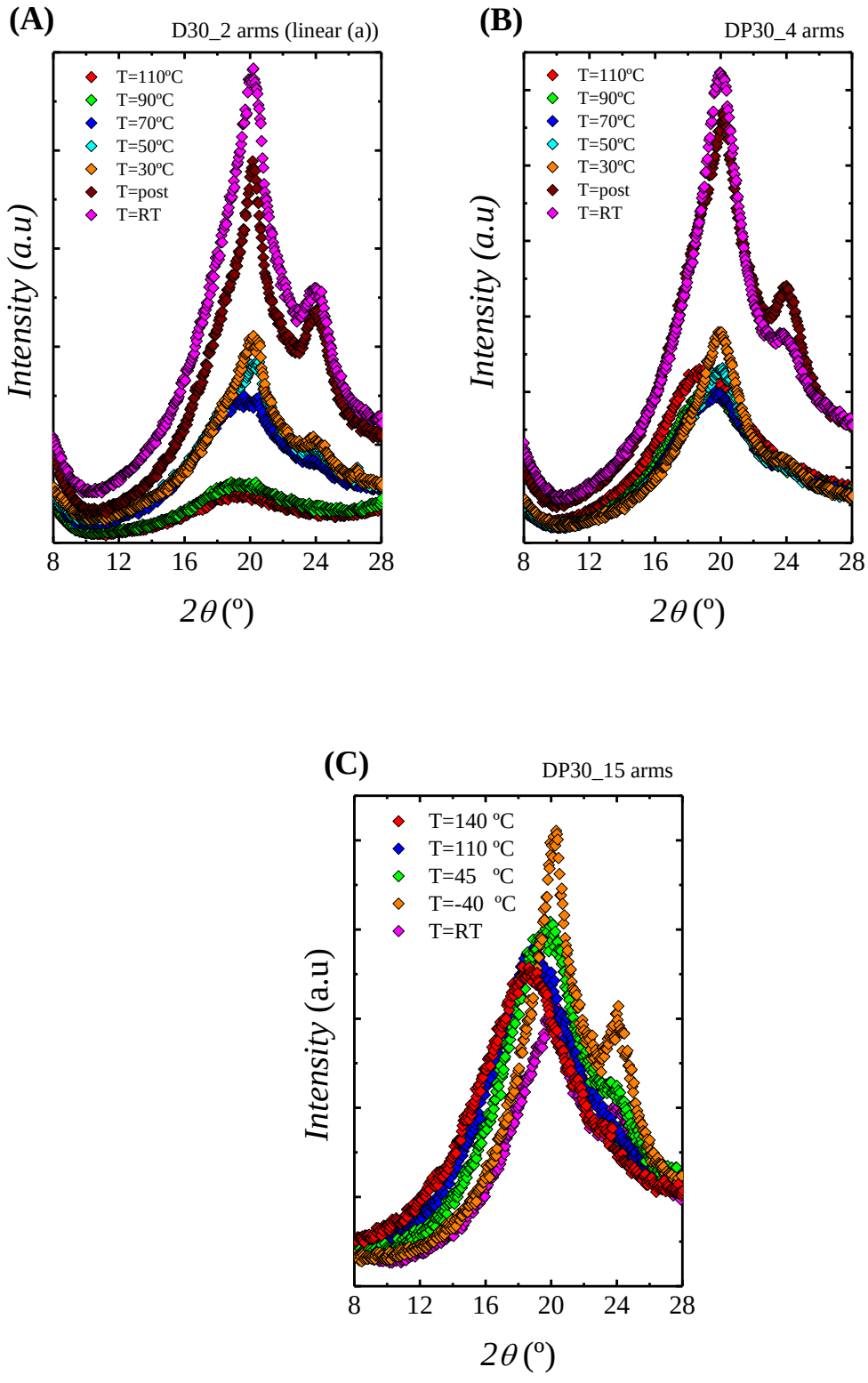

Figure 9.14. WAXS patterns of the samples taken at the indicated temperatures for (A) linear (a); (B) star-4 arms and (C) comb 15-arms copolymers with DP of 30.

Table 9.3 listed the *2θ* and *d* spacings calculated by Bragg´s law.

Table 9.3. Calculated diffraction spacings (*d*) according to the Bragg´s law for linear (a), star 4-arms and comb samples of 10, 15 and 20 arms at different temperatures.

Temperature (ºC)	***2θ* (º)**					***d* (nm)**				
	2	***4***	***10***	***15***	***20***	***2***	***4***	***10***	***15***	***20***
RT	20.2	20.0	19.9	20.3	19.8	0.439	0.445	0.446	0.437	0.448
	24.0	23.9	23.9	24.2	24.1	0.371	0.373	0.372	0.367	0.369
140	-	-	18.4	18.7	18.8	-	-	0.482	0.474	0.471
-40	-	-	20.2	20.3	20.2	-	-	0.439	0.437	0.439
			23.9	24.1	24.0			0.372	0.369	0.370
30	20.2	20.1	-	-	-	0.439	0.442	-	-	-
	23.9	24.0				0.373	0.370			
40	-	-	19.2	-	-	-	-	0.462	-	-
			24.6					0.361		
45	-	-	-	20	19.9	-	-	-	0.443	0.446
				24	24.2				0.370	0.367
50	20.5	20.1	-	-	-	0.434	0.441	-	-	-
	24.3	23.8				0.367	0.374			
70	19.7	19.6	-	-	-	0.451	0.452	-	-	-
	24.3					0.367				
90	19.4	19.3	-	-	-	0.458	0.461	-	-	-
110	18.9	19.1	18.5	18.9	19.2	0.480	0.464	0.479	0.469	0.462
post	20.2	20.1	-	-	-	0.440	0.441	-	-	-
	24.1	24.0				0.370	0.370			

SAXS experiments

Temperature-dependent SAXS experiments were performed with a similar protocol to those used in the temperature-dependent WAXS experiments. Figure 9.15 shows the SAXS patterns taken for different samples a selected temperatures.

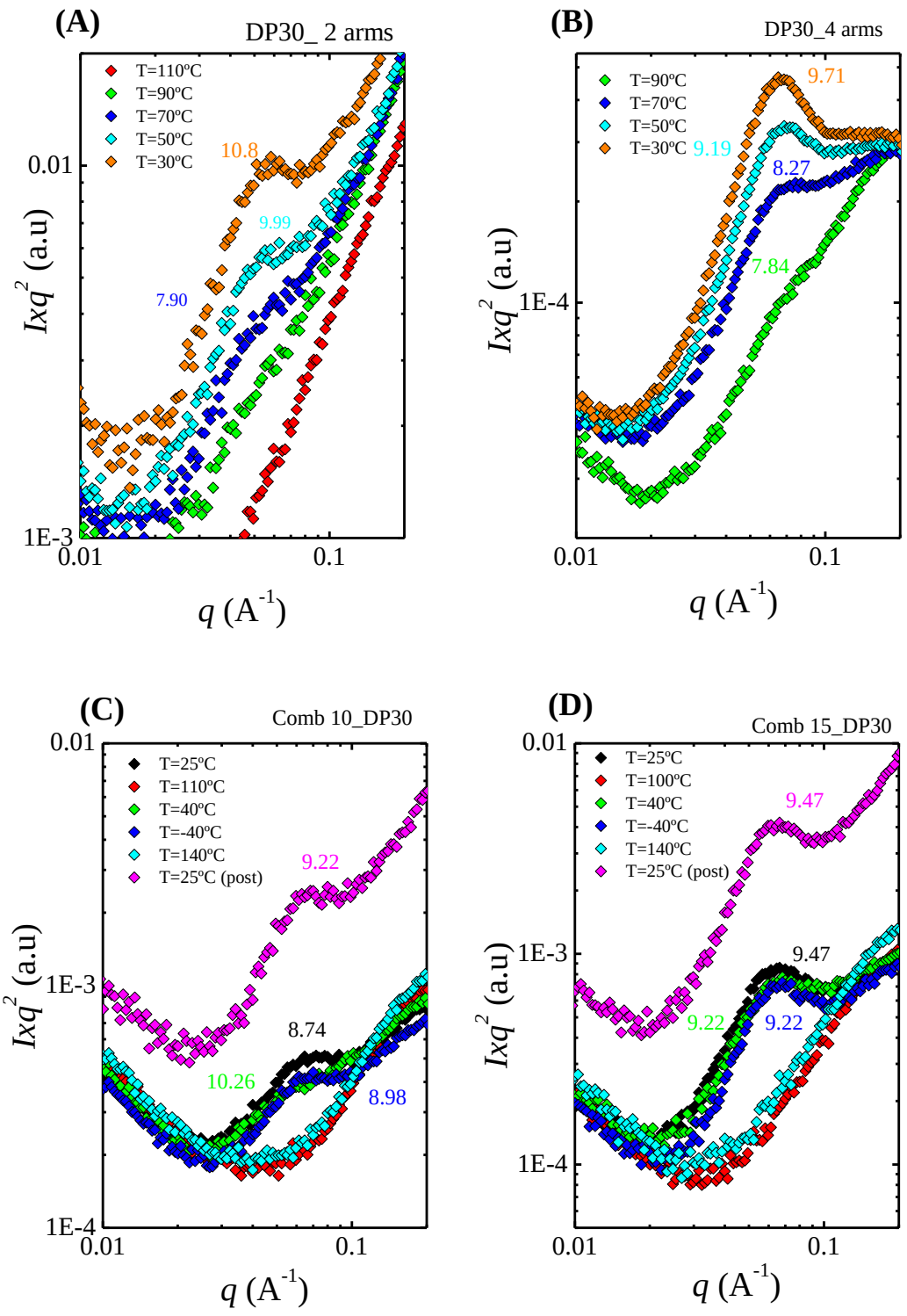

Figure 9.15. SAXS patterns of (A) linear (a); (B) star 4-arms; (C) comb 10-arms and (D) comb 15-arms copolymers with DP of 30 taken at the indicated temperatures. The *d**-value obtained from the maximum is labelled.

9.4 Appendix Chapter VI.

Morphological Study of PCL and PCL-g-lignin

Figure 9.16 shows the typical lamellar texture of PCL^{127}, $PCL_{29}^{13.7}$ and $PCL_6^{24.4}$ after isothermal crystallization at several temperatures. This micrograph shows lamellar stacks that share the same orientation. These lamellar stacks could be part of axialites or spherulites.
The staining with RuO_4 increases the electron density of the amorphous interlamellar regions (so they appear dark grey), as the heavy atoms can easily penetrate the less dense amorphous regions of the sample. On the other hand, the crystalline lamellae appear white under the electron beam. The parent lamellae are mostly straight, while some daughter lamellae branched out at shallow angles.

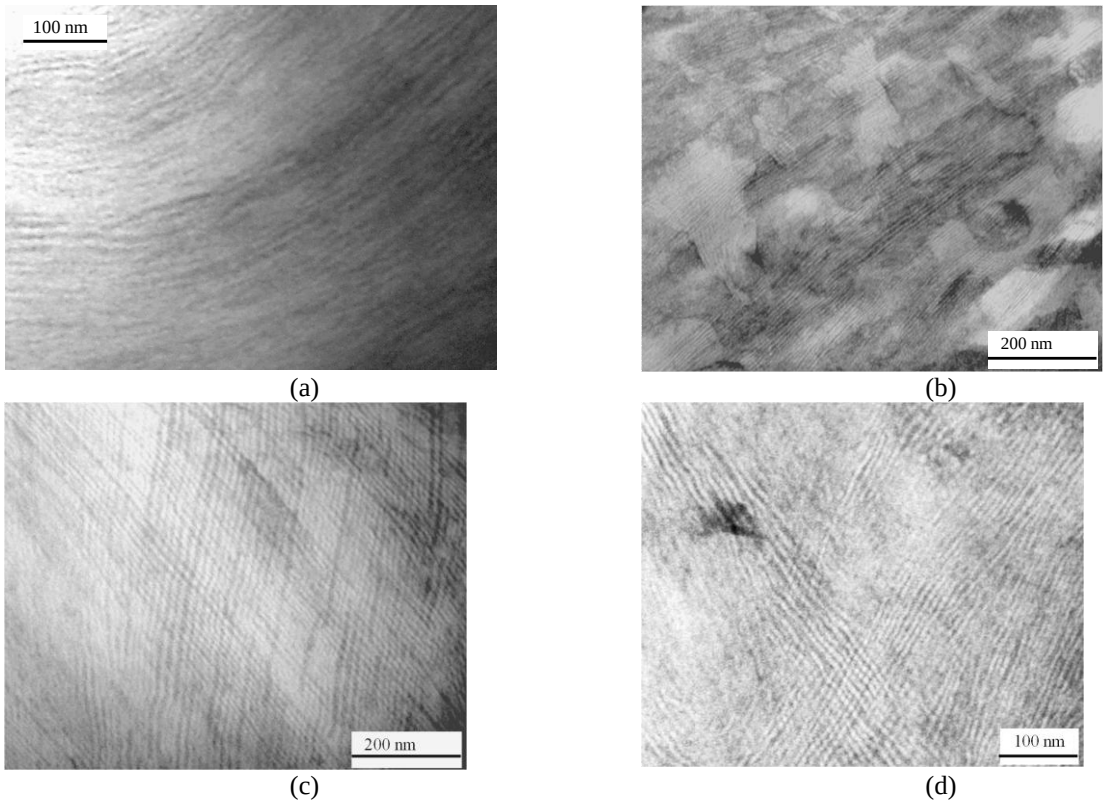

Figure 9.16. TEM micrograph of isothermally crystallized PCL and PCL-g-lignin samples at 40, 35, 30 and 25°C for 6 h at each step for (a) PCL^{127} (b) $PCL_{29}^{13.7}$ (c) and (d) $PCL_6^{24.4}$.

Detailed TEM observations were performed to try to see if the dispersion of the lignin blocks was observable and if lignin agglomerates (un–reacted) were present. In the samples with low lignin content it was very difficult to find areas of the sample that were unequivocally attributed to lignin, therefore it seems that most lignin is grafted to PCL chains and well dispersed with a non–significant amount of non–reacted lignin agglomerates.
In the sample with the highest content of lignin, *i.e.*, 29 wt%, low magnification micrographs, like that shown in Figure 9.16b, indicate a relatively good dispersion of areas with high and low electron densities. Darker areas (where staining with RuO_4 was most effective) are probably richer in lignin.
One interesting observation, common to all samples containing lignin, is the presence of areas where PCL crystalline lamellae exhibit a remarkable cross–hatched pattern. This is particularly pronounced in samples

with low lignin content. Figure 9.16c and d show examples of this morphology at two different magnifications for a PCL–*g*–lignin copolymer with 6 wt% lignin.
On the contrary, Figure 9.16a does not evidence such a PCL cross–hatched lamellar morphology seen for the grafted copolymers in Figure 9.16b to d, where daughter lamellae branched out perpendicularly or at wide angles from the parent ones.[4]

Avrami Fit
Table 9.4 to 9.7 shows the parameters obtained from the Avrami Fit for PCL and PCL-*g*-lignin samples.

Table 9.4. Parameters obtained by fitting the Avrami theory for neat PCLs

T_c (°C)	PCL^{127}					PCL^{15}					PCL^{149}				
	n	$K\times10^3$ min^{-n}	$\tau_{1/2t}$ min	$\tau_{1/2e}$ min	R^2	n	$K\times10^3$ min^{-n}	$\tau_{1/2t}$ min	$\tau_{1/2e}$ min	R^2	n	$K\times10^3$ min^{-n}	$\tau_{1/2t}$ min	$\tau_{1/2e}$ min	R^2
26	---	---	---	---	---	2.3	77530	0.13	0.15	1.0000	---	---	---	---	---
27	---	---	---	---	---	2.3	37317	0.18	0.20	1.0000	---	---	---	---	---
28	---	---	---	---	---	2.3	1801	0.25	0.25	0.9999	---	---	---	---	---
29	---	---	---	---	---	2.3	5365	0.42	0.42	0.9999	---	---	---	---	---
30	---	---	---	---	---	2.5	978.2	0.87	0.87	0.9997	---	---	---	---	---
31	---	---	---	---	---	2.8	160.7	1.67	1.67	0.9998	---	---	---	---	---
32	---	---	---	---	---	3.1	32.5	2.71	2.75	0.9999	---	---	---	---	---
33	---	---	---	---	---	3.0	10.8	4.1	4.1	1.0000	---	---	---	---	---
37	1.9	242.4	1.75	1.60	0.9993	---	---	---	---	---	1.9	815.4	0.92	1.02	0.9997
38	2.0	151.0	2.17	2.02	0.9995	---	---	---	---	---	2.0	570.7	1.10	1.22	0.9998
39	2.1	88.3	2.72	2.58	0.9998	---	---	---	---	---	2.2	331.8	1.41	1.57	0.9997
40	2.1	47.7	3.49	3.38	0.9999	---	---	---	---	---	2.3	179.3	1.81	2.02	0.9996
41	2.2	27.0	4.49	4.40	1.0000	---	---	---	---	---	2.3	92.7	2.38	2.60	0.9998
42	2.1	15.9	5.80	5.72	1.0000	---	---	---	---	---	2.3	45.0	3.28	3.53	0.9998
43	2.3	5.9	8.25	8.23	1.0000	---	---	---	---	---	2.3	19.8	4.62	4.83	1.0000
44	2.3	2.5	11.1	11.1	1.0000	---	---	---	---	---	2.3	9.8	6.4	6.6	1.0000

Table 9.5. Parameters obtained by fitting the Avrami theory for low lignin contents.

T_c (°C)	PCL$_6^{24.4}$					PCL$_2^{44}$					PCL$_3^{63.3}$				
	n	$K\times10^3$ min^{-n}	$\tau_{1/2t}$ min	$\tau_{1/2e}$ min	R^2	n	$K\times10^3$ min^{-n}	$\tau_{1/2t}$ min	$\tau_{1/2e}$ min	R^2	n	$K\times10^3$ min^{-n}	$\tau_{1/2t}$ min	$\tau_{1/2e}$ min	R^2
34	2.6	4643	0.48	0.47	0.9995	---	---	---	---	---	---	---	---	---	---
35	2.8	2627	0.62	0.60	0.9995	---	---	---	---	---	---	---	---	---	---
36	3.1	1143	0.85	0.85	0.9997	---	---	---	---	---	---	---	---	---	---
37	3.2	454	1.14	1.13	0.9998	---	---	---	---	---	---	---	---	---	---
38	3.5	143	1.58	1.58	0.9999	---	---	---	---	---	---	---	---	---	---
39	3.5	31	2.45	2.43	0.9999	2.5	1809	0.7	0.7	0.99954	2.4	1606	0.71	0.70	0.9999
40	3.1	22	3.04	3.02	0.9998	2.7	790	1.0	0.9	0.99955	2.7	679	1.01	1.00	1.0000
41	3.2	4.5	4.81	4.78	0.9999	2.9	260	1.4	1.4	0.99966	3.0	216	1.48	1.50	1.0000
42	---	---	---	---	---	2.9	120	1.8	1.8	0.9998	2.6	127	1.92	1.90	1.0000
43	---	---	---	---	---	2.9	40	2.7	2.6	0.99978	3.3	12	3.41	3.50	0.9999
44	---	---	---	---	---	2.8	14	4.0	3.9	0.9998	2.7	10	5.01	4.98	1.0000
45	---	---	---	---	---	2.7	5	6.2	6.0	0.99977	2.7	1.6	9.32	9.22	1.0000
46	---	---	---	---	---	2.5	3	9.3	9.0	0.99977	2.8	0.21	18.1	17.8	1.0000

Table 9.6. Parameters obtained by fitting the Avrami theory for intermediate lignin contents.

T_c (°C)	PCL$_{18}^{20}$					PCL$_{17}^{16.7}$					PCL$_{10}^{25}$				
	n	$K\times10^3$ min^{-n}	$\tau_{1/2t}$ min	$\tau_{1/2e}$ min	R^2	n	$K\times10^3$ min^{-n}	$\tau_{1/2t}$ min	$\tau_{1/2e}$ min	R^2	n	$K\times10^3$ min^{-n}	$\tau_{1/2t}$ min	$\tau_{1/2e}$ min	R^2
28	---	---	---	---	---	2.4	8552	0.35	0.38	0.99999	---	---	---	---	---
29	2.2	7491.0	0.34	0.37	1.0000	2.5	3202	0.54	0.58	0.99999	---	---	---	---	---
30	2.3	3044.5	0.52	0.53	0.9999	2.6	1065	0.85	0.87	0.99989	---	---	---	---	---
31	2.6	780.7	0.95	0.97	0.9999	2.9	259	1.40	1.42	0.99988	---	---	---	---	---
32	3.1	127.9	1.74	1.75	0.9999	2.9	86	2.06	2.03	0.99981	---	---	---	---	---

33	3.2	45.9	2.32	2.33	0.9999	2.9	39	2.72	2.67	0.99984	---	---	---	---	---
34	3.2	18.8	3.09	3.10	0.9999	2.9	16	3.72	3.65	0.99984	3.3	604	1.04	1.00	0.9990
35	3.1	9.1	4.13	4.12	0.9998	2.7	8	5.20	5.08	0.99983	3.4	230	1.38	1.33	0.9992
36	3.0	3.3	6.0	5.9	0.9999	---	---	---	---	---	3.5	74	1.91	1.83	0.9992
37	3.1	0.69	9.4	9.3	1.000	---	---	---	---	---	3.4	22	2.73	2.62	0.9991
38	2.7	0.93	12.0	12.1	1.000	---	---	---	---	---	3.5	4.2	4.28	4.10	0.9991
39	---	---	---	---	---	---	---	---	---	---	3.1	1.9	6.54	6.15	0.9990
40	---	---	---	---	---	---	---	---	---	---	2.7	1.5	9.97	9.13	0.9992
41	---	---	---	---	---	---	---	---	---	---	2.4	0.72	17.47	15.92	0.9995

Table 9.7. Parameters obtained by fitting the Avrami theory for high lignin contents.

T_c (°C)	$PCL_{37}^{11.9}$					$PCL_{29}^{13.7}$				
	n	***K*×10³ min⁻ⁿ**	**$\tau_{1/2t}$ min**	**$\tau_{1/2e}$ min**	**R^2**	***n***	***K*×10³ min⁻ⁿ**	**$\tau_{1/2t}$ min**	**$\tau_{1/2e}$ min**	**R^2**
21	2.1	621	1.05	1.15	0.99994	---	---	---	---	---
22	2.2	454	1.21	1.32	0.99993	---	---	---	---	---
23	2.1	329	1.42	1.50	0.99998	---	---	---	---	---
24	2.2	155	1.99	2.15	0.99993	---	---	---	---	---
25	2.2	73	2.74	2.95	0.99988	2.7	9999	0.37	0.40	0.99997
26	2.1	43	3.82	4.17	0.99995	2.8	2581	0.63	0.70	0.99993
27	2.3	10	6.46	6.85	0.99996	2.7	942	0.89	0.92	1.0000
28	---	---	---	---	---	2.5	323	1.36	1.35	0.99987
29	---	---	---	---	---	3.5	30	2.46	2.52	0.99999
30	---	---	---	---	---	3.2	17	3.21	3.28	1.0000
31	---	---	---	---	---	3.3	3	5.00	4.98	0.99949
32	---	---	---	---	---	2.9	4	5.88	5.80	0.99997

Polarized Light Optical Microscopy for PLA/lignin samples and PLA/talc

Figure 9.17 shows plots of spherulitic growth rate as a function of crystallization temperature for PLA and nucleated PLA systems with talc, Kraft lignin and Organosolv lignin.

Figure 9.18 shows Polarized Light Optical Micrographs taken at different temperatures for neat and nucleated PLA. Figure 9.18 evidences the higher nucleation capacities of the nucleated PLAs, especially the PLA/UT, in comparison with the neat PLA.

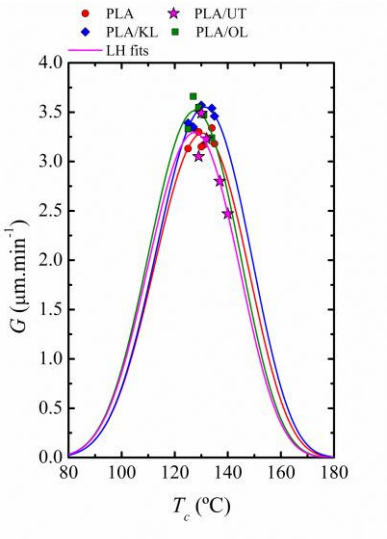

Figure 9.17. Spherulitic growth rate (G) as a function of crystallization temperature (T_c) for PLA and its nucleated compounds.

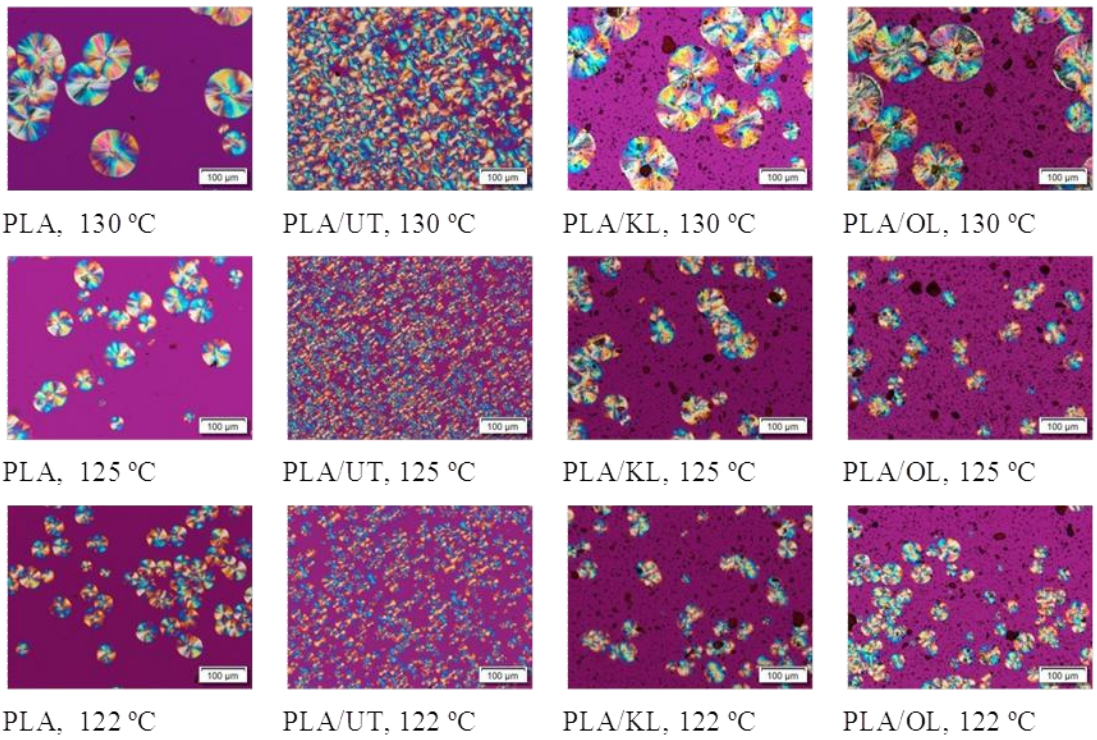

Figure 9.18. Micrographs taken for PLA and its blends at the indicated temperatures (i.e., 130, 125 and 122 ºC).

X-ray Scattering

The WAXS patterns taken after previously cooled the sample at 50 ºC/min as well as the *d*-spacings (long periods) of the samples obtained by SAXS are plotted in Figure 9.19.[5]

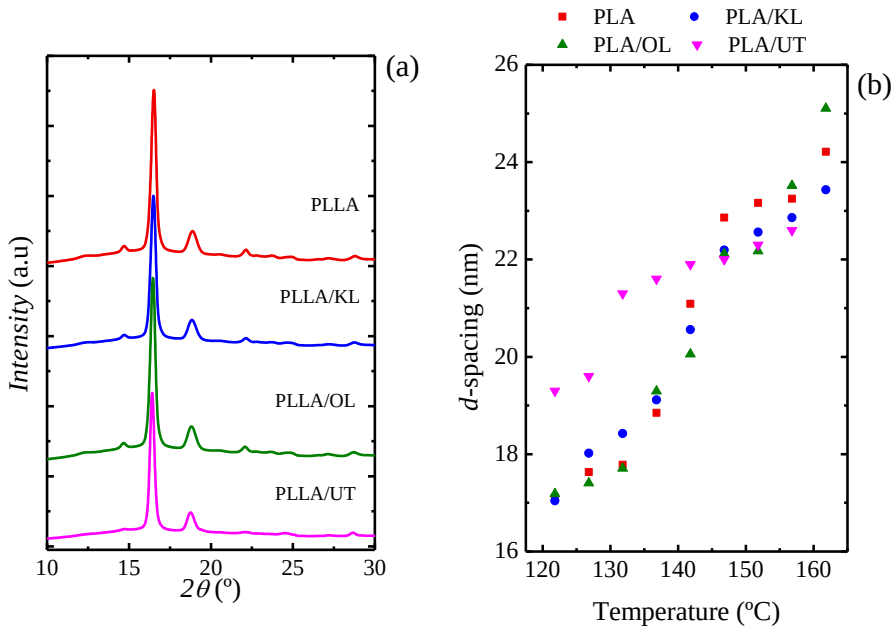

Figure 9.19. (a) WAXS patterns during the heating at 122 ºC after previously cooled the sample at 2 ºC min^{-1} (b) SAXS *d*-spacing obtained during heating at 5 ºC/min.

Avrami Fit

Table 9.8 shows the parameters obtained from the Avrami Fit for PLA/lignin and PLA/talc blends.

Table 9.8 Parameters obtained by fitting the Avrami theory.

T_c (°C)	PLA						PLA/UT						PLA/KL						PLA/OL					
	n	$kx10^3$ (min^{-n})	$kx10^3$ (min^{-1})	$t_{e50\%}$ (min)	$t_{t50\%}$ (min)	R^2	n	$kx10^3$ (min^{-n})	$kx10^3$ (min^{-1})	$t_{e50\%}$ (min)	$t_{t50\%}$ (min)	R^2	n	$kx10^3$ (min^{-n})	$kx10^3$ (min^{-1})	$t_{e50\%}$ (min)	$t_{t50\%}$ (min)	R^2	n	$kx10^3$ (min^{-n})	$kx10^3$ (min^{-1})	$t_{e50\%}$ (min)	$t_{t50\%}$ (min)	R^2
90	2.5	2.17	1.36	9.45	9.71	1	2.8	2400	16.1	0.64	0.64	1	3.4	17.6	2.3	3.01	2.94	0.99	2.6	30.1	3.7	3.25	3.29	1
95	2.7	7.16	2.07	5.53	5.49	0.99	2.4	6700	39.3	0.39	0.38	1	2.9	133	5.4	1.74	1.79	0.99	2.9	91.9	4.8	1.96	1.99	0.99
100	2.6	10.8	2.50	5.08	5.13	1	2.2	8550	61.3	0.32	0.33	0.99	3.0	283	6.6	1.33	1.35	1	3.6	136	3.9	1.60	1.57	0.99
105	2.6	11.7	2.58	4.92	4.96	1	2.6	6400	29.1	0.41	0.42	0.99	3.1	327	6.5	1.29	1.28	1	3.2	209	5.3	1.48	1.46	0.99
110	2.6	6.54	2.06	5.79	5.85	1	3.0	8270	20.2	0.44	0.44	0.99	3.0	1590	11.7	1.0	1.58	1	2.8	142	5.9	1.75	1.75	1
115	2.2	4.89	2.06	8.42	9.00	0.99	3.2	4510	13.9	0.55	0.55	1	2.8	67	4.5	2.25	2.28	1	3.4	27.2	2.6	2.68	2.63	0.99
120	1.8	2.82	1.78	18.8	23.1	0.99	3.1	583	7.8	1.05	1.06	1	2.8	7.94	2.1	5.02	5.09	1	2.7	6.94	2.0	5.46	5.59	1
123	1.8	1.67	1.33	25.5	30.8	0.99	3.3	202	4.8	1.45	1.44	1	3.9	0.412	0.8	7.11	6.80	0.99	3.5	0.318	0.7	9.38	9.11	0.99
125	1.5	3.45	2.28	34.1	32.1	0.99	3.3	71.2	3.6	2.00	2.00	1	2.6	1.6	1.2	10.2	10.3	1	2.4	1.78	1.3	12.0	12.4	1
126	1.7	1.54	1.29	38.8	35.2	0.99	3.5	35.8	2.8	2.35	2.32	0.99	2.9	0.191	0.6	16.2	16.5	1	2.9	0.224	0.6	16.7	16.7	1
128	2.3	0.203	0.50	39.1	32.6	0.99	3.5	11.2	2.0	3.26	3.20	0.99	3.7	0.0081	0.3	21.6	20.7	0.99	3.4	0.0219	0.3	21.9	21.3	0.99
130	2.1	0.166	0.43	55.5	50.9	0.99	3.2	6.71	1.8	4.24	4.12	0.99	3.0	0.0371	0.3	26.6	26.6	1	3.6	0.0079	0.3	24.2	23.5	0.99

*n is the Avrami index, k is the Avrami constant rate, $t_{t50\%}$ is the half-crystallization time determined theoretically, $t_{e50\%}$ is the half-crystallization time determined experimentally, R^2 is the correlation coefficient.

9.5 Appendix Chapter VII.

Avrami Fit

Table 9.9 and 9.10 shows the parameters obtained from the Avrami Fit for nanocomposites and nanohybrids, respectively.

Table 9.9. Parameters obtained by fitting the Avrami theory to the data obtained by isothermal crystallization experiments of non-functionalized samples.

Sample	T_c (°C)	n	K x10^5 (min^{-n})	K (min^{-1})	$\tau_{50\%,the}$ (min)	$\tau_{50\%,exp}$ (min)	1/ $\tau_{50\%,exp}$ (min^{-1})	R^2
PCL	35	2.8	36496	42.6	1.261	1.217	0.822	0.9998
	35.5	3.0	18518	26.5	1.545	1.516	0.660	1.0000
	36	3.1	11633	20.5	1.792	1.766	0.566	1.0000
	36.5	3.1	6873	17.3	2.096	2.083	0.480	1.0000
	37	3.2	3895	13.2	2.443	2.433	0.411	1.0000
	37.5	3.2	2466	11.5	2.833	2.816	0.355	1.0000
	38	2.7	3157	19.8	3.093	2.983	0.335	0.9999
	38.5	3.1	1175	9.8	3.681	3.666	0.273	1.0000
	39	3.0	994	10.0	4.133	4.117	0.243	1.0000
	39.5	3.0	573	8.3	4.846	4.850	0.206	1.0000
	40	2.9	468	8.3	5.688	5.616	0.178	1.0000
	40.5	2.8	284	7.5	6.891	6.734	0.149	1.0000
	41	2.7	243	7.6	8.366	8.017	0.125	0.9999
	41.5	2.7	118	5.9	10.516	9.917	0.101	0.9995
	42	3	30	3.1	12.918	12.317	0.081	0.9994
	42.5	2.7	33	3.7	16.403	14.950	0.067	0.9982
	43	3.1	6	1.8	20.653	19.100	0.052	0.9946
$PCL_{99.75}M_{0.25}$	48	2.2	3557	41.1	3.930	4.183	0.239	0.9999
	48.5	2.1	1998	37.3	5.239	5.700	0.175	0.9997
	49	2.2	917	22.2	7.065	7.734	0.129	0.9994
	49.5	2.1	496	19.2	10.618	11.750	0.085	0.9994
	50	1.9	562	28.0	13.157	13.317	0.076	1.0000
	50.5	1.8	325	24.9	19.119	19.067	0.052	1.0000
	51	1.9	140	13.5	27.893	28.067	0.036	1.0000
$PCL_{97}M_{0.3}$	48.5	1.7	5844	164.3	4.201	4.933	0.203	0.9959
	49	1.7	3528	122.1	5.645	6.283	0.159	0.9974
	49.5	1.9	1796	51.6	7.083	8.000	0.125	0.9985
	50	1.9	1108	40.0	8.695	10.133	0.099	0.9979
	50.5	1.7	1006	58.4	11.700	13.317	0.075	0.9982
	51	1.8	544	33.1	14.547	16.6	0.060	0.9980
	51.5	1.8	413	28.4	16.122	18.033	0.055	0.9985

	48.5	2.1	3533	48.9	4.110	4.384	0.228	0.9999
	49	2.2	1916	31.0	5.180	5.650	0.177	0.9998
	49.5	2.2	1107	24.2	6.470	7.133	0.140	0.9994
$PCL_{96}M_{0.4}$	50	2.1	734	23.2	8.780	9.600	0.104	0.9995
	50.5	1.9	647	30.2	11.086	11.450	0.087	0.9999
	51	2	286	16.9	16.088	16.733	0.060	0.9999
$PCL_{95}M_{0.5}$	49	2.3	1889	26.6	4.774	5.250	0.190	0.9997
	49.5	2.3	1025	20.4	6.367	7.166	0.140	0.9994
	50	2.2	741	20.2	7.687	8.283	0.121	0.9995
	50.5	2.1	425	17.8	11.165	12.000	0.083	0.9997
	51	1.9	0467	25.4	13.790	13.450	0.074	1.0000
	51.5	1.9	284	19.6	19.243	18.950	0.053	0.9999
	48	2.3	13901	63.3	1.982	2.167	0.461	0.9997
	48.5	2.2	10339	66.8	2.397	2.517	0.397	0.9999
	49	2.5	3015	24.6	3.577	3.900	0.256	0.9995
$PCL_{99.25}M_{0.75}$	49.5	2.6	1407	16.3	4.586	5.100	0.196	0.9996
	50	2.5	840	14.8	5.702	6.400	0.156	0.9990
	50.5	2.3	638	16.6	7.472	8.217	0.122	0.9992
	51	2.3	251	11.0	11.210	12.500	0.080	0.9992
	51.5	2.0	314	17.7	15.603	16.183	0.062	1.0000
	49	2.6	3517	23.1	3.207	3.483	0.287	0.9997
	49.5	2.8	1185	12.5	4.297	4.817	0.208	0.9992
	50	2.4	1093	18.5	5.504	6.184	0.162	0.9995
$PCL_{99}M_{1}$	50.5	2.1	963	26.3	7.543	8.333	0.120	0.9998
	51	2.1	457	18.5	10.996	12.033	0.083	0.9998
	51.5	2.2	257	12.5	13.275	13.683	0.073	0.9999
	52	1.9	247	18.2	19.619	19.333	0.052	0.9997
	49	2.5	11579	42.2	2.065	2.200	0.455	0.9999
	49.5	2.3	7505	48.4	2.588	2.700	0.370	1.0000
	50	2.7	2106	17.0	3.637	3.966	0.252	0.9997
$PCL_{98}M_{2}$	50.5	2.6	1215	15.4	4.652	5.067	0.197	0.9996
	51	2.6	677	12.3	6.047	6.516	0.153	0.9996
	51.5	2.3	548	15.5	8.566	8.983	0.111	0.9999
	52	2.1	365	16.6	12.167	12.350	0.081	1.0000
	52.5	2.2	166	10.2	14.716	14.500	0.069	1.0000
	50	2.8	3827	19.0	2.820	3.033	0.330	0.9999
	50.5	2.8	1625	14.0	3.743	4.067	0.246	0.9997
	51	2.5	1543	18.9	4.610	4.950	0.202	0.9999
$PCL_{97}M_{3}$	51.5	2.4	785	16.1	6.528	7.033	0.142	0.9999
	52	2.4	387	12.0	8.741	9.150	0.109	0.9999
	52.5	2.6	99	5.9	12.940	13.766	0.073	0.9998
	53	2.1	160	11.2	18.70803	18.150	0.055	0.9999
	50	2.5	7848	36.1	2.356	2.417	0.414	1.0000
	50.5	2.6	3543	23.2	3.132	3.267	0.306	1.0000
	51	2.8	1290	12.9	4.234	4.534	0.221	0.9998

$PCL_{95}M_5$	51.5	2.5	817	14.6	6.082	6.217	0.161	0.9999
	52	2.9	139	5.5	8.550	9.466	0.106	0.9990
	52.5	2.5	153	7.5	11.321	11.650	0.086	0.9999
	53	2.1	178	11.8	17.934	17.400	0.057	0.9998

Table 9.10. Parameters obtained by fitting the Avrami theory to the data obtained by isothermal crystallization experiments of functionalized samples.

Sample	T_c (°C)	n	K x10^5 (min^{-n})	K (min^{-1})	$\tau_{50\%,the}$ (min)	$\tau_{50\%,exp}$ (min)	1/ $\tau_{50\%,exp}$ (min^{-1})	R^2
	35	2.8	36496	42.6	1.261	1.217	0.822	0.9998
	35.5	3.0	18518	26.5	1.545	1.516	0.660	1.0000
	36	3.1	11633	20.5	1.792	1.766	0.566	1.0000
	36.5	3.1	6873	17.3	2.096	2.083	0.480	1.0000
	37	3.2	3895	13.2	2.443	2.433	0.411	1.0000
	37.5	3.2	2466	11.5	2.833	2.816	0.355	1.0000
PCL	38	2.7	3157	19.8	3.093	2.983	0.335	0.9999
	38.5	3.1	1175	9.8	3.681	3.666	0.273	1.0000
	39	3.0	994	10.0	4.133	4.117	0.243	1.0000
	39.5	3.0	573	8.3	4.846	4.850	0.206	1.0000
	40	2.9	468	8.3	5.688	5.616	0.178	1.0000
	40.5	2.8	284	7.5	6.891	6.734	0.149	1.0000
	41	2.7	243	7.6	8.366	8.017	0.125	0.9999
	41.5	2.7	118	5.9	10.516	9.917	0.101	0.9995
	42	3	30	3.1	12.918	12.317	0.081	0.9994
	42.5	2.7	33	3.7	16.403	14.950	0.067	0.9982
	43	3.1	6	1.8	20.653	19.100	0.052	0.9946
	48.5	2.3	26669	84.0	1.51	1.55	0.645	1.0000
	49	2.4	13602	52.8	1.99	2.07	0.483	1.0000
	49.5	2.5	4507	28.9	3.00	3.08	0.325	0.9999
$PCL_{99.75}NH_{0.25}$	50	2.7	1742	15.9	3.91	4.15	0.241	0.9999
	50.5	2.6	1040	14.5	4.95	5.23	0.191	1.0000
	51	2.6	573	11.5	6.43	6.83	0.146	0.9997
	51.5	2.2	566	17.8	8.81	8.88	0.113	1.0000
	52	2.1	268	14.3	13.51	13.12	0.076	0.9999
	48.5	2.4	3380	29.5	3.47	3.73	0.268	0.9999
	49	2.6	1423	16.3	4.41	4.82	0.207	0.9996
	49.5	2.4	1115	18.6	5.57	6.1	0.164	0.9994
$PCL_{95}NH_{0.5}$	50	2.1	1112	28.2	7.1	7.37	0.136	0.9999
	50.5	2.0	857	29.3	9.14	9.17	0.109	1.0000
	51	2.0	236	15.4	16.99	18.00	0.056	1.0000
	51.5	1.8	180	17.9	25.84	27.32	0.037	0.9999
	48	2.3	11658	58.6	2.19	2.28	0.439	1.0000

	48.5	2.2	4378	45.2	3.56	3.70	0.270	0.9999
	49	2.3	3114	33.0	3.82	4.02	0.249	1.0000
$PCL_{99.25}NH_{0.25}$	49.5	2.4	1628	21.8	4.74	5.03	0.199	0.9999
	50	2.3	1005	20.2	6.39	6.85	0.146	0.9997
	50.5	2.2	605	18.4	8.77	9.13	0.110	0.9998
	51	2.1	413	17.6	11.26	11.25	0.089	1.0000
	51.5	1.9	363	22.2	15.29	14.38	0.070	0.9999
	48	2.3	9656	54.0	2.31	2.48	0.403	0.9999
	48.5	2.3	6633	45.9	2.81	2.95	0.339	1.0000
$PCL_{99}NH_{1}$	49	2.4	2996	28.1	3.79	4.02	0.249	0.9999
	49.5	2.4	1564	21.4	4.77	5.10	0.196	0.9999
	50	2.3	1142	21.4	5.94	6.30	0.159	0.9998
	50.5	2.2	721	19.9	8.06	8.42	0.119	0.9998
	51	2.0	607	24.6	10.89	10.65	0.094	1.0000
	51.5	2.0	268	16.4	16.37	15.95	0.063	0.9998
	48.5	2.4	10710	47.8	2.17	2.33	0.429	0.9998
	49	2.3	7170	47.5	2.74	2.88	0.347	1.0000
	49.5	2.4	3006	28.1	3.73	3.93	0.254	1.0000
$PCL_{98.75}NH_{1.25}$	50	2.4	1454	20.8	4.93	5.33	0.188	0.9998
	50.5	2.4	931	17.3	6.09	6.48	0.154	0.9997
	51	2.1	781	23.8	8.20	8.40	0.119	1.0000
	51.5	2.1	389	17.1	11.89	11.90	0.084	1.0000
	52	2.1	192	12.2	16.24	15.98	0.063	1.0000
	52.5	1.8	212	19.6	23.26	21.51	0.046	1.0000
	48.5	2.4	11566	49.3	2.10	2.23	0.448	0.9999
	49	2.8	3038	17.5	3.09	3.37	0.297	0.9998
	49.5	2.4	3480	29.9	3.48	3.67	0.272	1.0000
$PCL_{98}NH_{2}$	50	2.3	1989	27.2	4.56	4.88	0.205	0.9999
	50.5	2.1	1466	32.2	6.08	6.40	0.156	0.9999
	51	2.2	663	19.2	8.11	8.28	0.121	0.9999
	51.5	2.1	496	19.2	11.09	10.90	0.092	1.0000
	52	2.2	200	11.1	14.87	14.25	0.070	0.9999
	49	2.4	11600	49.4	2.10	2.18	0.459	1.0000
	49.5	2.5	4816	29.7	2.87	3.00	0.333	1.0000
	50	3.5	622	6.3	3.90	4.33	0.231	0.9984
$PCL_{97}NH_{3}$	50.5	2.6	1012	14.3	5.00	5.38	0.186	0.9997
	51	2.5	610	13.0	6.89	7.25	0.138	0.9998
	51.5	2.2	393	15.1	10.34	10.71	0.093	1.0000
	52	2.5	77	5.7	15.41	16.12	0.062	0.9999
	52.5	2.0	124	11.1	22.09	21.2	0.047	0.9998

Rheological properties.

The melt rheological data have been superposed using the time-temperature superposition principle to obtain master curves at a reference temperature, T_R. Here we have selected a T_R = 70 °C. We have applied the method of Mavridis and Shroff, to determine horizontal, a_T, and vertical, b_T, factors. The a_T and b_T values were extracted from $tan\delta$ versus ω and $tan\delta$ versus $|G^*|$ data, respectively. Both the a_T and b_T factors for the nanocomposites studied are similar to those of the unfilled polymer and obey an Arrhenius-type temperature dependence with horizontal activation energy around 40 kJ/mol (reported in the range 35.0-40.0 kJ/mol for PCL) and vertical activation energies lower than 3.9 kJ/mol (< 1 kcal/mol).

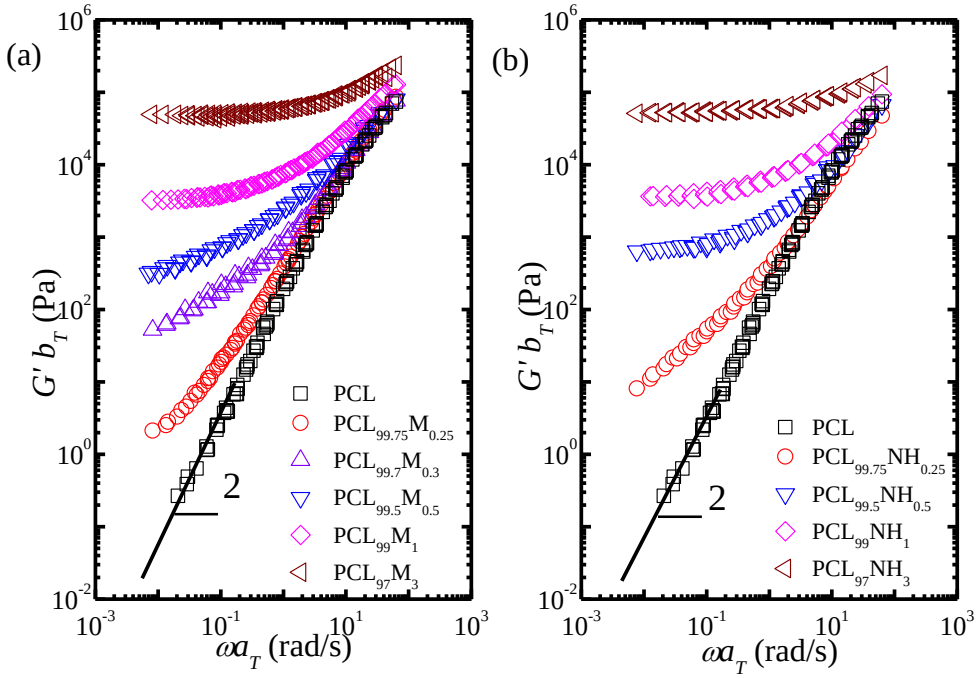

Figure 9.20. Reduced shear storage (G'_{bT}) modulus versus reduced angular frequency (ω_{aT}) of the materials studied at T_R=70 °C. (a) PCL_xM_y and (b) PCL_xNH_y.

The viscoelastic function storage moduli, G', for the neat polymer and the two families of nanocomposites are shown in Figure 9.20. The neat PCL behaves as a Newtonian liquid at low frequencies and shows the characteristic power law of the storage modulus, $G' \propto \omega^2$. However, the terminal behavior disappears with addition of MWCNTs either in PCL_xM_y or PCL_xNH_y. The low-frequency response for the samples display an increase of the values of G' and a decrease in the frequency dependence of G' (i.e., $G' \propto \omega^{\beta}$, with $\beta < 2$) within this region. This means that the long-time polymer dynamics in the terminal region is constrained by the presence of the MWCNTs.

As a result, the low-frequency complex viscosity, $|\eta^*|$, increases significantly in presence of MWCNTs especially at high compositions, and the Newtonian plateau of the viscosity curve for PCL progressively vanishes, as it can be readily observed in Figure 9.21. This is associated with the formation of a MWCNT network, which leads to the transformation of the liquid-like polymer to a solid-like material showing a remarkable yield, even at very low MWCNT concentrations. The divergence of $|\eta^*|$ in the low-frequency zone (*i.e.*, $|\eta^*| \propto \omega^{-\alpha}$, with $0 < \alpha < 1$) is clearly observed. Changes and improvements in the physical properties of polymers due to the addition of MWCNTs have been widely reported for polymeric nanocomposites with SWCNTs and MWCNTs, and it has been shown to depend on the MWCNT state of dispersion and aspect ratio, polymer-MWCNT interactions, but also on the molecular architecture of the polymeric matrix.

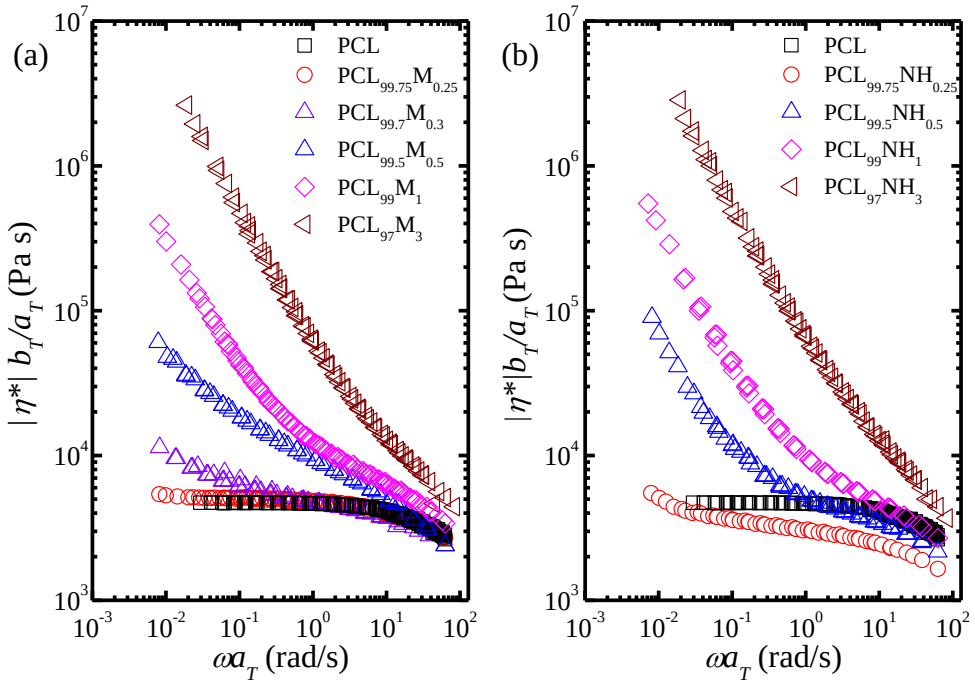

Figure 9.21. Reduced magnitude of the complex viscosity ($|\eta^*|\ b_T/a_T$) versus reduced angular frequency of the materials studied at T_R= 70 °C. (a) PCL_xM_y and (b) PCL_xNH_y.

In Figure 9.22, the exponents β and α (obtained by fitting in the lowest frequency decade experimentally available for *G'* and $|\eta^*|$), are plotted as a function of the MWCNT concentration. The value of β decreases monotonically from 2.0 to 0 with increasing MWCNT concentration and the values of α increase monotonically from 0 to 1.0, as it has been observed in well dispersed PCL/SWCNT nanocomposites obtained by solution mixing, which are included in Figure 9.22 for comparisons

purposes. The behavior observed seems to be independent of the type of the MWCNTs in our case (*i.e*, PCL_xM_y and PCL_xNH_y).

The results in Figures 9.19-9.22 are associated with the formation of a MWCNT network, which leads to the transformation of the liquid-like polymer to a solid-like material, even at very low MWCNT concentrations. This behavior has been typically observed in yield stress (viscoplastic) materials. The yield stress is classically defined in the non-linear viscoelastic range as the minimum shear stress that must be applied to a material (typically a multiphase system) to induce flow. The most common method to obtain the yield stress is to extrapolate the shear stress versus shear rate curve to zero shear rate, but there are other methods as stress relaxation, creep and recovery or shear stress ramp measurements. Dynamic oscillatory measurement is an alternative method for the determination of yield stress. Viscoplastic materials exhibit a low frequency plateau in *G'*, together with a characteristic power law increase of $|\eta^*|$. These trends have been suggested to be correlated to the yield stress. There is a general agreement in that these behaviors at low frequencies are characteristic features of yielding fluids.

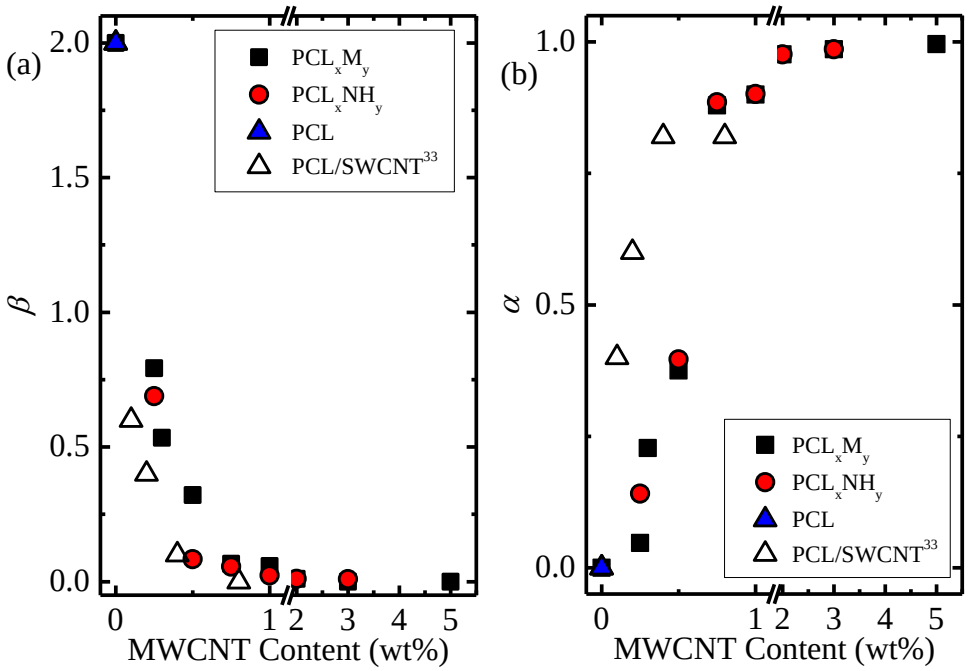

Figure 9. 22. Power law exponents of *G*' and $|\eta^*|$ obtained by fitting of the lowest frequencies.

Obtaining the percolation threshold requires a full characterization of the yield behavior at low frequencies. In Figure 9.23 it is observed the typical plot of $|\eta^*|$ versus $|G^*|$ used for the study of materials that show yield behavior applied to our samples. In general, a well-defined yield is obtained in all the cases except for the samples with the lowest content in MWCNTs. Some authors have suggested a linear

extrapolation of $|G^*|$ when $|\eta^*|$ tends to infinite (or the reciprocal tends to zero) in order to extract the typical modulus of the network. In our case, this procedure works well for compositions higher than 0.25 wt%, as it can be observed in Figure 9.23b. However, for the $PCL_{99.75}M_{0.25}$ and $PCL_{99.75}NH_{0.25}$ systems (those with the lowest MWCNT content) the application of this procedure would require very long extrapolations.

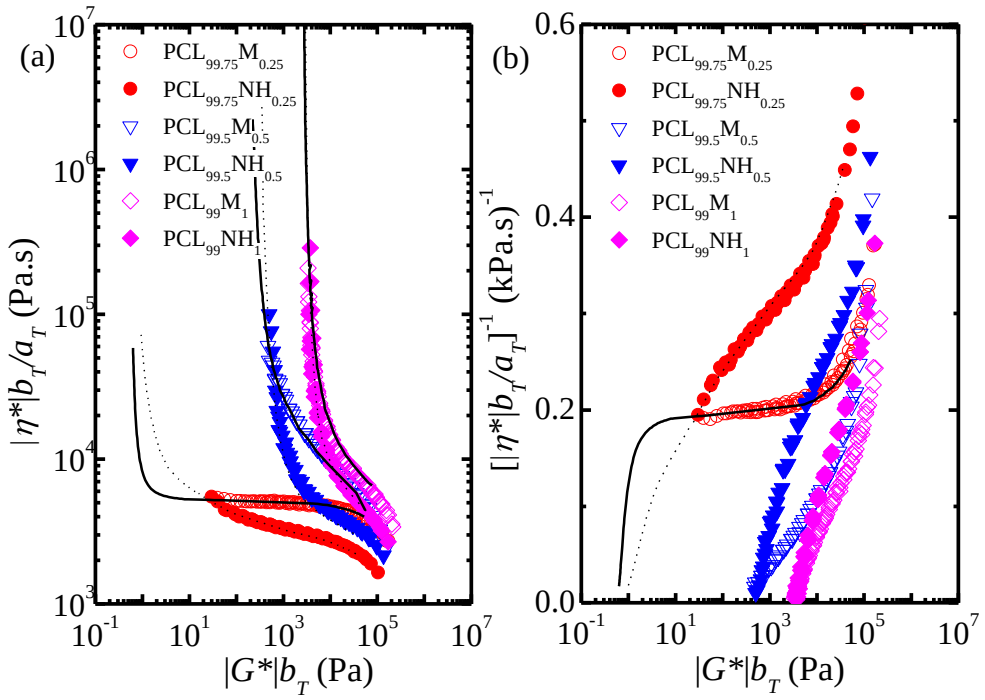

Figure 9.23. (a) Magnitude of the complex viscosity *versus* magnitude of the complex modulus of selected samples: (○) $PCL_{99.75}M_{0.25}$, (▽) $PCL_{99.5}M_{0.5}$, (◇) $PCL_{99}M_1$, (●) $PCL_{99.75}NH_{0.25}$, (▼) $PCL_{99.5}NH_{0.5}$, (◆) $PCL_{99}NH_1$. Lines represent the converted creep results to oscillatory data. (b) Extrapolation procedure using the creep results applied to obtain $|G^*|_0$ when $1/|\eta^*| \rightarrow 0$.

In order to further probe the existence and nature of this 'plateau', especially in these cases, we have performed long creep measurements at T=70 °C. The shear compliance, J_c, obtained from these measurements is shown in Figure 9.24 for selected samples. The results for J_c are within the linear viscoelastic region, as it is guaranteed by the identical trend obtained for each material irrespective of the shear stress applied in the range τ_0 = 6.25–100 Pa.

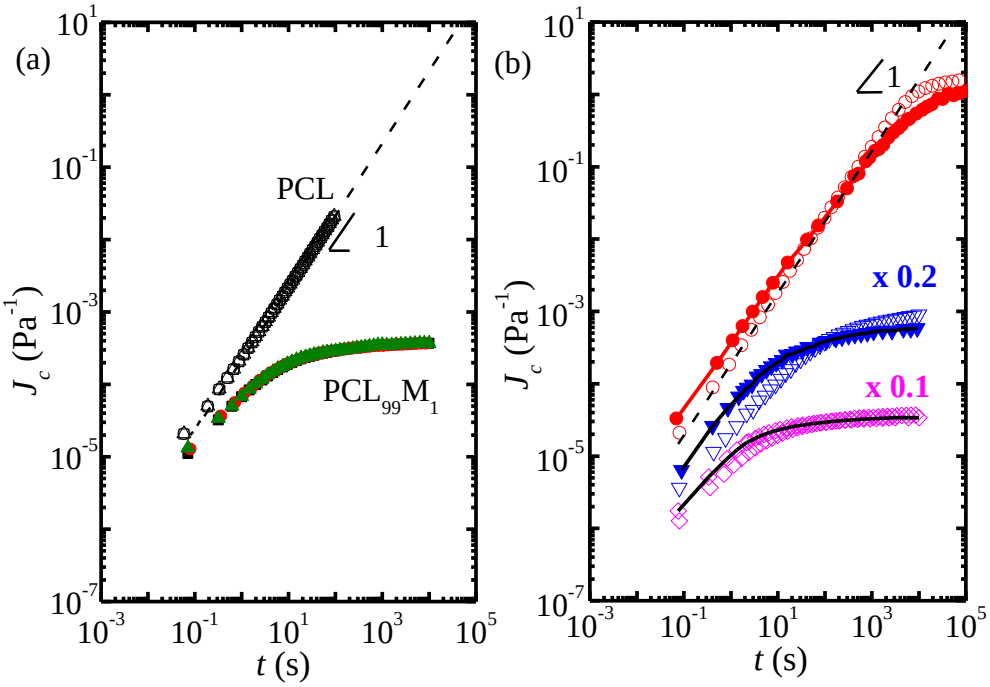

Figure 9.24. (a) Shear creep compliance, J_c, as a function of creep time for selected materials at T=70 °C. Applied shear stress, τ_0: (○) 6.25 Pa, (□) 12.5 Pa and (△) 25 Pa for PCL and (■) 50 Pa, (●) 75 Pa and (▲) 100 Pa for $PCL_{99}M_1$. Dotted lines indicate the extrapolated slope of the flow region for PCL. (b) Shear creep compliance, J_c, as a function of creep time at T=70 °C for pure PCL (dashed line); MWCNT samples: (○) $PCL_{99.75}M_{0.25}$, (▽) $PCL_{99.5}M_{0.5}$, (◇) $PCL_{99}M_1$; and the NH samples (●) $PCL_{99.75}NH_{0.25}$, (▼) $PCL_{99.5}NH_{0.5}$, (◆) $PCL_{99}NH_1$. The curves of the samples with 0.5 and 1 wt% MWCNT content in (b) have been vertically shifted for a better visualization, as indicated in the graph.

In Figure 9.24a the results obtained for PCL and $PCL_{99}M_1$ are shown as examples. The creep mode allows one to work in the terminal region providing application of low enough values of shear stress for long creep times. Typically, in polymeric materials it is possible to obtain the value of Newtonian viscosity, η_0, as $\eta_0 = \lim_{t\to\infty} t/J(t)$. This is the case of the neat PCL sample, which shows the typical behavior of a Newtonian polymer in the whole time window explored, with $J_c \propto t^1$. Lower values of J_c are observed as the MWCNT content in the sample increases (see Figure 9.24b). The terminal behavior however is not reached in any of the nanocomposites within the time window explored. The addition of the MWCNTs becomes evident by a general decrease of J_c over the whole ranges of time for the samples, either in PCL_xM_y or PCL_xNH_y samples. The most interesting result is that in all cases, including the samples with the lowest content in MWCNT, a constant 'plateau' in compliance is reached at long times, indicating the expected solid-like behavior of percolated networks. The equilibrium values of J_c at long times are quite similar in both families at a given content of MWCNTs, as it is shown in Figure 9.24b.

The values of J_c in Figure 9.24 have been converted to $|G^*|$ and $|\eta^*|$. The results obtained from the experiments can then be compared in a broad range of angular frequencies, as it is observed in Figure 9.23b for the $|G^*|$ *versus* $|\eta^*|$ plot. The strong effect of the MWCNTs can be seen, even for the lowest MWCNT compositions. From this plot the characteristic values of $|G^*|_0$ for the MWCNT network have been obtained. The values are listed in Table 9.11.

Table 9.11. Solid-like yield complex modulus for the materials under study at T = 70 °C.

PCL_xM_y	$\lvert G^*\rvert_0$ (Pa)	PCL_xNH_y	$\lvert G^*\rvert_0$ (Pa)
$PCL_{99.75}M_{0.25}$	0.63	$PCL_{99.75}NH_{0.25}$	1.0
$PCL_{99.3}M_{0.3}$	15	-	-
$PCL_{99.5}M_{0.5}$	220	$PCL_{99.5}NH_{0.5}$	340
$PCL_{99.25}M_{0.75}$	1,640	$PCL_{99.25}NH_{0.75}$	1,810
$PCL_{99}M_1$	2,710	$PCL_{99}NH_1$	2,960
$PCL_{98}M_2$	18,000	$PCL_{98}NH_2$	20,000
$PCL_{97}M_3$	52,500	$PCL_{97}NH_3$	55,000
$PCL_{95}M_5$	142,900	-	

The application of the percolation theory to the results obtained for $|G^*|_0$ from the combination of oscillatory and creep experiments as a function of the MWCNT content is shown in Figure 9.25. The determination of the critical concentration, ϕ_p, is made by fitting the data to the following scaling law:

$$|G^*|_0(\phi) = |G^*|_0\left(\phi - \phi_p\right)^t \qquad \text{Eq. 9.1}$$

The critical concentration was found to be quite similar in both families within the experimental uncertainty, 0.240% and 0.236 wt% for PCL_xM_y and PCL_xNH_y families, respectively. The volume fraction, ϕ_p, is around 1.5×10^{-3}, assuming a density $\rho_{PCL(melt)}$=1.06 g/cm^3 at T= 70 °C and ρ_{MWCNT}=1.74 g/cm^3. The critical exponent in Equation 9.1 is t=2.00, which is agreement with the universal value expected in the case of a 3D percolated network. The percolation threshold obtained is one order of magnitude lower than those obtained in previous determinations on PCL/CNT (2 - 3 wt%).

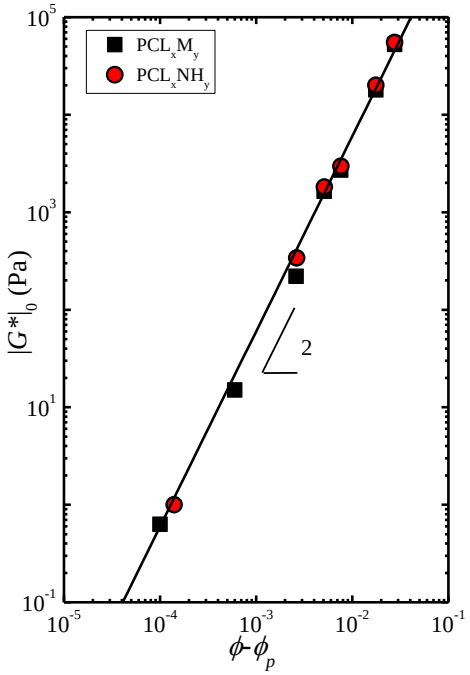

Figure 9.25. Linearization of the compositional dependence of the yield 'plateau' modulus for the systems under study. The line is the best fit to eq. 9.1.

A closer inspection of the results obtained for $|G^*|_0$ at given compositions suggests a slightly better dispersion for the PCL_xNH_y family (see Table 9.11). This is also clear in the complex viscosity plot shown in Figure 9.26. The figure includes a combination of oscillatory and creep results for selected samples at T = 70 °C. It is observed that both families reach in the low frequency region the expected yield behavior ($|\eta^*| \propto \omega^{-1}$). Additionally, PCL_xNH_y samples reach higher values of $|\eta^*|$ than the analogous PCL_xM_y. These results suggest that: (i) the MWCNT network dominates the dynamics of the systems within low frequency (long time) region in both families, restricting polymer chains terminal relaxation and (ii) the MWCNT network in the PCL_xNH_y family restricts more efficiently this relaxation than in PCL_xM_y samples, at least up to MWCNT content of 1 wt%.

More interesting differences between PCL_xM_y and PCL_xNH_y families can be observed for $|\eta^*|$ in the high frequency region. An enlargement of this specific region is observed in the right panel of Figure 9.26. It is remarkable that for those samples with the lowest NH content, $|\eta^*|$ diverges from that obtained for the neat PCL and PCL_xM_y family, decreasing in magnitude up to a 50 % (see the solid lines in Figure 9.26). The equivalent is observed for creep compliance in Figure 9.24b at short times, with a clear increase in J_c values with respect to that observed in neat PCL.

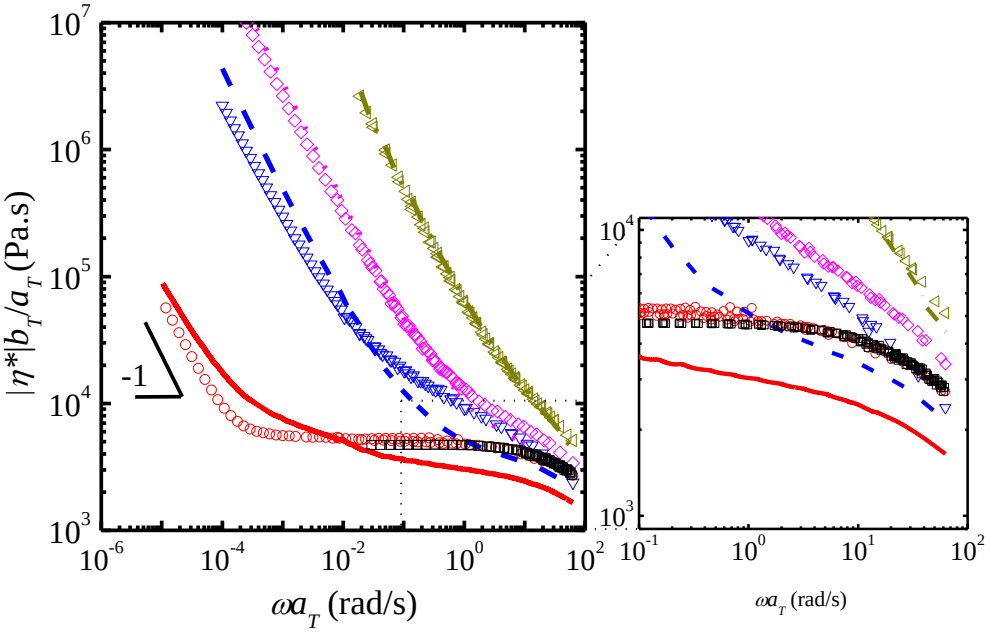

Figure 9.26. Reduced magnitude of the complex viscosity, obtained from oscillatory and transformed creep experiments, *versus* reduced angular frequency of selected samples: (□) PCL, (○) $PCL_{99.75}M_{0.25}$, (▽) $PCL_{99.5}M_{0.5,}$ (◇) $PCL_{99}M_1$, (◁) $PCL_{97}M_3$, (solid line) $PCL_{99.75}NH_{0.25}$, (dashed line) $PCL_{99.5}NH_{0.5}$, (dotted line) $PCL_{99}NH_{1,}$ (dash-dotted line) $PCL_{97}NH_3$.

The decreased viscosity and increased compliance is a result of the low molecular weight free and grafted PCL chains in PCL_xNH_y samples, as a consequence of the process of functionalization of the MWCNTs. At high frequencies the mechanical solicitation acts on a small size scale, being less sensitive to the MWCNT network, as it is demonstrated by the small changes observed for the PCL_xM_y family with respect to the neat PCL. For example, in this zone the $PCL_{99.75}M_{0.25}$ is virtually identical to neat PCL. However, this is not the case for the PCL_xNH_y, for which the effect of the low molecular weight species (either grafted or 'free') have a measurable effect. The influence of these low molecular weight species vanishes as the NH content increases. In fact, the plasticization effect disappears for compositions higher than 1 wt%, within the frequency range experimentally available, as it is observed in Figure 9.26. This is most probably due to a shift of the plasticization effect at higher frequencies as NH content increases. It should be noted that in the rheological analysis two competing mechanisms push in opposite directions as NH content increases: (i) an increase in the amount of low-M_w PCL component (decrease the magnitude of the rheological properties), and (ii) a decrease of the mesh size of the MWCNT network (increase the magnitude of the rheological properties). For the highest NH content the plasticization range may shift outside the experimentally accessible area due to the extremely low mesh size of the MWCNT network.

The results observed for the PCL_xNH_y family may have important implications in process operations, such as extrusion. It should be recalled here that PCL has been reported to show significant and undesirable extrudate distortions during this process. The results shown here are promising, as they anticipate a better performance and processability of the PCL_xNH_y samples in extrusion processes, preventing or delaying extrudate distortions, and also conferring a better dimensional stability, as it has been observed in polyolefins such as polypropylene and polyethyene.[6]

Polymer/masterbatch samples

The crystallization of PC due to the plasticization effect of PBS is show in Figure 9.27.[7]

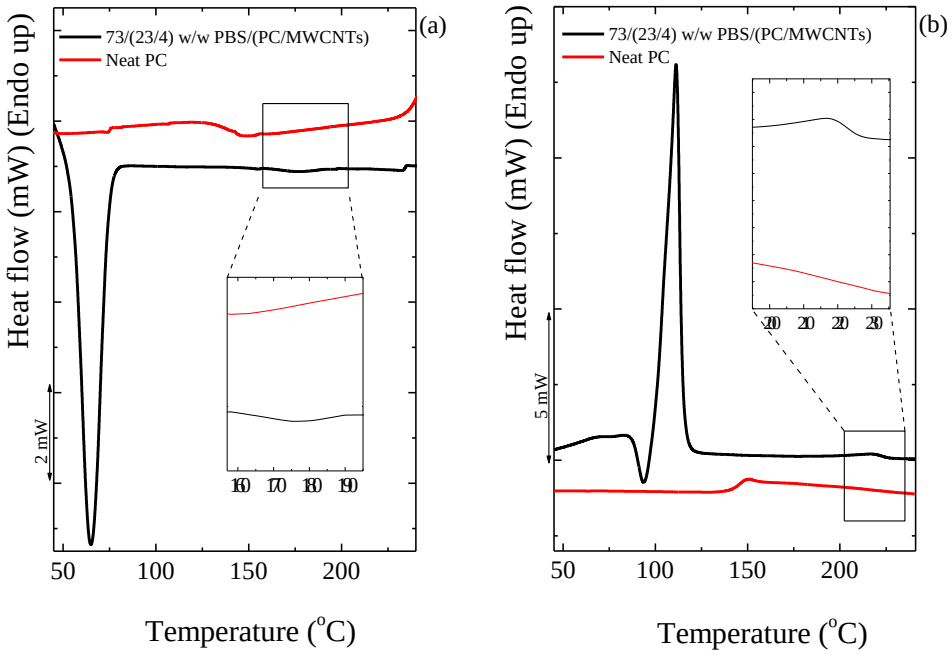

Figure 9.27. DSC (a) cooling and (b) second heating curves for neat polycarbonate (PC) and the 73/(23/4) w/w PBS/(PC/MWCNTs) nanocomposite. The zoomed regions correspond to the crystallization (see a) and melting (see b) of PC in the nanocomposites and its absence in the neat PC.

Simultaneous SAXS/WAXS experiments

Figure 9.28 shows the WAXS patterns taken during the heating after isothermally crystallize the neat components (*i.e.*, PCL and PBS, respectively) of the blends. In Table 9.12 is show the d-spacings calculated for the PBS systems.

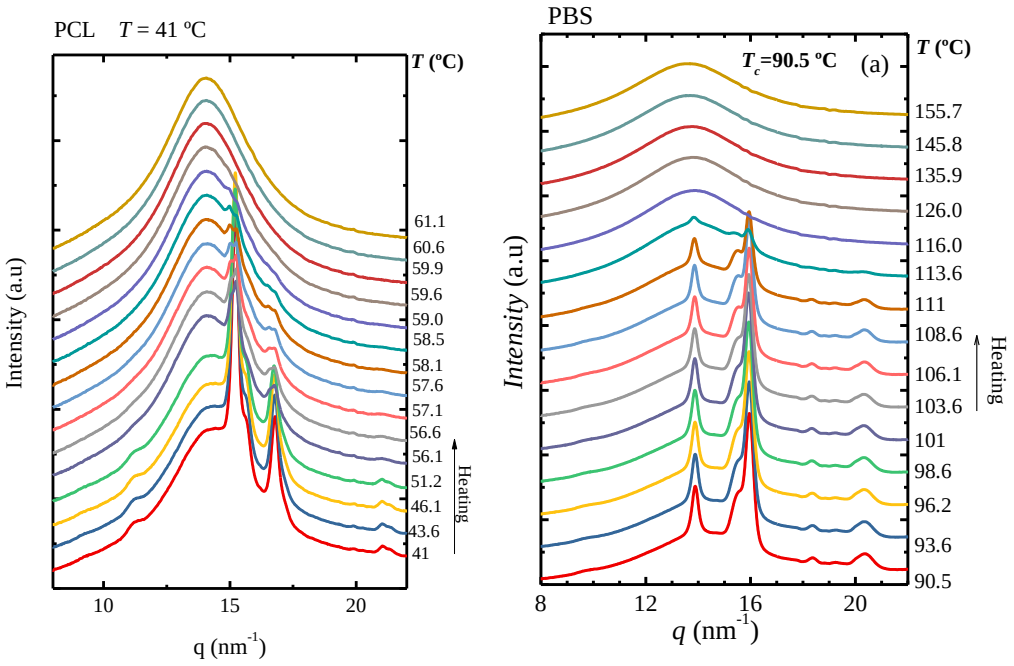

Figure 9.28. Heating of PCL and PBS after isothermal crystallization at 41 and 90.5 ºC, respectively.

Table 9.12. Calculated values of *d*-spacing (from WAXS experiments) and long period (*d**, obtained from SAXS experiments) for the neat PBS and its nanocomposites.

Sample	q (nm^{-1}) / *d*-spacing (nm) / (plane)	d^* (nm)
Neat PBS	13.88 / 0.426 / (002)	12.3
	15.54 / 0.381 / (012)	
	15.96 / 0.371 / (110)	
	18.38 / 0.322 / (121)	
	20.36 / 0.291 / (111)	
93/(6/1) w/w PBS/(PC/MWCNTs)	13.90 / 0.426 / (002)	11.9**
	15.52 / 0.381 / (012)	
	15.97 / 0.371 / (110)	
	18.35 / 0.323 / (12-1)	
	20.42 / 0.291 / (111)	
	12.34 / 0.479*	
73/(23/4) w/w PBS/(PC/MWCNTs)	13.88 / 0.426 / (002)	8.3**
	15.55 / 0.381 / (012)	
	15.95 / 0.371 / (110)	
	18.34 / 0.323 / (121)	
	20.36 / 0.291 / (111)	
	12.30 / 0.481*	

*PC signal
**overlap of PC and PBS signals

DMA experiments

Figure 9.29 and 9.31 shows the results of DMA experiments for PCL and PBS-based blends, which were performed in order to determined the glass transition temperature, which can be clearly seem in Figure 9.30 and 9.32 for PCL and PBS-based blends, respectively.[8]

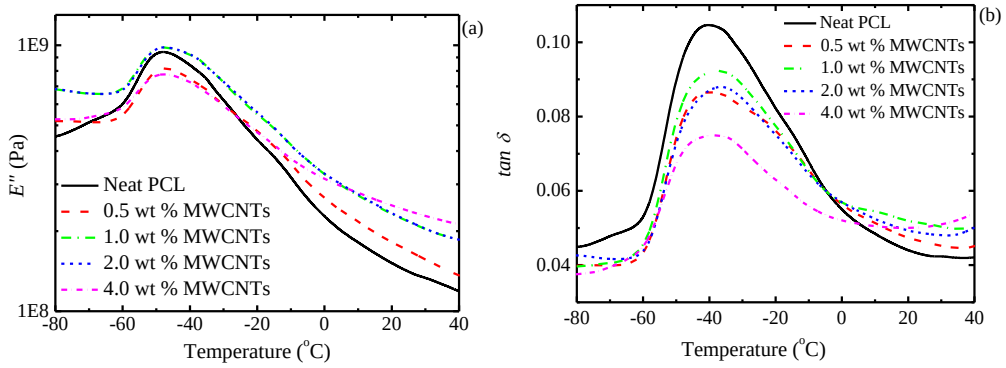

Figure 9.29 DMA (a) loss modulus (*E''*) and (b) tan δ curves for the PCL based blends.

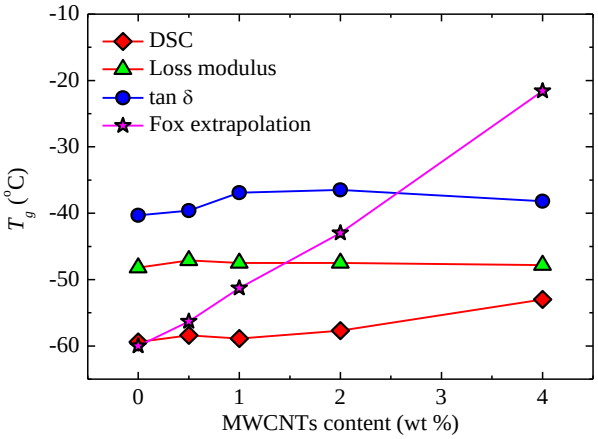

Figure 9.30. Glass transition temperatures of neat PCL and the PCL/(PC/MWCNT) nanocomposites as a function of MWCNT content.

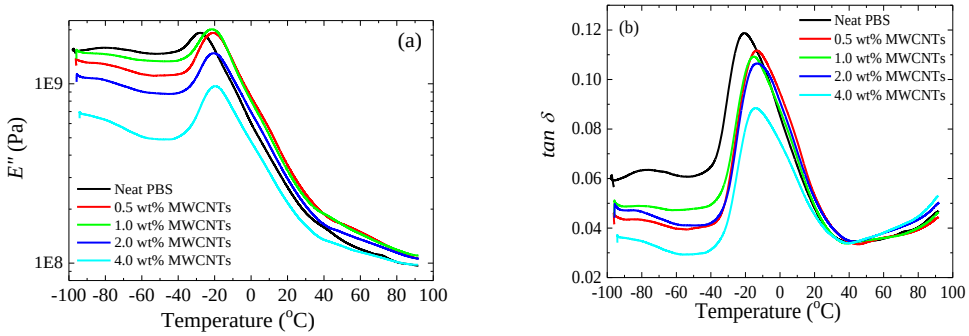

Figure 9.31. DMA (a) loss modulus (*E´´*) and (b) tan δ curves for the PBS-based blends.

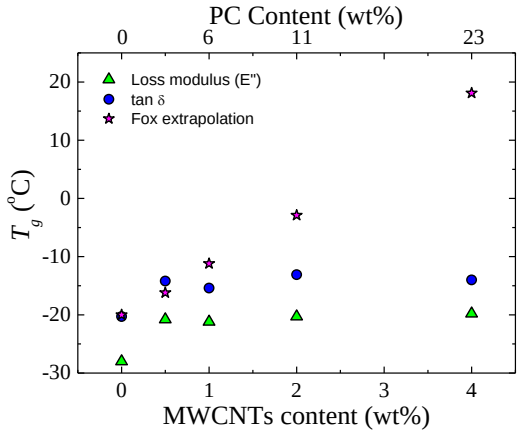

Figure 9.32. Glass transition temperatures of neat PBS and the PBS/(PC/MWCNTs) nanocomposites as a function of MWCNTs content (The corresponding PC content is indicated in the top x-axis). The Fox extrapolation T_g data was obtained using the *tan δ* values.

Electron Microscopy (SEM and TEM) and Atomic Force Microscopy (AFM)

SEM and TEM images for the PCL/(PC/MWCNT) nanocomposites with different PC/MWCNT contents were obtained to confirm the presence of two phases (PCL-rich and PC-rich phases), and to see whether any of the MWCNTs diffused into the PCL phase.

The SEM and TEM images in Figures 9.33 and 9.34 show that there are no clear phase boundaries separating the PCL-rich and PC-rich phases, and that the MWCNTs were fairly well dispersed throughout the blend matrix, although there were areas where the MWCNTs were more concentrated that correspond to the PC-rich phase. The results corroborate the partial miscibility of the blends. If the blends were immiscible, all MWCNTs would be confined to the PC phase (as a PC-based masterbatch was employed). However, it is clear that, due to partial miscibility and the establishment of PC-rich and PCL-rich phases, a fair number of MWCNTs diffused from the PC-rich phase to the PCL-rich phase, even though areas were found where MWCNTs agglomerates were still confined to the PC-rich pockets.

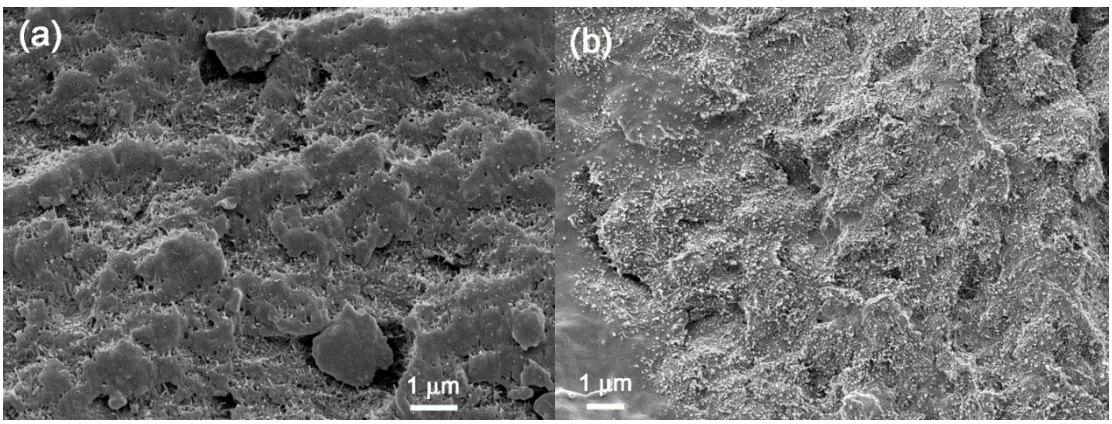

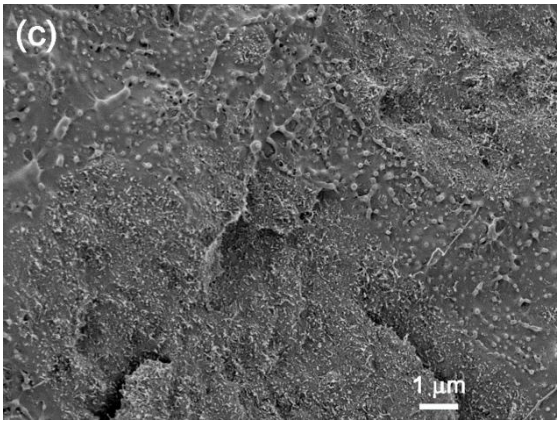

Figure 9.33. SEM micrographs for the PCL/(PC/MWCNT) nanocomposites, respectively, containing (a) 1.0, (b) 2.0, and (c) 4.0 wt % MWCNTs.

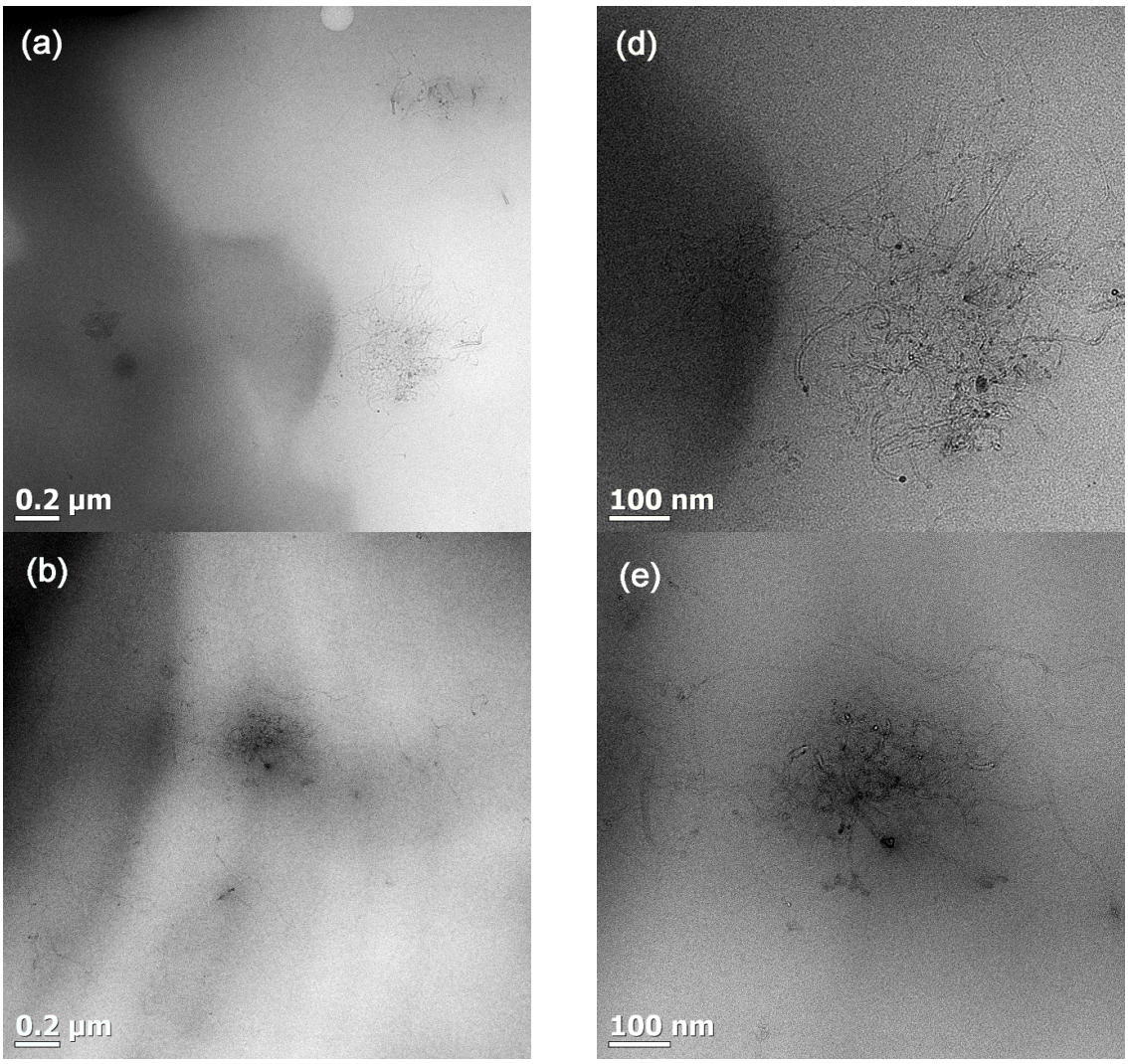

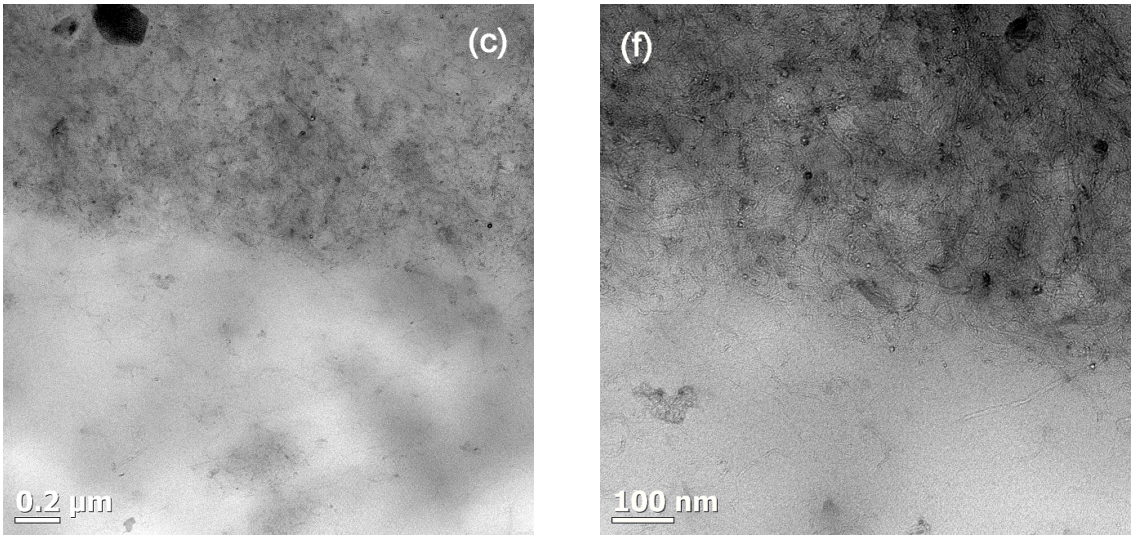

Figure 9.34. Figure 8. High and low magnification TEM micrographs for (a,d) 1.0 wt %, (b,e) 2.0 wt %, and (c,f) 4.0 wt % MWCNTs in the PCL/(PC/MWCNT) nanocomposites.

The molecular weight of PC (20,100 g mol^{-1}) in the masterbatch was appreciably lower than that of PCL (113,400 g mol^{-1}). The PC crystallized in the presence of the PCL, which acted as a plasticizer and imparted enough mobility to the PC chains.

The PC crystallization probably reduced the miscibility between PC and PCL, making them only partially miscible. Another reason why we did not observe complete miscibility in our system, is that the MWCNTs probably had a strong interaction with the PC and with each other, which restricted the PC flow during the mixing process and resulted in a fair amount of the PC chains being unable to diffuse into the PCL-rich phase.

Figure 9.35 shows the atomic force microscopy (AFM) phase images for the 4 wt % MWCNT nanocomposite at different magnifications. It can be seen at low magnification (Figure 9.35a) that an interphase exists between the PCL matrix and the PC/MWCNT-rich phase. The interphase is clear but reveals a very intimate contact between the phases, which probably stems from partial miscibility. At higher magnification (Figure 9.35b), the MWCNTs can clearly be seen in the PC-rich phase (the one with the higher amount of nanotubes). However, in addition, some nanotubes can be observed crossing the interface from the PC-rich phase to the PCL-rich phase (see Figure 9.35b). Figure 9.35c shows that the MWCNTs are well dispersed within the PC-rich phase.[8]

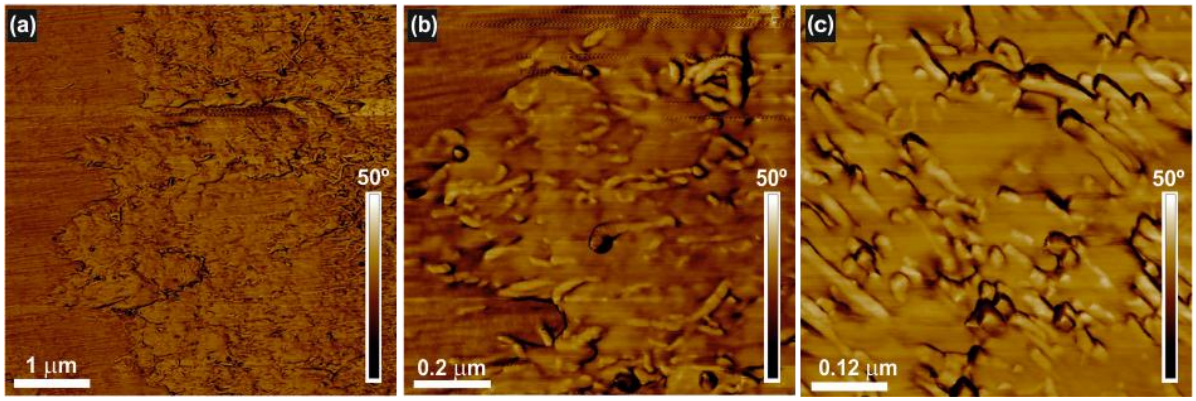

Figure 9.35. (a) Low and (b,c) high magnification AFM phase images for the 73/(23/4) *w*/*w* PCL/(PC/MWCNT) nanocomposite.

Self-nucleation (SN) experiments

Figure 9.36 shows the experimental data obtained during an SN experiment for neat PBS. The cooling scans after the isothermal step at T_s are presented in Figure 9.36a, and the subsequent heating scans are shown in Figure 9.36b. For the description of the different domains, see the Chapter II. General Concepts.

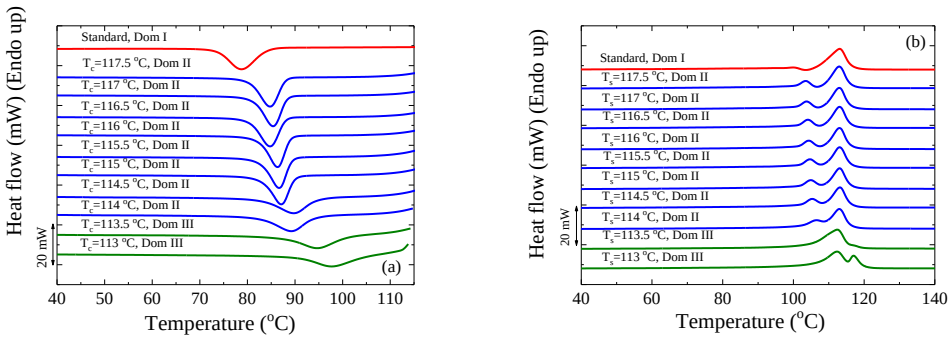

Figure 9.36.(a) DSC cooling scans for neat PBS after 5 min at the indicated T_s, and (b) subsequent heating scans after the cooling runs shown in (a).

Since 114 °C is the lowest T_s value in *Domain II*, it is called the ideal self-nucleation temperature, because it is the temperature in which there is maximum self-nucleation without any annealing. Employing the ideal T_s (114 °C), the T_c corresponding to the ideal T_s should be used as the maximum crystallization temperature ($T_{c,max}$) when determining the nucleation efficiency of the nanofiller. For the PBS used in this study, $T_{c,max}$ is 89.3 °C.

Avrami Fit

Table 9.13 shows the parameters obtained from the Avrami Fit for PCL-based blends.

Table 9.13. Kinetic parameters for all the investigated samples during isothermal crystallization.

PCL/(PC/MWCNTs) Sample	T_c [°C]	$t_{o\,[}$min]	ΔH [J.g^{-1}]	V_c range [%]	n	K [min^{-n}]	R^2	$\tau_{50\%\ Theo}$ [min]	$\tau_{50\%\ Exp}$ [min]	$(\tau_{50\%\ Exp})^{-1}$ [min^{-1}]	X_c [%]
100/0 w/w	41.0	0.35	52	3-20	2.5	8.21E-01	0.9998	0.93	0.90	1.1111	38
	42.0	0.52	53	3-20	2.5	3.86E-01	0.9999	1.26	1.22	0.8217	39
	43.0	0.50	54	3-20	2.6	1.77E-01	0.9999	1.68	1.63	0.6124	40
	44.0	0.67	55	3-20	2.6	8.13E-02	0.9999	2.25	2.20	0.4545	40
	45.0	1.03	56	3-20	2.7	3.20E-02	1.0000	3.09	3.03	0.3297	41
	46.0	1.13	60	3-20	2.8	1.03E-02	1.0000	4.40	4.37	0.2290	44
	47.0	1.63	59	3-20	2.9	3.64E-03	1.0000	6.16	6.07	0.1648	43
	48.0	1.82	59	3-20	3.0	8.24E-04	0.9999	9.15	9.03	0.1107	43
	49.0	1.02	63	3-20	3.4	8.36E-05	0.9995	14.76	14.43	0.0693	46
	50.0	2.27	51	3-20	3.0	7.94E-05	0.9976	20.21	18.87	0.0530	38
97/(2.5/05) w/w	42.0	0.35	45	3-20	2.6	2.86E+00	1.0000	0.58	0.62	1.6207	34
	43.0	0.47	48	3-20	3.0	1.14E+00	0.9998	0.85	0.90	1.1111	36
	44.0	0.43	52	3-20	3.1	3.95E-01	1.0000	1.20	1.27	0.7893	39
	45.0	0.67	52	3-20	2.8	1.89E-01	1.0000	1.59	1.63	0.6124	39
	46.0	0.67	55	3-20	3.3	3.62E-02	1.0000	2.44	2.53	0.3948	42
	47.0	1.46	51	3-20	2.7	3.79E-02	1.0000	2.97	2.98	0.3352	39
	48.0	2.25	51	3-20	2.7	1.50E-02	0.9999	4.22	4.18	0.2391	39
	49.0	3.10	52	3-20	2.7	5.04E-03	1.0000	6.15	6.10	0.1639	39
	50.0	4.63	56	3-20	2.8	1.39E-03	1.0000	9.35	9.40	0.1064	42
	51.0	5.67	57	3-20	3.1	1.54E-04	1.0000	15.45	15.58	0.0642	43
93/(6/1) w/w	44.0	0.32	50	3-20	3.3	2.07E+00	0.9998	0.72	0.72	1.3947	40
	45.0	0.50	52	3-20	3.5	6.30E-01	0.9998	1.03	1.03	0.9681	41
	46.0	0.53	50	3-20	3.6	2.02E-01	0.9999	1.42	1.42	0.7057	40
	47.0	0.77	50	3-20	3.5	5.81E-02	0.9999	2.01	2.02	0.4958	40

	48.0	0.95	51	3-20	3.8	9.17E-03	0.9999	3.11	3.13	0.3192	40
	49.0	1.48	53	3-20	3.5	3.20E-03	0.9995	4.71	4.65	0.2151	42
	50.0	1.92	55	3-20	4.0	2.19E-04	0.9999	7.65	7.72	0.1296	43
	51.0	3.68	47	3-20	3.8	7.89E-05	1.0000	10.77	10.85	0.0922	37
	52.0	2.53	47	3-20	3.6	1.23E-05	0.9959	21.82	20.35	0.0491	37
	53.0	14.85	30	3-20	3.1	5.35E-05	0.9997	20.34	19.70	0.0508	24
87/(11/2) w/w	45.0	0.33	43	3-20	3.4	2.63E+00	0.9999	0.68	0.68	1.4641	36
	46.0	0.57	43	3-20	3.3	8.52E-01	0.9999	0.94	0.93	1.0718	36
	47.0	0.67	43	3-20	3.2	3.10E-01	0.9998	1.29	1.27	0.7893	36
	48.0	0.90	45	3-20	3.2	8.34E-02	0.9998	1.92	1.90	0.5263	38
	49.0	0.80	47	3-20	4.1	4.93E-03	1.0000	3.30	3.35	0.2985	40
	50.0	1.98	48	3-20	3.3	5.26E-03	0.9999	4.39	4.40	0.2273	41
	51.0	3.75	45	3-20	3.0	2.87E-03	0.9999	6.26	6.20	0.1613	38
	52.0	5.35	49	3-20	3.0	6.52E-04	0.9999	10.34	10.22	0.0979	41
	53.0	11.22	46	3-20	2.7	5.95E-04	1.0000	14.13	14.08	0.0710	39
	54.0	20.92	44	3-20	2.7	1.96E-04	0.9996	20.38	21.63	0.0462	37
73/(23/4) w/w	46.0	0.28	30	3-20%	3.1	5.40E+00	1.0000	0.52	0.53	1.8762	30
	47.0	0.43	31	3-20%	3.5	1.93E+00	1.0000	0.75	0.77	1.3038	31
	48.0	0.47	33	3-20%	3.3	6.03E-01	0.9999	1.04	1.07	0.9372	33
	49.0	0.55	33	3-20%	3.7	1.21E-01	0.9999	1.61	1.63	0.6124	33
	50.0	0.85	35	3-20%	3.5	3.27E-02	0.9996	2.42	2.40	0.4167	35
	51.0	1.52	36	3-20%	3.5	8.79E-03	1.0000	3.54	3.58	0.2791	36
	52.0	2.20	37	3-20%	3.9	7.41E-04	1.0000	5.81	5.97	0.1676	37
	53.0	5.25	29	3-20%	2.9	2.22E-03	0.9996	7.50	7.23	0.1383	29
	54.0	9.62	24	3-20%	3.1	4.73E-04	1.0000	10.86	10.77	0.0929	24

The kinetic parameters for all the investigated PBS-based samples are plotted in Figure 9.37 and tabulated in Table 9.14.

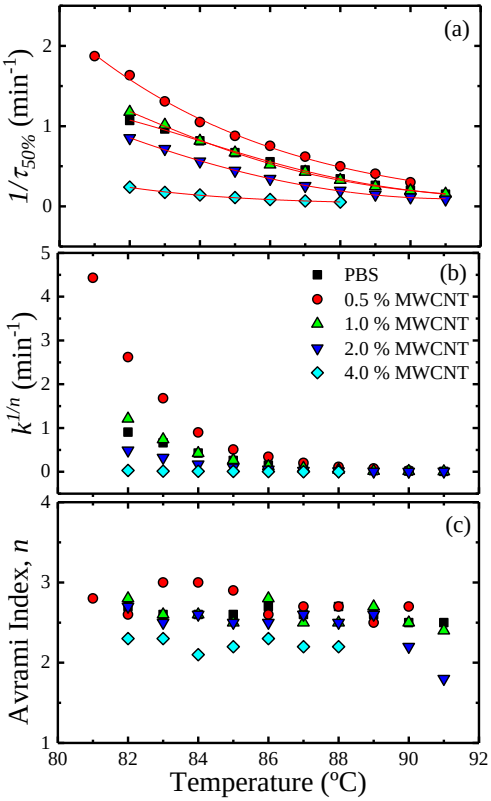

Figure 9.37. (a) Overall half-crystallization rate (the solid lines indicated the Lauritzen and Hoffman fitting); (b) Normalized crystallization constant of the Avrami model ($k^{1/n}$) and (c) Avrami index (n) as a function of the isothermal crystallization temperature (T_c) for all the samples.

Table 9.14. Kinetic parameters for all the investigated samples during isothermal crystallization.

PBS/(PC/MWCNTs) Sample	T_c [°C]	$t_{o\,I}$min]	ΔH [J.g^{-1}]	V_c range [%]	n	k [min^{-n}]	R^2	$\tau_{50\%\ Theo}$ [min]	$\tau_{50\%\ Exp}$ [min]	$(\tau_{50\%\ Exp})^{-1}$ [min^{-1}]
Neat PBS	82.0	1.46	30	3-20	2.7	9.05E-01	0.9999	0.91	0.94	1.0638
	83.0	1.58	33	3-20	2.6	6.62E-01	1.0000	1.02	1.04	0.9615
	84.0	1.62	37	3-20	2.6	4.27E-01	1.0000	1.20	1.22	0.8197
	85.0	1.68	40	3-20	2.6	2.57E-01	1.0000	1.46	1.50	0.6667
	86.0	1.72	41	3-20	2.7	1.49E-01	0.9999	1.76	1.80	0.5556
	87.0	1.84	49	3-20	2.6	9.19E-02	0.9999	2.16	2.21	0.4525
	88.0	1.89	53	3-20	2.7	4.17E-02	0.9998	2.81	2.92	0.3425
	89.0	1.99	57	3-20	2.6	2.23E-02	0.9999	3.76	3.84	0.2604
	90.0	2.13	61	3-20	2.5	1.24E-02	1.0000	4.97	5.00	0.2000
	91.0	2.18	64	3-20	2.5	6.19E-03	1.0000	6.58	6.63	0.1508
97/(2.5/0.5) w/w PBS/(PC/MWCNTs)	81.0	1.33	25	3-20	2.8	4.43E+00	1.0000	0.52	0.53	1.8868
	82.0	1.48	28	3-20	2.6	2.62E+00	1.0000	0.60	0.61	1.6393
	83.0	1.50	28	3-20	3.0	1.68E+00	0.9998	0.74	0.77	1.2987
	84.0	1.53	30	3-20	3.0	8.99E-01	0.9998	0.92	0.95	1.0526
	85.0	1.58	31	3-20	2.9	5.08E-01	0.9999	1.11	1.14	0.8772
	86.0	1.70	31	3-20	2.6	3.43E-01	1.0000	1.31	1.33	0.7519
	87.0	1.75	32	3-20	2.7	2.01E-01	1.0000	1.59	1.62	0.6173
	88.0	1.84	34	3-20	2.7	1.12E-01	0.9998	1.96	2.01	0.4975
	89.0	2.01	37	3-20	2.5	7.48E-02	1.0000	2.45	2.47	0.4049
	90.0	2.01	44	3-20	2.7	3.04E-02	0.9999	3.24	3.33	0.3003
93/(6/1) w/w PBS/(PC/MWCNTs)	82.0	1.51	19	3-20	2.8	1.21E+00	0.9999	0.82	0.85	1.1765
	83.0	1.70	19	3-20	2.6	7.40E-01	1.0000	0.98	0.99	1.0101
	84.0	1.79	21	3-20	2.6	4.23E-01	1.0000	1.21	1.22	0.8197
	85.0	1.92	22	3-20	2.5	2.63E-01	1.0000	1.47	1.50	0.6667

	86.0	1.94	22	3-20	2.8	1.24E-01	0.9996	1.84	1.92	0.5208
	87.0	2.11	24	3-20	2.5	8.65E-02	0.9999	2.28	2.33	0.4292
	88.0	2.21	27	3-20	2.5	4.35E-02	0.9999	2.97	3.04	0.3289
	89.0	2.28	17	3-20	2.7	1.81E-02	0.9997	3.86	4.01	0.2494
	90.0	2.60	30	3-20	2.5	1.25E-02	0.9999	4.93	5.05	0.1980
	91.0	2.98	31	3-20	2.4	7.87E-03	0.9999	6.27	6.40	0.1563
87/(11/2) w/w PBS/(PC/MWCNTs)	82.0	1.67	14	3-20	2.7	4.88E-01	0.9999	1.14	1.17	0.8547
	83.0	1.87	14	3-20	2.5	3.23E-01	0.9999	1.35	1.39	0.7194
	84.0	1.94	16	3-20	2.6	1.69E-01	0.9997	1.71	1.79	0.5587
	85.0	2.06	17	3-20	2.5	1.02E-01	0.9999	2.19	2.24	0.4464
	86.0	2.18	19	3-20	2.5	5.43E-02	0.9999	2.83	2.91	0.3436
	87.0	2.21	21	3-20	2.6	2.22E-02	0.9994	3.68	3.91	0.2558
	88.0	2.36	24	3-20	2.5	1.29E-02	0.9997	4.84	5.07	0.1972
	89.0	2.33	27	3-20	2.6	5.88E-03	0.9998	6.50	6.77	0.1477
	90.0	2.18	31	3-20	2.2	5.57E-03	0.9997	8.89	8.72	0.1147
	91.0	2.16	40	3-20	1.8	7.43E-03	0.9990	12.83	11.46	0.0873
73/(23/4) w/w PBS/(PC/MWCNTs)	82.0	2.30	30	3-20	2.3	2.99E-02	0.9998	4.00	4.18	0.2392
	83.0	2.43	36	3-20	2.3	1.47E-02	0.9998	5.48	5.73	0.1745
	84.0	2.77	36	3-20	2.1	1.09E-02	1.0000	6.95	7.07	0.1414
	85.0	2.94	36	3-20	2.2	5.57E-03	1.0000	8.92	9.04	0.1106
	86.0	2.94	34	3-20	2.3	2.73E-03	1.0000	11.64	11.71	0.0854
	87.0	3.32	33	3-20	2.2	1.64E-03	1.0000	14.96	14.84	0.0674
	88.0	3.59	27	3-20	2.2	1.05E-03	0.9999	19.84	18.48	0.0541

Table 9.15 and 9.16 shows the results obtained after applying the LH theory to PCL and PBS-based blends, respectively.

Table 9.15. Parameters for neat PCL. and the PCL/(PC/MWCNTs) nanocomposites

PCL/ (PC/MWCNTs)	K_g x 10^5	σ (erg/cm^2)	σ_e (erg/cm^2)	qx10^{-13} (erg)	T_m^o (ºC)	R^2
100/0	3.08	8.08	331.05	12.2	91.5	0.9915
97/(2.5/0.5)	1.11	8.08	124.44	4.59	75.4	0.9843
93/(6/1)	2.04	8.08	223.09	8.23	84.5	0.9941
87/(11/2)	1.47	8.08	163.29	6.03	80.5	0.9973
73/(23/4)	1.97	8.08	212.94	7.86	85.7	0.9947

Table 9.16. Parameters from the isothermal crystallization kinetics analyses for neat PBS and the PBS/(PC/MWCNTs) nanocomposites.

Sample	T_m^o (K)	K_g^{τ} x 10^4 (K^2)	σ (erg/cm^2)	σ_e (erg/cm^2)	q x 10^{-13} (erg)	R^2
100/0	394.0	8.16	8.08	81.13	2.99	0.9950
97/(2.5/0.5)	393.0	8.01	8.08	79.83	2.95	0.9975
93/(6/1)	392.1	7.91	8.08	79.04	2.92	0.9991
87/(11/2)	391.1	6.99	8.08	70.01	2.58	0.9868
73/(23/4)	389.1	6.79	8.08	68.32	2.52	0.9969

Tensile Properties of PBS-based blends

Figure 9.38 shows the stress-strain for PBS and its blends and Table 9.17 shows the testing tensile result for these samples.

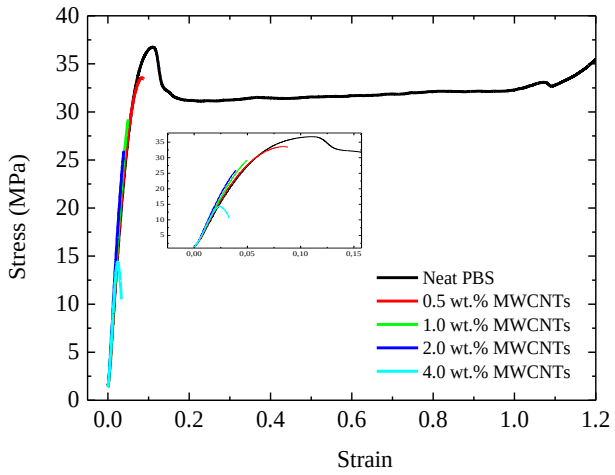

Figure 9.38. Stress-strain curves for neat PBS and the nanocomposites.

Table 9.17. Summary of tensile testing results for neat PBS and the nanocomposites.

w/w PBS/ (PC/MWCNTs)	σ_b (MPa)	ε_b (%)	E (MPa)
100/0	38.1 ± 2.1	210 ± 110	579 ± 139
97/(2.5/0.5)	28.3 ± 6.1	7.0 ± 2.9	641 ± 50
93/(6/1)	29.4 ± 0.5	5.0 ± 0.1	672 ± 44
87/(11/2)	26.0 ± 6.6	5.0 ± 1.0	715 ± 84
73/(23/4)	10.9 ± 0.6	4.0 ± 0.8	638 ± 79

σ_b – stress at break, ε_b – strain at break, E – Young's modulus

9.6 Appendix Chapter VIII.

Table 9.18 and 9.19 shows the Avrami Fit for Cyclic and linear PCL and their blends for average molecular weight of 3 and 12 kg/mol, respectively. [9]

Table 9.18. Parameters Obtained by Fitting the Avrami Theory to the 3kg/mol samples.

Sample	T_c (°C)	n	K x10^5 (min^{-n})	$K^{1/n}$x10^3 (min^{-1})	$\tau_{1/2t}$ (min)	$\tau_{1/2e}$ (min)	$1/\tau_{50\%}$ (min^{-1})	R^2
	45	3.6	20064	640	1.41	1.45	0.69	1.0000
	46	3.2	10307	492	1.81	1.83	0.55	1.0000
C–PCL 3k	47	3.4	2818	350	2.56	2.60	0.39	1.0000
	48	3.7	501	239	3.72	3.83	0.26	1.0000
	49	3.3	448	194	4.72	4.82	0.21	1.0000
	50	3.3	129	133	6.74	6.95	0.14	1.0000
	51	3.1	72	97	9.05	9.20	0.11	1.0000
	52	3.2	18	68	13.08	13.35	0.08	1.0000
	53	2.9	15	48	18.41	18.52	0.05	0.9999
	40	3.1	112843	1040	0.86	0.87	1.15	1.0000
	41	3.0	43520	758	1.17	1.17	0.86	0.9999
	42	3.2	13280	532	1.69	1.70	0.59	1.0000
C/L 95/5 3k	43	3.0	5644	384	2.30	2.28	0.44	0.9999
	44	3.0	2043	273	3.24	3.22	0.31	0.9999
	45	3.0	649	187	4.73	4.73	0.21	0.9999
	46	3.1	181	130	6.87	6.93	0.14	1.0000
	47	2.7	184	97	9.28	9.25	0.11	0.9999
	39	3.1	216424	1283	0.70	0.72	1.39	1.0000
	40	3.5	74904	921	0.98	1.02	0.98	1.0000
	41	3.3	31175	702	1.27	1.28	0.78	1.0000
C/L 90/10 3k	42	3.3	12744	536	1.67	1.68	0.59	1.0000
	43	3.5	3428	381	2.34	2.37	0.42	1.0000
	44	3.7	984	287	3.20	3.27	0.31	1.0000
	45	3.5	437	212	4.23	4.33	0.23	1.0000
	46	3.8	63	144	6.20	6.40	0.16	1.0000
	42	3.0	116916	1053	0.84	0.87	1.15	1.0000
	43	3.4	35200	736	1.22	1.28	0.78	1.0000
	44	3.4	11989	536	1.68	1.77	0.57	1.0000
C/L 80/20 3k	45	3.5	3281	377	2.38	2.50	0.40	1.0000
	46	3.5	1200	283	3.24	3.42	0.29	1.0000
	47	3.8	157	183	4.93	5.25	0.19	1.0000
	48	3.9	29	124	7.13	7.62	0.13	0.9999
	49	3.6	18	91	9.81	10.47	0.10	1.0000
	50	3.8	3	65	13.92	14.58	0.07	1.0000
	37	2.5	51106	765	1.13	1.22	0.82	0.9989
	38	2.2	23699	520	1.61	1.70	0.59	0.9995
	39	2.4	9735	379	2.30	2.45	0.41	0.9995
L–PCL 3k	40	2.4	4022	262	3.33	3.57	0.28	0.9996
	41	2.4	1429	170	5.02	5.42	0.18	0.9997
	42	2.4	570	116	7.25	7.82	0.13	0.9996
	43	2.4	236	80	11.18	12.03	0.08	0.9998

Table 9.19. Parameters Obtained by Fitting the Avrami Theory to 12 kg/mol samples.

Sample	T_c (°C)	n	K x10^5 (min^{-n})	$K^{1/n}$x10^3 (min^{-1})	$\tau_{1/2\,t}$ (min)	$\tau_{1/2e}$ (min)	$1/\tau_{50\%}$ (min^{-1})	R^2
	39	2.8	31986	666	1.32	1.35	0.74	1.0000
	40	3.0	14227	522	1.69	1.73	0.58	1.0000
	41	3.2	5862	412	2.19	2.25	0.44	1.0000
	42	3.2	2652	322	2.81	2.87	0.35	1.0000
C–PCL 12k	43	3.3	807	232	3.79	3.88	0.26	1.0000
	44	3.2	384	176	4.98	5.07	0.20	1.0000
	45	3.3	131	134	6.84	6.97	0.14	1.0000
	46	3.3	43	95	9.69	9.87	0.10	1.0000
	47	3.3	11	63	14.13	14.32	0.07	1.0000
	48	3.7	0.7	40	21.92	22.60	0.04	1.0000
	49	3.5	0.3	26	32.86	33.32	0.03	1.0000
	36	2.3	56892	783	1.09	1.05	0.95	0.9998
	37	2.3	30308	595	1.44	1.37	0.73	0.9998
	38	2.3	15475	444	1.91	1.83	0.55	0.9999

C/L 95/5 12k	39	2.3	8868	349	2.45	2.35	0.43	0.9999
	40	2.5	3448	260	3.33	3.27	0.31	1.0000
	41	2.5	1563	189	4.48	4.42	0.23	1.0000
	42	2.5	898	152	5.85	5.78	0.17	1.0000
	43	2.4	548	114	7.82	7.67	0.13	1.0000
	44	2.6	139	80	11.29	11.28	0.09	1.0000
	45	2.7	37	54	16.52	16.58	0.06	0.9999
C/L 90/10 12k	38	2.6	22017	559	1.57	1.53	0.65	1.0000
	39	2.5	13825	453	1.92	1.88	0.53	0.9999
	40	2.7	5467	341	2.56	2.55	0.39	1.0000
	41	2.8	2216	257	3.36	3.37	0.30	1.0000
	42	3.0	754	196	4.54	4.57	0.22	1.0000
	43	3.2	201	144	6.27	6.35	0.16	1.0000
	44	3.2	67	102	8.67	8.77	0.11	1.0000
	45	3.3	15	69	12.48	12.65	0.08	1.0000
	46	2.4	12	23	13.68	13.48	0.07	0.9998
C/L 80/20 12k	38	2.6	81841	926	0.94	0.95	1.05	1.0000
	39	3.0	32872	690	1.28	1.32	0.76	1.0000
	40	3.1	13406	523	1.69	1.75	0.57	1.0000
	41	3.4	4342	397	2.27	2.33	0.43	1.0000
	42	3.4	1598	296	3.00	3.07	0.33	1.0000
	43	3.3	704	223	3.98	4.05	0.25	1.0000
	44	3.5	166	161	5.60	5.70	0.18	1.0000
	45	3.8	25	113	8.10	8.30	0.12	1.0000
L–PCL 12k	37	2.3	15450	444	1.90	1.87	0.54	0.9999
	38	2.4	6806	326	2.61	2.58	0.39	0.9999
	39	2.4	3289	241	3.52	3.50	0.29	1.0000
	40	2.3	2052	185	4.54	4.50	0.22	1.0000
	41	2.5	735	140	6.19	6.20	0.16	1.0000
	42	2.4	411	101	8.25	8.30	0.12	1.0000
	43	2.4	221	78	11.03	11.13	0.09	1.0000
	44	2.3	128	55	15.38	15.43	0.07	1.0000

Lauritzen and Hoffman Fit

This Origin® plugin can be used not only to perform Avrami Fits but also to perform the Lauritzen–Hoffman Crystallization Fits. The parameters obtained from the LH theory are shown in Table 9.20 for cyclic, linear and C/L blends of both molecular weights (3 and 12 kg/mol).

Table 9. 20. Parameters Obtained from Fitting the Lauritzen and Hoffman Theory.

Sample	K_g^T (K^2)	σ_e (erg/cm^2)	R^2
C–PCL 3k	236319	254	0.99681
C/L 3k 95/5	329576	346	0.99711
C/L 3k 90/10	307817	315	0.99882
C/L 3k 80/20	297044	287	0.98808
L–PCL 3k	247079	274	0.99904
C–PCL 12k	298825	321	0.99904
C/L 12k 95/5	334344	351	0.99935
C/L 12k 90/10	307017	314	0.99434
C/L 12k 80/20	317940	310	0.99829
L–PCL 12k	186314	207	0.99439

Successive Self-Nucleation and Annealing (SSA)

The SSA experiments were performed with a fractionation windows of 3 ºC in 3 kg/mol sample, and the final DSC heating scan is show in Figure 9.39.

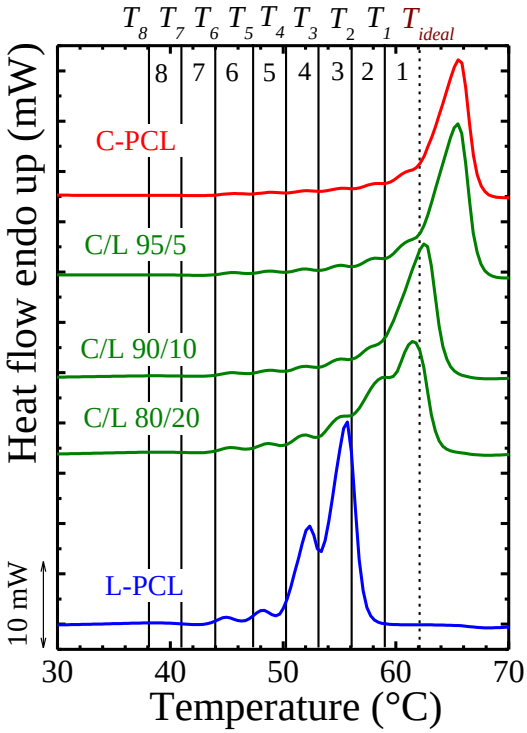

Figure 9.39. Final heating scan run after SSA thermal fractionation for C and L-PCLs and their C/L blends of 3kg/mol. The fractionation window was 3 ºC. Red and blue curves represent C-PCL and L-PCL, respectively, whereas green curves represent the C/L blends.

9.7 References

[1] T. Debuissy, P. Sangwan, E. Pollet, L. Avérous, Study on the structure-properties relationship of biodegradable and biobased aliphatic copolyesters based on 1,3-propanediol, 1,4-butanediol, succinic and adipic acids, Polymer 122 (2017) 105-116.
[2] T. Debuissy, E. Pollet, L. Avérous, Synthesis and characterization of fully biobased poly(propylene succinate-ran-propylene adipate). Analysis of the architecture-dependent physicochemical behavior, J. Polym. Sci., Part A: Polym. Chem. 55 (2017) 2738-2748.
[3] R.A. Pérez-Camargo, B. Fernández-d'Arlas, D. Cavallo, T. Debuissy, E. Pollet, L. Avérous, A.J. Müller, Tailoring the Structure, Morphology, and Crystallization of Isodimorphic Poly(butylene succinate-ran-butylene adipate) Random Copolymers by Changing Composition and Thermal History, Macromolecules 50 (2017) 597-608.
[4] R.A. Pérez–Camargo, G. Saenz, S. Laurichesse, M.T. Casas, J. Puiggalí, L. Avérous, A.J. Müller, Nucleation, Crystallization, and Thermal Fractionation of Poly (ε-Caprolactone)-Grafted-Lignin: Effects of Grafted Chains Length and Lignin Content, J. Polym. Sci., Part B: Polym. Phys. 53 (2015) 1736-1750.
[5] A. Kovalcik, R.A. Pérez-Camargo, C. Fürst, P. Kucharczyk, A.J. Müller, Nucleating efficiency and thermal stability of industrial non-purified lignins and ultrafine talc in poly(lactic acid) (PLA), Polym. Degrad. Stab. 142 (2017) 244-254.
[6] J.F. Vega, J. Fernández-Alcázar, J.V. López, R.M. Michell, R.A. Pérez-Camargo, B. Ruelle, J. Martínez-Salazar, M.L. Arnal, P. Dubois, A.J. Müller, Competition between supernucleation and plasticization in the crystallization and rheological behavior of PCL/CNT-based nanocomposites and nanohybrids, J. Polym. Sci., Part B: Polym. Phys. 55 (2017) 1310-1325.

[7] T. Gumede, A. Luyt, R. Pérez-Camargo, A. Tercjak, A. Müller, Morphology, Nucleation, and Isothermal Crystallization Kinetics of Poly(Butylene Succinate) Mixed with a Polycarbonate/MWCNT Masterbatch, Polymers 10 (2018) 424.
[8] T. Gumede, A. Luyt, M. Hassan, R. Pérez-Camargo, A. Tercjak, A. Müller, Morphology, Nucleation, and Isothermal Crystallization Kinetics of Poly(ε-caprolactone) Mixed with a Polycarbonate/MWCNTs Masterbatch, Polymers 9 (2017) 709.
[9] J.V. Lopez, R.A. Perez-Camargo, B. Zhang, S.M. Grayson, A.J. Muller, The influence of small amounts of linear polycaprolactone chains on the crystallization of cyclic analogue molecules, RSC Advances 6 (2016) 48049-48063.

List of Related Publications

Pérez-Camargo, R.A.; Arandia, I.; Safari, M.; Cavallo, D.; Lotti, N.; Soccio, M.; Müller, A.J. Crystallization of isodimorphic aliphatic random copolyesters: pseudo-eutectic behavior and double-crystalline materials. *European Polymer Journal* (featured article, in press), **2018,** 101: 233-247

Pérez-Camargo, R.A.; Fernández-d´Arlas, B.; Cavallo, D.; Debuissy, T.; Pollet, E.; Avérous, L.; Müller, A.J. Tailoring the structure, morphology and crystallization of isodimorphic poly (butylene succinate-*ran*-butylene adipate) random copolymers by changing composition and thermal history. *Macromolecules*, **2017**, 50, 597-608.

Pérez-Camargo, R.A; d' Arcy, R.; Iturrospe, A.; Arbe, A.; Tirelli, N.; Müller, A.J. The influence of chain primary structure and topology (branching) on crystallization and thermal properties; the case of polysulfides. *Macromolecules*, **2018** (in revision)

Kovalcik, A.; Pérez-Camargo, R.A.; Fürst, C.; Kucharczyk, P.; Müller, A.J. Nucleating efficiency and thermal stability of industrial non-purified lignins and ultrafine talc in poly (lactic acid) (PLA). *Polymer Degradation and Stability Testing*, **2017,** 142, 244-254

Pérez-Camargo, R.A.; Saenz, G.; Laurichesse, S. Avérous, L.; Casas, M.T.; Puiggalí, J.; Müller, A.J. Nucleation, Crystallization and Thermal Fractionation of Poly (ε-caprolactone)-Grafted-Lignin: Effects of Grafted Chains Length and Lignin Content. *Journal of Polymer Science, Part B: Polymer Physics*, **2015,** *53, 1736-1750.*

Gumede, T. P.; Luyt, A. S.; Pérez-Camargo, R.A.; Tercjak, A.; Müller, A.J. Morphology, nucleation and isothermal crystallization kinetics of poly (butylen succinate) mixed with polycarbonate/MWNCNT masterbatch. *Polymers*, **2018,** 10: 424.

Gumede, T. P.; Luyt, A.S.; Hassan, M. K.; Pérez-Camargo, R. A.; Müller, A. J. Morphology, nucleation and isothermal crystallization kinetics of poly (ε-caprolactone) mixed with polycarbonate/MWCNTs masterbatch. *Polymers*, **2017**, 9 (12): 709.

Vega, J.F.; Fernández-Alcázar, J.; López, J.V.; Michell, R.M.; Pérez-Camargo, R.A.; Ruelle, B.; Martínez-Salazar, J.; Arnal, M.L.; Dubois, Ph.; Müller, A.J. Competition between supernucleation and plasticization in the crystallization and rheological behaviour of PCL/CNT

based nanocomposites and nanohybrids. *Journal of Polymer Science, Part B: Polymer Physics*, **2017**, 55, 1310-1325

Pérez-Camargo, R.A.; Mugica, A.; Zubitur, M.; Müller, A.J. Crystallization of cyclic polymers. In *Polymer Crystallization I: From Chain Microstructure to Processing*, Auriemma, F.; Alfonso, G. C.; de Rosa, C., Eds., Springer International Publishing: Cham, **2017**; pp. 93-132.

López, J.V.; Pérez-Camargo, R.A.; Zhang, B.; Grayson, S.M.; Müller, A.J. The influence of small amounts of linear polycaprolactone chains on the crystallization of cyclic analogue molecules. *RSC Adv*. **2016**, 6, 48049-48063.

Müller, A.J.; Michell, R.M.; Pérez, R.A.; Lorenzo, A.T. Successive Self-nucleation and Annealing (SSA): Correct design of thermal protocol and applications. *European Polymer Journal*, **2015,** *65, 132-154.*

Other Publications from academic collaborations

Brüster, B.; Montesinos, A.; Reumaux, P.; Pérez-Camargo, R.A.; Mugica, A.; Zubitur, M.; Müller, A.J.; Dubois, Ph.; Addiego, F. Crystallization kinetics of polylactide: reactive plasticization and reprocessing effects. *Polymer Degradation and Stability*, **2018**, 148, 56-66.

Colonna, S.; Pérez-Camargo, R.A.; Chen, H.; Liu, G.; Wang, D.; Müller, A. J.; Saracco, G.; Fina, A. Super-nucleation and orientation of poly (butylene terephthalate) crystals in nanocomposites containing highly reduced graphene oxide. *Macromolecules*, **2017**, 50, 9380-9393.

Appiah, C.; Woltersdorf, G.; Pérez-Camargo, R.A.; Müller, A.J.; Binder, W.H. Crystallization behaviour of precision Polymers containing Azobenzenes defects. *European Polymer Journal*, **2017**, 97, 299-307.

Müller, A. J.; Pérez-Camargo, R.A.; López, J.V.; Grayson, S. Influencia de la topología de cadena (lineal versus cíclica) en la cristalización de policaprolactonas. *Revista Latinoamericana de Metalurgia y Materiales*, **2017**, S7, 3-7.

Gumede, T.P.; Luyt, A.S.; Pérez-Camargo, R.A.; Müller, A.J. The influence of paraffin wax addition on the isothermal crystallization of LLDPE. *Journal of Applied Polymer Science*, **2016**, 134, 44398.

Li, Z.; Wang, J.; Pérez-Camargo, R.A.; Müller, A.J.; Zhang, B.; Grayson, S.M.; Hu, W. Non-monotonic molecular weight dependence of crystallization rates of linear and cyclic poly (epsilon-caprolactone)s in a wide range. *Polymer International*, **2016**, 65, 1074-1079.

Gumede, T.P.; Luyt, A.S.; Pérez-Camargo, R.A.; Iturrospe, A.; Arbe, A.; Zubitur, M.; Mugica, A.; Müller, A.J. Plasticization and Cocrystallization in LLDPE/Wax Blends. *Journal of Polymer Science, Part B: Polymer Physics*, **2016**, 54, 1469-1482.

Wang, J.; Li, Z.; Pérez, R.A.; Müller, A.J.; Zhang, B.; Grayson, S.M.; Hu, W. Comparing crystallization rates between linear and cyclic poly (epsilon-caprolactones) via fast-scan chip-calorimeter measurements. *Polymer*, **2015**, *63*, *34-40*.